Author:
Mair, Chris R T

Title:
Stability Analysis of Whirl Flutter in Rotor-Nacelle Systems with Structural Nonlinearities

Stability Analysis of Whirl Flutter in Rotor-Nacelle Systems with Structural Nonlinearities

By

CHRISTOPHER R. T. MAIR

Department of Aerospace Engineering
UNIVERSITY OF BRISTOL

A thesis submitted to the University of Bristol
in accordance with the requirements of the degree of
DOCTOR OF PHILOSOPHY in the Faculty of Engineering

APRIL 2021

Word count: sixty-six thousand
Version: final/corrected

Abstract

Tiltrotor aircraft are steadily proliferating as the understanding of their design matures. Their large flight envelope is a combination of that of helicopters and that of turboprop aircraft, and as a result tiltrotors are highly attractive to both civilian and military operators. Ongoing improvements to their design include increasing their payload capacity and raising their cruising speed. However, addressing the latter is where whirl flutter is encountered. Whirl flutter is a destructive aeroelastic instability that becomes active above a certain airspeed. Occurrences have shown that it is able to destroy aircraft structures rapidly. In making tiltrotors go faster, tackling whirl flutter is unavoidable.

A substantial amount of research into whirl flutter has been conducted, using mathematical models sometimes validated by wind tunnel testing. However in deriving these models, some of the necessary simplifying assumptions might be faulty, preventing prediction of important results. Particular examples of such simplifications are using linear expressions in parts of the model where nonlinear expressions would be more accurate, or predicting the whirl flutter onset using stability analyses that are incompatible with the nonlinearities or their effects. It is these two examples, and their resulting impacts on whirl flutter, on which this work focuses.

This work uses two whirl flutter models to investigate the effects of two structural nonlinearities on the models' whirl flutter stability, a novel piece of work within the tiltrotor aeroelasticity field. The models are contrasting in complexity, covering (1) classical whirl flutter and (2) tiltrotor aeroelasticity, the latter being more complex. The two structural nonlinearities reflect features of real-world systems that might otherwise be overlooked. They are (1) a smooth, low-order polynomial stiffness representation, and (2) a quasi-nonsmooth freeplay nonlinearity. In this way, the effects of both model complexity and nonlinearity type may be understood. Continuation and Bifurcation Methods (CBM) are used to detect and quantify the new behaviours caused by the nonlinearities. Stability boundaries are used to summarise the changes compared to the linear versions of the models.

Both nonlinearities have a significant impact on the whirl flutter characteristics of both systems, leading to the creation of several whirl flutter solution branches. Some of these whirl flutter solution branches expand the parameter regions over which whirl flutter is possible, causing whirl flutter to be possible at higher structural stiffness values and at lower airspeeds than the predictions given by linear analysis for each model. In the more complex tiltrotor-specific model, some especially rich dynamics are predicted, including quasi-periodic and even chaotic behaviours.

Dedication and acknowledgements

To my grandparents:
Wanda Jędrzejkowska i Kazimierz Jędrzejkowski, Marion and Douglas Mair

Thanks are first due to my knowledgeable and friendly supervisors, Dr. Djamel Rezgui and Dr. Branislav Titurus. Their expertise has guaranteed the success of several manuscripts, and above all else they have made the last four years greatly enjoyable. I also thank all my family and friends for their invaluable support of many kinds, from enjoying this beautiful city with me to simply reminding me that life isn't all about work.

This research was only possible due to the Engineering and Physical Sciences Research Council (EPSRC), whose funding has allowed my continued existence.

Post-viva addendum: I also extend hearty thanks to my examiners Prof. Mark Lowenberg and Dr. Alex Shaw for such an enjoyable viva. It is always an honour and a pleasure to discuss one's work with experts.

Author's declaration

I declare that the work in this dissertation was carried out in accordance with the requirements of the University's Regulations and Code of Practice for Research Degree Programmes and that it has not been submitted for any other academic award. Except where indicated by specific reference in the text, the work is the candidate's own work. Work done in collaboration with, or with the assistance of, others, is indicated as such. Any views expressed in the dissertation are those of the author.

EXAM COPY SIGNED: .... DATE: ....

CORRECTIONS SIGNED: .... DATE: ....

Table of Contents

List of Tables

List of Figures

Figure **Page**

NOMENCLATURE

Symbol	Description	Unit
A_i, A_i'	Aerodynamic integrals (basic model)	-
C_p	Wing torsional damping (gimballed hub model)	$N.m.s.rad^{-1}$
C_{pq}^*	Normalised thrust contribution to pylon torsion due to flapwise bending (gimballed hub model)	-
C_ψ	Structural yaw damping (basic model)	$N.m.s.rad^{-1}$
C_{q1}	Wing beamwise damping (gimballed hub model)	N.m.s
C_{q2}	Wing chordwise damping (gimballed hub model)	N.m.s
C_θ	Structural pitch damping (basic model)	$N.m.s.rad^{-1}$
H	Vertical force (gimballed hub model)	N
$I_{P_x}^*$	Normalised pylon yaw moment of inertia (gimballed hub model)	-
$I_{P_y}^*$	Normalised pylon pitch moment of inertia (gimballed hub model)	-
I_b	Blade moment of inertia (gimballed hub model)	$kg.m^2$
I_β^*	Normalised blade cyclic flapping inertia (gimballed hub model)	-
$I_{\beta_0}^*$	Normalised blade collective flapping inertia (gimballed hub model)	-
I_n	Nacelle moment of inertia (basic model)	$kg.m^2$
$I_{p_w}^*$	Normalised wing torsion generalised mass (gimballed hub model)	-
$I_{q_w}^*$	Normalised wing bending generalised mass (gimballed hub model)	-
I_x	Rotor moment of inertia (basic model)	$kg.m^2$
I_ζ^*	Normalised blade cyclic lead-lag inertia (gimballed hub model)	-
$I_{\zeta_0}^*$	Normalised blade collective lead-lag inertia (gimballed hub model)	-
K_1	Linear pitch stiffness (basic model)	$N.m.rad^{-1}$
K_2	Cubic pitch stiffness (basic model)	$N.m.rad^{-3}$

Symbol	**Description**	**Unit**
K_3	Quintic pitch stiffness (basic model)	N.m.rad^{-5}
K_a	Consolidation of terms: $K_a = \frac{1}{2}\rho c_{l\alpha} R^4 \Omega^2$ (basic model)	N.m
$K_{\beta 1}$	Linear blade flap stiffness (gimballed hub model)	rad^{-1}
K_{β_2}	Cubic blade flap stiffness (gimballed hub model)	rad^{-3}
$K_{\beta 3}$	Quintic blade flap stiffness (gimballed hub model)	rad^{-5}
K_p	Wing torsional stiffness (gimballed hub model)	N.m.rad^{-1}
K_ψ	Structural yaw stiffness (basic model)	N.m.rad^{-1}
K_{q1}	Wing beamwise stiffness (gimballed hub model)	N.m
K_{q2}	Wing chordwise stiffness (gimballed hub model)	N.m^{-1}
K_θ	Structural pitch stiffness (basic model)	N.m.rad^{-1}
M_b^*	Normalised blade mass (gimballed hub model)	-
M_ψ	Aerodynamic yaw moment (basic model)	N.m
M_θ	Aerodynamic pitch moment (basic model)	N.m
N	Number of rotor blades comprising the rotor (both models)	-
R	Rotor radius (both models)	m
$S_{\beta_0}^*$	Normalised rotor coning inertial contribution to wing degrees of freedom (gimballed hub model)	-
S_w^*	Normalised wing bending-torsion inertial coupling (gimballed hub model)	-
S_ζ^*	Normalised rotor lead-lag inertial contribution to wing degrees of freedom (gimballed hub model)	-
T	Thrust force (gimballed hub model)	N
V	Airspeed/freestream velocity (both models)	m.s^{-1}
Y	Side force (gimballed hub model)	N
a	Ratio of pivot length to rotor radius (basic model)	m
c	Rotor blade chord (both models)	m
c_{l_α}	Blade 2D lift slope (both models)	rad^{-1}
c_w	Wing chord (gimballed hub model)	m
d	Freeplay deadband half-width (both models)	rad
g_{s_β}	Blade cyclic flapping structural damping ratio (gimballed hub model)	-
$g_{s_{\beta_0}}$	Blade collective flapping structural damping ratio (gimballed hub model)	-
g_{s_ζ}	Blade cyclic lead-lag structural damping ratio (gimballed hub model)	-

Symbol	Description	Unit
$g_{s_{\zeta_0}}$	Blade collective lead-lag structural damping ratio (gimballed hub model)	-
h	Shaft length (gimballed hub model)	m
m_P^*	Normalised pylon mass (gimballed hub model)	-
p	Wing torsion (gimballed hub model)	rad
q_1	Wing beamwise bending, normalised by y_{T_w} (gimballed hub model)	-
q_2	Wing chordwise bending, normalised by y_{T_w} (gimballed hub model)	-
t	Time	s
y_{T_w}	Wing span (gimballed hub model)	m
Ω	Rotor angular velocity (both models)	rad.s^{-1}
β_0	Rotor coning (gimballed hub model)	deg
β_{1C}	Gimbal pitch (gimballed hub model)	deg
β_{1C}	Gimbal yaw (gimballed hub model)	deg
β_m	Flapping angle of the m^{th} blade (gimballed hub model)	rad
ϵ	Freeplay deadband edge sharpness (both models)	rad
γ	Lock number $\gamma = \frac{\rho acR^4}{I_b}$ (gimballed hub model)	-
μ	Advance ratio $\mu = \frac{V}{\Omega R}$ (both models)	-
ν_β^*	Per-rev blade cyclic flapping natural frequency (gimballed hub model)	-
$\nu_{\beta_0}^*$	Per-rev blade collective flapping natural frequency (gimballed hub model)	-
ν_ζ^*	Per-rev blade cyclic lead-lag natural frequency (gimballed hub model)	-
$\nu_{\zeta_0}^*$	Per-rev blade collective lead-lag natural frequency (gimballed hub model)	-
ω	Modal undamped natural frequency	rad.s^{-1}
ψ	Yaw (basic model)	deg
ψ_m	Azimuth angle of the m^{th} blade (gimballed hub model)	rad
ρ	Air density (both models)	kg.m^{-3}
θ	Pitch (basic model)	deg
ζ	Modal damping ratio	-
ζ_0	Rotor collective lead-lag (gimballed hub model)	deg
ζ_{1C}	Rotor transverse CG position (gimballed hub model)	m
ζ_{1S}	Rotor vertical CG position (gimballed hub model)	m

Symbol	Description	Unit
ζ_m	Lead-lag angle of the m^{th} blade (gimballed hub model)	rad
$\mathbf{C}$	Damping matrix	
$\mathbf{J}$	Jacobian matrix	
$\mathbf{K}$	Stiffness matrix	
$\mathbf{M}$	Mass matrix	
$\mathbf{x}$	Vector of degrees of freedom	
$\mathbf{y}$	State vector	

Chapter 1

Introduction

1.1 Research Background and Motivation

1.1.1 Overview of tiltrotors

Tiltrotor aircraft such as those shown in Figures 1.1 to 1.4 are steadily proliferating. They are a particular type of fixed wing aircraft powered by rotors that may be tilted by the pilot so as to vector the thrust they produce. Their flight envelope is a combination of that of helicopters and that of turboprop aircraft, having both the VTOL[1] capabilities of the former and the range and speed of the latter. This large envelope provides great flexibility that is highly attractive to both military and civilian operators. In a military context this flexibility provides significant lifting agility to a fighting force, while in civilian usage tiltrotors offer a potential solution to the worldwide airport congestion problem. The names for the modes of operation are self-explanatory – "helicopter mode" and "airplane mode" – and the process of going from one mode to the other is known as transition/conversion.

Due to the engineering demands of realising the tiltrotor concept, most of the modern tiltrotor's ancestors did not fly, either failing to complete testing or to progress from the drawing board at all. The Weserflug P.1003 of 1938 was related to the tiltwing concept (described below) and contained a single engine within the fuselage. The Focke-Achgelis Fa 269 of 1941 had two rearward facing ("pusher") propellers that tilted downward, underneath the wing, when in helicopter mode. Although they resembled modern tiltrotors in several ways, neither managed to fly.

The first tiltrotor models to fly were the American company Transcendental's Model 1-G and

[1] VTOL: Vertical Take-Off and Landing.

(a) (b)

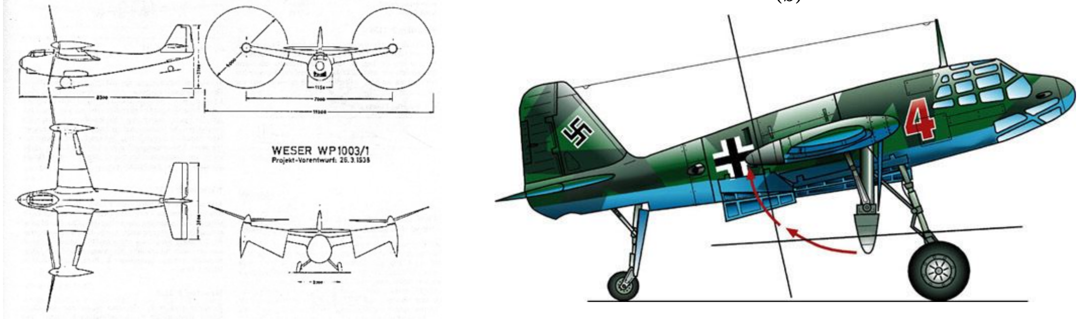

FIGURE 1.1. (a) Weserflug P.1003[2] (b) Focke-Achgelis Fa 269[3]

Model 2, shown in Figure 1.2. Starting work in 1945, the Model 1-G's first free flight was in 1954, though it did not manage to complete a full conversion cycle before the single prototype was destroyed in a crash in 1955. The Model 2 was larger, heavier and more powerful than the Model 1G, though little is known about the scope of its brief testing before the US Air Force's withdrawal of funding lead to its cancellation in 1957.

(a) (b)

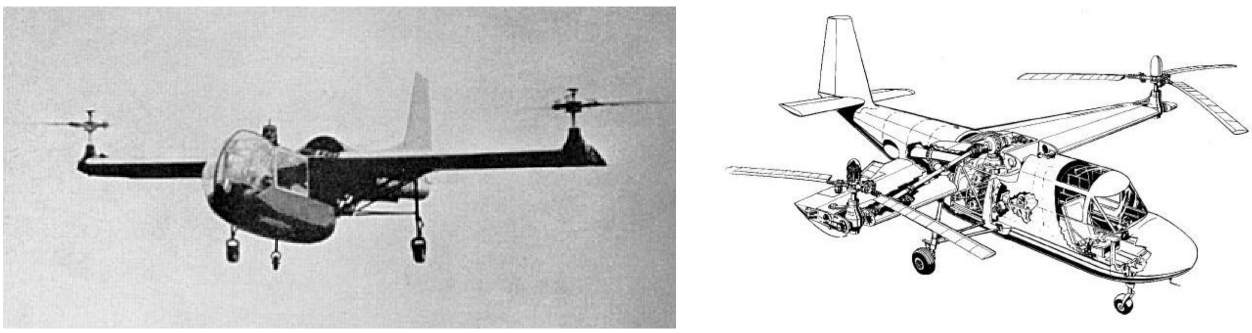

FIGURE 1.2. Transcendental tiltrotors: (a) Model 1-G[4] (b) Model 2[5]

The first truly successful tiltrotor model was the Bell XV-3 (see Figure 1.3, (a)), which flew from 1955 to 1966, achieving full conversions between airplane and helicopter modes. The modern era of tiltrotor design began with the Bell XV-15 (see Figure 1.3, (b)) in 1972, whose purpose was to ascertain what flight envelope could be expected from the tiltrotor configuration. A direct successor, the well-known Bell Boeing V-22 Osprey (see Figure 1.3, (c)) started development in 1981, building on the knowledge gained from the XV-3 and XV-15 programmes. It is the

[2] Dan Johnson **http://www.histaviation.com/Weserflug_P_1003_1_464x340.jpg**, creative commons

[3] Alchetron **https://alchetron.com/cdn/focke-achgelis-fa-269-4e2ec75c-e049-45c9-8267-247089324d9-resize-750.jpeg**, creative commons

[4] Aviastar **http://www.aviastar.org/foto/trans_1-g.jpg**, creative commons

[5] Stingray's List of Rotorcraft **https://sites.google.com/site/stingraysphotoarchive3/_/rsrc/1359519708865/page-two/Transcendental_Model-2.jpg**, creative commons

largest and most widespread operational production tiltrotor and is currently in service with the militaries of USA and Japan. Bell and Boeing collaborated in 1996 to produce a small tiltrotor aircraft of a similar size to the XV-15, though by 1998 Boeing had withdrawn from the venture and been replaced by then AgustaWestland, who took over full ownership of the project in 2011. The aircraft, known as the AW609 (see Figure 1.3, (d)), first flew in 2003 and remains in development. A comparison of the basic specifications of these flying tiltrotor models is given in Table 1.1.

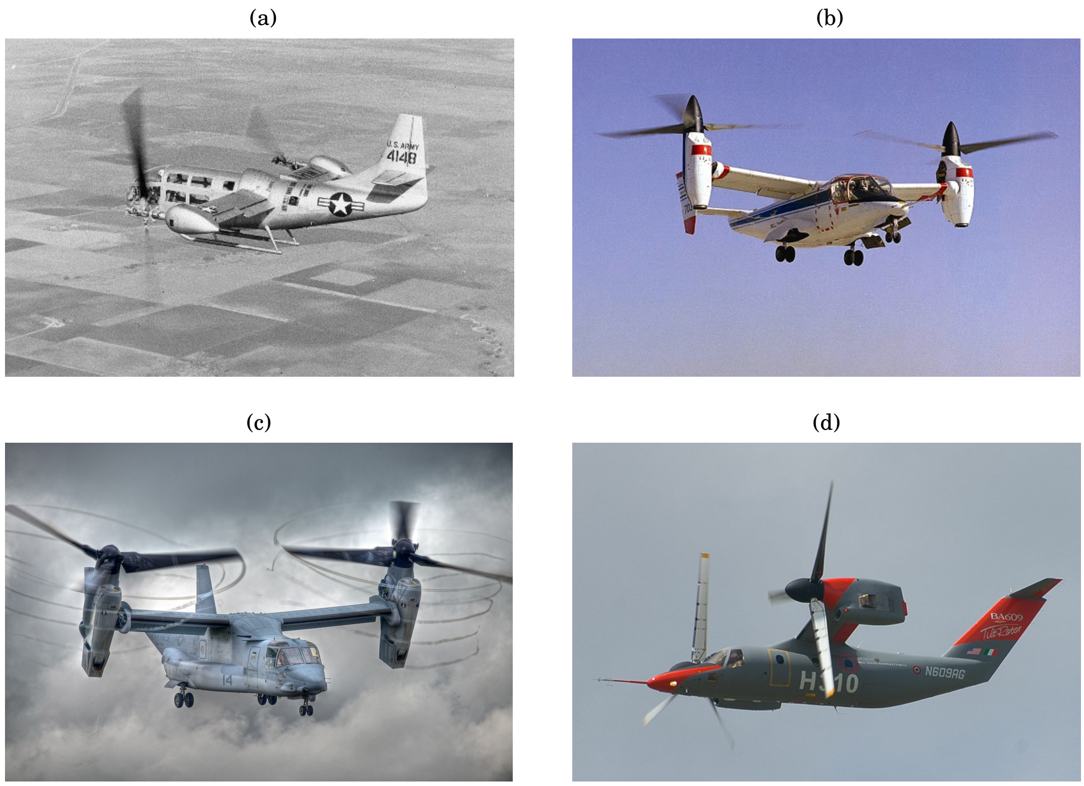

FIGURE 1.3. Examples of tiltrotor aircraft: (a) Bell XV-3[6], (b) Bell XV-15[7], (c) Bell Boeing V-22[8], (d) AgustaWestland AW609[9] (formerly Bell-Agusta BA609)

In the near future, Bell's V-280 Valor, shown in Figure 1.4, (a), is expected to enter service with the US military. Intended to provide troop insertion, the Valor is specifically designed for high manoeuvrability. A slightly further off development is Bell and Boeing's collaborative effort known as the Quad TiltRotor Concept (QTR) [1], shown in Figure 1.4, (b). The QTR is a large heavy-lift incarnation of the tiltrotor with an additional pair of tilting rotors added to the ends of a greatly enlarged horizontal stabiliser. The current design is the descendant of a series of projects starting in 1979 and is still in development. Tiltrotors of the more distant future are expected to

6 U.S. Army photo via San Diego Air & Space Museum, public domain.
7 NASA Photo ID EC80-75, public domain.
8 Peter Gronemann, creative commons licence.
9 Dmitry Mottl, public domain.

TABLE 1.1. Specifications of existing tiltrotor models

Model	First flight	MTOW (VTOL) [kg]	Maximum speed [kts]	Fuselage length [m]	Rotor radius [m]	Number produced[10]
XV-3	1955	1006	160	9.25	7.62	2
XV-15	1977	5897	332	12.83	7.60	2
V-22	1989	21546	305	17.48	12.00	400
AW609	2003	7620	275	13.4	7.90	2

include unmanned systems. Their development is already underway and their expected whirl flutter characteristics have been investigated by Floros et al. [2] and Shen [3].

(a) (b)

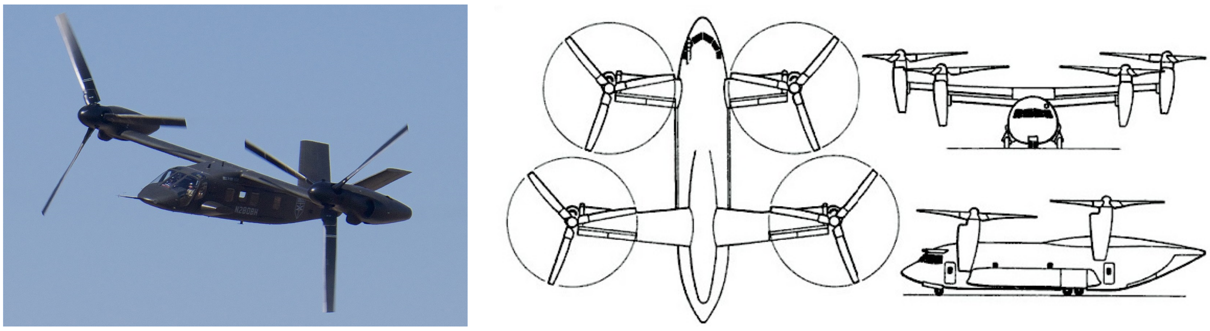

FIGURE 1.4. (a) Bell V-280 Valor[11] (b) Bell Boeing Quad TiltRotor concept[12]

A relative of the tiltrotor configuration is the tiltwing configuration, where part or all of the wing structure is tilted instead of just the wingtip-mounted rotors. Tiltwings generally have smaller proprotors than tiltrotors, leading to higher disc loading. The most well-known example of the concept is the XC-142, shown in Figure 1.5. As any part of the wing that tilts with the rotors is always aligned with the airstream produced by the rotor thrust, the drag losses from the wing are less than in tiltrotors, whose rotors' thrust impinges directly on the top wing surface when in helicopter mode. However, tiltrotors are less susceptible to crosswinds in helicopter mode due to their smaller side area, and have a higher hover efficiency due to their lower disc loading. The two configurations are linked both historically and in ongoing design as some models blur the line between them.

[10] 400 V-22s had been manufactured at the time of writing, with production ongoing.
[11] Danazar, creative commons licence.
[12] Frank86, creative commons licence.

FIGURE 1.5. XC-142 tiltwing aircraft[13]

1.1.2 Overview of whirl flutter

Like any other technology, there is an interest in tiltrotors' continued improvement. In addition to ubiquitous efforts such as "greener" performance, there is also particular interest in increasing their productivity, which is traditionally defined as the product of cruising speed and payload capacity. However, addressing the former is where the phenomenon known as whirl flutter is encountered.

Whirl flutter is an aeroelastic instability. Though it is sensitive to a number of parameters, a well-known mechanism through which it is activated is the exceeding of a certain onset airspeed. As such, it is regarded as an issue that affects the cruise flight regime. It comes about due to aerodynamic and gyroscopic forces acting on the rotor interacting with elastic structural modes of the rotor, nacelle and wing structure. Occurrences have shown that it is able to rapidly destroy aircraft structures. To make tiltrotors go faster is to tackle whirl flutter in a tiltrotor context: one of the designer's responsibilities is to predict the whirl flutter onset airspeed of a given tiltrotor. Whirl flutter limits the performance of tiltrotor aircraft, both directly through the need to stay beneath the onset airspeed, and indirectly through the aerodynamically-detrimental addition of stiffness (and therefore thickness) to the wing structure to guarantee aeroelastic stability up to the design speed [4]. As the literature survey in the following sections will show, a substantial amount of work has been devoted to finding design changes that raise the onset speed of whirl flutter, and similarly a great deal of literature exists on parametric sensitivity studies of whirl flutter. However, at the core of any whirl flutter research lies the need for an accurate way to predict the whirl flutter stability of a given system - which has also received dedicated research

[13] NASA, "Winds of Change, 75th Anniversary", public domain.

attention. The push for higher capacity tiltrotors only heightens the need for accurate prediction methods as the different technologies and materials that larger tiltrotors will likely need to employ may have different whirl flutter characteristics to current experience [5].

Accurate prediction of the onset speed is critical: under-prediction causes a waste of potential productivity, while over-prediction places the aircraft and those onboard at risk of loss. However, despite the fact that whirl flutter is in practice an intrinsically nonlinear phenomenon (see Section 1.1.4), much tiltrotor whirl flutter literature either lacks the use of nonlinear components, or uses stability analysis methods that are either not fully compatible with nonlinear influences or do not guarantee the discoverability of the solutions to nonlinear systems. Whirl flutter may still be predicted in these ways, though the accuracy of any predictions is endangered. This work investigates the impact of some structural nonlinearities on the whirl flutter characteristics of a typical tiltrotor rotor-nacelle system. The shortcomings of other modelling and/or analysis methods are shown by the mapping out of the parameter ranges in which whirl flutter behaviours are created. For brevity, the umbrella term "linear analysis" is used in this work to refer to both the use of linear models and the use of stability analysis methods that rely on linearisation. Chapter 2 provides an explanation of the process as well as why it is unsuitable for use with nonlinear systems.

1.1.3 Historical overview of whirl flutter

Although whirl flutter is now regarded as a serious aircraft design consideration, its path to appreciation has not been straightforward. Arguably it was discovered twice. It was first theorised by Taylor and Browne in 1938 [6] in research concerning the suppression of vibration caused by aircraft piston engines, although observation through experiment was not possible. Despite it remaining a theoretical construct at this stage, Wright Field personnel and some others made use of the suggested theory and instituted propeller whirl flutter calculation checks as a standard design practice for new aircraft [7]. However, the practice eventually fell out of use as only very large margins were ever found. That whirl flutter remained in the community's consciousness at least as late as 1950 is suggested by Scanlan and Truman's paper on the matter [8], however their model neglected aerodynamics, preventing any instability from being predicted and this likely denied whirl flutter any serious regard. Despite whirl flutter problems supposedly emerging in the test programme of the XV-3 [9, 10] tiltrotor (see Figure 1.3, (a)) as early as 1955, it was only after two disasters involving the Lockheed L-188 Electra aircraft (see Figure 1.6) in 1959 [11] and 1960 [12] that an earnest investigative effort was mounted. In both cases, whirl flutter had removed an entire wing from the airframe involved and all life onboard was lost.

NASA[14] was responsible for the official investigative response to the Electra disasters, with

[14] NASA: National Aeronautics and Space Administration. Founded in 1958 as a successor to NACA, the National Advisory Committee for Aeronautics, which had existed since 1915.

FIGURE 1.6. Lockheed L-188 Electra[15]. This particular aircraft (N121US) was the victim of the 1960 disaster, Northwest Flight 710

the NASA Langley site producing most of the research output throughout the 1960s. After it emerged that the Electra accidents quite possibly occurred due to structural damage weakening the engine mounts, official aircraft design regulations were updated accordingly in 1964 [13], decreeing that sufficient redundancy must exist in the engine support structure such that whirl flutter could not be possible following the failure of any single structural element. Whirl flutter has been a design consideration for aircraft with propellers and proprotors ever since, with supporting research conducted on a number of axes. Earlier work in the 60s and 70s tends to comprise parametric sensitivity studies, aiming to identify the parameters most influential in causing and sustaining whirl flutter. Later efforts tend to focus on finding design changes that raise the onset speed of whirl flutter. However, at the core of any research, regardless of the focus, lies the need for an accurate way to predict the whirl flutter stability of a given system. To this end, some research has been devoted purely to the development, validation and critique of whirl flutter prediction codes and mathematical methods, as will be summarised in Chapter 2. The complexity of analyses has also steadily increased, aided by digital computers, leading to the introduction and eventual widespread use of comprehensive analysis tools such as the CAMRAD family [14], which are commonly seen in contemporary research on the topic.

Whirl flutter remains a design consideration for turboprop aircraft [15] and similar configurations [16–18]. Its prevention remains a part of air regulations governing aircraft design [19]. It is the general consensus that whirl flutter was the cause of the loss of a Beechcraft 1990C twin-turboprop aircraft in 1991 [20–22], similar to the Electra disasters. Whirl flutter is even known to affect large wind turbines used for energy generation, requiring dedicated research [23, 24]. Where it does not immediately cause structural failure, it presents instead a fatigue

[15] Jeremy Carlisle (**https://jeremycarlisle.files.wordpress.com/2012/03/n121us-1.jpg**, creative commons)

hazard [25, 26].

1.1.4 Intrinsic nonlinearity

The observation of cases where the oscillation amplitude remained constant [27] implies that whirl flutter may exist as a limit cycle oscillation rather than just the "blow-up" of a linear system. Limit cycles are necessarily nonlinear phenomena, impossible in linear systems. Furthermore, tiltrotors – like any real world engineering system – are replete with sources of nonlinearity. Whirl flutter is therefore in practice a nonlinear phenomenon, which ideally should be studied with nonlinear models and stability analysis tools that are compatible with nonlinear systems. The important role of nonlinearities in aeroelasticity has long been appreciated: in 1955 Woolston et al. [28] investigated the impact of freeplay (then referred to as "flat spot"), hysteresis loop and cubic stiffness nonlinearities on the wing and control surface flutter onset speeds of a basic wing model, conducting a corresponding wind tunnel test with good agreement of results. The 1955 work was released as a technical report and was later followed by a journal paper in 1957 [29]. In both, the ability of nonlinearities to induce flutter below the linearly-predicted onset speed was clearly shown. However, despite the clear possibility that the same phenomenon could occur with whirl flutter in tiltrotor systems, many items of whirl flutter research neglect nonlinearities in their modelling for the sake of simplicity. Including nonlinearity represents adding complexity, which usually lengthens computation time and produces results that are more difficult to interpret. A key principle of modelling is balancing complexity with fidelity, including only elements that contribute meaningfully to a model's outputs. Despite this, the full role of nonlinearities in whirl flutter has been underestimated in much literature on the topic. Consideration of nonlinearities is vital for the complete description of whirl flutter, affecting both the size and nature of the whirl flutter solutions predicted and the parameter ranges in which they exist.

The forthcoming review of existing literature aims to explain simultaneously the history of tiltrotor whirl flutter study, the various avenues of investigation in which tiltrotor whirl flutter has been examined, and crucially, what methods have been used to assess tiltrotor whirl flutter stability. This will allow the shortcomings of these methods to be discussed, and in turn demonstrate the need for the present work. The categories of various themes and matters that constitute the field as a whole are listed in Table 1.2.

1.1.5 First era of whirl flutter study: classical theory

The earlier parametric studies chiefly employed a two-pronged approach comprising analytical models with corresponding wind tunnel testing to validate the predictions. An advantage of the parametric studies was that in addition to providing a way to understand whirl flutter, they also yielded the most efficient ways to avoid it as the sensitivity of each parameter was a direct

TABLE 1.2. Literature review categories

Theme	Sections
Methods for delaying whirl flutter onset	1.1.5, 1.1.6, 1.1.8
Improvements to the modelling description of whirl flutter	1.1.9, 1.1.16
Methods for predicting whirl flutter	1.1.3, 1.1.4, 1.1.10-13
Classical theory vs. tiltrotor-specific aeroelasticity	1.1.3, 1.1.4, 1.1.7
Presence and/or influence of nonlinearities	1.1.2, 1.1.15
CBM and the benefits it offers to the study of tiltrotor whirl flutter	1.1.17, 1.1.18

output. Reed and Bland's first work on the subject in 1961 [30] refers to whirl flutter as "propeller precession instability", and lays out the first iteration of what will become the canonical classical whirl flutter model. The paper is quite wide-ranging, investigating the effects of Mach number and location of the pitch and yaw axes among other parameters. The results are mainly presented as stability boundaries, indicating the relative influences of pairs of parameters. An example of such a stability boundary is shown in Figure 1.7, which is adapted from Figure 11 in [30]. The lines show what damping the wing and pylon structure must provide in the nacelle pitch degree of freedom in order to prevent whirl flutter, as a function of airspeed, thereby delineating the stable parameter-pair region (top left) from the unstable one (bottom right).

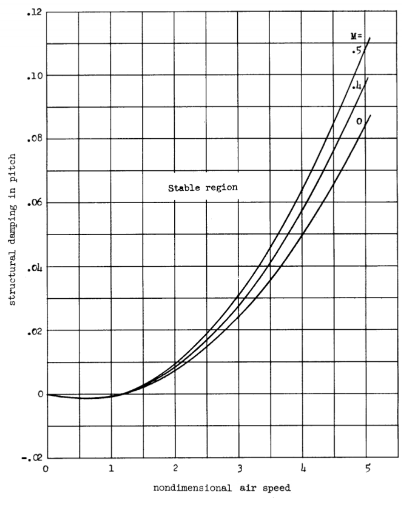

FIGURE 1.7. Stability boundary of structural pitch damping against nondimensional airspeed for a selection of three Mach numbers, adapted from [30]

The constant underprediction of the onset speed was noted as a limitation of the theory, and the discrepancy was attributed to the wing structure having some damping influence that was unmodelled by the theory. An early computer was also used to calculate some system responses in the time domain. The equations of motion were linear and thus simple eigenvalue analysis[16] was used to calculate the stability. Reed and Houbolt released their work to the wider aerospace community in 1962 [31]. Sewall [32] built on the results of [30] and [31] by extending the parameter ranges of analysis and adding further sweeps in parameters such as the ratio of the rotor's rotational moment of inertia to the nacelle's overall moment of inertia about the effective pitch point. In the same year, Zwaan and Bergh of the NLR[17] conducted an aeroelastic investigation that explicitly named the Electra aircraft as its focus [33]. Together, the aforementioned literature had assembled what is now known as **classical whirl flutter** theory. The defining features are the assumption of rigid proprotor blades and all motion of the system being expressed as pitching and yawing of the rotor shaft about an effective pivot point, at which the wing's properties are lumped.

Aware of the limitations of the classical whirl flutter theory, a number of institutions sought to augment the basic model with what they considered to be the most pressing omissions. Richardson and Naylor investigated the impact of hinged blades – as opposed to rigidly-attached ones as per the canonical theory – on whirl flutter in 1962 [34]. Bland and Bennett investigated the influence of the whole aircraft's static stability derivatives on whirl flutter stability in 1963 [35]. In the same year, Abbott et al. concluded an experimental investigation [36] which had used a "large dynamic-aeroelastic model of a four-engine turboprop transport airplane". Although neither the Electra aircraft nor the associated disasters were mentioned, the Figures of the wind tunnel rig show that the motivation of the report is nevertheless such. Ravera also investigated the effect of the blades' steady state angle of attack [37]. Bennett and Bland began to investigate the role of the wing in whirl flutter stability in their report of the following year [38], concluding it to be influential and mostly stabilising. Smith's 1966 computational-only investigation [39] added both nacelle flexibility and response of the wing to the basic whirl flutter formulation, noting the strong influence of damping on the onset speed, though interestingly the stabilising influence of the wing was less obvious and the main finding was that the wing flutter onset speed could be "reduced slightly by a coupling with an unstable power-plant whirl mode of comparable frequency". This first era of classical whirl flutter theory with minor extensions was largely bookended by Reed's summary reviews of 1965 [40] and 1967 [41], the latter of which explicitly noted that unequal values of pylon pitch and yaw stiffness could in some parameter configurations grant a greater stability margin than equal values.

[16] Eigenvalue analysis is a stability analysis tool comprising mathematical operations performed on the matrices that comprise the equations of motion, and its results are thereby a function of the parameter values in use and not the state vector. The operation finds the fixed point stability of the system and in the study of whirl flutter, the transition from stability to instability is taken as the whirl flutter onset point. It is described in more detail in Chapter 2.

[17] NLR: Nationaal Lucht- en Ruimtevaartlaboratorium (Dutch), Royal Netherlands Aerospace Centre (English). Formerly known as the National Aerospace Laboratory, the NLR is an aerospace research organisation in the Netherlands, founded in 1919.

1.1.6 Whirl flutter in tiltrotors

Soon after the Electra disasters it was recognised that other aircraft configurations could also be at risk. The search for feasible high-speed V/STOL[18] concepts had existed for some time and the tiltrotor configuration, now emerging, was a propitious lead to follow. However, with slender, flexible and highly twisted blades, and heavy engine nacelles mounted upon their wingtips to provide clearance of the blades from the fuselage, tiltrotors are prominently vulnerable to whirl flutter. They are not represented by the classical model, and the need to employ dedicated analyses when considering their aeroelastic properties was mentioned as early as 1962 [31], and formally examined in 1963 [7]. Previous studies of the dynamics of proprotors had only explored issues such as the destabilisation of aircraft rigid body modes due to blade flapping in high speed flight [42, 43]. Now however, the study of the aeroelastic stability of specifically proprotors – a byword at this time for tiltrotor configurations – was emerging as an area in its own right.

Motivated by the emergence of whirl flutter in the development of their XV-3 tiltrotor, the Bell Helicopter Company set forth an investigation specifically into tiltrotor whirl flutter in 1966 [44]. A work of some size, the research used wind tunnel and computational models of Bell's XV-3 aircraft, finding that "in-plane force[s] generated by blade flapping at high advance ratios" were the principal destabilising factor, and also provided an explanation of the physical origin of the instability. However, like all literature before it, a linear set of equations was used, which naturally was treated by eigenvalue analysis. Young conducted a computational study in 1967 [45] that centred on tuning the rotor's flapping stiffness to achieve optimal dynamic stability. Expressing the rotor blades' flapping stiffness in terms of the natural frequency of their flapping motion, the study advocated for a frequency around 1.1-1.2 per rev: a stiff[19] out-of-plane rotor. The whirl flutter onset speed was assessed using linear perturbations of the nonlinear equations of motion, and an energy-based approach was also used to assess the amplitudes of the LCOs (arising from the presence of nonlinearities) found to comprise the forward whirl mode, which transpired to be "self-limiting due to the non-linear aspects of the aerodynamic loads". The same phenomenon was not found in the backward whirl mode, nor was the forward whirl found to encroach meaningfully over the stability boundary predicted by eigenvalue analysis, i.e. existing at not much lower speeds than those predicted by eigenvalue analysis.

Edenborough from the Bell Helicopter Company released a 1968 report [27] on some wind tunnel testing that validated new whirl flutter stability theory that was under development, noting good agreement. The new theory in question had two components: a "linear closed-form analysis" which comprised a 4-DoF model to which linear eigenvalue analysis was applied, and a "digital open-form analysis" which numerically integrated the equations of motion in the

[18] V/STOL: Vertical and/or Short Take-Off and Landing.

[19] A rotor with a natural frequency above 1 per rotor revolution ("per rev") is known as "stiff", whereas one below 1 per rev is known as "soft". This terminology is applied to both the flapping/out-of-plane and lead-lag/in-plane motions.

time domain to produce time histories. The importance of the use of accurate parameter values in theoretical models was stressed. Work by Gaffey et al. in 1969 [46] used a combination of analytical and wind tunnel models of several tiltrotor configurations to show, among other things, the great influence of the relative placement of the wing and pylon[20] frequencies on the system's whirl flutter stability, echoing the work of Smith in 1966 [39]. DeLarm [47] addresses aeroelastic issues of both tiltrotor and tiltwing configurations in his paper dated the same year, providing analytical substantiation of some stability trends observed by Edenborough [27]. Although generic work on understanding proprotor aeroelasticity continued into the next decade [48, 49], by 1969 knowledge had matured sufficiently to allow summary works by Loewy [50] and Wernicke [51], which rounded up the key aspects and issues of the state of the art. However, they also made clear that linear approximations – both in the equations and the stability analysis methods – were very much still integral to the modus operandi of the various research projects involved, despite frequent acknowledgement of nonlinearities having a significant influence. For instance, Loewy states that "lag dampers frequently have non-linear characteristics", mentions "table look-up type procedures to allow for non-linear airfoil characteristics", says of helicopter rotor dynamics in general that "from the very earliest work...it has been clear that the governing equations are not of the linear, constant coefficient type", and mentions the observation of a "nonlinear, sub-harmonic flapping response".

1.1.7 Active control

A secondary outcome of Edenborough's 1968 research was the realisation that control coupling between the wing motion and the rotor swashplate could provide additional whirl flutter stability. Specifically, the active control could to a degree directly oppose any incipient whirl flutter motion and thereby raise the onset airspeed. The first tiltrotor application of active control however was gust alleviation through swashplate cyclic control, as detailed by Frick and Johnson in 1974 [52] and again by Johnson in 1977 [53]. The (uncontrolled) gust response of tiltrotors was also investigated, as shown in works such as that of Yasue in 1974 [54]. Although the primary motivation was the understanding of the loads generated, Yasue also demonstrated the strong influence that the choice of the mode shapes assumed in the model had on the reported damping ratios of the system, and consequently on the predicted stability boundaries. Curtiss in 1979 [55] investigated "single loop feedbacks of wing motion to cyclic pitch" and found them to "generally appear to stabilize one particular wing mode while destabilizing another". The maturation of the use of rotor cyclic control in this manner can be followed through Nasu (1986) [56], Vorwald et al. (1991) [57] and van Aken (1991) [58]. Nitzsche tried a different approach in 1994 [59], using instead the actuation of aerodynamic vanes which were to be installed on the engine nacelles. In contrast to rotor swashplate control, these vanes would allow the control of not just pylon

[20] The term "pylon" in this era of the literature refers collectively to the entire rotor-nacelle structure emanating from the wing, that is: the rotor, its nacelle along with structure connecting the nacelle to the wing, and the engine if the nacelle contained one.

bending but also pylon torsion, allowing a more specific targeting of individual wing modes. A further benefit of the approach was that it was also applicable to turboprops and propfans.

Hathaway and Gandhi [60] undertook a theoretical investigation into the use of flaperons for whirl flutter onset delay, finding that the additional damping provided to the wing beamwise[21] bending mode would be particularly useful for tiltrotors using soft in-plane rotors, which otherwise have inherently low damping in this mode. Paik et al. [61] added swashplate control in a subsequent, related investigation, finding that the flaperon control was very slightly more effective (90kts increase in flutter onset speed as opposed to 85kts). Other means of actuation were pursued in a resurgence of interest in the topic in the late 2010s: Richter et al. (2015) used trailing edge flaps [62], while Floros and Kang (2017) used wingtips [63].

Active control was also used for some related matters: although in-plane rotor loads play a large part in the instigation and sustenance of whirl flutter, their potential to exceed maximum allowable levels (as dictated by the materials comprising the rotor-nacelle system) was recognised in the development of the V-22, prompting research into the use of active control simply for their limitation. The most effective actuation method was deemed to be swashplate cyclic control, as detailed by Miller and Ham (1988) [64], Agnihotri et al. (1989) [65] and Miller et al. (1991) [66]. An example of corresponding work within European research is Manimala in 2004 [67]. A further application of active control in tiltrotors has been simply to improve the ride quality for those onboard, investigated by Bell in a series of wind tunnel tests. Settle in 1997 describes use of the wing flaperon [68], to which is later added higher harmonic control of the rotor swashplate, as described by Nixon in 1998 [69]. Reportedly, the aeroelastic stability was not compromised by the modifications, although pitch link loads increased 25% due to the swashplate control. Piatak reports further aeroelasticity results in 2001-2 [70, 71], noting that the use of R-134a heavy gas in wind tunnel testing to match the full-scale blade Mach number reveals current stability boundaries to be unconservative. Nguyen et al. produced a full-scale wind tunnel demonstration of the concept in 2001 [72]. Muro [73] later addressed the use of elevators, wing flaperons and the swashplate, although gust alleviation was the primary aim and aeroelastic stability was only checked after the fact rather than designed for.

1.1.8 Passive stabilisation

A contrasting philosophy of delaying the onset airspeed is the passive approach of building intrinsically stabilising features into the design. These features modify the aircraft's response in a manner that acts against physical drivers of the whirl flutter instability. Popelka et al. exploited the anisotropic properties of composite structures to create elastic couplings in a wing that were beneficial to whirl flutter stability [74, 75], a practice that is now known as "aeroelastic tailoring".

[21] Beamwise bending: up-down motion of the wingtip.

The studies found that influencing the wing torsion/bending coupling could improve the stability of one of the critical modes (symmetric[22] wing beamwise bending) but reduced the stability of the other (symmetric wing chordwise[23] bending), ultimately leading to limited gains due to the conflicting structural design requirements imposed by the two critical modes. The works were NASTRAN-based, with stability found by eigenvalue analysis performed by the ASAP code[24]. This work was followed up by a purely experimental segment of research by Corso et al. [76], which validated the linear damping predictions through measurements of the decay of various oscillations in the time domain. It was also suggested that such aeroelastic tailoring could be used to reduce wing thickness, recovering some of the aerodynamic efficiency lost due to aeroelastic stability requirements. Zhang et al. investigated the use of (uncontrolled) winglets and wing extensions using a finite element structural model coupled with a simple eigenvalue analysis code [77–79], achieving a 60-80kt increase in the whirl flutter onset airspeed of their model. A later analysis by the same group [80] used more sophisticated models though stability analysis was conducted through linearised equations.

Acree instead focused on modifications to the rotor, such as chordwise shifting of the blade section aerodynamic centre and adding tip masses and blade sweep [81–87]. Using models of the XV-15 and V-22 (see Figure 1.3), the impact on whirl flutter stability was assessed using modes of the linearised system. The conflict between whirl flutter stability and loads appears again in some of the research, and the sweeps of the aerodynamic centre suggest that the datum design point was selected based on loads minimisation rather than whirl flutter stability maximisation. These papers contrast with other blade optimisation papers that consider only the aerodynamics without examining the impact on whirl flutter stability, such as Liu and McVeigh's 1991 work [88]. Srinivas et. al investigated the introduction of favourable elastic couplings within the rotor blades, as well as aerodynamic refinements [89]. Soykasap et al. also investigated aeroelastic tailoring of the blades [90], though the focus was more on structural design methods. Barkai et al. developed a symbolically exact method [91] in 1998 which was also applied to the investigation of rotor blade and wing elastic couplings as a means of improving whirl flutter stability [92]. Nixon et al. added aeroelastic tailoring of the rotor blades to the wing tailoring undertaken by Popelka, once again using the linear eigenvalue analysis code "ASAP" in 2000 [93], which was supported in the same year by a wind tunnel test programme detailed by Corso et al. [94]. Singh and Chopra investigated whether the unique dynamic properties of a two-bladed proprotor could be beneficial for whirl flutter stability [95]. The results were mixed: the wing beamwise mode was found to be incapable of instability as a result, though a new wing torsion instability similar to divergence was observed.

[22] Symmetric: motion of one wing is mirrored by the other in phase. In anti-symmetric modes, the wings are in anti-phase, e.g. in anti-symmetric beamwise bending, when one wing is up, the other is down.

[23] Chordwise bending: forward-backward motion of the wingtip

[24] ASAP: Aeroelastic Stability Analysis of Proprotors. A proprietary code developed at the Bell Helicopter Company that describes itself as an "eigenvalue formulation".

The matter of preferential wing elastic couplings was revisited by Yang in 2011 [96], who used an adapted version of Johnson's 1974 model. Kim also investigated such wing couplings in 2012 [97]. Kambampati's 2015 investigation [98] into wing extensions and winglets for delaying the whirl flutter onset speed also conducted parametric sweeps in "stiffness, structural taper, composite couplings, winglet toe cant and sweep angles" about the modified design point. These parametric sweeps formed the basis of works employing optimisation methods that shortly followed [99, 100]. Muscarello later explored the optimisation of blade twist for the delay of whirl flutter onset [101]. In all cases, whirl flutter stability was determined through methods based on linear theory.

1.1.9 Soft in-plane rotors

Concerned about the weight of rotor systems used aboard tiltrotor aircraft, quite some research was dedicated to finding lighter alternatives. The use of a "soft in-plane" rotor – that is, a rotor with a lead-lag natural frequency below the rotor rotation frequency rather than above it ("stiff") – presented such an opportunity. Achieved by using a hingeless design, the concept was already in use on helicopters but Richardson's 1971 work on the concept [102] was dedicated to tiltrotors. The paper argues that the hingeless design offers the further benefits of greater reliability, less demanding maintainability and reduced drag. It focuses on optimising the design to maximise cruising efficiency and minimise loads, and does not discuss stability beyond showing the lag damping necessary to prevent ground resonance for a given lead-lag natural frequency. By 1972 Bell and Boeing had both began to develop their own tiltrotor models: while Bell's Model 300 kept a stiff in-plane gimballed[25] hub rotor design, Boeing's Model 222 used soft in-plane rotors and is described in Magee's large 1973 work [103] about wind tunnel testing thereof.

(a) (b)

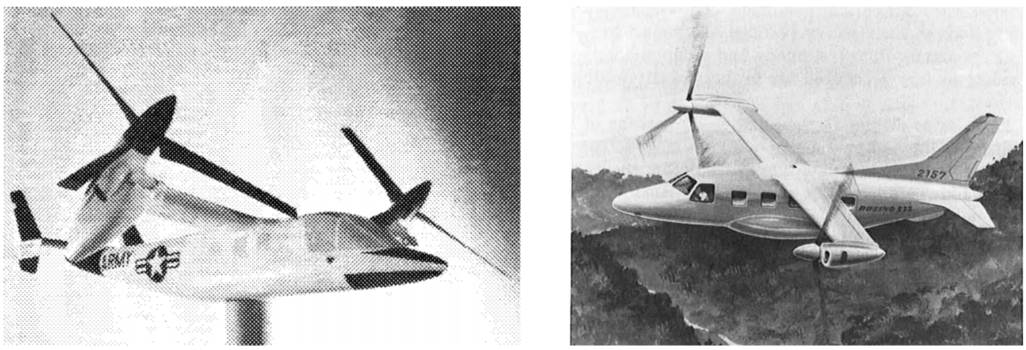

FIGURE 1.8. (a) Bell Model 300, taken from [104] (b) Boeing Model 222, taken from [105]

[25] In gimballed rotor hubs, the rotor may deflect relative to its driving shaft via elastic restraint provided at the connection point. They are described in more detail in Chapter 2.

In 1975, Alexander et al. [105] provided more work correlating wind tunnel aeroelasticity results with theoretical prediction methods being developed by Boeing. The paper also presents in complete detail the mathematical model being used, showing a reasonable collective understanding of the instability's components, such as the role of the wing, though linear eigenvalue analysis was used. Linear analysis was also used for Bell's venture: Edenborough [104] gives details of a Bell-proprietary 15-degree-of-freedom aeroelasticity code named DYN4, which again is underpinned by linear theory. Harendra's 1973 report [106] develops an aeromechanical model of the Model 301 (a relative of the Model 300) for the purpose of real-time simulation, though linear simplifications are used in the model to limit timesteps to 50ms and there is no mention of aeroelasticity being considered. Further details of the Bell Model 300 development tests were given by Wernicke in 1972 [107]. A more concrete explanation of the advantages and disadvantages of soft in-plane rotors was given by Ormiston in 1977 [108].

The use of soft in-plane rotors results in fairly significant changes to the rotor system's dynamic performance, however. Between the various works it is established that the softer in-plane rotor incurs lower loads (allowing the weight saving), at the price of less damping of the air resonance instability and the possibility of ground resonance. This forced designers of soft in-plane configurations to build in other sources of lead-lag damping. Whirl flutter airspeed boundaries were generally lower than equivalent stiff in-plane systems, though the lower loads allowed greater manoeuvring agility. Kloeppel [109] would later show that the cause of the adverse aeroelastic behaviour in the hingeless design was the pronounced inherent torsion-flap-lag coupling. In 2001, NASA and Bell showed renewed optimism in the soft in-plane proprotor design, using active control of the swashplate for stability augmentation. Formal development of the system, known as "Generalized[26] Predictive Control" (GPC), was initiated by Nixon et al. [110], who also noted that ground resonance behaviour for tiltrotors was "significantly different" to that for helicopters. Specifically, the participation of elastic wing modes in the instability makes it more complex in tiltrotors, and while ground resonance in helicopters may be obviated through appropriate design of the landing gear to supply the necessary damping, such adjustment of the tiltrotor's elastic wing modes is substantially more difficult. Gradual improvements to the soft in-plane concept were documented by Kvaternik et al. [111] and Nixon et al. [112].

1.1.10 The "stopped rotor" variant

The stopped rotor variant of tiltrotor attempted to design whirl flutter out of the tiltrotor configuration entirely. Investigated separately c. 1970 by Bell [113–115] and Boeing [116] (who called it the "folded rotor"), the principle was to obviate the issue of rotor-wing dynamical interaction at high speeds by folding the rotor blades away once airplane-mode flight had been achieved. “Convertible” engines that powered the proprotors during vertical operations then

[26] The US English spellings used in American works are retained here.

provided jet thrust for cruising. The transition process is illustrated in Figure 1.9, taken from [114]. Excessive blade flapping was discovered during rotor starting and stopping however, and combined with problems caused by shifting of the aerodynamic neutral point as flight conditions varied, further development of the concept was presumably not sufficiently attractive. A modern examination of the concept's aeroelastic stability was conducted in 2011 by Slaby and Smith [117], who concluded that a forward-swept wing was required for the concept to work. An imaginative extension of this novel concept was the addition of a "joined wing" (also known as a box wing), examined by Wolkovitch et al. in 1989 [118].

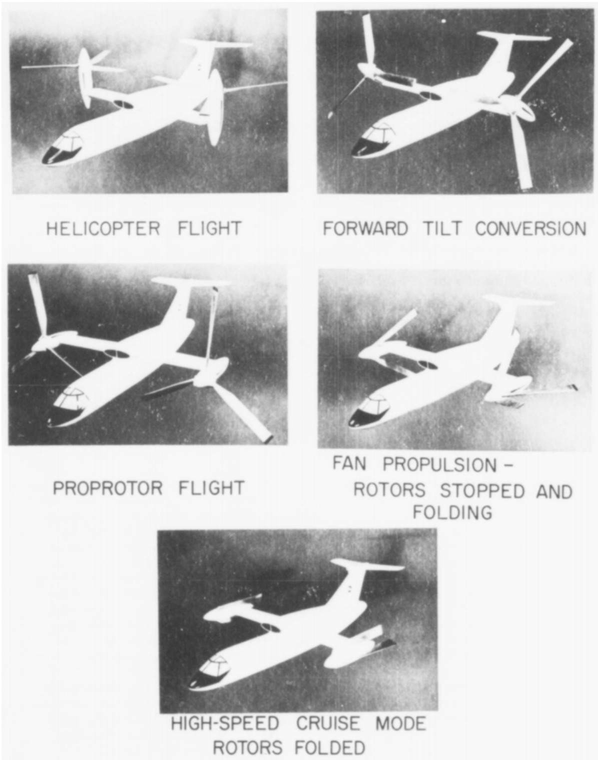

FIGURE 1.9. Process of transition for a stopped rotor tiltrotor, taken from [114]

1.1.11 Modelling improvements

Following the transition from classical theory to tiltrotor-specific contexts, research was also dedicated to improving the fidelity of the physical description of the problem, with a view to improving the accuracy of the models' predictions. Some summary works that give a good insight into which modelling elements were being targeted were released in the first half of the 1970s. The V/STOL Dynamics and Aeroelastic Rotor-Airframe Technology volume of reports [119] was a large work whose explanation of the state of the art included a comprehensive list of the assumptions made by individual models in use with Boeing and even specific known limitations of the general theory, i.e. experimental observations that couldn't be recreated. One such observation was the existence of limit cycle oscillations in certain parameter ranges, which is somehow attributed to "less precise knowledge of the model parameters", indicating a lack of understanding of what influences nonlinearities could exert on a system's behaviour. Specifically, the authors seem unaware that nonlinearities must be present for the limit cycles to exist. Some nonlinearity in the aerodynamics was modelled via table-based representations of blade lift curves, allowing effects such as stall and compressibility to be captured, though ultimately the stability analysis remained linear. Crucially, the majority of the aforementioned limit cycles occur on the stable side of the linearly-predicted boundary (Figure 18, Volume II of [119]). This observation was fairly major; it is a clear demonstration that linear predictions of the whirl flutter onset speed are not always valid.

This work was followed in 1974 by further survey works by Kvaternik [120] and Johnson [121]. The latter also provided the equations for a small collection of proprotor models, the most notable of which was a definitive 9-DoF proprotor-wing model that, using data first published in [122], allowed both stiff in-plane and soft in-plane rotors to be modelled. Linear analysis is once again used to define modes and determine their stability, though thorough discussion and explanation of key aeroelastic stability issues affecting configurations of the time was also provided. Perhaps prompted by the helicopter community modelling the coupling of blade torsion and bending modes (as shown by Huber in 1973 [123]), Johnson quickly followed up [121] with this refinement to the blades implemented in an updated model, released in the same year [124]. The results thereof were listed and discussed in a separate report approved in 1975 [125]. Curtiss made a further extension of this model to include "the effects of the longitudinal degrees-of-freedom of the body (pitch, heave and horizontal velocity)" [126]. Johnson also investigated the role that the engine and transmission system might play in influencing the lead-lag dynamics of the tiltrotor system [127]. By 1976, Johnson's theory of the modal classification he used to describe the aeroelastic stability of proprotors had developed to include a distinction between symmetric and antisymmetric instances of each of the modes originally defined [128].

Further summary works came in 1976 from Kvaternik [129] and Kingston et al. [130]. Unconvinced by proprotor aeroelastic stability predictions available at the time, Kvaternik and Kohn set out in 1977 to assemble a large body of data, structured as several single-parameter sweeps, to allow the robust validation of prediction methods [131]. Bell was at this point developing the XV-15 tiltrotor aircraft, as reported by Few and Edenborough [132], and Magee and Wernicke [133]. Few hints at parameter value prediction being a challenge, and echoes Johnson's 1975 work on engine and transmission system influences saying that "special concern centers around the thrust and power management system when flying at high speed when very small changes in rotor collective pitch represent large changes in thrust and power". Sikorsky stopped short of developing a full tiltrotor aircraft and instead focussed on developing solely the proprotor system at the heart of it; their bearingless "Elastic Gimbal Rotor", detailed by Carlson and Miao

[134], had both soft and stiff in-plane rotors tested with it in order to "explore the system's stiffness requirements". The design is shown in Figure 1.10. The document's conclusions note that either type could be chosen, though augmented structural damping may be required for the soft variant, and that the stiff variant was in general more stable. Nixon's 1993 study [135] is a further parametric study with an emphasis on physical mechanisms of the instability, concluding that "motion-dependent in-plane forces are the most significant contributor to the instability". A further key output was that the flutter onset speed was more dependent on the placement of wing frequencies relative to each other than relative to rotor frequencies, particularly the separation between the beam and torsion frequencies.

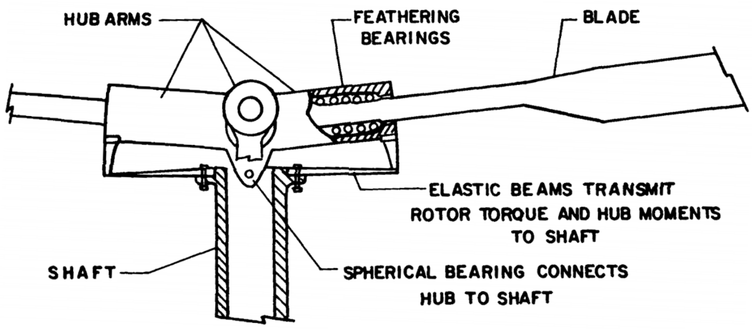

FIGURE 1.10. Sikorsky EGR, taken from [134]

The aerodynamic models used in analyses were also targeted for improvement, and progress was mainly inherited from aerodynamics-focused tiltrotor research and helicopter-based research. Janetzke and Kaza, in their work on the whirl flutter stability of wind turbines in 1983 [23], captured aerodynamic nonlinearities (such as the non-uniform lift slope) simply by using experimental data in a look-up table that was accessed iteratively as necessary. Abrego [136] and Betzina [137] investigated the aerodynamics of tiltrotors in descent, with vortex ring state in mind. Johnson in 2002 [138] developed tiltrotor wake models, followed in 2002 by Yamauchi [139] and in 2006 by Barla et al. who used PIV to measure and characterise the vortical wake left behind by tiltrotors [140]. Barla in the same year investigated how aerodynamic interaction between wing and rotor might be better modelled [141]. Kim and Shin in 2008 [142] focused specifically on whirl flutter, using three aerodynamic models of varying complexity: "normal" quasi-steady, Greenberg's unsteady aerodynamics [143] and full unsteady. Kim noted that the full unsteady model predicted the highest onset speed, though does not specify how this compared to experimental data. As a secondary axis of investigation, Kim also conducted time and frequency domain analysis (i.e. time histories and eigenvalue analysis respectively) of the effects of control system flexibility and wing sweep. A similar, related investigation [144] followed in 2009 where instead the swept parameters were pylon stiffness and swashplate geometric control coupling.

Yue and Xia [145] developed a wake bending model specifically for the conversion manoeuvre in the same year. Gennaretti and Greco [146, 147] analysed the effect of using a range of unsteady reduced-order aerodynamic models, though the rest of the model was as per the 1960s classical whirl flutter state of the art. Later in 2010, Gennaretti et al. [148] investigated the inclusion of wing-proprotor aerodynamic interaction in the aerodynamic model, with specific focus on the impact on the loads predictions. Droandi conducted wind tunnel tests that aimed to isolate and quantify this interaction [149, 150], later specifying the context of the conversion manoeuvre [151]. The conversion manoeuvre has been investigated in isolation: from a loads perspective by Staruk in 2017 [152], from a modelling fidelity perspective by Appleton et al. in 2018 [153] and from an aeroelastic stability perspective by Li in 2018 [154]. Garcia [155] dedicated attention toward building a CFD[27] solver capable of modelling both the hover and airplane regimes of tiltrotors, one of several objectives identified by the HiPerTilt project [156], which charts in terms of categorical objectives the path from the state of the art of tiltrotor-dedicated CFD to high-fidelity capabilities.

Structural modelling improvement has also received dedicated attention, although the close coupling with helicopter research meant that several landmark developments had helicopter contexts and the tiltrotor applicability was either secondary or only implied. Earlier work such as Johnson [121] used linear modal representations of the first harmonic only, while beam theory constituted an improvement in works such as Johnson's aforementioned work on gust response [53], before comprehensive analyses applied FEA-like methods as a standard. Hodges consolidated improvements in nonlinear beam theory [157], which were incorporated into the structural modelling of a number of works, such as Ormiston et al. [158] and Soykasap et al. [90]. Rigo et al. developed a new method known as MASST [159] in 2018 which was used for analysis of the AW609 (see Figure 1.3, (c)), while Gupta devised a methodology for identifying sources of damping in nonlinear composite beams [160].

The role of the pilot's biomechanics in a tiltrotor's overall dynamics was first investigated by Parham in 1991 within the context of the V-22 [161]. Interest was aroused by the observation of phenomena such as "collective bounce", where the vertical acceleration of the tiltrotor is fed back into the system as a control input due to acceleration of the pilot's arm on the collective lever, causing growing oscillations. Parham et al. later investigated the role of pilot biomechanics specifically in whirl flutter of the BA-609 [162], as well as influences from the dynamics of the FCS[28] and its actuation systems, a field known as aeroservoelasticity. Similar investigations were also conducted by Serafini et al. [163], Gennaretti et al. [164] and Muscarello [165]. These modelling inclusions were intended to improve the accuracy of whirl flutter predictions.

[27] CFD: Computational Fluid Dynamics.
[28] FCS: Flight Control System.

1.1.12 Multidisciplinary optimisations

By contrast, it is in optimisation-based works that the largest simplifications of whirl flutter stability assessment can be found. This shortcoming arises from the intrinsically iterative nature of optimisation, which places pressure on the cost function[29] to have as low a computational demand as possible. Most optimisations aim to be multidisciplinary to provide a breadth of analytical perspectives on the problem at hand. However, this diversification only exacerbates the issue of computational cost: the computation per iteration must be shared between the individual constituent analyses, and consequently the fidelity of each may suffer through excessive simplification of the theory applied. The influence of the relative placement of wing natural frequencies on the whirl flutter stability of a system – a conclusion from some of the foregoing literature – is readily translated into structural design constraints. However, this was the only consideration of whirl flutter stability in works by Rais-Rohani [166, 167], Brunson and Rais-Rohani [168] and Clements and Rais-Rohani [169], which aimed to find optimal wing structural designs. An interesting approach was Stettner 1992 [170], who sought to maximise tiltrotor productivity (as defined earlier), arguing that the true optimal design could only be found through simultaneous optimisation of both wing and rotor, rather than optimising the two areas in turn as was current practice. However, the responsibility for aeroelastic stability was handed off to an active control system assumed to be present, and it did not receive any dedicated attention. McCarthy [171] performed an aerodynamic optimisation of a tiltrotor wing but used linear theory for stability to determine the onset speed. Later, Park et. al [172] investigated the matter with a more advanced structural model though the stability analysis was conducted purely through time simulations. The optimisation studies employing the most advanced consideration of whirl flutter were those by Chattopadhyay in 1994 [173, 174], which employed CAMRAD/JA for the aeroelastic analysis. Kim et al. [175] employed fairly advanced structural modelling, though the stability analysis was similar to Park's. Optimisation has also been used directly in stability analyses to find the stability boundaries. Using a classical whirl flutter model with eigenvalue analysis, Cecrdle [15, 20, 176] used optimisation to find the most direct route to the stability boundary through two-parameter subspaces, effectively conducting several single-parameter sweeps at once and thereby bypassing considerable computational expenditure.

1.1.13 Rotorcraft comprehensive analyses

As analyses grew in size and complexity, and knowledge grew of which physical aspects required description in modelling, the concept of universal analysis packages that could be applied to any problem – rather than bespoke models and codes being developed for each investigation – became more and more attractive. These universal analysis packages are now known as rotorcraft

[29] The cost function assigns a figure of merit to each possible design point, calculated as a scalar function of the design variables that constitute the design point, where a lower cost indicates a better design. The optimisation's goal is therefore to find the point in the design space with the lowest cost function output.

comprehensive analyses and have since proliferated among industry and research institutions alike. The word "comprehensive" refers all at once to: the many analysis types covered by a single tool (structural, geometrical, aerodynamic, etc.), the high technology level of each analysis, the range of addressable rotorcraft configurations (conventional helicopter, tiltrotor, etc.), and the whole aircraft being under analysis rather than a subsection treated in isolation [177]. Some are available as commercial off-the-shelf products, others as in-house/proprietary tools belonging to a certain institution, though in all cases their useful application lies at the top of a learning gradient. Their usefulness is set only to increase as the rising costs of experimental testing places ever more of a demand on computational predictions [178]. There are several such analyses, and while some attempts are made at modelling nonlinearities, the whirl flutter stability analyses are simplistic, diminishing the accuracy of their predictions.

CAMRAD was one of the first codes to achieve applicability to a comprehensive range of vehicle types or problem types, and was developed in 1978-79 [158, 179] for NASA, following the growing independence of analysis codes in use [180]. Nixon notes in [135] that it was "one of the few comprehensive rotorcraft codes to allow treatment of a tiltrotor aircraft" available at the time of writing. Nonlinear model elements could be used, but the flutter analysis used linearised equations. This was followed by CAMRAD/JA, developed separately by the eponymous Johnson Aeronautics (JA) during 1986-88 [181], which incorporated a number of model extensions such as higher harmonic control simulation. This was followed by CAMRAD II in 1989-1996 [182], which implemented significant upgrades such as multibody dynamics and the allowance for multiple load paths, though the stability calculations were left unchanged throughout the software family. CAMRAD variants were used in the development of the V-22 [87, 183]. UMARC [184], from the University of Maryland, arose from developments of a previous wing finite element formulation coupled to rotor equations of motion [185], and used a wake model employed in CAMRAD/JA. A finite element model is used for the blades, allowing nonlinear geometry and multiple load paths. RCAS [186] was developed for the US Army in the late 1990s, in response to deficiencies concerning manoeuvre analysis and computational efficiency that were identified in 2GCHAS, its forerunner. RCAS's aerodynamic models are advanced, incorporating features such as dynamic inflow and dynamic wake. Ho et al. [187] further improved RCAS's capabilities by coupling it with the Helios CFD solver in 2019. Dymore [188] was developed at the Georgia Institute of Technology to provide modular and therefore flexible and expandable multibody dynamics modelling, and uses linearised equations for stability. MBDyn [189] is another multibody code, developed around 2000 at Politecnico di Milano, that has seen use in whirl flutter analyses of the ERICA tiltrotor concept. A history and brief guide of rotorcraft comprehensive analyses – itself a comprehensive work in several aspects – is provided by Johnson [177].

Although rotorcraft comprehensive analyses continue to proliferate, they have by no means replaced scratch-built analysis tools. Hathaway's work in the early 2000s [190, 191] presents a new analysis which models the distribution of blade flexibility while retaining separate gimbal and blade flapping degrees of freedom. Hylton [192] similarly uses an in-house code to build a basic whirl flutter model. Li [193] extends Johnson's 9-DoF model of 1974 to incorporate flexibility between the pylon and the wing structure upon which it is mounted.

Despite their power regarding the kinds of problem they are able to solve, each of the comprehensive analyses listed above assesses whirl flutter stability either through linearised equations, or linearisations of trim points, where the main effect of nonlinearities is to alter the trim points' value. Dymore assesses stability using the Prony method, which extracts modal damping ratios from time histories by assuming linear viscous damping. In all cases, linear theory is applied. Though this approach does produce a predicted whirl flutter onset speed, it is unable to predict LCOs, which is the form in which whirl flutter exists in practice. Although a linear-theory-based method exists for determining the stability of LCOs, the LCOs themselves must be found first. The inability of linear theory to predict LCOs becomes dangerous in systems where whirl flutter LCOs exist in parameter ranges that the linear stability analysis predicts to be stable, e.g. below the linear-predicted whirl flutter onset airspeed, as observed by Breitbach in [26] and by Alexander et al. in [119]. The shortcomings of at least CAMRAD, RCAS and Dymore's stability calculations is evidenced by the existence of a number of works dedicated to closing discrepancies between their predicted results for damping and the corresponding experimental data, as both earlier reports by Johnson [194, 195] and also recent, ongoing investigations by Kang, Kreshock and Shen [196–201] explain. The problems concerning damping prediction manifest as incorrect predictions of the stability boundary, and issues with blade load predictions arising from the structural modelling have also been discussed [195]. The general consensus is that the next (4th) generation of comprehensive rotorcraft analyses will make use of high performance computing [202], though there is no mention of plans to alter the stability analysis.

1.1.14 Multibody Dynamics approaches

Though they are grouped with comprehensive rotorcraft analyses, Dymore and MBDyn are fundamentally different in that they are dedicated multibody dynamics (MBD) codes. MBDyn was first applied to development of the V-22 by Ghiringhelli in 1999 [203], joining an established canon of commercial general purpose multibody codes, such as DADS [204], MECHANO [205] and ADAMS [206], though insufficiencies in aerodynamic representation and description of flexible bodies, and some problems caused by large rotations made them unsuitable for rotorcraft applications as Ghiringhelli further explains [207]. Ghiringhelli would in the same year use MBD to investigate a tiltrotor configuration fitted with active control [208], as did Mueller et al. in 2004 [209] and 2006 [210]. Quaranta et al. [211] used MBDyn to assess the stability of ground and air resonance in a soft in-plane rotor. The large size of multibody models could be reduced using a technique known as "proper orthogonal decomposition" [212] which was applied to a tiltrotor model by Masarati et al. [213] in 2003. Shen et al., applying multibody methods first to a model-scale tiltrotor in 2005 [3, 214, 215], assessed both stiff in-plane [178, 216] and soft in-plane [217, 218] rotors as a medium of comparison between MBDyn and Dymore.

Mattaboni [219, 220] used MBD to build on the Generalized Predictive Control work previously undertaken by Nixon et al., and found the high-speed aeroelastic stability to now be dominated by short-period flight mechanics. Shen et al. revisited their 2005 model-scale work in 2016 [215], this time incorporating nonlinear effects from the control system geometry and a freeplay nonlinearity in the drivetrain. The latter of these features was especially significant as the intermittent contact greatly altered the elastic restraint characteristics of the rotor's lead-lag motion, which previously was commonly assumed to be constant even by some comprehensive analyses, resulting in a constant rotor speed. The work helped to close prediction discrepancies regarding experimental observations of a large change in wing beamwise damping in the range of near-zero rotor mast torque, a phenomenon known as "damping bucket". Krueger [221] presented a multibody modelling approach that was the computational counterpart of an existing ADYN wind tunnel test, investigating the effects of the introduction of nonlinear springs in the computational model. Spring stops were also added to provide hard limits on model deflection and a good agreement with the wind tunnel test data was shown, with experimentally-observed LCOs being recreated successfully. Hoover used an MBD-based approach to re-attack the original propeller whirl flutter problem in 2019 [18] as part of development of the NASA X-57 Maxwell aircraft, determining the stability using the Prony method applied to the time histories output by Dymore.

A benefit of multibody solvers in general is the potential for higher fidelity kinematic representation, mainly arising from the ability to handle large[30] rotations and displacements. This allows better representation of nonlinearities, particularly those arising from nonlinear kinematics, including freeplay, which otherwise might be simplified unduly. However, stability must be assessed entirely in the time domain, often through long simulations [211]. This method is not robust as there is no guarantee that whirl flutter solutions, if they are present, will be found. A given whirl flutter solution has what is known as a "basin of attraction": a subset of the state space from which the system will converge upon that whirl flutter solution. When running time simulations as part of the MBD stability analysis, perturbations may be supplied to the system to encourage it to find whirl flutter solutions, but a solution will only be found if a time simulation starts within that solution's basin of attraction. Knowledge of the locations of basins of attraction is generally not available a priori, especially if it is not known what solutions are present. Furthermore, time simulation is only capable of finding stable solutions and the use of reverse time simulation to find unstable solutions is largely unreliable.

[30] As opposed to the mathematical definition of "small".

1.1.15 Other stability analysis methods

Although eigenvalue analysis is used by most of the foregoing literature, there is a small number of other known analyses, each with their own strengths and weaknesses. The basic problem that they address is that linear theory cannot predict LCOs, instead only producing a linear boundary for system-wide stability. The aforementioned work by Young and Lytwyn [45] included a stability criterion in the spirit of Lyapunov test functions that was based on the time derivative of the total energy in the system, viewing damping in a system-wide sense. This allowed LCOs to be predicted and their amplitudes estimated. Quaranta developed a method termed "robust stability analysis" [222] that was designed to handle uncertainties in parameter values, though linearised equations are used. In turboprop whirl flutter literature, one stability analysis method that has supplanted basic eigenvalue analysis is the PK method, as used by Cecrdle [20]. The method involves iterative curve fittings of the unsteady aerodynamic forces that cause the problem to be of the nonlinear eigenvalue type. Although the PK method was improved upon by Colo [223], it is more an iterative framework for finding stability boundaries efficiently and is still underpinned by linear theory, with nonlinearity lying with the complex Laplace variable and not with the state vector. More recently (2019), Karniel suggested a more general method [224] that he termed a "distributed aeroelastic energy approach", though the theory is fundamentally linear in nature, and fixed wing aircraft flutter was the focus.

The describing function method [225] can be useful for predicting the conditions for LCO existence, though the method struggles in circumstances where higher harmonics of the response are significant and in these cases requires adaptation as shown by Muscarello [226]. It also employs quasi-linearisation. The harmonic balance method [227] exploits the phenomenon of nonlinear systems reacting to sinusoidal forcing with a response comprising several harmonics of the fundamental frequency, and thus reconstructs steady state periodic solutions from a chosen number of harmonics. While compatible with strongly nonlinear functions, producing higher-order approximations can be laborious [228]. Furthermore, quasi-periodic solutions can only be predicted by including subharmonics in the representation, and aperiodic motions cannot be predicted at all.

1.1.16 Wing and control surface nonlinear aeroelasticity studies

Prediction fidelity in the foregoing literature was almost completely a function of the modelling choices (i.e. physical description) rather than the stability theory employed; the stability analysis methods in all the tiltrotor literature mentioned here have either been some application of linear theory or time simulations and therefore any improvement in prediction fidelity only came from improved modelling choices. The presence and consequent influences of system nonlinearities were acknowledged by the tiltrotor community but not fully engaged with; Kunz's 2005 survey of proprotor whirl flutter [229] has no mention of nonlinearity whatsoever. Some models included nonlinearities, though stability analyses remained linear. However, elsewhere in the wider aeroelasticity community, the full effects of structural nonlinearities were being investigated with simple wing and control surface flutter models. One of many successors to Woolston's aforementioned papers [28, 29] was Breitbach's 1977 AGARD[31] report [26], which uses a similar model and advocates strongly for the consideration of structural nonlinearities in modelling, knowing the strong influence that they can have on stability calculations. A similar range of nonlinearities is considered (backlash, solid friction, kinematic limitation, cubic softening, and some combinations thereof). Breitbach shows, for each nonlinearity, the amplitude of flutter LCOs existing below the linear-prediction flutter onset speed, created by each nonlinearity, as a function of airspeed. Harmonic balance was then used to manually construct a bifurcation diagram of the flutter solution branch from its origin at the linear flutter onset speed, distinguishing between stable and unstable segments. Impressive agreement with wind tunnel measurements was achieved, though naturally only the stable segments could be validated.

A closer step to the application of such a method to tiltrotors was Tongue's work [230, 231] which addressed ground resonance in helicopters. Analysis of the wing with control surface model deepened as the theory of nonlinear dynamics (and particularly chaos) developed and proliferated, allowing rather advanced studies such as that by Price et al. in 1994 [232], which investigated the behaviour of a 2-DoF pitch-heave 2D aerofoil with freeplay. Work by Conner et al. in 1997 [233] was similar, using a 3-DoF aerofoil and with experimental data for comparison. Survey works of theory by Dowell et al. in 2002 [234] and 2003 [235], and of experiment by Garrick in 1981 [236], show that an extensive body of research has been dedicated to nonlinear aeroelasticity, though a great deal of the work concerns basic wing systems capturing other instabilities than whirl flutter in a variety of applications other than tiltrotors [237–243]. The primary relevance of these works to this research is the same as that of Woolston and Breitbach: that the presence of structural nonlinearities adversely affects flutter characteristics, causing it to appear at lower airspeeds than linear analysis predicts. Further rotorcraft-specific studies of this nature – where the impacts of nonlinearities are tackled more directly through techniques such as symbolic manipulation and harmonic balance – are comparatively scarce. Some examples are Tang 1985 [244], Flowers 1988 [245], Tang 1993 [246], Robinson 1997 [247], Kunz 2000 [248] and Muscarello 2011 [226], though the focus is almost exclusively ground resonance of helicopters, rather than tiltrotors. Andersch [249] specifically tackles the impact of a stick-slip nonlinearity on ground resonance stability.

1.1.17 Nonlinearities in tiltrotors

However, various kinds of nonlinearity have been shown not only to be present in various tiltrotor systems, but also to have a non-negligible effect on system behaviour. Masarati et al. [218]

[31] AGARD: Advisory Group for Aerospace Research & Development. An advisory panel within NATO that existed from 1952 to 1996.

showed that nonlinear effects at the blade level can have a knock-on effect on overall system stability, specifically from deformability of the rotor blades. The appearance in tiltrotor-focused experimental results of the aforementioned "damping bucket", where a significant decrease in the damping of the wing beamwise bending mode occurs at very low values of rotor torque, was also recreated in Masarati's results and nonlinearities in the hub and drivetrain were suspected as being the cause. Specifically, the inclusion of a freeplay deadband in the model produced good correlation with experimentally-obtained results. Krueger [221] reports "considerable differences" between linear and nonlinear variants of the models he investigated in his aforementioned ADYN work. He further showed that nonlinearities introduced by the influence of the drivetrain, freeplay and backlash can create a behavioural discrepancy between rotors in windmill and thrust mode. A further explanation for this discrepancy is that the rotor blades deform under load when in thrust mode, altering the trim conditions. Given the aforementioned nonlinear nature of blade deformability, this effect would introduce nonlinearity into the behaviour of the blades.

A prolific source of nonlinearity in tiltrotors is their structure, such as geometrical nonlinearities between the various subsystems and components, or kinematic nonlinearities. Furthermore, their material properties may be intrinsically nonlinear, causing a nonlinear relationship to exist between deformation and external forces applied. Another source of structural nonlinearities in a tiltrotor rotor-nacelle system may be the drivetrain [221], as previously mentioned, where interfaces between the gears introduce small but finite amounts of freeplay. In general, a mechanical interface or joint may have a freeplay deadband [218]. The large degree of twisting in the rotor blades may couple their in-plane and out-of-plane bending motions. Krueger notes that a rotational spring element in the wind tunnel setup that his study recreated computationally was "a major source of nonlinearity". The gimbal may itself be a source of structural nonlinearity if elastomeric materials are used therein to provide elastic restraint, as specifically investigated by Gandhi et al. in 1996 [250]. Freeplay may exist at hinges and other mechanical interfaces [251], in addition to backlash and saturation nonlinearities.

In general, the assumption of linear stiffness of physical structures is only really representative when deformations are small – a condition that may well not hold for whirl flutter oscillations. While linear analysis does produce a figure for the onset airspeed, the presence of structural nonlinearities may not only alter the whirl flutter oscillations themselves, but also the parameter ranges over which they are possible. Low order polynomial functions may provide a more realistic description of structural stiffness at larger deflections [252], where a single stiffness does not exist for all deflections. Stiffness may increase as the deflection increases (known as hardening), decrease (softening), or some combination of both in different deflection ranges.

The effect of nonlinearities on whirl flutter stability is no merely academic interest: if nonlinearities are able to create the possibility of whirl flutter below the linear predicted onset speed, as is well known to happen in wing-control surface flutter, then a significant threat is posed to the design of tiltrotors. This threat may extend to other system parameters such as stiffness and damping. To use more general terms, the prevailing stability analyses may not detect some of the parametric regions in which the nonlinearities induce whirl flutter, causing incorrect, unconservative stability boundary predictions. This effect is illustrated in schematic form between two arbitrary parameters p_1 and p_2 in Figure 1.11, and has appeared in a number of the aforementioned works. Breitbach's work [26] showed the existence of flutter LCOs below the linear predicted onset speed. Lee and Tron [253] demonstrated that the existence of freeplay in a control surface significantly reduced the flutter onset speed itself. Nonlinear effects are not only an important modelling consideration for tiltrotor aeroelastic models, but the proper identification of the behaviours they can cause is crucial for tiltrotor design as a whole and the stability analyses generally used currently are insufficient.

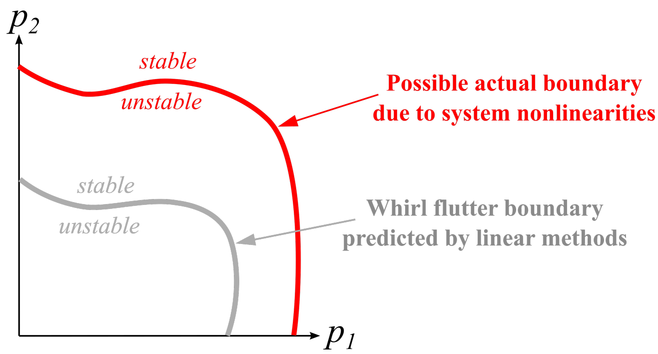

FIGURE 1.11. Schematic diagram of nonlinearities altering parameter ranges over which whirl flutter is possible

1.1.18 Further complications in future predictions

Furthermore, tiltrotor design is expected to develop in a way that may threaten the accuracy of whirl flutter prediction. A number of concept tiltrotors are under development around the world, whose primary goal is to establish what new technologies are necessary for future tiltrotors. In the case of developing larger tiltrotors, increasing the size and weight of tiltrotor designs looks likely to create complications due to changes to component-level configurations and/or designs that may become necessary, potentially affecting prediction methods. For instance, Acree et al. [254–257], found among other things that larger tiltrotors will require larger and slower-rotating rotors with four or more blades, for which gimballed hubs are unsuitable due to kinematic constraints [258]. Nixon [110] and Quaranta [211], among others, have also noted that soft in-plane rotors might be necessary, due to the weight saving arising from the lower blade loads. Furthermore, hingeless proprotors will have different per-rev frequencies and mode shapes than the gimballed rotors on current tiltrotors, so coupling between wing and rotor modes may differ from past experience [5].

1.1.19 Continuation and Bifurcation Methods

A newer body of theory that offers great potential in the analysis of nonlinear dynamical systems is Continuation and Bifurcation Methods (CBM). It is a practical tool with dedicated theory for investigating point changes in the qualitative nature of a system's steady state solutions as one or more of the system's parameters are varied. Continuation is an iterative numerical method that computes the steady state solutions of equations and their stability as one or more parameters are varied, while bifurcation theory classifies qualitative point changes in the solutions (bifurcations) [259–261]. Together, bifurcation diagrams are created that display the numerical values of the system's solutions, their stability, and any bifurcations present. The method requires a starting solution and incrementally constructs branches of solutions from it. Both equilibrium (static) solutions and periodic solutions can be found. The method is commonly applied to ordinary differential equations though other types of equation, such as delay differential equations, are also amenable to the method. Furthermore, the theory may be interfaced with the design of control laws to alter the behaviour of systems [262]. Stability analysis is only applied to the full numerical solutions obtained and therefore approximations do not need to be made to the nonlinear terms in the equations, with only few exceptions such as discontinuous representations. Though it has a significant computational demand, the increasing availability of computing power makes CBM ever more feasible and thus attractive as a tool.

Compared to other methods, CBM offers some simplicity of use as when it is used to solve ODEs, no manual working is required to transform the model into a usable form and the solver may be interfaced directly with it immediately. The stability of any solutions found is ordinarily output straight away, along with the numerical values of those solutions. A downside to CBM is that it is not amenable to problems with a large number of influential parameters, as the resulting high-dimensional parameter space that must be considered is unwieldy.

CBM had its debut in the aerospace field in the application to the flight dynamics of fighter aircraft, in work undertaken by Mehra and Carroll in 1977-9 [263–265] with examples of later contributions being Sibilski [266] and Jahnke [267]. Over time it has gradually been adopted by other aerospace engineering fields. Gordon [268] uses CBM to attack the flutter of a control surface on a wing, while Salles [269] addressed whole engine rotordynamics. NASA first engaged with CBM in 2005 [270] but usage since has mainly been restricted to fixed wing flight mechanics [271] in order to address loss of control incidents. CBM is in the gradual process of proliferation within the field of rotorcraft dynamics, and as a result has so far been limited in its application to a small number of problems [272], such as flight mechanics [262, 273, 274], ground resonance [275], dynamic impact of external load carriage [276] and rotor vortex ring state [277]. Their inclusion in rotary wing studies is steadily becoming more prevalent as they are powerful when applied to problems such as the identification of instability scenarios of rotor blades, as shown by Rezgui and Lowenberg [278, 279]. Continuation methods were used in the AW159/Wildcat Release To Service military certification document to assess the nonlinear dynamic behaviour of the tail rotor [280]. However, the application of CBM to tiltrotor systems was not uncovered by the literature survey conducted for this work, despite the great potential.

1.1.20 Summary and research gap

Tiltrotor aircraft are limited by whirl flutter, an aeroelastic instability that affects their design and performance. Nonlinearities, which are present in tiltrotor aircraft, have significant effects on their behaviour, and more general aeroelasticity studies have shown that nonlinearities can bring about the possibility of flutter at lower airspeeds than that predicted by linear stability analysis methods, as used by much contemporary literature. This occurs because linear prediction methods for establishing the flutter stability boundary of a given system are not compatible with these nonlinearities. Other analyses use time domain methods to look for instability, though there is no guarantee that they can find whirl flutter solutions if they are present. As most tiltrotor whirl flutter prediction tools in use have one of these weaknesses, the strong possibility exists that they are failing to detect instances where nonlinearities cause the early onset of tiltrotor whirl flutter. An investigation of whether nonlinearities can induce this phenomenon, using tools that are fully compatible with nonlinear systems, is therefore required.

Work on wing-control surface nonlinear aeroelasticity provides a robust categorisation of the stability impacts of various nonlinearities, but mostly uses generic, basic aerofoil pitch-heave models that do not bear much resemblance to tiltrotor systems. Multibody approaches do well to model nonlinearities, though their time-domain stability analysis is costly, unsystematic and un-robust as there is no guarantee of finding the whirl flutter solutions. Furthermore, only stable solutions can be found, and the use of reverse time simulation to find unstable solutions is largely unreliable. CFD, while importantly addressing the many nonlinearities found in aerodynamics, has not made a significant contribution to production flutter analyses [281], due to the unavoidably significant role of structural nonlinearities. Methods for predicting LCOs require significant manual working in order to produce useful results.

Given the available literature surveyed, a significant opening exists for the application of CBM to tiltrotor whirl flutter. By completing such a study, this work will achieve a novelty within the field of tiltrotor whirl flutter study. Much of the existing literature has either underestimated the role of nonlinearities in whirl flutter in its modelling, or prevented the full discovery of their impacts through insufficient stability analyses. The role of nonlinearities in tiltrotor whirl flutter is therefore not fully understood. More seriously this shortfall can lead to over-estimation of the whirl flutter onset speed and other unconservative stability boundary predictions, placing at risk tiltrotors designed using these unsuitable methods.

CBM offers the unparalleled capability of constructing a full picture of a nonlinear system's dynamics, showing what solutions exist at which parameter values, and their respective stabilities. Furthermore, its parameter-focused nature is appropriate both for the question of tiltrotor design and for the study of whirl flutter, as the design space of a tiltrotor is defined by parameter combinations and the use of whirl flutter stability boundaries encourages thought in terms of parameter ranges. Applied to tiltrotor aeroelasticity in the present work, it will reveal whirl flutter behaviours that linear methods cannot detect, providing accurate predictions of unsafe parametric regions in which whirl flutter can be experienced. That is, predictions that account for wider effects in the state-parameter space than the local boundaries that are determined by linear stability analysis. New and specific insight of the role of nonlinearities in tiltrotor whirl flutter will thus be gained.

1.2 Research Aim and Objectives

The aim of this research is to analyse the whirl flutter characteristics of a tiltrotor's rotor nacelle system that has had structural nonlinearities introduced into it. In practice, this work asks the following questions: *"What impact do structural nonlinearities have on the whirl flutter characteristics of a tiltrotor rotor-nacelle system? Are these effects common to rotor-nacelle systems in general?"*. As this work is the first of its kind, it is of the most use for it to establish an overview of the range of qualitative effects.

The term "characteristics" is used here to denote both where whirl flutter exists (in parametric terms), as well as the stability (stable/unstable) of the whirl flutter solutions found. Tiltrotor design is parametrically-focused, as is their operation: quantities such as airspeed are parameters in modelling analyses. The stability of whirl flutter solutions is important as, in addition to the numerical solution values, it comprises the full behaviour of a system. The impact on these characteristics is therefore any changes caused by the nonlinearities: while nonlinearity is not necessary for the models to experience whirl flutter, nonlinearities can cause additional instances of whirl flutter to be generated. CBM is therefore well-suited for this research as it is a dedicated tool for analysing dynamical systems in this way. The type of motion (periodic/aperiodic) is also of interest as individual complex behaviours can be symptomatic of overall dynamic complexity of a system. To this end, time simulations may be employed to predict specific behaviours in detail, as well as validating predictions made by CBM.

Choices must also be made regarding the structural nonlinearities to be portrayed and how they are modelled. While nonlinear finite element beam theory is at quite an advanced state, the focus of the investigation is to establish basic qualitative effects rather than examine specific designs, favouring CBM over such finite element methods. Nonlinearities that may be implemented directly in the equations of motion are valued as this allows a simple integration with CBM. Selection of which structural nonlinearities to model should follow the taxonomy established within existing nonlinear aeroelasticity literature, which identifies two main categories: **distributed** and **concentrated** [26]. Distributed nonlinearities manifest as macro-effects resulting from material property nonlinearities and geometric nonlinearities in beams, and are generally smooth in a mathematical sense. Concentrated nonlinearities are localised, generally associated with mechanical interfaces such as control mechanisms or connection points. In contrast to distributed nonlinearities, they are often discontinuous, or "hard".

Lastly, the results can be digested more readily if an appropriate basic model is investigated first. The dynamics of a tiltrotor model arise from both wing and rotor degrees of freedom, and though classical whirl flutter's consideration of wing contributions is limited, being only partially implicit in the angular deflections of the shaft, it is sufficient to enable the model to depict whirl flutter, and in a simpler form than is met in tiltrotor systems. Therefore, the analysis of a classical whirl flutter model may be used as a stepping stone to understanding the results of a tiltrotor model. Furthermore, classical whirl flutter remains relevant to the design of turboprops, and therefore the results of this study may be of use to both tiltrotor and turboprop aeroelasticity communities. The findings may also provide new perspectives to the wind turbine design community, given the various similarities between tiltrotor rotor systems and wind turbines.

The above considerations allow the following research objectives to be formalised. They are numbered O1-5 to allow their subsequent referencing:

- **O1**: assess the effect of a smooth nonlinearity on the whirl flutter dynamics of rotor-nacelle systems
- **O2**: evaluate the impact of a hard nonlinearity on the whirl flutter dynamics of rotor-nacelle systems
- **O3**: investigate the influence of model complexity (classical whirl flutter theory vs. tiltrotor aeroelasticity) on the impacts that the nonlinearities have on the whirl flutter dynamics of rotor-nacelle systems
- **O4**: explore what types of whirl flutter behaviour are observable over a range of design and operating parameters
- **O5**: synthesise guidelines for tiltrotor design against whirl flutter in the presence of structural nonlinearities, based on the findings

1.3 Research Process

Some consideration of practicalities allows a research process to be derived from the above objectives. Tiltrotor models are required that can produce reliable results of both linear and nonlinear types, in order for the influence of the nonlinearities to be clear. However, as this work is a first of its kind, no models could be found in the literature that can operate in both linear and nonlinear forms. Rather than develop models from scratch, using linear models from existing literature and adapting them to include nonlinearities has significant benefits. Firstly, the linear behaviour predicted by the models is reliable: the studies containing the models are usually validated by corresponding experimental tests. Secondly, significant effort is saved. Models are selected that are particularly amenable to adaptation.

The bifurcation diagrams that constitute the raw results need to be summarised in some way to allow the work's outcomes to be gathered. An ideal way to do this is to use stability boundaries. The de facto boundary of the nonlinear models across the whole domain of analysis can be shown in one diagram. Crucially however, stability boundaries are a common tool in expressing linear analysis results, and therefore summarising in this way allows a direct comparison with the original linear predictions.

The research process followed by this work is given below. The steps are again numbered for ease of reference:

- **P1**: Construct computational implementations of two existing linear whirl flutter models
- **P2**: Assess the linear stability boundaries of each as a baseline for comparison
- **P3**: Adapt each model to portray both a smooth and a discontinuous nonlinearity
- **P4**: Use CBM to find whirl flutter behaviours in each case
- **P5**: Interpret and understand the results using bifurcation diagrams
- **P6**: Use stability boundaries to summarise the impacts of the nonlinearities on the models' whirl flutter stability characteristics
- **P7**: Formulate guidelines for tiltrotor design practice regarding whirl flutter management

The ways in which the process steps serve the various objectives is shown in Figure 1.12.

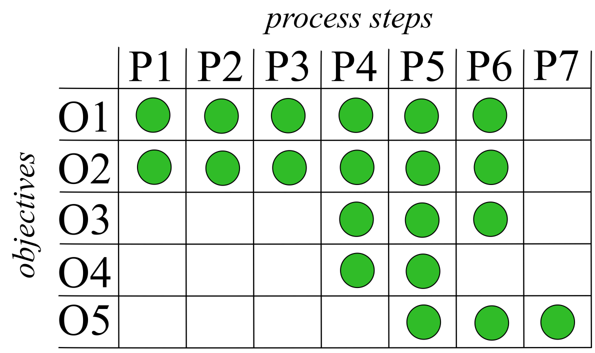

FIGURE 1.12. Grid relating process steps to research objectives

1.4 Thesis Structure

1.4.1 Sections

The work is structured so that not only is the research process above followed, but that the findings are ordered in a way that maximises their comprehensibility. That is, the aim is to provide as clear as possible a path from the simplest demonstration of whirl flutter to full understanding of all the new nonlinear cases considered. The research objectives can be boiled down to two axes of investigation: the type of nonlinearity and the complexity of the model. So that the differences between each combination of nonlinearity type and model type may remain clear, the results are presented in stages. The combinations form a 2-axis grid, shown in Figure 1.13, along with the chapter in which each is covered.

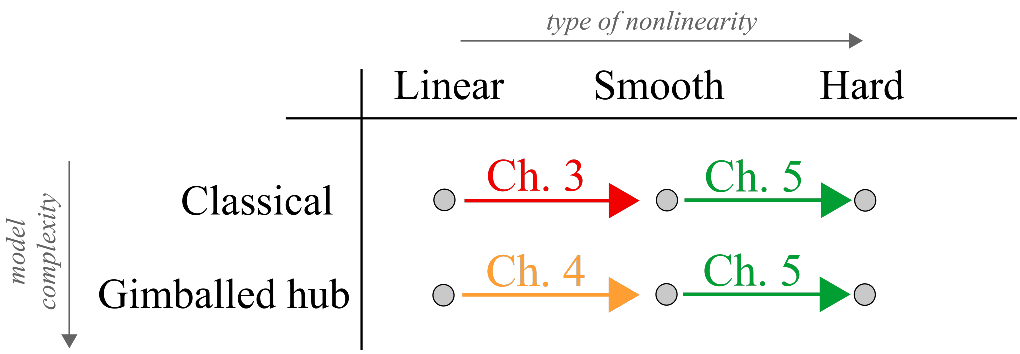

FIGURE 1.13. Flow of technical material within this work

First, the basic model is introduced and demonstrated in its original linear form (Chapter 3). The smooth nonlinearity is then introduced and the basic behavioural differences compared to the linear system are highlighted. The model complexity is then raised in Chapter 4. with the introduction of the tiltrotor-representative model in both its original linear and smooth nonlinearity forms. Finally, the discontinuous nonlinearity is integrated with both models in

Chapter 5, completing both axes of investigation. A chapter of theory and supporting concepts is given in Chapter 2, to provide a basic reference for the main technical material. The conclusions of the work form Chapter 6. The contributions of each chapter to the research objectives are shown in Figure 1.14.

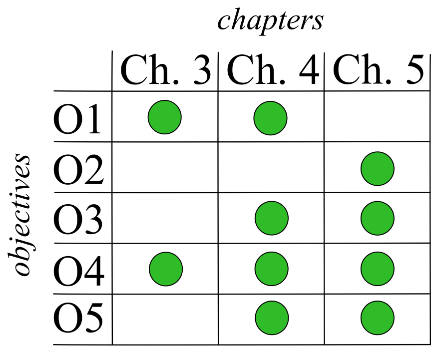

FIGURE 1.14. Grid relating chapters to research objectives

1.4.2 Basis of material in own existing publications

In the process of this research project, a selection of content from each of the individual work packages was published as each was completed, in conference proceedings and journals. They are now presented here in only a loosely adapted form.

Chapter 3, where the classical whirl flutter model is shown in both the linear form and with the smooth nonlinearity implemented, is adapted from preliminary work presented at the 43rd European Rotorcraft Forum in 2017 [282], and subsequently extended and published in full in the Journal of Nonlinear Dynamics in 2018 [283]. A greater breadth of explanatory material, including sensitivity analysis of the model in its original linear form, is included in the present work.

Chapter 4, where the tiltrotor-representative model is shown in both the linear form and with the smooth nonlinearity implemented, is adapted from a paper presented at the 75th Annual Forum of the Vertical Flight Society in 2019 [284]. Some new results in the study were subsequently discovered in addition to those reported in the VFS paper, and these are included here in addition to more comprehensive explanatory material and a sensitivity analysis of the model in its original form.

Chapter 5, where the hard nonlinearity is applied to both models, is based both on work presented at the 45th European Rotorcraft Forum in 2019 [285] and further work subsequently published in the Journal of Nonlinear Dynamics in 2021 [286]. Some additional bifurcation diagrams are shown in the present work, to show more clearly the effects that the nonlinearity's presence has caused.

Collectively, the papers mentioned here contribute to the conclusions in Chapter 6, as well as to the literature review conducted in this Chapter.

Chapter 2

Supporting Theory and Concepts

2.1 Tiltrotors

The most common and best known form of vertical flight in the current era is the helicopter configuration. However, helicopters have a number of performance disadvantages, such as low cruise speed and low range compared to fixed wing configurations. They additionally have higher accident rates due to operational factors and mechanical reliability issues directly related to their design [287]. Tiltrotors offer an improvement on helicopters by combining the vertical capabilities of helicopters with the flight envelope of a fixed wing turboprop aircraft. However, in combining the two configurations, designers have to contend with the design challenges of each.

2.1.1 General description

Tiltrotor aircraft mostly resemble modern mid-size turboprop aircraft, in the sense of their overall planform. However, their propulsion system employs two proprotors mounted on the wingtips as opposed to a turboprop's propellers. Proprotors are larger and slower-rotating than propellers, and tiltrotors typically employ turboshaft engines. Each rotor is swivelled by an actuation mechanism that can point the rotor upwards, forwards or anywhere in between, being rigidly held in place when not moving. All operational tiltrotor designs have their engines in the wingtips, collocated with the rotors and shielded within nacelles: pod-like structures that are aerodynamically optimised to reduce drag. In some older designs and modern conceptual designs, the engines are located within the fuselage, to alter the mass characteristics of the aircraft.

The wing is typically slightly swept forward and is substantially thicker than would be aerodynamically ideal so as to provide the necessary stiffness to guarantee aeroelastic stability up to a certain speed. This however makes them less efficient in cruise. The payload is stored in the fuselage, with access provided by side doors and/or a rear loading ramp depending on the design. An annotated system-level schematic diagram of the general tiltrotor configuration is shown in Figure 2.1.

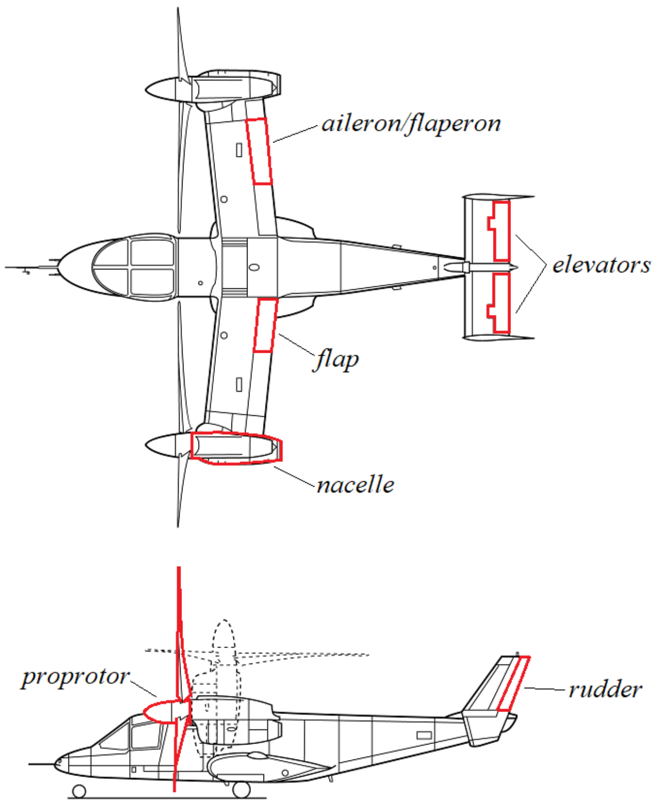

FIGURE 2.1. System-level schematic diagram of a tiltrotor[1]

The nacelle pointing angle is controlled by the pilot. Pointing the rotor upwards causes the tiltrotor to behave as a helicopter, known as "helicopter mode". In cruise, the rotors are pointed forward to provide thrust for flight as a conventional fixed wing aircraft, known as "airplane mode". Additionally, some tiltrotors such as the V-22 (see Figure 1.3, (c)) have a distinct operating mode known as the "80-jump" configuration, where the nacelles are pointed 80 degrees upward of the horizon for take-off, achieving altitude quickly while building speed. In helicopter mode, control of the aircraft is actuated through the proprotor blades in the same manner as a helicopter. In airplane mode, control is aerodynamic, using control surfaces similar to a conventional fixed wing aircraft. Elevators at the rear of the aircraft control pitch, ailerons near the wingtips control roll, and rudders at the rear control yaw. Flaps at the trailing edge of the wing can provide extra

[1] Adapted from NASA: **https://upload.wikimedia.org/wikipedia/commons/7/70/Bell_XV-15_line_drawing.png**, public domain.

lift at lower speeds, and additionally when deployed in helicopter mode they lower the area of the wing that obstructs the wash from the rotors. In some tiltrotor models the trailing edge surfaces function as both ailerons and flaps, and are referred to as flaperons.

The process of tilting the rotors to go from one mode of operation to the other is known as conversion, and requires the aircraft to keep its nacelle angle within a "corridor": upper and lower limits that are a function of its airspeed. The walls of the conversion corridor are defined by various constraints such as structural loading limits, or wing aerodynamic limits. The basic stages of conversion are illustrated in Figure 2.2. The aerodynamic design of the proprotors is a compromise between the conflicting requirements of high speed flight in airplane mode (propeller) and efficient hover in helicopter mode (rotor). In general, tiltrotors are unable to land in airplane mode due to their large rotors not being clear of the ground.

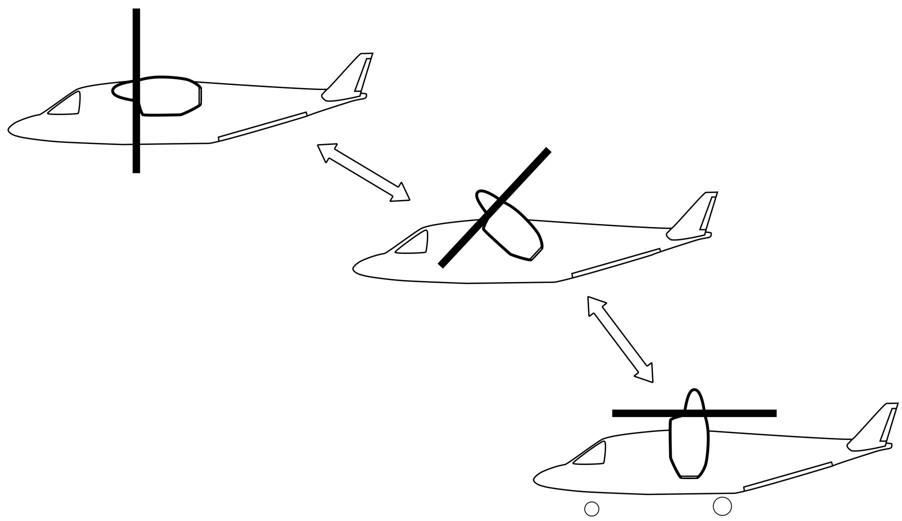

FIGURE 2.2. The conversion manoeuvre. Top: airplane mode (cruising). Middle: conversion. Bottom: helicopter mode (take-off/landing).

Given the large role that the wing degrees of freedom play in tiltrotor whirl flutter, the manners in which the wing may bend is of relevance to whirl flutter study. There are three distinct motions: flapwise (also known as beamwise) bending, chordwise bending, and torsion. They are shown in Figure 2.3, and are most readily described according to the motion of the wingtip that each bending type induces. Flapwise/beamwise bending is the up-down motion of the wingtip, chordwise bending is forwards-backwards, while torsion is the twisting of the wing about its root-to-span axis.

2.1.2 Rotor systems design

Tiltrotor rotor systems are in a number of ways similar to those of helicopters, in their overall assembly and the mechanisms by which control is administered. A number of rotor blades are

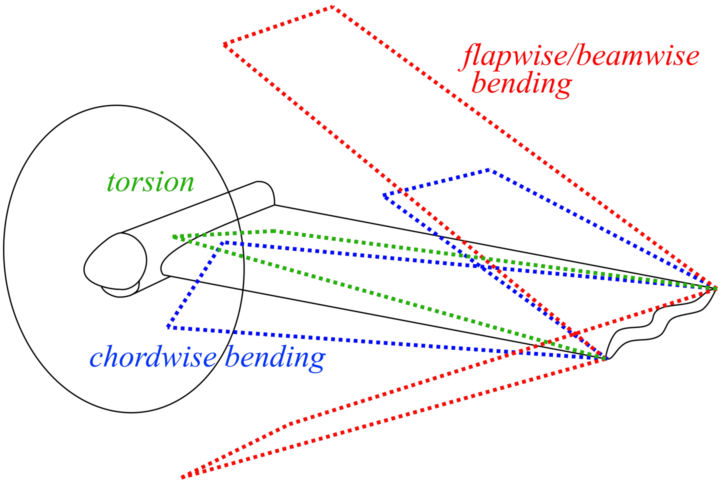

FIGURE 2.3. Types of wing bending

affixed to a hub via effective hinges which permit each rotor blade to bend elastically relative to the hub plane in response to the loads that it experiences. The hub plane exists at the hub where the blades are attached, perpendicular to the rotor shaft, and defines the plane in which the blades rotate if they are entirely undeflected. There are three fundamental types of blade motion, illustrated in Figure 2.4.

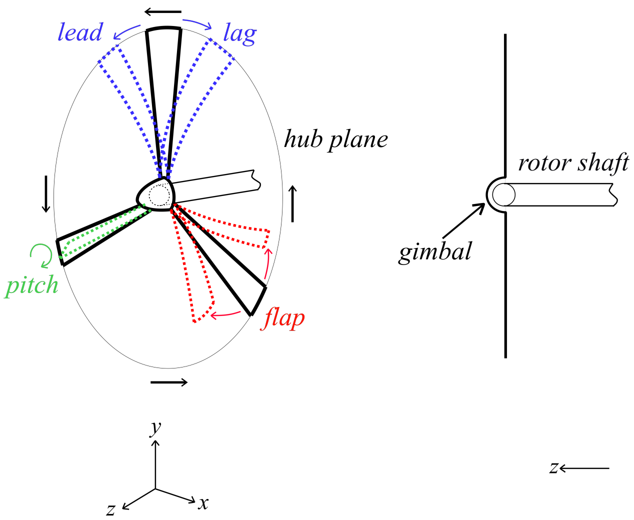

FIGURE 2.4. Illustrations of rotor blade motions and of a gimballed hub. An arbitrary coordinate system *(x,y,z)* is included to link the perspectives of the two drawings

The blade motions are most simply distinguished by their relation to the hub plane: flapping, lead-lag and pitching/feathering. The flapping motion is perpendicular to the hub plane; an up-down movement of the blade tip in helicopter mode, or forward-back in airplane mode. The lead-lag motion is parallel to the ordinary rotation of the rotors: when leading the rotors are ahead of their undeflected position, and vice versa when lagging. Pitching or feathering is the axial rotation of a blade about its attachment to the hub such that changes occur in the angle of attack made with the freestream surrounding the rotor. The flapping hinge axis is often offset from being perpendicular to the blade by an amount known as the "δ_3" angle, such that the flapping and pitching motions are coupled in a way that benefits that blade's stability. Specifically, the blade flapping in one direction (say upward/forward) reduces the blade's angle of attack, inducing it aerodynamically to return to its undeflected state.

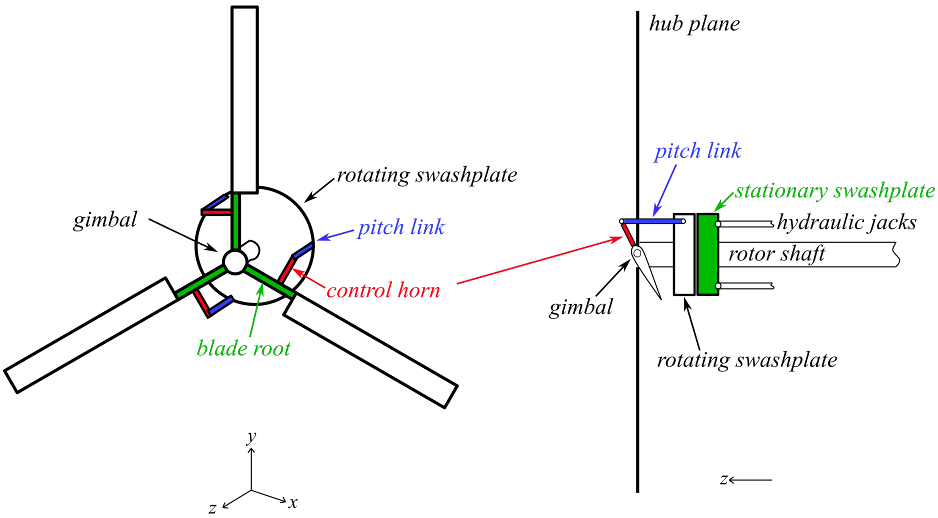

FIGURE 2.5. Schematic diagram of a tiltrotor rotor system. An arbitrary coordinate system *(x,y,z)* is included to link the perspectives of the two drawings

While the motion of the blades in all three of these senses occurs due to the time-varying loads that they each incur, the pitch motion is also controlled directly when in helicopter mode in order to control the motion of the entire aircraft. The control system is similar to that in helicopters and a schematic diagram of a typical tiltrotor rotor system is shown in Figure 2.5. The control is transferred to the blades via a swashplate: a two part assembly that is able to transmit control actuation from the non-rotating wing structure to the rotating hub. The hydraulic jacks actuated by the pilot move the stationary swashplate, which the rotor shaft passes through without connection. The stationary swashplate is mated with the rotating swashplate that is connected to the rotor shaft and rotates with it. The rotating swashplate is also connected to each of the rotor blades by a pitch link, a slender structural element which converts deflection of the swashplate assembly into pitch control of each of the rotor blades. This is used to control the aerodynamic forces produced by the rotor, in order to control the aircraft. Translation of the swashplate along the rotor shaft (without tilting) changes the pitch angle of the rotor blades equally and is referred to as collective control, changing the thrust produced by the rotor. Tilting of the swashplate changes the pitch angle of each rotor blade according to its azimuthal position, and is referred to as cyclic control. It produces pitching and rolling moments that are transferred to the tiltrotor aircraft as a whole.

The stiffness of the rotor blades is of qualitative significance in the overall dynamics of the rotor. The stiffness is usually quantified indirectly in terms of the undamped natural frequency of the rotor blades. Each of the three motions discussed above has its own natural frequency that is a function of the geometry of the blade and its material properties, though the torsional natural frequency is usually of lesser importance due to it normally being significantly higher than the flapping and lead-lag frequencies. The lead-lag natural frequency is of particular importance in tiltrotor rotor dynamics. As these frequencies vary with rotor rotational speed, due to the centrifugal and aerodynamic loads that depend on the speed, it is most convenient to express the natural frequency as a multiple of the rotor speed, usually referred to as the "per-rev[olution]" frequency. A natural frequency higher than the rotor speed (with a per-rev frequency above 1) is referred to as "stiff", e.g. a "stiff in-plane" rotor refers to a rotor whose lead-lag natural frequency is higher than the rotor speed. For per-rev frequencies below 1, the term "soft" is used.

The aeroelastic behaviours of the two types of rotor are notably different. Soft in-plane rotors generally have less favourable stability boundaries, and are vulnerable to ground resonance and air resonance. For a stiff in-plane rotor, although air resonance is avoided, there is instead the issue of a coupled blade flap and lag instability. Additionally, a stiff in-plane rotor can result in high hub loads, encouraging the use of soft in-plane rotors with adequate lead-lag damping [105, 112]. While the maximum speed of the XV-15 tiltrotor is limited by power available, it is in-plane rotor loads that limit the maximum speed of the V-22 tiltrotor [93]. The design compromise of their blades – between the opposing requirements of efficient hovering and performance in high speed flight – precipitated the idea of variable diameter rotors [288].

Current tiltrotor designs typically feature gimballed hubs. The rotor blades, their pitch control mechanisms and a central connecting portion are all elastically restrained about their connection point to the rotor shaft, as shown in Figure 2.4. The lack of bearings allows a weight saving, with potential reliability and maintainability benefits [102]. The flapping motion is thereby replaced with hub tilt, and the practical elimination of the one-per-rev flapping lowers Coriolis-induced loads [134]. The use of a gimbal at the hub may have a destabilising effect on the rotor's dynamics however, as Carlson and Miao [134] found in their examination of the aforementioned Sikorsky Elastic Gimbal Rotor, where the addition of the gimbal further worsened the aeroelastic stability characteristics of the soft in-plane rotor by placing what they termed the "coupled cyclic flap/body and gimbal roll mode" (a combination of individual blade flapping, rigid body behaviour of the assumed airframe as a whole, and tilting of the rotor tip path plane via the gimballed hub) in near resonance with the regressive lag mode (the lower frequency blade lead-lag mode) at the normal rotor speed. In addition, the gimbal system also introduces an extra low frequency body mode which further restricts the placement of the operating rotor speeds.

2.1.3 Whirl flutter in tiltrotors

The whirl flutter instability is slightly more complex in the tiltrotor context than in the classical form in which it was originally studied. Classical whirl flutter strictly refers to a basic system with rigid blades and a rigid shaft, all of which is able to pitch and yaw elastically about an effective pivot point. It is a limited representation with correspondingly limited behaviour predictions, though it was sufficient for the purposes of the NASA 1960s work. The dynamics of a system more representative of a tiltrotor – one with flexible blades, a gimballed hub and a flexible wing – are fundamentally different, however. Only backward whirl (where the whirl is in the opposite direction to the rotor rotation) may be unstable in the classical case, whereas both backward and forward whirl are possible in the tiltrotor proprotor system. The manner in which the precession-generated aerodynamic loads act on the pylon/wing is significantly different to the classical case [71]. Motion-dependent in-plane forces are the most significant contributor to the instability [135], and the physical origin is coupling between these rotor in-plane forces and the wing torsion motion [183].

For these reasons, some works prefer to use the term “rotor-pylon instability” instead of “whirl flutter”, or to declare their focus to be “tiltrotor aeroelastic stability”. Kvaternik refers to it in his doctoral thesis [289] as "proprotor/pylon instability", though also says that it is "akin to [classical] whirl flutter". As the dynamic behaviours found in the course of this work all pose the same overall threat to the aircraft’s structure, the term “whirl flutter” is used here both in classical and tiltrotor contexts.

2.1.4 Nonlinearities in tiltrotors

Nonlinearities are present in virtually all real world engineering systems. They can arise in any element of a system and be active in one or more aspects of the system’s dynamics (e.g. stiffness, damping, etc.). Although this work focuses on structural nonlinearities, other particularly notable sources of nonlinearity include the aerodynamics and the control actuation systems. Nonlinearities may be caused by single physical mechanisms or accumulations of physical mechanisms in concert.

Some formal words on stiffness: the stiffness of a structure is the gradient of internal elastic restoring forces or moments with respect to the deflection. It is separate from the concept of strength. A structure with a higher gradient – that is, a steeper accrual of restoring forces/moments with growing deflection – is said to be a stiffer structure. For linear structural elements, one gradient exists for all deflection values and so the stiffness profile is simply a straight line, characterised by a single stiffness value: e.g. $F = Kx$ where F is the restoring force/moment, x is the deflection or deformation, and K is the stiffness and is a constant. However for nonlinear structures, the gradient will vary with deflection: $F = K(x)x$. An expression linking structural deflection to the restoring force/moment that results will hereafter be referred to as a *stiffness profile*. As described in the research objectives in Section 1.2, two types of nonlinear structural stiffness are smooth nonlinearities and hard nonlinearities, and these are discussed here.

2.1.4.1 Smooth nonlinearities

Smooth nonlinearities, as required by Objective O1, may arise in aerospace structures due to geometric nonlinearities. Material properties may also be a cause. Smooth nonlinear stiffness is categorised according to whether the structure offers increasing stiffness with growing deflection (hardening) or decreasing stiffness (softening). Woolston [28] gives some examples of where each might arise: a hardening effect is found when a thin wing, or perhaps a propeller, is subjected to increasing amplitudes of torsion, while a soft spring effect may be associated with panel buckling. The softening and hardening varieties of smooth nonlinearity are shown in Figure 2.6.

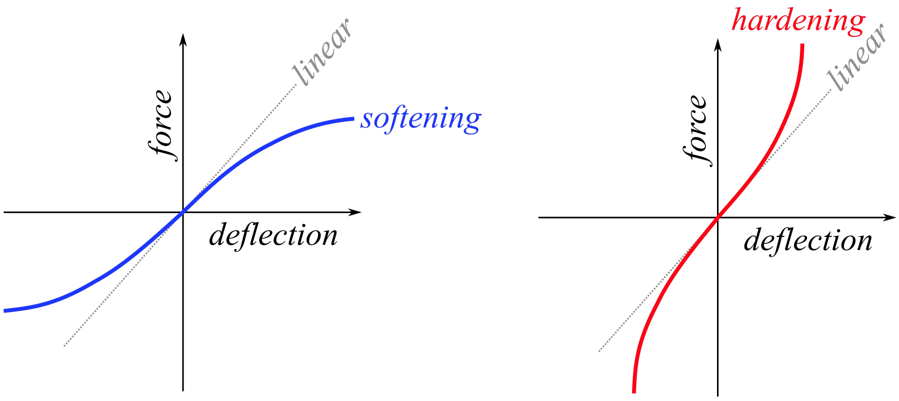

FIGURE 2.6. Types of smooth nonlinearities: softening *(left)* and hardening *(right)*

Low-order polynomials are commonly used for representing such smooth nonlinearities. They are frequently a better representation of stiffness profiles than linear examples as nonlinearities that may be negligible at low deflections can become significant at higher deflections. In tiltrotor whirl flutter oscillations, the deflections involved may well be too large for a linear stiffness profile to be assumed.

2.1.4.2 Hard nonlinearities

Hard nonlinearities, as required by Objective O2, cause gradient discontinuities in stiffness profiles. They usually arise from intermittency of contact in mechanical interfaces, causing point changes in stiffness as elements engage and disengage with each other. One example phenomenon is impacting, where one structural element strikes and bounces off a hard limit. Another example is freeplay, where an elastically-restrained structural element has a "deadband" of zero or highly reduced stiffness around the undeflected position. A relatable real world analogue is the behaviour of the steering mechanism in an old motor vehicle and the phenomenon is sometimes known simply as "play". A sample hard nonlinear profile is shown in Figure 2.7.

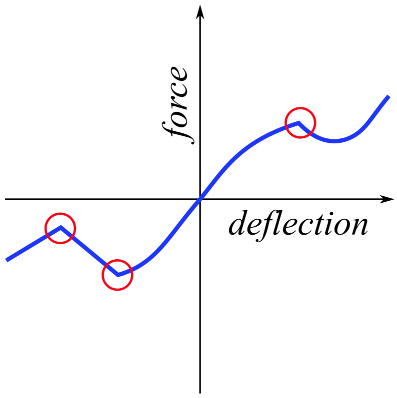

FIGURE 2.7. Overview of hard nonlinearities. The characteristic discontinuities are ringed with red

In order to fulfil their flight envelope, tiltrotor aircraft employ nacelle rotation actuators. These actuators are able to rotate each nacelle to any point between horizontal and vertical, and hold the nacelle there. Some illustrations of this mechanism within the surrounding wingtip-nacelle structure are shown in Figure 2.8.

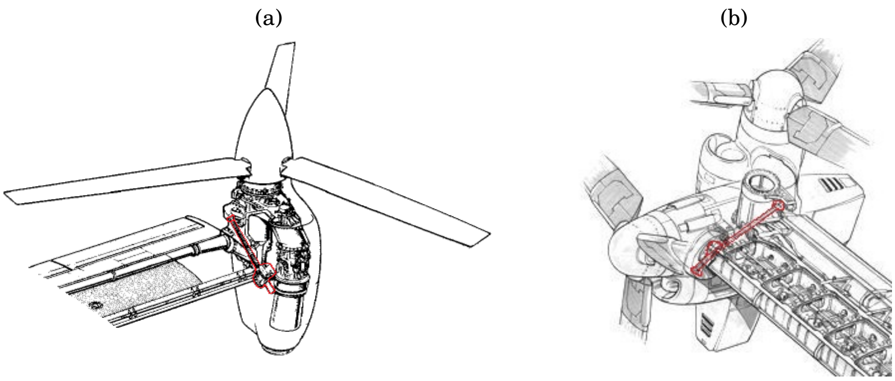

FIGURE 2.8. Nacelle tilting mechanisms (highlighted red) from (a) Bell XV-15[2] (b) Bell Boeing V-22[3]

The mechanism used is a two-stage telescopic ballscrew design [290, 291], driven by hydraulic motors. This choice of design was driven by a demanding set of requirements that not only specified particular loads to be withstood but also the ability to "operate after any single failure",

[2] Adapted from NASA: **https://upload.wikimedia.org/wikipedia/commons/e/e0/Bell_XV-15_tilt_rotor_research_aircraft.png**, public domain.

[3] Adapted from Flight Global: **https://i.pinimg.com/originals/f9/9c/e6/f99ce64a88027d6f894bdbaff2589707.jpg**, public domain.

have structural redundancy and produce as low a load on the power supplies as possible [290]. Other designs that were deemed unsuitable were hydraulic rams, single ballscrews and reduction gears.

The actuator undergoes a range of compressive and tensile axial loads within one operating cycle. For instance, at most nacelle angles, the actuator is in compression due to the weight of the nacelle and the thrust of the rotor. However in airplane mode, when the downstop preload is applied to hold the nacelle down to the wing, high tension loads are applied. Over time, this repeated cyclic loading may cause wear of the nacelle actuator components. Wear in general is the gradual removal or deformation of material from components in a mechanical system. While wear can cause the failure of mechanical systems, it is well known for causing freeplay. In aerospace design the freeplay of control surfaces such as ailerons is well studied. However, in the system at hand, wear of the end lug that attaches to the nacelle could cause this nacelle tilting actuator assembly to develop a degree of freeplay. The same effect could also be created through wear or damage of the housing trunnions that allow the actuator to fit into the wing end via split spindle arms (see Figure 2.9). Structural damage may cause freeplay deadbands to appear instantly, and freeplay oscillations themselves may directly cause their own deadband to grow, as shown by Padmanabhan [292].

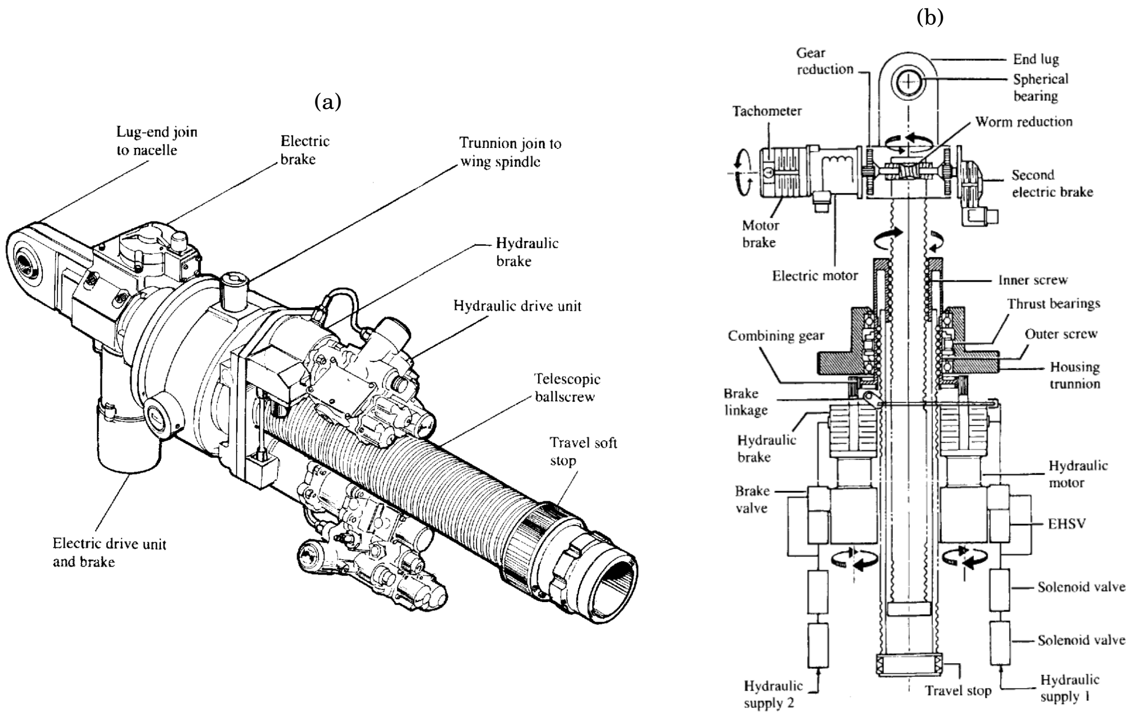

FIGURE 2.9. V-22 nacelle tilting actuation system. (a) Figure 6 from [290] (b) Figure 5 from [291]

Safi et al. [293] note from data they gathered that the ailerons of general aviation aircraft appear to accrue wear at approximately 0.6° per 1000 flying hours. Padmanabhan's investigation observed a much faster accrual of wear, with a 13-fold increase in the freeplay deadband width of a control surface in his investigation over 300 1-hour loading cycles [292]. Furthermore, while a standard industry model of wear depicts in-service wear as accruing at some steady linear rate, Padmanabhan found that the growth rate itself can increase with ongoing use, leading eventually to a runaway effect. If this same freeplay deadband growth rate occurred in the nacelle tilting actuator of a tiltrotor in regular operation, it would likely lead to unconservative estimates as to when to conduct appropriate maintenance. Freeplay in the nacelle tilting actuator is therefore not only a highly plausible eventuality, but also a significant threat to the tiltrotor aircraft in general.

2.2 Stability Analysis Methods

2.2.1 Dynamical systems

Dynamical systems generally fall into two classes according to the manner in which time evolves. Differential equations treat time as a continuous quantity, while iterated maps discretise time as a number of time steps [260]. While the equations that are dealt with in the present work are of the first kind, the concept of iterated maps is important in the formalisation of the stability of LCOs and the study of chaos, as will be discussed later. Continuous time systems are also known as *flows*. Within differential equations, the type of system this work uses are the ordinary differential equation type, as opposed to partial differential equations, as there is only one independent variable: time t. In this work, derivatives with respect to time use the well recognised "overdot" notation, e.g. $\frac{dx}{dt} = \dot{x}$. Furthermore, the systems are second order, as the highest derivative in the equation is the second time derivative $\frac{d^2}{dt^2}$. The equations may also be said to be autonomous (or time-invariant, or constant coefficient), as no part of the equations depends on the instantaneous value of time, and therefore the system's global dynamics are unchanged over time. This is consistent with the physics of the rotor-nacelle systems that will be modelled. The system of differential equations is of the form:

$$\frac{d}{dt}\mathbf{y}(t) = \dot{\mathbf{y}}(t) = \mathbf{f}(\mathbf{y}(t)) \tag{2.1}$$

where $\mathbf{f}$ is the system of ordinary differential equations and $\mathbf{y}$ is the state vector, composed of the n system states, the quantities that comprise the system and whose evolution in time is of interest. Such a system is said to be n-dimensional. As the equations used in this work describe mechanical systems, the states of the system are the position and velocity of each degree of freedom or generalised displacement, leading to the following relationship between the state vector $\mathbf{y}$ and the vector of degrees of freedom $\mathbf{x}$:

$$\mathbf{y} = \begin{bmatrix} \mathbf{x} \\ \dot{\mathbf{x}} \end{bmatrix} \tag{2.2}$$

Furthermore, the states are all real-valued: $\mathbf{y} \in \mathbb{R}^n$. Time histories of the system $\mathbf{y}(t)$ that satisfy the system of differential equations $\mathbf{f}$ are said to be *solutions* of the equations.

Two common solution types are fixed points and periodic solutions. A fixed point, also known as an equilibrium, is a system state $\mathbf{y}^*$ at which the system will remain motionless for all time:

$$\mathbf{f}(\mathbf{y}^*) = \mathbf{0} \quad \Rightarrow \mathbf{y}(t) = \mathbf{y}^* \tag{2.3}$$

for all t. Periodic solutions are trajectories that are closed in the phase space, forming loops. They therefore repeat with some period T:

$$\mathbf{y}(t) = \mathbf{y}(t+T) \tag{2.4}$$

A particular type of periodic solution is the Limit Cycle Oscillation (LCO). It is an isolated trajectory, as neighbouring trajectories are not closed like the LCO is, and they either approach the limit cycle or tend away from it [260]. LCOs are unique to nonlinear systems. Linear systems may experience ordinary periodic solutions, though they occur as infinitely large concentrically-nested families of such trajectories all with the same shape but varying continuously in amplitude. When solved numerically in time simulations, the motion is completely defined by the initial conditions used. This result can be deduced by theory concerning solutions to linear ODEs: if a trajectory $\mathbf{y}(t)$ is a solution to a system, then so is $c\mathbf{y}(t)$ for any constant c [260]. A schematic diagram of this phenomenon in an arbitrary phase plane (y_1, y_2) is shown in Figure 2.10.

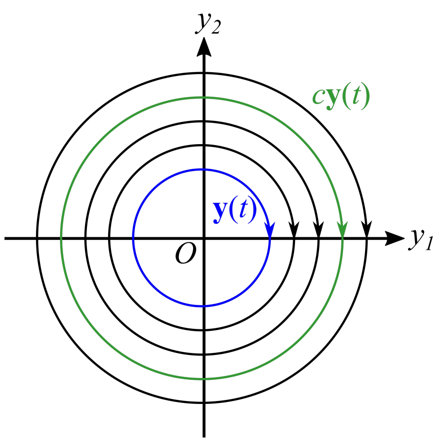

FIGURE 2.10. Schematic diagram of concentrically nested linear periodic solutions

There also more complex types of solutions. For instance, periodicity may be achieved by a combination of solution components with different but commensurate periods (forming a rational ratio). If the periods are incommensurate, then quasi-periodic solutions are formed as their trajectories in the phase space do not close. A relatively recent addition to the field of nonlinear dynamics is the ever-developing understanding of chaos: superficially random motion with a complex underlying structure. Chaos typically exists in certain parametric regions, rather than globally, and there are several mechanisms by which it may come about.

The geometrical approach[4] to dynamical systems involves viewing the system in an n-dimensional space known as the *phase space*, where each of the space's dimensions represents one of the system's n states. The instantaneous state of the system at any point in time is therefore represented as a point in the phase space, whose instantaneous coordinates are the instantaneous values of each of the states. This point is known as the *phase point*. The concepts of the phase space and phase point are demonstrated in Figure 2.11, part (a).

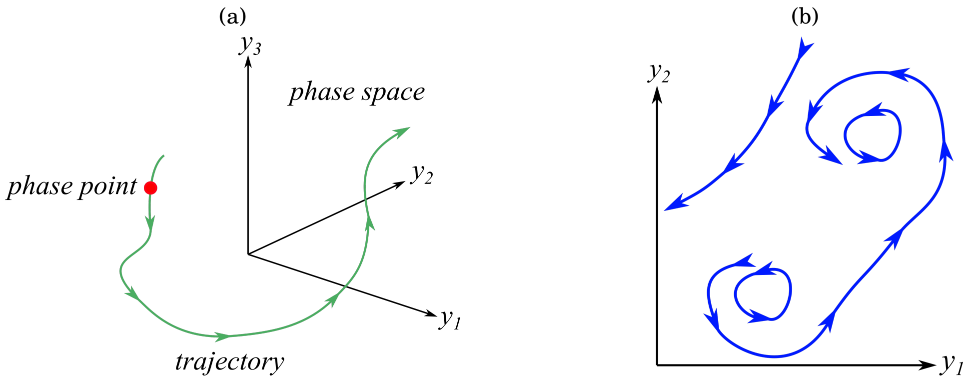

FIGURE 2.11. Illustrations of (a) a phase space with a phase point, and (b) a phase portrait. The states of the system are denoted y_i, $i \in 1,2...$

The evolution in time of a phase point starting at an arbitrary initial point (its initial conditions) will trace out a curve through the phase space, known as a trajectory or an orbit in some texts. The phase space is filled with trajectories which together pass through all points. The differential equations of motion dictate how the system evolves in time and they construct a vector field[5] within the phase space. In order for the equations of motion to define one and only one output for any arbitrary current state of the system, they must abide by the existence and uniqueness theorem, which specifies that if $\mathbf{f}$ and all its partial derivatives $\frac{\partial f_i}{\partial x_j}$, $i, j \in 1,2...n$ are continuous (smooth) in some open real-valued connected set, then all points in that set are each part of one unique solution to the system in time [260]. As a result of this theorem, the trajectories

[4] The French mathematician Henri Poincaré (1854–1912) is widely held to be the father of this approach. Another key aspect of his point of view was to ask qualitative questions of dynamical systems rather than quantitative ones, such as the nature of a system's long term behaviour (e.g. stable or divergence to infinity) rather than the exact state of the system at all times [260].

[5] Vector field: a space in which each point is assigned a vector. Here the vectors represent the rate of change of the system in all states, at each point, as defined by the equations of motion.

do not cross anywhere in the phase space. The phase space and motion of the phase point can be represented in a reduced level of detail using a phase plane, where two of the system's states are selected for the axes of a 2D projection of the phase space. A phase portrait is a particular kind of phase plane where a number of qualitatively different trajectories are displayed or sketched to demonstrate the variety of dynamical behaviours present in a system. An example illustration is given in Figure 2.11, part (b).

In this work, the computational implementations of the models to be used are constructed in MATLAB R2015a [294]. This choice is based on its availability, thorough documentation and prior experience of its use. Time simulations were generated using the inbuilt `ode45` numerical ordinary differential equation solver, which implements an explicit Runge-Kutta (4, 5) formula, the Dormand-Prince pair [295]. Solvers of this kind iteratively find numerical solutions in the time domain to ordinary differential equations. Discretising the desired time span into a number of steps, the `ode45` solver is able to adapt the time step size used at each point based on error tolerances specified. It offers good speed of computation and as the system type studied in this work does not feature stiff equations[6], this solver is a suitable choice.

2.2.2 Stability

Stability in the context of dynamical systems refers to the long-term tendency of the system (i.e. $\mathbf{y}(t)$ as $t \to \infty$) in reference to a given solution. As stability is related to how the amount of energy in a system changes over time, an important concept relating to stability is *damping*, which refers to mechanisms by which activity of a system causes energy to be bled from it. Damping can also be negative, where energy flows into the system instead of out. Periodic solutions in linear systems only exist if the system is both conservative (i.e. there is no damping) and autonomous. In nonlinear systems, damping is a function of both the system parameters and the system state. In autonomous physical systems, LCOs depict self-sustained oscillations [261], such as shimmy in tyres or self-exciting radio transmitters.

Solutions of all types have an associated stability, which qualifies whether the system, when in the near vicinity of that solution, will converge upon it or diverge away from it. Equivalently, it is a qualitative measure of the system's response to a perturbation away from that solution. An intuitive example for the fixed point case is a rigid pendulum: while both the vertically down and vertically up positions are fixed points at which the pendulum may rest, the former is stable and the latter unstable, in view of the behaviour that will follow any perturbation. If there is no tendency of either kind, the solution is said to be neutrally stable.

Based on this tendency, stable solutions may be said to be *attracting* while unstable ones

[6] Stiff equations: ODEs that demand unusually small timestep sizes even in very smooth regions of the solution curve.

may be said to be *repelling*. In addition to the basic definition, there are several more nuanced theoretical notions of stability. One notion is essentially linked to the perturbation size. While a given solution may be stable in response to small perturbations away from the solution in question, making it locally stable, the same may not be true for larger perturbations. This separates the concepts of local and global stability [260]. Mathematically speaking, all flows in the phase space approach a globally stable solution, allowing it to be reached from any initial conditions.

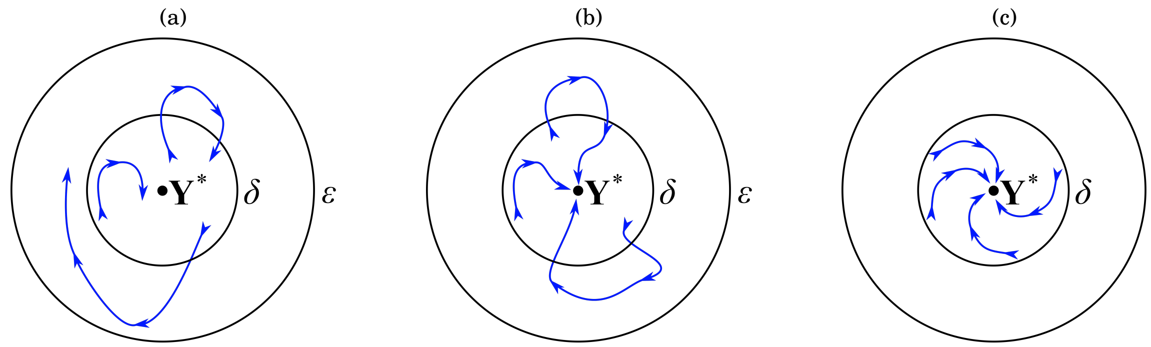

FIGURE 2.12. Three types of fixed point stability: (a) Lyapunov stability, (b) asymptotic stability, and c) exponential stability

The behaviour of flows that pass near fixed point solutions is another distinguishing notion [261]. The following classification of fixed point stability types has been adopted within the study of dynamical systems. The term $\mathbf{y}(0)$ indicates the state vector at $t = 0$, and the three stability types are illustrated in Figure 2.12.

- If all trajectories that start sufficiently close to a fixed point remain close to it for all time, the fixed point is said to be *Lyapunov*[7] *stable*. In mathematical language, if for every neighbourhood $\epsilon > 0$ of the fixed point $\mathbf{y}^*$, there exists a smaller neighbourhood $\delta > 0$ contained within ϵ such that every trajectory starting within δ remains within ϵ for all time, i.e. if $|\mathbf{y}(0) - \mathbf{y}^*| < \delta$ then $|\mathbf{y}(t) - \mathbf{y}^*| < \epsilon$ for all $t \geq 0$.

- Additionally, if a Lyapunov stable fixed point has all nearby trajectories eventually converge upon it (though they need not converge upon it monotonically), it is said to be *asymptotically stable*: i.e. in addition to the above conditions, if all trajectories starting within δ fulfil the condition $\lim_{t\to\infty} |\mathbf{y}(t) - \mathbf{y}^*| = 0$.

- An even stronger condition, *exponential stability* describes an asymptotically stable fixed point whose trajectories converge not only monotonically but at least as fast as some

[7] Aleksandr Mikhailovich Lyapunov (also spelt "Liapunov" in texts such as Strogatz [260]), 1857–1918. The concept of Lyapunov stability as defined above was first presented in Lyapunov's doctoral thesis of 1892, titled *The General Problem of the Stability of Motion*.

particular known rate $\alpha|\mathbf{y}(0)-\mathbf{y}^*|e^{-\beta t}$. In formal mathematical language: if there exists $\alpha > 0$ and $\beta > 0$ such that if $|\mathbf{y}(0)-\mathbf{y}^*| < \delta$, then $|\mathbf{y}(t)-\mathbf{y}^*| \leq \alpha|\mathbf{y}(0)-\mathbf{y}^*|e^{-\beta t}$.

Structural stability refers to how phase portraits respond to perturbations to the equations[261]. If the phase portrait's topology[8] cannot be changed by an arbitrarily small perturbation, such as the introduction of damping, then it is said to be structurally stable. Two phase portraits have the same topology if one can be stretched or warped into the other through a continuous one-to-one mapping[9] [259], without tearing or fusing. Some authoritative texts on dynamical systems and their study that are referred to here are Strogatz [260], Thompson and Stewart [261] and Kuznetsov [259].

Stable solutions, also known as attractors, have around them some neighbourhood in the phase space in which all trajectories converge upon that stable solution. That is, a flow passing through any point within this neighbourhood will converge upon the stable solution. This neighbourhood is known as a *basin of attraction*.

Stability analyses calculate the stability characteristics of a solution or an overall system, and in this sense stability can be both a quantitative matter and a qualitative one. Eigenvalue analysis is a dedicated stability analysis framework for linear systems as it simply uses components of linear systems theory, however it is in some circumstances incompatible with the nuances of nonlinear systems. CBM, a toolkit of methods and theory, is potentially more computationally expensive though it has the important ability of being able to find the new solutions created by the nonlinearities.

2.2.3 Eigenvalue analysis

2.2.3.1 Application to linear systems

Linear systems have one global stability characteristic that eigenvalue analysis finds, as opposed to individual solutions having their own stability characteristic. Assume an autonomous n-dimensional linear dynamical system of the continuous-time type whose equations of motion may be written as a flow (as opposed to a mapping) in the following matrix form that is typical of mechanical systems:

$$\mathbf{M}\ddot{\mathbf{x}} + \mathbf{C}\dot{\mathbf{x}} + \mathbf{K}\mathbf{x} = \mathbf{0} \tag{2.5}$$

where $\mathbf{x}$ is the vector of m degrees of freedom of the system with $\mathbf{x} \in \mathbb{R}^m$, $m = \frac{n}{2}$ and $\mathbf{x} = \mathbf{x}(t)$, over-dots indicate derivatives taken with respect to time t, and $\mathbf{M}$, $\mathbf{C}$ and $\mathbf{K}$ are the mass, damping

[8] Topology here refers to the qualitative form or structure of the phase portrait, defined by general features and their connectivity rather than specific dimensions.

[9] Mapping: a morphism that transforms one set into another.

and stiffness matrices respectively. The matrices are m-by-m square matrices with real-valued elements constituted of the various system parameters. The system's equations can be written instead in the form:

$$\dot{\mathbf{y}} = \mathbf{J}\mathbf{y} \tag{2.6}$$

where $\mathbf{y} = \begin{bmatrix} \mathbf{x} \\ \dot{\mathbf{x}} \end{bmatrix}$ and $\mathbf{J}$ is known as the Jacobian matrix, which may be expressed in terms of the matrices $\mathbf{M}$, $\mathbf{C}$ and $\mathbf{K}$:

$$\mathbf{J} = \begin{bmatrix} \mathbf{0} & \mathbf{I} \\ -\mathbf{M}^{-1}\mathbf{K} & -\mathbf{M}^{-1}\mathbf{C} \end{bmatrix} \tag{2.7}$$

The Jacobian matrix is useful as – providing it is diagonalisable (i.e. it can have its eigenvalues determined) – the general solution for $\mathbf{y}(t)$ is a function of its n eigenvectors and eigenvalues:

$$\mathbf{y}(t) = \sum_{k=1}^{n} (\mathbf{l}_k \cdot \mathbf{y}_0)\mathbf{r}_k e^{\lambda_k t} \tag{2.8}$$

where $\mathbf{l}_k$ are $\mathbf{J}$'s left eigenvectors, $\mathbf{r}_k$ are $\mathbf{J}$'s right eigenvectors and λ_k are the corresponding eigenvalues. If the Jacobian cannot be diagonalised it is said to be a defective matrix, which occurs when its eigenvectors are not linearly independent. In this case, the Jordan normal form of the Jacobian can be found, which is a matrix with the same properties and with the eigenvalues on the leading diagonal [296].

The eigenvalues are sometimes referred to as "roots" as they are the roots of the system's characteristic polynomial, given by $\det(\mathbf{J} - \lambda\mathbf{I})$. In a linear system, these eigenvalues and their corresponding eigenvectors describe the system's *modes*: isolated motions of which any response of the system is a linear combination. These modes have the property that if the system is given a perturbation composed solely of one particular mode, its response will also contain only that mode. While Equation (2.8) usefully gives the exact state of the system at any t, it also implies the asymptotic behaviour of the system, i.e. its stability. It is a function solely of the exponential component of each term, specifically the eigenvalues λ_k. The eigenvalues may be complex and therefore the k^{th} eigenvalue λ_k can be written as the sum of real and imaginary parts:

$$\lambda_k = \alpha_k + i\beta_k \tag{2.9}$$

where i is the imaginary constant. If $\beta_k \neq 0$ then λ_k and its complex conjugate (one of the other eigenvalues) will pertain to an oscillatory motion. If $\beta_k = 0$ then λ_k will by itself pertain to a monotonic first-order motion where the mode is non-oscillatory. In this case, the real part α_k determines the amplitude evolution over time, with $\alpha_k < 0$ causing a decay to 0 and $\alpha_k > 0$ causing

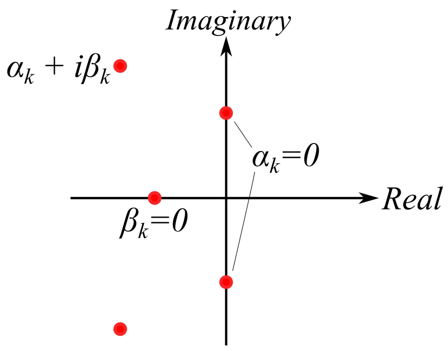

FIGURE 2.13. Argand diagram with example eigenvalues

a "blow-up" to infinitely large values. These behaviours may be called "stable" and "unstable", respectively. It is common to display such roots on an Argand diagram. An example eigenvalue plot on an Argand diagram is shown in Figure 2.13.

Furthermore, the only fixed point in a linear system is **0**, to which the decay or divergence of each eigenvalue is in relation. The response types discussed above are sketched in Figure 2.14. The knife-edge case of $\alpha_k = 0$ may be called "neutral stability" and for periodic solutions pertains to a constant amplitude of oscillation. For fixed points, the range of behaviours in the case of neutral stability may not be illustrated succinctly using the kind of diagram used in Figure 2.14 though very broadly speaking the system remains still if it is placed on the eigenvector corresponding to the zero eigenvalue.

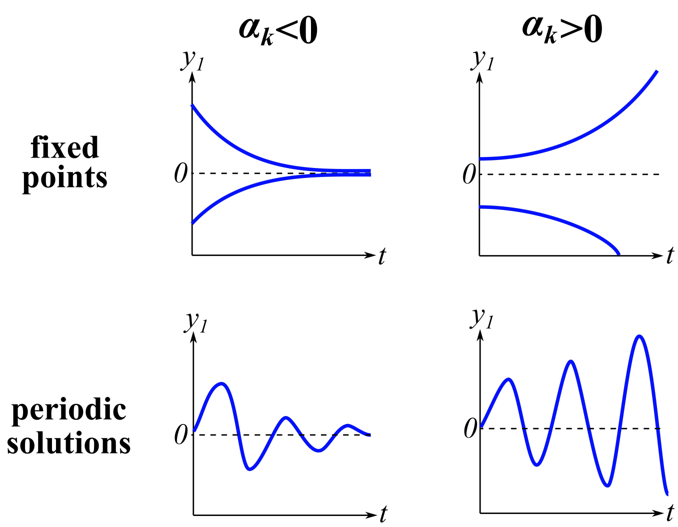

FIGURE 2.14. Sketches of response types of linear systems. The columns are organised according to stability characteristic (unstable - stable) and the rows according to the solution type (fixed point - oscillatory solution). Two responses are shown for each fixed point case

The stability of the system may therefore be viewed solely in terms of the real parts of its eigenvalues, and an eigenvalue with a positive real component may be called an unstable root. Inspection of Equation (2.8) shows clearly that only one of the n solution components needs to be unstable for the system as a whole to be unstable, i.e. one unstable root is sufficient.

Two important modal characteristics may be obtained from each eigenvalue's α_k and β_k and each of the system's n modes has associated with it an individual value for both. For the k^{th} mode, the damping ratio ζ_k captures the rate of amplitude change of that mode, as previously described, while the natural frequency ω_k gives the undamped (i.e. underlying) modal frequency. However, the damped frequency at which the oscillation actually occurs is a function of both ω and ζ. These characteristics are defined thus:

$$\zeta_k = \frac{-\alpha_k}{\omega_k} \tag{2.10}$$

$$\omega_k = \sqrt{\alpha_k^2 + \beta_k^2} \tag{2.11}$$

This set of methods will be used to calculate the overall system stability of the original linear version of the two rotor-nacelle models used in this work. For ease of reference, particularly when comparisons with CBM need to be made, the application of eigenvalue analysis to fixed point branches in order to determine the system's whirl flutter stability is termed *linear analysis*.

2.2.3.2 Eigenvectors and modeshapes

An oscillatory mode consists of a sinusoidal oscillation in all states at a frequency determined by the relevant eigenvalue's magnitude. The actual shape of the mode in terms of the system's states is encoded in each mode's right eigenvector $\mathbf{r_k}$, a vector the same size as the system's state vector whose components each pertain to the corresponding system state in the state vector in an element-wise fashion. In the systems that are studied in this work, the oscillatory modes not only have a complex eigenvalue but also a complex associated eigenvector. When these complex eigenvector components are plotted on an Argand diagram, their control of the modeshape becomes clear. Specifically, the relative magnitudes and the relative arguments of these eigenvector components are key. If the i^{th} component of $\mathbf{r_k}$ is notated $\mathbf{r_{k,i}}$, then its magnitude $|\mathbf{r_{k,i}}|$ and argument $\angle\mathbf{r_{k,i}}$ are:

$$|\mathbf{r_{k,i}}| = \sqrt{\mathrm{Re}(\mathbf{r_{k,i}})^2 + \mathrm{Im}(\mathbf{r_{k,i}})^2} \tag{2.12}$$

$$\angle\mathbf{r_{k,i}} = \tan^{-1}\left(\frac{\mathrm{Im}(\mathbf{r_{k,i}})}{\mathrm{Re}(\mathbf{r_{k,i}})}\right) \tag{2.13}$$

The relative magnitudes of the eigenvector components determine the relative amplitudes of the corresponding states' participations in the given mode, and the relative arguments between the various eigenvector components shows the phase difference between each state's time history. An alternative perspective is to view the mode shape as rotating: the set of eigenvectors rotates around the origin at the frequency dictated by the corresponding eigenvalue, and the value of each state at any given moment is given by the projection of the corresponding component onto one of the axes; the choice of axis is irrelevant as long as it is consistent across all states. This relationship is shown in an arbitrary context for a system with 3 states and neutral damping with an eigenvector $\mathbf{r_k}$ in Figure 2.15.

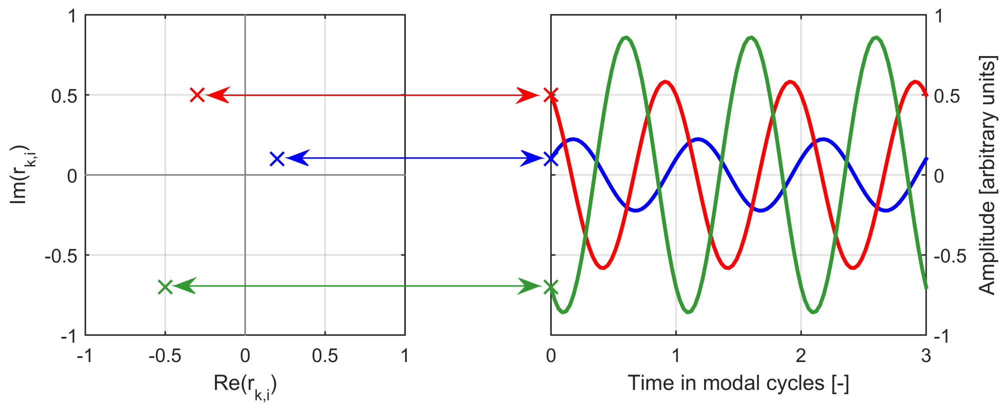

FIGURE 2.15. Relationship between eigenvector components and the time histories of their corresponding states, with damping excluded, in linear systems

2.2.3.3 Application of eigenvalue analysis to nonlinear systems

A model that has been derived with nonlinear terms in its equations may be linearised (i.e. manually made linear) to allow eigenvalue analysis to be conducted. This may be achieved by stipulating conditions under which the nonlinear terms may be neglected. For example, the model might be declared applicable only for numerically small values of its states, which in a dynamical system might pertain to small angles or small deformations. This way, small angle assumptions such as $\cos\theta \approx 1$ and $\sin\theta \approx \theta$ may be applied, and polynomial terms of states of order 2 and higher may be small enough to neglect. Nonlinear terms are then removed manually from the equations, leaving a linear system to which the eigenvalue analysis may be applied as described above.

However eigenvalue analysis can still be applied to nonlinear systems, which are markedly different to linear systems in a number of fundamental ways. They may contain LCOs, and fixed points away from $\mathbf{0}$. Furthermore, the system no longer has one single stability characteristic that is a function of the system parameters alone and does not depend on the system state. Each solution now has associated with it a stability characteristic, and therefore eigenvalue analysis must be applied on a solution by solution basis, by linearising specific fixed point solutions to find their stability. Such a nonlinear system takes the form of:

$$\dot{\mathbf{y}} = \mathbf{f}(\mathbf{y}) \tag{2.14}$$

where $\mathbf{f}$ is some nonlinear vector function operating on the elements of the state vector $\mathbf{y}$. The local linearisation of the system at a fixed point of interest is sometimes referred to as the underlying linear system. Geometrically speaking, it is the multivariate (n-dimensional) gradient at the fixed point within the vector field of the system's equations and the stability of the fixed point is therefore assessed using a linear approximation of the system's dynamics there [260, 261]. If $\mathbf{y}^*$ is a fixed point then

$$\boldsymbol{\eta}(t) = \mathbf{y}(t) - \mathbf{y}^* \tag{2.15}$$

is a perturbation away from that fixed point. The linearisation at the fixed point is obtained by expanding a Taylor series of the system's equations about the fixed point:

$$\mathbf{f}(\mathbf{y}^* + \boldsymbol{\eta}) = \mathbf{f}(\mathbf{y}^*) + \frac{\partial \mathbf{f}(\mathbf{y}^*)}{\partial \mathbf{y}}\boldsymbol{\eta} + O(\boldsymbol{\eta}^2) \tag{2.16}$$

where $\mathbf{f}(\mathbf{y}^*) = \mathbf{0}$ by definition, $O(\boldsymbol{\eta}^2)$ denotes small terms in $\boldsymbol{\eta}$ of quadratic order and above which are ignored due to their small size, and $\frac{\partial \mathbf{f}(\mathbf{y}^*)}{\partial \mathbf{y}}$ is the operation

$$\frac{\partial \mathbf{f}}{\partial \mathbf{y}} = \begin{bmatrix} \frac{\partial f_1}{\partial y_1} & \cdots & \frac{\partial f_1}{\partial y_n} \\ \vdots & \ddots & \vdots \\ \frac{\partial f_n}{\partial y_1} & \cdots & \frac{\partial f_n}{\partial y_n} \end{bmatrix} \tag{2.17}$$

evaluated at the fixed point $\mathbf{y}^*$. This leaves

$$\mathbf{f}(\mathbf{y}^* + \boldsymbol{\eta}) = \frac{\partial \mathbf{f}(\mathbf{y}^*)}{\partial \mathbf{y}}\boldsymbol{\eta} \tag{2.18}$$

The term $\frac{\partial \mathbf{f}(\mathbf{y}^*)}{\partial \mathbf{y}}$ is the nonlinear system's Jacobian matrix $\mathbf{J}$. It must be evaluated at each point of interest and the indications given are only valid in a small neighbourhood about that point. While $\mathbf{J}$ might be obtained directly through partial differentiation of the equations of motion, in some cases it may be quicker to calculate it numerically by applying a small perturbation in each state, evaluating $\mathbf{f}(\mathbf{y})$ and thereby calculating the linear gradient associated with each. The same eigenvalue analysis detailed above is applied to this Jacobian to obtain stability information. There are still cases where linearisation fails, when the method produces the zero matrix $\mathbf{0}$ and is thereby inconclusive. These cases occur when the $O(\boldsymbol{\eta}^2)$ terms are not negligible [260] and therefore it is unsuitable to assume that a linear representation of the local dynamics is sufficient.

This method will be used to calculate the local stability of the fixed point solutions found in the nonlinear versions (both soft and hard nonlinearity variants) of the two rotor-nacelle models used in this work. The stability of LCOs is calculated using a related linear method, though as it falls within the "toolbox" of CBM, it is discussed in the following section.

In linear systems, behaviour and therefore stability is solely a function of parameters rather than the state vector. In other words, one global stability characteristic alone exists for a given parameter value set, and therefore in linear systems depicting tiltrotor aeroelastic stability, this Jacobian eigenvalue analysis is all that must be considered to predict where whirl flutter exists. In nonlinear systems however, nonlinearities may not only create non-trivial additional solutions, but can also cause them to exist over ranges of parameter values. In the current context, LCO solutions constitute whirl flutter behaviour, and may exist in parameter regions that the foregoing fixed point analysis declares to be stable, resulting in incorrect predictions from the eigenvalue analysis. CBM can be used instead to prevent such solutions going undetected.

2.2.4 Continuation and Bifurcation Methods

Broadly speaking, there are two stages to the full application of CBM to a problem: (1) the finding of the steady state numerical solution values via the process of continuation, and (2) the application of bifurcation theory to the results. Continuation, or parameter continuation as it is more formally known, is a numerical technique for computing implicitly defined manifolds[10] [297]. Here, these manifolds are the solutions to the differential equations that constitute the various tiltrotor aeroelastic models under study. Key junctions between solution manifolds, where the solution changes stability or qualitatively changes type (i.e. bifurcations), may then be classified according to the canon of bifurcation theory. The output of the whole process is bifurcation diagrams that typically show the numerical values of solutions as a system parameter is varied, along with any bifurcations encountered. Where the solutions form continuous curves between the bifurcations, they are generally referred to as *solution branches*, and they can exist in both fixed point/equilibrium and LCO types.

2.2.4.1 Solution value finding

Continuation finds solutions to problems of the form:

$$\mathbf{f}(\mathbf{y}, \lambda) = \mathbf{0} \tag{2.19}$$

where $\mathbf{f}$ is a (sufficiently smooth) system of nonlinear equations. Here they comprise the model, $\mathbf{y}$ is the state vector as before and λ is some system parameter(s) of interest. Essentially all continuation packages are based on predictor-corrector methods with slight variations [259]. An

[10] A manifold is the n-dimensional generalisation of a surface. Implicit definition does not give a closed form for the manifold but rather some indirect expression(s) which hold true for the manifold.

initial solution $\mathbf{y}_0$ is required, from which the set of solutions is added to, or "continued". The initial solution may be obtained either analytically through mathematical reasoning applied to knowledge of the system's behaviour and/or properties, or through the use of a time simulation that allows the system to converge upon a stable solution of either the fixed point or periodic type. Though the latter method does not strictly find the exact values of the solution in question, the longer the simulation, the closer the system will be to that solution at the end of the simulation. Using a direction vector $\mathbf{y}'_0$ given by $\mathbf{y}'_0 = \frac{d\mathbf{y}}{d\lambda}$, and a parameter increment $\Delta\lambda$ defining the step size between this starting solution and the next solution point $\mathbf{y}_1$ that is being solved for, Newton's method is used to obtain convergence of the next solution point, providing the parameter increment is small enough. The process is then repeated for each new solution point to construct solution branches as described above.

For the continuation of periodic solution branches, equations can be set up in the form of boundary value problems. This involves discretising the LCO into a set of mesh intervals and then threading piecewise polynomials through a set of collocation points on each mesh interval. Although single parameter continuation has been described here, continuation can be conducted in more than one parameter at once. Three main types of continuation method that have seen much use are listed here:

- **Natural parameter continuation** is the most basic iterative case. In the limit the iteration approaches a solution of Equation (2.19) and the solution at one value of the continuation parameter is used as the initial guess for the next parameter point under evaluation. It is the simplest form of continuation although it cannot negotiate turning points of the solution branch, where the branch folds back upon itself in the continuation parameter axis.
- **Simplicial/piecewise linear continuation** uses $(n-1)$-dimensional simplexes[11] in the n-dimensional parameter-solution space, finding the unique linear interpolant in each and testing if it takes on the value 0 at any point inside the simplex and thereby satisfying $\mathbf{f}(\mathbf{y},\lambda) = \mathbf{0}$. While the method is simpler to visualise than the other two listed here, producing an efficient computational implementation of the method is significantly more complex than the basic statement of the method.
- The **pseudo-arclength method** parametrizes the solution curve with arclength rather than the value of the continuation parameter(s) and is thereby able to follow the solution branch around turning points. In addition to the system equations, the solution of each point solves an equation involving this arclength:

$$\mathbf{f}(\mathbf{y_1},\lambda_1) = \mathbf{0} \tag{2.20}$$

[11] Simplex: the n-dimensional generalisation of a triangle or tetrahedron.

$$(\mathbf{y}_1 - \mathbf{y}_0)\mathbf{y}'_0 + (\lambda_1 - \lambda_0)\lambda'_0 - \Delta s = 0 \tag{2.21}$$

where λ'_0 is the parameter component of the direction vector, λ_0 and λ_1 are the continuation parameter values at the current and next points respectively, and Δs is the increment of arclength along the solution curve [298].

The continuation package used in this work uses the last approach, the pseudo-arclength method. The other features of the package are described in Section 2.2.4.5.

2.2.4.2 Stability analysis

Once the solution values have been found, their stability may be assessed. Here, linear stability analysis is acceptable, as the solution of interest – wherever in the parameter space it may exist – has already been found. For fixed points, linearisation is employed at the solution point of interest, followed by an eigenvalue analysis of the resulting Jacobian matrix, as detailed in Section 2.2.3.3.

The assessment of periodic solution stability requires the application of Floquet[12] theory [299], which treats a periodically repeating motion in the phase space as a stroboscopic phenomenon at a single point through which it passes. Instead of considering the whole trajectory of the LCO within the n-dimensional phase space, an $(n-1)$-dimensional plane is placed at some point along the trajectory such that it is transverse[13] to the LCO at the point of intersection and to all other trajectories that intersect it. This plane is known as a Poincaré section and the concept is illustrated schematically for an arbitrary 3-state system in Figure 2.16.

In a sufficiently small neighbourhood of the phase space near the original LCO, nearby trajectories behave similarly to the LCO in that they too loop around in the phase space to re-join S from the other side. Unlike the LCO however, they do not re-join S at exactly the same point that they departed. The use of this plane therefore transforms the system from a continuous-time system to an iterated mapping: the trajectory emanating from an arbitrary point $\mathbf{y_a}$ on the Poincaré section S can be traced around in the phase space (blue line) using numerical integration of the system equations until it intersects S once again at $\mathbf{y_b}$, known as its *first return*. The group of mappings of all points on S, from S to itself, is known as the *Poincaré map*, an iterated mapping in discrete time. As the LCO in question (green) is a closed trajectory, its intersection point with S maps to itself on S and is therefore a fixed point of the Poincaré map, notated $\mathbf{y}^*$.

[12] Achille Marie Gaston Floquet, 1847–1920, is known mostly for his contributions to the theory of differential equations.

[13] The plane does not need to be orthogonal to any of the trajectories passing through it, but rather not parallel.

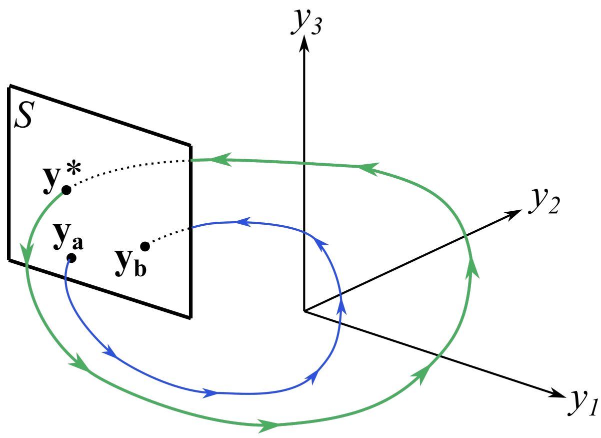

FIGURE 2.16. Schematic representation of a Poincaré section in an arbitrary 3-dimensional phase space

Floquet theory finds the stability of the LCO by measuring the tendencies of its nearby trajectories according to their first return on the Poincaré section. If a Poincaré section S is defined via one of the states (say y_1) as $y_1 = C$, where C is the value of the y_1 state at a point on the LCO trajectory where the Poincaré section is desired to be placed, then a small perturbation about the fixed point is applied in each of the remaining states in turn. The state values of each of the first return points constructs the *first return matrix*, known also as the *monodromy matrix*.

This approach linearises the dynamics of the LCO within a small neighbourhood of its intersection point with S, as this monodromy matrix is used as the Jacobian matrix of the iterated map's fixed point, which is an analogue for the stability of the LCO as a whole. Floquet theory further specifies that the monodromy matrix has the property that the above process can be performed for any point on the LCO with the same results obtained. Eigenvalues are taken of this matrix, which contain stability information, though here they are referred to as Floquet multipliers. One Floquet multiplier is always 1, which is the trivial indication that the trajectory at the intersection point with S is parallel to the LCO. While a positive real part is of significance in the eigenvalue analysis of fixed points, it is magnitude in excess of unity that has corresponding significance in Floquet analysis. The indication of the LCO's stability is the value of any of the real Floquet multipliers: any real multipliers with a magnitude above 1 indicate instability of the LCO under analysis.

The use of a Poincaré section is not restricted to the stability analysis of LCOs. They are also highly effective for uncovering the underlying structure of chaotic motions: a system can be simulated for a long period of time, allowing a pattern of intersections to build up on an appropriately positioned Poincaré section.

2.2.4.3 Bifurcation detection

While solution branches mostly vary smoothly with changes in the continuation parameter(s), junctions between branches and other non-smooth features occur at bifurcations, where the solution changes stability or type. Alternatively, there is no continuous one-to-one mapping of the phase portraits of the system either "side" of the bifurcation. Bifurcations may be categorised broadly according to the extent of the phase space that they affect. Local bifurcations such as the Hopf bifurcation affect only a single point, while global bifurcations affect swathes of the phase space and involve the creation, destruction or qualitative change of attractors within the phase space. Some bifurcations may be seen as a hybrid of the two categories, involving a "catastrophic" local bifurcation whose full repercussions depend on the system in which they occur. Some bifurcations that are common to the type of system studied by this work are listed here:

- **Fold bifurcation** - a fixed point solution branch changes direction on the continuation parameter axis, and in the process changes stability. Eigenvalue/multiplier indication: a single real eigenvalue crosses over the imaginary axis. Other names: limit point bifurcation, saddle-node bifurcation.

- **Pitchfork bifurcation** - a fixed point solution branch changes stability, and in the process spawns two new fixed point solution branches. The layout of the three branches emanating from one lends the bifurcation its name. Eigenvalue/multiplier indication: a single real eigenvalue crosses over the imaginary axis.

- **Hopf bifurcation** - a fixed point solution branch changes stability, and in the process spawns a periodic solution branch. The emergence of this periodic solution branch is smooth, in that at the Hopf bifurcation itself, the amplitude of the LCO is zero. Eigenvalue/multiplier indication: a complex conjugate eigenvalue pair crosses over the imaginary axis. Other names: Andronov-Hopf bifurcation

- **Cyclic fold bifurcation** - the periodic solution branch analogue of the ordinary fold bifurcation listed above. Though it is mathematically different and is detected via different means, its appearance on bifurcation diagrams is essentially identical. Eigenvalue/multiplier indication: a single real Floquet multiplier crosses over the unit circle.

- **Torus bifurcation** - a periodic solution branch changes stability, and in the process a torus-shaped manifold forms about the LCO, on which trajectories may flow. Flow of this kind is referred to in this work as *torus flow*. The emergence is smooth in the same manner as the Hopf bifurcation listed above, though torus manifolds of this kind may also be created/destroyed non-smoothly; such an occurrence does not constitute a torus bifurcation. Eigenvalue/multiplier indication: a complex conjugate pair of Floquet multipliers cross over the unit circle. Other names: Neimark-Sacker bifurcation, secondary Hopf bifurcation.

- **Homoclinic bifurcation** - a periodic solution branch annihilates upon collision with a separate fixed point branch. At the collision point, the LCO connects the fixed point to itself via a loop in the phase space; the "homo-" prefix indicates that the start and end points of this LCO are the same. Eigenvalue/multiplier indication: none.

- **Heteroclinic bifurcation** - similar to the homoclinic bifurcation listed above, except the collision involves two fixed point branches which the colliding LCO arcs between. The "hetero-" prefix indicates that the start and end points of this LCO are different. Eigenvalue/multiplier indication: none.

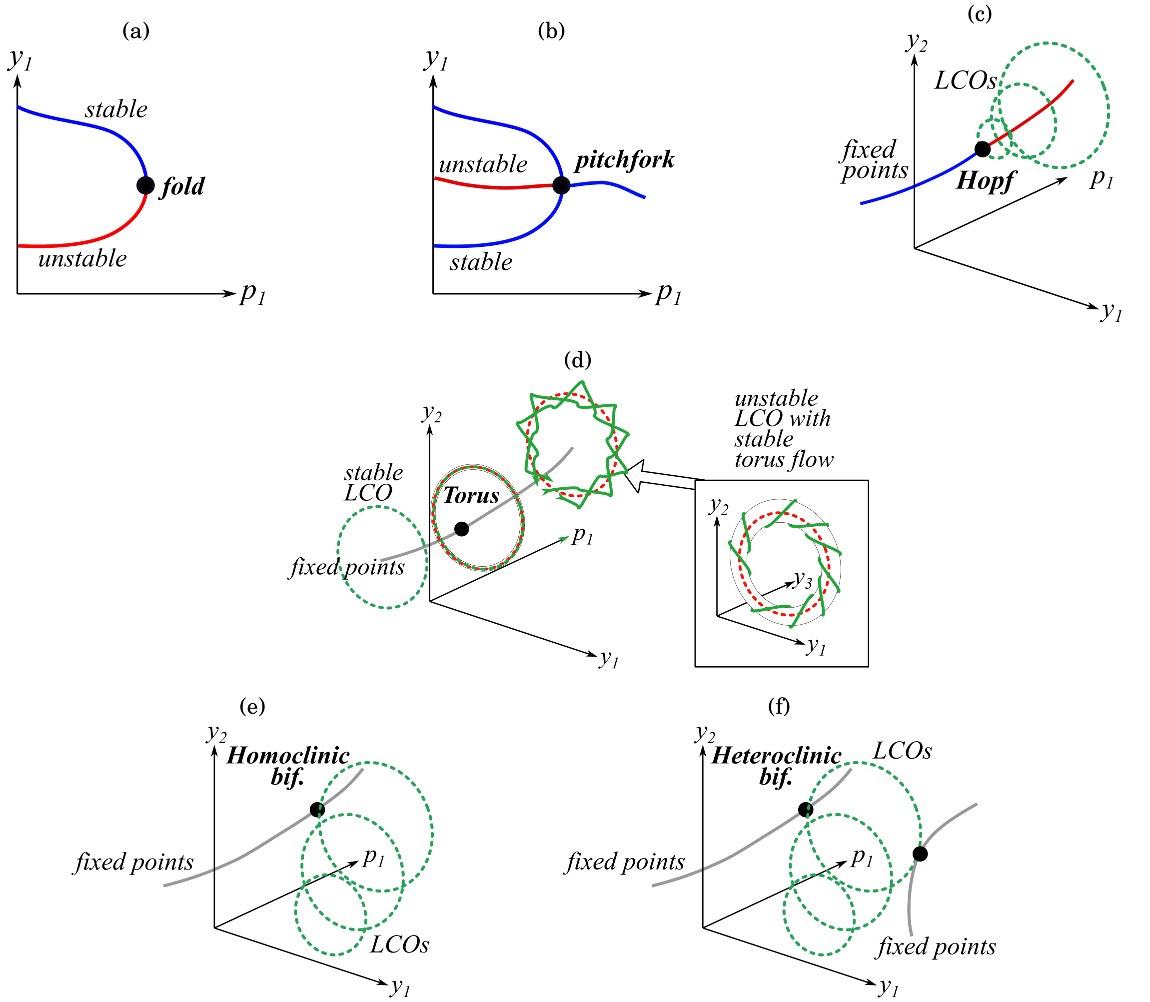

FIGURE 2.17. Types of bifurcation

These bifurcation types are shown in schematic detail in Figure 2.17. The bifurcation point in each case is indicated with a filled black dot.

Arguably, the emergence of a chaotic regime could be regarded as a bifurcation, in the sense that a qualitative change of the system's behaviour has occurred, from one recognisable type to another, and linked to the change of some system parameter. However, the canon of bifurcation theory does not describe chaos in this way, referring instead to the "onset of chaos", or the "emergence of chaos".

The *criticality* of certain types of bifurcation is a further sub-classification with qualitative impacts for a system's dynamics. The criticality refers to the stability of branches emanating from a bifurcation. Of the bifurcations listed above it applies to the pitchfork, the Hopf and the torus. A pitchfork or Hopf bifurcation is said to be *supercritical* if the emanating branches are stable, and *subcritical* if they are unstable. In the case of a torus bifurcation, if the torus manifold that is formed is stable (i.e. attracting) then that torus bifurcation is said to be supercritical. If it is unstable/repelling then it is said to be subcritical. The matter of criticality is demonstrated in schematic form in Figure 2.18.

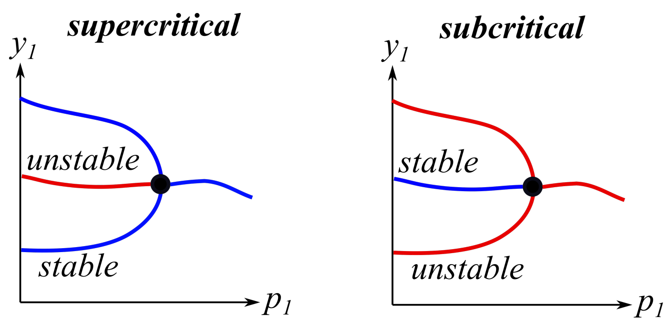

FIGURE 2.18. Schematic representation of bifurcation criticality

A key concept of nonlinear systems that Figure 2.17 also shows is the existence of a solution branch over a range of parameter values. This is in contrast to linear systems, which as described earlier produce trivial solution branches of concentrically-nested solutions that only exist at the parameter value that causes neutral stability. This phenomenon of a given solution type existing over a range of parameters is key to the stability analysis that the application of CBM will yield.

While the key eigenvalue/Floquet multiplier transitions have been listed for some of the bifurcations above, several have the same indication and the homoclinic and heteroclinic bifurcations have no such indication at all. Therefore the actual processes for detecting them are necessarily more complex than just monitoring the eigenvalues or Floquet multipliers in this way. There are a number of algorithms that continuation packages employ to detect specific bifurcations, which are explained in more detail by Kuznetsov [259], and Allgower and Georg [300].

A key to the symbols and lines used in the bifurcation diagrams shown in this work is given in Table 2.1. Particular attention is drawn to periodic solution branches. As a fixed point/equilibrium only exists at a single point in the phase space, its value can neatly be indicated on a bifurcation diagram. However, the same is not possible for periodic solution branches as at each parameter point, a whole LCO exists, covering a range of values in the states. The convention then is to indicate periodic solution branches via the maximum (i.e. most positive) value of the given projection state in the LCO at each point.

TABLE 2.1. Key for lines and symbols used in bifurcation diagrams

Graphic	Description	Meaning
———	solid green line	stable equilibrium branch
- - - -	dashed magenta line	unstable equilibrium branch
———	solid blue line	stable periodic solution branch
·········	dotted red line	unstable periodic solution branch
———	solid grey line	concentric periodic solution family
□	hollow square	Hopf bifurcation
★	black star	pitchfork bifurcation
●	black circle	fold bifurcation
▲	black triangle	homoclinic bifurcation
△	hollow triangle	heteroclinic bifurcation
○	hollow circle	torus bifurcation

2.2.4.4 Qualitative differences in stability analyses

With the fundamental differences between linear and nonlinear systems now demonstrated, it is logical to note that the results from their dedicated stability analyses are correspondingly different. Firstly, the philosophy behind the use of eigenvalue analysis for linear systems – and why it cannot be used for nonlinear systems – is clear. When applied to the classical whirl flutter problem, linear analysis only finds the onset point in whatever parameter is being swept: e.g. the airspeed or the stiffness value at which the whirl flutter mode roots become unstable. And because only unstable behaviour (i.e. divergence to infinitely large solution values) can be found beyond it, and only stable decay behaviour can be found before it – at least in the case of airspeed – it is sufficient in linear whirl flutter models to find this onset point and not consider any whirl flutter solutions pre- or post-instability. In terms of parametric regions, the parameter range before the instability onset is termed "stable" and the range after it "unstable".

It is however when this philosophy is applied to nonlinear systems that problems can occur. This is because nonlinearities can cause solution branches to "bend" within the parameter space. Although the whirl flutter solution branches still emanate from the linear-predicted instability onset parameter value, instead of a concentric family of solutions that only exists at that onset value, the solution branches may exist over ranges of the parameter value. In the case of whirl flutter, this parameter could represent airspeed, meaning that whirl flutter can be encountered at lower airspeeds than the linear analysis predicts. The bending of solution branches means that the parameter value at which a flutter branch emerges says nothing concrete about the range of parameter values that the whole branch could exist over.

Secondly, what the term "whirl flutter" refers to is dependent on whether the system representing it is linear or nonlinear. In a linear model of a system undergoing whirl flutter, the term refers to the post-instability behaviour where the system's oscillations diverge to infinity. However in a nonlinear representation, where solutions have their own individual stability and may exist over a range of parameter values, whirl flutter refers more generally to a periodic solution found in the system, including when it is stable. While this may seem contradictory, these periodic solutions still depict motion of the real world system that would damage it. The "self-limiting" nature of LCOs, where the same physical mechanisms that lead to a periodic solution arising also work against the oscillation amplitude increasing beyond some amount, does not make them any less dangerous, as the model fails to account for the structure being damaged through the LCO occurring and thereby the oscillation amplitude increasing. Furthermore, partitioning the parameter space into regions that are termed "stable" and "unstable" is insufficient here, given that a stable LCO presents a whirl flutter hazard and cannot be called "unstable". Instead, the term "unsafe" is used for any parametric regions where linear analysis predicts stability, but CBM finds whirl flutter.

2.2.4.5 Dynamical Systems Toolbox/AUTO-07P

The continuation package used in this work is the Dynamical Systems Toolbox (DST) [301] developed by Coetzee et al., a MATLAB-based interface for the pre-existing FORTRAN-powered AUTO-07P [302] continuation package. This package was chosen as it is widely used, performs robustly and is simple to use. With the simple class of system being solved in the present work, it has a considerable speed advantage over other available options such as COCO. While it has some analytical capabilities suited to problems of the form of Equation (2.19), the main algorithms are aimed at the solutions of systems of ordinary differential equations (ODEs) of the form:

$$\dot{\mathbf{y}}(t) = \mathbf{f}(\mathbf{y}(t), \lambda) \tag{2.22}$$

with $\mathbf{f} \in \mathbb{R}^n$ and $\mathbf{y} \in \mathbb{R}^n$, and λ representing parameters of interest that may be varied in the process of continuation. It uses the pseudo-arclength method of continuation and has a wide range of capabilities (listed in [302]) though some that are employed in this work are the computation of families of stable and unstable fixed point and periodic solutions, the computation of Floquet multipliers, the location of folds, cyclic folds, branch points, periodic doubling bifurcations and torus bifurcations. The main algorithms used by AUTO are explained in more detail by Doedel, Keller and Kernevez [303, 304]. Several other algorithms used by AUTO, such as the homoclinic bifurcation continuation algorithms and the Floquet multiplier algorithms were originally presented in [305–309]. AUTO is not however capable of continuing quasi-periodic solutions.

CHAPTER 3

Classical Whirl Flutter and a Smooth Nonlinearity

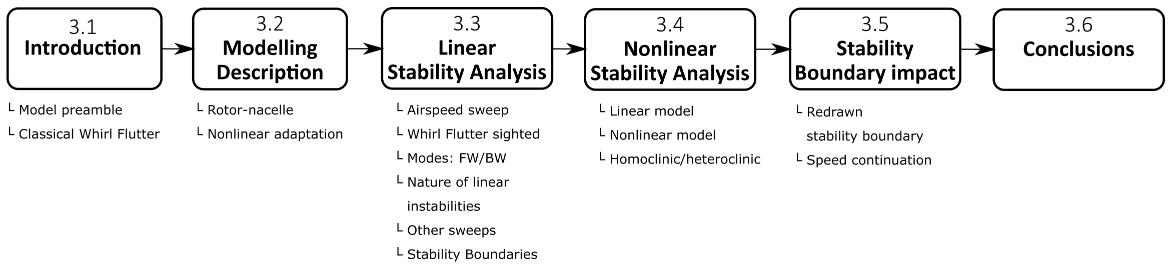

FIGURE 3.1. Chapter map

In this chapter, the effects of a smooth nonlinearity on the whirl flutter stability characteristics of a rotor-nacelle system are shown in an applied and integrated context, via the novel integration of a polynomial stiffness profile with the basic model. In terms of Research Objectives and Research Process steps, this chapter addresses objective O1, by performing steps P1-6 on the basic model and the smooth nonlinearity. Presenting these effects in isolation will assist the more complex analysis that follows later in this work. A summary of the chapter's content and structure is shown as a map in Figure 3.1.

First, whirl flutter and the basic model are introduced in tandem, each aiding the explanation of the other. Linear stability analysis (as introduced in Chapter 2) is employed, both to show the methods at work and also to show the sensitivity of the simple model's stability to various parameter changes. Stability boundaries are introduced as a tool for understanding and comparing stability impacts. Then, Continuation and Bifurcation Methods (CBM) are shown in practice by applying them to the basic model, demonstrating the similarities and differences compared to linear analysis. A smooth nonlinearity is then introduced and analysed with CBM. The impacts on the model's stability are discussed qualitatively, and the model's stability boundary is redrawn based on the findings. Finally, a continuation in speed is shown to illustrate the nonlinearity's impact on onset speed.

3.1 Introduction

Key ingredients in classical whirl flutter are aerodynamic and gyroscopic forces acting on the rotor, and the elastic restraint of the engine nacelle's structure. Recognising this, W. H. Reed III captured these aspects in a model developed during the 1960s. The model has since become the canonical form of classical whirl flutter, used for the introduction and explanation thereof, and it is for this reason that it is chosen for use in this work. Further benefits of using this model are the ease of its implementation and the availability of literature from the various studies that used it. The model changes slightly between its appearances in the various landmark publications released by Reed and his colleagues during the 1960s. The simplicity of the equations makes them amenable to manual analysis, something that was valued at the time of the model's development, when the limited performance of digital computers meant that computational analysis as a standard was not yet feasible. Such manual analysis might include forming explicit analytical expressions for root values necessary for specific instabilities, or relationships between parameter values that guarantee the existence of a periodic solution. A more compact version of the model was released later by Bielawa in his book [310] from 2005, which presents the aerodynamics and some of the inertias in a more succinct form. It is this version of the model that this work uses as the "basic model".

The model serves all the purposes of a canonical model: it represents the necessary physical phenomena in as concise a form as possible. This nevertheless comes at the expense of some features that, while not crucial for whirl flutter to appear or sustain, are nevertheless influential. The most significant of these omissions is the absence of rotor blade degrees of freedom such as flapping and lead-lag, while the inability of the pivot point to translate through wing bending is another. These omissions affect the model's predictions regarding the whirl flutter boundary and the nature of the instability's activation. However, the model does represent the most important influences of various stabilising and destabilising factors. Whirl flutter as depicted by this basic model – and accepting all the omissions – is known as classical whirl flutter.

The experimental rigs used for the practical elements of the 1960s research efforts were of a variety of sizes, ranging from full scale to small tabletop demonstrators. The parameter value set presented in Reed's 1965 summary work [40] pertains to the latter of these sizes and is used here due to its completeness. Though it is an existing model in the field, a derivation has been provided in Appendix A for completeness. Here, a description of the model is sufficient.

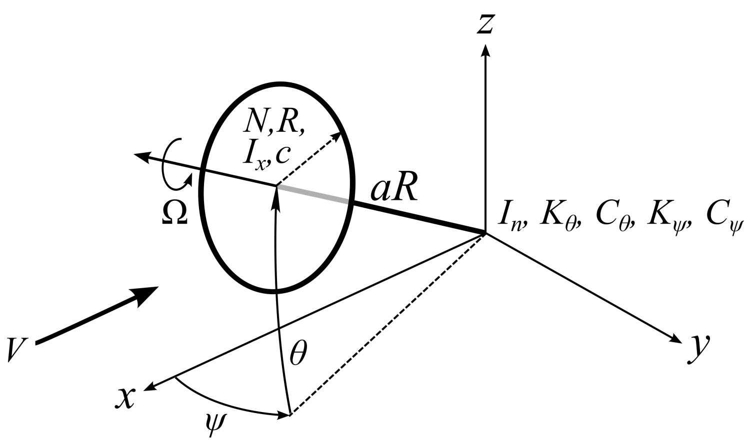

FIGURE 3.2. Schematic diagram of basic model

3.2 Modelling Description

3.2.1 Basic whirl flutter model

A rigid, N-bladed rotor of radius R rotates at an angular velocity of Ω about the end of a rigid shaft, to which it is rigidly attached. The rotation sense is clockwise if the rotor is viewed from the origin. The shaft's length is a multiple a of the rotor radius R, and the rotor has moment of inertia I_x about its axis of rotation. The rotor blades have chord c and sectional lift slope $c_{l\alpha}$. The rotor and shaft together represent the nacelle as a whole, and the opposite end of the shaft is elastically mounted at an effective pivot point, placed at the origin, which represents the connection of the nacelle to the wing. Through this connection, the rotor and shaft as a whole are able to rotate about the pivot point in pitch θ and yaw ψ. Though the wing is not modelled explicitly, the deformation that it would experience is lumped together into these degrees of freedom: wing torsion (contributing to pitch) and wing chordwise bending (contributing to yaw), in addition to flexure of the connection point itself. The nacelle rotations θ and yaw ψ are measured from an undeformed position where the shaft points down the global x-axis. The rotor and shaft's collective moment of inertia about the pivot point in each degree of freedom is I_n. The stiffness and damping properties of the pivot point are aggregated as single "lumped" quantities. The stiffness in each degree of freedom is assumed to be linear (proportional to angular deformation) and is denoted K. The structural damping is also assumed to be linear (proportional to angular deformation rate) and is denoted C. The structure is assumed not to contribute any coupling in either stiffness or damping. The whole assembly is immersed in a uniform freestream velocity V with air density ρ that is parallel to the x-axis, moving in the negative direction. The system is represented schematically in Figure 3.2.

The equations of motion, as given by Bielawa [310] are:

$$
\begin{aligned}
I_n\ddot{\theta} + C_\theta\dot{\theta} - I_x\Omega\dot{\psi} + K_\theta\theta &= M_\theta \\
I_n\ddot{\psi} + C_\psi\dot{\psi} + I_x\Omega\dot{\theta} + K_\psi\psi &= M_\psi
\end{aligned}
\tag{3.1}
$$

The aerodynamic forcing terms on the RHS[1] are:

$$M_\theta = \frac{N}{2}K_aR\left(-\left(A_3 + a^2A_1\right)\frac{\dot{\theta}}{\Omega} - A_2'\psi + aA_1'\theta\right) \tag{3.2}$$

$$M_\psi = \frac{N}{2}K_aR\left(-\left(A_3 + a^2A_1\right)\frac{\dot{\psi}}{\Omega} + A_2'\theta + aA_1'\psi\right) \tag{3.3}$$

where $K_a = \frac{1}{2}\rho c_{l\alpha}R^4\Omega^2$ and the aerodynamic integrals A_i are defined as:

$$A_1 = \int_0^1 \frac{c}{R}\frac{\mu^2}{\sqrt{\mu^2+\eta^2}}d\eta \tag{3.4}$$

$$A_2 = \int_0^1 \frac{c}{R}\frac{\mu\eta^2}{\sqrt{\mu^2+\eta^2}}d\eta \tag{3.5}$$

$$A_3 = \int_0^1 \frac{c}{R}\frac{\eta^4}{\sqrt{\mu^2+\eta^2}}d\eta \tag{3.6}$$

$$A_i' = \mu A_i \tag{3.7}$$

These integrals are radial summations of the aerodynamic forces acting on the blades. The integration variable η represents the distance away from the blade root in the radial direction, normalised by rotor radius. The advance ratio μ is defined as per contemporary convention: $\mu = \frac{V}{\Omega R}$, that is, without the factor of π that is commonly present in literature of Reed's time.

In the original text, Bielawa takes a more qualitatively-minded approach to the demonstration of whirl flutter and therefore does not provide numerical values, either for parameter values to be used with the model, or in the figures he includes. However, parameter values are provided in Reed's work [40] for use with his various iterations of the model. With some care they may be used in Bielawa's version of the model. Figure 3.3 shows results from the present work's implementation of the basic model compared to those shown in Figure 6 of [40], which shows a sweep of rotor speed with measurement of modal frequencies and damping ratios. The results from this work are shown with coloured lines, and those from Reed with black dots.

[1] RHS: Right Hand Side.

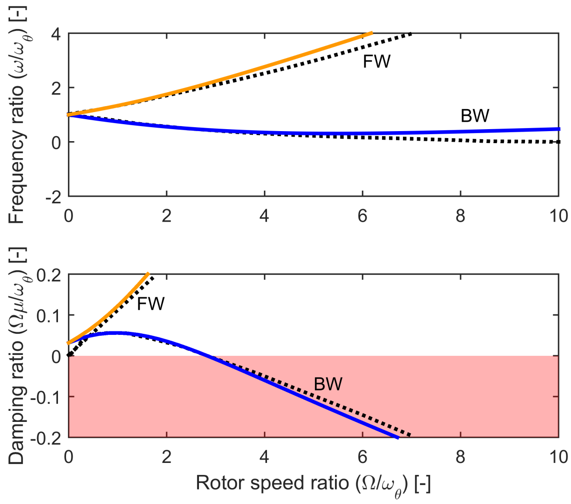

FIGURE 3.3. Variation of modal frequency *(top)* and damping ratio *(bottom)* with rotor speed Ω of the implemented basic model (solid coloured lines) and results from [40] (black dots)

The two distinct lines present, marked 'FW' and 'BW', correspond to the two modes of the system and are discussed in Section 3.3.3. There is good agreement between the results of the present work and those of Reed.

The model equations were written in state-space form, as shown in Equations (3.8) and (3.9):

$$\dot{\mathbf{y}} = \mathbf{f}(\mathbf{y}, \mathbf{p}), \quad \mathbf{y} \in \mathbb{R}^4, \quad \mathbf{p} \in \mathbb{R}^{13} \tag{3.8}$$

$$\mathbf{y} = \begin{bmatrix} \theta & \psi & \dot{\theta} & \dot{\psi} \end{bmatrix}^T \tag{3.9}$$

where $\mathbf{y}$ is the state vector and $\mathbf{p}$ is a vector of system parameters. The parameter values used throughout the investigation are shown in Table 3.1 and were retained, where possible, from Reed's original text. Where ranges of parameters were used in Reed's study, the midpoint value was taken for this parameter set. These values represent a scaled wind tunnel rotor-nacelle system, however the qualitative results achieved from the following analyses are applicable to full size aircraft for cases that approximate classical whirl flutter, such as very stiff blades (e.g. propellers) and a minimally translating pivot point.

3.2.2 Nonlinear adaptation

The shortcomings of assuming linear stiffness – specifically within the context of aeroelasticity – have been long known, as evidenced by Woolston's work [29], previously mentioned. One improvement is to replace the linear stiffness profile associated with a degree of freedom with a low order polynomial with odd-numbered power terms to relate deflection to restoring force/moment. This

TABLE 3.1. Basic model datum parameter values

Description	**Symbol**	**Value**
Rotor radius	R	0.152 m
Rotor angular velocity	Ω	40 rad.s^{-1}
Number of blades	N	4
Blade chord	c	0.026 m
Blade (2D) lift slope	$c_{l\alpha}$	2π rad^{-1}
Freestream velocity	V	6.7 m.s^{-1}
Ratio of pivot length to rotor radius	a	0.25
Rotor moment of inertia	I_x	0.000103 kg.m^2
Nacelle moment of inertia	I_n	0.000178 kg.m^2
Structural pitch damping	C_θ	0.001 N.m.s.rad^{-1}
Structural pitch stiffness	K_θ	0.4 N.m.rad^{-1}
Structural yaw damping	C_ψ	0.001 N.m.s.rad^{-1}
Structural yaw stiffness	K_ψ	0.4 N.m.rad^{-1}

polynomial is an improvement as it is often a more accurate representation of how stiffness varies at larger deflections. There are also a number of important constraints satisfied by this expression. In addition to being smooth, the zero point is crossed (i.e. zero restoring force/moment for zero deflection) and the function is odd (i.e. the graph of the function has rotational symmetry about the origin). The latter condition precludes the use of even-numbered powers in the polynomial expression. There are two general kinds of this polynomial stiffness representation: softening and hardening. Softening refers to profiles that accrue restoring force with a decreasing gradient as the deflection grows, while the opposite is the case for hardening. These two categories have differing hallmark influences on the dynamic behaviour of a system, as will be seen and explained later.

The pitch and yaw degrees of freedom in the basic model are qualitatively identical from a modelling point of view, as if the model is rotated 90° about the x-axis, it is completely unchanged in form. Furthermore, in the parameter value set used in this work, the values that control the respective physical attributes attached to the two degrees of freedom are also equal, giving the rotor-nacelle isotropic properties about the pivot point. For this reason, either degree of freedom could be selected for nonlinear adaption without any qualitative impact on the results. However, in a typical wing, the torsional degree of freedom is much less stiff than the chordwise bending degree of freedom, and therefore appreciable deformation may occur in the former in whirl flutter oscillations. In the Reed/Bielawa model, torsional motion of the wing is represented solely by motion in the nacelle pitch degree of freedom, θ, and it is therefore in this degree of freedom that the polynomial stiffness is implemented. In the nonlinear adaptation of the model, the polynomial stiffness expression replaces the linear expression ($K_\theta \theta$) specified in the original formulation of the model, and is of the form given in Equation (3.10), where “nl” denotes “nonlinear”. Note that

$K_{\theta,nl}$ is not a constant but rather a function of θ, which is in units of radians.

$$\begin{aligned} K_{\theta,nl}(\theta)\theta &= K_1\theta + K_2\theta^3 + K_3\theta^5 \\ &= (K_1 + K_2\theta^2 + K_3\theta^4)\theta \end{aligned} \tag{3.10}$$

The influence of each term is controlled via dedicated stiffness parameters K_i, which ultimately can provide softening behaviours by using negative values of K_2 and/or K_3, and hardening behaviours by using positive values. The cubic term is dominant at smaller deflections, while the quintic term is dominant at larger deflections, allowing both softening and hardening behaviours to be observed in the same stiffness profile if K_2 and K_3 have opposite signs. A fifth order polynomial is chosen as it is the simplest representation that allows softening and hardening behaviours to be combined. The following three cases are selected for investigation to both isolate the effects of each profile type and show them in concert:

$$K_2 = 10 \text{ N.m.rad}^{-3}, \quad K_3 = 0 \text{ N.m.rad}^{-5} \qquad \text{(cubic hardening)}$$

$$K_2 = -10 \text{ N.m.rad}^{-3}, \quad K_3 = 0 \text{ N.m.rad}^{-5} \qquad \text{(cubic softening)}$$

$$K_2 = -10 \text{ N.m.rad}^{-3}, \quad K_3 = 350 \text{ N.m.rad}^{-5} \qquad \text{(cubic softening - quintic hardening)}$$

The overall shape of these profiles compared to the original linear profile is shown in Figure 3.4. Note that the x-axis is expressed in degrees, rather than radians as in Equation (3.10).

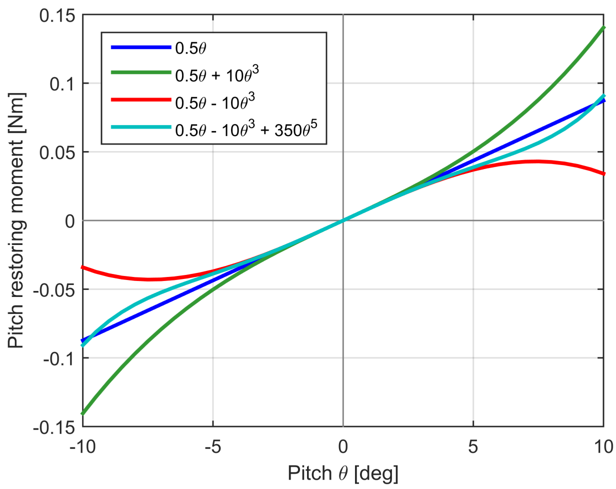

FIGURE 3.4. Polynomial stiffness profiles compared to linear profile (dark blue)

Covering these three cases allows the modelling of a variety of possibilities for how the stiffness of a tiltrotor's nacelle pitch might be characterised. These values were selected such that the desired form of the stiffness profile was readily apparent from its graph, and were ratified by comparison to the values used by Woolston [28] in his work on cubic stiffness in control surface flutter. K_1, the linear component of the stiffness profile, is used as the independent variable in each case and it is varied between -0.3 and 0.5 N.m.rad^{-1}. While the gradients of all the nonlinear stiffness profiles are quasi-linear near zero deflection, their tendencies at larger deflections are clear from Figure 3.4. The configurations of the model with each of these stiffness profiles are hereafter referred to as **model variants**, for instance, the "hardening model variant", etc. The cubic softening - quintic hardening case is referred to as the "combined variant".

3.3 Linear Stability Analysis

3.3.1 Parametric sweep in airspeed V

As a first step in the stability analysis of whirl flutter, the eigenvalue analysis is now applied to the basic model described above. As the most well known activation mechanism of whirl flutter is exceeding a critical whirl flutter onset airspeed, it is logical to first investigate a sweep in this model parameter, evaluating the linear stability at each point. The eigenvalues, damping ratio and frequency of the linear model's modes are shown in Figure 3.5 as the freestream velocity V is swept from 0 to 10 ms^{-1}. In the Argand diagram plot of the eigenvalues (a), the ends of the loci corresponding to 0 ms^{-1} are indicated with an 'x' and those corresponding to 10 ms^{-1} with an 'o'. The remaining parameter values used are those presented in Table 3.1.

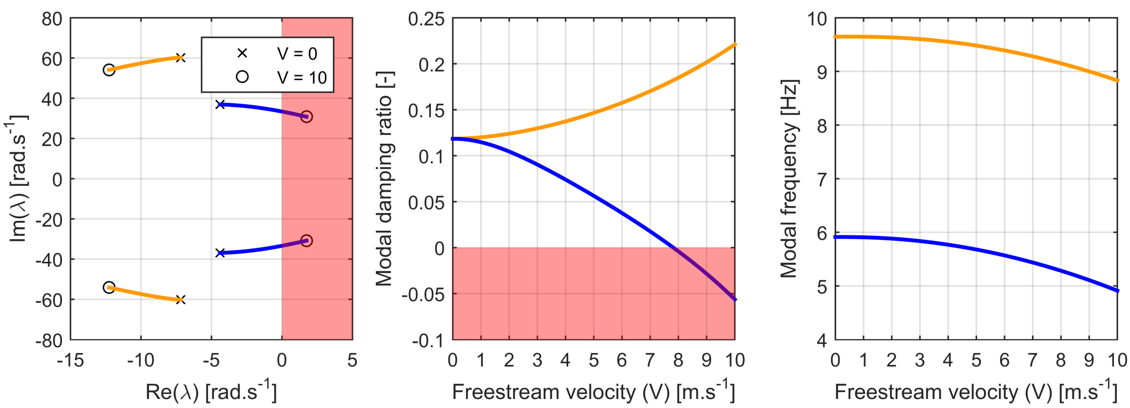

FIGURE 3.5. Argand diagram of eigenvalues *(left)* and their corresponding modal damping ratios *(centre)* and frequencies *(right)* for a sweep in airspeed V. Unstable regions are shaded red

The Argand diagram shows that within this domain of analysis, the four eigenvalues exist in two complex conjugate pairs and the plotted lines on the various subplots are coloured to reflect this. The identification of the modes is discussed shortly. Roots in a complex conjugate pair differ only by the sign of their imaginary component and therefore will have equal modal frequency and modal damping ratio. That is, if an eigenvalue pair – say, the pair coloured blue in Figure 3.5

– is in the form $\lambda_{1,2} = a \pm ib$, then:

$$\omega_2 = \sqrt{a^2 + (-b)^2} = \sqrt{a^2 + b^2} = \omega_1$$

$$\zeta_2 = -\frac{a}{\sqrt{a^2 + (-b)^2}} = -\frac{a}{\sqrt{a^2 + b^2}} = \zeta_1$$

Hence, only two distinct lines are visible in the damping and frequency plots. The system's stability is encoded solely in the damping ratio plot (middle): damping ratios above 0 imply stability of a mode, and damping ratios below 0 imply instability.

We may deduce that when configured with the datum set of parameters listed in Table 3.1 (i.e. V = 6.7 ms^{-1}), the system is stable. However, the damping ratio of one of the modes crosses through 0 from above at an airspeed of approximately 7.8 ms^{-1}, showing that this mode becomes unstable at this airspeed. Physically speaking, the freestream is the only source of energy in the system and when the system is unstable, energy is being supplied to the system at a greater rate than it can dissipate through the various features in the model that provide positive damping. As this unstable mode's eigenvalues are a complex conjugate pair, it is therefore oscillatory and is in fact the whirl flutter that this work concerns. As far as classical whirl flutter is concerned, this airspeed at which the damping ratio of one of the whirl flutter modes is 0 is the whirl flutter onset speed. Beyond this airspeed, the damping ratio of the mode continues to decrease, signifying greater and greater instability. The other mode, by contrast, becomes more and more stable with increasing airspeed, and at 0 ms^{-1} airspeed the damping ratio of the two modes is the same. This would suggest that the airspeed affects the mechanisms of energy transfer into and out of the system, acting to damp the orange-coloured mode but destabilise the blue-coloured mode. The frequencies of the two modes are always well separated within the domain of analysis, with a decrease in both modes as airspeed increases. The orange-coloured mode appears to be stiffer than the blue-coloured mode, but growing airspeed decreases the stiffness of both modes.

3.3.2 Visualising whirl flutter

With the system at the onset airspeed, a time history of the pitch θ and yaw ψ states over one second of the whirl flutter motion is shown in Figure 3.6. Being at the onset airspeed, the system's whirl flutter stability is neutral and therefore any amplitude can be chosen from the concentrically nested family of periodic solutions that exists here; for this Figure a value of 5° is chosen. To assist the reader in visualising the motion, a schematic diagram of the model at various points in the same whirling motion is shown in Figure 3.7. For clarity, both the shaft length and the oscillation amplitude have been exaggerated. The motion is a steady whirling of the nacelle about its undeformed position. Here, the path is circular as the respective values of damping and stiffness are set to be equal between the pitch and yaw degrees of freedom.

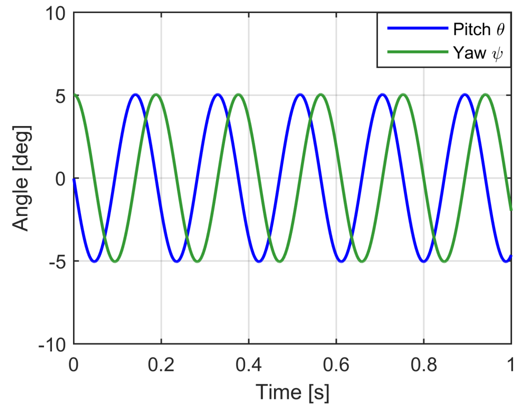

FIGURE 3.6. Time histories in pitch θ and yaw ψ of basic model, linear variant experiencing incipient whirl flutter

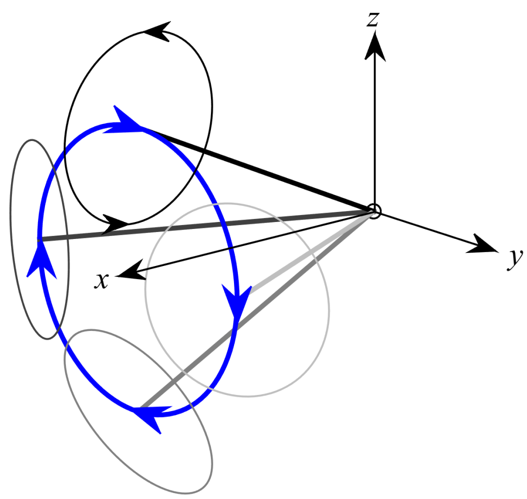

FIGURE 3.7. Schematic diagram of whirl flutter motion in basic model, linear variant. For clarity, both the shaft length and the oscillation amplitude have been drawn exaggerated

3.3.3 Classical whirl flutter mode identification

In Figure 3.7, the rotor whirls clockwise when viewed from the front (i.e. looking down the x axis in the negative direction). This is in the opposite direction to the rotor's spin, which is anti-clockwise. Classical whirl flutter is in fact characterised by the relationship between the whirl direction and the rotor spin direction: if the whirl is in the same direction as the rotor spin then it is known as **forward whirl**, while whirling against the spin direction is known as **backward whirl**. These are the only two types of periodic solutions that this basic model's linear variant is capable of exhibiting. For brevity, the shorthand 'FW' and 'BW' is used from here onwards to indicate forward whirl and backward whirl, respectively.

The mathematical distinction between the two whirl flutter modes lies in the phase differences between the various states and these can be identified from the phase relationships that exist within the system's eigenvectors. In the simplest possible case of whirl flutter, the motion is simply a circle of arbitrary radius A within the ψ-θ plane, as depicted in Figure 3.8.

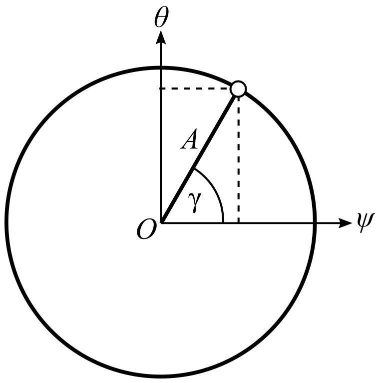

FIGURE 3.8. Schematic of hub motion in circular whirl flutter

If the hub whirls anti-clockwise (forward whirl in this system, given the rotor spin direction) with some arbitrary modal whirl frequency of ω_F, then its angular position γ, measured anti-clockwise from the positive ψ axis, at time t, is $\gamma = \omega_F t$, and therefore its position in the plane is:

$$\begin{aligned} \psi &= A\cos(\omega_F t) \\ \theta &= A\sin(\omega_F t) \end{aligned} \tag{3.11}$$

The velocity of the hub in this plane is given through differentiation of these expressions with respect to time:

$$\begin{aligned} \dot{\psi} &= -A\omega_F \sin(\omega_F t) \\ \dot{\theta} &= A\omega_F \cos(\omega_F t) \end{aligned} \tag{3.12}$$

And therefore ψ and $\dot{\theta}$ are in phase. Similarly, for clockwise whirl (backward whirl here, given the rotor spin direction), the hub's angular velocity is now $-\omega_F$ and therefore:

$$\begin{aligned} \psi &= A\cos(-\omega_F t) = A\cos(\omega_F t) \\ \theta &= A\sin(-\omega_F t) = -A\sin(\omega_F t) \end{aligned} \tag{3.13}$$

which gives:

$$\begin{aligned} \dot{\psi} &= -A\omega_F \sin(\omega_F t) \\ \dot{\theta} &= -A\omega_F \cos(\omega_F t) \end{aligned} \tag{3.14}$$

where here, θ and $\dot{\psi}$ are in phase. These phase relationships permit the identification of FW and BW from inspection of the eigenvector components of a given mode. The ordering of the eigenvector components corresponds to the ordering of the state vector.

Examination of the corresponding eigenvectors of the unstable whirl mode in Figure 3.5 (blue lines) corroborates the observation that it is backward whirl (BW). The other mode (orange line) is a FW mode, and one pair of each will typically exist when the parameters of the system are configured to produce oscillatory roots.

Importantly, **only the BW mode is capable of instability in this model**, regardless of what parameter value configuration is being used. This is due to the aerodynamic stiffness coupling, which always acts in the BW sense. This can be verified by inspection of the aerodynamic terms given in Equations (3.2) and (3.3), and the schematic diagram of the hub motion given in Figure 3.8.

If the nacelle is in the process of pitching upwards (i.e. $\dot{\theta}$ is positive) then the stiffness coupling term $A_2'\dot{\theta}$ in Equation (3.3) is also positive. On this side of the equation this denotes a positive yawing moment, i.e. in the positive ψ direction. Consulting Figure 3.8, this corresponds to BW motion, as if the nacelle is rising, it must be following the left side of the circle so that the positive yawing moment (to the right) is consistent with the motion to the right that follows. The reverse is true for pitching downwards: a negative yawing moment is generated and this corresponds to moving down the right hand side of the circle in Figure 3.8.

3.3.4 Parametric analysis

In the spirit of the investigations conducted by Reed et al., an elementary sensitivity analysis of the model's modes to the system parameters is shown here, conducted by means of some parametric sweeps. The modal damping ratio and modal frequency are calculated for a range of parameters as each is swept from a multiple of 0 to 4 of its datum value, a suitable range for capturing the trend of each. As only the BW mode is capable of instability, there is no need to show the FW mode here. Regarding the description of influences on stability, the terms "stabilising" and "destabilising" are simply used to indicate an increase or decrease (respectively) in the BW damping ratio rather than a transition from categorical instability to stability, or vice versa (respectively). Broadly speaking, the model divides into two regions: the shaft and pivot point, and the rotor. The sweeps are grouped by these regions and in each case, only the variable indicated is altered while all others are kept at their datum values. Hence, all curves intersect at a parameter multiple of 1.

The shaft and pivot point group comprises the nacelle moment of inertia I_n, pylon pitch damping C_θ (the yaw damping could equivalently be chosen here) and the ratio of pivot length to rotor radius a. The pylon stiffness is shown later as its increase destabilises the system in a non-oscillatory manner that requires dedicated explanation. The inertia is the only one of this group to cause instability through its increase, increasing the energy associated with a given deflection or deflection rate. Removing damping eventually destabilises the system. The increase of shaft length has a stabilising influence due to a given angular velocity inducing greater air velocities at the rotor and therefore greater aerodynamic damping, though its removal does not cause instability. The increase of all parameters causes the BW modal frequency to decrease. This set of sweeps is shown in Figure 3.9.

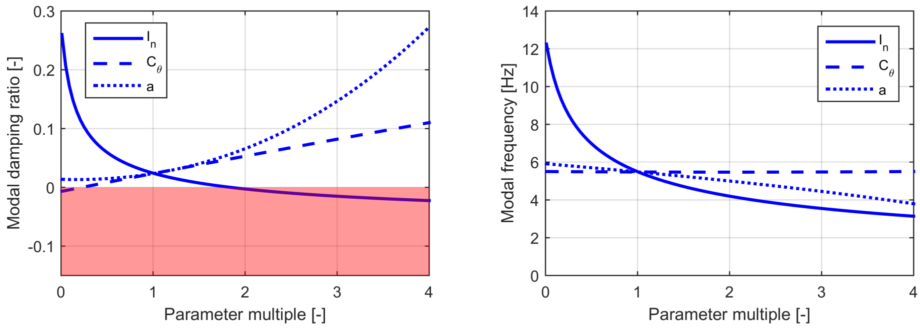

FIGURE 3.9. Parametric sweeps of pivot point parameters: nacelle inertia I_n, pylon pitch damping C_θ and pivot length ratio to rotor radius a

The modal frequency is similarly decreased by the increase of all parameters in the rotor group: rotor moment of inertia I_x, rotor angular velocity Ω and rotor radius R. However in contrast to the pivot point group, all rotor parameters are destabilising to various degrees when they are increased. While increasing the rotor speed only reduces the stability margin without causing instability, increases in the rotor moment of inertia – and therefore the gyroscopic moments – does cause instability. The rotor radius affects the magnitude of the aerodynamic forces and moments, and its increase causes a temporary increase in stability before eventual instability. This set of sweeps is shown in Figure 3.10.

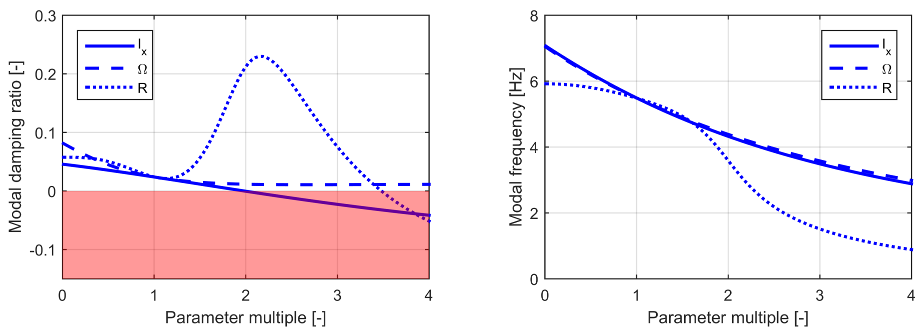

FIGURE 3.10. Parametric sweeps of rotor parameters: rotor moment of inertia I_x, rotor speed Ω and rotor radius R

The driver of the whirl flutter instability is of aerodynamic origin [310]. For instance, while gyroscopic influence is ordinarily able to destabilise the system as shown above, it is not able to do so if the aerodynamic stiffness coupling (the A_2' terms) is not present. This abstract case is shown in Figure 3.11. The BW's modal frequency is almost completely unchanged.

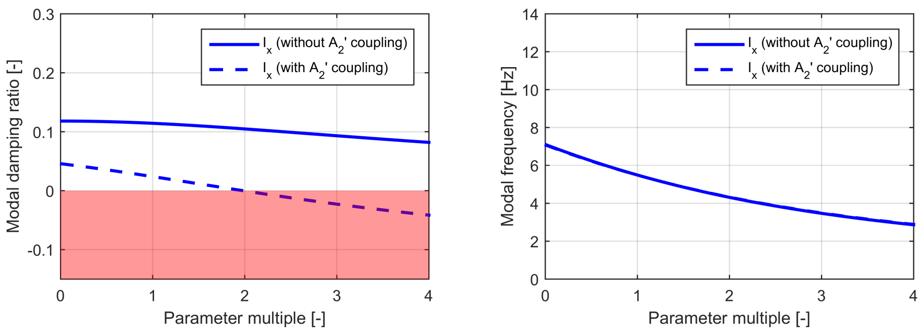

FIGURE 3.11. Parametric sweeps of rotor inertia I_x with and without A_2' coupling

As mentioned earlier, the system destabilisation caused by sweeping the pylon stiffness K_θ away from the datum parameter value set is non-oscillatory. Shown in Figure 3.12 is a sweep in pitch stiffness, similar to the preceding figures. For clarity however, the loci of the BW eigenvalues in the complex plane are instead shown, as the concepts of frequency and damping ratio do not apply to non-oscillatory modes. Note again that due to the mathematical similarity in how K_θ and K_ψ feature in the equations and their equal datum values, either could be used in this sweep.

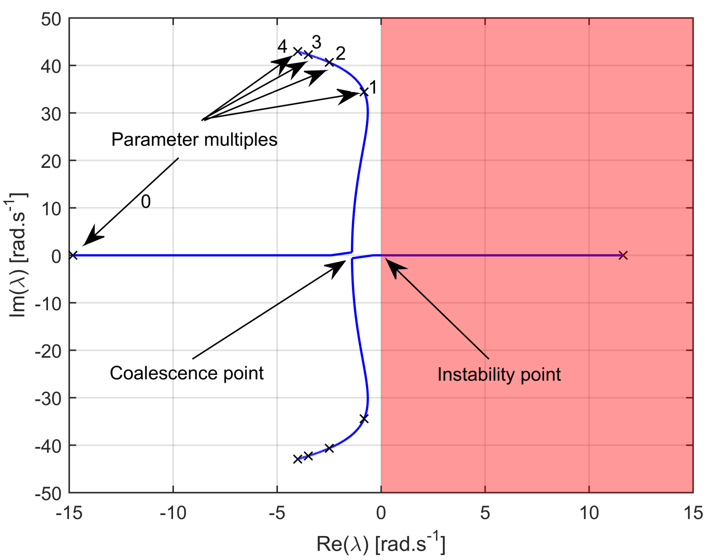

FIGURE 3.12. Argand diagram of eigenvalues during a parametric sweep of pylon pitch stiffness K_θ

Starting at a parameter multiple of 4, the BW root pair is a complex conjugate pair and therefore an oscillatory mode. It is comfortably stable at this point and the loci indicate that further increase of the parameter multiple would have a stabilising effect. However, as the parameter multiple is reduced, the roots first destabilise and then rapidly converge upon each other, representing a sharp increase in damping. The roots eventually coalesce at the marked coalescence point, taking on zero imaginary components. This represents the mode becoming overdamped and therefore non-oscillatory, and has occurred because the reduction in stiffness has not been accompanied by a corresponding reduction in damping. Following this coalescence, the two real roots shoot away from each other along the real axis, one in the positive direction across the imaginary axis and the other in the negative direction further into the left real half-plane. At the point that the rightward-heading root crosses the imaginary axis, it becomes unstable. As the instability of a single real root manifests in time domain behaviour as a monotonic non-oscillatory "blow-up" of the results (exponential divergence to infinity), in the study of aeroelasticity, it signifies *static divergence*: a structural failure where, in this case, the wing structure is soft enough to be overpowered by the aerodynamic pitch and yaw moments. This instability is distinct from the whirl flutter that this work concerns, though as it is part of the stability characteristics of the original linear variant of this basic model, knowledge of its existence will assist the comparison with the nonlinear variant results that will follow.

In summary, the parametric sensitivity analysis shows that the stability of classical whirl flutter, as depicted by the basic model, is sensitive to its constituent parameters in the manner shown in Table 3.2.

TABLE 3.2. Summary of basic model parametric sensitivity analysis

Parameter	**Influence of value increase**	**Influence of value decrease**
I_n	Destabilising, eventual instability	Stabilising
$C_{\theta,\psi}$	Stabilising	Destabilising, eventual whirl flutter
$K_{\theta,\psi}$	Stabilising	Destabilising, eventual static divergence
a	Stabilising	Destabilising without instability
I_x	Destabilising, eventual whirl flutter	Stabilising
Ω	Destabilising without instability	Stabilising
R	Destabilising, eventual whirl flutter	Stabilising

3.3.5 Stability boundaries

While single-parameter sweeps can provide good insight into system sensitivities, the stability boundary diagram between two parameters can also be useful, showing the balance of the two parameters' influences. Particularly useful parameters for such an understanding are those that are readily controllable in the design phase of a practical system such as an aircraft. Such a diagram can be produced from a grid of the combinations of different values for each parameter.

The Jacobian matrix is calculated at each grid point, and a surface is overlaid where the level at each point is determined by the maximum real component of the Jacobian's eigenvalues there. As the sign of the real component of an eigenvalue determines the stability of the corresponding mode – positive being unstable – and only one unstable eigenvalue is required for overall system instability, a horizontal plane cut of this surface at the level 0 will produce a contour that denotes the boundary between the stable and unstable regions of the parameter grid.

Two parameters that are readily controllable in the design phase of a tiltrotor aircraft are the two structural properties yaw stiffness K_ψ and pitch stiffness K_θ. Practically speaking, control of these parameter values would be achieved by alterations to the structure's design (e.g. thickness, materials used) albeit with an impact on the mass and cost of the design. They are relevant to the study of whirl flutter as stiffness is influential in determining natural frequency, as evidenced by the well-known relation $\omega = \sqrt{\frac{K}{I}}$ (where ω is natural frequency, K is stiffness and I is inertia), and natural frequency has been known to be impactful on whirl flutter characteristics, as previously mentioned. These two parameters are used here as the axes for the basic model's stability boundary. The surface with the $z = 0$ plane cut is shown on the left side of Figure 3.13 and the resulting 2D stability boundary is shown on the right side. Note that dimensional values (N.m.rad^{-1}) for the stiffnesses are now used as opposed to multiples of the datum value.

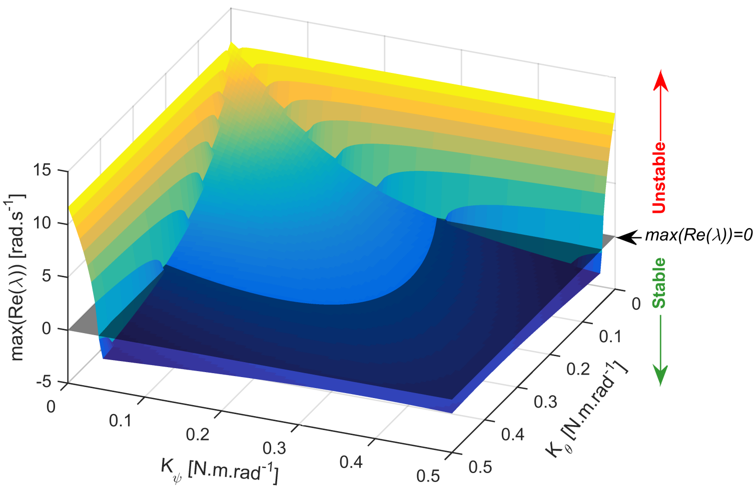

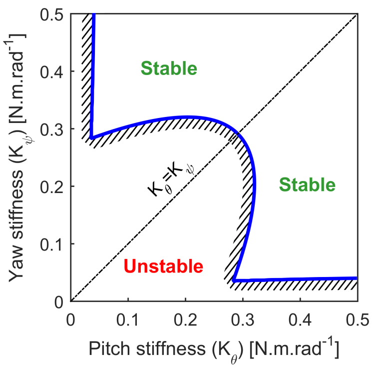

FIGURE 3.13. Stability surface *(left)* for structural pitch stiffness K_θ and structural yaw stiffness K_ψ, with a plane cut at $z = 0$ in translucent black, with corresponding stability boundary *(right)*

The parameter space partitions into two regions: an unstable region consisting of a round bubble-like form and two side lobes neighbouring the axes, and a stable region beyond it. Apparent again here is that the system is stable when configured with the datum set of parameter values:

the point $(K_\theta, K_\psi) = (0.4, 0.4)$ lies in the stable region. Furthermore, the stiffness sweep shown in Figure 3.12 can be related to this boundary: moving left from the datum point, the boundary of the unstable region is encountered at approximately $K_\theta = 0.04$, which corresponds to the point of instability in Figure 3.12.

As one might expect given the mathematical symmetry of these two structural stiffnesses (i.e. their role in the equations), the stability boundary between them is symmetric about the line $K_\theta = K_\psi$, although the two discontinuities where the round bubble meets each of the side lobes suggest that the boundary is defined by two different kinds of instability.

In this work, stability boundaries will form an important part of the investigative process detailed in Section 1.2. They will be the medium through which the comparison of the nonlinear results and the original linear results will take place, allowing the impact of the nonlinearities on the systems' whirl flutter characteristics to be ascertained. As mentioned before, nonlinearities can cause bending of solution branches within the parameter space, causing unsafe regions to emerge if stable LCO branches exist in parametric regions that the linear analysis (that is, eigenvalue analysis of fixed points) predicts to be safe. Not only will the stability boundaries summarise the nonlinear results in terms of these unsafe regions, but they also will provide direct comparison with the original linear stability boundaries.

3.4 Continuation and Bifurcation Analysis

3.4.1 Direct application to linear model

Figure 3.13 can also be generated by continuation methods, as the system has an equilibrium at $\mathbf{y} = \begin{bmatrix} 0 & 0 & 0 & 0 \end{bmatrix}^T$ that can be used as a starting solution. This phase point corresponds to the nacelle sitting at rest at the undeformed position. Generating the stability boundary this way in fact affords deeper insight than the contour cut method described in Section 3.3.5. Choosing $K_\psi = 0.3$ so that a continuation in K_θ will intersect the regions of interest in the contour-based stability boundary shown in Figure 3.13, the bifurcation diagram shown in Figure 3.14 is obtained. The pitch (θ) projection is shown. To link the bifurcations with the linear analysis discussed above, the BW eigenvalues and corresponding modal damping ratios are also shown.

In the bifurcation diagram (top right), note the Hopf bifurcations (square icons) at $K_\theta = 0.28$ and $K_\theta = 0.08$, and the pitchfork bifurcation (star icon) at $K_\theta = 0.03$. Only the fixed point solutions are plotted as the trivial periodic solution families (see Section 2.2.4.4) that emanate from the Hopf bifurcations are not of interest. The two Hopf bifurcations are labelled 'HB' for ease of reference. Although there is a separate mathematical basis for how CBM tracks solution values along branches, the subsequent eigenvalue analysis to determine if any bifurcations have occurred is essentially identical to the linear methods discussed, and therefore the position in K_θ of the

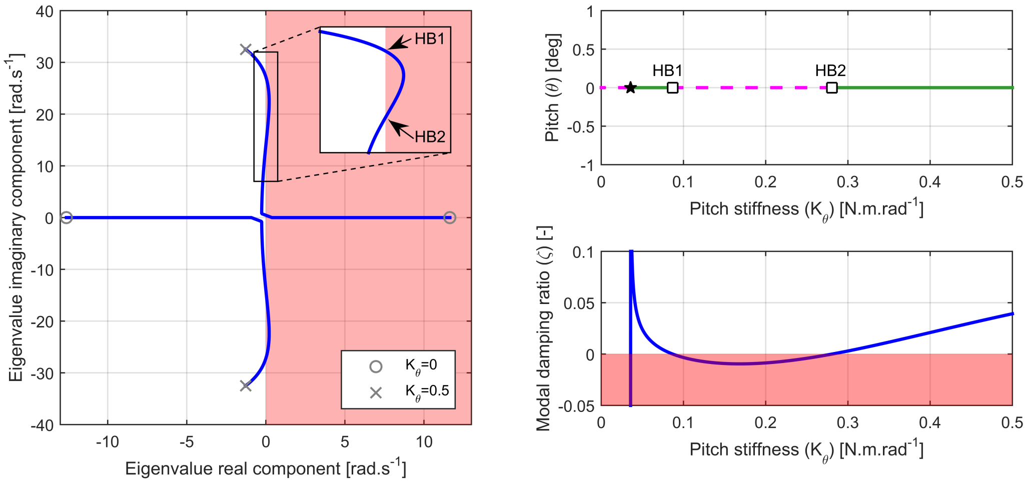

FIGURE 3.14. Bifurcation diagram *(top right)*, θ projection, with corresponding BW roots sweep *(left)* and modal damping ratio *(bottom right)*, as K_θ is varied

bifurcations correlates exactly with values at which the key eigenvalue transitions occur. The BW roots – the cause of any and all instabilities in this model – become unstable while oscillatory between $K_\theta = 0.28$ (HB2) and $K_\theta = 0.08$ (HB1), and then after becoming non-oscillatory near $K_\theta = 0.03$ one of the roots becomes unstable again. The damping ratio plot shows that the whirl flutter instability is only mild, and the pitchfork bifurcation manifests as a $1 \to -1$ snap merely as a mathematical technicality as the imaginary part of non-oscillatory roots is zero and the concept of damping ratio does not apply. The bifurcation diagram also shows that the solution remains at 0° pitch for the whole continuation. Physically speaking, whirl flutter occurs between $K_\theta = 0.28$ and $K_\theta = 0.08$, while static divergence may be encountered below $K_\theta = 0.03$. Looking at the sweep from the perspective of decreasing K_θ, the destabilisation at HB2 is physically intuitive: the reduction of stiffness fails to restrain the nacelle and allows oscillations. The re-stabilisation at HB1 occurs as the pitch stiffness is too low for enough elastic energy to be stored to sustain whirl flutter, but it is not yet low enough for the wing structure to be deformed by the freestream (the A'_1 terms in Equations (3.2) and (3.3)) in static divergence.

The K_θ-K_ψ stability boundary in Figure 3.13 could be built up iteratively by generating other bifurcation diagrams at a variety of "levels" of K_ψ and marking out the unstable regions found. However, if the sweep $(K_\theta, K_\psi) = ([0 \leftrightarrow 0.5], 0.3)$ is placed upon on the stability boundary (Figure 3.13), it becomes apparent that the round bubble and the side lobe present in that figure are defined by different types of instability. Therefore, two-parameter continuations in K_θ and K_ψ can be performed on either of the Hopf bifurcations and the branch point to trace their loci in the K_θ-K_ψ plane, and reconstruct the stability boundary in this way. Although manually tracking the relevant eigenvalue transitions through the plane could also reveal the underlying anatomy of the unstable region, progress toward the research objectives can be made if two-parameter continuation is used instead. Furthermore, the automation provided by continuation makes it a much more convenient method. These continuations are shown in Figure 3.15, and together they reconstruct the stability boundary obtained in Figure 3.13. Now however, the significance of each part of the boundary is known, as well as the path of some of the boundary segments once inside the unstable region.

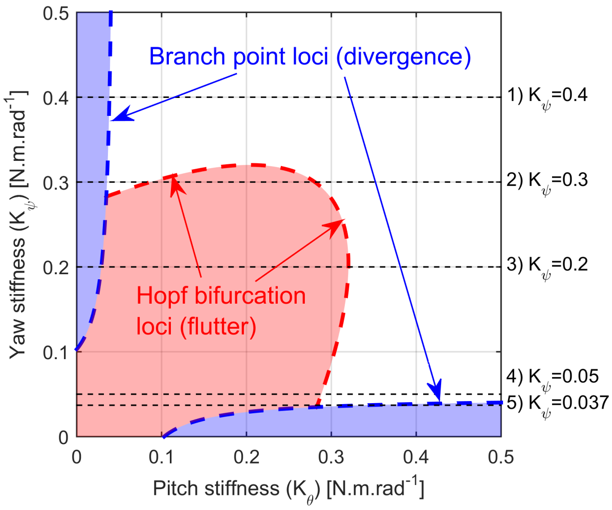

FIGURE 3.15. Basic model K_θ-K_ψ stability boundary regenerated through two-parameter continuations of the pitchfork and Hopf bifurcations

The red curved region in the bottom left corner of the diagram is defined by the location in K_θ of the Hopf bifurcation(s) for a given value of K_ψ. In the same way, the blue strips that are adjacent to the axes are defined by the branch point. Note that either HB1 or HB2 could have been used for the two-parameter continuation as they are part of the same boundary and both lead to the other via the continuation. These bifurcation loci together enclose the unstable region of the stability boundary. Therefore, all points that lie within the red region have oscillatory instability (i.e. whirl flutter). Similarly, all points that lie within the blue lobes have non-oscillatory instability and will experience static divergence. Note also that there is no overlap in these regions, because the BW roots that can cause instability cannot simultaneously exist as a complex conjugate pair (flutter) and two distinct real roots (static divergence). The dividing line between the unstable and stable regions – the stability boundary itself – corresponds to the neutral stability of the solution type in question. A number of K_ψ values are chosen as bifurcation analysis cases and are indicated on Figure 3.15.

As the Hopf and branch point are both on the equilibrium branch, which lies at zero displacement, the positions of the bifurcations do not change with the addition of any nonlinear stiffness terms. However, the dynamic behaviour outside the zero-deflection equilibrium branch calculated in Figure 3.14 (hereafter referred to as the *main branch*) is sensitive to the addition of nonlinear terms. It is further noted that constructing the main branch with CBM is functionally identical to conducting linear analysis, with the Hopf bifurcation marking the emergence of whirl flutter solution branches (in the nonlinear model variants) and thereby the onset point of instability. It is conducting continuations to find the periodic solution branches that emanate from this Hopf bifurcation that is the vital step to discovering how the system's whirl flutter characteristics have been affected by the presence of the nonlinearities.

In summary, the baseline stability characteristics of the original linear version of the basic model have been ascertained. It will serve as the basis for comparison with the nonlinear results which now follow. The stability boundary of structural stiffnesses (K_θ, K_ψ) has been set out and the areas that constitute whirl flutter are identified. It is therefore changes to these particular areas that are of interest when the nonlinearities are introduced. The use of CBM has also been demonstrated, as well as its links to eigenvalue analysis.

3.4.2 Nonlinear results: cubic hardening ($K_2 = 10$, $K_3 = 0$)

With the stability characteristics of the linear model thoroughly laid out as a baseline and the analysis tools demonstrated, the desired structural nonlinearities may now begin to be introduced. The first to be considered is cubic hardening, which uses a K_2 value of 10 and a K_3 value of 0 (see Figure 3.4 for an illustration of the profile). For ease of comparison with the linear model variant's analysis (Figure 3.14), the first continuation of the hardening variant is conducted with the same K_ψ value of 0.3. This corresponds to case 2) of the five identified in Figure 3.15. The bifurcation diagram of this continuation is shown in Figure 3.16. The continuation parameter is the linear stiffness K_1; it is equivalent to K_θ in the linear model variant though now the stiffness profile is of cubic form and the change of notation is required. The cubic stiffness nonlinearity causes a variety of nontrivial solution branches to be created, both of periodic solutions and equilibria.

Now the value of applying continuation to this problem is clear: the specific values of nontrivial solution branches are found in addition to any bifurcations on them. Specifically, the region of unbounded-amplitude whirl flutter, with Hopf bifurcations HB1 and HB2 at its ends, has been replaced by a whirl flutter LCO branch, connected to HB1 and HB2. Similarly, the onset of static divergence now marks the emergence of two such equilibrium branches where the nacelle is at rest but at a deflected position. These branches are hereafter referred to as *secondary branches* and they are mutually symmetrical about the continuation parameter axis, that is, $(\theta, \psi) \rightarrow (-\theta, -\psi)$. Here they are stable, and similar to the main branch, a small flutter branch is attached to each via two Hopf bifurcations, between which the equilibrium branch is unstable. This type of flutter is termed "secondary flutter" in the remainder of this work to distinguish it from flutter about the main branch. Lastly, it is typical in bifurcation analysis to extend the

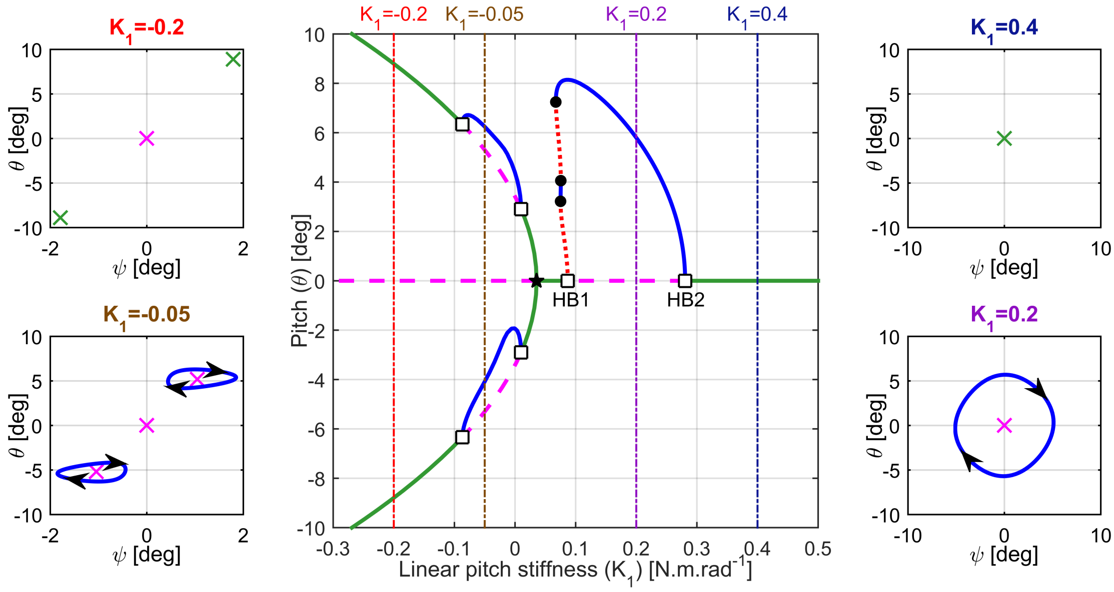

FIGURE 3.16. Bifurcation diagram for case 2 ($K_\psi = 0.3$) with phase planes showing solutions in detail at various K_1 values

continuation outside the physical range to search for any bifurcations which result in secondary branches extending back to the physical parameter range; this is why the lower limit used here is $K_1 = -0.3$.

To aid the reading of bifurcation diagrams throughout the work, the solutions at a variety of cuts in K_1 are shown in greater detail on ψ-θ phase planes to the left and right of the bifurcation diagram. The choice of coordinates (ψ, θ) approximately depicts the physical position of the rotor hub as observed in space. The cuts are chosen to provide a variety of different solution types and stabilities. Fixed point solutions are shown with crosses, while limit cycles have their complete path in the ψ-θ phase plane shown with a loop, with arrows indicating the direction of movement. The top left phase plane shows the two stable secondary branches aside the unstable main branch, while the bottom left phase plane shows the two stable secondary flutter LCOs about the now-unstable secondary branches, with the unstable main branch in the centre. The top right phase plane shows the main branch by itself, stable. The bottom right phase plane shows the main flutter LCO about the main branch, which at this point is unstable. The θ solution values of the fixed points on the phase planes can be directly cross-referenced with the y-value of the relevant branches at the corresponding K_1 cut. Similarly, the LCOs indicated on the relevant phase planes can be cross-referenced in the same way. In this representation it is clearer that the bifurcation diagram shows the maximum value of the state in question in the LCO present at that parameter value. All the instances of flutter are backward whirl, including those attached to the static divergence branches, however this deduction is made visually since the system's behaviour cannot reliably be described in modal terms now that it is nonlinear.

While bifurcation analysis is able to reveal complex behaviours of a system, a more profitable approach is to supplement continuation with time simulations at points of interest for a fuller understanding. Figure 3.17 shows time histories in pitch θ at the cuts in K_1 chosen in Figure 3.16, with different initial conditions to demonstrate the stability of various coexisting solutions by showing attraction or repulsion as relevant. Each time history is shown both for the pitch θ state alone and on the ψ-θ phase plane, and is colour-coded to correspond to Figure 3.16.

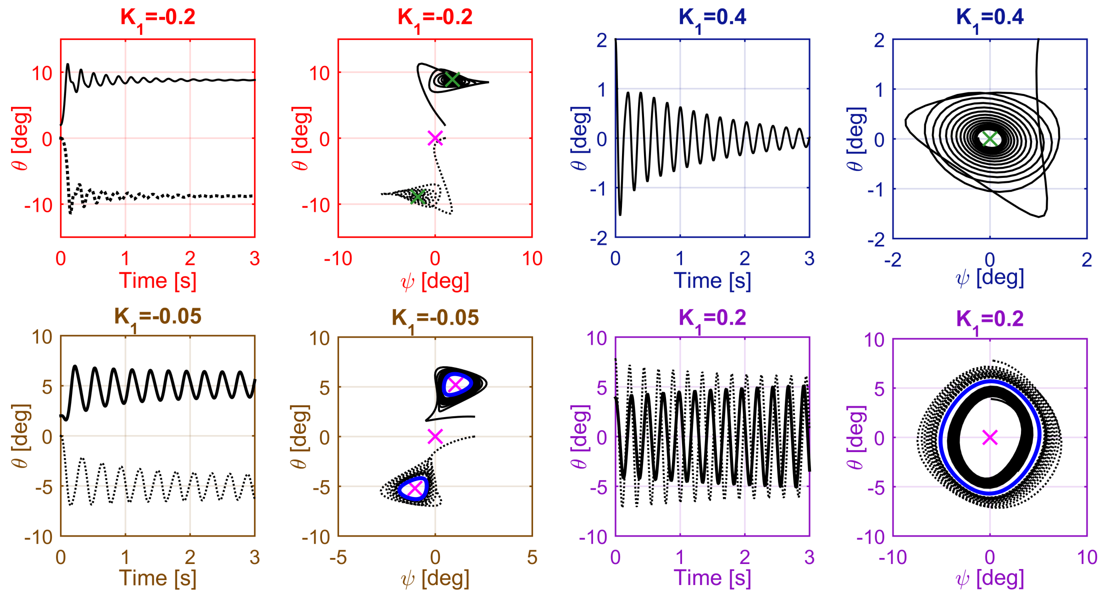

FIGURE 3.17. Time simulations for hardening variant, case 2 ($K_\psi = 0.3$), at the K_1 values used in Figure 3.16, with corresponding paths on ψ-θ phase planes

In order of ascending K_1, the simulations show convergence on either of the static divergence branch fixed points (red, $K_1 = -0.2$), joining either secondary branch flutter (brown, $K_1 = -0.05$), joining the main branch whirl flutter from both smaller and larger amplitudes (purple, $K_1 = 0.2$) and convergence on the main branch (dark blue, $K_1 = 0.4$).

Although it was touched upon in Section 2.2.4.4, it would serve well to establish a way of describing the theoretical findings of bifurcation analysis in terms of the practically-oriented language of aeroelasticity. This requires special care, despite the purportedly qualitative nature of both fields. The principal issue is the stability of solutions. When observed in practice, static divergence and whirl flutter are almost always fast, irreversible "runaway" unstable motions. However in continuation analysis, where exact values are found, both stable and unstable solution branches may be found for both equilibrium and periodic solutions, as is shown throughout this work. Unstable solution branches are often very difficult to recreate in time simulations, let alone to be observed in real-world systems. This leads to apparently contradictory terminology being used to describe the various behaviours observed in the model; the phrase “stable whirl flutter” is a contradiction in terms when viewed from the standpoint of aeroelasticity, though in the domain of nonlinear dynamical systems it refers quite clearly to a stable periodic solution branch that has emanated from a Hopf bifurcation on the main branch. Furthermore, in the same way that "whirl flutter" is applied to periodic solutions found in the nonlinear variants of the models used in this work, the term "static divergence" is applied to secondary equilibrium branches. This is because each is still occurring due to the same phenomena that cause them in the linear model; in the nonlinear models, the nonlinearities are simply able to prevent – in some parametric regions – the "runaway" motion. In order to preserve both the physical meaning of predicted behaviours and the insights afforded by bifurcation analysis, the terms “static divergence” and “whirl flutter” are used in direct conjunction with terms qualifying stability throughout the discussion sections of this work.

3.4.3 Effect of varying K_2

It is prudent to understand the effect of the value of K_2. Bifurcation diagrams with K_ψ set to 0.3 (case 2) for decreased and increased values of K_2 compared to the original value of 10 are shown in Figure 3.18. As is evident from the plots, increasing K_2 decreases the amplitude of both the flutter and the static divergence branches for a given value of K_1, due to increased structural stiffness. Furthermore, the concept of structural stability introduced in Section 2.2.2 is demonstrated here: the topology of the case 2 bifurcation diagram is unchanged by the value of K_2.

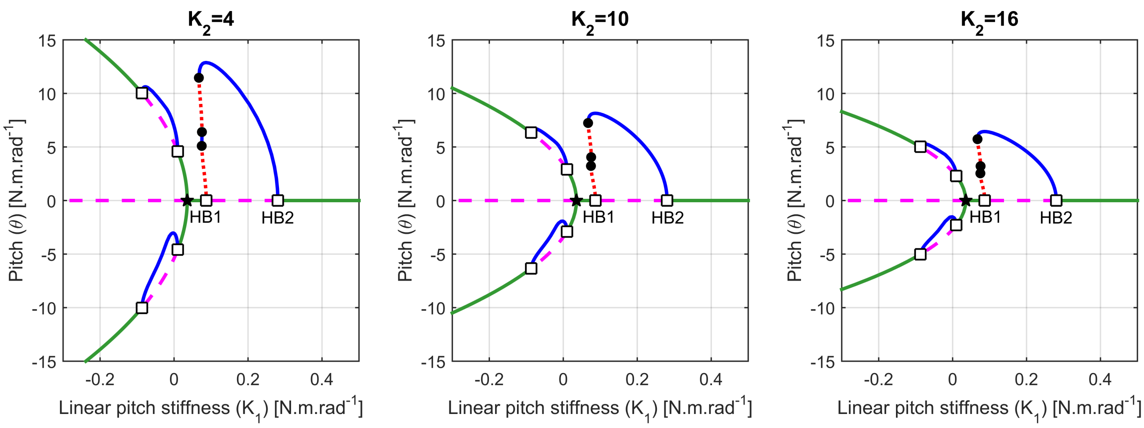

FIGURE 3.18. Effect of varying cubic stiffness K_2 in case 2

It is noted that the periodic solution branch connected to the main branch always leans over HB1, the Hopf bifurcation adjacent to the branch point. As a result a portion of the branch connecting to this bifurcation is unstable, which is present for all positive values of K_2. This is inevitable, as when a solution branch changes direction in the parameter space it must do so via a limit point/fold bifurcation, which involves a change of stability [260]. The effects of changing K_2 could also be explored for the other K_ψ cases shown in Figure 3.13, though given that the basic aspects of its effects are clear here, such exploration would be of limited value. Intuitively, the enlargement or compression effect described above can be expected for any given bifurcation diagram generated at some value of K_ψ.

3.4.4 Nonlinear results: cubic softening ($K_2 = -10$, $K_3 = 0$)

A softening yaw stiffness profile is now used, where the sign of the K_2 parameter is made negative ($K_2 = -10$, $K_3 = 0$). This profile is shown graphically in Figure 3.4. A bifurcation diagram for case 2 ($K_\psi = 0.3$) in this model variant, showing the pitch projection, is presented in Figure 3.19.

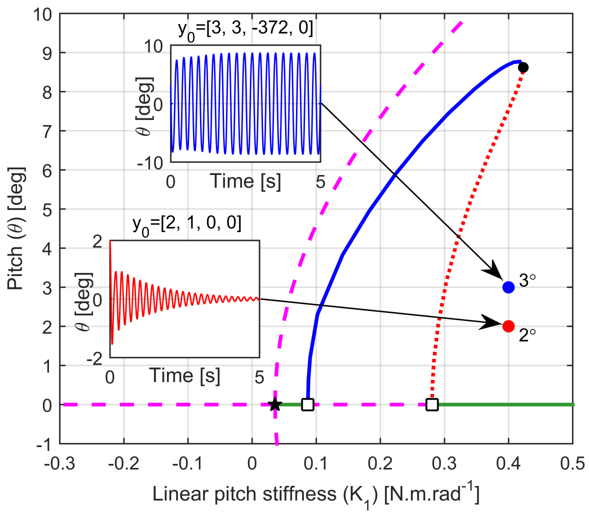

FIGURE 3.19. Bifurcation diagram of basic model, case 2, softening profile. Time simulations are shown in insets, with initial conditions y_0 shown in the title of each

The main branch bifurcations and the values of K_1 at which they exist are unchanged. The static divergence branches emanating from the branch point at $K_1 = 0.04$, though unstable, overhang the main branch, to the right of the Hopf bifurcation near $K_1 = 0.3$. While an unstable flutter solution emanates from this Hopf bifurcation, this branch eventually becomes stable through a limit point at approximately $K_1 = 0.42$, and both portions overhang the stable portion of the main branch (from $K_1 = 0.28$ upwards) as far as this limit point. This phenomenon, where a stable portion of the main branch is overhung by a flutter LCO, is hereafter referred to as *overhang*. Time simulations for selected points are shown in subplots.

A rotor nacelle mounted on an aircraft is subject to perturbations, from manoeuvring or gusts, for example. A perturbation of the rotor-nacelle may ultimately bring it sufficiently close to either of these solution branches to be attracted to them, and experience behaviour of that branch's type. The time simulations show that for $K_1 = 0.4$, where the main branch is stable, a pitch perturbation of 2° results in a decaying motion, but a stable flutter LCO develops almost immediately with a perturbation of 3°. In general, a perturbation may consist of any combination of individual state perturbations (i.e. angles and angular rates). Provided sufficient angular rates, attraction to the stable flutter branch overhanging $K_1 = 0.4$ could be possible from even lower angles than 3°. The regions of attraction for these two solutions are certainly not readily apparent from the bifurcation diagram alone.

However, a further risk exists in this analysis case. An unstable solution branch may be part of a separatrix[2] between two basins of attraction. Here, the unstable static divergence branches leading off indefinitely to the right are part of separatrices between attraction to the stable main branch, and "blow-up" divergence to infinity. That is, if the system crosses beyond this separatrix, via a perturbation, it will diverge to an infinitely large solution. Physically speaking, this means structural failure of the system. The linear stability analysis is unable to predict the above results. The flutter boundary it predicts is simply the location of the Hopf bifurcation at $K_1 = 0.28$, though flutter and static divergence behaviours are shown to exist and may be encountered for values of K_1 that lie within the stable region. As separatrices are manifolds in the state space, and bifurcation diagrams typically only show one dimension of the state space, an arbitrary point shown on a bifurcation diagram could be on either side of a given separatrix. In this system, for a phase point to be subject to the aforementioned divergence to infinity, all its state coordinates must place it on the divergence side of the separatrix.

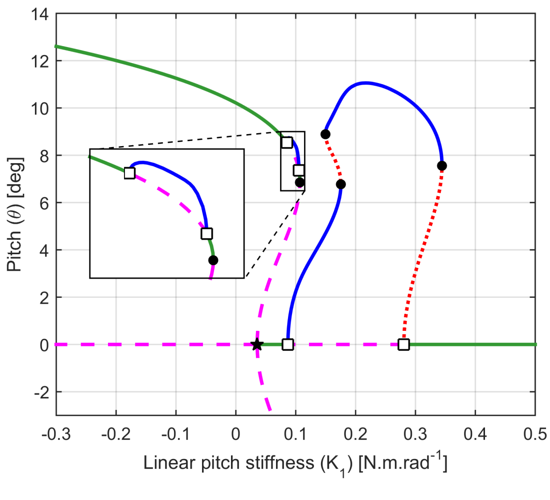

FIGURE 3.20. Bifurcation diagram of basic model, case 2, combined softening-hardening profile

[2] Separatrix: an $(n-1)$-dimensional manifold within an n-dimensional space that separates regions of the phase space, such as distinct basins of attraction [261].

3.4.5 Nonlinear results: combined softening – hardening ($K_2 = -10$, $K_3 = 350$)

A hardening quintic stiffness component (K_3) is now introduced into the softening stiffness profile used in Section 3.4.4. The value of K_3 chosen was 350, so that the stiffness curve is in the neighbourhood of the linear profile within the angle range of [-10°, 10°] (see Figure 3.4), a physically reasonable range of deflection. Initially, the bifurcation diagram for case 2 is presented in Figure 3.20.

Compared with the softening variant's results, here the hardening component bends the static divergence branches back round to the left, allowing a small branch of secondary flutter LCOs to exist on each, as seen in the hardening variant. There is also some bending back of the flutter branch attached to the main branch, in the same manner. These observations are consistent with the contrasting influences of the hardening and softening components. As the softening component dominates at lower deflections due to being in the lower power, it influences the direction of departure of the branches from the bifurcations that attach them to the main branch. These features are seen in the softening-only case above. However, the behaviour of the system at larger deflections, both the equilibria and periodic solutions, is dominated by the hardening component in the quintic power, which helps to bound the solution amplitudes and make them stable.

To provide a level comparison between the behaviours of each stiffness type (hardening, softening, combined), the projections for all states for case 2 are shown in Figure 3.21. As before, the secondary equilibrium branches in the pitch and yaw projections (first two rows of Figure 3.21) show the static divergence position for a given value of K_1. As static divergence branches are fixed points, these secondary branches appear to overlap the main branch in the pitch rate and yaw rate projections (last two rows of Figure 3.21) in all three models, as in both branches pitch rate and yaw rate are by definition zero. In the hardening and combined variants (left and right columns of Figure 3.21), each static divergence branch has its own secondary flutter LCO branch.

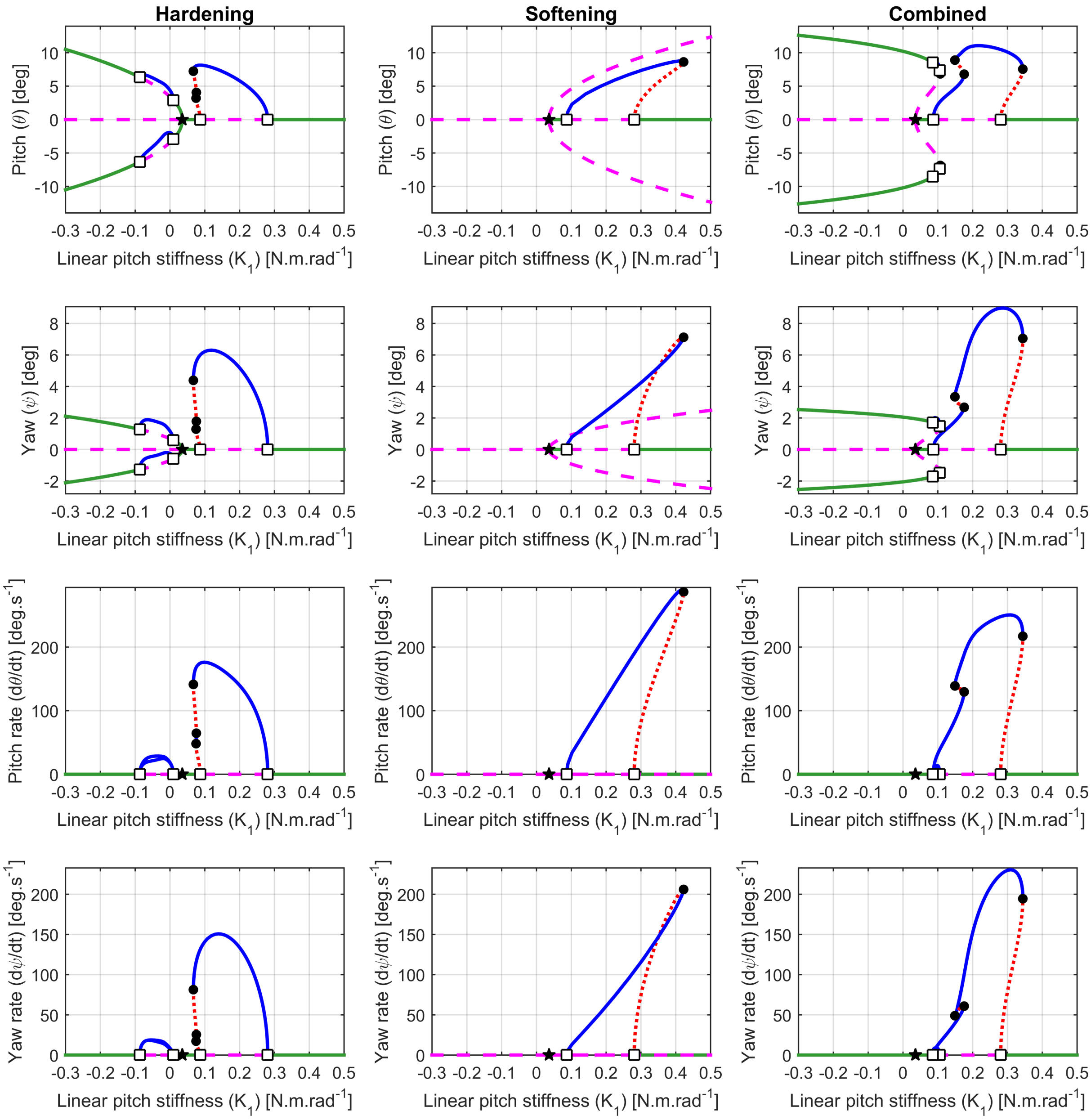

FIGURE 3.21. Bifurcation diagram of basic model, case 2, all projections, all profiles

The pitch projections for all five K_ψ cases from all three variants are summarised in Figure 3.22. Considering a given diagram from right to left, i.e. for descending K_1: case 1 ($K_\psi = 0.4$, top row) shows divergence only, case 2 ($K_\psi = 0.3$, second row) shows a separate region of flutter only followed by divergence, case 3 ($K_\psi = 0.2$, third row) shows flutter which eventually coexists with static divergence, case 4 ($K_\psi = 0.05$, fourth row) shows flutter only, and case 5 ($K_\psi = 0.037$, bottom row) shows a separate region of divergence followed by flutter. Only the projection in pitch θ is shown in Figure 3.22, though projections in any of the other state variables would present the same qualitative results.

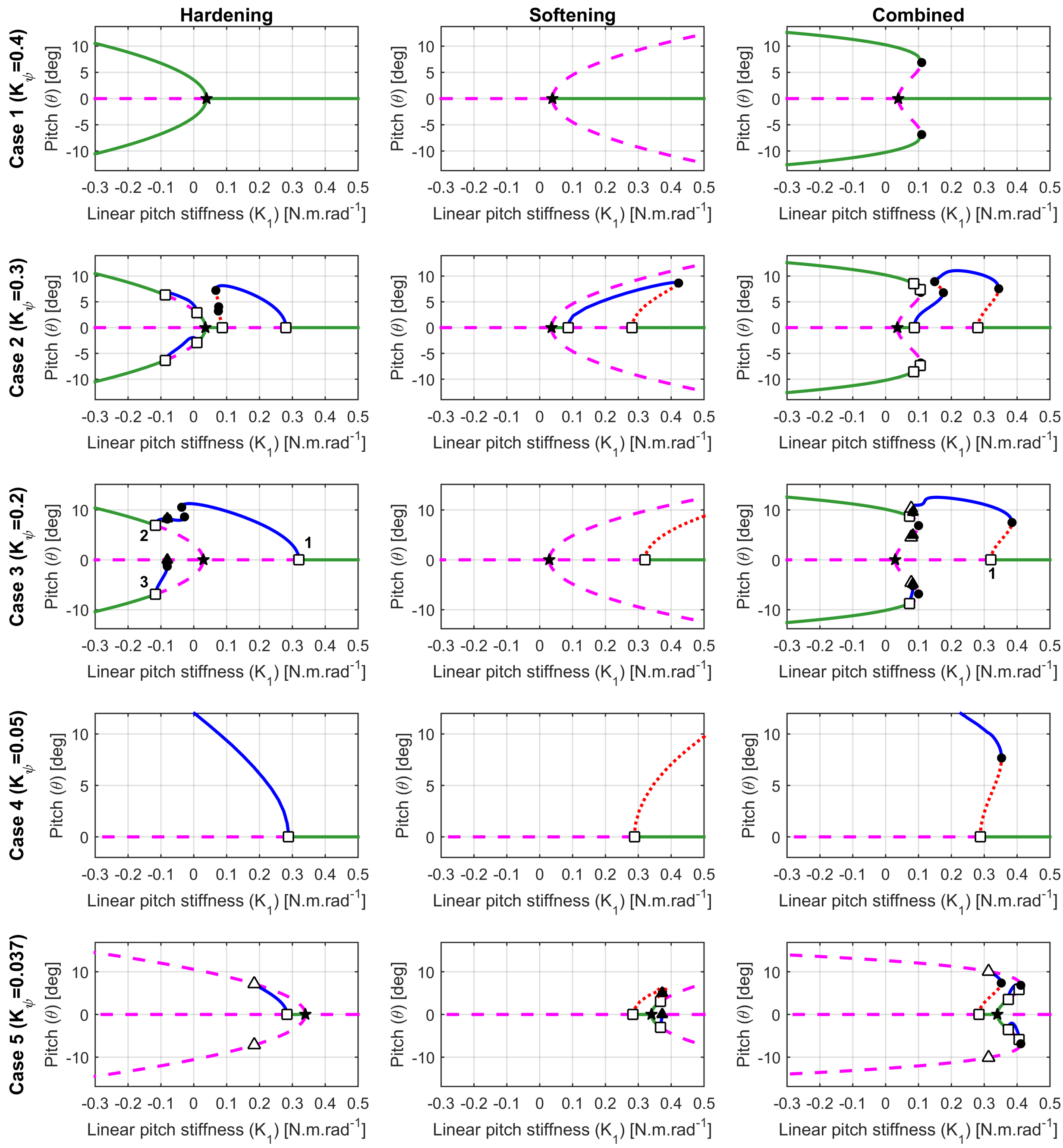

FIGURE 3.22. Bifurcation diagram of basic model, all cases, pitch projection, all profiles

Each of the diagrams can be cross-referenced with Figure 3.13 to confirm that the bifurcations present on the main branch correspond to the extent of the unstable regions at the relevant value of K_ψ. As the value of yaw stiffness is gradually decreased, the amplitude of the limit cycles increases significantly.

Interesting to note is the complex interaction in case 3 ($K_\psi = 0.2$) in the hardening and combined variants (Figure 3.22, middle column, left and right) that occurs between the limit cycles emanating from the main branch and those emanating from the two secondary branches. In case 2, these periodic solution branches are entirely distinct and unconnected. However in case 3, these limit cycle branches have collided due to a homoclinic bifurcation, covered in more detail in Section 3.4.7. On the other hand, a collision between a flutter branch and a static divergence branch occurs in case 5 ($K_\psi = 0.037$), due to a heteroclinic bifurcation.

Regarding the results from the softening variant, the bifurcations on the main branch still occur in the same left-to-right order as in Figure 3.16, as nonlinear stiffness terms do not affect their location. Moreover, the regions of stability of the main branch are unaffected. However, both the static divergence and flutter branches are reversed left-to-right in the direction of their departure from the main branch. With the exception of case 5, all the static divergence branches are unstable and no secondary limit cycle branches were found to emanate from them, as seen in cases 2 and 3 of the hardening variant. The flutter branches in case 3 are no longer bounded or stable as they were in the hardening variant, continuing to grow as K_1 is increased. Furthermore, the flutter branch in case 5 is now connected to the secondary flutter branches through a homoclinic bifurcation.

The values of K_1 at which the bifurcations on the main branch occur is still unchanged in the combined softening-hardening variant, as is to be expected. The static divergence branches depart from the main branch in the same manner as in the softening variant in terms of direction and stability, though at larger deflections (i.e. further away from the main branch) the quintic hardening overpowers the cubic softening and the branches are bent back in the direction of the hardening variant's branches, i.e. decreasing K_θ.

The flutter branches in the combined variant cases mainly resemble those of the hardening variant cases in terms of shape, however the regions of stability on the branches have more in common with the softening cases. This seems to be another effect of the differing dominant regions of the cubic and quintic terms. The cubic softening's dominance at low deflections influences the direction of a branch's departure from the main branch. By contrast, the quintic hardening's dominance at higher deflections plays a greater part in influencing the path of the branch through the state space, specifically which other bifurcations the branch is connected to. This affects the overall shape of the branch and causes resemblance of the hardening variant's diagrams. As the stability of periodic solution branches changes through limit points, it is the combination of departure direction and overall shape that influences the regions of stability along a given branch. For example, a branch that departs a bifurcation in one direction, but eventually connects to another bifurcation on the opposite side of its emanation point, will have both stable and unstable portions. In contrast, if the branch spanned the two bifurcations without a change in direction and therefore a limit point, there would not necessarily be a change in stability.

Taking a broader view of the bifurcations and branch shapes in each system allows some links to become clear. The branch points with their stable equilibrium branches in the hardening variant can be directly attributed to the hardening term (K_2) in the stiffness function due to the close resemblance of the supercritical pitchfork bifurcation normal form. Similarly, the softening term present in the softening and combined variants closely resembles the subcritical pitchfork bifurcation normal form.

3.4.6 Effect of varying K_3

In the same manner that the effect of the value of the cubic stiffness parameter K_2 was investigated in Section 3.4.3, the effect of the value of the quintic stiffness parameter K_3 on the combined softening-hardening variant's behaviour is investigated here. Bifurcation diagrams for increased and decreased values of K_3 are shown in Figure 3.23.

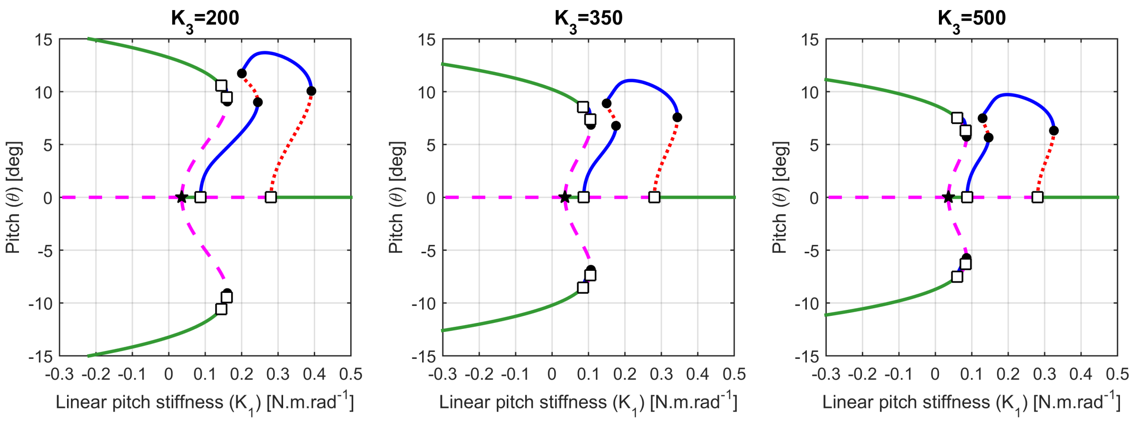

FIGURE 3.23. Effect of varying quintic stiffness K_3 in case 2

The effect of K_3 is similar to the effect of K_2 in that a higher value makes for a stiffer structure than a lower value, and the effect is to restrict the extent of the static divergence branches and the amplitude of periodic solutions. However, as the quintic hardening controlled by K_3 acts in opposition to an existing cubic softening component, the respective influences of each are in conflict. Specifically, the softening's influence of bending the flutter branches to the right and making them unstable is contested by the hardening's influence of bending them leftward and making them stable. The prevalence of each influence is dictated by the ratio of the respective parameters, which now varies with K_3 being varied. This influences the extent of the previously mentioned overhang phenomenon: as K_3 is weakened, it takes larger deflections for the quintic hardening to overpower the cubic softening, which increases the extent of the overhang. The reverse is true for larger K_3. Physically speaking, the more pronounced a structure's hardening characteristic is in relation to its softening characteristic, the less susceptible it is to overhang effects and therefore the less inaccurate its linear-predicted onset speed is.

3.4.7 Homoclinic and heteroclinic bifurcations

In the hardening and combined variants of case 3 ($K_\psi = 0.2$; Figure 3.22, middle row, left and right sides), the disappearance of the limit cycle branches upon contacting the secondary branches is explained by the homoclinic and heteroclinic bifurcations that they undergo. As a continuation parameter is varied, a portion of a limit cycle may approach a fixed point. Although the fixed point may be unstable, the vector field (as described by the differential equations of motion) in its near vicinity will describe smaller and smaller rates of change of the system states. Therefore the period of the limit cycle will increase as it approaches the fixed point, reaching infinity when the collision occurs and the homoclinic/heteroclinic trajectory is created. This runaway increase can be used as an indication of the presence of such a bifurcation[3]. The homoclinic and heteroclinic trajectories were illustrated in schematic form in Figure 2.17. The process of creating such a homoclinic or heteroclinic trajectory is known as a homoclinic/heteroclinic (as appropriate) bifurcation. Taking the hardening variant first, a phase portrait is shown in Figure 3.24 to demonstrate how the limit cycles collide with a fixed point to create a homoclinic trajectory.

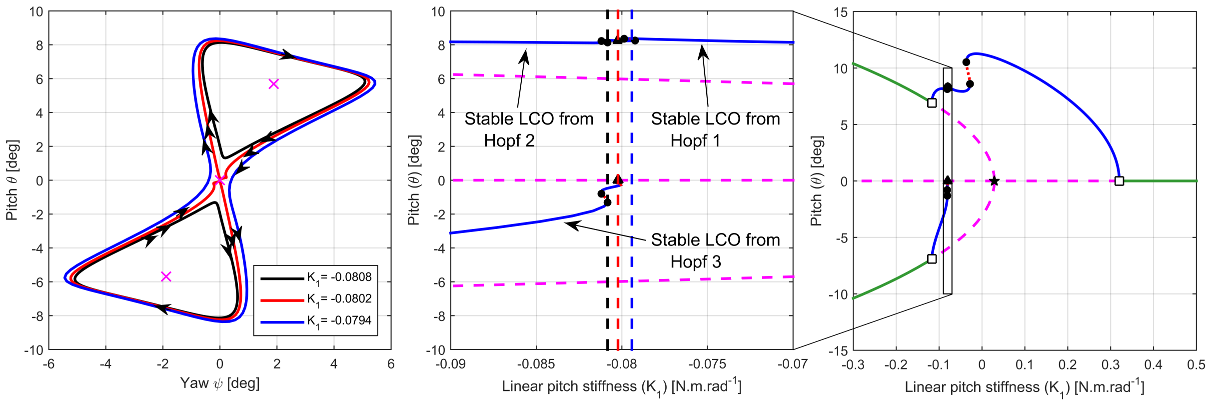

FIGURE 3.24. Phase plane of trajectories before, during and after a homoclinic bifurcation in hardening case 3 *(left)*, with excerpt of corresponding bifurcation diagram *(centre)* and full corresponding bifurcation diagram *(right)* for cross-reference

[3] One method of pinpointing the location of homoclinic and heteroclinic bifurcations if the collision itself is not visible is to fit a $1/x$ curve to the Period vs. Parameter graph. The Parameter value over which the asymptote falls is then taken to be the location of the bifurcation, as this is where the Period would be infinite.

The solutions for three values of K_1 are illustrated – two limit cycles, one on either side of the homoclinic bifurcation (blue and black), and the homoclinic trajectory itself (red). The various elements of the phase portrait can be cross-referenced with the excerpt of the bifurcation diagram provided on the right side of the figure. The numbering of the Hopf bifurcations used to identify the various periodic solution branches in the right side of the figure is illustrated in the relevant subplot of Figure 3.22. Some simplifications have been made to improve the figure's readability. Firstly, although the cut indicated with the black line intersects the secondary flutter branch (from Hopf 3) twice in different places, only the LCO closest to the homoclinic bifurcation is shown. Additionally, the fixed points (magenta crosses) from the static divergence branches move very slightly between the K_1 plane cuts chosen, though only their locations at the homoclinic point are shown.

In both of these plots, the maximum (positive) amplitude of each limit cycle and the position of the fixed point branches is visible. To the left of the bifurcation point, two separate limit cycles exist (black), each about one of the static divergence branches. As K_1 increases, the innermost corner of each limit cycle nears the equilibrium at the origin – the main branch mentioned in previous sections. The limit cycles simultaneously make contact with the origin fixed point at $K_1 = -0.0802$, fusing to form a homoclinic trajectory (red). Beyond this value of a K_1, a single limit cycle forms whose trajectory loosens, taking on the appearance of a bow tie (blue).

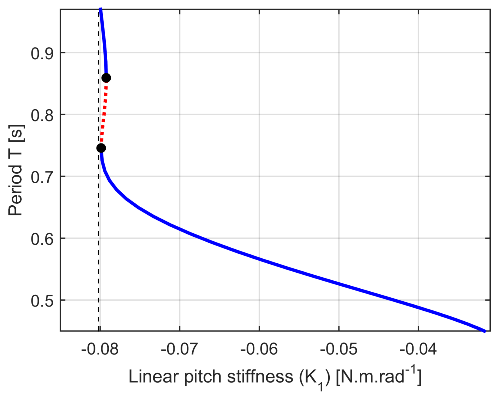

FIGURE 3.25. Plot of limit cycle period near the homoclinic bifurcation shown in Figure 3.24, hardening case 3

The homoclinic bifurcation itself is therefore at (ψ, θ, K_1) = (0, 0, -0.0802), as this is the point at which the two limit cycles collide and fuse. On the bifurcation diagram shown in Figure 3.24 (left), the limit cycle branches are indicated by their maximum amplitude, and therefore the secondary flutter branches seem to disappear on this projection. To indicate their annihilation via a homoclinic bifurcation, the ends of the branches are also marked with the homoclinic bifurcation symbol. The period of the larger single limit cycle approaching the homoclinic bifurcation (from the right) is shown in Figure 3.25. The stability and limit points are also included for cross-referencing with Figure 3.22 (middle row, left side) and Figure 3.24 (right). The characteristic asymptotic increase in period near the bifurcation is clearly visible.

The combined variant's results in case 3 ($K_\psi = 0.2$) feature homoclinic bifurcations and a heteroclinic bifurcation. The heteroclinic bifurcation at $K_1 = 0.0779$ is explored here. Unlike the homoclinic bifurcations seen previously, the heteroclinic bifurcation involves a heteroclinic trajectory that joins two equilibria. A phase portrait showing trajectories at and near the bifurcation is shown in Figure 3.26.

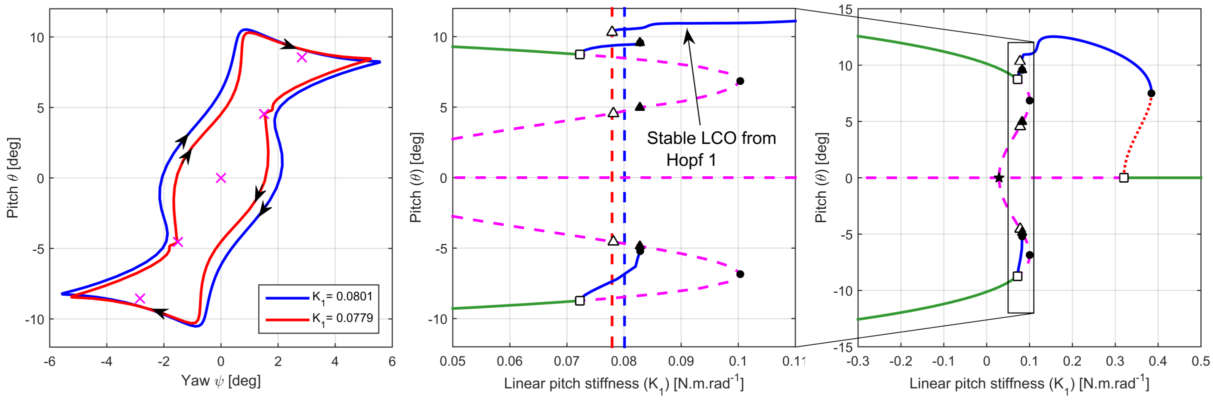

FIGURE 3.26. Phase plane of trajectories before, during and after a heteroclinic bifurcation in combined case 3 *(left)*, with excerpt of corresponding bifurcation diagram *(centre)* and full corresponding bifurcation diagram *(right)* for cross-reference.

The two equilibria that are joined by the heteroclinic trajectory are the inner pair of fixed points at $(\psi, \theta) = \pm(1.5, 4.5)$. As the complete motion strictly comprises two trajectories, one from left to right and the other vice versa, it is termed a heteroclinic cycle [311]. As the bifurcation point is approached from beneath (increasing K_1), certain corners of the limit cycle move toward the fixed points mentioned, eventually colliding with them simultaneously at $K_1 = 0.0779$. The period of the limit cycle approaching the heteroclinic bifurcation (from the right) is shown in Figure 3.27.

There are also two homoclinic bifurcations at $K_1 = 0.0828$ where the secondary flutter branches collide with the same inner pair of fixed points involved in the heteroclinic bifurcation. Homoclinic and heteroclinic bifurcations are also visible in case 5 ($K_\psi = 0.037$). In the hardening variant (Figure 3.22, bottom row, left side) the periodic branch's maximum and minimum extents simultaneously make contact with the static divergence branches, annihilating after forming a heteroclinic cycle between the two equilibria. In the softening variant (Figure 3.22, bottom row, centre), the unstable flutter branch folds back to become stable at approximately $K_1 = 0.38$, and very shortly afterwards splits into two limit cycles via a homoclinic bifurcation at (ψ, θ)

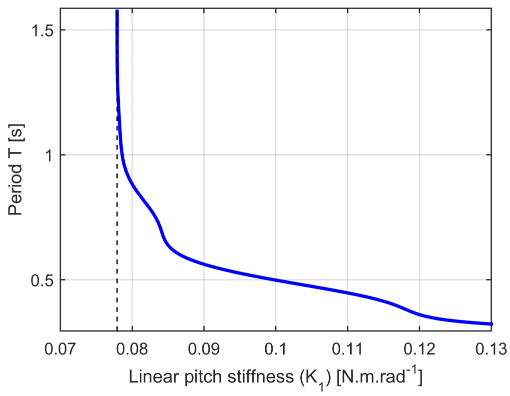

FIGURE 3.27. Plot of limit cycle period near the heteroclinic bifurcation shown in Figure 3.26, combined case 3

= (0, 0). These two new limit cycles are secondary flutter motions about the static divergence branches. This is the same process that occurred in the hardening variant for case 3 (K_ψ = 0.2), interpreted in reverse. In the combined variant (Figure 3.22, bottom row, right side), the main flutter branch collides with both static divergence branches simultaneously, in the same manner as in the hardening variant.

The aeroelastic implications for homoclinic and heteroclinic bifurcations are based on their linking of periodic solution branches with equilibrium branches. If a rotor-nacelle system is undergoing a reduction in stiffness over time, due to damage being incurred from aeroelastic activity, then it may pass from one solution type (periodic solution/equilibrium) to the other, depending on the layout of the bifurcation diagram for a given system. This may manifest as a "jump" in the case of transitioning from an undeflected equilibrium (the main branch in the above figures) to a whirl flutter branch that surrounds that equilibrium in the phase space.

A further threat exists that is connected specifically to homoclinic bifurcations. The Shilnikov criterion links the existence of homoclinic orbits to some forms of chaos [259]. As chaos is dynamic activity of the system, if it were found in this model it would constitute just as much of a threat to the structural integrity of a nacelle-wing structure as periodic motions do.

3.5 Implications for Stability Boundaries

3.5.1 K_θ-K_ψ stability boundary

The overhang phenomenon has repercussions for the whirl flutter stability characteristics of the model. As shown in Figures 3.21 and 3.22, overhang occurs in the softening and combined variants, meaning that flutter can be encountered in parametric regions that linear eigenvalue analysis predicts to be stable. In the softening variant, this overhang occurs in the approximate region $0.28 < K_\psi < 0.32$. In this region, bifurcation diagrams take the form of case 2 ($K_\psi = 0.3$; Figure 3.22, second row, centre). That is, a stable flutter branch exists but is connected only to the main branch, and the static divergence branches each have a secondary flutter branch about a small portion of them. The region is bounded by the existence of all the necessary bifurcations; at approximately $K_\psi = 0.28$ the left-most Hopf (HB1) and the pitchfork collide and the left-most Hopf annihilates as detailed in Section 3.4.5. This is because instability of the system can only originate from the BW pair and therefore both kinds of instability cannot coexist. For values of K_ψ lower than 0.28, the whirl flutter branch emanating from HB2 no longer has a second main branch Hopf bifurcation to fold back to, and therefore while it continues to overhang the main branch on its right side, it does not contain any stable regions (Figure 3.22, middle to last rows, centre). The greater threat however is posed by the two unstable equilibrium branches, which, as part of separatrices in the phase space as discussed previously, causes divergence if the system strays sufficiently far from the main branch. These overhanging equilibrium branches exist for all K_1 and all K_ψ: the phenomenon cannot be prevented by any increase of either of these stiffnesses.

In the combined variant, stable overhang of the main flutter branch exists for a much greater range of K_ψ. Overhang exists from $K_\psi = 0.32$ downwards as in the softening variant (Figure 3.22, second row, right side). However, after HB1 has collided with the branch point at approximately $K_\psi = 0.28$, stable flutter branch portions still overhang a stable portion of the main branch. Continuing to descend in K_ψ, this overhang exists until the static divergence region near the K_1 axis is met. Here, at $K_\psi = 0.037$, the main branch rightward of the branch point does experience stable flutter branch overhang (albeit connected to the static divergence branches), though the main branch itself is unstable (Figure 3.22, bottom row, right side).

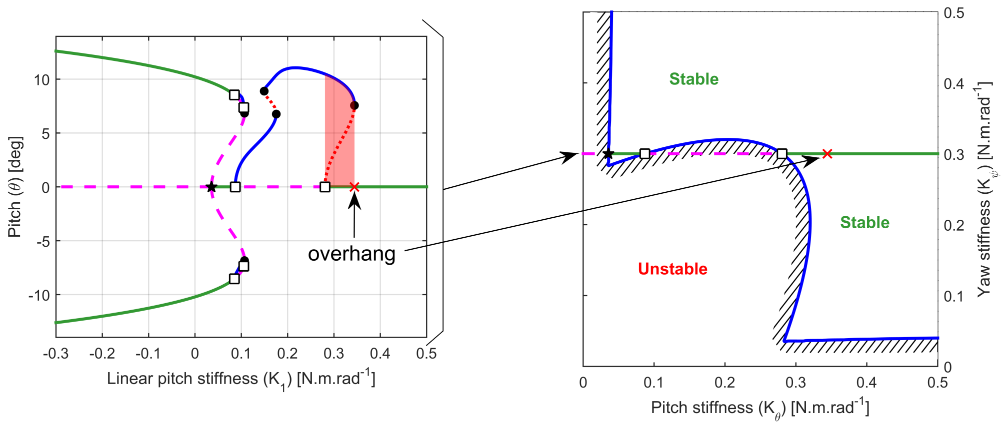

FIGURE 3.28. Bifurcation diagram for combined softening-hardening model variant case 2, with overhang region shaded red and overhang extent indicated with a red 'x' (*left*), next to stability boundary with the bifurcation diagram's main branch superimposed at the relevant value of K_ψ, along with overhang extent (*right*)

The danger of the overhang is that it invalidates the linear eigenvalue analysis stability predictions. This is best understood graphically by relating the overhang in a given bifurcation diagram to the parametric position of the overhanging whirl flutter behaviours within the stability boundary that was constructed in Figure 3.13. This is shown in Figure 3.28 for the combined softening-hardening variant, case 2.

Although the right-most Hopf bifurcation, which the linear analysis takes to be the whirl flutter onset point, is at $K_\theta = 0.2806$, the whirl flutter LCO reaches as far right as $K_\theta = 0.3443$. The linear analysis predicts this value of K_θ to be stable, however a perturbation of the system could cause it to join this overhanging whirl flutter branch.

A revised stability boundary accounting for the rightward reach of any overhanging flutter branch with a stable portion can be generated. This can be achieved either through iterated one-parameter continuation over a variety of K_ψ values, or through two-parameter continuation of the right-most limit point found on the flutter branch to trace its path in K_ψ and K_1 simultaneously. Such a revised stability boundary for the combined model variant is shown in Figure 3.29. The original linear model boundary and the enclosed unstable region are shown in grey. The additional unsafe area due to the aforementioned overhang phenomenon in the combined variant is shown in red. Some of the boundaries are coincident though the overhang region extends to the right of the Hopf loci. The new region is termed "unsafe" as the whirl flutter behaviours present are stable, and the word "unstable" is here more of a relic from the nature of the linear whirl flutter instability.

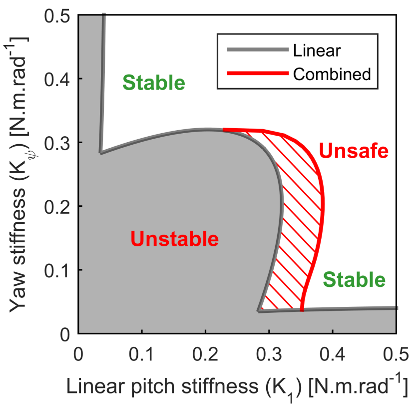

FIGURE 3.29. Revised K_1-K_θ stability boundary accounting for overhanging whirl flutter branches

It is also important to note that CBM's prediction of stable solution branches existing well into parametric regions that linear analysis declared to be unstable is not an indication that these parametric regions have been made safe by the presence of the nonlinearities. Rather, the model does not account for any structural damage that the occurrence of whirl flutter LCOs would likely cause the rotor system, leading to potentially catastrophic structural failure.

3.5.2 Airspeeds at which whirl flutter may be encountered

As stated earlier, whirl flutter is often thought of as being activated aerodynamically, and this was accordingly its first demonstration in this work. So far in this chapter, the ability of polynomial stiffness nonlinearities to cause whirl flutter branches to overhang stable parameter regions has been shown in the structural stiffness domain. To close this chapter, a return to the aerodynamic case is now made and the overhang effect is now demonstrated in airspeed. Figure 3.30 shows a continuation in airspeed V of the undeflected main branch in the combined model variant, between the datum value of 6.7 ms^{-1} and 8 ms^{-1}. The other parameters are left at their datum values as indicated in Table 3.1.

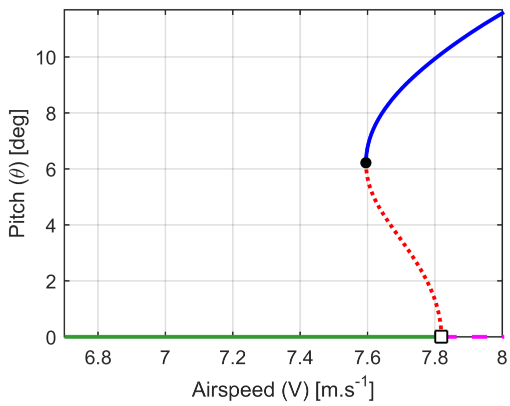

FIGURE 3.30. Airspeed continuation for basic model, combined variant, datum parameter values

The main branch becomes unstable at about $V = 7.8$ ms^{-1}, as the eigenvalues sweep shown in Figure 3.5 also shows. However, due to the polynomial stiffness nonlinearity (and invisible to linear stability analysis), the whirl flutter branch bends back to 7.6 ms^{-1}. Whirl flutter may therefore be encountered from 7.6 ms^{-1} onwards, although linear analysis predicts the onset to be 7.8 ms^{-1}.

3.6 Conclusions

A summary of this chapter's activity is given here. The relevant research process steps (e.g. P1) are also indicated for each item. This chapter has:

- introduced the basic model used in this work (P1)
- introduced and demonstrated classical whirl flutter (P1, P2)

- used linear stability analysis to investigate the parametric sensitivity of classical whirl flutter (P2)
- introduced the smooth nonlinearity and discussed its implementation in the basic model (P3)
- applied CBM to the basic model (P3, P4) when configured with:
  - the original linear stiffness profile
  - a hardening stiffness profile
  - a softening stiffness profile
  - a combined hardening-softening profile
- demonstrated the concept of **overhang** (P5)
- discussed the homoclinic and heteroclinic bifurcations found (P5)
- redrawn the structural stiffness stability boundary (K_θ-K_ψ) for the combined model variant to account for the overhang caused by the nonlinearity (P6)
- performed a continuation in airspeed to show the overhang existence in this parameter (P4, P5)

This contributed to the following research objectives:

- **O1**: assess the effect of a smooth nonlinearity on the whirl flutter dynamics of rotor-nacelle systems
  - The presence of nonlinearities was found to create whirl flutter LCOs and secondary equilibrium branches involving static deflection of the rotor-nacelle. These solution branches have their own associated stability and are the nonlinear equivalents of the well known linear phenomena, whirl flutter and static divergence, respectively. In linear stability analysis of whirl flutter, the whole system's stability is assessed using eigenvalue analysis, and the whirl flutter onset point of a parameter is taken as the value at which oscillatory instability emerges. The solution branches found in the nonlinear model variants were found to exist over a range of values of the chosen continuation parameter, pitch stiffness, in places coexisting with the main branch at values outside of the linear stability analysis' predicted unstable region. This important phenomenon, referred to as **overhang**, creates new **unsafe** parametric regions where it occurs, as whirl flutter may be encountered via perturbations despite the linear prediction that it cannot.

- Conversely, the prediction of stable solution branches existing in parametric regions that linear analysis declares to be unstable is not an indication that these parametric regions have been made safe by the presence of the nonlinearities. This is because the model does not account for any structural damage that the occurrence of whirl flutter LCOs would likely cause the rotor system, leading to potentially catastrophic structural failure.
- Hardening variant: The hardening component of the stiffness profile created largely stable solution branches, bounding the system response in the parametric regions that in the linear model variant contained linear (i.e. exponentially divergent) whirl flutter and static divergence behaviours. Overhang was not observed in the analysed cases.
- Softening variant: The softening component of the stiffness profile generally led to larger values of fixed point solutions and increased amplitudes of LCOs, that were largely unstable. While some overhang was observed, the greatest practical risk is the presence of unstable secondary equilibrium branches, which overhang the stable main branch in the same way. Rather than posing the risk of whirl flutter, these secondary equilibrium branches are part of separatrices between attraction to the stable main branch and divergence to infinity.
- Combined variant: The influences of both hardening and softening profile components were visible, with the lower amplitude parts of the solution branches resembling those in the softening variant's results, and the higher amplitude parts resembling those in the hardening variant's results. The stabilising influence of the added hardening component caused the overhanging secondary equilibrium branches seen in the softening variant to be bent back, away from the stable region of the main branch. The same was true of the whirl flutter branch connected to the main branch. Overhang was visible in several of the analysis cases examined, and the unsafe region created as a result was mapped out within the K_θ-K_ψ stability boundary, which was used to characterise the whirl flutter stability characteristics of the linear system.

- **O4**: explore what types of whirl flutter behaviours are observable over a range of design and operating parameters
  - Within the analysis of the basic model, periodic solutions and equilibrium branches were found. Quasi-periodic behaviours were not found to be present, nor was chaos observed in any time simulations generated.
  - In addition, homoclinic and heteroclinic bifurcations were observed in two of the hardening variant cases, one of the softening variant cases and two of the combined variant cases. Homoclinic bifurcations are known to be associated with some kinds of chaos, though no such behaviour was observed.

CHAPTER 4

Moving Toward a Gimballed Hub Model

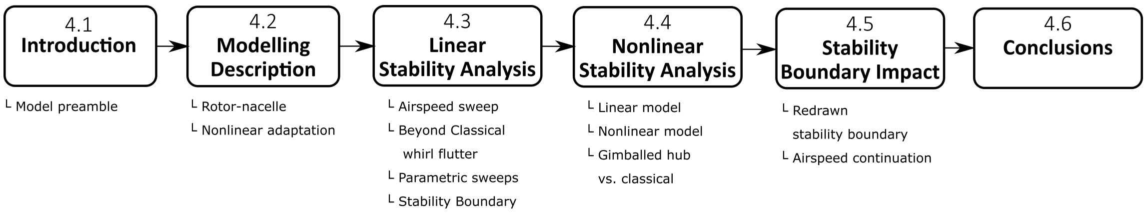

FIGURE 4.1. Chapter map

In this chapter, the three smooth nonlinearities (hardening, softening, combined) explored in the previous chapter are applied to the gimballed hub model, a novel extension thereof. This completes the work constituting research objective O1, but is also done to achieve an understanding of how the model complexity affects the impact that a given nonlinearity has on rotor-nacelle whirl flutter characteristics, as required by research objective O3. The greater complexity of this second model is reflected in the substantially more complex dynamics that are observed.

The chapter's flow, shown in Figure 4.1, closely follows that of the previous chapter. First, the gimballed hub model is introduced. Linear stability analysis is employed to explain the system's modes and how whirl flutter manifests in this system compared to the basic model. The stability boundary used for characterising the linear system's whirl flutter stability characteristics and assessing the impacts of the nonlinearities is then established. CBM is applied to the model first in its original linear form, then to its three nonlinear variants. The stability boundary is redrawn based on the findings, and a continuation in airspeed is shown to illustrate the impact of the nonlinearities on the range of airspeeds within which whirl flutter is possible.

4.1 Introduction

Following the work done by Reed and his contemporaries during the 1960s, the usefulness of understanding whirl flutter had gone beyond merely solving the Electra accidents. The ever-present push from both military and civil communities for the development of a successful VTOL concept had at some point lead to the recognition of the tiltrotor configuration as a promising candidate. The various research institutions accordingly focussed on developing dedicated tiltrotor models. They were further incentivised to do so by the appreciation of the powerful role that aeroelastic considerations would need to play in the design of a successful tiltrotor aircraft.

Regarding the research objective that is to be addressed in this chapter, a model is required that is more representative of a full-size tiltrotor aircraft, both in the modelling description and in the parameter values that are used. A key aspect of a dedicated tiltrotor rotor-nacelle model is the inclusion of a gimballed rotor hub where the rotor is able to rotate elastically about the end of the shaft, which itself may still rotate in space due to flexure of the wing. This design feature is explained and illustrated in Section 2.1.2. Additionally, flexibility of the wing is an important modelling inclusion.

The model used in this chapter is one developed by Johnson in 1974 [121]. It was published as a NASA technical note, and similar to the Reed investigations before it, was just one element of a joint theoretical-practical investigation. The publication includes the equations and parameter values that constitute the model, along with a wealth of discussion of findings directly from the model and from smaller sub-analyses such as criteria for blade stability, loads in the structure, classical whirl flutter and contribution of a tiltrotor's proprotors to its whole-aircraft stability derivatives. The parameter values cover two full-size test rigs, each a rigidly-supported cantilever wing mounted in axial flow, with a rotor-nacelle mounted at the wingtip, as per their wind tunnel counterparts. The main distinguishing feature of the model compared to the Reed/Bielawa model is the presence of a gimballed rotor[1]. Compared to other tiltrotor rotor-nacelle models that have appeared in publications, the transparent and complete presentation of its constituent equations make it the most straightforward to construct and implement. It has formed the basis of several works in tiltrotor literature and in this regard is somewhat familiar.

The presence of the gimballed hub, in addition to several other degrees of freedom, mainly in the rotor but also in the wing, amount to a system whose dynamics are far more complex than the Reed/Bielawa model, and is much more representative of a tiltrotor aircraft system. As will be shown and explained, classical whirl flutter terminology no longer suffices for interpreting the dynamical results; concepts such as forward/backward whirl direction fall apart in the face of the

[1] Strictly speaking, the gimballed nature of the rotor attachment is achieved through the usage of the Bell rotor parameter value set rather than the Boeing set; see the comments on the datum parameter set used. Due to the usage of solely the Bell parameter set in this work, the model is referred to as the "gimballed hub model".

complexity of the dynamics. Similar to the Reed/Bielawa model, Johnson's model is an existing model in the field and is the basis of several published works. For completeness however, a full derivation is provided in Appendix B, original to this work.

4.2 Modelling Description

4.2.1 Gimballed hub whirl flutter model

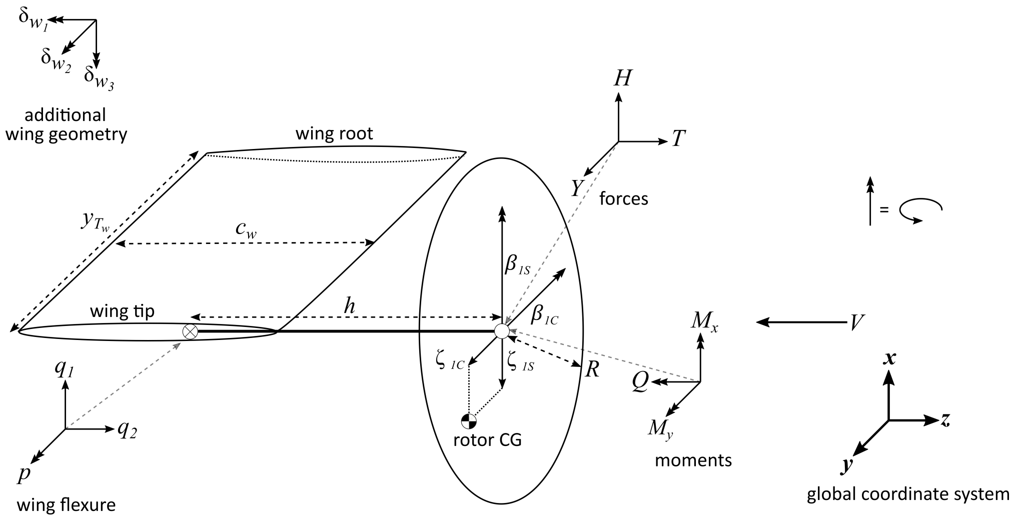

FIGURE 4.2. Schematic diagram of gimballed hub model, showing rotor and wing degrees of freedom, and axis conventions

The system represents the wing of a tiltrotor aircraft, along with its rotor-nacelle mounted on the wingtip, operating in "airplane mode" flight. A schematic diagram of the system is shown in Figure 4.2, including the global coordinate system used. A rotor of radius R with N blades rotates with angular velocity Ω about the end of a rigid shaft of length h. The shaft is connected rigidly to a flexible cantilever wing of span y_{T_w} and chord c_w, which may deform elastically in three ways: flapwise bending, chordwise bending and torsion. Flapwise bending (denoted q_1) involves the wingtip moving up and down in x. Chordwise bending (denoted q_2) involves the wingtip moving forwards and backwards in z. Wing torsion (denoted p) involves the wing twisting about its spanwise elastic axis, which in this model is parallel with the y-axis. Lumped stiffness (K) and damping (C) parameters are assigned to each of these degrees of freedom, with the inertial properties of the pylon and wing being specified separately. Rigid body modes of the aircraft are not considered as they are typically of low frequency and negligibly coupled to the other degrees of freedom used in the model. As such, the wing root is assumed to be attached rigidly to an immovable base. The shaft is pointed directly forward of the wing down the z^+ axis and the whole system is immersed in a freestream velocity V, incident on the system along z^-

which represents "airplane mode" flight of the tiltrotor aircraft. The flow is accordingly of high advance ratio (also referred to as "inflow ratio") where $\mu = \frac{V}{\Omega R}$ is assumed to be of order 1. This reflects the cruise conditions in which whirl flutter may be expected, as mentioned previously. A modal representation is used for the wing degrees of freedom, considering only the first (lowest frequency) mode for each. This choice is motivated by the fact that higher modes are well above 1-2 per-rev and therefore do not couple significantly with the rotor's motion. The modeshape assumed for both wing bending modes is $\eta_w(y) = \frac{y^2}{y_{T_w}}$, and the modeshape assumed for the wing torsion is $\xi_w(y) = \frac{y}{y_{T_w}}$. These capture the fundamental features of the respective deflections of the real world system, while satisfying the necessary constraint of zero deflection and zero slope at the root. An illustration of these modeshapes is shown in the derivation (Appendix B), in Figure B.11. The wing has some additional geometry: dihedral angle (denoted δ_{w_1}), wing angle of attack angle (or setting angle, denoted δ_{w_2}), and wing sweep angle (denoted δ_{w_3}). These are specified as rigid-body rotations of the wing about its root.

The rotor generates aerodynamic forces and moments that act upon the wing. Of the forces, there is thrust T, positive forwards in z^+; vertical force H, positive upwards in x^+; and side force Y, positive outwards in Y^+. The moments are yawing moment M_x, positive for turning inward to the wing root; pitching moment M_y, positive for pitching upward; and torque Q, positive for clockwise rotation if the system is viewed from the front, looking along z^-. The wing also makes a small aerodynamic contribution to the system's dynamics. All aerodynamics are obtained using quasi-steady strip theory. Only c_{L_α} terms are retained in the aerodynamic coefficients due to their dominance in the system's behaviour in high inflow (airspeed), and the effects of compressibility are neglected entirely.

The motion of the m^{th} blade within the rotating frame of reference is defined by flap β_m and lag ζ_m degrees of freedom, all with respect to the hub plane. The flap degree of freedom is pure out-of-plane deflection of the blade spar, with which the shear axis is assumed to be coincident such that there is no coupling with blade pitch. The lead-lag degree of freedom is likewise pure in-plane deflection. The mode shape for both types of blade deflection is assumed to be rigid-body rotation about the hub (i.e. without bending/curving of the blade itself), with the relevant hinge assumed to be coincident with the hub, represented in mathematical notation as $\eta(r) = r$ where r is radial station outward from the hub. β_m is defined positive for forward displacement of the blade tip from the disc plane. ζ_m is defined positive for deflection opposing the rotor direction of rotation, i.e. consistent with the notion of lagging. The flapping and lead-lag motions of the individual blades manifest in the non-rotating frame of reference in four ways. Cyclic flapping of the blades manifests as tilting of the rotor disc in pitch and yaw, while collective flapping manifests as coning. Cyclic lead-lag manifests as rectilinear motion of the rotor's CG within the hub plane, while collective lead-lag manifests as perturbations in the rotor's rotational speed Ω. Blade structural damping is included, with a dedicated quantity for each of cyclic flapping, collective flapping, cyclic lead-lag and collective lead-lag.

A summary of the major steps of the derivation is given here so that the fundamental features of the model may be understood. Generalising the motion of the rotor shaft's connection point at the wingtip as a set of translations and rotations within the global coordinate system, $(x_P, y_P, z_P, \alpha_x, \alpha_y, \alpha_z)$, an equation for the flapping motion of the m^{th} blade, β_m, within the hub's rotating frame of reference, is first derived:

$$I_\beta \ddot{\beta}_m + I_{\beta\alpha}\left[-(\ddot{\alpha}_y - 2\Omega\dot{\alpha}_x)\cos\psi_m + (\ddot{\alpha}_x + 2\Omega\dot{\alpha}_y)\sin\psi_m\right] + I_\beta \Omega^2 \nu_\beta^2 \beta_m + S_\beta \ddot{z}_P = M_{F_m} \tag{4.1}$$

which includes inertial terms, influence from the motion of the shaft-wing connection point, Coriolis terms and aerodynamic terms. The azimuth angle of the m^{th} blade relative to the global coordinate system is ψ_m and the total aerodynamic flapping moment acting upon it is M_{F_m}. Converting the measure of time to be per-rotor-revolution rather than seconds, and nondimensionalising the terms using the blade inertia, the following is obtained:

$$I_\beta^*(\beta_m'' + \nu_\beta^2 \beta_m) + I_{\beta\alpha}^*\left[-(\alpha_y'' - 2\alpha_x')\cos\psi_m + (\alpha_x'' + 2\alpha_y')\sin\psi_m\right] + S_\beta^* z_P'' = \gamma \frac{\bar{M}_{F_m}}{a\bar{c}} \tag{4.2}$$

where the dash superscript (e.g. x') indicates a derivative with respect to time in terms of rotor revolutions as opposed to seconds (e.g. $\dot{x}$), and the bar over M_{F_m} indicates that the nondimensionalisation has been applied. A similar equation is obtained for the lead-lag motion of the m^{th} blade:

$$I_\zeta^*\left(\zeta_m'' + \nu_\zeta^2 \zeta_m\right) - I_{\zeta\alpha}^* \alpha_z''\left[-(y_P'' - h\alpha_x'')\cos\psi_m + (x_P'' + h\alpha_y'')\sin\psi_m\right] = \gamma \frac{\bar{M}_{L_m}}{a\bar{c}} \tag{4.3}$$

As the influence of the wing is relative to the non-rotating (i.e. inertial) external frame of reference, the rotor blade motions need to be transformed from their rotating frame to the external frame to be consistent. Through a Fourier coordinate transform, the flapping and lead-lag of the N blades is aggregated to form degrees of freedom in the external non-rotating frame from which the whole system is viewed. This process is known as a multi-blade coordinate transform. This is done through application of the following summations to the N blade flapping equations and N blade lead-lag equations:

$$\frac{1}{N}\sum_{m=1}^{N}[\ldots] \tag{4.4}$$

$$\frac{2}{N}\sum_{m=1}^{N}[\ldots\cos\psi_m] \tag{4.5}$$

$$\frac{2}{N}\sum_{m=1}^{N}[\ldots\sin\psi_m] \tag{4.6}$$

where "..." indicates the full contents of the m^{th} blade (flap or lead-lag) equation. The cyclic (i.e. individual) flapping of the blades amounts to gimballing of the rotor disc (or hub plane) about the point where the rotor is attached to the shaft. Gimbal yaw (denoted β_{1S}) is defined positive for the rotor turning inward toward the wing root, and gimbal pitch (denoted β_{1C}) is defined positive for the rotor pitching downwards. The collective flapping of the blades – the component of the blades' motion that is synchronised such that the tip path plane moves forward-backward relative to the rotor shaft – amounts to coning and is denoted β_0. The cyclic (i.e. individual) lead-lag motion of the blades amounts to rectilinear motion of the rotor's overall CG within the hub plane, due to the individual blade CGs moving relative to each other. Transverse CG motion (denoted ζ_{1C}) is defined positive away from the wing root, and vertical CG motion (denoted ζ_{1S}) is defined positive downwards. Collective lead-lag motion of the blades – the component of the blades' motion that is such that they all move together, synchronised – amounts to perturbations in the rotor's rotational speed Ω. As with the wing degrees of freedom, only the first modes are considered for each of the motions discussed here, due again to their dominance in the overall dynamics of the system.

The application of these summations results in the following blade flapping equations in the non-rotating frame:

$$I^*_{\beta_0}\left(\beta_0''+g_{s_{\beta_0}}\sqrt{\nu^2_{\beta_0}-1}\,\beta_0'+\nu^2_{\beta_0}\beta_0\right)+S^*_\beta z_P''=\frac{\gamma}{a\bar{c}}\bar{M}_{F_0} \tag{4.7}$$

$$I^*_\beta\left(\beta_{1C}''+g_{s_\beta}\sqrt{\nu^2_\beta-1}\,\beta_{1C}'+2\beta_{1S}'+\left(\nu^2_\beta-1\right)\beta_{1C}\right)+I^*_{\beta\alpha}(-\alpha_y''+2\alpha_x')=\frac{\gamma}{a\bar{c}}\bar{M}_{F_{1C}} \tag{4.8}$$

$$I^*_\beta\left(\beta_{1S}''+g_{s_\beta}\sqrt{\nu^2_\beta-1}\,\beta_{1S}'-2\beta_{1C}'+\left(\nu^2_\beta-1\right)\beta_{1S}\right)+I^*_{\beta\alpha}(\alpha_x''+2\alpha_y')=\frac{\gamma}{a\bar{c}}\bar{M}_{F_{1S}} \tag{4.9}$$

The lead-lag equations in the non-rotating frame are:

$$I^*_{\zeta_0}\left(\zeta_0''+g_{s_{\zeta_0}}\nu_{\zeta_0}\zeta_0'+\nu^2_{\zeta_0}\zeta_0\right)-I^*_{\zeta_{0\alpha}}z_P''=\frac{\gamma}{a\bar{c}}\bar{M}_{L_0} \tag{4.10}$$

$$I^*_\zeta\left(\zeta_{1C}''+g_{s_\zeta}\nu_\zeta\zeta_{1C}'+2\zeta_{1S}'+\left(\nu^2_\zeta-1\right)\zeta_{1C}\right)+S^*_\zeta(-y_P''+h\alpha_x'')=\frac{\gamma}{a\bar{c}}\bar{M}_{L_{1C}} \tag{4.11}$$

$$I^*_\zeta\left(\zeta_{1S}''+g_{s_\zeta}\nu_\zeta\zeta_{1S}'-2\zeta_{1C}'+\left(\nu^2_\zeta-1\right)\zeta_{1S}\right)+S^*_\zeta(x_P''+h\alpha_y'')=\frac{\gamma}{a\bar{c}}\bar{M}_{L_{1S}} \tag{4.12}$$

The aerodynamic coefficients are assessed by considering the nondimensional forces acting on an arbitrary section of the rotor blade aerofoil. They are integrated along the radius of each blade and only the terms corresponding to the sectional lift slope $\frac{\partial c_l}{\partial \alpha}$ are retained, as they strongly dominate the expressions and the basic aspects of the behaviour of the forces are retained.

Modeshapes $\eta_w(y_w)$ and $\xi_w(y_w)$ for the wing bending and torsional motions (respectively) are defined, and the motion of the shaft-wing connection point is now expressed in terms of the wing degrees of freedom originally set out:

$$\begin{bmatrix} \alpha_x \\ \alpha_y \\ \alpha_z \end{bmatrix} = \begin{bmatrix} -\eta'_w(y_{T_w})\delta_{w_2} & -\eta'_w(y_{T_w}) & \delta_{w_1} \\ -\eta'_w(y_{T_w})\delta_{w_3} & \eta'_w(y_{T_w})\delta_{w_1} & 1 \\ -\eta'_w(y_{T_w}) & \eta'_w(y_{T_w})\delta_{w_2} & -\delta_{w_3} \end{bmatrix} \begin{bmatrix} q_1 \\ q_2 \\ p \end{bmatrix} \tag{4.13}$$

$$\begin{bmatrix} x_P \\ y_P \\ z_P \end{bmatrix} = \begin{bmatrix} y_{T_w} & -\delta_{w_2} y_{T_w} & -\xi_w(y_{B_w})\delta_{w_3} y_{T_w} \\ -\delta_{w_1} y_{T_w} & -\delta_{w_3} y_{T_w} & 0 \\ -\delta_{w_2} y_{T_w} & -y_{T_w} & -\xi_w(y_{B_w})\delta_{w_1} y_{T_w} \end{bmatrix} \begin{bmatrix} q_1 \\ q_2 \\ p \end{bmatrix} \tag{4.14}$$

The equations of motion attached to each wing degree of freedom are then derived:

$$\left(I_{q_w} + m_P y_{T_w}^2\right)\ddot{q}_1 + C_{q_1}\dot{q}_1 + K_{q_1} q_1 + S_w \ddot{p} = M_{q_{1_{aero}}} + M_{q_{1_{rotor}}} \tag{4.15}$$

$$\left(I_{q_w} + I_{P_x}\eta'_w(y_{T_w})^2 + m_P y_{T_w}^2\right)\ddot{q}_2 + C_{q_2}\dot{q}_2 + K_{q_2} q_2 + S_w \delta_{w_2}\ddot{p} = M_{q_{2_{aero}}} + M_{q_{2_{rotor}}} \tag{4.16}$$

$$\left(I_{p_w} + I_{P_y}\right)\ddot{p} + C_p\dot{p} + K_p p + S_w \ddot{q}_1 - S_w \delta_{w_2}\ddot{q}_2 = M_{p_{aero}} + M_{p_{rotor}} \tag{4.17}$$

The wing aerodynamic coefficients are evaluated in terms of the wing geometry and the assumed modeshapes, and when all terms are brought together, the result is a set of linear ordinary differential equations for the nine degrees of freedom:

β_{1C} cyclic flap (longitudinal tip path plane tilt/pitch)

β_{1S} cyclic flap (lateral tip path plane tilt/yaw)

ζ_{1C} cyclic lead-lag (lateral rotor centre-of-gravity offset)

ζ_{1S} cyclic lead-lag (longitudinal/vertical rotor centre-of-gravity offset)

β_0 collective flap (coning)

ζ_0 collective lag (or rotor speed perturbation)

q_1 wing vertical/beamwise/flapwise bending

q_2 wing chordwise bending

p wing torsion

which are arranged in the degree of freedom vector **x** thus:

$$\mathbf{x} = \begin{bmatrix} \beta_{1C} & \beta_{1S} & \zeta_{1C} & \zeta_{1S} & \beta_0 & \zeta_0 & q_1 & q_2 & p \end{bmatrix}^T \tag{4.18}$$

which allows the full equations to have the form:

$$\mathbf{A}_2\mathbf{x}'' + \mathbf{A}_1\mathbf{x}' + \mathbf{A}_0\mathbf{x} = \mathbf{0} \tag{4.19}$$

where $\mathbf{A}_{0,1,2}$ are the coefficient matrices for stiffness, damping and inertia, respectively. Here, the state vector $\mathbf{y} = \begin{bmatrix} \mathbf{x} \\ \mathbf{x}' \end{bmatrix}$. The equations are too large to display in matrix form due to the dense algebra they contain, and thus a conventional line-by-line format is adopted here:

$$\begin{aligned} & I^*_\beta \beta''_{1C} + I^*_{\beta\alpha}\delta\eta q''_1 - I^*_{\beta\alpha} p'' \\ & + \left(I^*_\beta g_\beta \sqrt{\nu^2_\beta - 1} - \gamma M_{\dot\beta}\right)\beta'_{1C} + 2I_\beta \beta'_{1S} + \gamma M_{\dot\zeta}\zeta'_{1C} - \gamma M_{\dot\beta}\delta\eta q'_1 - \left(2I^*_{\beta\alpha}\eta + \gamma M_\mu(\eta\bar{h} - \delta y_{T_w})\right) q'_2 + \gamma M_{\dot\beta} p' \\ & + \left(I^*_\beta(\nu^2_\beta - 1) + K_P\gamma M_\theta\right)\beta_{1C} - \gamma M_{\dot\beta}\beta_{1S} + \gamma M_{\dot\zeta}\zeta_{1S} + \gamma(\mu) M_\mu \eta q_2 = 0 \end{aligned} \tag{4.20}$$

$$\begin{aligned} & I^*_\beta \beta''_{1S} - \eta I^*_{\beta\alpha} q''_2 \\ & - 2I^*_\beta \beta'_{1C} + \left(I^*_\beta g_\beta \sqrt{\nu^2_\beta - 1} - \gamma M_{\dot\beta}\right)\beta'_{1S} + \gamma M_{\dot\zeta}\zeta'_{1S} + \left[\gamma M_\mu (y_{T_w} - \delta\eta\bar{h}) - 2I_{\beta\alpha}\delta\eta\right] q'_1 + \gamma M_{\dot\beta}\eta q'_2 \\ & + \left(2I_{\beta\alpha} + \gamma M_\mu(\bar{h} - \delta\xi y_{T_w})\right) p' \\ & + \gamma M_{\dot\beta}\beta_{1C} + \left(I^*_\beta(\nu^2_\beta - 1) + K_P\gamma M_\theta\right)\beta_{1S} - \gamma M_{\dot\zeta}\zeta_{1C} + \gamma M_\mu \delta\eta\mu q_1 - \gamma M_\mu \mu p = 0 \end{aligned} \tag{4.21}$$

$$\begin{aligned} & I^*_\zeta \zeta''_{1C} - S^*_\zeta(\eta\bar{h} - \delta y_{T_w}) q''_2 \\ & + \gamma Q_{\dot\beta}\beta'_{1C} + \left(\gamma Q_{\dot\zeta} + I^*_\zeta g_\zeta \nu_\zeta\right)\zeta'_{1C} + 2I^*_\zeta \zeta'_{1S} - \gamma Q_{\dot\beta}\delta\eta q'_1 - \gamma Q_\mu(\eta\bar{h} - \delta y_{T_w}) q'_2 + \gamma Q_{\dot\beta} p' \\ & + \gamma K_P Q_\theta \beta_{1C} - \gamma Q_{\dot\beta}\beta_{1S} + I^*_\zeta(\nu^2_\zeta - 1)\zeta_{1C} + \gamma Q_{\dot\zeta}\zeta_{1S} + \gamma Q_\mu \eta\mu q_2 = 0 \end{aligned} \tag{4.22}$$

$$\begin{aligned} & I^*_\zeta \zeta''_{1S} + S\zeta^*(y_{T_w} - \delta\eta\bar{h}) q''_1 + S^*_\zeta(\bar{h} - \delta\xi y_{T_w}) p'' \\ & - \gamma Q_{\dot\beta}\beta'_{1S} - 2I^*_\zeta \zeta'_{1C} + \left(\gamma Q_{\dot\zeta} + I^*_\zeta g_\zeta \nu_\zeta\right)\zeta'_{1S} + \gamma Q_\mu(y_{T_w} - \delta\eta\bar{h}) q'_1 + \gamma Q_{\dot\beta}\eta q'_2 + \gamma Q_\mu(\bar{h} - \delta\xi y_{T_w}) p' \\ & + \gamma Q_{\dot\beta}\beta_{1C} + \gamma Q_\theta K_P \beta_{1S} - \gamma Q_{\dot\zeta}\zeta_{1C} + I^*_\zeta(\nu^2_\zeta - 1)\zeta_{1S} + \gamma Q_\mu \delta\eta\mu q_1 - \gamma Q_\mu \mu p = 0 \end{aligned} \tag{4.23}$$

$$\begin{aligned} & I^*_{\beta_0}\beta''_0 - S^*_{\beta_0} y_{T_w} q''_2 \\ & + \left(I^*_{\beta_0} g_{\beta_0}\sqrt{\nu^2_{\beta_0} - 1} - \gamma M_{\dot\beta}\right)\beta'_0 + \gamma M_{\dot\zeta}\zeta'_0 + \gamma M_{\dot\zeta}\eta q'_1 + \gamma M_\lambda y_{T_w} q'_2 + \gamma M_{\dot\zeta}\delta p' \\ & + \left(I^*_{\beta_0}\nu^2_{\beta_0} + \gamma K_P M_\theta\right)\beta_0 = 0 \end{aligned} \tag{4.24}$$

$$
\begin{aligned}
(4.25)\quad & I^*_{\zeta_0}\zeta_0'' + \eta I^*_{\zeta_0\alpha} q_1'' + I_{\zeta_0\alpha}\delta p'' \\
&\quad - \gamma Q_{\dot\beta}\beta_0' + \left(I^*_{\zeta_0} g_{\zeta_0}\nu_{\zeta_0} + \gamma Q_{\dot\zeta}\right)\zeta_0' + \gamma Q_{\dot\zeta}\eta q_1' + \gamma Q_\lambda y_{T_w} q_2' + \gamma Q_{\dot\zeta}\delta p' \\
&\qquad + \gamma K_P Q_\theta \beta_0 + I^*_{\zeta_0}\nu^2_{\zeta_0}\zeta_0 = 0
\end{aligned}
$$

(4.26)

$$
\begin{aligned}
& S^*_\zeta(y_{T_w} + \delta\eta\bar h(\xi-1))\zeta''_{1S} + 2\eta I_{\zeta_0\alpha}\zeta_0'' + \left(I_{q_w} + m^*_P + 2M_b(y_{T_w} + \delta\eta\bar h(\xi-1))(y_{T_w} - \delta\eta\bar h) + 2\eta^2\right) q_1'' \\
&\quad + \left(S^*_w + 2\delta\eta + 2M_b(y_{T_w} + \delta\eta\bar h(\xi-1))(\bar h - \delta\xi y_{T_w})\right) p'' \\
&\quad - \gamma H_{\dot\beta}\left(y_{T_w} + \delta\eta\bar h(\xi-1)\right)\beta'_{1S} + \gamma H_{\dot\zeta}(y_{T_w} + \delta\eta\bar h(\xi-1))\zeta'_{1S} - 2\gamma Q_{\dot\beta}\eta\beta_0' + 2\gamma Q_{\dot\zeta}\eta\zeta_0' \\
&\quad + \left(C^*_{q_1} + 2\eta^2\gamma Q_{\dot\zeta} + \gamma\left(H_\mu + R_\mu\right)(y_{T_w} + \delta\eta\bar h(\xi-1))(y_{T_w} - \delta\eta\bar h) - \gamma M_{q_1 q_1'}\right) q_1' \\
&\quad + \left(2\eta y_{T_w}\gamma Q_\lambda + \gamma H_{\dot\beta}\eta\left(y_{T_w} + \delta\eta\bar h(\xi-1)\right)\right) q_2' \\
&\quad + \left(\gamma\left(H_\mu + R_\mu\right)\left(y_{T_w} + \delta\eta\bar h(\xi-1)\right)(\bar h - \delta\xi y_{T_w}) + 2\gamma Q_{\dot\zeta}\delta\eta - \gamma M_{q_1 p'}\right) p' \\
&\quad + \left(\gamma H_{\dot\beta}\left(y_{T_w} + \delta\eta\bar h(\xi-1)\right) + I^*_\beta\delta\eta(\nu^2_\beta - 1)(\xi-1)\right)\beta_{1C} + \gamma K_P H_\theta\left(y_{T_w} + \delta\eta\bar h(\xi-1)\right)\beta_{1S} \\
&\quad - \gamma H_{\dot\zeta}\left(y_{T_w} + \delta\eta\bar h(\xi-1)\right)\zeta_{1C} + 2\gamma Q_\theta\eta K_P\beta_0 \\
& + \left(K_{q_1} + \gamma\left(H_\mu + R_\mu\right)\delta\eta\mu\left(y_{T_w} + \delta\eta\bar h(\xi-1)\right) - \gamma M_{q_1 q_1}\right) q_1 - \left(\gamma\left(H_\mu + R_\mu\right)\mu\left(y_{T_w} + \delta\eta\bar h(\xi-1)\right) + \gamma M_{q_1 p}\right) p = 0
\end{aligned}
$$

(4.27)

$$
\begin{aligned}
& -S^*_\zeta\left(\eta\bar h + \delta y_{T_w}(\xi^2-1)\right)\zeta''_{1C} - S^*_\zeta\delta\eta\bar h(\xi-1)\zeta''_{1S} - 2y_{T_w}S_{\beta_0}\beta_0'' - 2M_b\delta\eta\bar h\left(y_{T_w} - \delta\eta\bar h\right)(\xi-1)q_1'' \\
& + \left(I^*_{q_w} + m_P + I_{P_x}\eta^2 + 2M_b(\eta\bar h - \delta y_{T_w})(\eta\bar h + \delta y_{T_w}(\xi^2-1)) + 2y^2_{T_w}M_b\right) q_2'' - 2M_b\delta\eta\bar h\left(\bar h - \delta\xi y_{T_w}\right)(\xi-1)p'' \\
& + \gamma H_{\dot\beta}\left(\eta\bar h + \delta y_{T_w}(\xi^2-1)\right)\beta'_{1C} + \gamma H_{\dot\beta}\delta\eta\bar h(\xi-1)\beta'_{1S} - \gamma H_{\dot\zeta}\left(\eta\bar h\delta y_{T_w}(\xi^2-1)\right)\zeta'_{1C} - \gamma H_{\dot\zeta}\delta\eta\bar h(\xi-1)\zeta'_{1S} \\
&\quad + 2\gamma T_{\dot\beta} y_{T_w}\beta_0' - 2\gamma T_{\dot\zeta} y_{T_w}\zeta_0' \\
&\quad + \left(\gamma H_{\dot\beta}\delta\eta\left(\eta\bar h + \delta y_{T_w}(\xi^2-1)\right) - 2\gamma T_{\dot\zeta}\eta y_{T_w} - \gamma\left(H_\mu + R_\mu\right)\delta\eta\bar h\left(y_{T_w} - \delta\eta\bar h\right)(\xi-1)\right) q_1' \\
&\quad + \left(C^*_{q_2} + \gamma\left(H_\mu + R_\mu\right)\left(\eta\bar h + \delta y_{T_w}(\xi^2-1)\right) - 2\gamma T_\lambda y^2_{T_w} - \gamma H_{\dot\beta}\delta\eta^2\bar h(\xi-1)\right) q_2' \\
&\quad - \left(\gamma H_{\dot\beta}\left(\eta\bar h + \delta y_{T_w}(\xi^2-1)\right) + 2\gamma T_{\dot\zeta}\delta y_{T_w} + \gamma\left(H_\mu + R_\mu\right)\delta\eta\bar h\left(\bar h - \delta\xi y_{T_w}\right)(\xi-1)\right) p' \\
&\quad - \left(\gamma H_\theta K_P\left(\eta\bar h + \delta y_{T_w}(\xi^2-1)\right) + \gamma H_{\dot\beta}\delta\eta\bar h(\xi-1)\right)\beta_{1C} \\
&\quad + \left(\eta I^*_\beta(\nu^2_\beta - 1) + \gamma H_{\dot\beta}\left(\eta\bar h + \delta y_{T_w}(\xi^2-1)\right) - \gamma H_\theta K_P\delta\eta\bar h(\xi-1)\right)\beta_{1S} \\
& + \gamma H_{\dot\zeta}\delta\eta\bar h(\xi-1)\zeta_{1C} - \gamma H_{\dot\zeta}\left(\eta\bar h + \delta y_{T_w}(\xi^2-1)\right)\zeta_{1S} - 2\gamma T_\theta K_P y_{T_w}\beta_0 - \gamma\left(H_\mu + R_\mu\right)\delta^2\eta^2\bar h\mu(\xi-1)q_1 \\
&\quad + \left(K^*_{q_2} - \gamma\left(H_\mu + R_\mu\right)\eta\mu\left(\eta\bar h + \delta y_{T_w}(\xi^2-1)\right)\right) q_2 + \gamma\left(H_\mu + R_\mu\right)\delta\eta\bar h\mu(\xi-1)p = 0
\end{aligned}
$$

$$
\begin{aligned}
S_\zeta^*\zeta_{1S}'' - 2I_{\zeta_0\alpha}^*\delta(\xi-1)\zeta_0 + \left(S_w^* + 2M_b^*\bar{h}\left(y_{T_w} - \delta\eta\bar{h}\right) - 2\delta\eta(\xi-1)\right)q_1'' \\
+ \left(I_{p_w}^* + I_{P_y}^* + 2M_b^*\bar{h}\left(\bar{h} - \delta\xi y_{T_w}\right) - 2\delta^2(\xi-1)\right)p'' \\
- \gamma H_{\dot\beta}\bar{h}\beta_{1S}' + \gamma H_{\dot\zeta}\bar{h}\zeta_{1S}' + 2\gamma Q_{\dot\beta}\delta(\xi-1)\beta_0' - 2\gamma Q_{\dot\zeta}\delta(\xi-1)\zeta_0' \\
+ \left(\gamma\left(H_\mu + R_\mu\right)\bar{h}\left(y_{T_w} - \delta\eta\bar{h}\right) - 2\gamma Q_{\dot\zeta}\delta\eta(\xi-1) - \gamma M_{pq_1'}^*\right)q_1' + \left(\gamma H_{\dot\beta}\eta\bar{h} - 2\gamma Q_\lambda\delta y_{T_w}(\xi-1) - \gamma M_{pq_2'}^*\right)q_2' \\
+ \left(C_p^* + \gamma\left(H_\mu + R_\mu\right)\bar{h}\left(\bar{h} - \delta\xi y_{T_w}\right) - 2\gamma Q_{\dot\zeta}\delta^2(\xi-1) + M_{pp'}^*\right)p' \\
+ \left(I_\beta^*(\nu_\beta^2 - 1) + \gamma H_{\dot\beta}\bar{h}\right)\beta_{1C} + \gamma H_\theta K_P\bar{h}\beta_{1S} - \gamma H_{\dot\zeta}\bar{h}\zeta_{1C} \\
- 2\gamma Q_\theta K_P\delta(\xi-1)\beta_0 + \left(\gamma\left(H_\mu + R_\mu\right)\delta\eta\bar{h}\mu - \gamma M_{pq_1}^* + C_{pq}^*\right)q_1 - \left(\gamma\left(H_\mu + R_\mu\right)\bar{h}\mu + \gamma M_{pp}^*\right)p = 0
\end{aligned} \tag{4.28}
$$

The datum parameter values were taken directly from [121] and are listed in Table 4.1. Two parameter sets are included in Johnson's text, both describing full-size rotor-wing test rigs. The sets differ only in the finer details of the rotors: one is a stiff in-plane gimballed rotor designed by Bell and the other a soft in-plane hingeless rotor designed by Boeing. Due to the relevance to existing tiltrotor configurations, the former is selected for use in this work. Furthermore, the parameter sets allow for autorotation to be modelled by freeing the collective lead-lag degree of freedom ζ_0 to allow the rotor to find its windmilling speed, acting as a perturbation from the nominal rotor speed Ω. This freeing up (implemented by setting the relevant stiffness to zero) sets the eigenvalue associated with ζ_0 to 0, which can cause problems for continuation solvers as the local Jacobian is not of full rank, preventing the solver from finding the ζ_0 coordinate of solutions. To circumvent this problem, the parameter set for the powered flight condition is used for all gimballed hub model results in this work. A further benefit of doing so is that it fully represents the cruising flight case, where whirl flutter might be most plausibly expected.

4.2.2 Nonlinear adaptation

For the nonlinear adaptation of this model, the same polynomial stiffness profile is used as in the previous chapter, along with the same lines of investigation. Of importance here is the choice of which of the model's degrees of freedom to adapt in this way. A direct analogue to the basic model's adaptation of pitch stiffness K_θ (leading to results being assessed on the K_θ-K_ψ stability boundary) would be to select the wing torsional stiffness K_p for polynomial adaptation, with results being assessed on the K_p-K_{q_2} stability boundary. The wing chordwise bending degree of freedom q_2 in this case is the closest analogue of shaft yaw ψ in the basic model. However, pursuing such an analysis does not make use of the highly influential new rotor degrees of freedom present in the gimballed hub model. By selecting the rotor blade flapping stiffness for the polynomial adaptation, the opportunity to explore the influence of the rotor degrees of freedom may be capitalised upon. Furthermore, some insight into the influence of the presence of these new degrees of freedom – i.e. the increase of model complexity – may be gained by comparing the

TABLE 4.1. Gimballed hub model datum parameter values

Description	Symbol	Value
Rotor radius	R	3.82 m
Rotor angular velocity	Ω	48 rad.s^{-1}
Number of blades	N	3
Blade chord	c	0.356 m
Blade (2D) lift slope	$c_{l\alpha}$	5.7 rad^{-1}
Freestream velocity	V	128.6 m.s^{-1}
Shaft length	h	1.306 m
Wing semispan	y_{T_w}	5.092 m
Wing chord	c_w	1.578 m
Wing flapwise damping	C_{q_1}	9030 N.m.s.rad^{-1}
Wing flapwise stiffness	K_{q_1}	9200000 N.m.rad^{-1}
Wing chordwise damping	C_{q_2}	27300 N.m.s.rad^{-1}
Wing chordwise stiffness	K_{q_2}	25000000 N.m.rad^{-1}
Wing torsional damping	C_p	955 N.m.s.rad^{-1}
Wing torsional stiffness	K_p	1770000 N.m.rad^{-1}
Normalised pylon mass	m_P^*	76.9
Normalised pylon yaw moment of inertia	$I_{P_x}^*$	1.086
Normalised pylon pitch moment of inertia	$I_{P_y}^*$	1.206
Normalised wing bending generalised mass	$I_{q_w}^*$	4.03
Normalised wing torsion generalised mass	$I_{p_w}^*$	0.0141
Normalised thrust contribution to pylon torsion	C_{pq}^*	0.667
Normalised wing bending-torsion inertial coupling	S_w^*	2.88
Blade moment of inertia	I_b	142 kg.m^2
Normalised blade cyclic flapping inertia	I_β^*	1
Normalised blade collective flapping inertia	$I_{\beta_0}^*$	0.779
Normalised blade cyclic lead-lag inertia	I_ζ^*	0.670
Normalised blade collective lead-lag inertia	$I_{\zeta_0}^*$	0.670
Normalised rotor lead-lag inertial contribution to wing	S_ζ^*	1.035
Normalised rotor coning inertial contribution to wing	$S_{\beta_0}^*$	1.212
Normalised blade mass	M_b^*	6.16
Per-rev blade cyclic flapping natural frequency	ν_β	1.0175
Per-rev blade collective flapping natural frequency	ν_{β_0}	1.85
Per-rev blade cyclic lead-lag natural frequency	ν_ζ	1.3847
Per-rev blade collective lead-lag natural frequency	ν_{ζ_0}	1.3847
Blade cyclic flapping structural damping ratio	g_{s_β}	0.1%
Blade collective flapping structural damping ratio	$g_{s_{\beta 0}}$	0.5%
Blade cyclic lead-lag structural damping ratio	g_{s_ζ}	0.5%
Blade collective lead-lag structural damping ratio	$g_{s_{\zeta 0}}$	0.5%

linear analyses of the two models. Regarding the second axis of the stability boundary on which to assess the stability results, the greatest insight can be expected to be gained from considering a wing degree of freedom. Of those wing coordinates, the wing torsion is one of the most influential and therefore the corresponding torsional stiffness K_p is chosen as the second axis.

In the same manner that the basic model's linear version was converted to a nonlinear form by replacing the linear stiffness profile in the nacelle pitch degree of freedom with a polynomial expression, the same is performed here with the blade flapping stiffness profile. However, the complete adaptation of this model requires some care. The nonlinear blade flapping stiffness must be applied first to each blade within the rotating frame of reference, and the multi-blade coordinate transform reapplied to obtain the full equations. The nonlinear blade flapping expression for the m^{th} blade $K_{\beta,nl}$, within the rotating frame of reference, is therefore:

$$\begin{aligned} K_{\beta_{nl}}(\beta_m)\beta_m &= K_{\beta 1}\beta_m + K_{\beta 2}\beta_m^3 + K_{\beta 3}\beta_m^5 \\ &= \left(K_{\beta 1} + K_{\beta 2}\beta_m^2 + K_{\beta 3}\beta_m^4\right)\beta_m \end{aligned} \tag{4.29}$$

with dedicated coefficients K_i for controlling the influence of each term, as used in Chapter 3. In the original linear formulation of Johnson's model, the normalised effective flapping stiffness of the m^{th} blade $K^*_{\beta_e}$ is specified implicitly in terms of the per-rev natural flapping frequency ν_β that is present in the equations. The link between $K^*_{\beta_e}$ and ν_β is:

$$K^*_{\beta_e}\beta_m = \nu_\beta^2\beta_m \tag{4.30}$$

as the dimensional natural flapping frequency $\omega_\beta(= \nu_\beta\Omega)$ is related to the dimensional effective flapping stiffness K_{β_e} and the flapping moment of inertia I_β thus:

$$\omega_\beta = \sqrt{\frac{K_{\beta_e}}{I_\beta}} \tag{4.31}$$

and with the conversion of the time domain from seconds to per-rev:

$$\nu_\beta = \sqrt{\frac{K_{\beta_e}}{I_\beta\Omega^2}} \tag{4.32}$$

Therefore:

$$\nu_\beta^2 = \frac{K_{\beta_e}}{I_\beta\Omega^2} \tag{4.33}$$

or, substituting $K^*_{\beta_e} = \frac{K_{\beta_e}}{I_\beta\Omega^2}$:

$$\nu_\beta^2 = K^*_{\beta_e} \tag{4.34}$$

The original linear term $K_{\beta 1}$ appears as $\nu_\beta^2\left(= K^*_{\beta_e}\right)$ in the original linear model, and as it is still present in the new nonlinear expression, the original set of terms produced by the application of the Fourier coordinate transform may be retained. It is the new cubic and quintic terms that must be processed by the transform to obtain the relevant new terms that are then added on to the inertial frame equations:

$$K_{\beta 2}\beta_m^3 + K_{\beta 3}\beta_m^5 \tag{4.35}$$

As specified in the original derivation, the relation between the flapping angle of the m^{th} blade and the various degrees of freedom defined in the coordinate transform is:

$$\beta_m = \beta_0 + \beta_{1C}\cos\psi_m + \beta_{1S}\sin\psi_m \tag{4.36}$$

where ψ_m is the instantaneous azimuth position of the m^{th} blade as defined in Figure B.2 in Appendix B. The transform is performed by applying the following summation operations to the N blade equations:

$$\frac{1}{N}\sum_{m=1}^{N}[...] \tag{4.37}$$

$$\frac{2}{N}\sum_{m=1}^{N}[...\cos\psi_m] \tag{4.38}$$

$$\frac{2}{N}\sum_{m=1}^{N}[...\sin\psi_m] \tag{4.39}$$

where "..." indicates the full contents of the m^{th} blade flapping equation. This precipitates the β_0, β_{1C} and β_{1S} equations respectively. By substituting β_m for the definition provided in Equation (4.36), an expanded form of Equation (4.35) can be obtained in terms of powers of trigonometric terms. When the summations (4.37)-(4.39) are then applied, useful identities can be used to simplify the results greatly. The expanded form of Equation (4.35) is:

(4.40)

$$\begin{aligned}
K_{\beta 2}\beta_m^3 + K_{\beta 3}\beta_m^5 =& K_{\beta 2}\left(\beta_0 + \beta_{1C}\cos\psi_m + \beta_{1S}\sin\psi_m\right)^3 + K_{\beta 3}\left(\beta_0 + \beta_{1C}\cos\psi_m + \beta_{1S}\sin\psi_m\right)^5 \\
=& K_{\beta 3}\beta_0^5 + 5K_{\beta 3}\beta_0^4\beta_{1C}\cos\psi_m + 5K_{\beta 3}\beta_0^4\beta_{1S}\sin\psi_m + 10K_{\beta 3}\beta_0^3\beta_{1C}^2\cos^2\psi_m \\
&+20K_{\beta 3}\beta_0^3\beta_{1C}\beta_{1S}\cos\psi_m\sin\psi_m + 10K_{\beta 3}\beta_0^3\beta_{1S}^2\sin^2\psi_m + K_{\beta 2}\beta_0^3 \\
&+10K_{\beta 3}\beta_0^2\beta_{1C}^3\cos^3\psi_m + 30K_{\beta 3}\beta_0^2\beta_{1C}^2\beta_{1S}\cos^2\psi_m\sin\psi_m + 30K_{\beta 3}\beta_0^2\beta_{1C}\beta_{1S}^2\cos\psi_m\sin^2\psi_m \\
&+3K_{\beta 2}\beta_0^2\beta_{1C}\cos\psi_m + 10K_{\beta 3}\beta_0^2\beta_{1S}^3\sin^3\psi_m + 3K_{\beta 2}\beta_0^2\beta_{1S}\sin\psi_m \\
&+5K_{\beta 3}\beta_0\beta_{1C}^4\cos^4\psi_m + 20K_{\beta 3}\beta_0\beta_{1C}^3\beta_{1S}\cos\psi_m^3\sin\psi_m + 30K_{\beta 3}\beta_0\beta_{1C}^2\beta_{1S}^2\cos^2\psi_m\sin^2\psi_m \\
&+3K_{\beta 2}\beta_0\beta_{1C}^2\cos^2\psi_m + 20K_{\beta 3}\beta_0\beta_{1C}\beta_{1S}^3\cos\psi_m\sin^3\psi_m + 6K_{\beta 2}\beta_0\beta_{1C}\beta_{1S}\cos\psi_m\sin\psi_m \\
&+5K_{\beta 3}\beta_0\beta_{1S}^4\sin^4\psi_m + 3K_{\beta 2}\beta_0\beta_{1S}^2\sin^2\psi_m + K_{\beta 3}\beta_{1C}^5\cos^5\psi_m \\
&+5K_{\beta 3}\beta_{1C}^4\beta_{1S}\cos^4\psi_m\sin\psi_m + 10K_{\beta 3}\beta_{1C}^3\beta_{1S}^2\cos^3\psi_m\sin^2\psi_m + K_{\beta 2}\beta_{1C}^3\cos^3\psi_m \\
&+10K_{\beta 3}\beta_{1C}^2\beta_{1S}^3\cos^2\psi_m\sin^3\psi_m + 3K_{\beta 2}\beta_{1C}^2\beta_{1S}\cos^2\psi_m\sin\psi_m \\
&+5K_{\beta 3}\beta_{1C}\beta_{1S}^4\cos\psi_m\sin^4\psi_m + 3K_{\beta 2}\beta_{1C}\beta_{1S}^2\cos\psi_m\sin^2\psi_m + K_{\beta 3}\beta_{1S}^5\sin^5\psi_m \\
&+K_{\beta 2}\beta_{1S}^3\sin^3\psi_m
\end{aligned}$$

The summations (4.37)-(4.39) are now applied to these extra terms to produce the additional contributions to the β_0, β_{1C} and β_{1S} equations respectively, e.g.:

$$\frac{1}{N}\sum_{m=1}^{N}\left[K_{\beta 2}\beta_m^3+K_{\beta 3}\beta_m^5\right]=\frac{1}{N}\sum_{m=1}^{N}\left[K_{\beta 3}\beta_0^5+...+K_{\beta 2}\beta_{1S}^3\sin^3\psi_m\right] \tag{4.41}$$

The following identities allow most of the terms to either be removed or replaced with a single number. Note that their respective continuous (integral form) equivalents evaluate to the same values.

$$\sum_{m=1}^{N}\left[\cos\psi_m\right]=0 \qquad \sum_{m=1}^{N}\left[\sin\psi_m\right]=0 \qquad \sum_{m=1}^{N}\left[\sin\psi_m\cos\psi_m\right]=0$$

$$\sum_{m=1}^{N}\left[\cos^2\psi_m\right]=\frac{1}{2} \qquad \sum_{m=1}^{N}\left[\sin^2\psi_m\right]=\frac{1}{2}$$

$$\sum_{m=1}^{N}\left[\cos^2\psi_m\sin\psi_m\right]=0 \qquad \sum_{m=1}^{N}\left[\sin^2\psi_m\cos\psi_m\right]=0$$

$$\sum_{m=1}^{N}\left[\cos^3\psi_m\right]=0 \qquad \sum_{m=1}^{N}\left[\sin^3\psi_m\right]=0 \; \sum_{m=1}^{N}\left[\cos^3\psi_m\sin\psi_m\right]=0 \qquad \sum_{m=1}^{N}\left[\sin^3\psi_m\cos\psi_m\right]=0$$

$$\sum_{m=1}^{N}\left[\cos^4\psi_m\right]=\frac{3}{8} \qquad \sum_{m=1}^{N}\left[\sin^4\psi_m\right]=\frac{3}{8} \qquad \sum_{m=1}^{N}\left[\sin^2\psi_m\cos^2\psi_m\right]=\frac{1}{8}$$

$$\sum_{m=1}^{N}\left[\cos^3\psi_m\sin^2\psi_m\right]=0 \qquad \sum_{m=1}^{N}\left[\sin^3\psi_m\cos^2\psi_m\right]=0 \; \sum_{m=1}^{N}\left[\cos^4\psi_m\sin\psi_m\right]=0 \qquad \sum_{m=1}^{N}\left[\sin^4\psi_m\cos\psi_m\right]=0$$

$$\sum_{m=1}^{N}\left[\cos^5\psi_m\right]=0 \qquad \sum_{m=1}^{N}\left[\sin^5\psi_m\right]=0$$

$$\sum_{m=1}^{N}\left[\cos^5\psi_m\sin\psi_m\right]=0 \qquad \sum_{m=1}^{N}\left[\sin^5\psi_m\cos\psi_m\right]=0 \; \sum_{m=1}^{N}\left[\cos^4\psi_m\sin^2\psi_m\right]=\frac{1}{16} \qquad \sum_{m=1}^{N}\left[\sin^4\psi_m\cos^2\psi_m\right]=\frac{1}{16}$$

$$\sum_{m=1}^{N}\left[\cos^5\psi_m\sin\psi_m\right]=0 \qquad \sum_{m=1}^{N}\left[\sin^5\psi_m\cos\psi_m\right]=0$$

$$\sum_{m=1}^{N}\left[\cos^6\psi_m\right]=\frac{5}{16} \qquad \sum_{m=1}^{N}\left[\sin^6\psi_m\right]=\frac{5}{16} \qquad \sum_{m=1}^{N}\left[\sin^3\psi_m\cos^3\psi_m\right]=0$$

Following these simplifications, the additions to the β_0 equation are:

$$\begin{aligned}\frac{\beta_0}{8}\Big[&8K_{\beta 3}\beta_0^4+40K_{\beta 3}\beta_0^2\beta_{1C}^2+40K_{\beta 3}\beta_0^2\beta_{1S}^2+8K_{\beta 2}\beta_0^2+15K_{\beta 3}\beta_{1C}^4\\&+30K_{\beta 3}\beta_{1C}^2\beta_{1S}^2+12K_{\beta 2}\beta_{1C}^2+15K_{\beta 3}\beta_{1S}^4+12K_{\beta 2}\beta_{1S}^2\Big]\end{aligned} \tag{4.42}$$

The additions to the β_{1C} equation are:

$$\begin{aligned}\frac{\beta_{1C}}{8}\Big[&40K_{\beta 3}\beta_0^4+60K_{\beta 3}\beta_0^2\beta_{1C}^2+60K_{\beta 3}\beta_0^2\beta_{1S}^2+24K_{\beta 2}\beta_0^2+5K_{\beta 3}\beta_{1C}^4\\&+10K_{\beta 3}\beta_{1C}^2\beta_{1S}^2+6K_{\beta 2}\beta_{1C}^2+5K_{\beta 3}\beta_{1S}^4+6K_{\beta 2}\beta_{1S}^2\Big]\end{aligned} \tag{4.43}$$

Lastly, the additions to the β_{1S} equation are:

$$\frac{\beta_{1S}}{8}\Big[40K_{\beta 3}\beta_0^4+60K_{\beta 3}\beta_0^2\beta_{1C}^2+60K_{\beta 3}\beta_0^2\beta_{1S}^2+24K_{\beta 2}\beta_0^2+5K_{\beta 3}\beta_{1C}^4 \\ +10K_{\beta 3}\beta_{1C}^2\beta_{1S}^2+6K_{\beta 2}\beta_{1C}^2+5K_{\beta 3}\beta_{1S}^4+6K_{\beta 2}\beta_{1S}^2\Big] \tag{4.44}$$

The same three model variants as in Chapter 3 are used here and the coefficient values used for each are listed below. As the expression has been normalised by blade inertia and rotor speed to convert from dimensional quantities in the ordinary time domain to dimensionless quantities in the per-rev time domain, the K_β parameters are dimensionless.

$$K_{\beta 2} = 10 \text{ rad}^{-3}, \quad K_{\beta 3} = 0 \text{ rad}^{-5} \qquad \text{(cubic hardening)}$$
$$K_{\beta 2} = -10 \text{ rad}^{-3}, \quad K_{\beta 3} = 0 \text{ rad}^{-5} \qquad \text{(cubic softening)}$$
$$K_{\beta 2} = -10 \text{ rad}^{-3}, \quad K_{\beta 3} = 100 \text{ rad}^{-5} \qquad \text{(cubic softening - quintic hardening)}$$

To obtain the dimensional values of $K_{\beta 1,2,3}$, they should be multiplied by $I_b\Omega^2$. These profiles are illustrated in Figure 4.3. Once again, $K_{\beta 1}$ is selected as the independent variable in these profiles and is therefore the continuation parameter in the continuations shown. It is identical to $K^*_{\beta_e}$ in the original linear variant of the model, shown in Equations (4.30)-(4.33). However, it will be controlled not by its absolute value but rather as a multiple of its datum value, obtained from Table 4.1 as ν_β^2. This variable, termed $K^\#_\beta$, is defined as $\frac{K_{\beta 1}}{\nu_\beta^2}$.

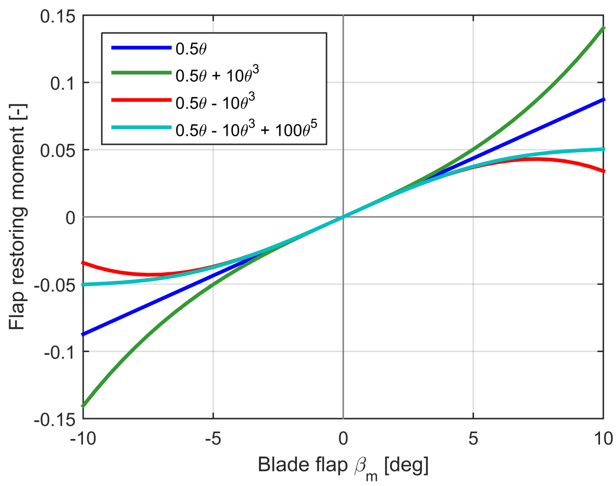

FIGURE 4.3. Polynomial stiffness profiles compared to linear profile (dark blue)

The qualitative features of the profiles are visible within the range shown, and all the nonlinear profiles are approximately linear at very low angles of deflection. The deflection angle that gives zero stiffness (i.e. zero profile gradient) in the softening profile shown here is ±7.4°. The combined softening-hardening profile does not have zero stiffness at any deflection values as the quintic hardening component causes the gradient to steepen again before this can happen.

4.3 Linear Stability Analysis

4.3.1 Parametric sweep in airspeed

The various modes are identified and named by Johnson in [121]. The naming scheme approximately follows the naming of the degrees of freedom, as is common in aeroelastic study. Johnson explains that the choice is informed partially by proximity of a given modal frequency to a system uncoupled natural frequency, and partially by prominence of participation of a degree of freedom in a given mode. Once again, the eigenvectors contain this information: the relative amplitudes of the states' participations in a mode are given by the relative magnitudes of the corresponding components within the relevant eigenvector, while the phasing between states is given by the relative arguments of the eigenvector components. The names and symbols of the modes, along with the colours used to represent them in the figures of this section, are shown in Table 4.2.

TABLE 4.2. Names of and keys to gimballed hub model modes (from Johnson [121])

Description	Symbol	Colour
High-frequency flap	$\beta+1$	orange
Low-frequency flap	$\beta-1$	purple
High-frequency lead-lag	$\zeta+1$	magenta
Low-frequency lead-lag	$\zeta-1$	light green
Coning	β	cyan
Collective lead-lag	ζ	dark green
Wing vertical bending	q_1	red
Wing chordwise bending	q_2	yellow
Wing torsion	p	blue

To introduce the gimballed hub model's behaviour, a sweep in airspeed V is first conducted. Shown in Figure 4.4 are plots of the eigenvalues, damping ratios and modal frequencies of the system as the airspeed V is varied from 0 to 340 ms^{-1}. This range is wide compared to the speeds that current tiltrotors can achieve (see Table 1.1; 340 ms^{-1} = 661 kts) though due to the neglection of compressibility effects in the model, the onset of certain effects is possibly over-predicted in speed. The remaining parameter values used are those in Table 4.1.

The greater complexity of this system – 9 degrees of freedom as opposed to 2 in the basic model – is immediately apparent from the figure. All 18 roots of the system manifest as complex conjugate pairs, indicating that the system response is composed of 9 oscillatory modes. Some modes appear to be stabilised with increasing airspeed, and others destabilised. Crucially, the figure shows that there is no longer just one mechanism of instability as in the basic model, but several. A magnified plot of the higher end of the sweep is shown in Figure 4.5 to show the changes in system stability. The frequency plot has been omitted to allow more space for the eigenvalue and damping ratio plots.

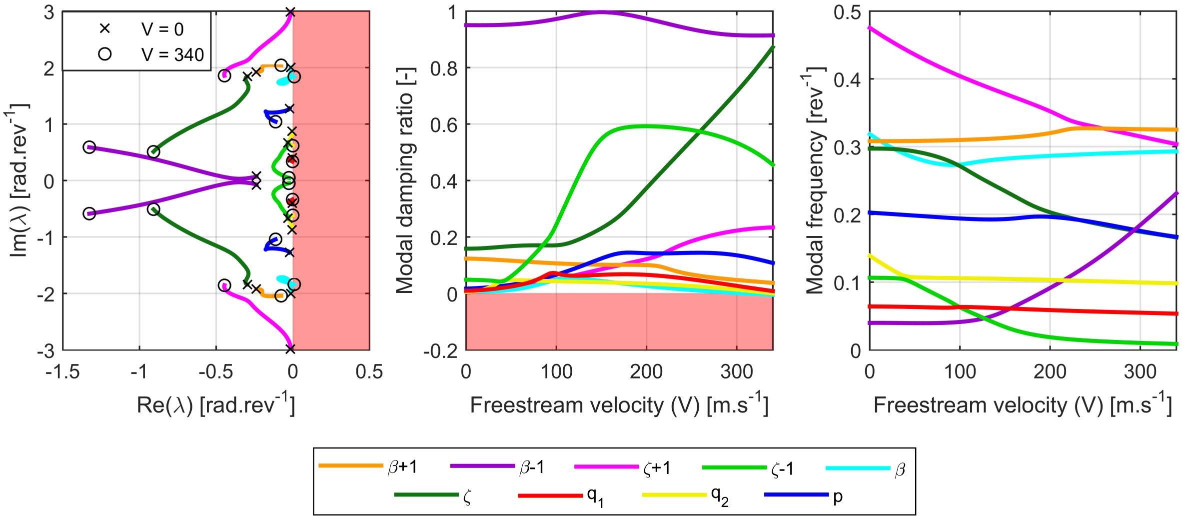

FIGURE 4.4. Eigenvalues *(left)* and their corresponding modal damping ratios *(centre)* and frequencies *(right)* for a sweep in airspeed V, powered condition. Unstable regions are shaded red

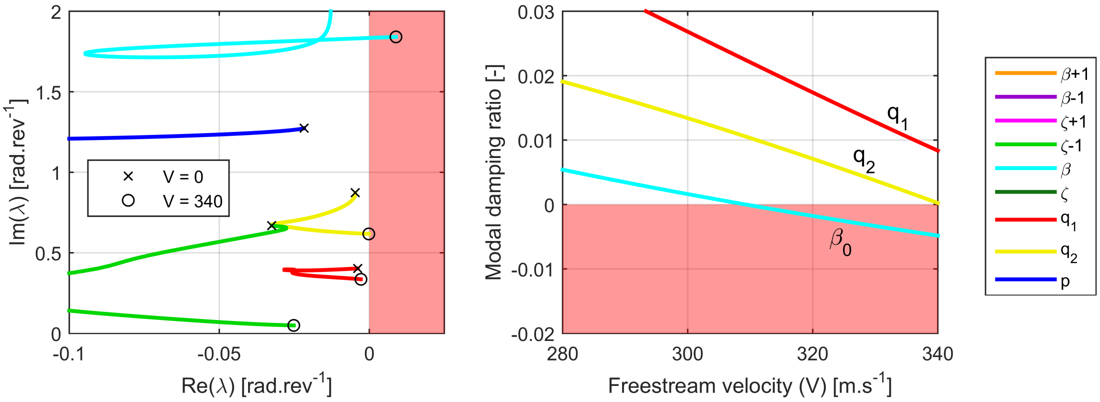

FIGURE 4.5. Eigenvalues *(left)* and their corresponding modal damping ratios *(right)* for a subset of Fig. 4.4. Unstable regions are shaded red

Within the domain of analysis shown here, we see that it is the β mode that loses stability at 310 ms^{-1}, and the q_2 mode that loses stability at 340 ms^{-1}. Once again, the very high airspeeds at which these stability changes take place is due to neglection of compressibility effects in the aerodynamic model. Nevertheless, the sweep has only been continued approximately as far as the speed of sound at sea level, 340 ms^{-1}.

The data shown in Figures 4.4 and 4.5 pertains to the powered case, as is the norm for this model's data in the rest of the work. However for comparison a similar sweep is shown for the autorotation case (i.e. a windmilling rotor) in Figure 4.6. This figure corresponds to Fig. 18 within [121] and therefore can also serve as validation, as Johnson does not include such a figure for the powered case. Johnson's figure uses an airspeed range of 25 to 600 knots, uses the damped definition of natural frequency (i.e. $\omega = b$ rather than $\omega = \sqrt{a^2+b^2}$), only shows the positive-imaginary root of each complex conjugate pair, and uses two co-located x-axes of different scales. The plots in this original figure have been imported to Figure 4.6 and are shown in thin, beaded black lines. In the original figure, the damping ratio data is only provided in the bracket of $\zeta \in [0, 0.15]$. Furthermore, the eigenvalue loci data for the complete sweep are not shown in all modes. All the data that is given is shown here.

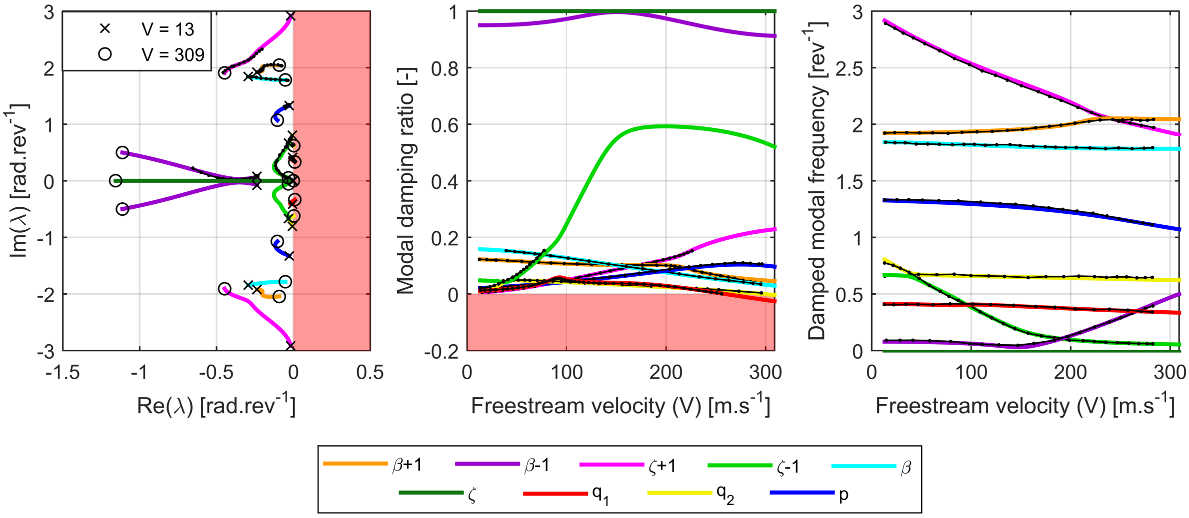

FIGURE 4.6. Eigenvalues *(left)* and their corresponding modal damping ratios *(centre)* and frequencies *(right)* for a sweep in airspeed V, autorotation condition. Unstable regions are shaded red and Johnson's original data is shown with thin, beaded black lines.

Here, the β mode does not go unstable within the domain of analysis, though it appears that it will do so shortly beyond the upper limit of the sweep. Instead, the q_1 mode goes unstable at approximately 260 ms^{-1}, followed by the q_2 mode at approximately 300 ms^{-1}. Now that the rotor is no longer being driven, there is no longer any elastic restraint of the lead-lag motion of the rotor relative to the nominal rotor speed, and therefore the ζ mode roots become non-oscillatory as the rotor instead converges upon its windmilling speed. In general there is very good agreement between the implementation's results and the original data.

4.3.2 Defining whirl flutter and visualising whirl flutter modes

The gimballed hub model is considerably more complex than the basic model, and consequently its modes are correspondingly more complex. Illustrations of a selection of the modeshapes are shown in Figure 4.7. The two modes that become unstable in the autorotation airspeed sweep (Figure 4.6), q_1 and q_2, are shown on the left and in the centre, while the first mode that becomes unstable in the powered condition airspeed sweep (Figure 4.4), β, is shown on the right.

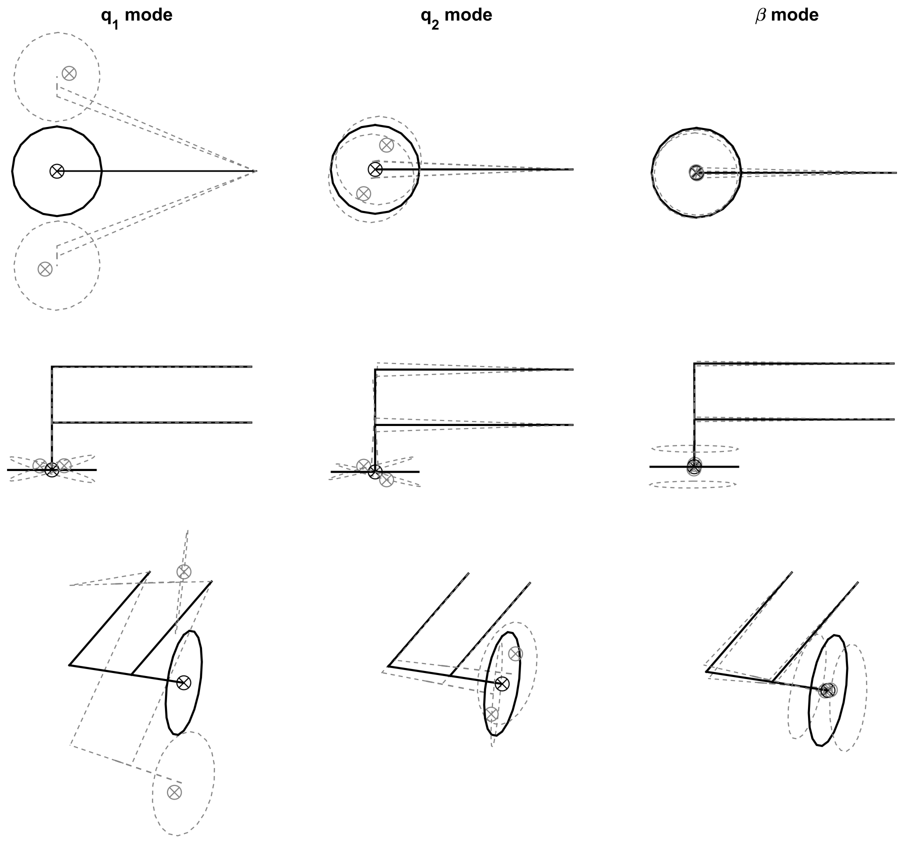

FIGURE 4.7. Illustrations of a selection of modeshapes at V = 250 ms^{-1}. The rotor CG, a function of ζ_{1C} and ζ_{1S}, is indicated by a cross within a circle.

The q_1 mode is dominated by flapwise bending of the wing, with some participation of wing torsion and rotor cyclic flapping, and almost no wing chordwise bending. The q_2 mode exhibits significant wing chordwise bending, with almost no participation of other states apart from cyclic flapping of the rotor. The β mode features almost no wing motion at all other than a small amount of torsion, consisting almost entirely of large amplitude coning (collective flapping) oscillations of the rotor blades.

As a result of this additional complexity, the forward/backward classification scheme for whirl flutter is not usable with the gimballed hub model. Instead, the naming of the modes as shown in Table 4.2 is the most useful classification scheme available and it is therefore retained. Furthermore, modern literature investigating whirl flutter in gimballed hub rotor-nacelle systems, such as [86, 135], tends to present stability arguments in terms of these modes, most usually those dominated by wing motion. As it is typically the wing structure that experiences failure in the known occurrences of whirl flutter, such as the aforementioned Electra disasters, this focus on the wing modes is logical and therefore this work defines whirl flutter in the gimballed hub model as any periodic solutions with meaningful wing participation. This will however require the direct inspection of the nonlinear model's periodic solution branches found by CBM, rather than relying on the modes reported by linear eigenvalue analysis. This is because the nonlinearity will significantly alter the dynamic behaviour of the system, preventing the linear modes from being of much use. This is due to the stiffness nonlinearities playing a significant role in the system's dynamics, due to the non-negligible deflections occurring.

4.3.3 Further parametric sweeps

To familiarise with the gimballed hub model, an elementary sensitivity analysis of the kind shown in Section 3.3.4 for the basic model is conducted here. That is, the original linear version of the model is probed by conducting sweeps on some of the parameters listed in Table 4.1 and observing how the stability of the model changes. Comparing these results to the corresponding linear study of the basic model will yield an initial understanding of the effect that model complexity has on whirl flutter characteristics, as required by research objective O3. Instead of single parameters being swept, some of the following sweeps will be conducted on groups of similar parameters simultaneously, as there is a great number of parameters and some have very low influence when in isolation. To aid clarity, each sweep is allotted a figure of its own. Once again, the terms "stabilising" and "destabilising" are simply used to indicate an increase or decrease (respectively) in a mode's damping ratio rather than a transition from categorical instability to stability, or vice versa. The first set of three sweeps involves the wing and corresponds to Figure 3.9's analogous treatment of pylon and pivot point parameters in the basic model.

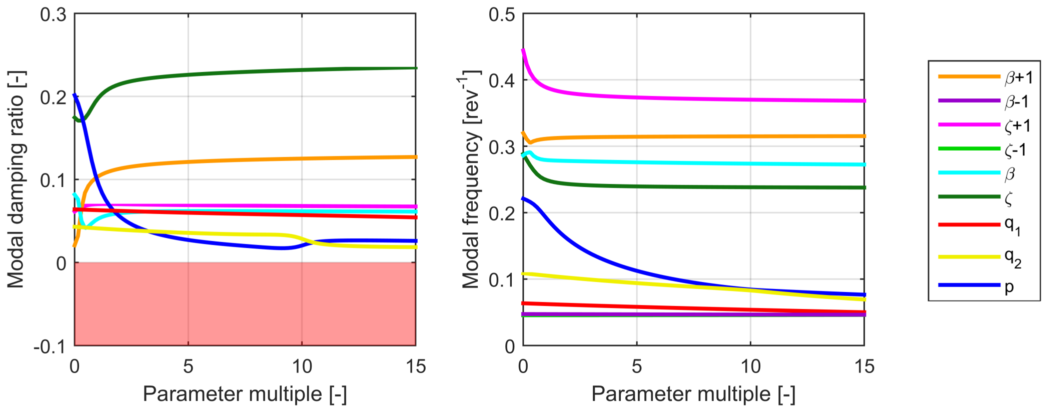

FIGURE 4.8. Simultaneous parametric sweep of wing inertias I_{P_x}, I_{P_y}, I_{q_w} and I_{p_w}

A sweep of the wing inertias is shown in Figure 4.8: pylon yaw moment of inertia I_{P_x}, pylon pitch moment of inertia I_{P_y}, wing bending (flapwise and chordwise) generalised mass I_{q_w} and wing torsion generalised mass I_{p_w} are swept simultaneously as a multiple of their respective datum values, from 0 to 15. It can be seen that in contrast to the basic model, the addition of inertia does not cause instability in the system, and close to zero inertia some modes rapidly gain stability while others destabilise. This implies that resonance could be occurring between two modes – perhaps the high frequency rotor flapping (orange) and coning (light blue) modes – leading to energy flowing from the latter to the former. The impact on modal frequencies is consistent with basic theory in that increasing inertia causes a reduction in natural frequency.

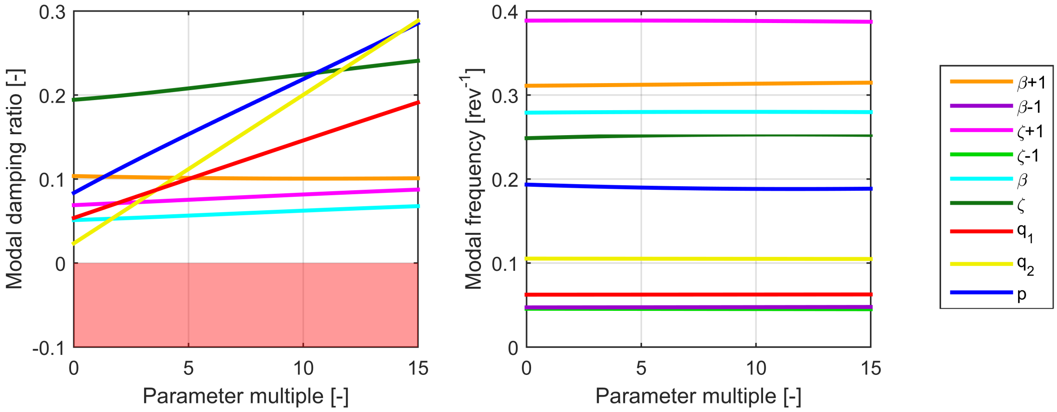

FIGURE 4.9. Simultaneous parametric sweep of wing damping constants C_{q_1}, C_{q_2} and C_p

A sweep of the wing damping constants is shown in Figure 4.9: wing flapwise damping C_{q_1}, wing chordwise damping C_{q_2} and wing torsional damping C_p are varied in the same way. There is minimal impact on the system's modal frequencies, though the damping ratio of some of the rotor-based modes (e.g. ζ) is also improved by increasing the wing damping. An absence of damping does not cause instability in any of the modes and the figure suggests that to do so would require negative wing damping. This suggests that the aerodynamics of the system provide some damping of their own, both at the wing and at the rotor.

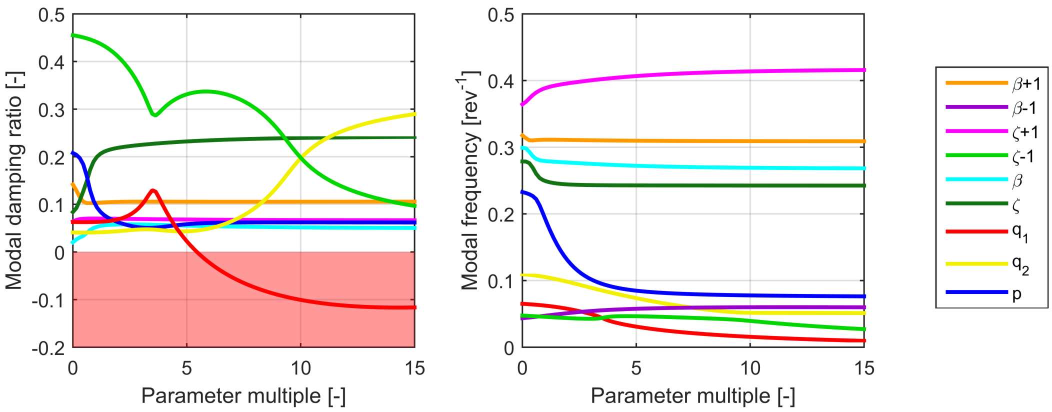

FIGURE 4.10. Parametric sweep of shaft length h

A sweep of the shaft length h (referred to as "mast height" by Johnson) is shown in Figure 4.10. Here, increasing the shaft length causes the system to go unstable in the q_1 mode – in contrast to growing stability in the basic model – as the greater in-plane velocities induced by a given angular motion contribute to destabilising aerodynamic forces and moments in the rotor. Other than at low h, the modal frequencies are only weakly affected.

A sweep of the rotor flapping natural frequencies ν_β (cyclic) and ν_{β_0} (collective) is shown in Figure 4.11. To recap, these parameters are how the flapping stiffness is controlled within the model, and the values refer to uncoupled frequencies. There is a direct, broadly linear impact on some of the rotor mode frequencies, specifically β, $\beta+1$ and $\zeta+1$. At low values in the sweep, the effect is destabilising, causing instability in the p mode and briefly in the q_2 mode, showing the mutual influence the rotor and wing have on one another.

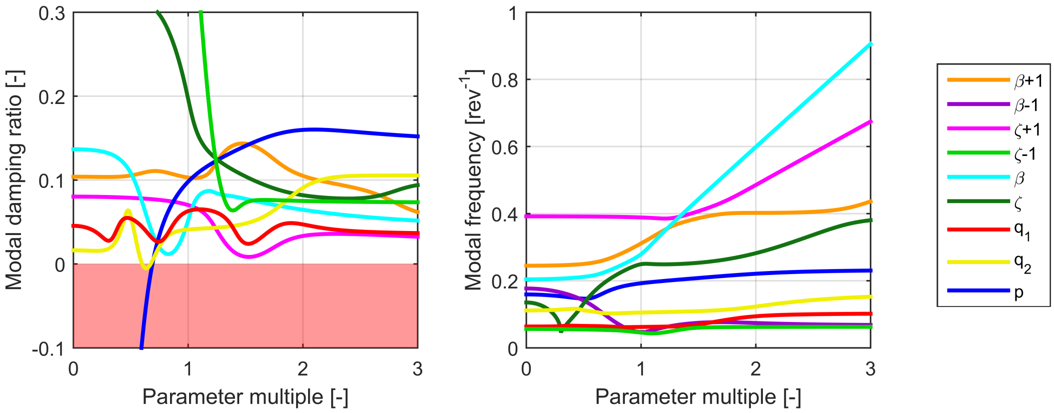

FIGURE 4.11. Simultaneous parametric sweep of rotor flap frequencies ν_β and ν_{β_0}

A sweep of the rotor lead-lag natural frequencies ν_ζ (cyclic) and ν_{ζ_0} (collective) is shown in Figure 4.12. The frequencies of some of the rotor modes are increased toward the higher end of the sweep, and once again low values in the sweep see instability in the system. Here however, the three modes that become unstable are all associated with the rotor's lead-lag dynamics: ζ (collective lead-lag), $\zeta-1$ (low-frequency lead-lag) and $\zeta+1$ (high frequency lead-lag). That is, no wing modes are made unstable as in the previous sweep of ν_β and ν_{β_0}, and this sheds some light on the system's primary physical mechanism of instability.

A sweep of the rotor speed Ω is shown in Figure 4.13. As the model uses a per-rev timescale (rather than seconds), sweeping of the rotor speed and therefore this timescale causes changes in the effective value of various physical properties such as stiffness and damping. The sweep here is therefore started at a parameter multiple of 1 (i.e. the datum parameter value) to avoid the strong numerical issues that arise as Ω approaches 0. These issues are caused by Ω frequently appearing in the denominator of various terms in the equations, such as the aerodynamic coefficients which are functions solely of advance ratio μ.

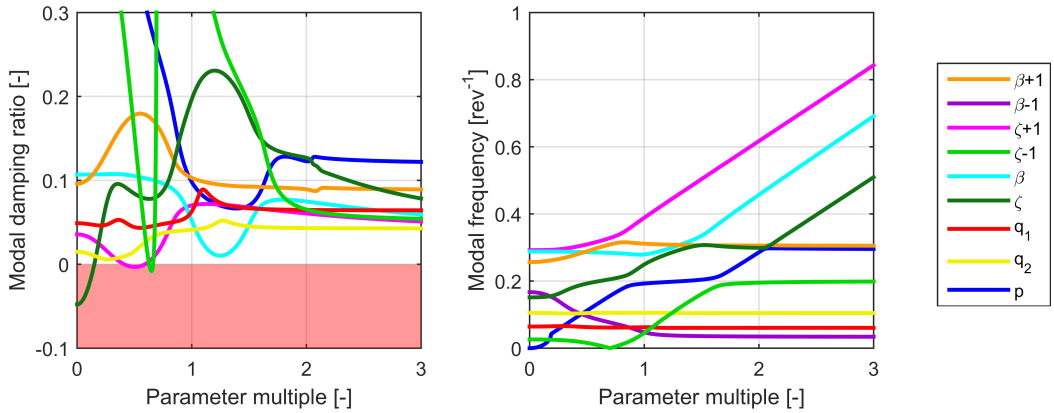

FIGURE 4.12. Simultaneous parametric sweep of rotor lead-lag frequencies ν_ζ and ν_{ζ_0}

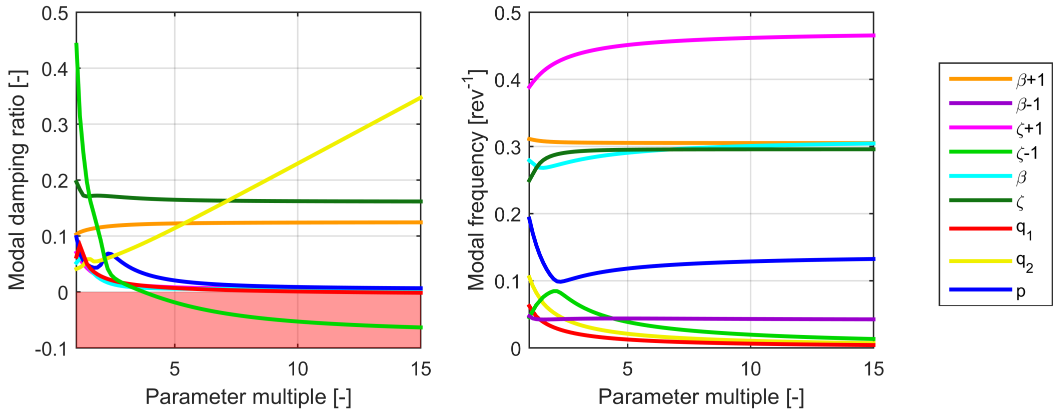

FIGURE 4.13. Parametric sweep of rotor speed Ω

Increasing the rotor speed causes an instability in one of the rotor modes ($\zeta - 1$) followed by one of the wing modes (q_1). This occurs despite the higher rotor speed causing a lower advance ratio μ, as another effect of the rotor speed is to diminish the effective wing stiffness and damping values as experienced by the system. This happens because in the model, the dimensional values for the wing stiffnesses and damping constants are normalised by a factor of $I_b\Omega^2$, where I_b is the moment of inertia of a single blade. The stiffnesses and damping constants of the wing "seen" by the model therefore vary with Ω.

A sweep of rotor radius R is shown in Figure 4.14. As several lengths in the equations are nondimensionalised by R, numerical issues are encountered when R is very small, and therefore this sweep is also started at a multiple of 1. Similar to the basic model, the system has greater stability at the low end of the sweep, and there is a limit to the influence of R toward the higher end. Here however, the modal frequencies also tend asymptotically to some set of values, rather than decreasing as in the basic model.

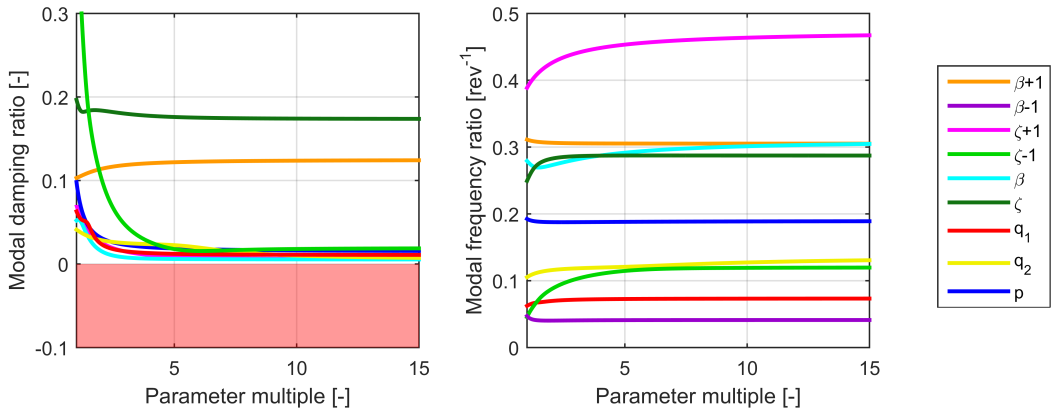

FIGURE 4.14. Parametric sweep of rotor radius R

A summary of these parametric studies is shown in Table 4.3.

TABLE 4.3. Summary of gimballed hub model parametric sensitivity analysis

Parameter	**Influence of value increase**	**Influence of value decrease**
$I_{P_x}, I_{P_y}, I_{q_w}, I_{p_w}$	Destabilising without instability	Destabilising without instability
C_{q_1}, C_{q_2}, C_p	Stabilising	Destabilising without instability
h	Destabilising, eventual whirl flutter	Destabilising without instability
$\nu_\beta, \nu_{\beta 0}$	Destabilising without instability	Destabilising, eventual whirl flutter
$\nu_\zeta, \nu_{\zeta 0}$	Destabilising without instability	Destabilising, eventual whirl flutter
Ω	Destabilising, eventual whirl flutter	Stabilising
R	Destabilising without instability	Stabilising

As the freestream is the only source of energy in the system, it is also the source of any instability, as stability is a matter of how the amount of energy in the system changes over time. While the aerodynamic component of the model is relatively simple in comparison to contemporary literature, it introduces a number of couplings between the rotor and the wing degrees of freedom. For instance, forces on the rotor that are dependent on axial velocity through the rotor disc are influenced by chordwise bending of the wing, and aerodynamic forces acting on the wing contend with the influence of the rotor in how they act on the wing's motion. However, the specific mechanism by which whirl flutter occurs that is mentioned in existing literature is the coupling between the wing torsional motion and motion-dependent in-plane forces [135, 183]. Further, a number of works emphasise the contribution from blade flapping to these in-plane forces [105, 162]. The stronger influence of blade flapping on system stability (as opposed to lead-lag) was apparent in Figures 4.11 and 4.12, however the destabilising influence of the interaction between the motion-dependent in-plane forces and the wing torsional motion can be seen in isolation by temporarily removing the relevant terms in the model. This has the effect of removing the physical mechanism of this interaction. Shown in Figure 4.15 is a sweep in airspeed V with removal of some of the aerodynamic coupling coefficients, as well as removal of aerodynamic feedback of the wing torsion motion $\dot{p}$ into the blade cyclic flapping equations of β_{1C} and β_{1S}, Equations (4.20) and (4.21). That is, all terms of aerodynamic origin involving $\dot{p}$ in these equations were temporarily removed. The neutralised aerodynamic coupling coefficients are $H_{\dot{\zeta}}$ (blade drag/in-plane force induced by blade lead-lag motion) and $Q_{\dot{\beta}}$ (hub in-plane torque induced by blade flapping motion), and these were removed from all the equations in which they appear.

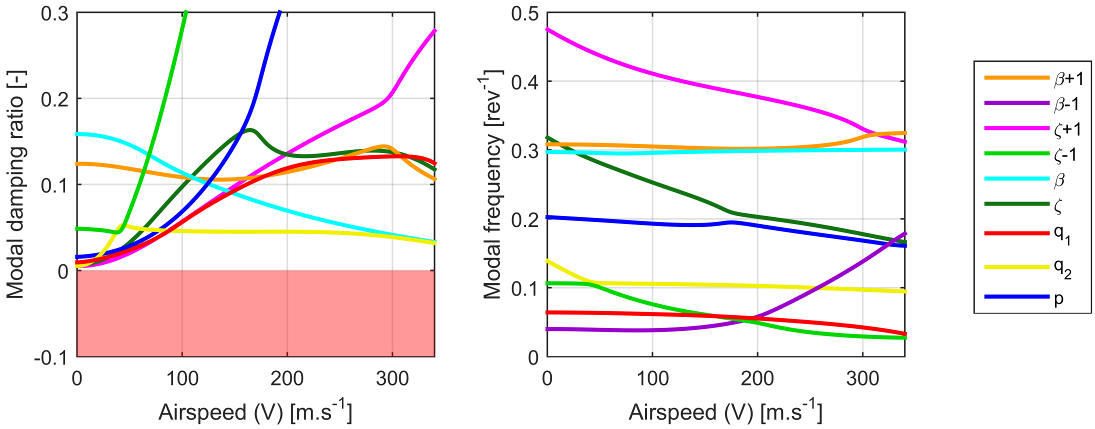

FIGURE 4.15. Parametric sweep of airspeed V with primary instability mechanism removed

The system's modes are stabilised within the domain of analysis, which extends from an absence of freestream velocity up to the speed of sound, beyond which key simplifications in the aerodynamic model such as the neglection of compressibility can no longer be ignored. Due to the complexity of the system, there are likely to be a number of aerodynamic mechanisms by which the system may become unstable – such as coupling between the rotor coning and the wing chordwise bending – with the case demonstrated here only being the most critical.

4.3.4 Stability boundary

Regarding the choice of stability boundary axes, the greatest insight will be gained from a parameter space comprised of one rotor parameter and one wing parameter, as explained in Section 4.2.2. As discussed previously, the linear component of the nonlinear stiffness profiles, normalised by ν_β^2 and indicated $K_\beta^\#$, is the independent variable in this chapter and it therefore is used as the x-axis of the stability boundary. The wing torsion degree of freedom is one of the most influential, being part of the model's primary whirl flutter instability mechanism, and therefore the corresponding stiffness K_p is chosen for the second axis of the stability boundary. Lastly, due to the varying orders of magnitude of the model's parameters, it is most convenient to also apply datum-normalisation to the K_p parameter. That is, the values used on graph scales in the figures shown here are decimal multiples of the datum value shown in Table 4.1. The notation $K_p^\#$ is therefore used, where $K_p^\# = \frac{K_p}{K_{p\,\text{datum}}}$.

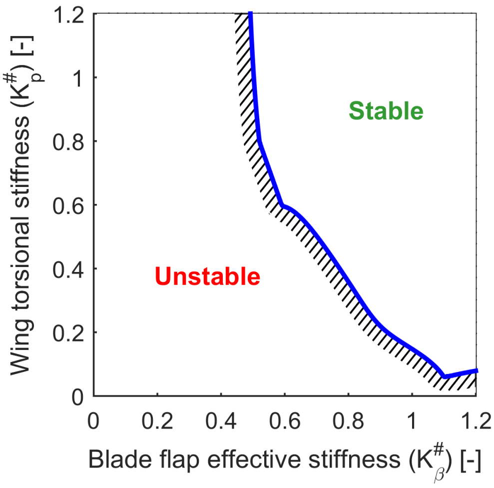

FIGURE 4.16. Stability boundary between datum-normalised blade flapping stiffness $K_\beta^\#$ and datum-normalised wing torsional stiffness $K_p^\#$. All other parameters are at their datum values

The $K_\beta^\#$-$K_p^\#$ stability boundary of the gimballed hub model (original linear version) is shown in Figure 4.16. It will serve as the baseline to which the nonlinear model variant's results will be compared. Similar to the basic model's K_θ-K_ψ stability boundary, the unstable region is placed in the bottom left corner of the analysis domain, indicating that a reduction of both parameters results in a reduction of stability. Once again, the presence of a number of subtle but noticeable discontinuities in the boundary suggests that it is composed of the loci of a number of different modes on the knife edge of instability (or alternatively, bifurcations).

4.4 Continuation and Bifurcation Analysis

4.4.1 Direct application to linear model

As with the basic model, the inner structure of the stability boundary's unstable region is best revealed using two-parameter continuation. A single-parameter continuation is performed in $K_\beta^\#$, the (linear) blade flapping stiffness. The undeformed and at-rest position of the system, $\mathbf{y} = \mathbf{0}$, is used as a starting solution. Choosing $K_p^\# = 0.55$ so that a continuation in $K_\beta^\#$ will intersect a region of interest in the stability boundary, the bifurcation diagram shown in Figure 4.17 (top right) is obtained. The loci of the system's eigenvalues over this sweep are indicated on the left on an Argand diagram, with the modal damping ratios shown in the bottom right.

Considering the sweep in the $K_\beta^\#$-decreasing sense, the $\beta - 1$ mode (purple) becomes non-oscillatory (i.e. overdamped) and then oscillatory again, moving off to the left of the Argand diagram. Interestingly, the β mode (cyan) is almost entirely unaffected by the sweep. The p mode (blue) becomes unstable and monotonically continues to become more and more unstable, as confirmed by the damping plot (bottom right). Once again, the presence of several different "types" of whirl flutter is demonstrated, rather than just one. There are five Hopf bifurcations (hollow square icons) found through the continuation (top right of the figure), and when their $K_\beta^\#$ coordinates are cross-referenced with the damping ratio plot, it becomes apparent that they may signal either the loss of stability or the re-stabilisation of an individual whirl flutter mode.

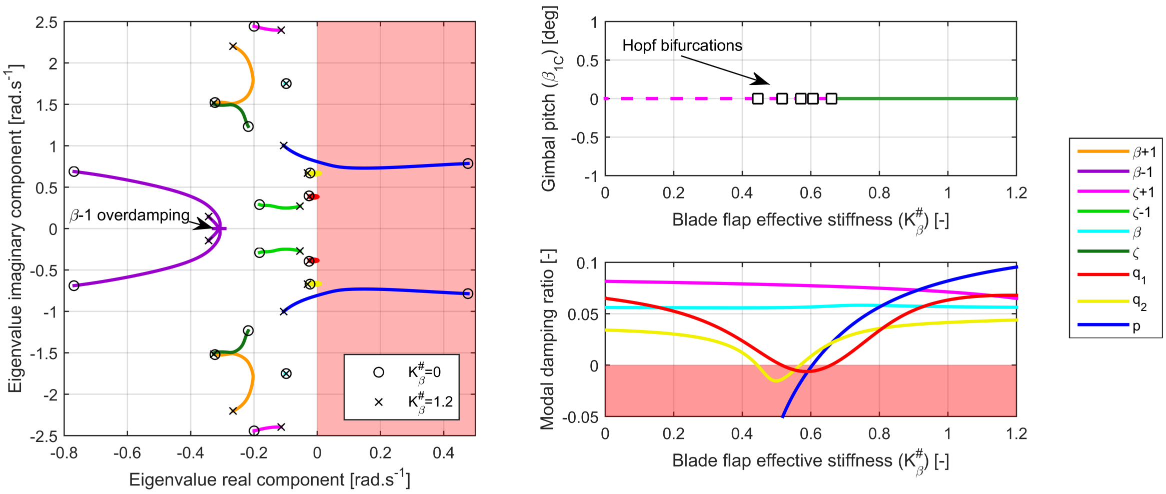

FIGURE 4.17. Bifurcation diagram *(top right)*, β_{1C} projection, with corresponding roots sweep *(left)* and modal damping ratios *(bottom right)*, as $K_\beta^\#$ is varied

Moving in the sense of decreasing blade flap stiffness on the damping ratio plot, the q_1 mode (red) is the first to lose stability, followed by the p mode as previously mentioned, followed by the q_2 mode (yellow). However the q_1 mode restabilises shortly afterward, and by approximately $K_\beta^\# = 0.45$ the q_2 mode has also restabilised. While this variety of types of whirl flutter is not in itself a hazard, it is their coexistence in the parameter space that may pose a threat, as if more than one stable whirl flutter solution exists at a certain value, it increases the likelihood that a perturbation will cause the system to encounter whirl flutter. The stability is not visible here however, and requires further application of CBM.

Performing two-parameter continuations in $K_\beta^\#$ and $K_p^\#$ on each of these Hopf bifurcations reconstructs the stability boundary and this is shown in Figure 4.18. The very bottom-right segment of the boundary is defined by a pitchfork bifurcation that is found by a separate continuation downward in $K_p^\#$ at any fixed value of $K_\beta^\#$ (not shown). This pitchfork gives rise to secondary equilibrium branches in much the same manner as shown in Chapter 3, though as they do not relate to whirl flutter, they are not explored. Regions shaded red are subject to oscillatory instability (an unstable complex conjugate root pair) and regions shaded blue are subject to non-oscillatory instability (an unstable single real root). The modal identification of the Hopf bifurcations in Figure 4.17, together with the smoothness of the bifurcation loci in Figure 4.18, might suggest that each enclosed region pertains to the instability of a specific mode. However, due to the occurrence of veering between the modes, the matter of modal regions in this stability boundary is substantially more complex.

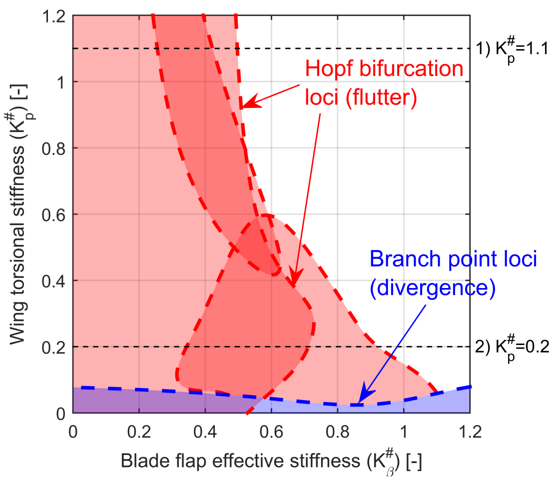

FIGURE 4.18. $K_\beta^\#$-$K_p^\#$ stability boundary regenerated through two-parameter continuations of the pitchfork and Hopf bifurcations

Veering is a phenomenon of linear system modes where two eigenvalues moving in the complex plane during a parameter sweep come very close to one another and swap trajectories, appearing to bounce off one another. In some cases, the eigenvalues can overlap, with their corresponding eigenvectors also becoming equal to one another. A more comprehensive explanation of veering is given by Arnold [312]. Here, the phenomenon makes it impossible to unambiguously attribute each Hopf bifurcation locus, and the area that it bounds, to a given mode. Furthermore, as the nonlinear results presented later are not interpretable in terms of these linear modes, a comprehensive characterisation of the modal regions in this boundary is not of value and is therefore not undertaken. This means that it is not possible to tell from this figure alone which of these oscillatory instabilities contains meaningful wing activity and therefore qualify as whirl flutter under the definition of this work. Nevertheless, the phenomenon of several different types of instability existing – and coexisting at that – can now be appreciated: the shaded regions overlap in several places forming darker sub-regions where multiple instabilities are present. Furthermore, the figure gives a map of where periodic solution branches will emerge from when CBM is applied to the nonlinear model variant, as the position of these Hopf bifurcations is unchanged by nonlinear terms.

Two levels of $K_p^\#$ are chosen as analysis cases for the rest of the chapter: $K_p^\# = 1.1$ and $K_p^\# = 0.2$. They are also indicated in the figure. This choice of cases provides a concise demonstration of the influence of $K_p^\#$ as they span the range of analysis: one at high pitch stiffness and one at lower stiffness.

4.4.2 Nonlinear results: cubic hardening ($K_{\beta 2} = 10$, $K_{\beta 3} = 0$)

The nonlinear results may now be obtained, using blade flap effective stiffness $K_\beta^\#$ as the continuation parameter. The hardening profile is examined first and a bifurcation diagram for the first analysis case, $K_p^\# = 1.1$, is shown in Figure 4.19. In the gimballed hub model, the behaviours of both the rotor and the wing are of interest, and therefore the projections of both gimbal pitch β_{1C} and wing torsion p are shown for each bifurcation diagram. The p projection is also useful in determining whether a given branch contains meaningful wing activity, and therefore may be called whirl flutter.

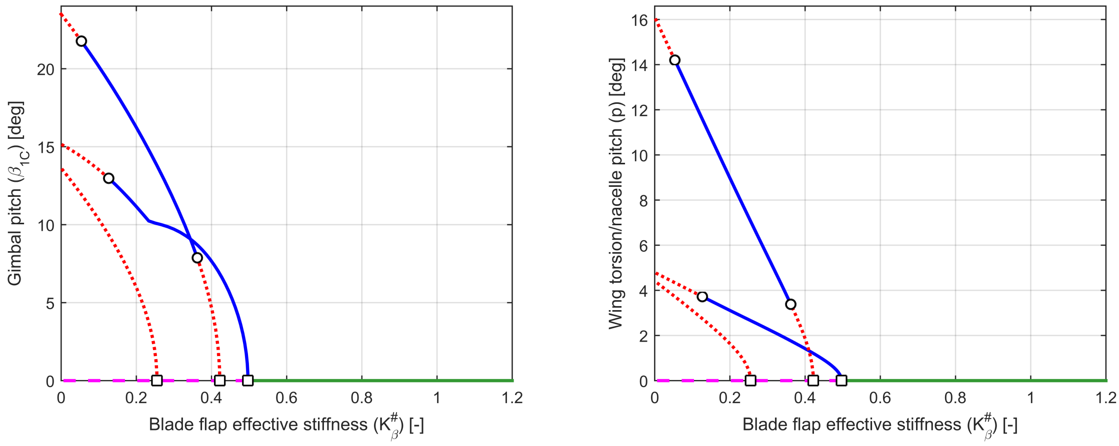

FIGURE 4.19. Bifurcation diagram for case 1 ($K_p^\# = 1.1$), hardening variant, β_{1C} and p projections

Three Hopf bifurcations are visible, whose locations in $K_\beta^\#$ correspond to the three intersections of a line at $K_p^\# = 1.1$ with the Hopf loci present at that level (see Figure 4.18). As the p projection shows, the wing participation in all three of these periodic solution branches is significant, so all may be identified as whirl flutter. The ability of CBM to uncover this information is a further benefit it has over linear analysis and/or linear models. The most significant wing torsion participation occurs in the periodic solution branch emanating from the middle Hopf bifurcation, with much less prominent participation in the branches emanating from the left and right Hopf bifurcations. The hardening component in the blade flap stiffness profile bends the periodic solutions leftward. Furthermore, all three Hopf bifurcations are supercritical, resulting in no overhang of the stable main branch ($K_\beta^\# >\sim 0.5$). As $K_\beta^\#$ is lowered, the amplitude of all three whirl flutter branches increases in both projections. The periodic solution branches mostly coexist – that is, at a given continuation parameter value, more than one periodic solution branch is generally present – and the system may join any stable solution branches depending on what perturbation it receives. This constitutes the possibility of whirl flutter. It is once again important to note that CBM's prediction of stable branches in parametric regions that lie very much within the unstable region predicted by linear analysis does not indicate that these regions have been made safe by the presence of the nonlinearity. The model does not account for any damage that the occurrence of whirl flutter LCOs would likely cause to the system, leading to the widening of the oscillations and likely structural failure.

New here however, compared to the basic model results, is the presence of **torus bifurcations**, indicated with hollow circles. Torus bifurcations, also known as Neimark-Sacker bifurcations or secondary Hopf bifurcations, are present on all three branches. The bifurcation acts on periodic solutions: at the bifurcation point, a stable LCO becomes unstable and a torus-shaped manifold forms about it in the phase space. This type of manifold was shown in schematic form in Figure 2.17, in Section 2.2.4.3. This torus can itself be stable or unstable, either attracting or repelling trajectories from both inside and outside. Trajectories on the torus are closely bundled and not closed, producing **quasi-periodic** behaviour. In this work, the phenomenon of the system following a torus manifold in this way is referred to as torus flow. The torus bifurcation is explained in more detail in Section 4.4.8, though for now it suffices to say that a torus bifurcation only guarantees the existence of a torus flow in some neighbourhood near it on the periodic solution branch on which it exists, and the torus flow does not necessarily require a second torus bifurcation at which to terminate. This is because torus flows can also be created or destroyed abruptly through a different process. Unlike the torus bifurcation, there is no signal in the movement of the Floquet multipliers for this destruction, and therefore the presence of a torus bifurcation only presents the possibility of torus flow in some neighbourhood of the torus bifurcation. Conversely, torus flow can in principle exist about LCOs without a nearby torus bifurcation, if the LCO segment of torus flow both starts and ends with torus creation/destruction. As far as the above figure is concerned, all that can be deduced with certainty is that quasi-periodic behaviour exists in at least some of the diagram.

The lower of the two torus bifurcations on the middle Hopf bifurcation's periodic solution branch is responsible for the branch emerging unstable despite departing to the left, suggesting a supercritical form. The torus bifurcation manifests mathematically as two complex conjugate Floquet multipliers crossing the unit circle, and on this branch the Floquet multiplier pair remain outside the unit circle throughout the lower portion between the aforementioned torus bifurcation and the Hopf bifurcation from which the branch emanates. This causes AUTO to mark this portion as unstable, although there is no guarantee that the torus flow exists over all of the branch portion. For reference, the movement of the Floquet multipliers along this middle periodic solution branch is shown in Figure 4.20.

The 18 Floquet multipliers manifest mostly as 9 complex conjugate pairs, though during the sweep a number of the pairs collapse temporarily into two distinct real multipliers, giving the full set of loci a complex appearance. Where the branch emanates at $K^{\#}_{\beta} = 0.422$, the two multipliers on the left of the figure are outside the unit circle, making the LCO unstable, although there is

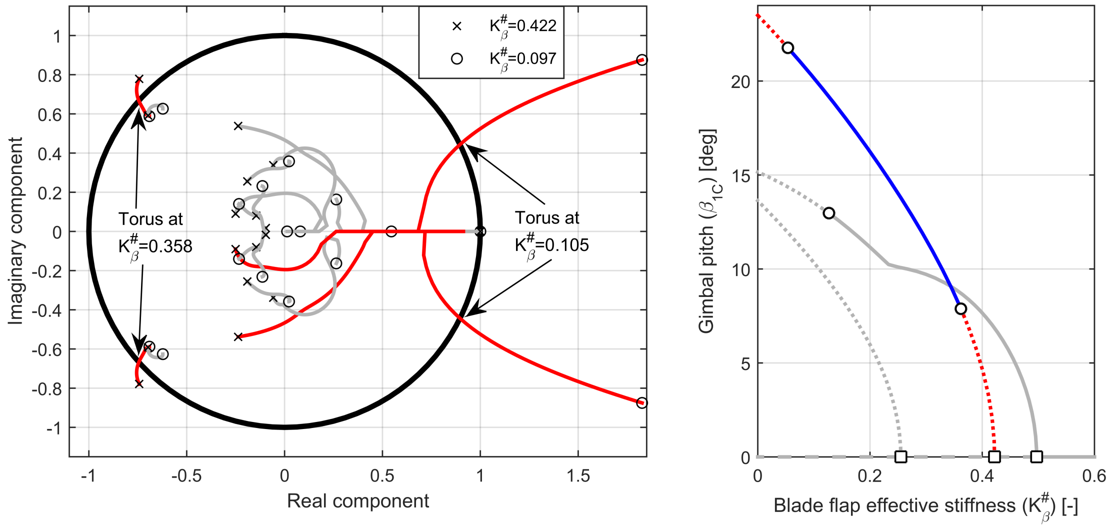

FIGURE 4.20. Argand diagram of Floquet multiplier loci (*left*) on middle periodic solution branch, hardening variant, case 1. The loci of the multipliers that signal the torus bifurcations are coloured red. The unit circle is indicated in black. The corresponding bifurcation diagram is included for reference (*right*)

no guarantee that torus flow of the kind described above is occurring about the LCO at this point. The left-most Hopf's whirl flutter branch is unstable for the entire extent within the domain of analysis. To aid the reader in visualising the bifurcation diagrams presented in Figure 4.19, Figure 4.21 shows the β_{1C} projection with a selection of β_{1S}-β_{1C} phase planes showing the stable and unstable solutions present at each cut.

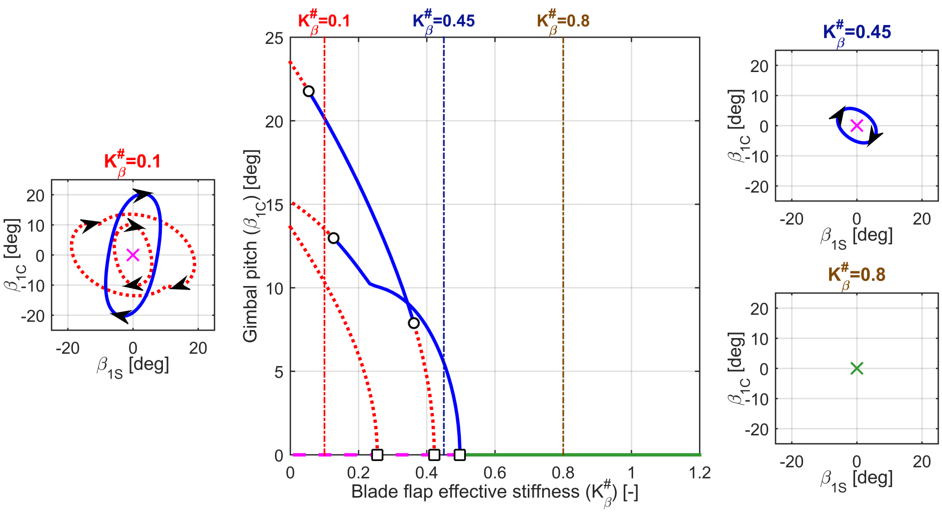

FIGURE 4.21. Bifurcation diagram for case 1 ($K_p^{\#} = 1.1$), hardening variant, β_{1C} projection, with phase plane planes showing solutions in detail at various $K_{\beta}^{\#}$ values

Observing the figure from right to left, the first cut at $K_\beta^\# = 0.8$ shows the stable main branch with no other solutions present, the second at $K_\beta^\# = 0.45$ shows the main branch now unstable with a single stable whirl flutter LCO present, and the third shows three whirl flutter LCOs all present at the $K_\beta^\#$ value of 0.1. Some torus flow was located at this value of $K_\beta^\#$ on the branch emanating from the right-most Hopf bifurcation at $K_\beta^\# = 0.497$, shortly after the torus bifurcation has made the LCO unstable. The LCO at this point is visible on the left-most phase plane of Figure 4.21; it is the larger of the two unstable LCOs (red). This torus flow is demonstrated in Figure 4.22 in a 3-dimensional projection of the phase space using gimbal pitch β_{1C}, gimbal yaw β_{1S} and wing torsion p, produced by a time simulation over a period of 250 rotor revolutions.

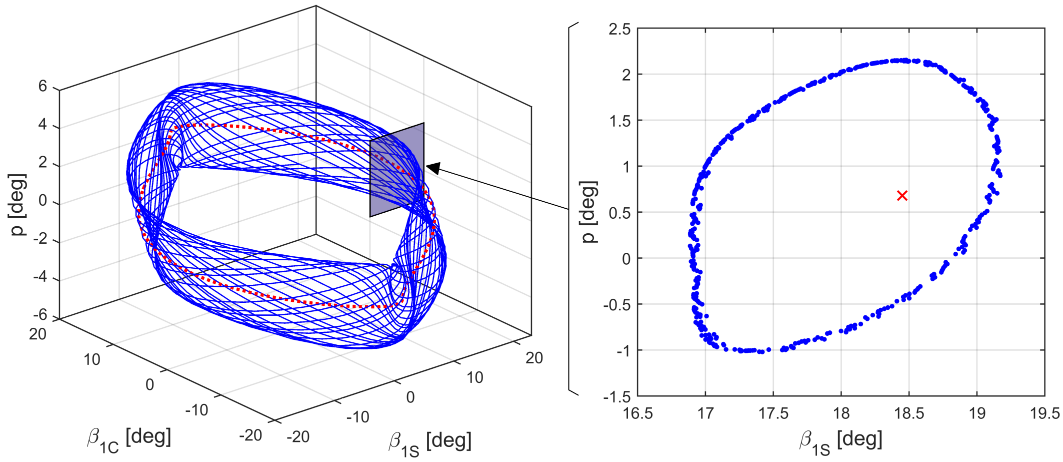

FIGURE 4.22. Torus flow found at $K_\beta^\# = 0.1$ in hardening variant, case 1, shown in $(\beta_{1C}, \beta_{1S}, p)$ space (*left*), with Poincaré section placed at $\beta_{1C} = 0°$ (*right*).

A Poincaré section placed at $\beta_{1C} = 0°$ on the positive β_{1S} side of the LCO shows a cross-section of the torus' 3D projection at this point in the LCO, over a period of 5000 rotor revolutions. The torus can clearly be seen surrounding the LCO.

The second analysis case ($K_p^\# = 0.2$) for the hardening model variant is now considered, shown in Figure 4.23. Once again, there are three supercritical Hopf bifurcations present. The middle and left periodic solution branches are both unstable within the domain of analysis. The right-most Hopf's flutter branch is the only one of the three to contain stable portions, and after emanating from the main branch it folds back and forth in $K_\beta^\#$ a number of times before eventually departing to the left. In this folded part, the torus bifurcations potentially cause several branch portions that would otherwise be stable to be unstable, as the Floquet multipliers that signalled the torus bifurcation are still placed outside of the unit circle. Without the torus bifurcations, the regions of stability would be placed like in the basic model's hardening variant: stable for branches growing with decreasing $K_\beta^\#$, and unstable for branches growing with increasing $K_\beta^\#$. The torus bifurcations exist just before fold bifurcations.

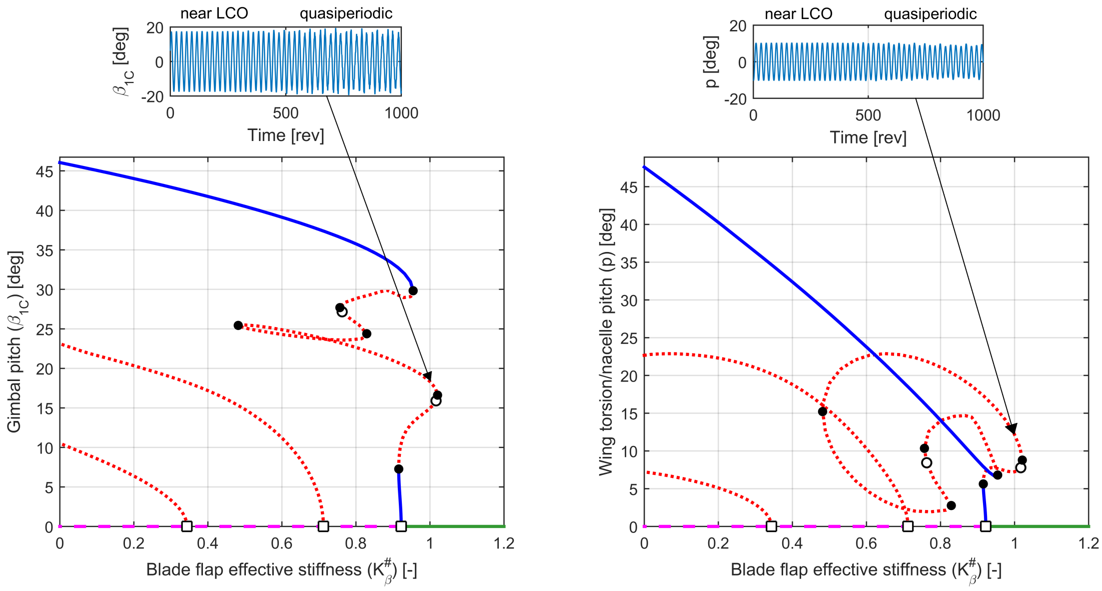

FIGURE 4.23. Bifurcation diagram for case 2 ($K_p^\# = 0.2$), hardening variant, β_{1C} and p projections. A time simulation starting close to the LCO branch at $K_\beta^\# = 1.015$ is also shown, with the relevant state for each projection.

The much lower wing torsional stiffness value of case 2 allows all three whirl flutter branches to be much larger in amplitude than those in case 1. Most pressing however is the overhanging of the stable main (equilibrium) branch by a portion of the first Hopf's whirl flutter branch which, due to the torus bifurcation at approximately $K_\beta^\# = 1$, is surrounded by torus flow in at least some neighbourhood of that torus bifurcation. A time simulation with $K_\beta^\# = 1.015$ is shown to demonstrate the system's ability to be attracted to whirl flutter behaviours in this vicinity. The time histories of the β_{1C} and p states from this simulation are shown next to the relevant projections in Figure 4.23. The simulation of 2000 rotor revolutions is started with initial conditions 99% the size of a point on the LCO (in all states) and the transition from the LCO to the quasi-periodic behaviour on the torus surrounding the LCO is noticeable in the time histories for each state shown. The earlier portion of the time history shows neat oscillation of only one frequency component, though in the latter portion there are several frequencies components visible. This overhang stretches as far in $K_\beta^\#$ as the torus bifurcation, and is partially shadowed by a lesser overhang by the same branch at a larger amplitude, which provides stable LCOs up to approximately $K_\beta^\# = 0.95$.

While this overhang may seem unusual given the results from case 1 above, and the hardening model variant results from the basic model, it is likely due to the nonlinearity causing the effective natural frequencies of some system components to be closer to each other than they would otherwise be. As natural frequency is in general a function of stiffness, and stiffness in the nonlinear profiles is a function of deflection, the instantaneous effective natural frequency of the rotor blade motions is a function of the deflection of the rotor. Therefore, when the system is configured with $K_\beta^\#$ set between 0.9 and 1, its properties are such that oscillation at the amplitudes indicated by Figure 4.23 gives the rotor blades the necessary natural frequencies for energy to be received from other system components and the motion to therefore be sustained as an LCO.

4.4.3 Effect of varying $K_{\beta 2}$

In the same way as was done in the basic model, the effect of the cubic stiffness coefficient $K_{\beta 2}$ must be explored briefly. Shown in Figure 4.24 are bifurcation diagrams with $K_p^\#$ set to 0.2 (as per case 2), with increased and decreased values of $K_{\beta 2}$ compared to the standard value of 10.

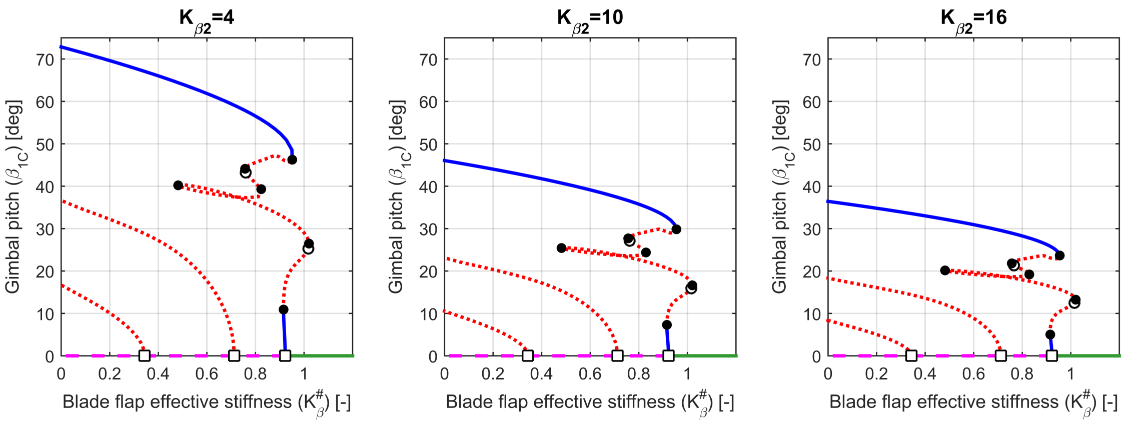

FIGURE 4.24. Effect of varying cubic stiffness $K_{\beta 2}$ in case 2

As before, higher values of $K_{\beta 2}$ have the effect of stiffening the structure, reducing the amplitude of any solution branches. The reverse is true for lower values of $K_{\beta 2}$, and in fact the structure of the solution branches is almost completely unchanged apart from this scaling of amplitude. The change in $K_{\beta 2}$ neither improves nor worsens the extent of the overhang, meaning that the position of the unsafe region within the stability boundary created by the overhang is not a function of the "strength" of this nonlinearity. This further implies that the overhang cannot be removed simply by designing a structure with strong hardening stiffness properties. The amplitude of the solutions is however restricted by increasing the hardening effect.

4.4.4 Nonlinear results: cubic softening ($K_{\beta 2} = -10$, $K_{\beta 3} = 0$)

Attention can now be turned to the softening profile, shown in Figure 4.3. A continuation in $K_\beta^\#$ is conducted and the β_{1C} and p projections of the resulting bifurcation diagram are shown in Figure 4.25.

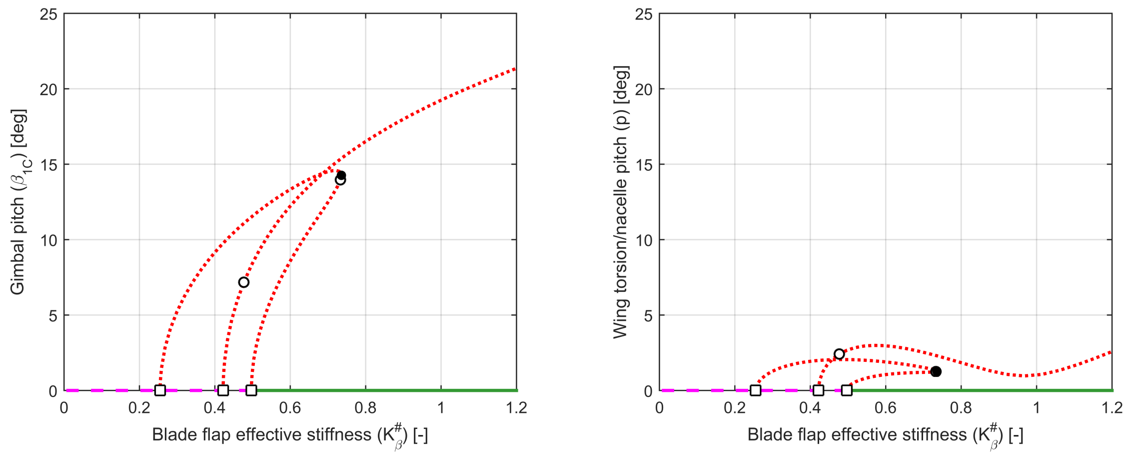

FIGURE 4.25. Bifurcation diagram for case 1 ($K^{\#}_{p} = 1.1$), softening variant, β_{1C} and p projections

There are three Hopf bifurcations, situated at the same $K^{\#}_{\beta}$ locations as in the corresponding hardening variant diagram (Figure 4.19), as their positions are functions only of the linear components of the system and are therefore unaffected by the value of $K_{\beta 2}$ (or $K_{\beta 3}$). Now however, the Hopf bifurcations are subcritical and their branches depart to the right. Furthermore, the right-most and left-most Hopfs are joined together via the whirl flutter branch that emanates from each. The flutter branch connecting them is unstable at the right-most Hopf, but following a torus bifurcation very close to the fold, the left side of the branch is possibly the centre of a torus. The middle Hopf's whirl flutter branch is unstable and disappears off to the right, unstable and overhanging the main branch. A torus bifurcation fairly close to the branch's origin signals the potential presence of torus flows on the branch.

While it might appear that the overhang threat from this analysis case is the torus surrounding part of the whirl flutter branch connecting the right-most and left-most Hopf bifurcations, the unstable branch emanating from the middle Hopf is actually a more severe threat. Being an attractor, the main branch has a basin of attraction around it in the phase space, as does divergence to infinitely-large solutions, and the unstable LCO here is equally attracted by both of them, resulting in zero net attraction. The manifold that is defined by where the two basins of attraction meet acts as a separatrix between them, and therefore also between behaviours seen in time simulations: decay to the main branch or an infinite blow-up of solutions. That is, a perturbation that pushes the system over the separatrix and into the basin of attraction of infinitely large solutions will experience divergence. While the LCO does not fully characterise this separatrix manifold (as it is only a curve within the phase space rather than a manifold), it does lie within the manifold and can still be used to demonstrate its role as a separatrix.

The effect is shown in Figure 4.26. The system is configured with $K_\beta^\# = 1$ and two time simulations are started whose initial conditions are fractional multiples of an arbitrary point on the LCO: one inside the LCO at 80% of the arbitrary point (in all states), and one outside the LCO at 120%. The time simulation started inside the LCO is run for 200 rotor revolutions' time and quickly decays, converging on the main branch. However, the time simulation started outside the LCO has left the domain shown in the phase plane within 1.5 rotor revolutions, quickly diverging to infinitely large solution values in all states. Physically, this may be interpreted as a catastrophic structural failure of the system.

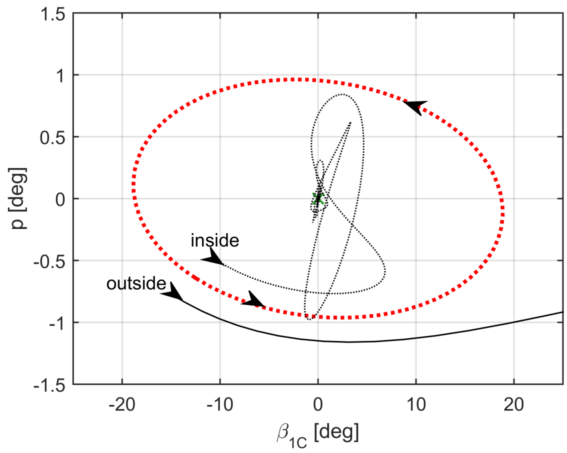

FIGURE 4.26. Time simulations on β_{1C}-p phase plane for case 1 ($K_p^\# = 1.1$), softening variant, with $K_\beta^\# = 1$. The LCO is shown in red

The second analysis case ($K_p^\# = 0.2$) is shown in Figure 4.27.

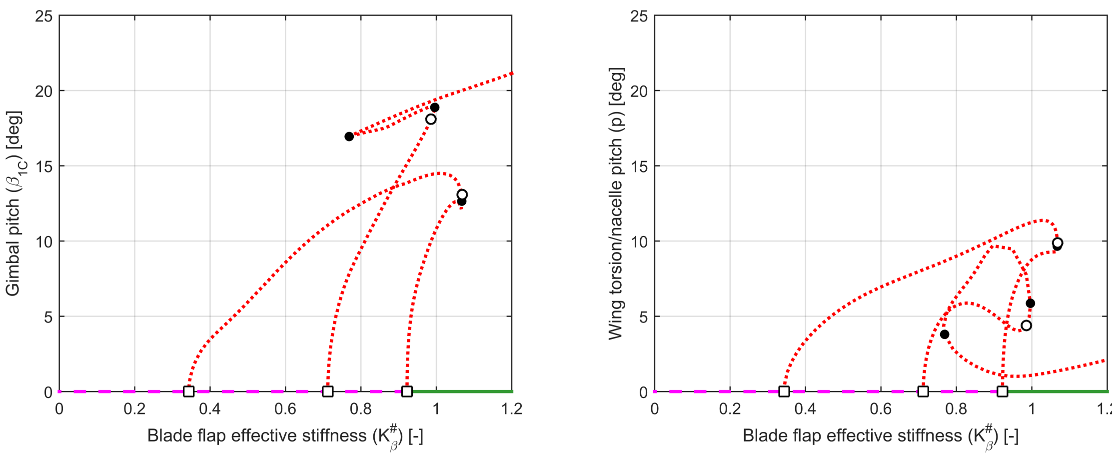

FIGURE 4.27. Bifurcation diagram for case 2 ($K_p^\# = 0.2$), softening variant, β_{1C} and p projections

The results are in a number of ways similar to those from case 1 (Figure 4.25). The three Hopf bifurcations are subcritical, and the right-most and left-most Hopf bifurcations are connected through the whirl flutter branch that they share, with some portion potentially as the centre of a torus. The middle Hopf gives rise to an indefinitely-overhanging unstable branch whose LCO at any point is part of a separatrix in the phase space between decay down to the stable main branch and blow-up to infinite amplitudes, in the same manner as shown for case 1 above. Interestingly, the lower torsional stiffness of this case amplifies only the wing torsional response and not also the gimbal pitch response, as it did in the hardening model variant. This indicates that the rotor and wing are interacting in a different way here to how they did in the hardening case.

4.4.5 Nonlinear results: combined softening – hardening ($K_{\beta 2} = -10$, $K_{\beta 3} = 100$)

The combined profile is now used, which as in the previous chapter has a softening cubic component tempered by a hardening quintic component. The results are shown in Figure 4.28. The three Hopf bifurcations are present as expected, and due to the softening component of the profile dominating at lower deflections (through its cubic influence), the Hopfs are subcritical with their whirl flutter branches departing to the right, unstable. The middle and left-most Hopfs' branches are born with two unstable Floquet multipliers, and the middle Hopf's branch contains a torus bifurcation, indicating the possible presence of a torus flow about both. The solution branches are bent back round to the left by the hardening component, and are all of greater amplitude than in the hardening case, owing to the softening effects at lower deflections.

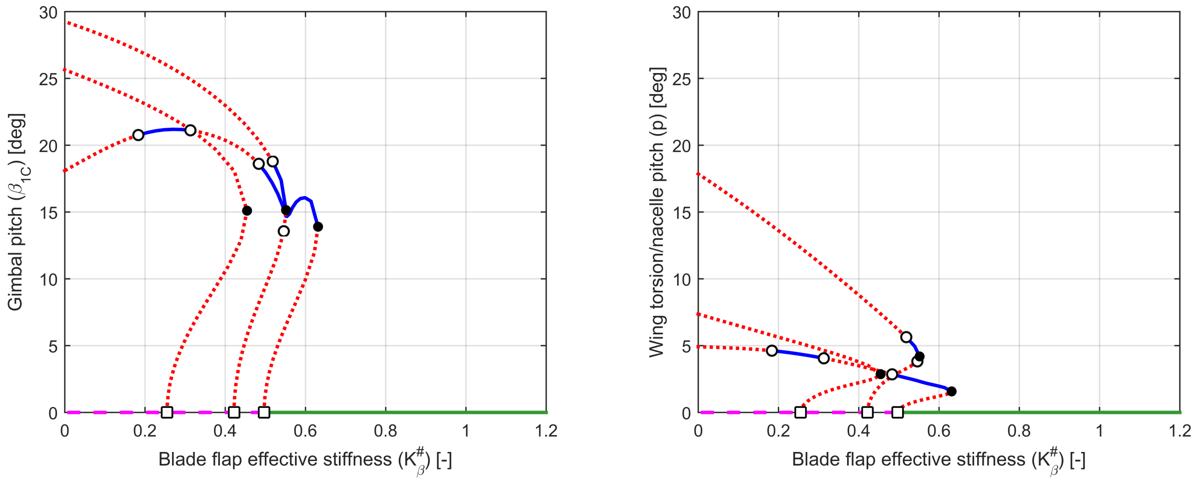

FIGURE 4.28. Bifurcation diagram for case 1 ($K^{\#}_{p} = 1.1$), combined variant, β_{1C} and p projections

There are two sources of overhang in this case. The first segment of the middle Hopf's branch contains a torus bifurcation, overhanging up to approximately $K^{\#}_{\beta} = 0.55$, though the main overhang threat comes from the right-most Hopf's branch, which, free from torus bifurcations, provides a segment of stable LCO that reaches out to approximately $K^{\#}_{\beta} = 0.63$. Therefore here, there is the coexistence of two distinct overhanging whirl flutter branches, as opposed to the two overhanging instances of the same branch in the hardening model, case 2 (see Figure 4.23).

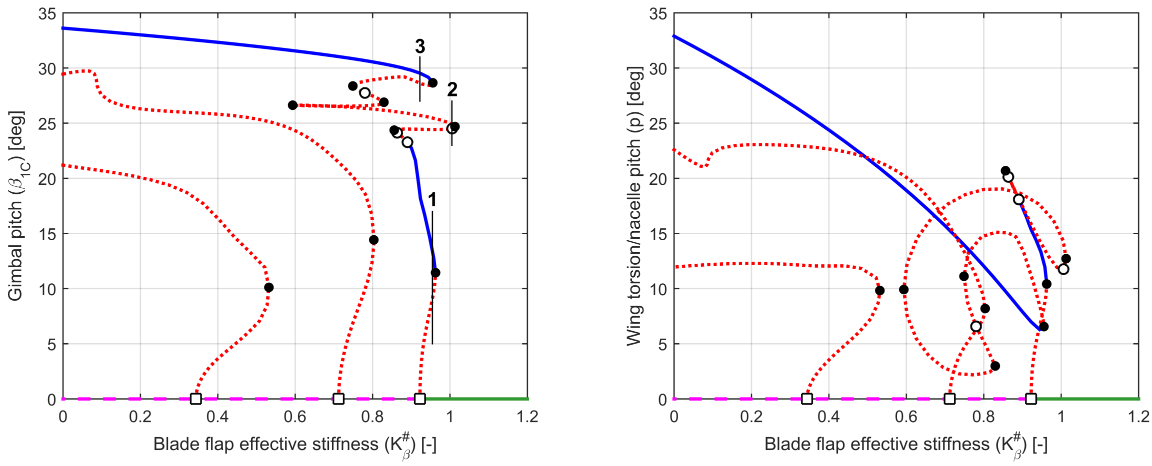

FIGURE 4.29. Bifurcation diagram for case 2 ($K^{\#}_{p} = 0.2$), combined variant, β_{1C} and p projections. The locations of the time simulations shown in Fig. 4.30 are numbered 1-3

Lastly, case 2 ($K^{\#}_{p} = 0.2$) is analysed for the combined model variant, shown in Figure 4.29. The combination of softening behaviours at lower deflections and hardening behaviours at higher deflections is once again apparent here. The Hopf bifurcations are all subcritical, with branch departures to the right. Once they have been bent back round to the left, the whirl flutter branches belonging to the left-most and middle Hopf bifurcations take after those in the hardening model variant for this case (see Figure 4.23), remaining unstable within the domain of analysis and exiting the figure on the left side without any overhanging of the stable main branch. The right-most Hopf's whirl flutter branch folds back and forth several times and contains a number of torus bifurcations, as in the hardening case. Here, it provides two attracting, overhanging segments, which are most clearly visible in the β_{1C} projection (left side of Figure 4.29). They are LCO portions which overhang as far as approximately $K^{\#}_{\beta} = 0.95$. The outcrop in between them, though it overhangs, does not attract the system. Although the torus bifurcation suggests the presence of torus flow, none could be found, indicating either that the torus flow created was only very weakly stable, unstable, or that the torus flow only exists in a very small neighbourhood of the torus bifurcation. Time histories for these three points of interest are shown in Figure 4.30. At point **1** ($K^{\#}_{\beta} = 0.9546$), the system is shown joining the larger stable LCO and being repelled from the smaller unstable LCO to decay to the stable main branch. At point **2** ($K^{\#}_{\beta} = 1.0049$), the time simulation is started on the LCO, though the system is soon repelled and decays back to the stable main branch. At point **3** ($K_\beta^\# = 0.9222$), the system is shown joining the stable LCO from two distinct initial conditions.

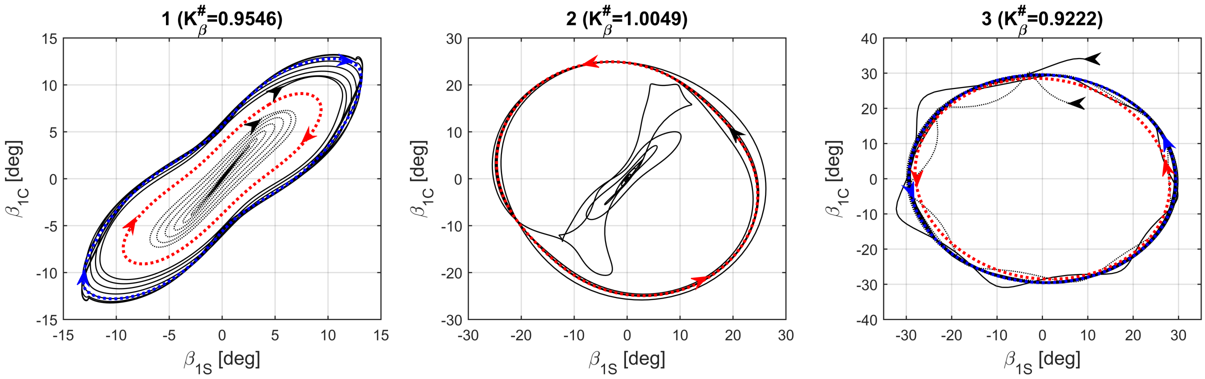

FIGURE 4.30. Time simulations for case 2 ($K_p^\# = 0.2$), combined variant. The title numbers correspond to the locations indicated in Fig. 4.29

4.4.6 Effect of varying $K_{\beta 3}$

The influence of the magnitude of the quintic stiffness can now be investigated. Shown in Figure 4.31 are bifurcation diagrams with $K_p^\#$ set to 0.2 (as per case 2), β_{1C} projection, with increased and decreased values of $K_{\beta 3}$ compared to the standard value of 100.

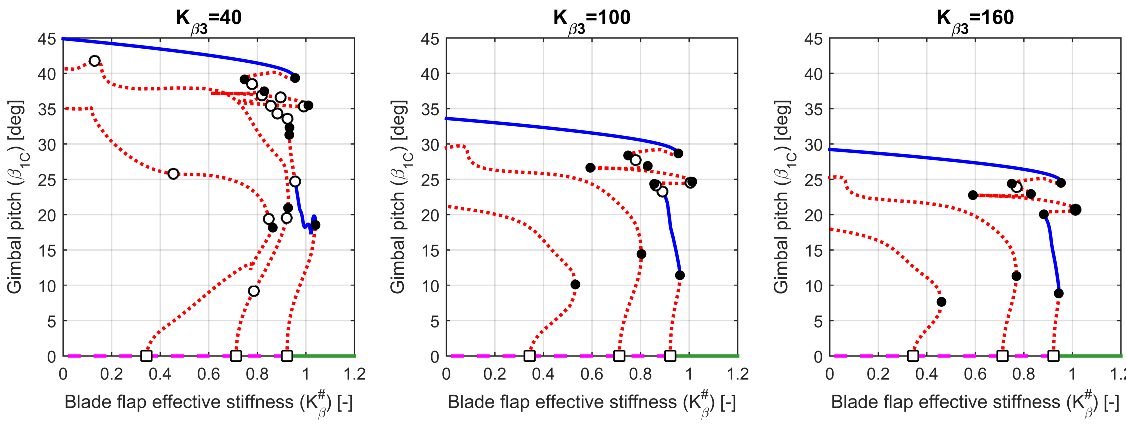

FIGURE 4.31. Effect of varying quintic stiffness $K_{\beta 3}$ in case 2, combined model variant

$K_{\beta 3}$ appears to have a wider influence than $K_{\beta 2}$: while altering $K_{\beta 2}$ only affects the amplitudes of the solution branches, $K_{\beta 3}$ is also able to change their shape, even influencing to a small degree how far the whirl flutter branch from the right-most Hopf overhangs the stable main branch. While increasing the quintic stiffness above the standard value merely compresses the branch amplitudes while maintaining the topology, reducing the quintic stiffness substantially complicates the whirl flutter branch connected to the right-most Hopf. These effects are all due to the presence of the cubic softening component $K_{\beta 2}$, which here is left at the standard value of -10. As the quintic stiffness value is varied, its influence relative to that of the cubic stiffness changes correspondingly. At the reduced quintic stiffness, the softening component is relatively strong, causing the slightly more pronounced overhang.

As the overhang defines the unsafe region, where whirl flutter may be encountered despite the linear prediction of stability, it is in the interest of a tiltrotor design for any softening component to be minimised, or diluted as much as possible with a hardening component in the stiffness profile. Minimising the softening component would also reduce the complexity of system's dynamics, simplifying analysis work undertaken during design processes.

4.4.7 Summary of results

For ease of comparison, a summary of the gimballed hub model's results is shown here. The β_{1C} projections are shown in Figure 4.32, while the p projections are shown in Figure 4.33. As stated at the end of Section 4.3.2, in order to be identifiable as whirl flutter, a periodic solution branch found in this model must contain meaningful participation of the wing in the motion. Figure 4.33 shows that all branches found fulfil this criterion.

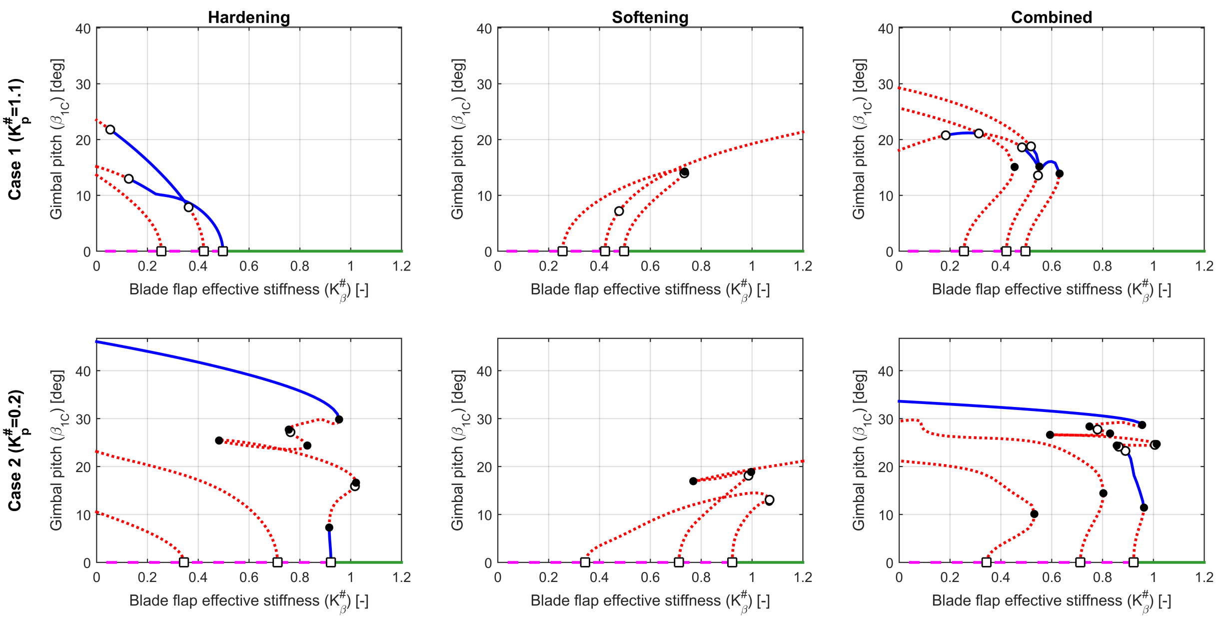

FIGURE 4.32. Summary of results, β_{1C} projections

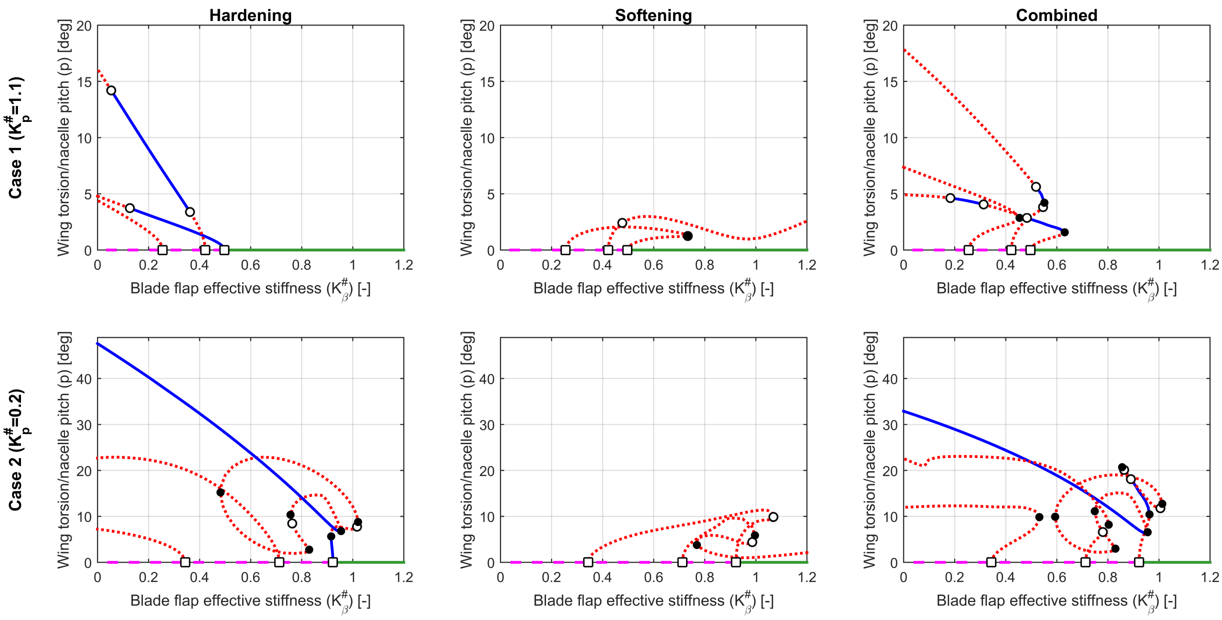

FIGURE 4.33. Summary of results, p projections

In summary, both hardening and combined model variants experience the overhang phenomenon. The softening model variant has overhanging unstable LCO branches that are part of separatrices between areas of the phase space in which the system will decay to the main branch and others in which the system will diverge to infinitely large solutions. These separating branches stretch at least as far as the upper $K^{\#}_{\beta}$ end of the domain of analysis. The reduced wing torsional stiffness $K^{\#}_{p}$ in case 2 is shown to increase the response amplitude of both the wing and the rotor, as evidenced by the increase in amplitudes in both the p and β_{1C}. Torus bifurcations are abundant, and are discussed in the following section.

4.4.8 Torus bifurcations

A salient feature of this model, when compared to the basic model, is the prevalence throughout the results of torus bifurcations. Not only are some branches seen transitioning from LCOs to torus flows through torus bifurcations, but some branches were found to be "born" with a torus potentially already surrounding them. In contrast to LCOs which follow a set, repeating path, torus flows cover a range of values that is larger than the LCO which the torus surrounds.

In the simplest case of a torus, the movement of trajectories around the torus has two components and they are easiest to visualise when considering a round, symmetrical torus. One component is in the same sense of the LCO, moving round the torus. The other moves orthogonally to this direction, in a radial sense relative to the very middle of the torus, curling around the ring-like cross-section, as demonstrated in Figure 4.34.

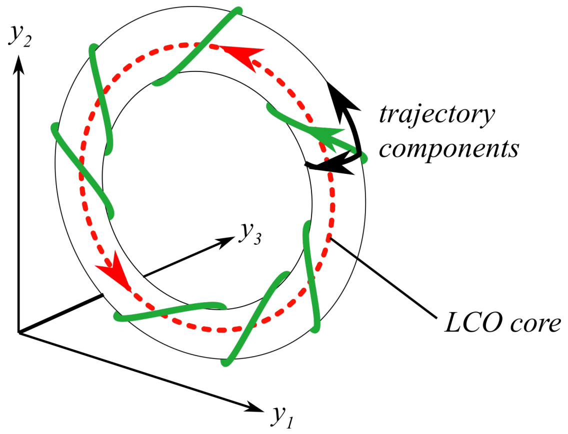

FIGURE 4.34. Schematic diagram of a torus flow

Each of these motion components has its own fixed period, though crucially the periods form an irrational ratio. This means that no trajectory on the torus ever quite closes, and that the motion is therefore quasi-periodic. With passing time, a trajectory will cover more and more of the torus' surface[2], though not all of it, even with infinite time[3]. Instead, it is said that the trajectories are "dense" on the torus [260]. In practice, a torus structure is likely not round and symmetrical like this example, but rather stretched isomorphically so that it maintains its toroidal topology. This structure is clear in Figure 4.22.

Torus bifurcations are generally associated with distinct LCO branches interfering with each other [313], in that where two LCO branches draw close to each other, torus bifurcations may reasonably be expected. This phenomenon may occur due to the LCO branches from two separate Hopf bifurcations drawing near to each other, or due to Hopf-Hopf bifurcations (a.k.a. "double-Hopf" bifurcations) where two Hopf bifurcations are coincident. Five such Hopf-Hopf bifurcations exist within the stability boundary considered for the gimballed hub model, created by the intersection of the Hopf loci[4]. They are indicated in Figure 4.35, which shows the $K_\beta^\#$-$K_p^\#$ stability boundary in terms of the bifurcation loci that define it. Kuznetsov discovered that in the kinds of equations that typically describe dynamical systems, two branches of torus bifurcations will emanate from a Hopf-Hopf bifurcation, though they are short-lived. The five Hopf-Hopf

[2] The generalised concept of "surface" here is an $n-1$ dimensional manifold within the n-dimensional space.

[3] This would necessarily mean that the trajectory was closed, a contravention of the foregoing statement. Furthermore, such a condition would isolate the torus from the surrounding phase space.

[4] Hopf-Hopf bifurcations are therefore codimension-2 bifurcations, where the codimension of a bifurcation is the number of parameters that must be varied or "tuned" to reach that bifurcation. Hopf bifurcations are by contrast codimension-1 bifurcations, drawing a line-shaped locus within the 2-parameter stability boundary considered in this work. Were a 3-parameter stability boundary to be used, the torus bifurcation loci would become lines within the 3D space, while the Hopf loci would become surfaces.

bifurcations are most likely the source of the torus bifurcations observed in the gimballed hub model.

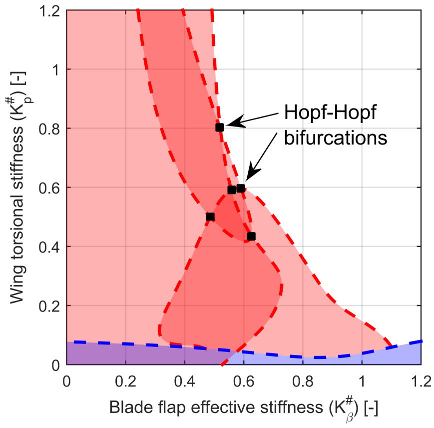

FIGURE 4.35. $K_\beta^{\#}$-K_p stability boundary with Hopf-Hopf bifurcations marked

A torus bifurcation refers specifically to the smooth emergence of a torus from an LCO, in much the same way that a Hopf bifurcation consists of the smooth emergence of a periodic solution from a fixed point branch. This bifurcation is signalled via the transition of a complex conjugate pair of Floquet multipliers over the unit circle, i.e. attaining a magnitude of 1. However, tori may also be instantaneously created or destroyed (depending on the perspective), and this occurrence is not signalled in any way by the Floquet multipliers. That is, a complex conjugate pair of Floquet multipliers that has signalled a torus bifurcation will continue to draw loci in the complex plane once they have exited the unit circle, though the existence of two complex conjugate Floquet multipliers outside of the unit circle does not in itself guarantee the existence of torus flow at that point on the LCO branch, due to the possibility of torus destruction. To further complicate matters, a torus manifold does not necessarily have to remain attached to the LCO from which it emanated (within the phase space), and depictions of torus flow such as Figure 4.34 where the torus still surrounds the LCO may only be reliably expected in the close neighbourhood of torus bifurcations.

Similarly, the Floquet multipliers do not have encoded in them the stability of the torus that has been created[5], or whether the torus is supercritical or subcritical (and therefore also in which direction along the LCO branch the torus first emanates). The one piece of additional information that is encoded in Floquet multipliers is that of resonances, where an LCO is spawned that exists on the torus surface. As mentioned before, trajectories on or near the torus surface are usually quasi-periodic owing to the irrational ratio of the frequencies of their constituent motions. In the case of resonance, the frequency ratio is rational – making the trajectory closed, periodic and therefore an LCO – and the ratio is given by the departure angle of the Floquet multipliers on the unit circle. More rigorous explanations of torus bifurcations are available in [259, 260].

[5] Tori tend to inherit stability characteristics from the LCO from which they are born.

AUTO is not able to track torus flows through parameter continuations. The locus and extent of a torus branch must therefore be found manually if it is desired: iteratively through time simulations. Furthermore, only stable tori may be tracked in this way. Combined with the limited Floquet multiplier indications, the possibility for the torus branch to disconnect from the LCO branch from which it emanated, and the possibility of collapse/destruction without warning, torus flows are rather difficult to track.

From an aeroelastic perspective, the fact that a structure undergoes motion described by a torus flow in the phase space means that it will experience larger amplitude oscillations than those that the LCO at that point describes. This may place the structure under greater loads and therefore increase the risk of structural failure. However, as far as parameter regions are concerned, the torus only exists within the phase space about an LCO and therefore does not itself cause any further overhang within the parameter space. Therefore, tracking of torus flows along LCO branches is not required to assess the overhang of an LCO branch.

4.5 Implications for Stability Boundaries

The whirl flutter branches created by the nonlinearities are seen to overhang the stable main branch (the undeflected position of the rotor-nacelle system) at several points in the results. The softening variant of the model only produces unstable overhanging whirl flutter branches, which as discussed earlier are part of separatrices in the state space, separating decaying motions that converge on the main branch from divergent motions that grow to infinitely large values. Although these overhanging branches exist at least as far as the maximum $K_\beta^\#$ value covered by the domain of analysis, the hazard that it depicts is not whirl flutter and therefore within this work's scope, the stability boundary for the softening variant does not need redrawing. However, a finite extent of overhang exists in the hardening and combined model variants, allowing a revised stability boundary to be produced for each.

As mentioned previously, the greater complexity of the gimballed hub model over the basic model leads to the possibility of more than one whirl flutter branch existing at a particular parameter value. Due to the nonlinearities causing the solution branches to bend within the parameter space, the possibility of more than one whirl flutter branch overhanging the stable main branch also arises. The redrawing of the stability boundary therefore requires the separate tracking of individual instances of overhang observed in the bifurcation diagrams produced for the two $K_p^\#$ analysis cases. This is done through a variety of different continuations: continuations in $K_\beta^\#$ at levels of $K_p^\#$ that are otherwise not used for analysis cases, continuations in $K_p^\#$ at various positions in $K_\beta^\#$, and two-parameter continuations in $K_\beta^\#$ and $K_p^\#$ simultaneously.

4.5.1 Redrawn stability boundary for hardening variant

In the hardening variant, there are three instances of overhang that require investigation, shown in Figure 4.36, left and centre. The first is an LCO overhang, marked 'H1'. In case 1 it originates from the middle Hopf bifurcation (the connection is not visible within the $K_\beta^\#$ range shown), and overhangs as far as approximately $K_p^\# = 0.76$, while in case 2 it originates from the right-most Hopf bifurcation and overhangs as far as approximately $K_p^\# = 1$. The other overhang present in the hardening variant is an outcrop of the right-most whirl flutter branch which contains a torus bifurcation, marked 'H2' in Figure 4.36. It does not have a corresponding presence in the previously-shown case 1 diagrams due to not having any Hopf connections there, and exists there solely due to a large overhang in $K_p^\#$. Tracking these overhangs within the $K_\beta^\#$-$K_p^\#$ plane renders the redrawn stability diagram shown on the right side of Figure 4.36.

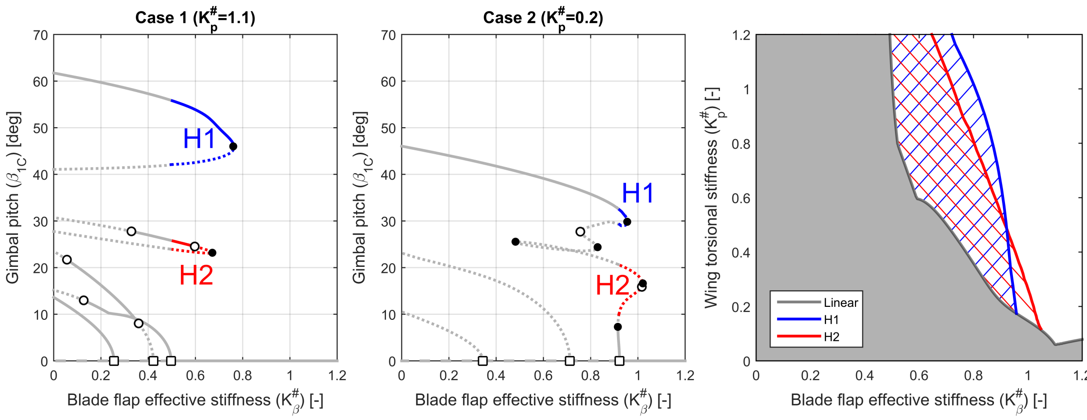

FIGURE 4.36. Overhang instances in hardening variant *(left, centre)* with redrawn $K_\beta^\#$-$K_p^\#$ stability boundary *(right)*

The existence of the H1 overhang in both analysis cases may at first seem strange due to the fact that different Hopf bifurcations exist in each case, with distinct attached LCOs. However, the H1 overhang exists continuously between the two $K_p^\#$ levels, due to a seamless change in "ownership" of the LCO portion causing the overhang. That is, the Hopf bifurcation from which the LCO containing H1 emanates, changes according to the level of $K_p^\#$ on the boundary. This change occurs suddenly at a specific parameter value: where two LCOs emanating from two distinct Hopf bifurcations draw close to each other, a portion of one LCO is suddenly swapped to the other LCO. There are in fact two such changes, at $K_p^\# = 0.32$ and at $K_p^\# = 0.63$, and the first of these transitions is shown in Figure 4.37. Before the swap at $K_p^\# = 0.318$, the largest amplitude LCO emanates from the right-most Hopf bifurcation and the mid-amplitude LCO from the middle Hopf bifurcation. However after the swap at $K_p^\# = 0.321$, this order is reversed. At the swap itself, the two LCOs are in contact. This type of transition is a known phenomenon, referred to as a "saddle transition", and it is given a more complete and technical treatment by Golubitsky and Schaeffer [314].

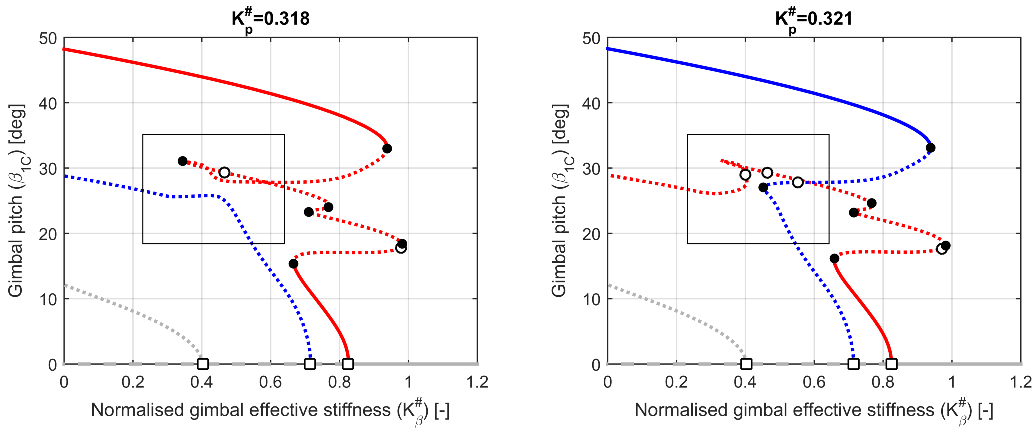

FIGURE 4.37. LCO portion swapping in hardening variant. The LCOs attached to the right-most and middle Hopf bifurcations are coloured red and blue respectively

4.5.2 Redrawn stability boundary for combined variant

There are four instances of overhang in the combined variant, shown in the left and centre of Figure 4.38. The first, ‘C1’, is an incursion from the whirl flutter branch emanating from the middle Hopf in case 1, presenting both a portion of stable LCO and the possibility of torus flow. It is not present in case 2. ‘C2’ is an LCO and is visible in both analysis cases, emanating from the right-most Hopf in case 1 and the middle Hopf in case 2. It is only overhanging in case 1, however. The remaining two overhang threats are only visible in case 2, and exist at other $K_p^\#$ levels only through overhang in this parameter. ‘C3’ and ‘C4’ are LCO overhangs, and the outcrop between them was shown in an earlier section not to contain stable torus flow despite the presence of the Hopf bifurcation. Tracking these overhangs within the $K_\beta^\#$-$K_p^\#$ plane renders the redrawn stability diagram shown in the right side of Figure 4.38.

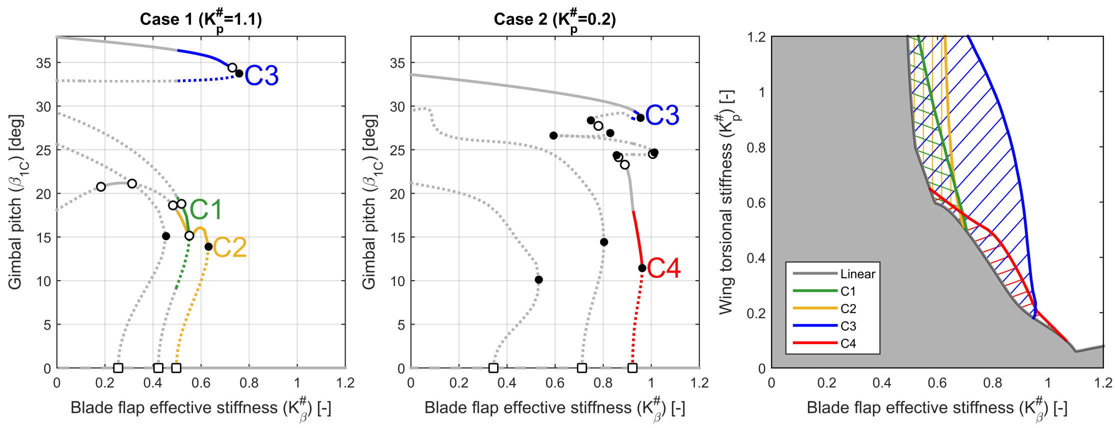

FIGURE 4.38. Overhang instances in the combined variant *(left, centre)* with redrawn $K_\beta^\#$-$K_p^\#$ stability boundary *(right)*

Like the H2 overhang shown previously, the C3 overhang is not visible in the previously-shown case 1 bifurcation diagrams, despite existing at the corresponding value of $K_p^{\#}$, as it is not connected to any of the Hopf bifurcations present in the case 1 analysis. Despite this, it is still present in case 1, its stable LCO portions posing the threat of attracting the system to them, and it is shown in Figure 4.38.

Once again, the effect of nonlinearity on the system's stability boundary is to add unsafe regions to the existing unstable region. This shows that the linear stability analysis used to construct the original stability boundary is unconservative in the presence of the nonlinearities investigated here. If the new unsafe regions went undetected during the design process of a tiltrotor aircraft, the final selected design point could lie within the unsafe region, placing it at the risk of structural failure.

The existence of so many coexisting whirl flutter attractors is in itself a threat. As each one has its own basin of attraction, each brings with it the possibility of whirl flutter for the set of perturbations that lie within its basin of attraction. Together, they compete to diminish the size of the stable neighbourhood surrounding the main branch, and increase the risk of whirl flutter being encountered.

It was shown in this chapter that hardening components are beneficial for stability, restricting the amplitude of LCOs (both $K_{\beta 2}$ and $K_{\beta 3}$) and slightly reducing the extent of the overhang ($K_{\beta 3}$). However, if the stiffness profile of the wing torsion degree of freedom contains sufficiently large hardening components such that whirl flutter LCOs are small compared to the ones shown in the results here, then their appearance still causes problems for the system. The vibration of the system in this way will accelerate the wear of its components, and the ride quality could be reduced for those aboard.

4.5.3 Airspeeds at which whirl flutter may be encountered

As in the basic model, this chapter is concluded by returning to the initial motivating phenomenon of whirl flutter being encountered via airspeed. This is shown via a continuation in V for the combined variant, with all other parameters set to their datum values, shown in Figure 4.39.

The overhang in this parameter is fairly pronounced; the location of the Hopf bifurcation from which the whirl flutter originates – and therefore the predicted onset speed via linear analysis – is 309 ms^{-1}, though the whirl flutter branch reaches as far as 297 ms^{-1}. Though the values of airspeeds depicted here are beyond the flight envelope of current tiltrotor models, the principle stands of overhang existing in the airspeed parameter due to a structural nonlinearity. Furthermore, a torus bifurcation exists at 302 ms^{-1}, and at some airspeed values in its neighbourhood, torus flow is observed. Time simulations are shown in Figure 4.40.

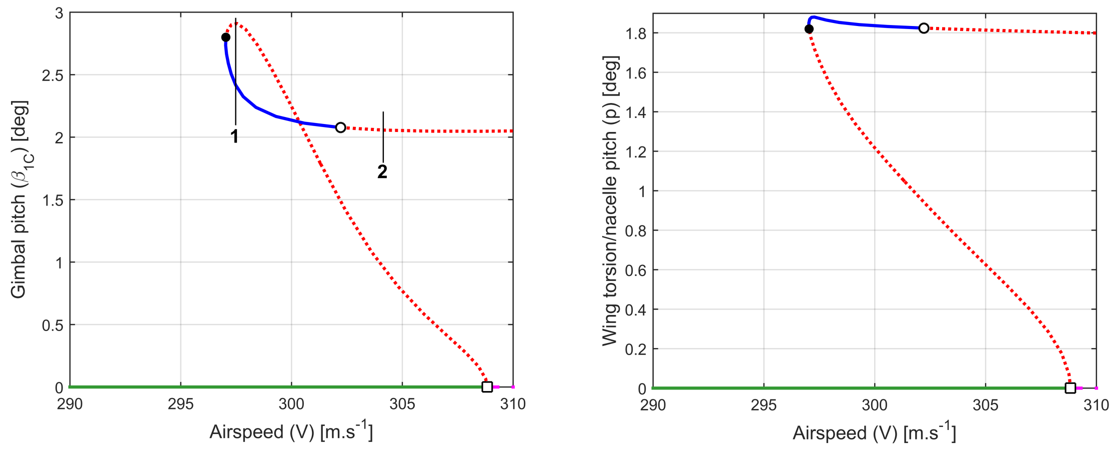

FIGURE 4.39. Continuation in airspeed V for gimballed hub model, combined variant. The locations of the time simulations shown in Fig. 4.40 are numbered 1-2.

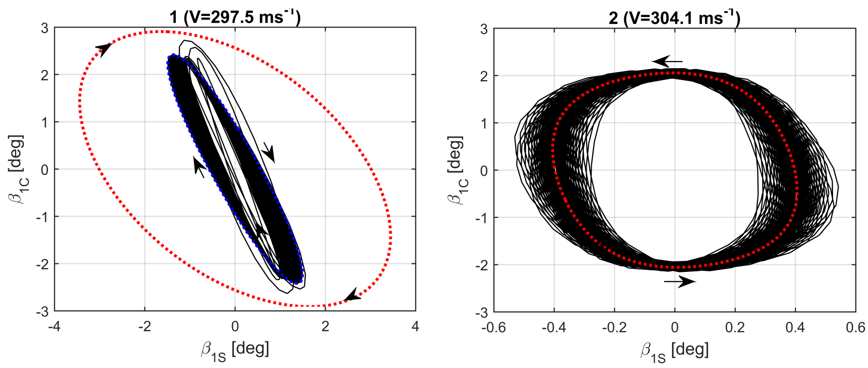

FIGURE 4.40. Time simulations corresponding to the indicated points in Fig. 4.39

In frame **1**, the system converges upon the stable LCO present there, while clear torus flow exists in frame **2**, surrounding the unstable LCO there. Crucially, both these behaviours occur at airspeeds below the linear-predicted onset speed. Due to changes occurring in the shape of the LCO along the branch, the LCO appears to have changed direction within the β_{1S}-β_{1C} phase plane used to display the results here.

4.6 Conclusions

In summary, this chapter has:

- introduced the gimballed hub model used in this work (P1)
- introduced and demonstrated tiltrotor aeroelasticity and whirl flutter in a tiltrotor (gimballed hub) context (P1, P2)

- used linear stability analysis to investigate the parametric sensitivity of tiltrotor aeroelasticity in comparison to classical whirl flutter (P2)
- applied CBM to the gimballed hub model (P3, P4) when configured with:
  - the original linear stiffness profile
  - a hardening stiffness profile
  - a softening stiffness profile
  - a combined hardening-softening profile
- discussed the torus bifurcations and the torus flows that exist near them (P5)
- redrawn the structural stiffness stability boundary ($K^{\#}_{\beta}$-$K^{\#}_{p}$) to account for the influence of the nonlinearities in both the hardening model variant and the combined model variant (P6)
- performed a continuation in airspeed to show the overhang existence in this parameter (P4, P5)

This contributed to the following research objectives:

- **O1**: assess the effect of a smooth nonlinearity on the whirl flutter dynamics of rotor-nacelle systems
  - The presence of nonlinearities was once again found to create whirl flutter LCOs. Secondary equilibrium branches, the nonlinear equivalent of static divergence, were not explored but are known to exist in this system. The phenomenon of overhang, where stable portions of whirl flutter branches are found to exist in parameter regions that linear analysis declares to be stable, was observed in a number of the analysis cases. The unsafe regions created as a result were mapped out within the $K^{\#}_{\beta}$-$K^{\#}_{p}$ stability boundary.
  - Hardening variant: while several stable branches were found, many more unstable ones were observed due to the presence of torus bifurcations. Overhang was observed throughout the domain of analysis. Variation of the cubic stiffness $K^{\#}_{\beta 2}$ does not improve or worsen the overhang extent, instead only scaling the amplitude of the various solution branches.
  - Softening variant: the whirl flutter branches found were unstable without exception, with some of the instability being due to the possibility of torus flow. In both cases, one of the whirl flutter branches reached out to overhang the stable main branch at least as far as the upper end of the domain of analysis. While it was not stable, it was found to be part of a separatrix separating the system's responses to perturbations from

decay to the stable main branch and divergence to infinitely large solutions. Overhang of stable LCO portions was not found.

  - Combined variant: the quintic hardening component once again exerted a stabilising influence on the LCO branches, causing them to resemble the softening variant's branches at low amplitude but the hardening variant's branches at higher amplitudes. Several instances of overhang – some coexisting – were visible in the analysis cases and the unsafe regions created as a result was mapped out within the $K_\beta^\#$-$K_p^\#$ stability boundary. One overhanging feature (C3) demonstrated that overhanging LCOs can be present even if they are not connected to any Hopf bifurcations present within a given bifurcation diagram. While this overhang was primarily demonstrated in the context of the stiffness parameters that characterise the wing structure (K_p) and the rotor blades (K_β), it was also observed in the case of airspeed, making the linear prediction of onset speed unconservative. The lowering of the quintic stiffness $K_{\beta3}^\#$ was found to greatly complicate the whirl flutter branches, both in their structure and the types of behaviours found on them. Their overhang extent was also affected.

- **O3**: investigate the influence of model complexity (classical whirl flutter theory vs. tiltrotor aeroelasticity) on the impacts that the nonlinearities have on the whirl flutter dynamics of rotor-nacelle systems

  - Due to the greater system complexity involved in tiltrotor aeroelasticity, there are correspondingly more whirl flutter modes that may each be unstable. Veering between modes, where the modes appear to swap properties when their roots have similar values, was observed. These instabilities may coexist at certain parameter values, and therefore in the nonlinear version of the system, multiple whirl flutter attractors may coexist.
  - Overhang was not observed in the hardening variant of the basic model. Its appearance in the hardening variant of the gimballed hub model is likely due to the relative placement of the wing and rotor natural frequencies, such that the nonlinearity's effect caused them to coalesce at certain oscillation amplitudes.
  - In the softening variant of the gimballed hub model, rather than secondary equilibrium branches overhanging rightward to the limit of the domain of analysis, unstable LCO branches were found instead. It is part of a separatrix delineating decaying responses from divergent ones, as previously mentioned. This is similar to the role of the aforementioned secondary equilibrium branches in the basic model. It is certainly a possibility that overhanging secondary equilibrium branches of this kind also exist elsewhere in the gimballed hub model.
  - The quintic hardening coefficient $K_{\beta3}$ was found to influence not only the amplitude of the solution branches (as it did in the basic model) but also the extent of any overhang

present. This is likely attributable to the fact that the hardening influence in the gimballed hub model is able to cause overhang itself.

- The greater system complexity of the tiltrotor-representative gimballed hub model was reflected in the richer, more complex dynamics observed. Solution branches were in general more convoluted, and torus bifurcations and their associated quasi-periodic behaviour – unseen in the basic model – were abundant. This was linked to the presence of several Hopf-Hopf bifurcations, which are known to be associated with torus bifurcations. However, neither homoclinic or heteroclinic bifurcations were observed in the gimballed hub model, as they were in the basic model.

- **O4**: explore what types of whirl flutter behaviours are observable over a range of design and operating parameters

  - Within the analysis of the basic model, periodic solutions and equilibrium branches were found. Quasi-periodic behaviours were also found to be present in the gimballed hub model, though chaos was not observed in any time simulations generated.
  - While the presence of torus flows does not affect the overhang extent of the LCO branches that they surround, the larger amplitude and multi-frequency motions that they involve are likely to accelerate the degradation of the tiltrotor system's structure, leading either to fatigue in the best case or catastrophic structural failure in the worst.
  - The difficulties of tracking torus bifurcations and their associated quasi-periodic behaviours through a parameter space were shown. Specifically, their detection is heavily reliant on time simulations, and therefore their tracking is an iterative effort. Furthermore, only stable tori can be found in the time domain, and there is no indication of a torus' stability in the Floquet multipliers.

- **O5**: synthesise guidelines for tiltrotor design against whirl flutter in the presence of structural nonlinearities, based on the findings

  - The use of margins between operating points and predicted stability boundaries is strongly recommended. This reduces the risk of structural damage that any undetected solution branches can pose to the tiltrotor system.
  - Design processes of tiltrotors should use models which include all necessary nonlinearities, and should be analysed with CBM. The shortcomings of linear analysis in the presence of nonlinearities are clear from the foregoing results.
  - The application of CBM should be as thorough as possible in order to create as complete as possible a "map" of the system's dynamic behaviours. The invisibility of the H2 overhang in case 1 of the hardening variant, and of the C3 overhang in case 1 of the combined model variant, shows not only that overhanging branches could

be anywhere, but also that one bifurcation diagram does not reveal the entirety of a system's dynamics.

- There is potentially limited gain of building strong cubic hardening stiffness into structures, if a softening component is known to exist. Although the extent of the overhang present is not improved by doing so, the oscillation amplitudes may be reduced from those that cause structural failure to those that only constitute fatigue damage.

Chapter 5

Investigating the Effects of Freeplay

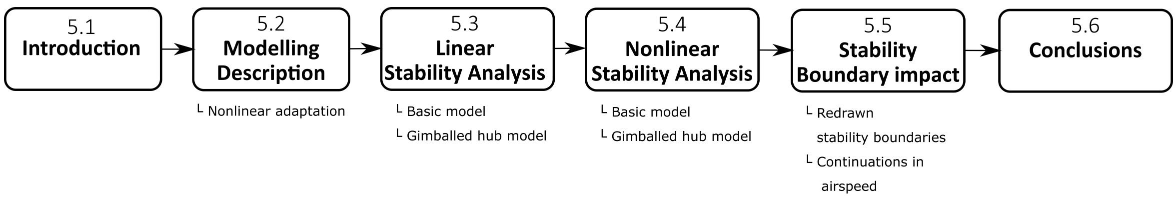

FIGURE 5.1. Chapter map

In this chapter, the hard nonlinearity known as freeplay is introduced and applied simultaneously to the two models discussed earlier in the work, satisfying research objectives O2 and O3. The big picture painted by the results also allows research objectives O4 and O5 to be satisfied. Some of the more complex results in the work are obtained here, although a number of features are recognisable from previous results.

This chapter proceeds straight to the freeplay nonlinearity's modelling and the results obtained with it, as the models have already been introduced and described in previous chapters. The chapter is organised by stages of analysis and then by model, with each analysis stage being applied to both models in turn. First, the nonlinearity is implemented in each model and bifurcation diagrams are generated to find instances of overhang i.e. where whirl flutter branches exist in supposedly stable parameter regions. The stability boundary is then redrawn for each model, based on these instances of overhang. Finally, continuations in airspeed are shown to demonstrate the nonlinearity's effect of lowering the onset speed through overhang in the airspeed parameter. A schematic map of the chapter structure is shown in Figure 5.1.

5.1 Introduction

Freeplay is well-known for causing important instabilities in the form of LCOs and aperiodic oscillations [313]. Such instabilities may exist below the nominal onset speed of any instabilities in an equivalent linear system neglecting the freeplay. As a result, airworthiness regulations such as those of the FAA [315] stipulate maximum limits on the freeplay deadband width to avoid placing aircraft and those onboard at risk. It is considered a non-smooth nonlinearity due to the shape of the stiffness profile at the edges of the deadband, and is commonly represented with a piecewise linear stiffness profile. Where this is done, the system's statespace may be viewed as being comprised of sub-domains, where the freeplay deadband is viewed as one sub-domain, one side of it another sub-domain, and the other side of it a further sub-domain. The piecewise linear system is a specific case of a piecewise smooth system, where the system is smooth at all points except at the boundaries between the sub-domains. As the piecewise linear stiffness profile is partitioned according to these sub-domains, each sub-domain is a distinct linear system. Obtaining solutions to systems with discontinuous nonlinearities can be difficult, whether time simulation of the system is used, or continuation methods. However a number of workarounds exist:

- **smoothing** replaces the non-smooth nonlinearity with a smooth approximation
- **event-driven integration** concatenates a number of variable-step time integrations, with each integration modelling the system according to the equations of motion that apply within each of the sub-domains of the state space as given by the piecewise description. Event detection is used to locate the transitions between these sub-domains so that the final timestep of each separate simulation may be placed correctly.
- **time-stepping with constant steps** simply applies ordinary time simulation methods to the equations of motion to produce one single time simulation. The integrated value of the non-smooth function (over the time-step) is used rather than an instantaneous value.

While each of these methods is used by a substantial number of studies and is discussed at length therein, it suffices to summarise here that:

- smoothing is practical but never perfectly representative of a truly non-smooth system
- event-driven integration is highly accurate though may become computationally expensive if many events/transitions occur
- time-stepping is less accurate and the accuracy further depends on the degree of smoothness of the system, but is less computationally demanding than event-driven integration

Crucially, smoothing is considered the most practical option in this work given the use of CBM and it is employed here. No adaptation or alteration of the continuation solver is required, and the absence of events/transitions constitutes a saving in computational cost. Although a small number of continuation solvers such as TĈ [316] have been developed for piecewise smooth systems, they are less well known than AUTO and their specialised nature steepens the learning gradient associated with their effective use. Furthermore, expertise of their use is less accessible than that of AUTO. The level of smoothing used can influence computation time and the rate of convergence upon solutions.

As freeplay may exist at mechanical interfaces such as hinges and gears, there is also a potential for friction to exist. While friction – whether it is viscous damping from lubricated surfaces in contact, or dry friction – usually has a stabilising effect, it adds considerable complexity to the analysis and therefore for simplicity it is not considered in this work.

5.2 Modelling Description

5.2.1 Freeplay stiffness profile

As freeplay is viewed as a non-smooth nonlinearity, its simplest non-smooth mathematical description is a bilinear profile [317]:

$$M = \begin{cases} K(\alpha - d) & \alpha > d \\ 0 & -d \le \alpha \le d \\ K(\alpha + d) & \alpha < -d \end{cases} \tag{5.1}$$

For some deflection quantity α that ordinarily has associated with it some linear restoring force or moment $M = K\alpha$, there instead exists a region of zero M, centred about $\alpha = 0$ and with width $2d$. This region is known as a *deadband*. Stiffness is, in general, the gradient at which restoring force/moment is accrued with increasing deflection, or in mathematical terms, $\frac{\partial M}{\partial \alpha}$. In the linear profile $M = K\alpha$, the stiffness is uniformly K at all values of α, whereas in the freeplay profile it is now a function of α: zero within the deadband and K everywhere else.

As mentioned above, the use of a non-smooth expression can be problematic as the gradient discontinuities at the deadband edges can cause numerical issues for continuation solvers. These issues are avoided in this work by using a smooth expression instead, which in the limit is able to approximate a non-smooth equivalent expression via a tuning parameter. This work uses the arctangent expression shown in Equation (5.2), as used by Howcroft et al. [251]. Howcroft further explains that deadbands in real engineering systems are unlikely to have truly non-smooth edges as in the bilinear representation.

$$M = \frac{K}{\pi}\left[(\alpha + d)\left(\frac{\pi}{2} + \tan^{-1}\frac{-(\alpha + d)}{\epsilon}\right) + (\alpha - d)\left(\frac{\pi}{2} + \tan^{-1}\frac{(\alpha - d)}{\epsilon}\right)\right] \tag{5.2}$$

The symbols M, α etc. retain their meanings from the bilinear equation. The tuning parameter ϵ primarily controls the turning radius of the profile at the edges of the deadband. Furthermore, the width (in α) of the transition between the deadband and the rest of the stiffness profile is approximately 2ϵ; a smaller ϵ results in sharper edges. Additionally, ϵ influences the gradient within the deadband, with the gradient of all points in the deadband approaching zero as ϵ tends to zero, in the limit. Outside of this region the stiffness, hereafter termed "out-of-deadband gradient", asymptotically approaches the original linear gradient K. Therefore, this smooth arctangent function converges asymptotically on representing "true" freeplay as ϵ tends to 0, in the sense of having perfectly sharp discontinuous edges and zero in-deadband stiffness. Furthermore, it is more intuitive to consider the ratio $\frac{\epsilon}{d}$ rather than ϵ by itself. The ratio $\frac{\epsilon}{d}$ more usefully gives an indication of what proportion of the deadband is used up in turning, and is therefore of non-negligible gradient. While the nature of the loading present in a real world system may cause the freeplay to not be centred about zero deflection, to have an offset in M, to have one out-of-deadband gradient on one side of the deadband and another on the other side, or to have a non-zero deadband gradient, this work neglects these possibilities for simplicity.

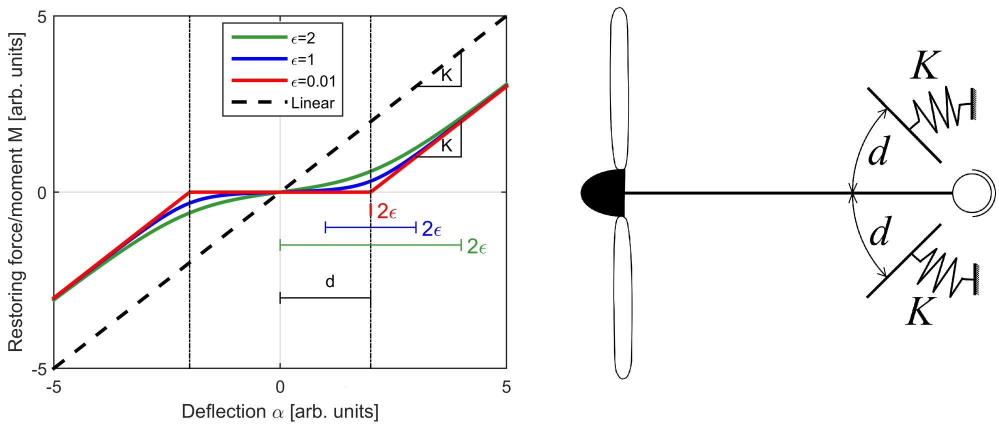

FIGURE 5.2. Example freeplay stiffness profiles as described by Equation (5.2), with $K = 1$, $\epsilon = [2, 1, 0.01]$, $d = 2$ *(left)*, with schematic diagram of freeplay presence within the model *(right)*

If ϵ is small enough, or if a bilinear expression is used, then the system behaves as one of two linear systems depending on whether its current state is within the deadband or outside of it. Within the deadband, it behaves as the nominal system but with the linear stiffness of the freeplay-affected degree of freedom (i.e. K here) set to 0, referred to as the *underlying linear system*. At sufficiently large deflections, the α-offset of the stiffness gradient caused by the deadband becomes negligible, and the system behaves more or less as the equivalent freeplay-less system. This is referred to as the *overlying linear system*. As the two models' parameter sets differ by orders of magnitude, the profile is demonstrated in a neutral context in Figure 5.2 (left), with an equivalent linear stiffness profile also included for comparison. A schematic diagram of the presence of the freeplay within the models in which it is placed is shown in the right half of the figure.

5.2.2 Parameter value selection and implementation in models

As zero ϵ cannot in practice be used due to its presence in the denominator, a non-zero deadband gradient is inevitable, though it can be minimised by using as small a value of ϵ as possible. As will be shown later, the sensitivity to $\frac{\epsilon}{d}$ of the two models varies in both nature and severity, and therefore the value chosen in each case requires dedicated discussion. However in the bifurcation diagrams used for the results of each model, the deadband gradient is small. Following consultation of other freeplay studies [26, 253, 318] which are informed by the examination of real-world systems, a value of $0.1°$ for the deadband half-width d is, though small, deemed to be representative of wear accrued in an aerospace structure joint during its service life [253, 318] and is therefore suitable for use in the present work. The value of K used is the value of the linear stiffness parameter associated with the degree of freedom used for the nonlinear adaptation in each model. This parameter is also used as the continuation parameter in each model's investigation.

The objective of this chapter is to investigate the impact of freeplay at the rotor tilting mechanism where, as explained earlier, there is a strong case for it to exist. In the basic model, there is only one degree of freedom for nacelle pitch, θ, and therefore the freeplay adaption is applied in place of the associated linear stiffness profile $K_\theta \theta$. Despite the fact that in the gimballed hub model, the wing torsion has an assumed mode shape, the degree of freedom p only represents the rotation in pitch at the wingtip. As the nacelle is mounted and rotated at the tip, any freeplay in the nacelle mechanism is coincident with the wing torsion degree of freedom and therefore it is the most suitable part of the model to receive the freeplay adaptation. The original linear expression $K_p^{\#} p$ describes how the wing deforms in torsion in response to torque loads of whatever kind (inertial, aerodynamic etc.), so to perform the nonlinear adaptation, this term is removed and replaced with an expression of the form shown in Equation (5.2). Physically, this stiffness profile implies a rigid wing, as the only motion that is described is freeplay at the wingtip between the nacelle and the wing. This is done to isolate the effect of the freeplay. While the wing aerodynamics are in theory affected by the altered behaviour of p, they are in practice negligible and therefore no influence on the results is missed.

5.3 Linear Stability Analysis

The K_θ-K_ψ stability boundary from Chapter 3 is retained for use with the basic model. However a different stability boundary is used in this chapter for the gimballed hub model rather than that used in Chapter 4. The $K_\beta^{\#}$-$K_p^{\#}$ boundary used previously provided a useful oversight of the influences of both the rotor and the wing on the overall system's dynamics, especially as the nonlinearity was present in the blades. Here however, the nonlinearity is present in the wing, in the torsion degree of freedom. Selecting the $K^{\#}_{p}$-$K^{\#}_{q2}$ boundary not only achieves focus on the wing, but also equivalence with the boundary used in the basic model: the wing torsion p in the gimballed hub model approximates the nacelle pitch θ in the basic model, while the wing chordwise bending q_2 approximates the nacelle yaw ψ. Once again, datum-normalised quantities are used for the gimballed hub model, indicated with a superscript '#'. The two linear baseline boundaries are shown in Figure 5.3.

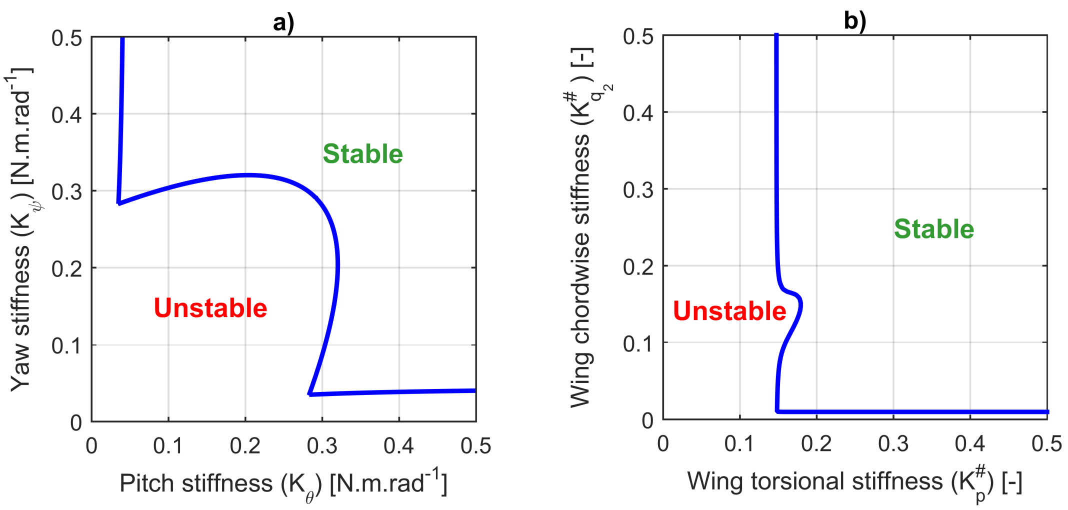

FIGURE 5.3. Baseline (linear variant) stability boundaries for a) the basic model, and b) the gimballed hub model

5.4 Continuation and Bifurcation Analysis

5.4.1 Nonlinear analysis of the basic model

The continuation parameter used for this model is the linear stiffness of the nacelle pitch degree of freedom, K_θ. With the freeplay adaptation made as described in Equation (5.2), this parameter primarily controls the out-of-deadband gradient of the stiffness profile: a linear profile to which the freeplay profile tends asymptotically at large deflections. With the freeplay adaptation implemented, the undeformed at-rest position $\mathbf{y} = \mathbf{0}$ is uniformly unstable within the K_θ domain of analysis, due to the near-zero stiffness around $\theta = 0°$ which is overpowered by the aerodynamic forces and moments. For non-trivial continuation results a new, stable equilibrium must be found for the initial solution. Intuitively, the nacelle must lie stably at some pitch angle outside of the deadband, where the structural restoring moment is non-zero and able to oppose the aerodynamic moments that act to push the nacelle further away from the undeflected position. Being deflected in pitch, the nacelle in turn experiences an aerodynamic yaw moment pushing it further away from $\mathbf{y} = \mathbf{0}$ that must be countered by yaw structural stiffness, which requires some amount of yaw deflection to act. Two such non-zero equilibria exist due to the structural symmetry of the system, mirrored in θ and ψ about $\mathbf{0}$. These new equilibria were found by solving the equations of motion with all time derivatives set to zero. Due to the presence of the arctangent terms, iterative numerical methods were employed.

An $\frac{\epsilon}{d}$ value of 10^{-4} is set for this model, as it provides suitably sharp deadband edges without causing numerical difficulties for the AUTO solver. The stiffness profile of the pitch (θ) degree of freedom as configured with these values is shown in Figure 5.4. As the pitch stiffness K_θ is the independent variable in the continuations, three profiles are plotted corresponding to three values of K_θ. It can be seen that the deadband edges are sharp in all three profiles.

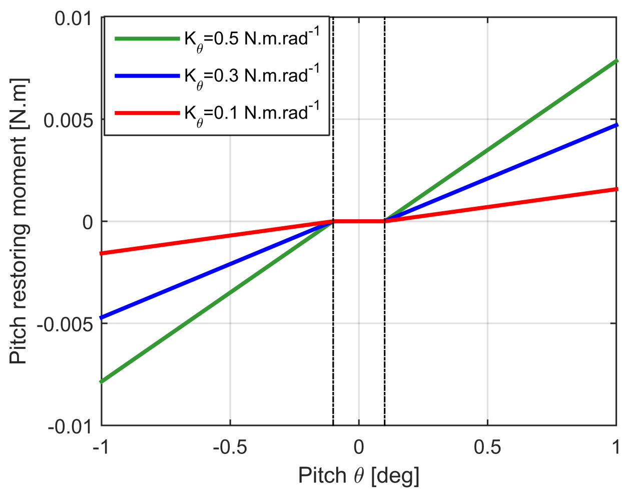

FIGURE 5.4. Freeplay stiffness profiles used in the basic model. The deadband edges are indicated with dash-dot lines

A continuation in K_θ is now performed and is presented in Figure 5.5, left side. A validation of the chosen $\frac{\epsilon}{d}$ value is shown after the main features of the diagram have been discussed. The periodic solution branches emanating from the Hopf bifurcations are also shown. As the freeplay deadband exists within the projection shown, its extent is indicated with black dash-dot lines. A phase plane taken at a cut of $K_\theta = 0.15$ is shown on the right of the figure. In the bifurcation diagrams shown in this chapter, the minimum value of the projection state in the LCO at each continuation parameter value point is also shown, in addition to the maximum values as before. The minimum values are indicated with a thin line and using a fainter colour. The maximum and minimum values of the flutter LCOs on the bifurcation diagram in Figure 5.5 can be cross-referenced with the full LCO in the phase plane, along with the positions of the zero and non-zero main branches which are indicated with 'X's, magenta to denote their instability.

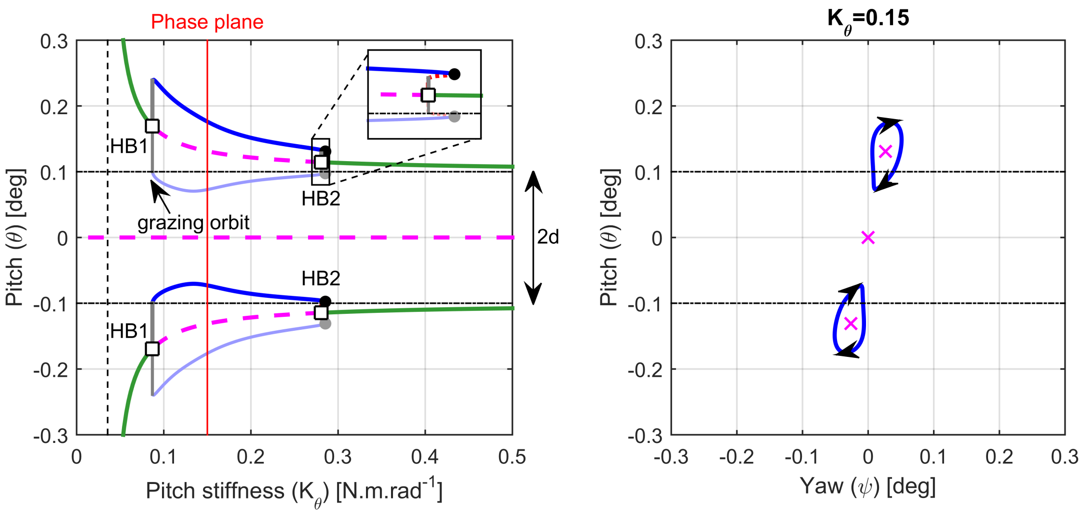

FIGURE 5.5. Bifurcation diagram *(left)* for $K_\psi = 0.3$, with $d = 0.1°$ and $\frac{\epsilon}{d} = 10^{-4}$. A phase plane *(right)* is shown for $K_\theta = 0.15$

The first notable feature of Figure 5.5 is that for most of the range of the continuation parameter, three *main* solution branches exist instead of one as in the linear model. Either side of the uniformly unstable zero main branch ($\mathbf{y} = \mathbf{0}$), the two new non-zero equilibria described earlier have appeared as branches whose positions are influenced by the continuation parameter K_θ. These branches diverge to infinitely large solution values with decreasing K_θ. The divergence to infinity is asymptotic to the K_θ value of the onset of static divergence in the linear system (approximately 0.03; see Figure 3.14), indicated on the figure as a black dashed vertical line. With increasing K_θ, the non-zero main branches converge asymptotically on the boundaries of the deadband. This occurs as the structural restoring moments – which balance the aerodynamic moments acting to push the system further away from $\mathbf{0}$ – require non-zero deflection (beyond the deadband) in order to exist, regardless of the value of K_θ, to which the out-of-deadband stiffness tends. Two Hopf bifurcations are positioned on each of the non-zero main branches at the same values as those on the main branch in the original linear variant of the model (see Chapter 3). They are the same bifurcations; the presence of the freeplay has simply caused what was originally the main branch to exist outside the freeplay deadband, with a mirror image about its original position, $\mathbf{y} = \mathbf{0}$. The labelling of these Hopf bifurcations ('HB1' and 'HB2') has been retained from Chapter 3.

Here, periodic solution branches link HB1 and HB2 together on each non-zero branch. These non-trivial solution branches constitute whirl flutter motion and they are almost entirely stable (i.e. attracting). Pitch stiffness decreases from the right side of the diagram to the left, so at HB2 the pylon has become loose enough to begin to oscillate, while at HB1 the stiffness has reduced to a level where it is not able to store sufficient potential energy when deflected for flutter motion to be sustained. Where each flutter branch joins HB2 at approximately 0.28, it first overhangs the stable non-zero main branch by a small amount, shown in the zoomed inset box in the left plot. In plain terms, this means that flutter is possible for a slightly larger range of parameter values than the linear analysis of the freeplay-less system predicts. The ψ-θ phase plane at $K_\theta = 0.15$ shown on the right side of the figure shows the path in this plane taken by the two LCOs found at this point on the bifurcation diagram.

It is worth noting that it is no coincidence that the LCOs that form the periodic solution branches that connect HB1 and HB2 together always exist both in and out of the deadband. Rather, this positioning is necessary for their existence. If ϵ is small enough, the arctangent expression becomes almost entirely equivalent to a bilinear stiffness profile with a zero in-deadband gradient, which is a piecewise linear expression. As mentioned in this chapter's Introduction, the presence of the deadband partitions the system's statespace into sub-domains, each of which behaves as a distinct linear system. LCOs, being necessarily nonlinear phenomena, require net (i.e. overall) nonlinearity in order for them to exist and therefore in a piecewise linear system (or a system that approximates a piecewise linear system sufficiently closely) they must span at least two of the linear sub-domains.

Furthermore, HB1 and HB2 are not ordinary Hopf bifurcations. In an ordinary Hopf bifurcation, the periodic solution branch emanates smoothly from the fixed point at which the Hopf bifurcation exists, having initially zero amplitude. Here however, the periodic solution branch is created with non-zero amplitude, as the fixed point branch containing the Hopf is comfortably within one of the linear sub-domains, but the LCOs it creates need to span more than one sub-domain in order to exist, as discussed above. As Figure 5.5 shows, the LCO attached to each branch is, at each of its ends, just grazing the deadband (known as a "grazing orbit"). As a further reduction in amplitude would place the LCO solely outside of the deadband where it cannot exist, due to the local dynamics being essentially linear, the branch disappears abruptly after this grazing orbit, when the LCO has non-zero amplitude. HB1 and HB2 are therefore a discontinuous equivalent of the ordinary Hopf bifurcation, covered in greater detail by Leine and Nijmeijer [319]. The connection between HB1/HB2 and the grazing orbits near to them is the same concentrically-nested family of neutrally-stable orbits of the same shape as was described in Section 2.2.4.4, and here it is coloured grey to set it apart from the LCOs.

Before any further analysis is conducted, some validation of the choice to use $\frac{\epsilon}{d} = 10^{-4}$ is prudent. The bifurcations HB1 and HB2 define the topology of Figure 5.5, and using two-parameter continuation in K_θ and $\frac{\epsilon}{d}$, the location in K_θ of these bifurcations can be tracked over a range of $\frac{\epsilon}{d}$ values to detect any variation, indicating sensitivity to $\frac{\epsilon}{d}$. More specifically, it can be said that $\frac{\epsilon}{d} = 10^{-4}$ is a suitable choice if the bifurcations do not exhibit a sensitivity to further decreasing $\frac{\epsilon}{d}$. This two-parameter continuation is shown in Figure 5.6. The value of $\frac{\epsilon}{d} = 10^{-4}$ as used in Figure 5.5 is also indicated. While there is a very slight increase in the K_θ location of HB2 at $\frac{\epsilon}{d} = 10^{-3}$ (right line, top of figure), the variation in either Hopf bifurcation is imperceptible below the chosen value of 10^{-4}. The overall shape of the solution branches was also checked and found not to change over the range of $\frac{\epsilon}{d}$ considered, and therefore it may be concluded that this $\frac{\epsilon}{d}$ value is sufficient for the purposes of the present work.

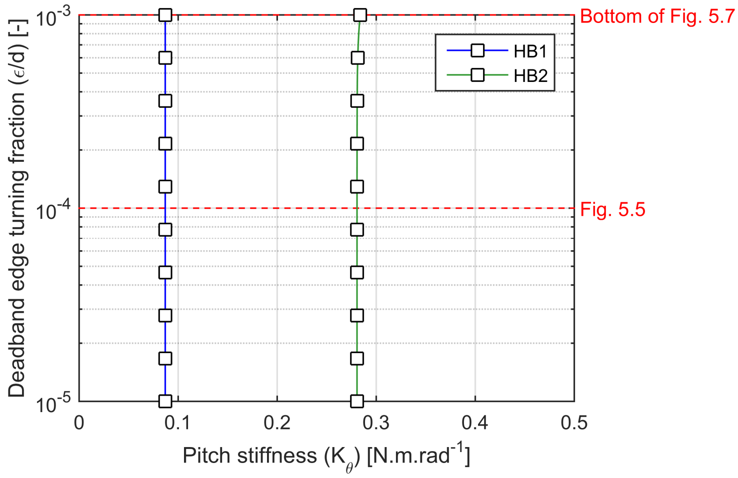

FIGURE 5.6. Two-parameter continuation of Hopf bifurcations at $K_\psi = 0.3$, $d = 0.1°$ within the K_θ-$\frac{\epsilon}{d}$ plane

It is also useful to gain a basic understanding of how $\frac{\epsilon}{d}$ affects the bifurcation diagrams that are produced when it is raised (or "loosened") as well as lowered. Figure 5.7 picks up from where Figure 5.6 left off: two-parameter continuations are performed on HB1 and HB2 as $\frac{\epsilon}{d}$ is swept from 0.001 (or 10^{-3}) to 0.01.

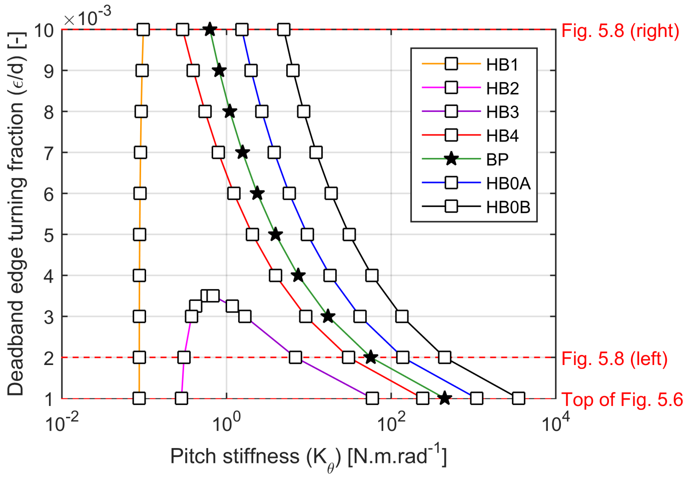

FIGURE 5.7. Two-parameter continuation of various bifurcations at $K_\psi = 0.3$, $d = 0.1°$ within the K_θ-$\frac{\epsilon}{d}$ plane

A variety of other bifurcations become visible in the process. It emerges that as $\frac{\epsilon}{d}$ is loosened, the double non-zero main branches eventually attach to the zero main branch via a pitchfork bifurcation (labelled 'BP' in Fig. 5.7). The zero main branch is stable at K_θ values above this point, with the exception of a pocket of a periodic solution that exists between the Hopf bifurcations marked 'HB0A' and 'HB0B'. Lastly, there are some regions of alternating stability on the double non-zero main branches that only become visible when this sweep is performed. Some Hopf bifurcations HB1-4 are present on the double non-zero main branches at lower values of $\frac{\epsilon}{d}$, with a flutter branch existing between HB1 and HB2, and between HB3 and HB4. The layout of the regions simplifies as $\frac{\epsilon}{d}$ is raised, as the Hopf bifurcations HB2 and HB3 only exist below approximately $\frac{\epsilon}{d} = 0.035$, where they emerge from the same point. The HB3, HB4, BP, HB0A and HB0B bifurcations were detected when generating a bifurcation diagram for the $\frac{\epsilon}{d} = 0.01$ case, and their loci were subsequently traced back down to $\frac{\epsilon}{d} = 0.001$. As $\frac{\epsilon}{d}$ is lowered, these bifurcations rapidly move to the right in K_θ. The bifurcation diagram for the $\frac{\epsilon}{d} = 0.01$ case is shown in Figure 5.8.

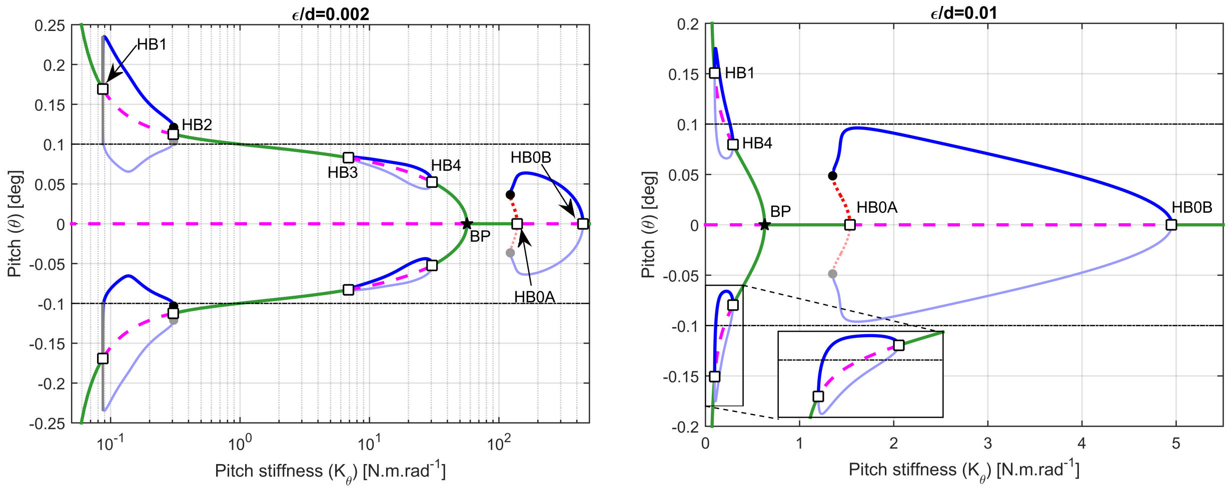

FIGURE 5.8. Bifurcation diagram for $K_\psi = 0.3$, with $\frac{\epsilon}{d} = 0.002, 0.01$

In the cases of "loose" $\frac{\epsilon}{d}$ as explored in Figures 5.7 and 5.8, the LCOs on the branches that span HB3 and HB4, and HB0A and HB0B exist at pitch values that are solely within the nominal freeplay deadband, as opposed to spanning a number of sub-domains as described above. This occurs because at these relatively high values of ϵ, the stiffness profile no longer represents freeplay. Its relatively round deadband edges and significantly non-zero gradient within the deadband cause it to more resemble a cubic profile, and the resulting bifurcation diagrams are reminiscent of some of those seen in the hardening cases in Chapter 3. Additionally, the HB3, HB4, HB0A and HB0B Hopf bifurcations are ordinary Hopf bifurcations as opposed to the discontinuous Hopf bifurcation discussed above. At $\frac{\epsilon}{d} = 0.01$, the stiffness profile is so smooth that all the bifurcations – including HB1 – are ordinary Hopf bifurcations, without any concentric periodic solution families joining the Hopf to where the LCO branch truly begins.

With the selection of the $\frac{\epsilon}{d}$ value validated, time simulations may now be employed to explore this nonlinear adaptation of the system. Figure 5.9 shows the same bifurcation diagram as in Figure 5.5, however time simulations in the pitch state θ are shown for two selected points. For this and the remaining figures, only the upper half of each figure (i.e. the positive pitch branch) is shown as the system is symmetrical about the origin in all states, and therefore so are any solution branches. Convergence on the stable flutter branch attached to the positive non-zero main branch is shown on the left of the figure ($K_\theta = 0.15$). Divergence away from the unstable zero main branch and convergence on the stable non-zero main branch is shown on the right ($K_\theta = 0.4$). Even though the system is being attracted to a non-oscillatory solution, the slow decay means that it incurs considerable cyclic loading in the process, constituting fatigue.

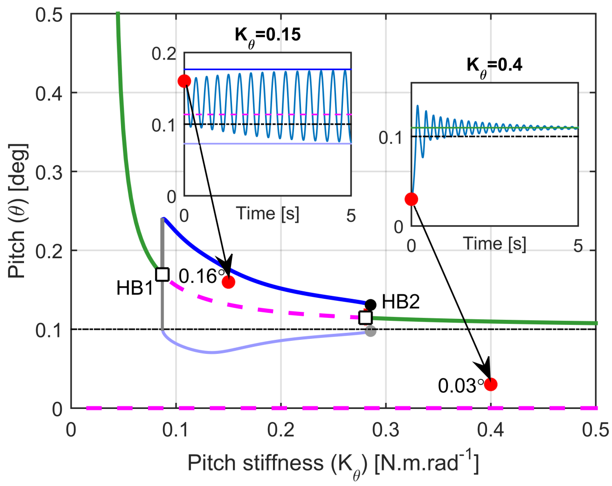

FIGURE 5.9. Bifurcation diagram of basic model with freeplay in pitch θ for $K_\psi = 0.3$, $d = 0.1°$, pitch projection, K_θ as the continuation parameter, $\frac{\epsilon}{d} = 0.0001$. Time simulations are shown in inset plots, with initial conditions indicated by red dots

The foregoing results exist only at $K_\psi = 0.3$ and further exploration of the K_θ-K_ψ plane is required. As K_ψ is lowered, the Hopf bifurcations HB1 and HB2 move apart from each other. Furthermore, the flutter branches grow in amplitude, reaching toward the unstable zero-branch. Their eventual collision with the zero-branch happens simultaneously due to the symmetry of the system. At this collision point, the two flutter LCOs make contact with each other at the unstable zero branch, forming a homoclinic trajectory similar to that observed and explained in Chapter 3. This fusing of orbits constitutes a homoclinic bifurcation and it occurs below $K_\psi = 0.28$, when HB1 is no longer present to re-attach the flutter branches (that have emanated from HB2) to the non-zero main branches. A continuation in K_θ with K_ψ now set to 0.2 is shown in Figure 5.10, accompanied by a phase plane showing the trajectories before ($K_\theta = 0.346$), at ($K_\theta = 0.366$) and after ($K_\theta = 0.389$) fusing. At K_θ values above the homoclinic collision point (approximately 0.366), the homoclinic trajectory opens up into a new LCO of finite period which, near the collision, resembles a bow tie. It is a product of the fusing of the two flutter branches and is of comparatively large amplitude. This LCO was also observed in Chapter 3 (see Figure 3.24), and was named the "bow tie" LCO on account of its appearance on the phase planes used to study it.

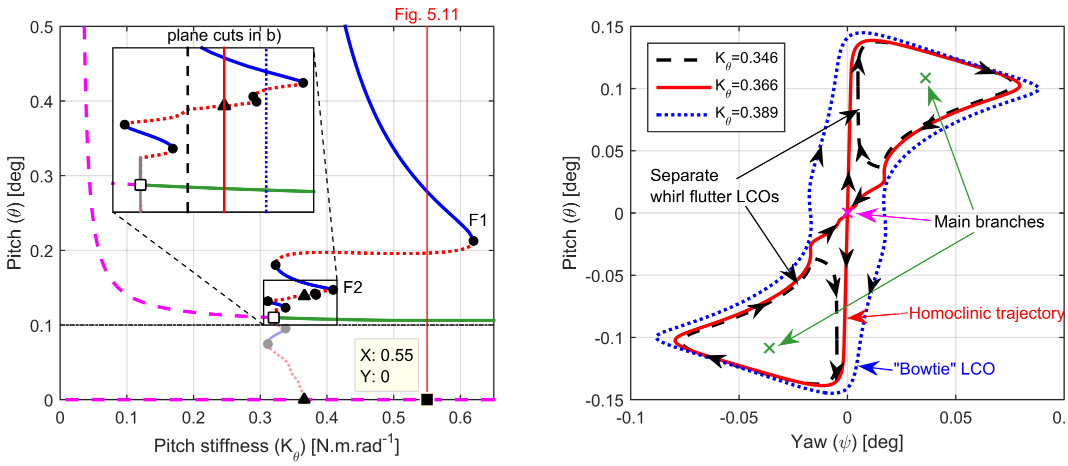

FIGURE 5.10. Bifurcation diagram *(left)* for $K_\psi = 0.2$, with phase plane at $K_\theta = 0.55$ *(right)*

As Figure 5.10 shows, the bow tie LCO branch folds back and forth between $K_\theta = 0.32$ and 0.62 as it increases in amplitude. However, it can also be seen that throughout this parameter range, the non-zero main (equilibrium) branches are stable, and in literature employing linear stability analysis methods it is effectively only equilibrium branches that are considered when determining overall system stability. The linear methods discussed earlier only show the parameter values at which periodic solution branches emanate from a fixed point branch. Any bending of periodic solution branches back into supposedly stable regions due to nonlinearities – as has happened here – is not captured by linear theory and therefore goes undetected. Linear stability analysis declares the system to be stable for $K_\theta > 0.32$ based on the location of HB2, though clearly this is not correct. The hazard posed by the bow tie LCO branch is therefore twofold: it is largely stable (and therefore attracts), and overhangs the non-zero main branches at K_θ values as high as 0.62: well into the supposedly stable region of the stability boundary.

The fact that part of the overhanging bow tie branch is stable means that the system can be attracted to it following a sufficiently large perturbation. In practice, such a perturbation might be supplied by a gust, or by manoeuvring of the aircraft. Figure 5.11 (left) shows two time simulations with $K_\psi = 0.2$, $K_\theta = 0.55$, showing one insufficient perturbation causing the system to join the upper non-zero main equilibrium branch (green line), and a similar but sufficient perturbation causing the system to be attracted to the bow tie LCO (blue line). For comparison, these time simulations are also shown on a phase plane on the right side. Two parts of this LCO branch are present at $K_\theta = 0.55$; in addition to the stable LCO of pitch amplitude 0.3° shown in the time simulation, a smaller unstable LCO with a pitch amplitude of approximately 0.25° is also present, surrounded by the stable LCO.

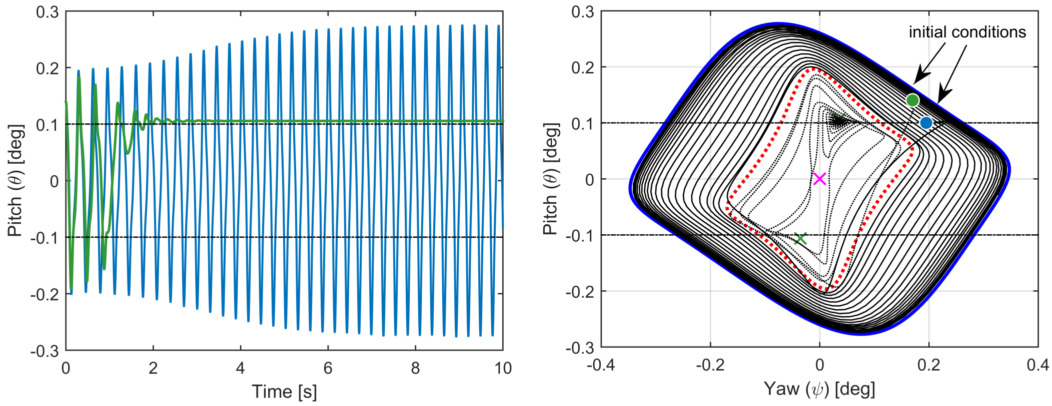

FIGURE 5.11. Time simulations *(left)* with $K_\psi = 0.2$, $K_\theta = 0.55$, also shown on a phase plane *(right)*. Starting from different initial conditions, the system can join one of the non-zero main branches (green) or join the bow tie LCO (blue)

5.4.1.1 Effect of deadband half-width d

Here, the effect of d on the system's predicted dynamics is assessed by performing a continuation with d set to 1°, a value ten times larger than that used for the main investigation. Figure 5.12 shows the bifurcation diagrams for the $K_\psi = 0.3$ case for both $d = 0.1°$ and $d = 1°$, normalised by their respective d values and shown overlaid. The $\frac{\epsilon}{d}$ ratio is kept at 0.0001 in both cases.

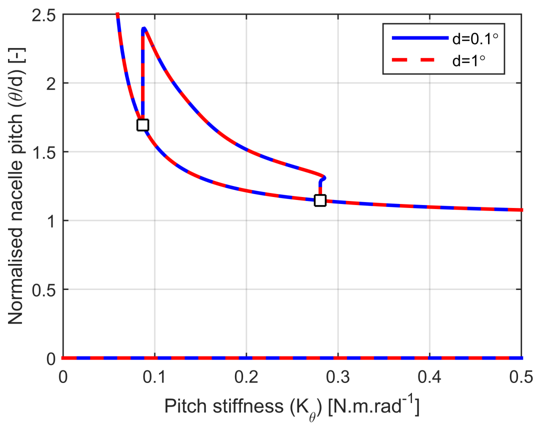

FIGURE 5.12. Overlaid normalised bifurcation diagrams for $K_\psi = 0.3$, $d = 0.1°$ and 1°, basic model

As the system's response scales linearly with the value of d, the two plots are entirely coincident. The redrawn stability boundary is therefore unaffected by the value of d, as d does not affect the overhang extent.

5.4.2 Nonlinear analysis of the gimballed hub model

The gimballed hub model's analysis is conducted at $K^{\#}_{q2} = 0.4$ (that is, 40% of the datum value used in [121]). As the entire left side of the boundary is made by the locus of one bifurcation, choosing a relatively high value of $K^{\#}_{q2}$ within the domain of analysis allows the observation of system dynamics that are representative of the datum parameter values (i.e. at $K^{\#}_{q2} = 1$), while permitting visibility of the same whirl flutter solution branches that are present at lower values of $K^{\#}_{q2}$. The freeplay nonlinearity exists in the wing torsion degree of freedom p as discussed earlier. A deadband half-width d of 0.1° was used, as with the basic model. However, reprising $\frac{\epsilon}{d} = 10^{-4}$ for the deadband edge sharpness introduces intricate complications into the periodic solution branches that cause great difficulties for the AUTO solver.

An alternate method to obtain a bifurcation diagram for the gimballed hub model is to employ a similar method to the $\frac{\epsilon}{d}$ sensitivity analysis shown in Figure 5.6. The strategy is to start with a value of $\frac{\epsilon}{d}$ that is too large to represent freeplay fairly but is amenable to the application of AUTO, and subsequently sweep ϵ downwards, noting how the bifurcation diagram changes as the stiffness profile becomes more representative of freeplay. This approach not only allows numerical complexities to be circumvented but also lends further insight into how the freeplay nonlinearity alters the system's solution branch structure. Figure 5.13 shows bifurcation diagrams with $\frac{\epsilon}{d}$ set to 0.010, 0.007 and 0.005, continuing in $K^{\#}_{p}$. The boundaries of the deadband are once again indicated with dash-dot lines.

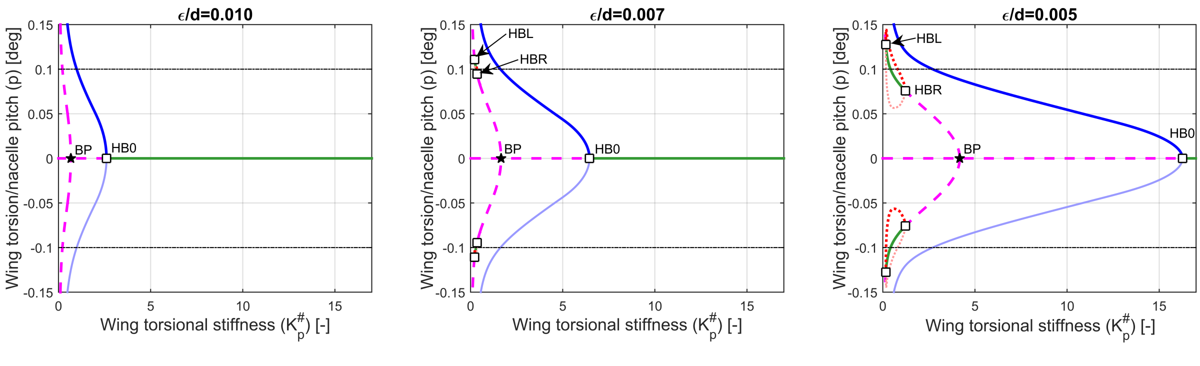

FIGURE 5.13. Bifurcation diagrams for gimballed hub model, $K^{\#}_{q2} = 0.4$, $d = 0.1°$, $\frac{\epsilon}{d} = 0.010, 0.007, 0.005$

Some of the changes seen here caused by the nonlinearity are similar to those in the basic model. For instance, the zero branch becomes unstable, two mirroring non-zero equilibrium branches are created about the zero main branch (unstable branches emanating from BP), and a bow tie LCO is spawned. Furthermore, the zero branch is only unstable at $K_p^\#$ values below a Hopf bifurcation, labelled 'HB0', which is the source of the bow tie LCO. However, the bow tie LCO exists over the rest of the domain of analysis and reaches unbounded amplitude as $K_p^\#$ tends to 0. It is stable over its entire extent. The zero branch also has a pitchfork bifurcation, labelled 'BP', between $K_p^\# = 0$ and HB0, from which the two double main branches emanate. When $\frac{\epsilon}{d} \leq 0.007$, a region of stability exists on both, bounded by a pair of Hopf bifurcations ('HBR' and 'HBL') that share a small unstable LCO (i.e. whirl flutter) branch. HBR, BP and HB0 all move rightward as $\frac{\epsilon}{d}$ is lowered, while HBL moves slightly leftward. While Figure 5.13 bears several similarities to Figure 5.9 and Figure 5.10, there is no homoclinic bifurcation connecting the bow tie LCO to the whirl flutter branch from each non-zero double main branch.

With the basic topology of the bifurcation diagram established, further lowering of $\frac{\epsilon}{d}$ is achieved by conducting two-parameter continuations in $\frac{\epsilon}{d}$ and $K_p^\#$ on each of the aforementioned topology-defining bifurcations (HB0, etc.). Their loci in the $K_p^\#$-$\frac{\epsilon}{d}$ plane as $\frac{\epsilon}{d}$ is lowered down to 0.001 is shown in Figure 5.14 (left). The positions in $K_p^\#$ of the bifurcations can be cross-referenced with the relevant diagrams in Figure 5.13. A plot of the stiffness at $p = 0°$ when $K_p^\# = 1$ is also shown on the right of Figure 5.14.

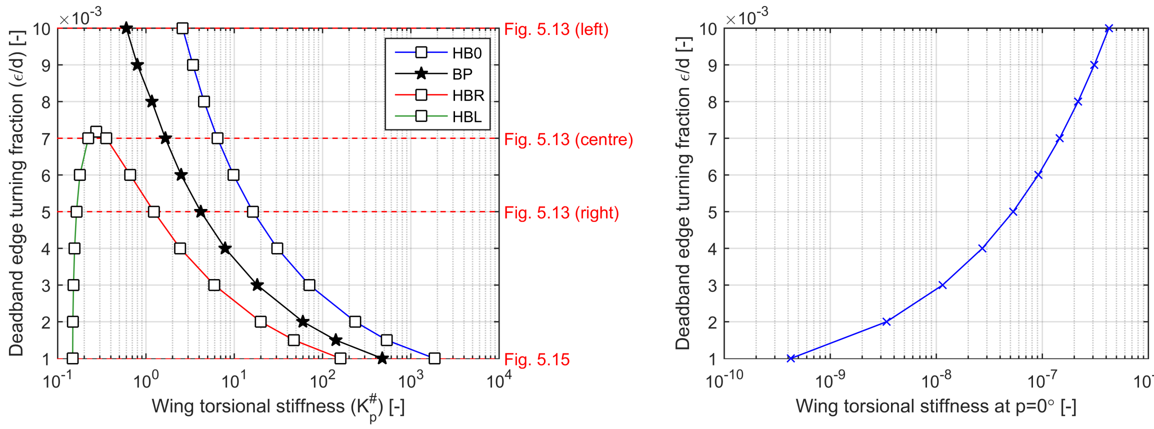

FIGURE 5.14. Two-parameter continuation of Hopf bifurcations at $K_{q2}^\# = 0.4$, $d = 0.1°$ within the $K_p^\#$-$\frac{\epsilon}{d}$ plane *(left)*, with plot of wing torsional stiffness (i.e. stiffness profile gradient) at deadband centre $p = 0°$ *(right)*

The double branch Hopf bifurcations HBL and HBR are coincident with each other slightly above $\frac{\epsilon}{d} = 0.007$ and do not exist above this value. This makes the non-zero main branches uniformly unstable when $\frac{\epsilon}{d}$ is large, due to the attracting influence of the bow tie LCO. Meanwhile, the distance moved leftward by HBL decreases with each further downward increment of $\frac{\epsilon}{d}$, however the rightward movement of HB0, BP and HBR increases. A logarithmic scale is required for the $K_p^\#$ axis in order for the full form of the diagram to be visible.

Physically speaking, this runaway occurs due to the flattening of the gradient within the deadband: as the structure becomes softer in-deadband, the out-of-deadband stiffness ($K_p^\#$ in this model) becomes less and less influential as a stabilising influence. Outside the deadband, $K_p^\#$ still controls the amplitude of the bow tie LCO, and at the Hopf bifurcation HB0 it has increased to a level sufficient to prevent whirl flutter. An interesting effect is the lowering of $\frac{\epsilon}{d}$ causing a stabilisation of a portion of the double main branches. This portion is near the deadband edge and is present at low values of $K_p^\#$, which flatten the stiffness profile. At low values of $K_p^\#$, some values of edge sharpness can give the stiffness profile a gradient near its edges that produces a stable fixed point. The unstable flutter LCOs attached to the Hopfs bounding these portions are part of separatrices in the phase space between the basins of attraction of these stable double main branch portions and of the bow tie LCO.

The movement of the bifurcations HBR, BP and HB0 to infinity in $K_p^\#$ as $\frac{\epsilon}{d}$ tends to 0 is intuitive as no amount of out-of-deadband stiffening would be able to stabilise a truly zero-stiffness deadband. The form of the bifurcation diagram for bilinear or "true" freeplay, within a physically reasonable range of analysis, is already provided by that for $\frac{\epsilon}{d} = 0.005$ shown in Figure 5.13 (right). Specifically, the $\frac{\epsilon}{d} = 0$ diagram would resemble the $\frac{\epsilon}{d} = 0.005$ diagram for $K_p^\# <$ approximately 1.2, that is, up to but not including HBR on the double main branches. The diagram therefore comprises two non-zero equilibrium branches which are stable except below HBL, and the uniformly unstable zero main branch, all surrounded by the bow tie LCO.

The positions of HBR, BP and HB0 were tracked as far as $\frac{\epsilon}{d} = 0.001$ in Figure 5.14. However, time simulations reveal that as this value is approached, complex dynamical structures begin to surround the nominal bow tie LCO branch. At first, patches of quasiperiodic behaviour caused by the creation of torus bifurcations emerge at various points on the bow tie branch. Further obfuscation of the torus structures with decreasing $\frac{\epsilon}{d}$ leads to the collapse of some, precipitating pockets of chaotic behaviour. Other pockets of chaos in the region may exist due to other onset mechanisms, such as period doubling cascades or intermittency [260, 261].

A subsection of the bifurcation diagram for $\frac{\epsilon}{d} = 0.001$ is shown in Figure 5.15, overlaid with a selection of phase planes showing the various steady state behaviours present at some points on the bow tie LCO branch. The secondary flutter branch attached at $K_p^\# = 0.1477$ to the double main branch shown could not be computed in full due to strong numerical issues prevalent at this value of $\frac{\epsilon}{d}$ (0.001), and it is therefore not shown. Each phase plane shows the gimbal pitch β_{1C} and wing torsion p coordinates of the various forms of the bow tie LCO. These states are chosen to give simultaneous insight into how the bow tie LCO manifests in both the rotor and the wing, the two macro-components of the system. An ordinary period-1 oscillation is present at $K_p^\# = 1.468$, while a period-2 variation is at $K_p^\# = 0.636$ where the trajectory approaches its starting point but completes another similar cycle before closing as a loop. A well-formed torus can be seen at $K_p^\# = 0.918$ and a chaotic trajectory is found at $K_p^\# = 0.646$.

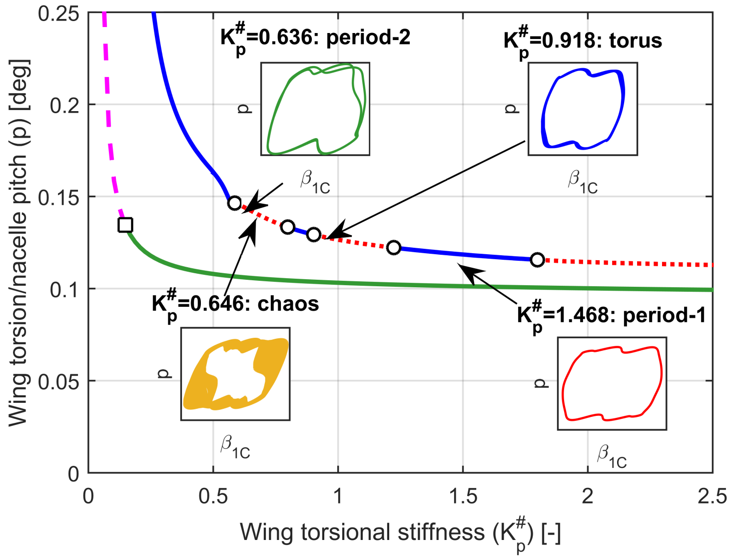

FIGURE 5.15. Subsection of bow tie LCO for $\frac{\epsilon}{d} = 0.001$ within the region of $K_p^\# \in [0, 2.5]$, pitch projection. The inset windows contain β_{1C}-p phase planes. The hollow circles indicate Neimark-Sacker (torus) bifurcations

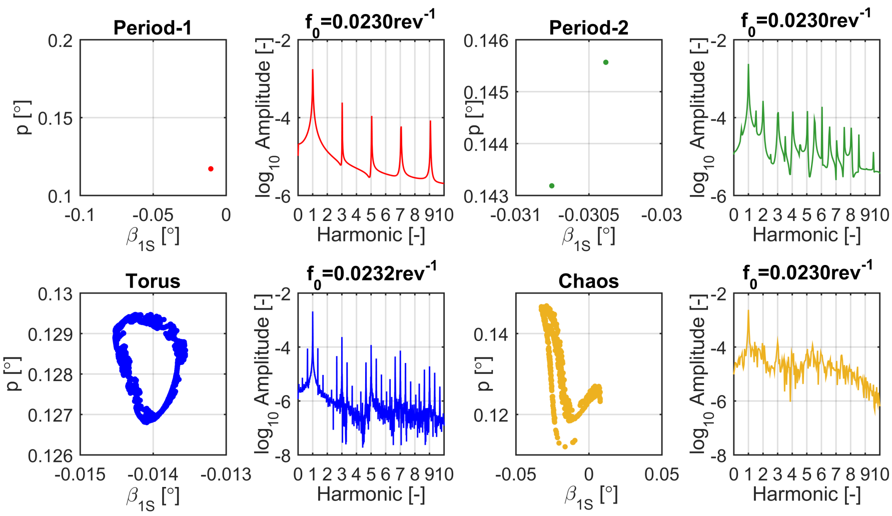

FIGURE 5.16. Poincaré sections and frequency spectra for each behaviour found in Fig. 5.15

Some torus bifurcations were sufficiently well-defined for AUTO to detect and they are indicated with hollow circles. However, efforts in the present work to create a complete behaviour map of this branch region proved to be impossible due to its fractal nature: no amount of “zooming in" revealed a fundamental structure or resolution for the intervals in which these behaviours exist. Fractal structuring of this kind is a common feature of chaotic regimes [261].

Recognition of the various behaviours shown in Figure 5.15 was possible via Poincaré sections and frequency spectra, shown in Figure 5.16. The Poincaré sections in Figure 5.16 were taken at $\beta_{1C} = 0°$, monitoring positive to negative transitions. The frequency spectra are generated using the time history of the β_{1C} state. The most powerful frequency in each spectrum is notated f_0 and the harmonics on each spectrum scale are multiples of it. The period-1 trajectory has only a single intersection with the Poincaré section, while the period-2 trajectory has two that are passed through in alternation. The torus' structure is once again evident from its Poincaré section, while the chaotic trajectory clearly exhibits some underlying structure despite the superficially random appearance of its phase plane time history. The period-1 trajectory has frequency components only on odd harmonics, a manifestation of the Fourier series reconstruction of the freeplay stiffness profile. The period-2 trajectory has significant components at all harmonics with some spikes at non-integer harmonic numbers. The structure of the torus' spectrum is less obvious though an oscillating pattern in the harmonic amplitudes is subtly evident. The spectrum for the chaotic trajectory is akin to white noise.

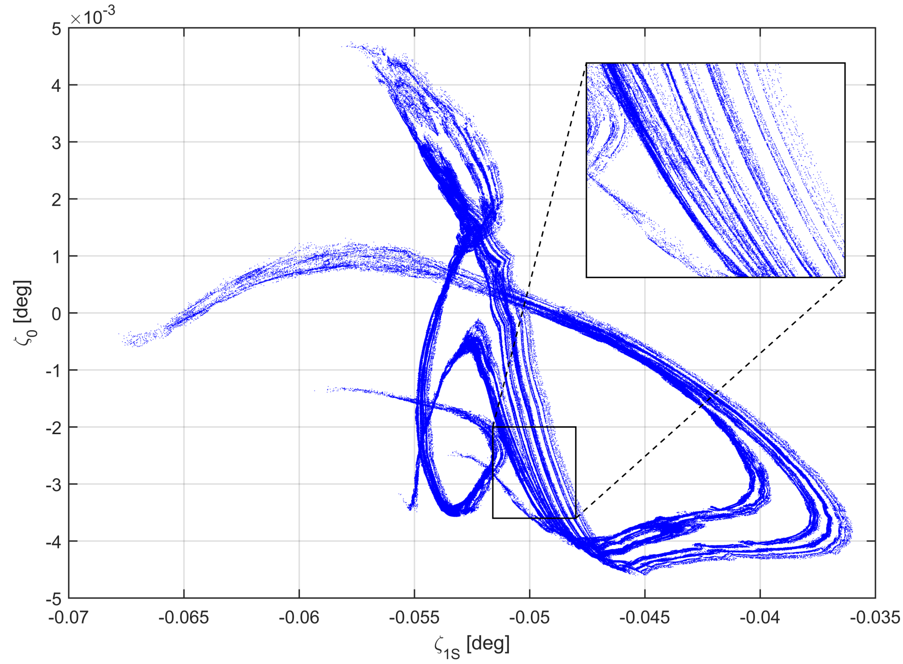

FIGURE 5.17. Poincaré section at $p = 0°$ for a chaotic trajectory found at $K_p^{\#} = 0.646$ showing values of rotor CG lateral offset ζ_{1S} and rotor collective lead lag ζ_0 upon intersecting the section over the period of 5×10^7 rotor revolutions

More use of the Poincaré section can be made in order to gain further insight into the underlying structure of the chaotic attractor. Figure 5.17 shows a Poincaré section defined by

$p = 0°$, monitoring transitions from positive to negative p, for the chaotic trajectory found in Figure 5.15. Created by the folding and mixing of the state space [261], the chaotic attractor's layered structure is clearest in the ζ_{1S}-ζ_0 plane.

5.4.2.1 Effect of deadband half-width d

The effect of d on the system's predicted dynamics is assessed in the same way as was done for the basic model, by performing a continuation with d set to 1°. Figure 5.18 shows the bifurcation diagrams for the $K^{\#}_{q2} = 0.4$ case for both $d = 0.1°$ and $d = 1°$ normalised by their respective d values and shown overlaid. Due to the aforementioned issues caused by low values of ϵ, the continuation shown here is performed at the relatively "loose" value of 0.01. It can be seen that the effect of d here appears to be the same as in the basic model, only scaling the amplitude of the various solution branches created by the presence of the freeplay nonlinearity and not altering the parameter regions over which they exist. The redrawn stability boundary is therefore also unaffected for this model.

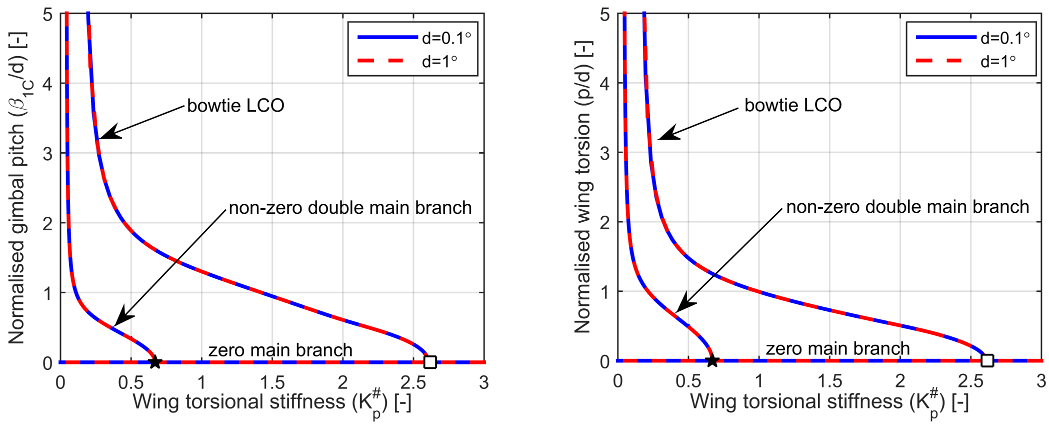

FIGURE 5.18. Overlaid normalised bifurcation diagrams for $K^{\#}_{q2} = 0.4$, $d = 0.1°$ and 1°, gimballed hub model

5.5 Implications for Stability Boundaries

5.5.1 Redrawn stability boundary for basic model

The existence of the bow tie LCO – specifically created by the presence of the freeplay nonlinearity – is a significant problem. In practical terms, a whirl flutter oscillation is possible in parameter ranges declared safe by linear stability analysis, a commonly-used standard prediction tool. Strictly speaking, this new parameter range cannot be termed "unstable" as the danger lies in attraction to stable solutions, and so "unsafe" is a more suitable term. The extent (in K_θ) of the bow tie LCO's overhang can be tracked in the K_θ-K_ψ plane to see what range of K_ψ it occurs at. This adds a new "unsafe" region to the stability boundary and is presented in Figure 5.19.

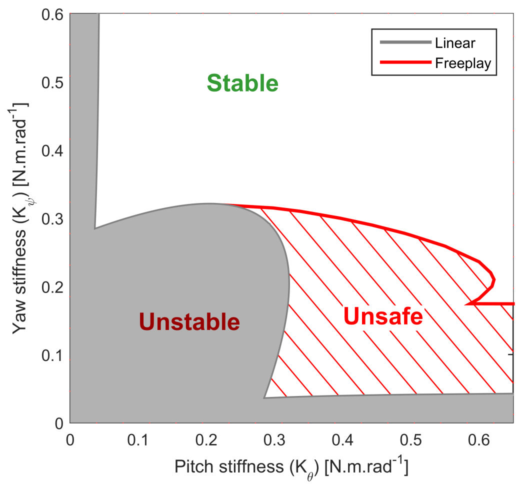

FIGURE 5.19. Redrawn stability boundary for the basic model, based on overhang of the bow tie LCO

The findings also show that the presence of freeplay in a system capable of classical whirl flutter can invalidate previous guidance regarding the role of structural stiffnesses. Several publications on classical whirl flutter explain that the shape of the Hopf-bulge – see Figure 5.3 a) – means that a design point with particularly dissimilar values of pitch and yaw stiffness will have a greater stability margin (in speed) than one with similar or equal values. However, in the case of low yaw stiffness, very much the opposite was found in the present work and therefore following the guidance in this manner could prove to be ruinous.

The discontinuity in the boundary of the new unsafe region at approximately $K_\theta = 0.6$ is caused by a rapid distension of one of the features on the bow tie LCO. The overhang extent is mostly defined by the position of the fold seen at $K_\theta = 0.65$, $\theta = 0.2°$ in Figure 5.10, marked 'F1'. However, the second fold underneath it marked 'F2', at $K_\theta = 0.41$, $\theta = 0.15°$, begins to move rightward with decreasing K_ψ. By $K_\psi \approx 0.18$ it emerges from underneath the first fold and becomes the furthest-right feature on the bifurcation diagram, defining the extent of the unsafe region.

Furthermore, the tracing in two parameters of the bow tie LCO reveals that though it exists at $K_\psi = 0.3$, it was undetected in the analysis conducted at that level as it exists as an isola. This is shown in Figure 5.20. The two free ends of the isola at the top of the figure rapidly depart to very high values of pitch θ and their eventual connection exists at some very high or even infinite value of θ. The K_θ value of the isola's overhang (i.e. its right-most extent at the fold bifurcation) may be cross-referenced with the unsafe region's extent shown in Figure 5.19.

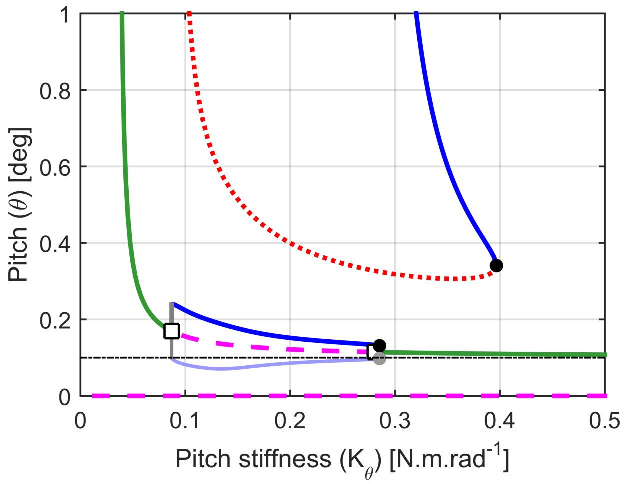

FIGURE 5.20. Bifurcation diagram for $K_\psi = 0.3$ showing bow tie LCO isola

5.5.2 Redrawn stability boundary for gimballed hub model

Although the presence of freeplay creates an overhanging bow tie LCO, it is not possible to redraw the stability boundary for the "true" freeplay case of $\epsilon = 0$. The position in $K_p^\#$ of HB0 may at first seem like a robust definition of the new boundary: it bounds the extent of the bow tie LCO and its overhang of the double main branches, the zero branch is stable thereafter and its position is in theory always finite and findable for $\epsilon > 0$. However as previously discussed, for $\epsilon = 0$ it lies at infinity and therefore the overhang is unbounded in $K_p^\#$. Attracting solution structures of various kinds (i.e. periodic, quasi-periodic and chaotic) are therefore predicted to exist on the bow tie branch at all values of $K_p^\#$, constituting a risk of whirl flutter without the possibility of restabilising using $K_{q2}^\#$ or any other parameter. The runaway effect of HB0 as ϵ tends to zero and the correspondingly growing "unsafe" region on the stability boundary is shown in Figure 5.21. The $K_p^\#$ values of the three boundaries at the level $K_{q2}^\# = 0.4$ can be cross-referenced with Figure 5.14.

In practical terms, no safe region is predicted to exist, and therefore some responsibilities exist on the designer and on the operator in the form of preventative measures. The designer must ensure that the structure has sufficient strength and stiffness for the tiltrotor to fulfil its required performance envelope with suitable margin between operating points and aeroelastic instabilities. Ideally, the structure would also be fatigue-resistant such that stresses that the components may undergo during very small whirl flutter LCOs lead to the slowest possible growth of the deadband width in the course of ordinary operation. The amplitude of these small whirl flutter oscillations is not reduced meaningfully by increasing the out-of-deadband gradient $K_p^\#$ to very large values, and therefore a design optimum may be reached by a structure that

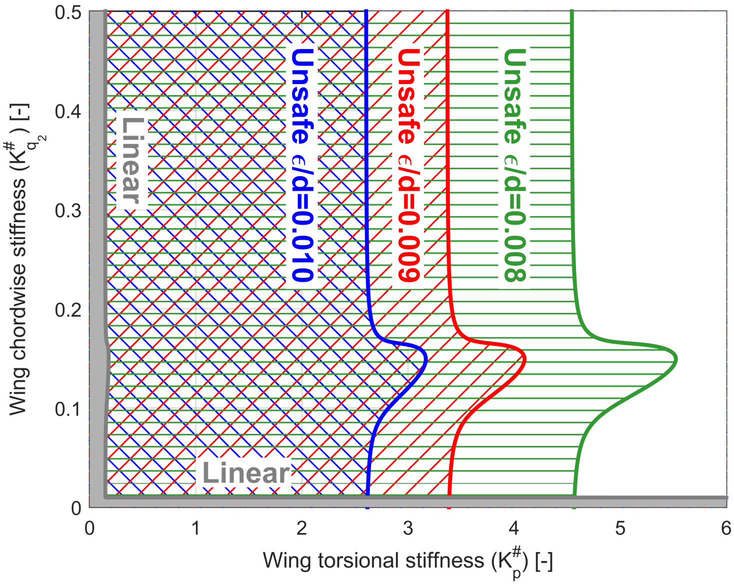

FIGURE 5.21. Redrawn stability boundaries for the gimballed hub model, based on overhang of the bow tie LCO for $\frac{\epsilon}{d} = 0.010, 0.009, 0.008$. The original linear boundary is shaded grey

fulfils its required performance envelope but is not excessively strong (and therefore needlessly heavy).

The tiltrotor operator may adopt a preventative approach that involves periodic monitoring of the deadband width and conducting component replacement as appropriate when the deadband width reaches some critical value. The selection of this critical value could be based on the growth rate of the deadband as a function of its width, and further practical investigations into the phenomenon could inform this choice more intelligently. As mentioned previously, freeplay oscillations induce their own deadband to widen through cyclic wear in a manner similar to fatigue, and such monitoring would prevent whirl flutter oscillations reaching a size that could lead to structural failure. Preloading of the tilting mechanism could be also be employed, to reduce the rate of the deadband's growth and also the effects of its presence.

Lastly, the impact of the freeplay's presence on the whirl flutter onset speed of both models is investigated here. In both cases, the models are reconfigured with their datum values and a continuation in airspeed is conducted. The continuation uses a point on one of the non-zero double main branches as the starting solution and finds the Hopf bifurcation associated with the onset of whirl flutter.

5.5.3 Airspeed continuation of basic model

The datum values for the basic model are given in Table 3.1 in Chapter 3, and the continuation is shown in Figure 5.22. An $\frac{\epsilon}{d}$ ratio of 0.0001 is maintained from the analysis above. Only one of the non-zero main branches is shown as the other is symmetric about the origin. The whirl flutter onset speed of approximately 7.8 m.s^{-1} is overhung by approximately 0.05 m.s^{-1}. The Hopf bifurcation marking the linear onset speed is a discontinuous Hopf bifurcation due to the LCO branch being born with non-zero amplitude, spanning both the in-deadband and out-of-deadband sub-domains.

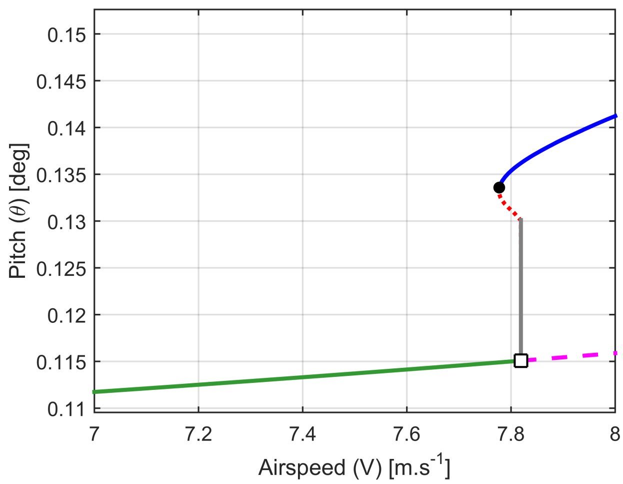

FIGURE 5.22. Airspeed continuation for the basic model

5.5.4 Airspeed continuation of gimballed hub model

The datum values for the gimballed hub model are given in Table 4.1 in Chapter 4, and the continuation is shown in Figure 5.23. A value of $\frac{\epsilon}{d} = 0.001$ is used. The continuation does not find an overhang as is found in the basic model. This is because the mode that goes unstable at 309 m.s^{-1}, the β mode, is heavily dominated by gimbal activity and therefore the nonlinearity, positioned in the wing torsion, does not have much influence. This leads to the whirl flutter more closely resembling that in the linear case, where the solution branches do not bend within the parameter space.

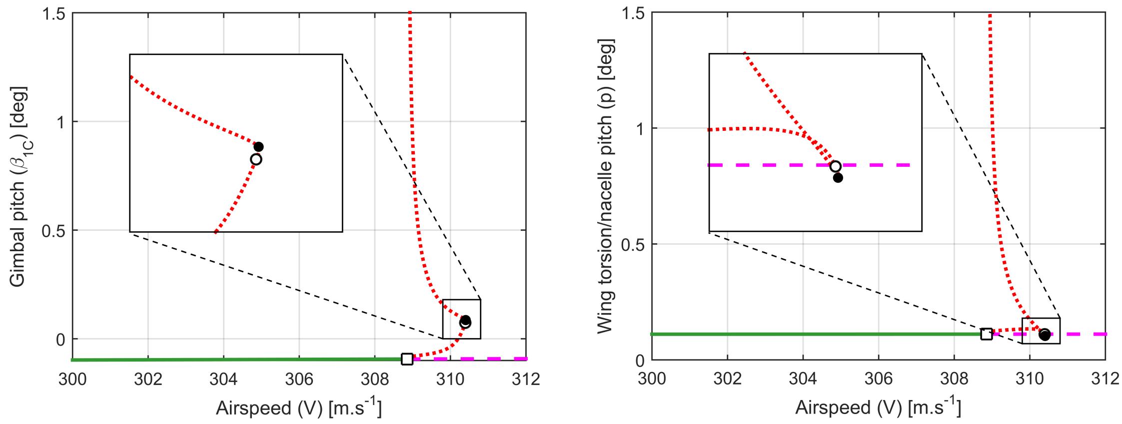

FIGURE 5.23. Airspeed continuation for the gimballed hub model

By contrast, when the gimballed hub model is configured with the autorotation parameters (release of the elastic restraint of the collective lead-lag degree of freedom) that were briefly used for validation in Figure 4.6, the first mode to go unstable is the q_1 mode at 254 m.s^{-1}, which features much more prominent participation of wing degrees of freedom, including torsion. In this case, some overhang is present, as shown in Figure 5.24. Here, the whirl flutter onset speed is lowered from about 254 m.s^{-1} to 247 m.s^{-1}.

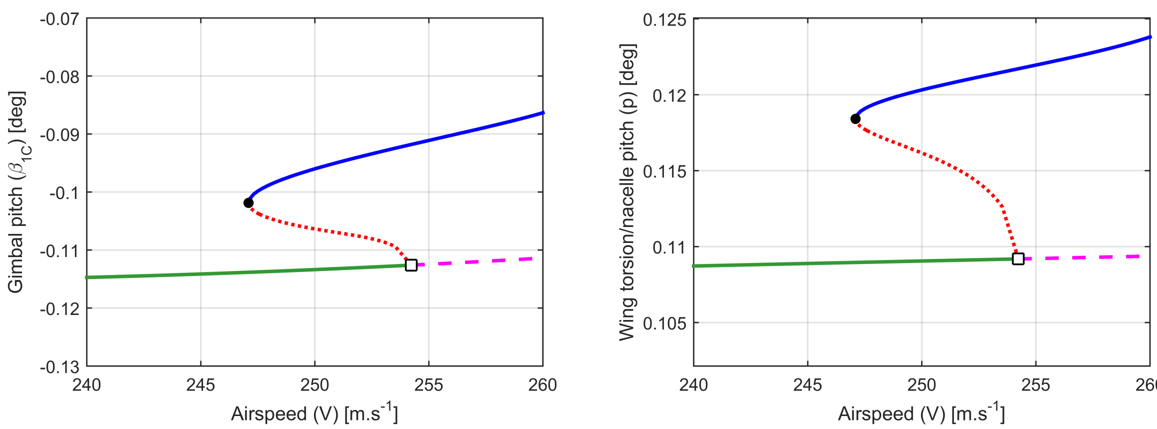

FIGURE 5.24. Airspeed continuation for the gimballed hub model, autorotation condition

5.6 Conclusions

In summary, this chapter has:

- introduced the hard nonlinearity and discussed its implementation in both models (P3)
- applied CBM (P3, P4) to:
  - the basic model with freeplay implemented in the nacelle pitch degree of freedom θ
  - the gimballed hub model with freeplay implemented in the wing torsion degree of freedom p
- investigated the impact of the smoothness parameter ratio $\frac{\epsilon}{d}$ in each model (P4, P5)
- investigated the impact of the freeplay deadband half-width d in each model (P4, P5)
- explored the quasi-periodic and chaotic behaviour found in the gimballed hub model (P5)
- redrawn the stability boundary for each model based on overhang caused by the freeplay (P6)
- performed a continuation in airspeed in each model to show the overhang existence in this parameter (P4, P5)

This contributed to the following research objectives:

- **O2**: evaluate the impact of a hard nonlinearity on the whirl flutter dynamics of rotor-nacelle systems
  - The presence of a hard nonlinearity was found to create whirl flutter LCOs. The nonlinearity also altered the equilibrium branches of the system, causing two new secondary branches (termed "non-zero main branches") to appear either side of the freeplay deadband. The original "zero" main branch was made largely unstable throughout most of the domain of analysis. Convergence on the non-zero main branches was found in some cases to have a slow decay rate, causing fatigue wear to system components.
  - The phenomenon of overhang, where stable portions of whirl flutter branches are found to exist in parameter regions that linear analysis declares to be stable, was observed in a number of the analysis cases, due to the creation of a bow tie LCO similar to that found arising from the smooth nonlinearity. The unsafe regions created as a result of the overhang were mapped out within the relevant stability boundary for each model. The overhang was bounded in the basic model, but unbounded in the gimballed hub model. This contrasts with the smooth nonlinearity, in which the overhang extent was bounded in both models.

  - The sharpness of the deadband, though more of a modelling consideration than a physical aspect of the real world system, was found to have a considerable impact on the bifurcation diagrams. Higher or "looser" values of ϵ were found to make the connection of the non-zero main branches to the zero main branch more visible, while specifically in the gimballed hub model, smaller values affected the shapes of the solution branches and resulted in more complex dynamics (quasi-periodic behaviour and chaos) existing on the branches.
  - The effect of the deadband width d was found to be a linearly-proportional scaling of the amplitudes of the solution branches, providing that the ratio $\frac{\epsilon}{d}$ was held constant. The parametric extent of branches, including any overhang, was not affected by d. This was the case in both models.

- **O3**: investigate the influence of model complexity (classical whirl flutter theory vs. tiltrotor aeroelasticity) on the impacts that the nonlinearities have on the whirl flutter dynamics of rotor-nacelle systems
  - The size of the new unsafe region, created by the presence of the hard nonlinearity, was found to be bounded in the basic model, but unbounded in the gimballed hub model. This indicates that the adjustment of other parameters may be used to circumvent the unsafe region in the basic model, but not in the gimballed hub model.
  - The complexity of the gimballed hub model's dynamics was found to be sensitive to the deadband edge sharpness, though this was not found for the basic model.
  - The gimballed hub model was once again found to have the richer dynamics. While heteroclinic bifurcations were observed in the basic model, the gimballed hub model's dynamics were found to contain quasi-periodic behaviour and even chaos.

- **O4**: explore what types of whirl flutter behaviours are observable over a range of design and operating parameters
  - Within the analysis of the basic model, periodic solutions and equilibrium branches were found in both models.
  - Quasi-periodic behaviours and chaos were also found to be present in the gimballed hub model.
  - The complexity of the gimballed hub model's dynamics were sensitive to the sharpness of the deadband's edges.

- **O5**: synthesise guidelines for tiltrotor design against whirl flutter in the presence of structural nonlinearities, based on the findings
  - The results suggest that the basic model, which is representative of propeller whirl flutter that may occur in turboprop aircraft, may have its new unsafe region avoided

by appropriate adjustment of the structural design parameters. However, previous guidance regarding the use of particularly dissimilar values of pitch and yaw stiffness could prove to be ruinous given the positioning of the new unstable region.

- The unsafe region may not be avoided through adjustment of structural design parameters however, as it is predicted to be infinitely large for truly sharp-edged deadbands.
- Instead, the tiltrotor structure can be made as fatigue-resistant as possible, so that the rate of the deadband's growth due to LCOs occurring is minimised. A design optimum for the structure's stiffness may be reached such that the required performance envelope is fulfilled without making the structure excessively heavy.
- From an operational perspective, the deadband width should be measured periodically. This will allow components to be replaced when the deadband width reaches some critical value, beyond which the growth rate would be too high. The tilting mechanism could be also be preloaded to reduce the effects of the deadband's presence, though this would increase the load on hydraulic motors at the heart of the actuator, increasing the power that they consume.

Chapter 6

Conclusions

The work presented in this thesis has provided a new approach to the dynamic analysis of the impact of some basic structural nonlinearities on the whirl flutter stability characteristics of rotor-nacelle systems. The results primarily apply to tiltrotors although the basic model's results are also applicable to turboprop propellers. To the best of the author's knowledge, such an analysis has not been undertaken previously and its absence constitutes an omission in the proper understanding of such systems, given the unignorable role that nonlinearities play in their behaviour and stability characteristics.

The tiltrotor systems were represented by two well-established models from existing literature in the field: a basic model by Reed and a gimballed hub model by Johnson. Both models are capable of predicting whirl flutter. The basic model is a rotor-nacelle system that represents classical whirl flutter, and the gimballed hub model represents tiltrotor aeroelasticity more specifically, constituting a rotor mounted on a flexible wing. The contrasting complexities of the two models lends an insight into the role of system complexity in the whirl flutter problem, though both are highly amenable to computational implementation and analysis. Both models are linear in their original forms and they were adapted to include structural nonlinearities specifically for this work, by replacing the original linear stiffness expression with a nonlinear stiffness profile appropriate for each case. These adaptations are the first of their kind in the field and derivations were provided where necessary. The nonlinearities chosen for analysis were a smooth nonlinearity and a hard (non-smooth) nonlinearity. The smooth nonlinearity provides a more realistic stiffness profile for a structure undergoing large deformations and was modelled by a low order polynomial with odd-numbered powers, while the hard nonlinearity represented freeplay in the nacelle tilting mechanism. Of the smooth nonlinearity, three subvariants were considered: a hardening profile, a softening profile and a combined softening-hardening profile.

These subvariants together explore the range of possible stiffness characterisations of the real world systems that are modelled.

The main enabling tools applied in this research were Continuation and Bifurcation Methods (CBM), which were used to calculate the stability characteristics in all cases. The application of CBM to the tiltrotor whirl flutter problem is without precedent, and lends new insights. Rather than conventional linear analyses that assess nonlinear systems in terms of linear modes, or time simulation analyses that try to find instances of whirl flutter through perturbations, CBM constructs maps of the full nonlinear system's solutions that help to interpret the various solution types that exist in different parametric ranges. As CBM is also able to find unstable solution branches as well as stable ones, it can also explain "jump" phenomena that may be observed in time simulations where a system will suddenly be drawn to an attractor of some variety. It is further able to detect whirl flutter solutions in parametric regions that linear analysis declares to be stable, as was seen in a number of instances in the results. Stability boundaries between selected system parameters were used as the principal tool for assessing changes in the stability characteristics. Doing so provided a concise summary of the nonlinearities' respective impacts, while making use of a well-established tool that is well-known in conventional linear analyses. The analysis of both the original linear versions of the models and the nonlinear adaptations included the sweeping of both design parameters such as structural stiffness and operational parameters such as airspeed.

In the original linear versions of the two models, whirl flutter was only found to be possible at and beyond the onset speed predicted by conventional eigenvalue analysis. Furthermore, the predicted instability was a simple "blow-up" of solutions to infinite values. A comprehensive literature review corroborates this observation. However, this work found that both nonlinearities created *new periodic solution branches* that are the nonlinear equivalent of the linear blow-up instability. Crucially, these new whirl flutter solution branches were found to exist over a range of parameter values, in many cases *existing in parameter regions predicted to be safe from whirl flutter by linear analysis*. This existence of whirl flutter solution branches in supposedly stable parameter regions was termed *"overhang"* on account of its appearance on bifurcation diagrams. The danger of overhang is that although the undeflected position of the rotor-nacelle system remains stable, some perturbations - such as manoeuvring of the aircraft or encountering gusts – can cause the system to join these overhanging solution branches, initiating whirl flutter behaviour. The extents of the various instances of overhang were tracked in the plane of each stability boundary affected, drawing *new "unsafe" regions: parametric regions that linear analysis declared to be stable but were subsequently found through CBM to contain whirl flutter solution branches*. Both nonlinearities were found to cause whirl flutter to be possible at lower speeds than the linearly-predicted onset airspeed, through overhang, in both models.

The research objectives of this work have been achieved. Insights into the effect of structural nonlinearities on rotor-nacelle systems have been achieved in a number of directions, ranging from nonlinearity type to the impact of model complexity. The use of CBM was instrumental in gaining these insights, and its application to the tiltrotor whirl flutter problem was a novelty in the field. The bespoke modification of the existing Reed and Johnson models is also unique to this work. The use of these models together in one investigation, also previously unseen, allowed for a gradual build-up of complexity in the results that aids their comprehensibility. Additional novelty is provided by the comprehensive derivation of Johnson's model, including the terms which for simplicity Johnson omits from his statement of the final equations. This derivation will be of great value to other researchers seeking to understand this model, which continues to be of use to the field. The research objectives of this work are:

- **O1**: assess the effect of a **smooth nonlinearity** on the whirl flutter dynamics of rotor-nacelle systems
- **O2**: evaluate the impact of a **hard nonlinearity** on the whirl flutter dynamics of rotor-nacelle systems
- **O3**: investigate the influence of **model complexity** (classical whirl flutter theory vs. tiltrotor aeroelasticity) on the impacts that the nonlinearities have on the whirl flutter dynamics of rotor-nacelle systems
- **O4**: explore what **types of whirl flutter behaviour** are observable over a range of design and operating parameters
- **O5**: synthesise **guidelines** for tiltrotor design against whirl flutter in the presence of structural nonlinearities, based on the findings

Objective **O1** is addressed by Chapters 3 and 4, and Objective **O2** by Chapter 5. The effect of both types of nonlinearity is to create a new unsafe region on the stability boundary of each model, due to the phenomenon of overhang. Objective **O3** is addressed by the comparison of Chapters 3 and 4 with each other, and by Chapter 5: Chapter 3 deals with the basic model, Chapter 4 deals with the gimballed hub model, and Chapter 5 deals with both. The effect of the two nonlinearities is slightly different in the models: the overhang only occurs in the combined variant of the basic model, but in the gimballed hub model it occurs in both the combined and the hard variants. Furthermore, the non-smooth nonlinearity added a finite unsafe region to the stability boundary of the basic model but added an unbounded unsafe region to the gimballed hub model. In general, the more complex gimballed hub model has accordingly more complex dynamics. Not only is it able to experience a number of different types of whirl flutter, whose solutions may coexist, but torus bifurcations and chaotic behaviours exist in the system. The torus bifurcations caused some instances of quasi-periodic behaviour. In addition to being more complex and time consuming to analyse, *these complex behaviours constitute a greater whirl flutter risk to tiltrotor rotor systems than regular LCOs* due to the multi-frequency motions that they involve, which are likely to accelerate the degradation of the tiltrotor system's structure. Meanwhile, the basic model dynamics' most complex features were homoclinic and heteroclinic bifurcations. Collectively, this group of observed behaviours informs Objective **O4**. Some simple features shared by both models were Hopf bifurcations, fold bifurcations and pitchfork bifurcations.

In fulfilment of **O5**, some practical recommendations were made based on the findings. Regarding the smooth nonlinearity, the results indicate that the new unsafe regions can be avoided with sufficient structural stiffness, and therefore the designer must only position the tiltrotor's design point comfortably within the stable region in order to obviate the possibility of whirl flutter. This finding applies to both models, with the exception of the softening variant of the smooth nonlinearity, whose overhanging branches were found to be part of separatrices beyond which the system would diverge to infinitely large solution values. The designer must therefore design structures so that their stiffness profiles do not contain a softening component, so that these separatrices do not exist. If this is unavoidable, a hardening component should be included to counteract the softening component as much as possible.

Regarding the hard nonlinearity, while the basic model's results suggest that the unsafe region can again be avoided through design, the same is not true for the gimballed hub model and therefore the designer should instead focus on fatigue resistance. While additional stiffness built into the design will limit the amplitude of any whirl flutter LCOs, a fatigue-resistant structure will limit the growth rate of the freeplay deadband. In either case, the desired performance envelope of the aircraft must be fulfilled in terms of the necessary strength and stiffness of the aircraft's components. Operators of tiltrotors can minimise the risk of freeplay resulting in the loss of an aircraft by regularly monitoring the freeplay deadband width of the nacelle actuators on their tiltrotor aircraft and conducting maintenance and replacement of components when the deadband width reaches some critical value. The choice of this critical value could be informed by further studies of both theoretical and practical types. The monitoring could even by conducted by an onboard system in real-time (i.e. HUMS) if the minimisation of aircraft down-time was valued by the operator.

This work has also shown some guidance previously issued in the field's literature to be faulty. Regarding classical whirl flutter models, it was remarked in earlier literature that having dissimilar values of pitch and yaw stiffness could lead to a greater margin between the operating point and whirl flutter instability. However in the cases investigated in this work, the positioning of the new unsafe region could make following this advice ruinous, to some extent in the soft nonlinearity case but to a significant extent in the hard nonlinearity case. Furthermore, the presence of the wing was thought in classical whirl flutter literature to provide a stabilising influence. While this may be true for linear models, in the presence of freeplay it is very much not the case, given that the basic model's unsafe region is bounded and the gimballed hub model's unsafe region is infinitely large.

Looking beyond the results, some more general points can be made regarding the application of CBM to the tiltrotor whirl flutter problem. Firstly, the role of time simulations in the CBM-based investigation of tiltrotor systems should not be underestimated. While it is true to say that time simulations alone are insufficient for determining the whirl flutter stability of a system given the discoverability of solutions, it was apparent at a number of points in this work that CBM also cannot be used by itself. In the gimballed hub model's results, a whirl flutter isola – an isolated solution branch that may attract the system but be difficult to find – present in the combined softening-hardening variant was only discovered because of a direct connection to a bifurcation diagram constructed in another analysis case. Were this other analysis case not to have been used, the isola could still have been discovered by the use of time simulations alone. Additionally, the separatrices that were seen so often in this work's results require time simulation for their proper exploration, as do quasi-periodic behaviours and chaos. However, the importance of using CBM prevails, as the bifurcation diagrams it produces can explain behaviours such as the rapid divergence to infinitely large solution values that crossing a separatrix entails, as well as helping to explain why other behaviours are present and what other behaviours they are connected to.

However, several avenues exist for further work. It is very reasonable to postulate that the "overhang" effect that was found in the stiffness and airspeed parameters could also exist in several other parameters involved in tiltrotor design or operation. Future work in the same vein as this investigation could look into other system parameters or explore larger parameter spaces at once, or further increase the complexity of the models used.

Although the structure of a tiltrotor is known to be a prolific contributor of nonlinearity, the range of nonlinearity sources that are investigated in the manner shown in this work could be expanded. The aerodynamics are also known to be nonlinear, and some of the more advanced models already in use in other studies could be applied here. Although some discrepancies need to be closed between the predictions made by comprehensive rotorcraft analyses and corresponding experimental data, these analyses can in theory be coupled with CBM solvers to investigate their behaviour in the same way as shown in this work. Alternatively, specific stiffness profiles obtained from existing aerospace structures could be used in CBM-based investigations of tiltrotor whirl flutter, using multi-dimensional tables where explicit functions cannot be used. Investigating the influence of nonlinearity in the drivetrain would be a suitable successor to the field's longstanding recognition of the strong influence of this degree of freedom even in linear representations. A broader area of research, the use of active control to delay whirl flutter could be re-investigated in a CBM-based context which would uncover hidden whirl flutter behaviours in the manner shown in this work.

Research from more mathematical perspectives could also be undertaken. For instance, obtaining criteria for the existence of torus flows in regions where torus bifurcations are known to exist would reduce the reliance on time simulations to find the torus flows iteratively. Alternatively, the bifurcations found in this work could be investigated specifically to uncover what factors influence their criticality. The structural stability of the results found in this work could also be investigated, which would show how sensitive the topology of the bifurcation diagrams is to variations in the system parameters, and therefore what results can be expected both in similar systems and in real world equivalent systems, whose exact parameter values may have some degree of uncertainty or variability associated with them.

Despite the rising cost and difficulty of undertaking experimental work, practical validation of mathematical models' predictions is always of use and some dedicated studies could be conducted to produce experimental observation of the overhang effect in conjunction with any of the aforementioned research leads. A number of tiltrotor-specific test rigs have been built in recent years, facilitating dedicated testing.

Furthermore, the wider adoption of CBM in industry could be accelerated by efforts dedicated to improving the accessibility of such techniques. While a number of free CBM software packages exist, they are add-ons to existing programs such as MATLAB that are typically only prevalent in research institutions rather than industrial enterprises. The development of dedicated CBM software – whether it is a stand-alone application or an upgrade to a comprehensive rotorcraft analysis – would expedite the proliferation of CBM in aerospace applications.

APPENDIX A

Derivation of Basic Model

Though well established, the derivation for the basic model, embodying classical whirl flutter and used in Chapters 3 and 5, is presented here. It is mostly reproduced directly from [310] with only minor changes in nomenclature and with the addition of some further explanatory comments. The original text focuses almost solely on the strip theory aerodynamics and so the derivation of the inertial and structural terms is included here for completeness, original to this work. A schematic diagram of the derivation is shown in Figure A.1.

A.1 Derivation Structure

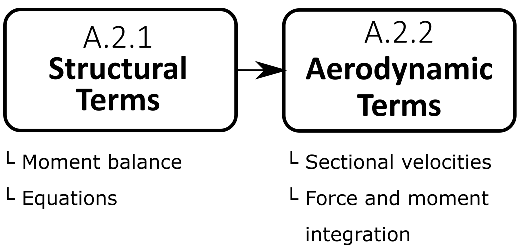

FIGURE A.1. Schematic diagram of derivation structure

A.2 Derivation Proper

A.2.1 Structural terms

A rotor of radius R rotates at an angular velocity of Ω about the end of a shaft with length a multiple a of the rotor radius, to which it is otherwise rigidly attached. The rotor has N blades, each with chord c, and it has a moment of inertia of I_x about its rotational axis. The system is characterised entirely by the deflection of the shaft's deflection in pitch and yaw, and is immersed in a uniform steady freestream velocity V. A free body diagram of the system is shown in Figure A.2, including the global coordinate system. Each degree of freedom has associated with it the overall moment of inertia of the whole rotor-nacelle about the pivot point, I_n. The wing structure provides – in each degree of freedom – elastic restoring moments that oppose deflection and viscous damping moments that oppose deflection rate. Both stiffness and damping are assumed to be linear: the moment induced is always in the same proportion with the deflection or deflection rate causing it. The constants of proportionality are elastic stiffness K and damping C. A subscript is used to indicate which degree of freedom a given constant pertains to. It is assumed that there is no coupling between the degrees of freedom in either stiffness or damping.

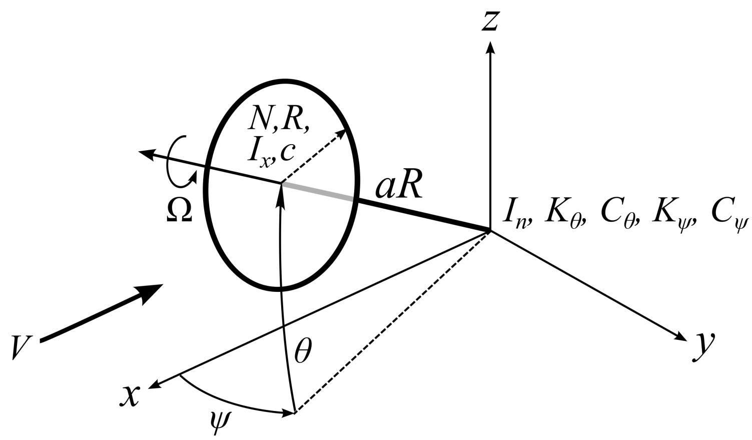

FIGURE A.2. Schematic diagram of basic model

The rotation of the rotor blades causes gyroscopic moments to be induced as a response to rotation of the rotor disc within the global frame of reference. A manifestation of Coriolis effects, the gyroscopic torque reaction $\mathbf{T}$ to a rotation $\mathbf{Q}$ of an object spinning with rotation vector $\boldsymbol{\Omega}$ and moment of inertia about that rotational axis I is given by

$$\mathbf{T} = -2I\boldsymbol{\Omega} \times \mathbf{Q} \tag{A.1}$$

The sign convention for Equation (A.1) is consistent with being situated on the left-hand side of an equation of motion (e.g. $m\ddot{x} + ... = ...$). For the case of this model's rotor disc, the pitching and yawing motions are orthogonal to the axis of rotor rotation, and it can be shown that only half of the moment of inertia about that rotational axis participates in pitching and yawing motion. Within this derivation, rotation in each of the degrees of freedom will be indicated by a rotation vector with the appropriate symbol. The rotation vector for the rotor's own rotation is indicated with $\boldsymbol{\Omega}$. A pitching motion $\mathbf{Q} = \dot{\theta}\boldsymbol{\theta}$ will induce a gyroscopic moment $\mathbf{M}_{\mathbf{g},\psi}$ in the yawing degree of freedom $\boldsymbol{\psi}$ and is

$$\mathbf{M}_{\mathbf{g},\psi} = -2\left(\frac{I_x}{2}\right)\Omega\boldsymbol{\Omega}\times\dot{\theta}\boldsymbol{\theta} = -I_x\Omega\dot{\theta}\left(-\boldsymbol{\psi}\right) = I_x\Omega\dot{\theta}\boldsymbol{\psi} \tag{A.2}$$

Similarly, a yawing motion $\mathbf{Q} = \dot{\psi}\boldsymbol{\psi}$ will induce a gyroscopic moment $\mathbf{M}_{\mathbf{g},\theta}$ in the pitching degree of freedom $\boldsymbol{\theta}$ and is

$$\mathbf{M}_{\mathbf{g},\theta} = -I_x\Omega\dot{\psi}\boldsymbol{\psi} \tag{A.3}$$

The system is immersed in a uniform freestream velocity V, incident on the rotor directly along the x-axis. Together with the rotation of the rotor, this induces aerodynamic moments on the rotor blades in the pitch and yaw directions, M_θ and M_ψ, respectively. These forces and moments are derived in a manner similar to work done by Ribner in 1947 [320] and may be classified as quasi-stead strip theory. The equations of motion at this stage in the derivation are therefore:

$$\begin{aligned} I_n\ddot{\theta} + C_\theta\dot{\theta} - I_x\Omega\dot{\psi} + K_\theta\theta &= M_\theta \\ I_n\ddot{\psi} + C_\psi\dot{\psi} + I_x\Omega\dot{\theta} + K_\psi\psi &= M_\psi \end{aligned} \tag{A.4}$$

A.2.2 Aerodynamic terms

The perturbational aerodynamic loads can be formulated using strip theory, wherein only the vector diagram of the air velocities at a typical section need be considered. The principal quantities that must be mathematically modelled are the total air velocity at the section and its components in and out of the plane of the rotor disc; the geometric angle of attack change caused by pitch and yaw α_1; and the change in the inflow angle caused by the perturbational velocities caused by pitch and yaw rates. As viewed from the front of the rotor, Figure A.3 shows a typical section located at an arbitrary spanwise location r of a blade positioned at some azimuth angle Ωt and with the hub displaced at an arbitrary small position in pitch and yaw.

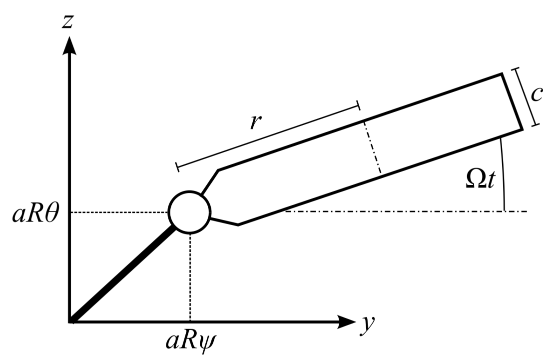

FIGURE A.3. Geometry of deflected hub, with one blade shown

The pertinent geometrical features of the typical airfoil section are then shown in Figure A.4.

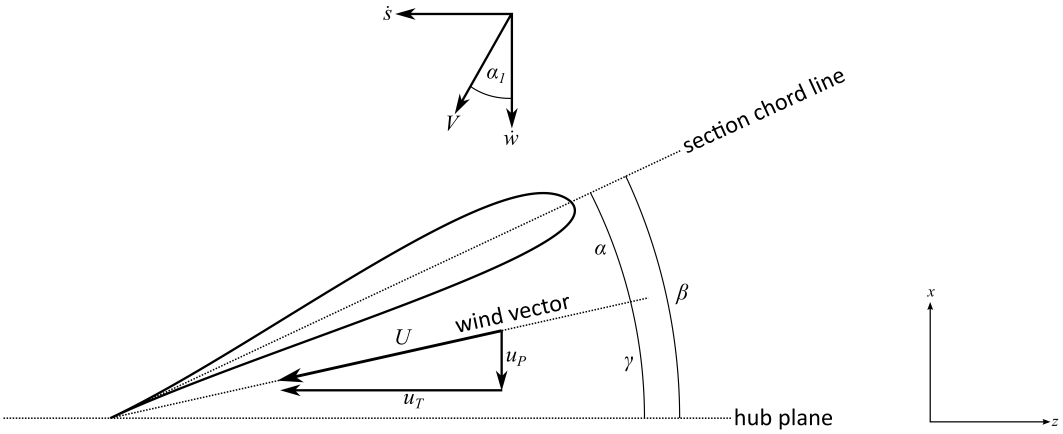

FIGURE A.4. Section velocities

The tangent and perpendicular components of velocity at the blade section are given by

$$U_T = \Omega r + \dot{s} + V \sin\alpha_1 \tag{A.5}$$

$$U_P = \dot{w} + V \cos\alpha_1 \tag{A.6}$$

where the geometric angle of attack change caused by pitch and yaw is

$$\alpha_1 = \psi \sin\Omega t - \theta \cos\Omega t \tag{A.7}$$

the additional perpendicular air velocity at an arbitrary section due to hub plane motion is

$$\dot{s} = aR\left(\dot{\theta}\cos\Omega t - \dot{\psi}\sin\Omega t\right) \tag{A.8}$$

and the additional tangential air velocity at an arbitrary section due to hub plane motion is

$$\dot{w} = -r\left(\dot{\psi}\cos\Omega t + \dot{\theta}\sin\Omega t\right) \tag{A.9}$$

The square of the effective resulting velocity U_e (that producing dynamic pressure) is then approximated by

$$U_e^2 = \Omega^2 r^2 + V^2 + 2\Omega r\dot{s} + 2V\dot{w}_2\Omega rV\alpha_1 + (H.O.T.) \tag{A.10}$$

Note that the first two terms $\Omega^2 r^2 + V^2 = U^2$. The lift at the airfoil section l can then be expressed in terms of the effective dynamic pressure and the angle of attack of the section:

$$\begin{aligned} l = \frac{\mathrm{d}L(r,t)}{\mathrm{d}r} &= \frac{1}{2}\rho U_e^2 . c_l . c \\ &= \frac{1}{2}\rho U_e^2 . c_{l_\alpha}\alpha . c \\ &= \frac{1}{2}\rho\left[\Omega^2 r^2 + V^2 + 2\Omega r\dot{s} + 2V\dot{w}_2\Omega rV\alpha_1\right] c_{l\alpha}\left(\beta-\gamma\right) c \end{aligned} \tag{A.11}$$

where β is the angle between the chord line of the aerofoil and the rotor plane, and is comprised of the angle between the local wind vector and the rotor plane γ, and the angle of attack of the aerofoil α. Furthermore:

$$\begin{aligned} \alpha &= \beta - \gamma = \beta - \arctan\left(\frac{U_P}{U_T}\right) \\ &= \beta - \arctan\left(\frac{V}{\Omega r}\right) - \frac{\Omega r}{U^2}\dot{w} + \frac{V}{U^2}\dot{s} + \frac{V^2}{U^2}\alpha_1 \end{aligned} \tag{A.12}$$

After the various formulations are combined, the resulting expression can be expanded wherein only the linear terms are retained. The following expression for the lifting load distribution is then obtained:

$$\frac{\mathrm{d}L(r,t)}{\mathrm{d}r} = \frac{1}{2}\rho c_{l\alpha} c U^2 \left[\alpha_0 - \frac{\Omega r}{U^2}\left(1 - \frac{2V}{\Omega r}\right)\dot{w} + \frac{V}{U^2}\left(1 + \frac{2\Omega r}{V}\right)\dot{s} + \frac{V^2}{U^2}\left(1 + \frac{2\Omega r}{V}\right)\alpha_1\right] \tag{A.13}$$

or, after including the expressions for $\dot{w}$, $\dot{s}$ and α_1:

$$\begin{aligned} \frac{\mathrm{d}L(r,t)}{\mathrm{d}r} &= \frac{1}{2}\rho c_{l\alpha} c U^2 \left[\alpha_0 + \frac{\Omega r}{U^2}\left(1 - \frac{2V}{\Omega r}\right) r\left(\dot{\psi}\cos\Omega t + \dot{\theta}\sin\Omega t\right)\right] \\ &+ \frac{1}{2}\rho c_{l\alpha} c U^2 \left[\frac{V}{U^2}\left(1 + \frac{2\Omega r}{V}\right) aR\left(\dot{\theta}\cos\Omega t - \dot{\psi}\sin\Omega t\right)\right] \\ &+ \frac{1}{2}\rho c_{l\alpha} c U^2 \left[\frac{V^2}{U^2}\left(1 + \frac{2\Omega r}{V}\right)\psi\sin\Omega t - \theta\cos\Omega t\right] \end{aligned} \tag{A.14}$$

The lift distribution can then be used to calculate the total perturbational in-plane forces and pitching and rolling moments at the hub accruing from all of the blades. Within the context of the quasi-steady assumption, the terms involving α_0 can be neglected resulting in the following expressions for the perturbational forces and moments at the hub:

$$L_y = \frac{N}{2}K_a\left(A_1'\psi - aA_1\frac{\dot{\psi}}{\Omega} + A_2\frac{\dot{\theta}}{\Omega}\right) \tag{A.15}$$

$$L_z = \frac{N}{2}K_a\left(A_1'\theta - aA_1\frac{\dot{\theta}}{\Omega} - A_2\frac{\dot{\psi}}{\Omega}\right) \tag{A.16}$$

$$M_y = \frac{N}{2}K_a R\left(A_2'\psi - aA_2\frac{\dot{\psi}}{\Omega} + A_3\frac{\dot{\theta}}{\Omega}\right) \tag{A.17}$$

$$M_z = \frac{N}{2}K_a R\left(A_2'\theta - aA_2\frac{\dot{\theta}}{\Omega} - A_3\frac{\dot{\psi}}{\Omega}\right) \tag{A.18}$$

where

$$K_a = \frac{1}{2}\rho c_{l\alpha} R^4\Omega^2 \tag{A.19}$$

The various integrals given in the preceding expressions are defined as follows:

$$A_1 = \int_0^1 \frac{c}{R} \frac{\mu^2}{\sqrt{\mu^2 + \eta^2}} d\eta \tag{A.20}$$

$$A_2 = \int_0^1 \frac{c}{R} \frac{\mu\eta^2}{\sqrt{\mu^2 + \eta^2}} d\eta \tag{A.21}$$

$$A_3 = \int_0^1 \frac{c}{R} \frac{\eta^4}{\sqrt{\mu^2 + \eta^2}} d\eta \tag{A.22}$$

$$A_i' = \mu A_i \tag{A.23}$$

where the advance ratio μ is defined as per contemporary convention: $\mu = \frac{V}{\Omega R}$. The total pitching and yawing moments about the pivot point are then given by:

$$M_\theta = -M_y + aRL_z \tag{A.24}$$

$$M_\psi = M_z + aRL_y \tag{A.25}$$

which result in the following final forms:

$$M_\theta = \frac{N}{2} K_a R \left(-\left(A_3 + a^2 A_1\right) \frac{\dot{\theta}}{\Omega} - A_2' \psi + a A_1' \theta \right) \tag{A.26}$$

$$M_\psi = \frac{N}{2} K_a R \left(-\left(A_3 + a^2 A_1\right) \frac{\dot{\psi}}{\Omega} + A_2' \theta + a A_1' \psi \right) \tag{A.27}$$

Appendix B

Derivation of Gimballed Hub Model

Like the Reed/Bielawa basic model, the Johnson gimballed hub model is well known in literature and is the basis of a number of works on tiltrotor aeroelasticity. Originally presented in [121], the accompanying derivation provides a thorough justification for each of the model's features. It is reproduced here for the reader's convenience, largely in Johnson's original phrasing. Only a few (entirely cosmetic) alterations have made.

Johnson frequently includes commentary on the physical significance and/or typical behaviour of certain quantities, and where these appear in the derivation (as opposed to separate discussion sections) they have largely been retained in this Appendix. However, due either to a desire to contain the length of the work, or to the falling out of use of some algebraic shortcuts that were common at the time (1974), some steps in the original algebraic manipulation might appear undesirably large. As a remedy, intermediate steps and corresponding commentary have been added here and not explicitly indicated. Furthermore, nondimensionalisation – a key tool of the dynamicist at a time when limited digital computing power made manual analysis of equations an important skill – is employed very liberally in the original work (as are subscripts of subscripts, such as $M_{q_{1_{rotor}}}$) though sadly the consistency of the nomenclature does not benefit from a commensurate rigour. This too is addressed below.

To save space, the structure of the derivation is condensed somewhat. In the original text, Johnson first derives a relatively simple 4-DoF model (2 rotor DoF, 2 wing DoF), going into considerable detail so as to demonstrate the principles employed. Following this, Johnson then derives a much more comprehensive 12-DoF model (6 rotor DoF, 6 generalised pivot DoF), but mainly as an extension to the 4-DoF model derivation from before and with far less discussion. The final 9-DoF model is then derived by generating 3-DoF equations of motion for a wing expressing the generalised pivot degrees of freedom in terms of the wing degrees of freedom, and thereby substituting the wing equations into the 12-DoF model, producing the full 9-DoF rotor-wing model.

In this work, the 12-DoF model is obtained directly and the derivation thereof is presented in the same level of detail as the 4-DoF model in the original text, saving considerable space. The introduction and integration of the wing degrees of freedom is unchanged, however. Where logical, some items are brought forward in the derivation.

B.1 Derivation Structure

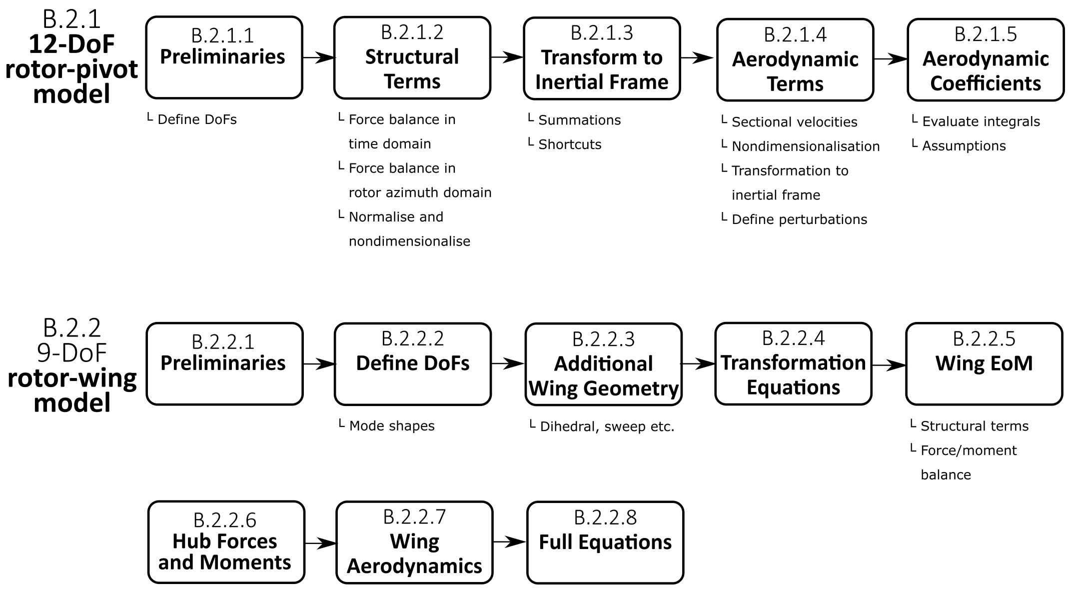

FIGURE B.1. Schematic diagram of derivation

B.2 Derivation Proper

B.2.1 12-DoF rotor – generalised pivot model

B.2.1.1 Preliminaries

Consider a flapping rotor on a pylon with pitch and yaw degrees of freedom operating in high inflow axial flight. The model is shown in Figure B.2.

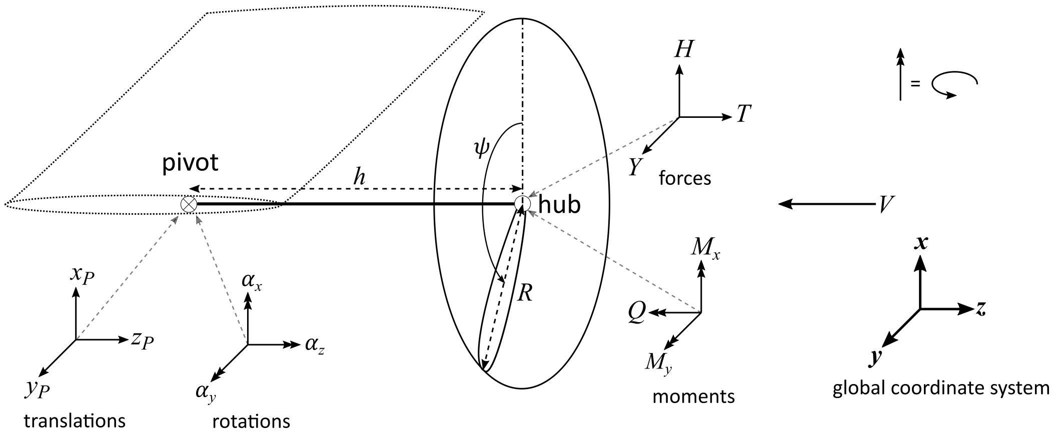

FIGURE B.2. Schematic diagram of the gimballed hub model

The rotor is mounted on the end of a pylon a distance h (known as the mast height) forward from the pivot point, with a freestream velocity of V. The inflow ratio $\mu = \frac{V}{\Omega R}$ is assumed to be of order 1. Only rotor aerodynamics are considered; any pylon aerodynamic forces are neglected. Shown also in Figure B.2 are the axis conventions for the hub forces and moments, and pylon degrees of freedom.

The pylon motion is considered to be 6-DoF rigid-body and is defined about the pivot point. The pivot linear displacement degrees of freedom are x_P (vertical; positive upward), y_P (lateral; positive rightward from the pylon's perspective) and z_P (longitudinal; positive into the oncoming freestream). The rotational degrees of freedom of the pylon are named using the right-hand rule on the system axes, and are α_x (yaw), α_y (pitch) and α_z (roll). Their respective positive senses are consistent with rotation vector representation. The rigid-body pitch and yaw motion has inertia, damping, and elastic restraint about the pivot. At the hub is a rotor with N blades that rotates with angular velocity Ω rad.s^{-1}.

The net forces exerted by the rotor on the hub from all N blades are rotor thrust T (positive forwards), rotor vertical force H (positive upwards), rotor side force Y (positive to the right when viewed from behind) and rotor torque Q (positive in the opposite sense to the rotor's motion). The rotor has clockwise rotation when viewed from the rear, with azimuth angle ψ measured from vertically upward. The azimuth position of the m^{th} blade, $m = 1, 2 \ldots N$ is $\psi_m = \Omega t + m\Delta\psi$ where $\Delta\psi = \frac{2\pi}{N}$ is the angle between succeeding blades and t is time in seconds. As the pylon is rotated in roll by α_z, the rotational velocity of the blade with respect to space is $\Omega + \dot{\alpha}_z$ (without blade flap or lag motion).

The motion of each blade is defined by flap and lag degrees of freedom and blade pitch input, all with respect to the hub plane. The flap degree of freedom is pure out-of-plane deflection of the blade spar, and likewise the lead-lag degree of freedom is pure in-plane deflection. The mode shape of the blade deflection is represented by $\eta_\beta(r)$ for flap and $\eta_\zeta(r)$ for lead-lag. These modeshapes are functions of radial station r and are normalised to 1 at the tip $r = R$. The out-of-plane deflection of a point at a radial station r is therefore $\beta(\psi)\eta_\beta(r)$ normal to the hub plane, with β defined positive for forward displacement of the blade tip from the disc plane. ζ is defined positive for deflection opposing the rotor direction of rotation, i.e. consistent with the notion of lagging.

Rotating mode shapes are used, that is, natural vibration modes including the centrifugal spring due to blade rotation. A major influence on the mode shape is the type of root restraint, i.e. hinged or a cantilever root. However, the centrifugal stiffening is so strong in comparison that the effect of the root restraint on the lowest flap and lag mode shapes is restricted mainly to the root area (where the centrifugal effects are lesser). The influence of the root restraint on the natural frequencies of the modes is of primary importance. The first (lowest frequency) flap and lag modeshapes for either type of blade (hinged/cantilever) are then nearly $\eta = r$, a linear relationship resembling rigid body rotation about the root where the blade remains un-curved. However, near the root of a cantilever blade, the mode shape must deviate from this, of course, to satisfy the boundary condition of zero slope.

The final form for the equations of motion is in terms of the nonrotating rotor degrees of freedom. It is possible to have different mode shapes for the various nonrotating degrees of freedom. For example, one for the coning mode and one for the tip path plane tilt modes, depending on how the hub restraint appears during deflection of the blades in that particular rotor model. Two rotors are considered in the applications of this theory; a cantilever rotor and a gimballed rotor. For the cantilever rotor, the mode shape for all nonrotating degrees of freedom of the blade is that of elastic bending with cantilever root restraint. For the gimballed rotor, the mode shape for tip path plane tilt degrees of freedom β_{1C} and β_{1S} is that of an articulated blade, namely, rigid-body motion about a hinge at the centre of rotation, with the modeshape $\eta = r$ as indicated previously. For all other nonrotating modes of the gimballed rotor (specifically coning and all blade lag modes), the rotor blade acts as a cantilever blade, with corresponding blade deflection mode shapes.

The motion of a real cantilever rotor blade in elastic bending is actually more complex than the representation used here. The in-plane and out-of-plane deflections are highly coupled due to the collective pitch and built-in twist of the blade, both of which are usually large for a proprotor. Consequently, although the lowest frequency bending modes are usually still identifiable as predominantly flap or lag motion, there is actually both in-plane and out-of-plane motion in both modes. The neglect of this effect, by assuming that the blade flap and lag degrees of freedom are pure out-of-plane and pure in-plane deflections respectively, is probably the severest limitation of the theory presented here. The basic features of the flap and lag motion are represented, so this model may be expected to predict proprotor behaviour fairly well.

The dimensionless rotating natural frequency of the flap motion (that is, the natural frequency normalised against rotor speed Ω to produce a quantity per rotor revolution) is allowed to be greater than 1/rev so that blades with cantilever root constraint or a flap hinge offset or spring providing restoring stiffness may be treated as well as articulated blades (which have an actual hinge at or near the centre of rotation). In the latter case, the stiffness present is not modelled explicitly, but implicitly as a contribution to the natural frequency. The mode shape for the flap motion is assumed proportional to the radial distance r, that is, rigid body rotation about the hub centre with no bending of the blade.

The equations of motion are derived for a constant rotor rotational speed Ω (with respect to the pylon). This assumes that the engine powering the rotor has a perfect governor, i.e. the engine always supplies the instantaneous torque required to hold the rotor rotational speed Ω constant during any perturbed motion. For an actual rotor in powered flight, the engine/drivetrain/governor dynamics must be included to give a complete representation of the behaviour.

The blade also has pitch motion about the feathering axis at the blade root (given by θ), with the actual blade pitch measured from the hub plane. The pitch has trim and perturbation contributions as before. The trim value is due to root collective and built-in twist; the perturbation value is due to a control input and pitch/flap coupling. Pitch/flap coupling (δ_3) is included for the gimballed rotor.

B.2.1.2 Structural terms

The equations of motion for flap and lag degrees of freedom are obtained from equilibrium of moments on the blade. The flapping equation is considered first. Blade flap of the m^{th} blade with respect to space is composed of flap with respect to the hub plane β_m, plus α_y and α_x, which give the tilt of the hub plane in space, and finally plus any longitudinal movement of the shaft z_P. The linearized equations of motion, that is, for small angles of the blade and pylon displacement, are then obtained. For the m^{th} blade, in the rotating frame, the flap equation is:

$$I_\beta \ddot{\beta}_m + I_{\beta\alpha}\left[-\ddot{\alpha}_y \cos\psi_m + \ddot{\alpha}_x \sin\psi_m\right] + I_\beta \omega_\beta^2 \beta_m + S_\beta \ddot{z}_P = M_{F_m} \tag{B.1}$$

where I_β is the basic blade flapping inertia, $I_{\beta\alpha}$ is the blade inertia in response to pylon rotational excitation, S_β is the blade inertia in response to pylon longitudinal translational excitation, and M_{F_m} is the aerodynamic flap moment on the m^{th} blade. Note that the (aggregate) elastic restraint of the blade flapping is expressed implicitly in terms of that motion's natural frequency:

$$\omega_\beta = \sqrt{\frac{K_\beta}{I_\beta}} \Rightarrow K_\beta = I_\beta \omega_\beta^2 \tag{B.2}$$

As we wish to view the motion from within the hub/disc plane, Coriolis terms must be added. The hub plane does not rotate with the blades, but does rotate due to movement of the shaft α_y and α_x. Within the inertial frame (defined by the unit rotation vectors $[\hat{\boldsymbol{\alpha}}_x, \hat{\boldsymbol{\alpha}}_y, \hat{\boldsymbol{\alpha}}_z]$) the hub plane rotation vector $\boldsymbol{\Omega}_{hp}$ is:

$$\boldsymbol{\Omega}_{hp} = [\dot{\alpha}_x, \dot{\alpha}_y, 0] \tag{B.3}$$

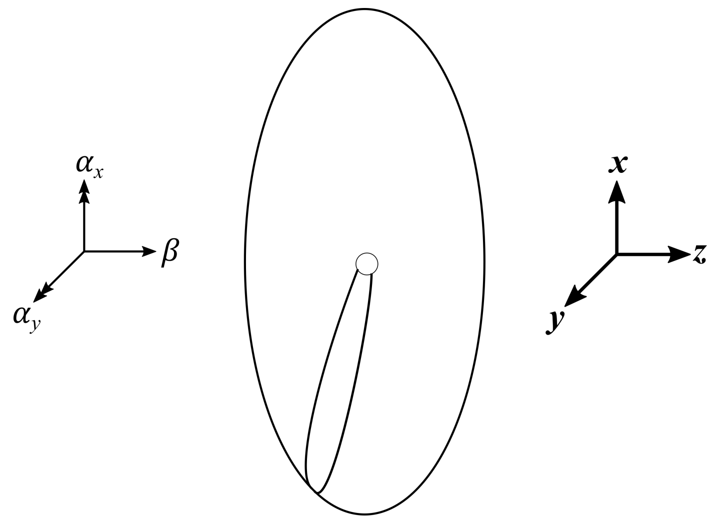

FIGURE B.3. Coordinate system adopted for deriving Coriolis accelerations (left) compared to global coordinate system (right)

The instantaneous velocity of a blade element within the hub plane depends on its position in that plane. If the angles α_y and α_x are assumed to be small, then the hub plane can be approximated as lying within the x-y plane of the inertial frame, and consequently points in the hub plane can be described using $(\hat{\boldsymbol{\alpha}}_x, \hat{\boldsymbol{\alpha}}_y, \hat{\boldsymbol{\beta}})$, where $\hat{\boldsymbol{\beta}}$ is a unit vector (of translation, not rotation) normal to the hub plane, positive forwards (i.e. parallel with z^+ in order to be consistent with the definition for flapping described above. This coordinate system is shown in Figure B.3, in the context of the global coordinate system. The use of a translation vector for flapping avoids the need for a rotation vector that itself rotates with time within the x-y plane. The angular position of the blade within the hub plane is:

$$\mathbf{r}_{blade} = [\cos\psi_m, \sin\psi_m, 0] \tag{B.4}$$

where $\psi_m = \Omega t + m\Delta\psi$. The instantaneous angular velocity of this element is therefore:

$$\mathbf{v}_{blade} = [-\Omega\sin\psi_m, \Omega\cos\psi_m, 0] \tag{B.5}$$

The Coriolis acceleration, when on this side of the equation, is $2\boldsymbol{\Omega}_{hp} \times \mathbf{v}_{blade}$:

$$
\begin{aligned}
2\boldsymbol{\Omega}_{hp} \times \mathbf{v}_{blade} &= 2\begin{vmatrix} \hat{\boldsymbol{\alpha}}_x & \hat{\boldsymbol{\alpha}}_y & \hat{\boldsymbol{\beta}} \\ \dot{\alpha}_x & \dot{\alpha}_y & 0 \\ -\Omega\sin\psi_m & \Omega\cos\psi_m & 0 \end{vmatrix} \\
&= 2\left[\hat{\boldsymbol{\alpha}}_x(0-0) - \hat{\boldsymbol{\alpha}}_y(0-0) + \hat{\boldsymbol{\beta}}(\dot{\alpha}_x\Omega\cos\psi_m - -\dot{\alpha}_y\Omega\sin\psi_m)\right] \\
&= 2\hat{\boldsymbol{\beta}}\left(\dot{\alpha}_x\Omega\cos\psi_m + \dot{\alpha}_y\Omega\sin\psi_m)\right) \\
&= 2\Omega\dot{\alpha}_x\cos\psi_m + 2\Omega\dot{\alpha}_y\sin\psi_m)
\end{aligned}
\tag{B.6}
$$

And so these terms may be added to the equation to give:

$$I_\beta\ddot{\beta}_m + I_{\beta\alpha}\left[-(\ddot{\alpha}_y - 2\Omega\dot{\alpha}_x)\cos\psi_m + (\ddot{\alpha}_x + 2\Omega\dot{\alpha}_y)\sin\psi_m\right] + I_\beta\omega_\beta^2\beta_m + S_\beta\ddot{z}_P = M_{F_m} \tag{B.7}$$

It is more convenient to work with the nondimensional (i.e. per-rev) blade flapping frequency ν_β (1/rev for an articulated blade with no hinge spring or offset; greater than 1/rev for a cantilever blade) which is related to the dimensional natural frequency thus:

$$\nu_\beta = \frac{\omega_\beta}{\Omega} \tag{B.8}$$

and making this substitution gives:

$$I_\beta\ddot{\beta}_m + I_{\beta\alpha}\left[-(\ddot{\alpha}_y - 2\Omega\dot{\alpha}_x)\cos\psi_m + (\ddot{\alpha}_x + 2\Omega\dot{\alpha}_y)\sin\psi_m\right] + I_\beta\Omega^2\nu_\beta^2\beta_m + S_\beta\ddot{z}_P = M_{F_m} \tag{B.9}$$

This prompts us also to nondimensionalise the time in the same way, giving time in rotor rotations rather than seconds t. Given that the azimuth position of the m^{th} blade ψ_m is defined as:

$$\psi_m = \Omega t + m\Delta\psi \tag{B.10}$$

then we therefore can obtain

$$\frac{\mathrm{d}\psi_m}{\mathrm{d}t} = \Omega \tag{B.11}$$

Choosing dash notation to indicate a per-rev derivative $\beta'_m = \frac{\mathrm{d}\beta_m}{\mathrm{d}\psi}$, the relation to the dot notation per-second derivative $\dot{\beta}_m = \frac{\mathrm{d}\beta_m}{\mathrm{d}t}$ can be obtained using the chain rule for derivatives:

$$\dot{\beta}_m = \frac{\mathrm{d}\beta_m}{\mathrm{d}t} = \frac{\mathrm{d}\psi_m}{\mathrm{d}t}\frac{\mathrm{d}\beta_m}{\mathrm{d}\psi} = \Omega\beta'_m \tag{B.12}$$

By extension:

$$\ddot{\beta}_m = \Omega^2\beta''_m \tag{B.13}$$

and the same is true for time derivatives of the pylon degrees of freedom. The flapping equation of the m^{th} blade becomes:

(B.14)

$$I_\beta\Omega^2\beta''_m + I_{\beta\alpha}\left[-(\Omega^2\alpha''_y - 2\Omega^2\alpha'_x)\cos\psi_m + (\Omega^2\alpha''_x + 2\Omega^2\alpha'_y)\sin\psi_m\right] + I_\beta\Omega^2\nu_\beta^2\beta_m + S_\beta\Omega^2 z''_P = M_{F_m}$$

which can be simplified:

$$I_\beta(\beta''_m + \nu_\beta^2\beta_m) + I_{\beta\alpha}\left[-(\alpha''_y - 2\alpha'_x)\cos\psi_m + (\alpha''_x + 2\alpha'_y)\sin\psi_m\right] + S_\beta z''_P = \frac{M_{F_m}}{\Omega^2} \tag{B.15}$$

The lead-lag equation for the m^{th} blade follows in much the same way:

$$I_\zeta\left(\zeta''_m + \nu_\zeta^2\zeta_m\right) - I_{\zeta\alpha}\alpha''_z\left[-(y''_P - h\alpha''_x)\cos\psi_m + (x''_P + h\alpha''_y)\sin\psi_m\right] = \frac{M_{L_m}}{\Omega^2} \tag{B.16}$$

However here there are no Coriolis terms, as the only manifestations of Coriolis effects are in the flapping direction $\hat{\boldsymbol{\beta}}$, as shown in Equation (B.6). Furthermore, the pylon motion has more prominent influence.

The inertia constants are integrals of the blade section mass distribution according to the relevant modeshapes:

$$I_\beta = \int_0^1 \eta_\beta^2(\bar{r})md\bar{r} \tag{B.17}$$

$$I_{\beta\alpha} = \int_0^1 \eta_\beta(\bar{r})\bar{r}md\bar{r} \tag{B.18}$$

$$S_\beta = \int_0^1 \eta_\beta(\bar{r})md\bar{r} \tag{B.19}$$

$$I_\zeta = \int_0^1 \eta_\beta^2(\bar{r})md\bar{r} \tag{B.20}$$

$$I_{\zeta\alpha} = \int_0^1 \eta_\zeta(\bar{r})\bar{r}md\bar{r} \tag{B.21}$$

$$S_\zeta = \int_0^1 \eta_\zeta(\bar{r})md\bar{r} \tag{B.22}$$

where $\bar{r}$ is the nondimensional radial station (normalised by rotor radius R). The rotating natural frequencies of the flap and lag motions are ν_β and ν_ζ, respectively. A subscript '0' will be added to the mode shape, inertias and natural frequencies for the collective modes (coning and collective lag) since these terms may not be identical to those for the cyclic modes (e.g. for the gimballed rotor).

The flap equation is forced by pure out-of-plane aerodynamic forces (F_z) and the lag by pure in-plane forces (F_x), because of the assumption of decoupled flap and lag bending modes. The flap mode shape η_β influences the effective inertias of the flap motion and the shaft angular acceleration; here, rigid-body flap motion $\eta_\beta(\bar{r}) = \bar{r}$ is found to be sufficient for representation of first mode motion and is therefore assumed. The lag motion couples with in-plane acceleration of the rotor hub (resolved into the rotating frame) and with roll angular acceleration of the rotor shaft. The Coriolis inertial coupling of the flap and lag equations has been neglected. The coefficients of these terms would be proportional to the rotor trim coning angle, which is of order $\gamma\frac{C_T}{\sigma a}$. However, aerodynamic terms also contribute to this coupling, and for high inflow these coefficients are of order 1. Hence the Coriolis inertia coupling may be neglected compared with the high inflow aerodynamic forces. The nominal dimensional blade inertia I_b is defined:

$$I_b = \int_0^1 \bar{r}^2 m d\bar{r} \tag{B.23}$$

and the inertias in the equations are normalised and nondimensionalised by dividing them by this quantity. Quantities normalised in this way are denoted by an asterisk superscript:

$$\frac{I_\beta}{I_b} = I^*_\beta \tag{B.24}$$

Furthermore, it is the nominal blade inertia value that is used in the definition of the Lock number γ, as opposed to any of the other blade inertias:

$$\gamma = \frac{\rho a c R^4}{I_b} \tag{B.25}$$

where a is the blade 2D lift slope (dimensionless), and c is the dimensional rotor blade chord. Normalising the various blade inertias with I_b gives the following blade equations:

$$I^*_\beta(\beta''_m + \nu^2_\beta \beta_m) + I^*_{\beta\alpha}\left[-(\alpha''_y - 2\alpha'_x)\cos\psi_m + (\alpha''_x + 2\alpha'_y)\sin\psi_m\right] + S^*_\beta z''_P = \frac{M_{F_m}}{I_b\Omega^2} \tag{B.26}$$

$$I^*_\zeta\left(\zeta''_m + \nu^2_\zeta\zeta_m\right) - I^*_{\zeta\alpha}\alpha''_z\left[-(y''_P - h\alpha''_x)\cos\psi_m + (x''_P + h\alpha''_y)\sin\psi_m\right] = \frac{M_{L_m}}{I_b\Omega^2} \tag{B.27}$$

The right-hand sides of the equations can be rewritten in terms of some relevant and familiar nondimensional quantities. The Lock number γ as defined above in (B.25) is one of these, and we introduce also the solidity σ, the ratio of total blade area to disc area:

$$\sigma \;\left(= \frac{NcR}{\pi R^2}\right)\; = \frac{Nc}{\pi R} \tag{B.28}$$

Taking the right-hand side of the flapping equation:

$$\begin{aligned}\frac{M_{F_m}}{I_b\Omega^2} &= \gamma\frac{1}{\gamma}\frac{M_{F_m}}{I_b\Omega^2}\\ &= \gamma\frac{I_b}{\rho a c R^4}\frac{M_{F_m}}{I_b\Omega^2}\\ &= \gamma\frac{1}{\rho a c R^4}\frac{M_{F_m}}{\Omega^2}\end{aligned} \tag{B.29}$$

and defining a nondimensional rotor blade chord $\bar{c}$ by normalising the dimensional rotor blade chord c by rotor radius R gives:

$$\begin{aligned}\gamma\frac{1}{\rho acR^4}\frac{M_{F_m}}{\Omega^2} &= \gamma\frac{1}{\rho a(\bar{c}R)R^4}\frac{M_{F_m}}{\Omega^2}\\ &= \frac{\gamma}{a\bar{c}}\frac{M_{F_m}}{\rho R^5\Omega^2}\end{aligned} \tag{B.30}$$

The quantity $\frac{M_{F_m}}{\rho R^5\Omega^2}$ is nondimensional and it therefore can be used as the definition for a nondimensional flapping aerodynamic moment:

$$\frac{M_{F_m}}{\rho R^5\Omega^2} = \bar{M}_{F_m} \tag{B.31}$$

and the nondimensional lead-lag aerodynamic moment $\bar{M}_{L_m}$ follows in the same way. Structural damping of the rotor blades is also added to this model; however, since the blade flap and lag damping are high already because of the high inflow aerodynamic forces, the low structural damping of the rotors considered here is not very important to the dynamics. A term $I^*_\beta g_{s_\beta}\sqrt{\nu_\beta^2-1}\,\beta'_m$ is added to the rotating flap equation, and a term $I^*_\zeta g_{s_\zeta}\nu_\zeta\zeta'_m$ is added to the rotating lead-lag equation of motion. Similar to the blade's stiffnesses, these damping terms are also defined implicitly. For instance, for the lead-lag term:

$$C_\zeta = g_{s_\zeta}\sqrt{K_\zeta I_\zeta} = g_{s_\zeta}I_\zeta\sqrt{\frac{K_\zeta}{I_\zeta}} = g_{s_\zeta}I_\zeta\nu_\zeta$$

$$\Rightarrow C^*_\zeta = \frac{C_\zeta}{I_b} = g_{s_\zeta}\frac{I_\zeta}{I_b}\nu_\zeta = g_{s_\zeta}I^*_\zeta\nu_\zeta \tag{B.32}$$

where the structural damping parameter g_s is twice the fraction of critical damping (2ζ in modern nomenclature convention) and is typically 0.5 to 1% for the cantilever rotor blades considered here. The structural damping does not act on the centrifugal spring term in ν_β. This gives the following blade equations:

$$I^*_\beta(\beta''_m + g_{s_\beta}\sqrt{\nu_\beta^2-1}\,\beta'_m + \nu_\beta^2\beta_m) + I^*_{\beta\alpha}\left(-(\alpha''_y - 2\alpha'_x)\cos\psi_m + (\alpha''_x + 2\alpha'_y)\sin\psi_m\right) + S^*_\beta z''_P = \gamma\frac{\bar{M}_{F_m}}{a\bar{c}} \tag{B.33}$$

$$I^*_\zeta\left(\zeta''_m + I^*_\zeta g_{s_\zeta}\nu_\zeta\zeta'_m + \nu_\zeta^2\zeta_m\right) - I^*_{\zeta\alpha}\alpha''_z\left(-(y''_P - h\alpha''_x)\cos\psi_m + (x''_P + h\alpha''_y)\sin\psi_m\right) = \gamma\frac{\bar{M}_{L_m}}{a\bar{c}} \tag{B.34}$$

If the rigid body mode shape is assumed for both flap and lag modes regardless of root restraint type ($\eta_\beta(\bar{r}) = \eta_\zeta(\bar{r}) = \bar{r}$), and a constant blade mass distribution is assumed ($m(\bar{r}) = m$), then following values are achieved for the inertias:

$$I^*_\beta = \frac{I_\beta}{I_b} = \frac{m\int_0^1 \bar{r}^2 d\bar{r}}{m\int_0^1 \bar{r}^2 d\bar{r}} = 1 \qquad \left(= I^*_\zeta\right) \tag{B.35}$$

(B.36)
$$I^*_{\beta\alpha} = \frac{I_{\beta\alpha}}{I_b} = \frac{m\int_0^1 \bar{r}^2 d\bar{r}}{m\int_0^1 \bar{r}^2 d\bar{r}} = 1 \qquad \left(= I^*_{\zeta\alpha}\right)$$

(B.37)
$$S^*_\beta = \frac{S_\beta}{I_b} = \frac{m\int_0^1 \bar{r} d\bar{r}}{m\int_0^1 \bar{r}^2 d\bar{r}} = \frac{1/2}{1/3} = \frac{3}{2} \qquad \left(= S^*_\zeta\right)$$

With usual blade construction, the I^* terms are slightly less than 1, and the S^* terms around 1.

B.2.1.3 Transformation to non-rotating frame of reference

The N individual blade flapping equations for each of the flap and lead-lag degrees of freedom exist within the rotating hub frame. To convert them into the inertial frame in order to be consistent with the pylon equations, a coordinate transform of the Fourier type is introduced, whose new degrees of freedom for the flapping motion are defined as:

(B.38)
$$\beta_0 = \frac{1}{N}\sum_{m=1}^{N} \beta_m$$

(B.39)
$$\beta_{nC} = \frac{2}{N}\sum_{m=1}^{N} \beta_m \cos(n\psi_m)$$

(B.40)
$$\beta_{nS} = \frac{2}{N}\sum_{m=1}^{N} \beta_m \sin(n\psi_m)$$

(B.41)
$$\beta_{N/2} = \frac{1}{N}\sum_{m=1}^{N} \beta_m (-1)^m$$

Each of these is a summation across all blades, with n being fixed where it is present. The first degree of freedom is average flap angle and represents coning of the rotor, positive with positive β_m. The second and third are twice the average blade pitch and yaw (respectively) at the n^{th} harmonic. At the first harmonic they simply represent the rotor disc tilt in pitch and yaw, positive downward and left (when viewed from behind), respectively. Higher harmonics only represent internal rotor motion, that is, motion of the blades relative to each other. The fourth summation is a mode where alternating rotor blades split into two groups and flap antagonistically, known as the reactionless flapping mode on account of the zero net force transferred to the hub.

Time derivatives of β_m are preserved in the above descriptions (B.38)–(B.41), i.e.:

(B.42)
$$\beta'_0 = \frac{1}{N}\sum_{m=1}^{N} \beta'_m$$

and so forth for the other degrees of freedom. These new degrees of freedom are related to the flapping of the m^{th} blade via:

$$\beta_m = \beta_0 + \sum_{n=1}^{\Delta} \left[\beta_{nc}\cos(n\psi_m) + \beta_{ns}\sin(n\psi_m)\right] + \beta_{N/2}(-1)^m \tag{B.43}$$

where the summation's upper limit is

$$\Delta = \begin{cases} \frac{N-1}{2} & \text{if } N \text{ is odd} \\ \frac{N-2}{2} & \text{if } N \text{ is even} \end{cases} \tag{B.44}$$

The $\beta_{N/2}$ degree of freedom is only included if N is even; for odd N it is not part of the definition of β_m and is not present in the model. Furthermore, N determines via the summation limit Δ how many harmonics need to be included for the description to be complete, i.e. it ensures that there are N equations. As the present work only uses a 3-bladed rotor for all analysis, the choice $N = 3$ and the corresponding mathematical description generated by (B.43) and (B.44) may be set in stone now. The $\beta_{N/2}$ degree of freedom may therefore be discarded immediately and only the first harmonics β_{1C} and β_{1S} are retained. These represent tilt of the rotor disc plane about the end of the shaft: the gimballing of the rotor. The gimbal pitch is β_{1C}, positive for pitching downwards, and the gimbal yaw is β_{1S}, positive for the rotor yawing inward toward the wing root.

Similarly, the new degrees of freedom for the lead-lag motion are:

$$\zeta_0 = \frac{1}{N}\sum_{m=1}^{N} \zeta_m \tag{B.45}$$

$$\zeta_{1C} = \frac{2}{N}\sum_{m=1}^{N} \zeta_m \cos\psi_m \tag{B.46}$$

$$\zeta_{1S} = \frac{2}{N}\sum_{m=1}^{N} \zeta_m \sin\psi_m \tag{B.47}$$

Similar to the flapping motion, the choice $N = 3$ excludes higher harmonics of the lead-lag motion. The collective lag mode ζ_0 is simultaneous lagging motion of all the blades (with respect to the hub rotating at constant speed Ω). The cyclic lag modes ζ_{1C} and ζ_{1S} produce rectilinear in-plane motion of the net rotor centre of gravity: laterally for ζ_{1C}, positive in the $-y$ direction (to the left as viewed by the pylon), and vertically for ζ_{1S}, positive in the x direction (upwards). The rotor's cyclic degrees of freedom are illustrated in Figure B.4.

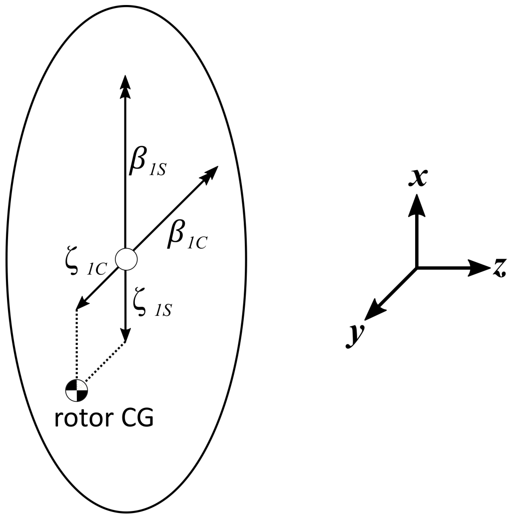

FIGURE B.4. Rotor cyclic degrees of freedom

The usefulness of the Fourier coordinate transformation lies in the simplifications it produces in the equations of motion. The above equations of motion have periodic coefficients because of the nonrotating degrees of freedom in the rotating equations of motion and vice versa; the periodic coefficients only appear explicitly so far with the pylon inertia terms in the flapping equation, but there are actually many more in the aerodynamic forces in all the equations. Since the Fourier coordinate transform converts the rotor degrees of freedom and equations of motion to the nonrotating frame, the result is constant coefficients for the inertia terms, and also for the aerodynamic terms for axial flow through the rotor (as considered here).

In addition, only a limited number of the rotor nonrotating degrees of freedom couple with the pylon degrees of freedom; in this case, only the β_{1C} and β_{1S} degrees of freedom couple with α_y and α_x. The other rotor degrees of freedom are decoupled from the pylon motion and represent only internal rotor motion, that is, motion of the blades relative to each other. Thus the transformation reduced a set of equations with periodic coefficients (the ψ_m terms) to a set with constant coefficients (considering only those influenced by the pylon motion). The rotor behaviour for this problem is basically part of the nonrotating system, so the transformation which converts the rotor degrees of freedom and equations of motion to that frame is the appropriate one.

These degrees of freedom describe the rotor motion as seen in the nonrotating frame, while the β_m terms describe the motion in the rotating hub frame. This coordinate transform must now be implemented in the equations of motion, and summation operators that correspond in form to the new degrees of freedom are introduced to allow the concise summing of the N blade equations:

$$\frac{1}{N}\sum_{m=1}^{N}[\ldots] \tag{B.48}$$

$$\frac{2}{N}\sum_{m=1}^{N}[\ldots\cos\psi_m] \tag{B.49}$$

$$\frac{2}{N}\sum_{m=1}^{N}[\ldots\sin\psi_m] \tag{B.50}$$

where "..." indicates the full contents of the m^{th} blade (flap or lead-lag) equation. To allow summation of the aerodynamic right hand side of the blade equations, the following definitions are now introduced:

$$\bar{M}_{F_0} = \frac{1}{N}\sum_{m=1}^{N}[\bar{M}_{F_m}] \tag{B.51}$$

$$\bar{M}_{F_{1C}} = \frac{2}{N}\sum_{m=1}^{N}[\bar{M}_{F_m}\cos\psi_m] \tag{B.52}$$

$$\bar{M}_{F_{1S}} = \frac{2}{N}\sum_{m=1}^{N}[\bar{M}_{F_m}\sin\psi_m] \tag{B.53}$$

which are the aerodynamic coning, pitch and yaw moments respectively for the flapping degree of freedom. The corresponding quantities for the lead-lag degree of freedom are defined similarly:

$$\bar{M}_{L_0} = \frac{1}{N}\sum_{m=1}^{N}[\bar{M}_{L_m}] \tag{B.54}$$

$$\bar{M}_{L_{1C}} = \frac{2}{N}\sum_{m=1}^{N}[\bar{M}_{L_m}\cos\psi_m] \tag{B.55}$$

$$\bar{M}_{L_{1S}} = \frac{2}{N}\sum_{m=1}^{N}[\bar{M}_{L_m}\sin\psi_m] \tag{B.56}$$

The first of the summation operations (B.48) is applied to both sides of the N blade flapping equations thus:

$$\frac{1}{N}\sum_{m=1}^{N}\left[I_\beta^*(\beta_m''+g_{s_\beta}\sqrt{\nu_\beta^2-1}\,\beta_m'+\nu_\beta^2\beta_m)+I_{\beta\alpha}^*\left(-(\alpha_y''-2\alpha_x')\cos\psi_m+(\alpha_x''+2\alpha_y')\sin\psi_m\right)+S_\beta^* z_P''\right] = \frac{1}{N}\sum_{m=1}^{N}\left[\gamma\frac{\bar{M}_{F_m}}{a\bar{c}}\right]$$

(B.57)
$$\frac{1}{N}\sum_{m=1}^{N}\left[I_\beta^*\beta_m''\right]+\frac{1}{N}\sum_{m=1}^{N}\left[I_\beta^* g_{s_\beta}\sqrt{\nu_\beta^2-1}\,\beta_m'\right]+\frac{1}{N}\sum_{m=1}^{N}\left[I_\beta^*\nu_\beta^2\beta_m\right]-\frac{1}{N}\sum_{m=1}^{N}\left[I_{\beta\alpha}^*(\alpha_y''-2\alpha_x')\cos\psi_m\right]$$
$$+\frac{1}{N}\sum_{m=1}^{N}\left[I_{\beta\alpha}^*(\alpha_x''+2\alpha_y')\sin\psi_m\right]+\frac{1}{N}\sum_{m=1}^{N}\left[S_\beta^* z_P''\right]=\frac{1}{N}\sum_{m=1}^{N}\left[\gamma\frac{\bar{M}_{F_m}}{a\bar{c}}\right]$$

Constants such as the blade inertias (I_β^* etc.) can be brought outside the blade summations. The pylon degrees of freedom (e.g. α_y'') are independent of azimuth position and therefore also behave as constants:

(B.58)
$$I_\beta^*\frac{1}{N}\sum_{m=1}^{N}\left[\beta_m''\right]+I_\beta^* g_{s_\beta}\sqrt{\nu_\beta^2-1}\,\frac{1}{N}\sum_{m=1}^{N}\left[\beta_m'\right]+I_\beta^*\nu_\beta^2\frac{1}{N}\sum_{m=1}^{N}\left[\beta_m\right]-I_{\beta\alpha}^*(\alpha_y''-2\alpha_x')\frac{1}{N}\sum_{m=1}^{N}\left[\cos\psi_m\right]$$
$$+I_{\beta\alpha}^*(\alpha_x''+2\alpha_y')\frac{1}{N}\sum_{m=1}^{N}\left[\sin\psi_m\right]+S_\beta^* z_P''\frac{1}{N}\sum_{m=1}^{N}[1]=\frac{\gamma}{a\bar{c}}\frac{1}{N}\sum_{m=1}^{N}\left[\bar{M}_{F_m}\right]$$

which contains the explicit definitions for the new degrees of freedom β_0 and $\bar{M}_{F_0}$, allowing their substitutions. Furthermore, $\frac{1}{N}\sum_{m=1}^{N}[1]=\frac{1}{N}(1+1+\ldots+1)=\frac{1}{N}N=1$:

$$I_\beta^*\beta_0''+I_\beta^* g_{s_\beta}\sqrt{\nu_\beta^2-1}\,\beta_0'+I_\beta^*\nu_\beta^2\beta_0-I_{\beta\alpha}^*(\alpha_y''-2\alpha_x')\frac{1}{N}\sum_{m=1}^{N}\left[\cos\psi_m\right]$$
$$+I_{\beta\alpha}^*(\alpha_x''+2\alpha_y')\frac{1}{N}\sum_{m=1}^{N}\left[\sin\psi_m\right]+S_\beta^* z_P''=\frac{\gamma}{a\bar{c}}\bar{M}_{F_0} \quad \text{(B.59)}$$

As discussed earlier, the root restraint type for the coning mode β_0 is different to that for the other degrees of freedom, and therefore distinct values for natural frequency ν_{β_0} and inertia $I_{\beta_0}^*$ are permitted. Similarly, different damping coefficients are allowed for the rotor cyclic and collective modes, specifically to account for the collective lag mode and the coning mode of the gimballed rotor:

$$I_{\beta_0}^*\left(\beta_0''+g_{s_{\beta_0}}\sqrt{\nu_{\beta_0}^2-1}\,\beta_0'+\nu_{\beta_0}^2\beta_0\right)-I_{\beta\alpha}^*(\alpha_y''-2\alpha_x')\frac{1}{N}\sum_{m=1}^{N}\left[\cos\psi_m\right]$$
$$+I_{\beta\alpha}^*(\alpha_x''+2\alpha_y')\frac{1}{N}\sum_{m=1}^{N}\left[\sin\psi_m\right]+S_\beta^* z_P''=\frac{\gamma}{a\bar{c}}\bar{M}_{F_0} \quad \text{(B.60)}$$

The trigonometric sums are best understood using a geometrical approach. Consider the related summation of complex numbers on the Argand plane:

$$\sum_{m=1}^{N}\left[e^{j\psi_m}\right] \quad \text{(B.61)}$$

which is of concern here as:

$$\mathrm{Re}\left(e^{j\psi_m}\right)=\cos\psi_m \qquad \text{and} \qquad \mathrm{Im}\left(e^{j\psi_m}\right)=\sin\psi_m$$

Manipulating the summation makes the form of the result clearer:

$$\begin{aligned}\sum_{m=1}^{N}\left[e^{j\psi_m}\right] &= \sum_{m=1}^{N}\left[e^{j(\Omega t+m\frac{2\pi}{N})}\right]\\ &= \sum_{m=1}^{N}\left[e^{j\Omega t}e^{jm\frac{2\pi}{N}}\right]\\ &= e^{j\Omega t}\sum_{m=1}^{N}\left[e^{jm\frac{2\pi}{N}}\right]\end{aligned} \tag{B.62}$$

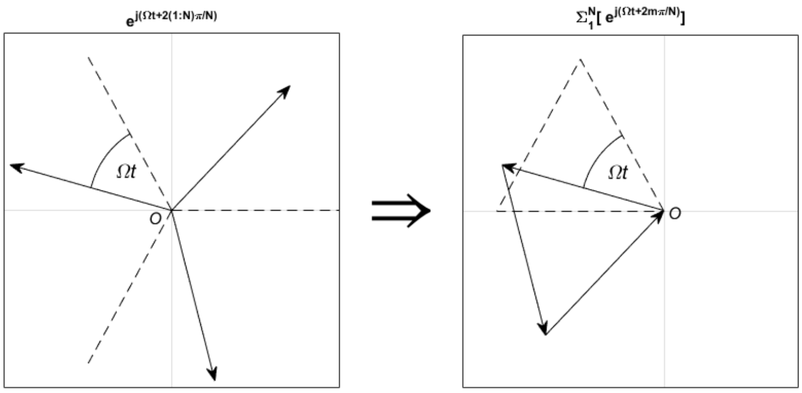

FIGURE B.5. Summation of complex numbers in vector form.

Although the commutativity of addition means that this summation can be done in any order, if the summation is done in sequence of $m = 1...N$ then it can be clearly seen that it amounts to **0** as it forms a closed polygon with N unit-length sides with one vertex at the origin; the factor of $e^{j\Omega t}$ merely rotates the whole polygon about the origin by the angle Ωt and does not affect the value of the sum. It can immediately be seen then that the trigonometric sums $\sum_{m=1}^{N}\left[\cos\psi_m\right]$ and $\sum_{m=1}^{N}\left[\sin\psi_m\right]$ are both are equal to zero as both real and imaginary parts of the sum value are 0. Therefore (B.60) reduces to:

$$I^*_{\beta_0}\left(\beta_0''+g_{s_{\beta_0}}\sqrt{\nu^2_{\beta_0}-1}\,\beta_0'+\nu^2_{\beta_0}\beta_0\right)+S^*_\beta z_P''=\frac{\gamma}{a\bar{c}}\bar{M}_{F_0} \tag{B.63}$$

and this is the equation of motion for the coning (collective flapping) mode. The next summation operator, (B.49), constitutes multiplication of each equation by the cosine of its own ψ_m, summing all equations and multiplying the result by 2. This is applied thus to the flapping equations:

(B.64)

$$\frac{2}{N}\sum_{m=1}^{N}\left[\left(I^*_\beta(\beta_m''+g_{s_\beta}\sqrt{\nu^2_\beta-1}\,\beta_m'+\nu^2_\beta\beta_m)+I^*_{\beta\alpha}\left(-(\alpha_y''-2\alpha_x')\cos\psi_m+(\alpha_x''+2\alpha_y')\sin\psi_m\right)+S^*_\beta z_P''\right)\cos\psi_m\right]$$
$$=\frac{2}{N}\sum_{m=1}^{N}\left[\gamma\frac{\bar{M}_{F_m}}{a\bar{c}}\cos\psi_m\right]$$

Separating summations, distributing the $\cos\psi_m$ terms and bringing constants outside of the summation operators:

$$\text{(B.65)}\quad I^*_\beta \frac{2}{N}\sum_{m=1}^{N}\left[\beta''_m \cos\psi_m\right] + I^*_\beta g_{s_\beta}\sqrt{\nu^2_\beta - 1}\,\frac{2}{N}\sum_{m=1}^{N}\left[\beta'_m \cos\psi_m\right] + I^*_\beta \nu^2_\beta \frac{2}{N}\sum_{m=1}^{N}\left[\beta_m \cos\psi_m\right]$$
$$- I^*_{\beta\alpha}(\alpha''_y - 2\alpha'_x)\frac{2}{N}\sum_{m=1}^{N}\left[\cos^2\psi_m\right]$$
$$+ I^*_{\beta\alpha}(\alpha''_x + 2\alpha'_y)\frac{2}{N}\sum_{m=1}^{N}\left[\sin\psi_m \cos\psi_m\right] + S^*_\beta z''_P \frac{2}{N}\sum_{m=1}^{N}\left[\cos\psi_m\right] = \frac{\gamma}{a\bar{c}}\frac{2}{N}\sum_{m=1}^{N}\left[\bar{M}_{F_m}\cos\psi_m\right]$$

The z''_P term can be removed as $\sum_{m=1}^{N}\left[\cos\psi_m\right] = 0$ as shown previously. Furthermore, the explicit definitions for the new degrees of freedom β_{1C} and $\bar{M}_{F_{1C}}$ are present, allowing their substitutions:

$$\text{(B.66)}\quad I^*_\beta\left(\beta''_{1C} + g_{s_\beta}\sqrt{\nu^2_\beta - 1}\,\beta'_{1C} + \nu^2_\beta \beta_{1C}\right) - I^*_{\beta\alpha}(\alpha''_y - 2\alpha'_x)\frac{2}{N}\sum_{m=1}^{N}\left[\cos^2\psi_m\right]$$
$$+ I^*_{\beta\alpha}(\alpha''_x + 2\alpha'_y)\frac{2}{N}\sum_{m=1}^{N}\left[\sin\psi_m \cos\psi_m\right] = \frac{\gamma}{a\bar{c}}\bar{M}_{F_{1C}}$$

Attention is now turned to the $\frac{2}{N}\sum_{m=1}^{N}\left[\sin\psi_m \cos\psi_m\right]$ term. As this sum is slightly more complex than the summations evaluated above, an intuitive geometric analogy is harder to find. The quantity $\sin\psi_m \cos\psi_m$ is the area of a rectangle swept out corner-to-corner by the corresponding complex vector $e^{j\psi_m}$ within the complex plane. The value of the summation is simply the sum of these areas. However, it is easy to show that the sum of the areas is not necessarily equal to the area swept out by the resultant vector, and with this the analogy collapses. Instead, it is simplest to show the relation between these finite summations and the operation of integration. The summation:

$$\text{(B.67)}\quad \frac{1}{N}\sum_{m=1}^{N}\left[f(\psi_m)\right]$$

effectively finds the average value of the function $f(\psi_m)$ by sampling it at N evenly-spaced points. Within the context of this work, $f(\psi_m)$ is a trigonometric function, and is therefore periodic in ψ_m with a period of 2π. As the sampling points are evenly-spaced due to the definition of the blade azimuth positions, it is also true to say that any sampling scheme is periodic in blade index m with a period of N, the number of blades. Therefore, the summation over $m \in [1, N]$ finds the average value of the function $f(\psi_m)$ over one period $\psi \in [0, 2\pi]$. However, integration can be used as an equivalent continuous method to find the average value of a periodic function over one period T, starting at some value x_0:

$$\text{(B.68)}\quad \frac{1}{T}\int_{x_0}^{x_0+T} f(x)dx$$

The integration itself simply finds the area between the curve of $f(x)$ and the x-axis, while the division by the period T treats the area as rectangle and finds the height given that it is of width

T. Furthermore, the even-spacing condition applies here too: integration, each sampling "strip" has the same infinitesimal width. The following two expressions are therefore analogous:

$$\frac{1}{N}\sum_{m=1}^{N}\left[f(\psi_m)\right] = \frac{1}{2\pi}\int_{x_0}^{2\pi} f(\psi_m)d\psi_m \tag{B.69}$$

Furthermore, the right hand side of (B.69) is equal to the left hand side for the case $\lim_{N\to\infty}$. We can therefore evaluate any discrete summations by use the equivalent integral alternative. Regarding the $\sin\psi_m\cos\psi_m$ summation, we find:

$$\frac{2}{N}\sum_{m=1}^{N}\left[\sin\psi_m\cos\psi_m\right] = \frac{1}{\pi}\int_{x_0}^{2\pi}\left(\sin\psi_m\cos\psi_m\right)d\psi_m = 0 \tag{B.70}$$

and in the same way:

$$\frac{2}{N}\sum_{m=1}^{N}\left[\cos^2\psi_m\right] = \frac{1}{\pi}\int_{0}^{2\pi}\left(\cos^2\psi_m\right)d\psi_m = 1 \tag{B.71}$$

And therefore equation (B.66) reduces to:

$$I_\beta^*\left(\beta_{1C}'' + g_{s_\beta}\sqrt{\nu_\beta^2-1}\,\beta_{1C}' + \nu_\beta^2\beta_{1C}\right) + I_{\beta\alpha}^*(-\alpha_y'' + 2\alpha_x') = \frac{\gamma}{a\bar{c}}\bar{M}_{F_{1C}} \tag{B.72}$$

Applying the similar sine summation operator (B.50) to the blade flapping equations yields a similar result:

$$I_\beta^*\left(\beta_{1S}'' + g_{s_\beta}\sqrt{\nu_\beta^2-1}\,\beta_{1S}' + \nu_\beta^2\beta_{1S}\right) + I_{\beta\alpha}^*(\alpha_x'' + 2\alpha_y') = \frac{\gamma}{a\bar{c}}\bar{M}_{F_{1S}} \tag{B.73}$$

The Coriolis terms to account for the hub plane moving relative to the inertial frame have been added, however another set of Coriolis terms needs to be added to account for the blades spinning within the hub plane. The rotation vector coordinate system $[\hat{\boldsymbol{\beta}}_{1S}, \hat{\boldsymbol{\beta}}_{1C}, \hat{\boldsymbol{\Omega}}]$ is adopted, in line with the definition of the rotor cyclic degrees of freedom shown in Figure B.4. This rotation vector coordinate system is shown in Figure B.6. The rotation vector for the blades $\boldsymbol{\Omega}_{\text{blade}}$ is simply:

$$\boldsymbol{\Omega}_{\text{blade}} = [0,0,1] \tag{B.74}$$

Note that the $\hat{\boldsymbol{\Omega}}$ coordinate of $\boldsymbol{\Omega}_{\text{blade}}$ is 1 rather than Ω as the system has already been normalised by the rotor speed in order to work with nondimensionalised time, as explained before. The angular velocity of the hub within the inertial plane, $\mathbf{v}_{\text{hp}}$, is:

$$\mathbf{v}_{\text{hp}} = \left[\dot\beta_{1S}, \dot\beta_{1C}, 0\right] \tag{B.75}$$

Once again, the Coriolis acceleration, when transferred to the $m\ddot{x}$... side of the equation, is found thus:

$$\begin{aligned}
2\boldsymbol{\Omega}_{\text{blade}} \times \mathbf{v}_{\text{hp}} &= 2\begin{vmatrix} \hat{\boldsymbol{\beta}}_{1S} & \hat{\boldsymbol{\beta}}_{1C} & \hat{\boldsymbol{\Omega}} \\ 0 & 0 & 1 \\ \dot\beta_{1S} & \dot\beta_{1C} & 0 \end{vmatrix} \\
&= 2\left[\left(0-\dot\beta_{1C}\right)\hat{\boldsymbol{\beta}}_{1S} - \left(0-\dot\beta_{1S}\right)\hat{\boldsymbol{\beta}}_{1C} + (0-0)\hat{\boldsymbol{\Omega}}\right] \\
&= 2\left[-\dot\beta_{1C}\hat{\boldsymbol{\beta}}_{1S} + \dot\beta_{1S}\hat{\boldsymbol{\beta}}_{1C}\right] \\
&= -2\dot\beta_{1C}\hat{\boldsymbol{\beta}}_{1S} + 2\dot\beta_{1S}\hat{\boldsymbol{\beta}}_{1C}
\end{aligned} \tag{B.76}$$

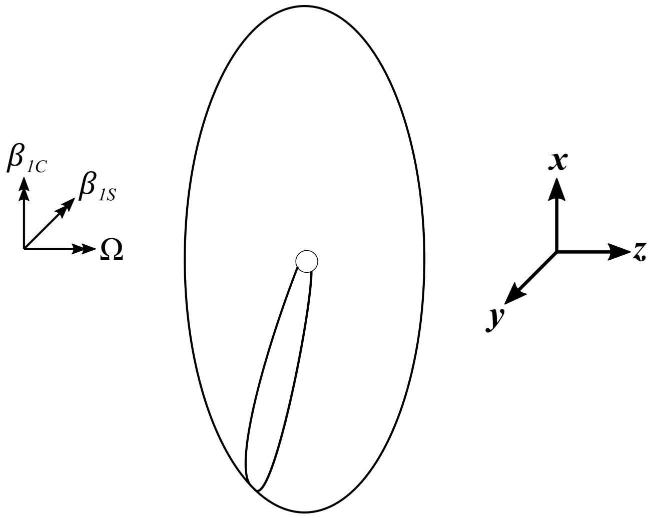

FIGURE B.6. Gimbal coordinate system

That is, a quantity of $2\dot{\beta}_{1S}$ is to be added to the $\bar{M}_{F_{1C}}$ equation, and a quantity of $-2\dot{\beta}_{1C}$ is to be added to the $\bar{M}_{F_{1S}}$ equation.

The centrifugal terms are found via $\boldsymbol{\Omega}_{\text{blade}} \times (\boldsymbol{\Omega}_{\text{blade}} \times \mathbf{R}_{\text{hp}})$ where $\boldsymbol{\Omega}_{\text{blade}}$ is defined as before and $\mathbf{R}_{\text{hp}}$ is the rotation vector of the hub plane:

$$\mathbf{R}_{\text{hp}} = [\beta_{1S}, \beta_{1C}, 0] \tag{B.77}$$

and therefore:

$$\begin{aligned}
\boldsymbol{\Omega}_{\text{blade}} \times \mathbf{R}_{\text{hp}} &= \begin{vmatrix} \hat{\boldsymbol{\beta}}_{1S} & \hat{\boldsymbol{\beta}}_{1C} & \hat{\boldsymbol{\Omega}} \\ 0 & 0 & 1 \\ \beta_{1S} & \beta_{1C} & 0 \end{vmatrix} \\
&= (0-\beta_{1C})\,\hat{\boldsymbol{\beta}}_{1S} - (0-\beta_{1S})\,\hat{\boldsymbol{\beta}}_{1C} + (0-0)\,\hat{\boldsymbol{\Omega}} \\
&= -\beta_{1C}\hat{\boldsymbol{\beta}}_{1S} + \beta_{1S}\hat{\boldsymbol{\beta}}_{1C} \\
&= [-\beta_{1C}, \beta_{1S}, 0]
\end{aligned} \tag{B.78}$$

Consequently:

$$\begin{aligned}
\boldsymbol{\Omega}_{\text{blade}} \times (\boldsymbol{\Omega}_{\text{blade}} \times \mathbf{R}_{\text{hp}}) &= \begin{vmatrix} \hat{\boldsymbol{\beta}}_{1S} & \hat{\boldsymbol{\beta}}_{1C} & \hat{\boldsymbol{\Omega}} \\ 0 & 0 & 1 \\ -\beta_{1C} & \beta_{1S} & 0 \end{vmatrix} \\
&= (0-\beta_{1S})\,\hat{\boldsymbol{\beta}}_{1S} - (0--\beta_{1C})\,\hat{\boldsymbol{\beta}}_{1C} + (0-0)\,\hat{\boldsymbol{\Omega}} \\
&= -\beta_{1S}\hat{\boldsymbol{\beta}}_{1S} - \beta_{1C}\hat{\boldsymbol{\beta}}_{1C}
\end{aligned} \tag{B.79}$$

That is, a quantity of $-\beta_{1C}$ is to be added to the $\bar{M}_{F_{1C}}$ equation, and a quantity of $-\beta_{1S}$ is to be added to the $\bar{M}_{F_{1S}}$ equation. With all these extra terms added, the three inertial frame (i.e.

nonrotating) flapping equations are:

$$I^*_{\beta_0}\left(\beta''_0 + g_{s_{\beta_0}}\sqrt{\nu^2_{\beta_0}-1}\,\beta'_0 + \nu^2_{\beta_0}\beta_0\right) + S^*_\beta z''_P = \frac{\gamma}{a\bar{c}}\bar{M}_{F_0} \tag{B.80}$$

$$I^*_\beta\left(\beta''_{1C} + g_{s_\beta}\sqrt{\nu^2_\beta-1}\,\beta'_{1C} + 2\beta'_{1S} + \left(\nu^2_\beta-1\right)\beta_{1C}\right) + I^*_{\beta\alpha}(-\alpha''_y + 2\alpha'_x) = \frac{\gamma}{a\bar{c}}\bar{M}_{F_{1C}} \tag{B.81}$$

$$I^*_\beta\left(\beta''_{1S} + g_{s_\beta}\sqrt{\nu^2_\beta-1}\,\beta'_{1S} - 2\beta'_{1C} + \left(\nu^2_\beta-1\right)\beta_{1S}\right) + I^*_{\beta\alpha}(\alpha''_x + 2\alpha'_y) = \frac{\gamma}{a\bar{c}}\bar{M}_{F_{1S}} \tag{B.82}$$

The inertial frame lead-lag equations follow in much the same way, via the application of the summation operators on the blade lead-lag equations of motion followed by the addition of Coriolis and centrifugal terms as appropriate:

$$I^*_{\zeta_0}\left(\zeta''_0 + g_{s_{\zeta_0}}\nu_{\zeta_0}\zeta'_0 + \nu^2_{\zeta_0}\zeta_0\right) - I^*_{\zeta_{0\alpha}} z''_P = \frac{\gamma}{a\bar{c}}\bar{M}_{L_0} \tag{B.83}$$

$$I^*_\zeta\left(\zeta''_{1C} + g_{s_\zeta}\nu_\zeta\zeta'_{1C} + 2\zeta'_{1S} + \left(\nu^2_\zeta-1\right)\zeta_{1C}\right) + S^*_\zeta(-y''_P + h\alpha''_x) = \frac{\gamma}{a\bar{c}}\bar{M}_{L_{1C}} \tag{B.84}$$

$$I^*_\zeta\left(\zeta''_{1S} + g_{s_\zeta}\nu_\zeta\zeta'_{1S} - 2\zeta'_{1C} + \left(\nu^2_\zeta-1\right)\zeta_{1S}\right) + S^*_\zeta(x''_P + h\alpha''_y) = \frac{\gamma}{a\bar{c}}\bar{M}_{L_{1S}} \tag{B.85}$$

Note that the equations separate into a lateral/vertical group (subscripts $1C$, $1S$, x, y) and a longitudinal group (0, z), with no inertial coupling between them. This decoupling is maintained by the aerodynamics also (because of the trim axial flow); the shaft motion due to the actual wing degrees of freedom will, in general, couple the two groups of equations.

The hub pitch and yaw moments (in the normalised-time domain) due to the rotor, $\bar{M}_y$ and $\bar{M}_x$ respectively, could be found by integrating the forces on the blade (as is done for the other forces on the hub), but it is simpler to express them directly in terms of the rotor flapping motion. The source of the hub moment is the bending moment at each of the blade roots due to flapping, which for the m^{th} blade is:

$$\bar{M}_m = I_b\left(\nu^2_\beta - 1\right)\beta_m \tag{B.86}$$

Therefore the components of this flapping moment in the pitching and yawing directions are, respectively:

$$\bar{M}_{m_y} = -I_b\left(\nu^2_\beta - 1\right)\beta_m\cos\psi_m \tag{B.87}$$

$$\bar{M}_{m_x} = I_b\left(\nu^2_\beta - 1\right)\beta_m\sin\psi_m \tag{B.88}$$

Note that positive flapping β_m at the top of the disc ($\psi_m = 0$) is in the opposite sense to α_y, hence the negative sign in the $\bar{M}_{m_y}$ equation. Transforming the moment into the nonrotating frame by summing over all N blades gives the hub pitch and yaw moments that are able to be expressed in terms of the existing nonrotating degrees of freedom:

$$\begin{aligned}\bar{M}_y &= \sum_{m=1}^{N}\left[-I_b\left(\nu_\beta^2-1\right)\beta_m\cos\psi_m\right]\\ &= -I_b\left(\nu_\beta^2-1\right)\sum_{m=1}^{N}\left[\beta_m\cos\psi_m\right]\\ &= -I_b\left(\nu_\beta^2-1\right)\frac{N}{2}\beta_{1C}\end{aligned} \tag{B.89}$$

And similarly for hub yawing moment:

$$\bar{M}_x = I_b\left(\nu_\beta^2-1\right)\frac{N}{2}\beta_{1S} \tag{B.90}$$

where the definition of the tip path plane coordinates β_{1C} and β_{1S} has been applied; ν_β is the rotating natural frequency of the flap motion. If the rotor blade has a flap hinge at the centre of rotation, then the only spring restraint of the blade is due to the centrifugal forces, resulting in $\nu_\beta = 1$; in that case, no moment on the hub is produced by tip path plane tilt β_{1C} and β_{1S}, as required for a hinged blade. With hinge offset, hinge spring, or a cantilever root, the natural frequency is greater than 1 per rev and so tip path plane tilt does produce a hub moment. Dividing $\bar{M}_y$ by $\gamma\frac{N}{2}I_b$ gives:

$$\begin{aligned}\frac{\bar{M}_y}{\gamma\frac{N}{2}I_b} &= -\frac{I_b\left(\nu_\beta^2-1\right)\frac{N}{2}\beta_{1C}}{\gamma\frac{N}{2}I_b}\\ &= -\frac{\left(\nu_\beta^2-1\right)}{\gamma}\end{aligned} \tag{B.91}$$

and the LHS can be written in coefficient form. The definition of the rotor pitching moment coefficient C_{M_y} is:

$$C_{M_y} = \frac{M_y}{\rho\pi R^3(\Omega R)^2} \tag{B.92}$$

and therefore:

$$M_y = C_{M_y}\rho\pi R^3(\Omega R)^2 \tag{B.93}$$

Though here M_y is in the dimensional time domain. Conversion is simple:

$$M_y = \Omega^2\bar{M}_y \tag{B.94}$$

or rather

$$\begin{aligned}\bar{M}_y &= \frac{M_y}{\Omega^2}\\ &= \frac{C_{M_y}\rho\pi R^3(\Omega R)^2}{\Omega^2}\\ &= C_{M_y}\rho\pi R^5\end{aligned} \tag{B.95}$$

which can now be substituted into the LHS of (B.91):

$$\begin{aligned}\frac{\bar{M}_y}{\gamma \frac{N}{2} I_b} &= \frac{C_{M_y} \rho \pi R^5}{\gamma \frac{N}{2} I_b} \\ &= \frac{2 C_{M_y} \rho \pi R^5}{\gamma N I_b}\end{aligned} \tag{B.96}$$

Remembering that $\sigma = \frac{Nc}{\pi R}$ we obtain $\frac{\pi}{N} = \frac{c}{\sigma R}$, allowing a substitution:

$$\begin{aligned}\frac{\bar{M}_y}{\gamma \frac{N}{2} I_b} &= \frac{2 C_{M_y} \rho R^5}{\gamma I_b} \frac{c}{\sigma R} \\ &= \frac{2 C_{M_y} \rho R^4}{\gamma I_b} \frac{c}{\sigma} \frac{a}{a} \\ &= \frac{2 C_{M_y}}{\sigma a \gamma} \frac{\rho a c R^4}{I_b} \\ &= \frac{2 C_{M_y}}{\sigma a \gamma} \gamma \\ &= \frac{2 C_{M_y}}{\sigma a}\end{aligned} \tag{B.97}$$

which allows (B.91) to be written thus:

$$\frac{2 C_{M_y}}{\sigma a} = -\frac{\left(\nu_\beta^2 - 1\right)}{\gamma} \tag{B.98}$$

Similarly, for yaw:

$$\frac{2 C_{M_x}}{\sigma a} = \frac{\left(\nu_\beta^2 - 1\right)}{\gamma} \tag{B.99}$$

There are similar inertial contributions to vertical force H, side force Y, thrust T and torque Q, which when written in the nondimensional azimuth time domain are:

$$H_{in} = -\frac{N}{2} S_\zeta \zeta''_{1S} - N M_b \left(x''_P + h \alpha''_y\right) \tag{B.100}$$

$$Y_{in} = \frac{N}{2} S_\zeta \zeta''_{1C} - N M_b \left(y''_P - h \alpha''_x\right) \tag{B.101}$$

$$T_{in} = -N S_{\beta 0} \beta''_0 - N M_b z''_P \tag{B.102}$$

$$Q_{in} = -N I_{\zeta 0 \alpha} \zeta''_0 + N I_b z''_P \tag{B.103}$$

where M_b is the mass of a single rotor blade. When normalised (by I_b), M_b^* is around 3 for a uniform mass distribution, though greater than 3 for usual rotors. The contributions to vertical force H and side force Y are the net in-plane acceleration of the rotor due to the motion of the shaft and blade; similarly, the thrust is the net longitudinal acceleration of the rotor; and the torque, the net angular acceleration.

In a manner similar to before, the coefficient form of these equations can be obtained by dividing the vertical and side forces by $\frac{N}{2}I_b\gamma$ and the thrust and torque by $NI_b\gamma$:

$$\left(\frac{2C_H}{\sigma a}\right)_{in} = -\frac{S^*_\zeta}{\gamma}\zeta''_{1S} - \frac{2}{\gamma}M^*_b\left(x''_P + h\alpha''_y\right) \tag{B.104}$$

$$\left(\frac{2C_Y}{\sigma a}\right)_{in} = \frac{S^*_\zeta}{\gamma}\zeta''_{1C} - \frac{2}{\gamma}M^*_b\left(y''_P + h\alpha''_x\right) \tag{B.105}$$

$$\left(\frac{C_T}{\sigma a}\right)_{in} = -\frac{S^*_{\beta 0}}{\gamma}\beta''_0 - \frac{1}{\gamma}M^*_b z''_P \tag{B.106}$$

$$\left(\frac{C_Q}{\sigma a}\right)_{in} = -\frac{I^*_{\zeta 0\alpha}}{\gamma}\zeta''_0 + \frac{1}{\gamma}\alpha''_z \tag{B.107}$$

B.2.1.4 Aerodynamic terms

Quasi-steady strip theory is used for the aerodynamic elements of the model. A schematic diagram of the air velocities incident on an arbitrary section are shown in Figure B.7.

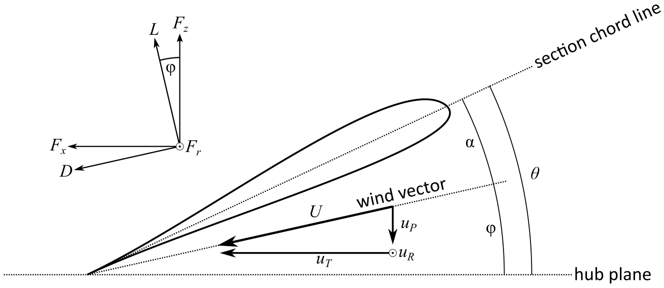

FIGURE B.7. Rotor blade sectional velocities and forces

A hub plane reference frame is used, that is, a coordinate frame fixed to the end of the shaft and tilting with it in pylon pitch and yaw (α_y and α_x respectively). All forces and velocities are resolved with respect to the hub plane coordinate system, and the blade pitch angle and flap angle are measured from the hub plane. The velocities seen by the blade section are u_T (T for tangential, in the hub plane, positive in the blade drag direction), u_P (P for perpendicular, normal to the hub plane, positive rearward through the disc), and u_R (R for radial, in the hub plane, positive outward along the blade). The resultant of u_T and u_P in the blade section plane (i.e. not u_R) is U. At a particular radial station, the blade pitch angle θ relative to the hub plane is composed of collective root pitch (i.e. the setting angle of the blades), built-in twist along the blade span and any increment due to the perturbed blade motion. The inflow angle is $\phi = \arctan \frac{u_P}{u_T}$, measured from the hub plane, and the section angle of attack is $\alpha = \theta - \phi$. The aerodynamic forces on the blade section are lift L, drag D and radial force F_r. As per convention, lift and drag are oriented relative to the airflow rather than the section's chord line, and as such are rotated from the hub plane axes by an angle of ϕ about the radial axis. The radial force is positive outward and has contributions from the tilt of the lift vector due to blade flapping, and from the radial drag due to u_R. The section lift and drag are resolved with respect to the hub plane into normal and in-plane forces F_z and F_x respectively.

As the air velocity – and therefore the aerodynamic forces – vary with radial position, expressions for sectional forces are required that may be integrated along the blade lengths to obtain total forces. The section aerodynamic lift and drag forces L_s and D_s, that is, the lift and drag forces per unit blade length, are expressed in terms of the lift and drag coefficients c_l and c_d:

$$L_s = \frac{1}{2}\rho c \left(u_T^2 + u_P^2\right) c_l = \frac{1}{2}\rho c U^2 c_l \tag{B.108}$$

$$D_s = \frac{1}{2}\rho c \left(u_T^2 + u_P^2\right) c_d = \frac{1}{2}\rho c U^2 c_d \tag{B.109}$$

where the resultant air velocity incident on the section $U = \sqrt{u_T^2 + u_P^2}$. Working with dimensionless quantities from this point on, we obtain dimensionless sectional lift and drag by nondimensionalising air density ρ with itself, blade chord c with rotor radius R, and freestream velocity U with blade tip velocity ΩR, which gives:

$$\bar{L}_s = \frac{1}{2}\frac{\rho}{\rho}\frac{c}{R}\frac{U^2}{(\Omega R)^2} c_l = \frac{L_s}{\rho R (\Omega R)^2} = \frac{1}{2}\bar{c}\bar{U}^2 c_l \tag{B.110}$$

$$\bar{D}_s = \frac{1}{2}\frac{\rho}{\rho}\frac{c}{R}\frac{U^2}{(\Omega R)^2} c_d = \frac{L_s}{\rho R (\Omega R)^2} = \frac{1}{2}\bar{c}\bar{U}^2 c_d \tag{B.111}$$

where $\bar{U}$ denotes nondimensional freestream velocity. The lift and drag coefficients are functions of the section angle of attack α (as defined above) and Mach number M:

$$c_l = c_l(\alpha, M) \tag{B.112}$$

$$c_d = c_d(\alpha, M) \tag{B.113}$$

$$M = \frac{U}{a} = \frac{U}{\Omega R}\frac{\Omega R}{a} = \bar{U} M_{tip} \tag{B.114}$$

where M_{tip} is the tip Mach number: the tip velocity ΩR divided by the speed of sound. The section forces can then be resolved into the hub plane. Taking dimensionless normal force F_z first, the contributing components of $\bar{L}_s$ and $\bar{D}_s$ can be obtained intuitively from Figure B.7:

$$\begin{aligned} \bar{F}_z &= \bar{L}_s \cos\phi - \bar{D}_s \sin\phi \\ &= \bar{L}_s \frac{u_T}{U} - \bar{D}_s \frac{u_P}{U} \end{aligned} \tag{B.115}$$

where trigonometric definitions have been substituted in regarding the inflow angle ϕ . Although the quotients are ultimately nondimensional, it will prove useful later to nondimensionalise both numerator and denominator now:

$$\bar{u}_T = \frac{u_T}{\Omega R} \tag{B.116}$$

$$\bar{u}_P = \frac{u_P}{\Omega R} \tag{B.117}$$

and U is nondimensionalised with tip speed ΩR, as before. Therefore (B.115) can be rewritten:

$$\begin{aligned} \bar{F}_z &= \bar{L}_s \frac{\bar{u}_T}{\bar{U}} - \bar{D}_s \frac{\bar{u}_P}{\bar{U}} \\ &= \frac{\bar{L}_s \bar{u}_T - \bar{D}_s \bar{u}_P}{\bar{U}} \end{aligned} \tag{B.118}$$

The dimensionless in-plane force $\bar{F}_x$ follows in a similar manner:

$$\bar{F}_x = \frac{\bar{L}_s \bar{u}_P + \bar{D}_s \bar{u}_T}{\bar{U}} \tag{B.119}$$

and the dimensionless radial force $\bar{F}_r$ has terms due to radial dag and due to the tilt of $\bar{F}_z$ inward by the flap angle β_m of the blade in question:

$$\begin{aligned} \bar{F}_r &= \frac{\bar{D}_s \bar{u}_R}{\bar{U}} - \sin(\beta_m) \bar{F}_z \\ &\cong \frac{\bar{D}_s \bar{u}_R}{\bar{U}} - \beta_m \bar{F}_z \end{aligned} \tag{B.120}$$

A small angle approximation has been made for the flapping angle. The radial drag term $\frac{\bar{D}_s \bar{u}_R}{\bar{U}}$ is derived assuming that the viscous drag force on the section is in the same direction as the local section velocity. Such a model for the radial drag force is only approximate, but is adequate for proprotors since this term is not important in high inflow aerodynamics. Substituting prior expressions in for $\bar{L}_s$ and $\bar{D}_s$ and dividing by $a\bar{c}$ (where a is the two-dimensional section lift curve slope and $\bar{c}$ is the dimensionless blade section chord) yields, for dimensionless normal force $\bar{F}_z$:

$$\begin{aligned}\frac{\bar{F}_z}{a\bar{c}} &= \frac{1}{a\bar{c}}\frac{\bar{L}_s\bar{u}_T - \bar{D}_s\bar{u}_P}{\bar{U}} \\ &= \frac{\left(\frac{1}{2}\bar{c}\bar{U}^2 c_l\right)\bar{u}_T - \left(\frac{1}{2}\bar{c}\bar{U}^2 c_d\right)\bar{u}_P}{\bar{U}a\bar{c}} \\ &= \frac{\bar{U}c_l\bar{u}_T - \bar{U}c_d\bar{u}_P}{2a} \\ &= \bar{U}\left(\bar{u}_T\frac{c_l}{2a} - \bar{u}_P\frac{c_d}{2a}\right)\end{aligned} \tag{B.121}$$

And similarly for dimensionless in-plane force $\bar{F}_x$:

$$\frac{\bar{F}_x}{a\bar{c}} = \bar{U}\left(\bar{u}_P\frac{c_l}{2a} + \bar{u}_T\frac{c_d}{2a}\right) \tag{B.122}$$

The dimensionless radial force $\bar{F}_r$ is slightly different:

$$\begin{aligned}\frac{\bar{F}_r}{a\bar{c}} &= \frac{1}{a\bar{c}}\left[\frac{\bar{D}_s\bar{u}_R}{\bar{U}} - \beta_m\bar{F}_z\right] \\ &= \frac{1}{a\bar{c}}\left[\frac{\frac{1}{2}\bar{c}\bar{U}^2 c_d\bar{u}_R}{\bar{U}} - \beta_m\bar{F}_z\right] \\ &= \bar{U}\bar{u}_R\frac{c_d}{2a} - \beta_m\frac{\bar{F}_z}{a\bar{c}}\end{aligned} \tag{B.123}$$

The net dimensionless rotor aerodynamic forces and moments are obtained by integrating the section forces over the span of the blade (normalised against R) and summing over all N blades. The dimensionless quantities are thrust $\bar{T}$, rotor vertical force $\bar{H}$, rotor side force $\bar{Y}$, blade flap moment $\bar{M}_{F_m}$, blade lead-lag moment $\bar{M}_{L_m}$ and rotor torque $\bar{Q}$. Note that all these quantities arise from the rotor as a whole, with the exception of the flap moment which refers only to the contribution of the m^{th} blade. These quantities are:

$$\bar{T} = \sum_{m=1}^{N}\left[\int_0^1 \bar{F}_z d\bar{r}\right] \quad \text{(thrust)} \tag{B.124}$$

$$\bar{H} = \sum_{m=1}^{N}\left[\cos\left(\psi_m\right)\int_0^1 \bar{F}_r d\bar{r} + \sin\left(\psi_m\right)\int_0^1 \bar{F}_x d\bar{r}\right] \quad \text{(vertical force)} \tag{B.125}$$

$$\bar{Y} = \sum_{m=1}^{N}\left[\sin\left(\psi_m\right)\int_0^1 \bar{F}_r d\bar{r} - \cos\left(\psi_m\right)\int_0^1 \bar{F}_x d\bar{r}\right] \quad \text{(side force)} \tag{B.126}$$

$$\bar{M}_{F_m} = \int_0^1 \bar{r}\bar{F}_z d\bar{r} \quad \text{(blade flapping moment)} \tag{B.127}$$

(B.128) $$\bar{M}_{L_m} = \int_0^1 \bar{r}\bar{F}_x d\bar{r} \quad \text{(blade lead-lag moment)}$$

(B.129) $$\bar{Q} = \sum_{m=1}^{N} \left[\int_0^1 \bar{r}\bar{F}_x d\bar{r} \right] \quad \text{(torque)}$$

However, in the equations of motion derived thus far, these quantities appear in coefficient form, so the equivalent integrals must be found. To begin with, the dimensional thrust T can be converted to nondimensional thrust $\bar{T}$ by normalising thus:

(B.130) $$\bar{T} = \frac{T}{\rho R^2 (\Omega R)^2}$$

And therefore, with some manipulation:

(B.131) $$\begin{aligned} \bar{T}\frac{1}{Na\bar{c}}\frac{\pi}{\pi} &= \frac{T}{\rho R^2 (\Omega R)^2}\frac{1}{Na\bar{c}}\frac{\pi}{\pi} \\ &= \frac{T}{\rho \pi R^2 (\Omega R)^2}\frac{1}{a}\frac{\pi R}{Nc} \end{aligned}$$

The first term is the explicit definition of the well-recognised thrust coefficient C_T and the last is the explicit definition for σ^{-1}:

(B.132) $$\bar{T}\frac{1}{Na\bar{c}}\frac{\pi}{\pi} = C_T\frac{1}{a}\frac{1}{\sigma} = \frac{C_T}{\sigma a}$$

And combining this with the integral expression for $\bar{T}$ given previously in (B.124):

(B.133) $$\begin{aligned} \frac{C_T}{\sigma a} &= \bar{T}\frac{1}{Na\bar{c}} \\ &= \frac{1}{Na\bar{c}} \sum_{m=1}^{N} \left[\int_0^1 \bar{F}_z d\bar{r} \right] \\ &= \frac{1}{N} \sum_{m=1}^{N} \left[\int_0^1 \frac{\bar{F}_z}{a\bar{c}} d\bar{r} \right] \end{aligned}$$

Similar substitutions follow for $\bar{H}$, $\bar{Y}$, $\bar{M}_{F_m}$, $\bar{M}_{L_m}$ and $\bar{Q}$:

(B.134) $$\frac{2C_H}{\sigma a} = \frac{2}{N} \sum_{m=1}^{N} \left[\cos(\psi_m) \int_0^1 \frac{\bar{F}_r}{a\bar{c}} d\bar{r} + \sin(\psi_m) \int_0^1 \frac{\bar{F}_x}{a\bar{c}} d\bar{r} \right] \quad \text{(vertical force)}$$

(B.135) $$\frac{2C_Y}{\sigma a} = \frac{2}{N} \sum_{m=1}^{N} \left[\sin(\psi_m) \int_0^1 \frac{\bar{F}_r}{a\bar{c}} d\bar{r} - \cos(\psi_m) \int_0^1 \frac{\bar{F}_x}{a\bar{c}} d\bar{r} \right] \quad \text{(side force)}$$

(B.136) $$\frac{\bar{M}_{F_m}}{a\bar{c}} = \int_0^1 \bar{r}\frac{\bar{F}_z}{a\bar{c}} d\bar{r} \quad \text{(blade flapping moment)}$$

(B.137) $$\frac{\bar{M}_{L_m}}{a\bar{c}} = \int_0^1 \bar{r}\frac{\bar{F}_x}{a\bar{c}} d\bar{r} \quad \text{(blade lead-lag moment)}$$

$$\frac{C_Q}{\sigma a} = \frac{1}{N}\sum_{m=1}^{N}\left[\int_0^1 \bar{r}\frac{\bar{F}_x}{a\bar{c}}d\bar{r}\right] \quad \text{(torque)} \tag{B.138}$$

Which neatly gives the dimensionless force terms a factor of $\frac{1}{a\bar{c}}$ as obtained previously in (B.121) to (B.123), which give the sectional forces (e.g. $\bar{F}_z$ etc.) in terms of the sectional velocities. These expressions can be substituted into the per-blade summing integrals to obtain the total force or moment for a whole blade:

$$\int_0^1 \frac{\bar{F}_z}{a\bar{c}}d\bar{r} = \int_0^1 \bar{U}\left(\bar{u}_T\frac{c_l}{2a} - \bar{u}_P\frac{c_d}{2a}\right) \quad \text{(normal force)} \tag{B.139}$$

$$\int_0^1 \frac{\bar{F}_x}{a\bar{c}}d\bar{r} = \int_0^1 \bar{U}\left(\bar{u}_P\frac{c_l}{2a} + \bar{u}_T\frac{c_d}{2a}\right) \quad \text{(in-plane force)} \tag{B.140}$$

$$\int_0^1 \frac{\bar{F}_r}{a\bar{c}} = \int_0^1 \left[\bar{U}\bar{u}_R\frac{c_d}{2a} - \beta_m\frac{\bar{F}_z}{a\bar{c}}\right] = \int_0^1 \bar{U}\bar{u}_R\frac{c_d}{2a}d\bar{r} - \beta_m\int_0^1 \frac{\bar{F}_z}{a\bar{c}} \quad \text{(radial force)} \tag{B.141}$$

$$\int_0^1 \bar{r}\frac{\bar{F}_z}{a\bar{c}}d\bar{r} = \int_0^1 \bar{r}\bar{U}\left(\bar{u}_T\frac{c_l}{2a} - \bar{u}_P\frac{c_d}{2a}\right) \quad \text{(flapping moment)} \tag{B.142}$$

$$\int_0^1 \bar{r}\frac{\bar{F}_x}{a\bar{c}}d\bar{r} = \int_0^1 \bar{r}\bar{U}\left(\bar{u}_P\frac{c_l}{2a} + \bar{u}_T\frac{c_d}{2a}\right) \quad \text{(torque)} \tag{B.143}$$

Note that each of these integrals computes the contributions from the m^{th} blade. There is the net blade force normal to the hub plane i.e. thrust (B.139), the net blade force in the hub plane i.e. blade drag force (B.140), the net blade radial force (B.141), the moment about the hub created by the blade thrust i.e. the flapping moment (B.142), and the moment about the hub of the blade's net drag force i.e. the drag torque (B.143).

To evaluate these blade force and moment expressions, the blade section pitch angle θ and the velocity components at the blade section are required. Each velocity component has a trim term (additional subscript 'T') and a perturbation term (prefixed with δ), the latter due to the movement caused by activity in the blade and pylon degrees of freedom, and any gusts present:

$$u_T = u_{TT} + \delta u_T \tag{B.144}$$

$$u_P = u_{PT} + \delta u_P \tag{B.145}$$

$$u_R = u_{RT} + \delta u_R \tag{B.146}$$

When the differential equations of motion are linearised, the perturbation components of the velocity are assumed to be small. The trim velocity components for a blade section at radial station r for operation in purely axial flow are:

$$u_{TT} = \Omega r \tag{B.147}$$

(B.148)
$$u_{PT} = V + v$$

(B.149)
$$u_{RT} = 0$$

The velocity u_{TT} is due to the rotation of the blade, and inflow u_{PT} is composed of the forward velocity V plus the induced inflow v. In the trim condition, the rotor is operating in purely axial flow and there is therefore no radial velocity component. The trim resultant air velocity incident on an arbitrary section, U_T, is therefore:

(B.150)
$$U_T = \sqrt{u_{TT}^2 + u_{PT}^2}$$

As before, all speeds are nondimensionalised by tip speed ΩR, giving:

(B.151)
$$\bar{u}_{TT} = \frac{u_{TT}}{\Omega R} = \frac{\Omega r}{\Omega R} = \bar{r}$$

(B.152)
$$\bar{u}_{PT} = \frac{u_{PT}}{\Omega R} = \frac{V + v}{\Omega R} = \mu + \bar{v}$$

(B.153)
$$\bar{u}_{RT} = \frac{u_{RT}}{\Omega R} = \frac{0}{\Omega R} = 0$$

(B.154)
$$\bar{U}_T = \frac{U_T}{\Omega R} = \frac{\sqrt{u_{TT}^2 + u_{PT}^2}}{\Omega R} = \sqrt{\bar{u}_{TT}^2 + \bar{u}_{PT}^2} = \sqrt{\bar{r}^2 + (\mu + \bar{v})^2}$$

Although defining nondimensional forward velocity $\bar{V} = \frac{V}{\Omega R}$ would give consistency with the other nondimensional nomenclature used, this quantity is the definition of the well-known advance ratio μ and therefore this symbol is used instead. Note also the dimensionless induced inflow $\bar{v} = \frac{v}{\Omega R}$. Momentum theory gives the latter to be:

(B.155)
$$\bar{v} = -\frac{\mu}{2} + \sqrt{\left(\frac{\mu}{2}\right)^2 + \frac{C_T}{2}}$$

Or alternatively:

$$\begin{aligned}
\bar{v} &= -\frac{\mu}{2} + \mu\sqrt{\left(\frac{\mu}{2\mu}\right)^2 + \frac{C_T}{2\mu^2}} \\
&= -\frac{\mu}{2} + \mu\sqrt{\left(\frac{1}{2}\right)^2 + \frac{C_T}{2\mu^2}}
\end{aligned}$$

If high inflow (i.e. large μ) is assumed, then the following expansion can be used with the $\left(\frac{C_T}{2\mu^2}\right)^2$ term being small enough to neglect:

$$\bar{v} \cong -\frac{\mu}{2} + \mu\sqrt{\left(\frac{1}{2} + \frac{C_T}{2\mu^2}\right)^2}$$

and this allows:

$$\begin{aligned}\bar{v} &\cong -\frac{\mu}{2} + \mu\left(\frac{1}{2} + \frac{C_T}{2\mu^2}\right)\\ &\cong \frac{C_T}{2\mu^2}\end{aligned}$$

The induced inflow $\bar{v}$ will, in fact, be very small (i.e. $\frac{\bar{v}}{\mu} << 1$) for typical proprotor operation; this is due to the high inflow μ and the low working C_T of a proprotor in cruise. Consequently, induced inflow is generally not an important factor in high inflow proprotor aerodynamics, and the assumption of uniform induced inflow, or even neglecting it entirely, is reasonable for an investigation of the rotor aeroelastic behaviour. The term is therefore dropped from the algebra from this point forwards and forward airspeed incident on the rotor is taken to be solely μ.

The trim blade pitch angle θ_T is determined by the setting angle of the blades on the rotor and the blade built-in twist. The perturbation velocities are due to motion caused by the rotor

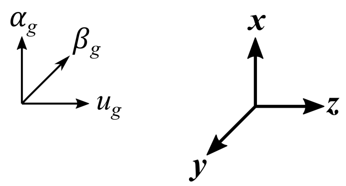

FIGURE B.8. Gust velocities coordinate system

and pylon degrees of freedom, and aerodynamic gusts. The axis convention used for these gust velocities is shown in Figure B.8 and the gust velocity vector $\mathbf{v}_g$ is:

$$\mathbf{v}_g = \left[\alpha_g \hat{\boldsymbol{\alpha}}_g, \beta_g \hat{\boldsymbol{\beta}}_g, u_g \hat{\mathbf{u}}_g\right] \tag{B.156}$$

Note that the lateral gust $\hat{\boldsymbol{\beta}}_g$ is in the opposite sense to the global y axis. The gust velocities are normalised by forward speed V:

$$\bar{\alpha}_g = \frac{\alpha_g}{V} \tag{B.157}$$

$$\bar{\beta}_g = \frac{\beta_g}{V} \tag{B.158}$$

$$\bar{u}_g = \frac{u_g}{V} \tag{B.159}$$

Such that:

$$\mathbf{v}_g = \left[V\bar{\alpha}_g \hat{\boldsymbol{\alpha}}_g, V\bar{\beta}_g \hat{\boldsymbol{\beta}}_g, V\bar{u}_g \hat{\mathbf{u}}_g\right] \tag{B.160}$$

Or, nondimensionally, as used later:

(B.161)
$$\bar{\mathbf{v}}_g = \left[\mu\bar{\alpha}_g\hat{\boldsymbol{\alpha}}_g, \mu\bar{\beta}_g\hat{\boldsymbol{\beta}}_g, \mu\bar{u}_g\hat{\mathbf{u}}_g\right]$$

And therefore the axial component $\bar{u}_g$ is a fractional change in forward speed μ, while $\bar{\alpha}_g$ and $\bar{\beta}_g$ are – following the application of a small angle assumption – angles at which the freestream velocity is incident upon the axes due to the presence of upward and sideways gusts. For instance, if the resultant angle of attack of the incident freestream velocity due to forward speed V and upward gust velocity $V\alpha_g$ denoted γ_α, then by simple trigonometry:

(B.162)
$$\tan\left(\gamma_\alpha\right) \cong \gamma_\alpha = \frac{V\bar{\alpha}_g}{V} = \bar{\alpha}_g$$

This convention follows the usual practice for aircraft stability and control investigations. The gust velocities are a small perturbation to the direction and magnitude of the forward velocity V, assumed uniform over the entire flow field. The gust influence is entirely aerodynamic; the gust velocities do not involve a change of the aircraft velocity with respect to the inertial frame, but only a change with respect to the air. Therefore, the gust velocities do not appear in the inertia terms of the equations of motion, but only in the aerodynamic terms.

Returning to the rotor blade section, the perturbation velocities (already nondimensionalised by ΩR for convenience) are:

(B.163)
$$\begin{aligned}\delta\bar{u}_T =& \bar{r}\left(\alpha_z' - \zeta_m'\right) - \bar{h}\left(\alpha_y'\sin\psi_m + \alpha_x'\cos\psi_m\right) + \mu\left(\alpha_y\sin\psi_m + \alpha_x\cos\psi_m\right)\\ &+ \mu\left(\bar{\beta}_g\cos\psi_m + \bar{\alpha}_g\sin\psi_m\right) + \left(y_P'\cos\psi_m - x_P'\sin\psi_m\right)\end{aligned}$$

(B.164)
$$\delta\bar{u}_P = \bar{r}\left(\beta_m' - \alpha_y'\cos\psi_m + \alpha_x'\sin\psi_m\right) + \mu\bar{u}_g + z_P'$$

(B.165)
$$\begin{aligned}\delta\bar{u}_R =& \bar{h}\left(-\alpha_y'\cos\psi_m + \alpha_x'\sin\psi_m\right) + \mu\left(\alpha_y\cos\psi_m - \alpha_x\sin\psi_m\right)\\ &+ \mu\left(-\bar{\beta}_g\sin\psi_m + \bar{\alpha}_g\cos\psi_m\right) - \left(y_P'\sin\psi_m + x_P'\cos\psi_m\right)\end{aligned}$$

The terms in these equations have a variety of sources. There are in-plane hub velocities due to the angular velocity of the pylon about the pivot (α_y' and α_x'; second term in $\delta\bar{u}_T$ and first term in $\delta\bar{u}_R$), in-plane components of the forward velocity (μ) due to the tilt of the pylon (third term in $\delta\bar{u}_T$ and second term in $\delta\bar{u}_R$), and in-plane velocities due to vertical lateral gusts (fourth term in $\delta\bar{u}_T$ and third term in $\delta\bar{u}_R$). Furthermore, the first term of $\delta\bar{u}_T$ is a further in-plane component arising from additional rotation of the blades induced by lead-lag motion and shaft axial rotation (note that this term is proportional to radial position $\bar{r}$). The last term in each expression arises from translational motion of the shaft.

In $\delta\bar{u}_P$ the first two terms are: flapwise velocity with respect to the air, due to both flapping with respect to the shaft and angular velocity of the shaft itself (proportional to radial position $\bar{r}$); and longitudinal gusts (note that this term is independent of $\bar{r}$).

As both $\delta\bar{u}_T$ and $\delta\bar{u}_P$ contain terms proportional to $\bar{r}$, useful simplifications later on will become possible if they are written in the following form:

$$\delta\bar{u}_T = \bar{r}\delta\bar{u}_{T1} + \delta\bar{u}_{T2} \tag{B.166}$$

$$\delta\bar{u}_P = \bar{r}\delta\bar{u}_{P1} + \delta\bar{u}_{P2} \tag{B.167}$$

as $\delta\bar{u}_{T1}$, $\delta\bar{u}_{T2}$, $\delta\bar{u}_R$, $\delta\bar{u}_{P1}$ and $\delta\bar{u}_{P2}$ are all independent of $\bar{r}$ and may therefore be factored out of the integrands in the aerodynamic forces.

The blade pitch angle θ is also expressed in the format of trim and perturbation terms:

$$\theta = \theta_T + \delta\theta \tag{B.168}$$

As stated earlier, the trim term θ_T is the sum of the root setting angle of the blades and any built-in twist along the span. The perturbation term $\delta\theta$ is the sum of the any dynamic control of the pitch of a given blade (both cyclic and collective) plus any additional pitching of an individual blade in question due to pitch-flap coupling with that blade's current flapping angle β_m. Therefore the perturbation of the blade pitch $\delta\theta_m$ of the m^{th} blade:

$$\delta\theta_m = \theta_{C_m} - K_P\beta_m \tag{B.169}$$

Where θ_{C_m} is control of the pitch of the m^{th} blade, an input variable in the equations of motion, also available for feedback control. Since this pitch perturbation is made through the control system and supplied at the blade root, it is uniform over the blade span (independent of $\bar{r}$). The second term is the pitch-flap coupling, with K_P the gain of the negative feedback of blade flap angle to pitch angle. This feedback is usually accomplished by mechanical means inherent in the control system geometry; it is usually referred to as δ_3 coupling, where $K_P = \tan\delta_3$. As the section velocities are expressed in terms of a trim component and a perturbation component, quantities that are functions of them that appear in the integrals (e.g. α, which is a function of u_T, u_P and θ) consequently also have a trim component and a perturbation component. For instance, for sectional lift coefficient:

$$c_l = c_{lT} + \delta c_l \tag{B.170}$$

Expressions for the perturbation components of quantities such as α are now formed. The general expression for infinitesimal change in a quantity F that is a function of variables x_1, x_2 etc., arising from infinitesimal changes in those variables, is:

$$\delta F = \frac{\partial F}{\partial x_1}\delta x_1 + \frac{\partial F}{\partial x_2}\delta x_2 + ... \tag{B.171}$$

As all perturbations in this system are assumed to be small, the formula (B.171) is assumed to be adequate for describing those perturbations that are functions of other quantities.

As stated before, the lift and drag coefficients are functions of angle of attack α and Mach number M, so their expressions are fairly straightforward:

(B.172) $$\delta c_l = \frac{\partial c_l}{\partial \alpha}\delta\alpha + \frac{\partial c_l}{\partial M}\delta M$$

(B.173) $$\delta c_d = \frac{\partial c_d}{\partial \alpha}\delta\alpha + \frac{\partial c_d}{\partial M}\delta M$$

Perturbation in Mach number M is quite simple:

(B.174) $$\delta M = M_{tip}\delta\bar{U}$$

And therefore:

(B.175) $$\delta c_l = \frac{\partial c_l}{\partial \alpha}\delta\alpha + \frac{\partial c_l}{\partial M}M_{tip}\delta\bar{U}$$

(B.176) $$\delta c_d = \frac{\partial c_d}{\partial \alpha}\delta\alpha + \frac{\partial c_d}{\partial M}M_{tip}\delta\bar{U}$$

The perturbation in angle of attack $\delta\alpha$ requires more working. Considering the definition of α:

(B.177) $$\alpha = \theta - \phi$$

then:

(B.178) $$\delta\alpha = \delta\theta - \delta\phi$$

From the schematic we have defined:

(B.179) $$\phi = \arctan\left(\frac{\bar{u}_P}{\bar{u}_T}\right)$$

therefore:

(B.180) $$\delta\phi = \frac{\partial\phi}{\partial\bar{u}_P}\delta\bar{u}_P + \frac{\partial\phi}{\partial\bar{u}_T}\delta\bar{u}_T$$

Which may be solved if a temporary intermediate variable C is defined thus:

(B.181) $$C = \frac{\bar{u}_P}{\bar{u}_T} \Rightarrow \phi = \arctan C$$

And this allows:

(B.182) $$\frac{\partial\phi}{\partial\bar{u}_P} = \frac{\partial\phi}{\partial C}\frac{\partial C}{\partial\bar{u}_P}$$

with a similar expression for $\frac{\partial\phi}{\partial\bar{u}_T}$. Firstly:

(B.183) $$\begin{aligned}\frac{\partial\phi}{\partial C} &= \frac{1}{1+C^2}\\ &= \frac{1}{1+\left(\frac{\bar{u}_P}{\bar{u}_T}\right)^2}\\ &= \frac{\bar{u}_T^2}{\bar{u}_T^2+\bar{u}_P^2}\end{aligned}$$

Furthermore:

$$\frac{\partial C}{\partial \bar{u}_P} = \frac{1}{\bar{u}_T} \tag{B.184}$$

$$\frac{\partial C}{\partial \bar{u}_T} = -\frac{\bar{u}_P}{\bar{u}_T^2} \tag{B.185}$$

and therefore:

$$\begin{aligned}
\delta\phi &= \frac{\partial\phi}{\partial C}\frac{\partial C}{\partial \bar{u}_P}\delta\bar{u}_P + \frac{\partial\phi}{\partial C}\frac{\partial C}{\partial \bar{u}_T}\delta\bar{u}_T \\
&= \frac{\partial\phi}{\partial C}\left(\frac{\partial C}{\partial \bar{u}_P}\delta\bar{u}_P + \frac{\partial C}{\partial \bar{u}_T}\delta\bar{u}_T\right) \\
&= \frac{\bar{u}_T^2}{\bar{u}_T^2+\bar{u}_P^2}\left(\frac{1}{\bar{u}_T}\delta\bar{u}_P - \frac{\bar{u}_P}{\bar{u}_T^2}\delta\bar{u}_T\right) \\
&= \frac{1}{\bar{u}_T^2+\bar{u}_P^2}\left(\bar{u}_T\delta\bar{u}_P - \bar{u}_P\delta\bar{u}_T\right)
\end{aligned} \tag{B.186}$$

And as $\bar{U}^2 = \bar{u}_T^2 + \bar{u}_P^2$:

$$\delta\phi = \frac{\bar{u}_T\delta\bar{u}_P - \bar{u}_P\delta\bar{u}_T}{\bar{U}^2} \tag{B.187}$$

Substituting into (B.178) gives:

$$\delta\alpha = \delta\theta - \frac{\bar{u}_T\delta\bar{u}_P - \bar{u}_P\delta\bar{u}_T}{\bar{U}^2} \tag{B.188}$$

The (normalised) velocity perturbation $\delta\bar{U}$ is:

$$\delta\bar{U} = \frac{\partial\bar{U}}{\partial\bar{u}_P}\delta\bar{u}_P + \frac{\partial\bar{U}}{\partial\bar{u}_T}\delta\bar{u}_T \tag{B.189}$$

Defining a temporary variable C thus:

$$C = \bar{U}^2 \Rightarrow C = \bar{u}_T^2 + \bar{u}_P^2 \tag{B.190}$$

allows:

$$\frac{\partial\bar{U}}{\partial\bar{u}_P} = \frac{\partial\bar{U}}{\partial C}\frac{\partial C}{\partial\bar{u}_P} \tag{B.191}$$

with a similar expression for $\frac{\partial\phi}{\partial\bar{u}_T}$. Evaluating the constituent terms:

$$\frac{\partial\bar{U}}{\partial C} = \frac{1}{2\bar{U}} \tag{B.192}$$

$$\frac{\partial C}{\partial\bar{u}_P} = 2\bar{u}_P \tag{B.193}$$

$$\frac{\partial C}{\partial \bar{u}_T} = 2\bar{u}_T \tag{B.194}$$

Therefore we have:

$$\begin{aligned}
\delta\bar{U} &= \frac{\partial \bar{U}}{\partial C}\left(\frac{\partial C}{\partial \bar{u}_P}\delta\bar{u}_P + \frac{\partial C}{\partial \bar{u}_T}\delta\bar{u}_T\right) \\
&= \frac{1}{2\bar{U}}\left(2\bar{u}_P\delta\bar{u}_P + 2\bar{u}_T\delta\bar{u}_T\right) \\
&= \frac{\bar{u}_P\delta\bar{u}_P + \bar{u}_T\delta\bar{u}_T}{\bar{U}}
\end{aligned} \tag{B.195}$$

Note that, for simplicity, where quantities appear as constituent terms in these perturbation expressions, they are evaluated using only their trim components rather than their full expression involving the perturbation component also. For instance, where $\bar{u}_P$ appears, $\bar{u}_{PT}$ is intended rather than $\bar{u}_{PT} + \delta\bar{u}_P$ and the same goes for all other quantities. Strictly speaking then, (B.188) and (B.195) are therefore written:

$$\delta\alpha = \delta\theta - \frac{\bar{u}_{TT}\delta\bar{u}_P - \bar{u}_{PT}\delta\bar{u}_T}{\bar{U}_T^2} \tag{B.196}$$

$$\delta\bar{U} = \frac{\bar{u}_{PT}\delta\bar{u}_P + \bar{u}_{TT}\delta\bar{u}_T}{\bar{U}_T} \tag{B.197}$$

Returning to the per-blade aerodynamic integrals (B.139 - B.143), the full expressions (i.e. trim + perturbation) for each quantity can be substituted in, and the expressions for $\delta\alpha$ and $\delta\bar{U}$ may then subsequently substituted in. The resulting expressions are then entirely in terms of the trim and perturbation components of the sectional velocities and the blade pitch angle θ, and can be expanded as a linear combination of them. Applying this first to the thrust integral (B.139):

(B.198)

$$\begin{aligned}
\int_0^1 \frac{\bar{F}_z}{a\bar{c}}d\bar{r} &= \int_0^1 \left(\bar{U}_T + \delta\bar{U}\right)\left((\bar{u}_{TT} + \delta\bar{u}_T)\frac{(c_{lT} + \delta c_l)}{2a} - (\bar{u}_{PT} + \delta\bar{u}_P)\frac{(c_{dT} + \delta c_d)}{2a}\right) \\
&= \int_0^1 \left(\bar{U}_T + \delta\bar{U}\right)\left((\bar{u}_{TT} + \delta\bar{u}_T)\frac{(c_{lT} + \frac{\partial c_l}{\partial \alpha}\delta\alpha + \frac{\partial c_l}{\partial M}M_{tip}\delta\bar{U})}{2a} - (\bar{u}_{PT} + \delta\bar{u}_P)\frac{(c_{dT} + \frac{\partial c_d}{\partial \alpha}\delta\alpha + \frac{\partial c_d}{\partial M}M_{tip}\delta\bar{U})}{2a}\right)
\end{aligned}$$

However, before the expression becomes unwieldy, some simplification is possible before going any further. As the perturbations are assumed to be small, it is assumed that in expanding this expression, terms that are products of two or more perturbation quantities are assumed to be small enough to be neglected. For the sake of clarity, the c_l and c_d parts are considered separately. Examining the c_l part of (B.198) first:

$$\int_0^1 \left(\frac{c_{lT}}{2a}\left(\bar{U}_T\bar{u}_{TT} + \delta\bar{U}\bar{u}_{TT} + \bar{U}_T\delta\bar{u}_T\right) + \frac{\partial c_l}{\partial \alpha}\frac{\delta\alpha}{2a}\bar{U}_T\bar{u}_{TT} + \frac{\partial c_l}{\partial M}\frac{M_{tip}\delta\bar{U}}{2a}\bar{U}_T\bar{u}_{TT}\right)d\bar{r} \tag{B.199}$$

Separating terms further:

$$\int_0^1 \frac{c_{lT}}{2a}\bar{U}_T\bar{u}_{TT}d\bar{r} + \int_0^1 \frac{c_{lT}}{2a}\delta\bar{U}\bar{u}_{TT}d\bar{r} + \int_0^1 \frac{c_{lT}}{2a}\bar{U}_T\delta\bar{u}_T d\bar{r} + \int_0^1 \frac{\partial c_l}{\partial\alpha}\frac{\delta\alpha}{2a}\bar{U}_T\bar{u}_{TT}d\bar{r} + \int_0^1 \frac{\partial c_l}{\partial M}\frac{M_{tip}\delta\bar{U}}{2a}\bar{U}_T\bar{u}_{TT}d\bar{r} \tag{B.200}$$

The definition of $\delta\bar{U}$ as given by (B.196) can be substituted into the second integral of the above equation:

$$\begin{aligned}\int_0^1 \frac{c_{lT}}{2a}\delta\bar{U}\bar{u}_{TT}d\bar{r} &= \int_0^1 \frac{c_{lT}}{2a}\frac{\bar{u}_{PT}\delta\bar{u}_P + \bar{u}_{TT}\delta\bar{u}_T}{\bar{U}_T}\bar{u}_{TT}d\bar{r}\\ &= \int_0^1 \frac{c_{lT}}{2a}\frac{\bar{u}_{PT}\delta\bar{u}_P}{\bar{U}_T}\bar{u}_{TT}d\bar{r} + \int_0^1 \frac{c_{lT}}{2a}\frac{\bar{u}_{TT}\delta\bar{u}_T}{\bar{U}_T}\bar{u}_{TT}d\bar{r}\end{aligned} \tag{B.201}$$

and also into the last integral:

$$\begin{aligned}\int_0^1 \frac{\partial c_l}{\partial M}\frac{M_{tip}\delta\bar{U}}{2a}\bar{U}_T\bar{u}_{TT}d\bar{r} &= \int_0^1 \frac{\partial c_l}{\partial M}\frac{M_{tip}\frac{\bar{u}_{PT}\delta\bar{u}_P + \bar{u}_{TT}\delta\bar{u}_T}{\bar{U}_T}}{2a}\bar{U}_T\bar{u}_{TT}d\bar{r}\\ &= \int_0^1 \frac{\partial c_l}{\partial M}\frac{M_{tip}}{2a}\frac{\bar{u}_{PT}\delta\bar{u}_P}{\bar{U}_T}\bar{U}_T\bar{u}_{TT}d\bar{r} + \int_0^1 \frac{\partial c_l}{\partial M}\frac{M_{tip}}{2a}\frac{\bar{u}_{TT}\delta\bar{u}_T}{\bar{U}_T}\bar{U}_T\bar{u}_{TT}d\bar{r}\end{aligned} \tag{B.202}$$

Similarly the definition of $\delta\alpha$ can now be substituted in to the fourth integral of (B.200):

$$\begin{aligned}\int_0^1 \frac{\partial c_l}{\partial\alpha}\frac{\delta\alpha}{2a}\bar{U}_T\bar{u}_{TT}d\bar{r} &= \int_0^1 \frac{\partial c_l}{\partial\alpha}\frac{\delta\theta - \frac{\bar{u}_{TT}\delta\bar{u}_P - \bar{u}_{PT}\delta\bar{u}_T}{\bar{U}_T^2}}{2a}\bar{U}_T\bar{u}_{TT}d\bar{r}\\ &= \int_0^1 \frac{\partial c_l}{\partial\alpha}\frac{\delta\theta}{2a}\bar{U}_T\bar{u}_{TT}d\bar{r} - \int_0^1 \frac{\partial c_l}{\partial\alpha}\frac{\bar{u}_{TT}\delta\bar{u}_P}{2a\bar{U}_T^2}\bar{U}_T\bar{u}_{TT}d\bar{r} + \int_0^1 \frac{\partial c_l}{\partial\alpha}\frac{\bar{u}_{PT}\delta\bar{u}_T}{2a\bar{U}_T^2}\bar{U}_T\bar{u}_{TT}d\bar{r}\end{aligned} \tag{B.203}$$

Now (B.199) can be expressed purely in terms of the trim and perturbation components of the sectional velocities and the blade pitch angle θ. This allows all the terms to be collected according to which type of trim or perturbation quantity they contain:

$$\begin{aligned}&\int_0^1 \frac{c_{lT}}{2a}\bar{U}_T\bar{u}_{TT}d\bar{r} + \int_0^1 \left[\frac{c_{lT}}{2a}\left(\frac{\bar{u}_{TT}^2}{\bar{U}_T} + \bar{U}_T\right) + \frac{\partial c_l}{\partial\alpha}\frac{\bar{U}_T\bar{u}_{TT}\bar{u}_{PT}}{2a\bar{U}_T^2} + \frac{\partial c_l}{\partial M}\frac{M_{tip}}{2a}\frac{\bar{u}_{TT}}{\bar{U}_T}\bar{U}_T\bar{u}_{TT}\right]\delta\bar{u}_T d\bar{r}\\ &+ \int_0^1 \left[\frac{c_{lT}}{2a}\frac{\bar{u}_{PT}\bar{u}_{TT}}{\bar{U}_T} - \frac{\partial c_l}{\partial\alpha}\frac{\bar{U}_T\bar{u}_{TT}^2}{2a\bar{U}_T^2} + \frac{\partial c_l}{\partial M}\frac{M_{tip}}{2a}\frac{\bar{u}_{PT}}{\bar{U}_T}\bar{U}_T\bar{u}_{TT}\right]\delta\bar{u}_P d\bar{r} + \int_0^1 \frac{\partial c_l}{\partial\alpha}\frac{\delta\theta}{2a}\bar{U}_T\bar{u}_{TT}d\bar{r}\end{aligned} \tag{B.204}$$

And finally, making the substitutions $\delta\bar{u}_T = \bar{r}\delta\bar{u}_{T1} + \delta\bar{u}_{T2}$ and $\delta\bar{u}_P = \bar{r}\delta\bar{u}_{P1} + \delta\bar{u}_{P2}$ allows a representation where all perturbation quantities are independent of $\bar{r}$, as stated earlier:

(B.205)
$$\begin{aligned}
&\int_0^1 \frac{c_{lT}}{2a}\bar{U}_T\bar{u}_{TT}d\bar{r} + \int_0^1 \bar{r}\left[\frac{c_{lT}}{2a}\left(\frac{\bar{u}_{TT}^2}{\bar{U}_T}+\bar{U}_T\right)+\frac{\partial c_l}{\partial\alpha}\frac{\bar{U}_T\bar{u}_{TT}\bar{u}_{PT}}{2a\bar{U}_T^2}+\frac{\partial c_l}{\partial M}\frac{M_{tip}}{2a}\frac{\bar{u}_{TT}}{\bar{U}_T}\bar{U}_T\bar{u}_{TT}\right]\delta\bar{u}_{T1}d\bar{r}\\
&+\int_0^1\left[\frac{c_{lT}}{2a}\left(\frac{\bar{u}_{TT}^2}{\bar{U}_T}+\bar{U}_T\right)+\frac{\partial c_l}{\partial\alpha}\frac{\bar{U}_T\bar{u}_{TT}\bar{u}_{PT}}{2a\bar{U}_T^2}+\frac{\partial c_l}{\partial M}\frac{M_{tip}}{2a}\frac{\bar{u}_{TT}}{\bar{U}_T}\bar{U}_T\bar{u}_{TT}\right]\delta\bar{u}_{T2}d\bar{r}\\
&+\int_0^1 \bar{r}\left[\frac{c_{lT}}{2a}\frac{\bar{u}_{PT}\bar{u}_{TT}}{\bar{U}_T}-\frac{\partial c_l}{\partial\alpha}\frac{\bar{U}_T\bar{u}_{TT}^2}{2a\bar{U}_T^2}+\frac{\partial c_l}{\partial M}\frac{M_{tip}}{2a}\frac{\bar{u}_{PT}}{\bar{U}_T}\bar{U}_T\bar{u}_{TT}\right]\delta\bar{u}_{P1}d\bar{r}\\
&+\int_0^1\left[\frac{c_{lT}}{2a}\frac{\bar{u}_{PT}\bar{u}_{TT}}{\bar{U}_T}-\frac{\partial c_l}{\partial\alpha}\frac{\bar{U}_T\bar{u}_{TT}^2}{2a\bar{U}_T^2}+\frac{\partial c_l}{\partial M}\frac{M_{tip}}{2a}\frac{\bar{u}_{PT}}{\bar{U}_T}\bar{U}_T\bar{u}_{TT}\right]\delta\bar{u}_{P2}d\bar{r}\\
&+\int_0^1\frac{\partial c_l}{\partial\alpha}\frac{\delta\theta}{2a}\bar{U}_T\bar{u}_{TT}d\bar{r}
\end{aligned}$$

The c_d parts of (B.198) can be manipulated in the same way as the c_l terms were just above, producing a similar collection of terms, and the resulting expressions combined with (B.204) to obtain an alternative representation for (B.198) with the form of:

(B.206) $$\int_0^1\frac{\bar{F}_z}{a\bar{c}}d\bar{r} = T_0+T_\zeta\delta\bar{u}_{T1}+T_\mu\delta\bar{u}_{T2}+T_\beta\delta\bar{u}_{P1}+T_\lambda\delta\bar{u}_{P2}+T_\theta\delta\theta \quad \text{(normal force)}$$

which is the expansion of linear combinations previously mentioned. The coefficients T_0 etc. tidily represent the groups of integrals shown above and their evaluation is demonstrated in a later section.

Repeating the treatment shown in (B.199 - B.204) with the remaining force and moment integrals (B.140 - B.143) results in the same linear expansion representation:

(B.207) $$\int_0^1\frac{\bar{F}_x}{a\bar{c}}d\bar{r} = H_0+H_\zeta\delta\bar{u}_{T1}+H_\mu\delta\bar{u}_{T2}+H_\beta\delta\bar{u}_{P1}+H_\lambda\delta\bar{u}_{P2}+H_\theta\delta\theta \quad \text{(in-plane force)}$$

(B.208) $$\int_0^1\frac{\bar{F}_r}{a\bar{c}}d\bar{r} = R_\mu-\beta_m\int_0^1\frac{\bar{F}_z}{a\bar{c}}d\bar{r} \quad \text{(radial force)}$$

(B.209) $$\int_0^1\bar{r}\frac{\bar{F}_z}{a\bar{c}}d\bar{r} = M_0+M_\zeta\delta\bar{u}_{T1}+M_\mu\delta\bar{u}_{T2}+M_\beta\delta\bar{u}_{P1}+M_\lambda\delta\bar{u}_{P2}+M_\theta\delta\theta \quad \text{(flapping moment)}$$

(B.210) $$\int_0^1\bar{r}\frac{\bar{F}_x}{a\bar{c}}d\bar{r} = Q_0+Q_\zeta\delta\bar{u}_{T1}+Q_\mu\delta\bar{u}_{T2}+Q_\beta\delta\bar{u}_{P1}+Q_\lambda\delta\bar{u}_{P2}+Q_\theta\delta\theta \quad \text{(torque)}$$

The coefficients in this representation are named according to their type and their origin. They are constants, and since all their constituent terms are trim quantities that are independent of rotor azimuth ψ, they too are independent of rotor azimuth. They are integrals of the blade aerodynamics over the span, and expressions for them are obtained later. The full-size letter denotes the type and the naming convention is maintained from the inertial segment of the derivation earlier: thrust forces on the blade are T, flap moments M, blade drag forces H, blade radial forces R and hub torques Q. Terms with subscript 0 are trim forces and moments, subscript $\dot{\zeta}$ are from lead-lag velocity of the blade, subscript μ from hub in-plane velocity, subscript $\dot{\beta}$ from flapwise velocity of the blade, subscript λ from the axial velocity of the rotor, and subscript θ from blade pitch control. The coefficients may be grouped as in-plane and out-of-plane forces, so the H and Q terms have similar behaviour, and the M and T terms have similar behaviour. Alternatively the coefficients may be grouped as in-plane and out-of-plane velocities so the coefficients with subscripts μ and $\dot{\zeta}$ have similar behaviour. The only difference between the coefficients within a particular group (say, the out-of-plane forces due to out-of-plane velocities: $M_{\dot{\beta}}$, M_λ, $T_{\dot{\beta}}$, T_λ) is a factor of $\bar{r}$ more or less in the spanwise integration (the difference between force and moment, and between the translation and rotational velocities), hence just slightly different numerical constants. The behaviour of the coefficients with a variation in the parameters (in particular, with forward velocity μ), is basically the same within a group; that is, it is determined primarily by whether an in-plane or out-of-plane force is involved, and whether an in-plane or out-of-plane velocity or pitch control is the input. The fundamental set of coefficients is considered to be the M and H terms with subscripts μ, $\dot{\beta}$, and θ - one each of in-plane and out-of-plane types - together with T_0 and Q_0 for the trim values. The the behaviour of all other coefficients may be inferred from a knowledge of the behaviour of this set.

Lastly, the nonrotating frame coordinates are required for control of the blade collective pitch θ_C. The following degrees of freedom are defined in the same way as previous quantities already discussed:

(B.211)
$$\theta_0 = \frac{1}{N}\sum_{m=1}^{N} \theta_{C_m}$$

(B.212)
$$\theta_{1C} = \frac{2}{N}\sum_{m=1}^{N} \theta_{C_m} \cos\psi_m$$

(B.213)
$$\theta_{1S} = \frac{2}{N}\sum_{m=1}^{N} \theta_{C_m} \sin\psi_m$$

The blade forces may now be summed over all N blades to find the net rotor forces. If the most recent expressions for the individual blade forces (B.206 - B.210) are substituted into the equations for the whole rotor forces (B.133 - B.138), the aerodynamic coefficients T_0 etc. are independent of blade index m, so that summation operates only on the perturbations of the blade velocities and pitch. The aerodynamic coefficients may therefore be immediately brought outside the summation operators, and any summation terms may be replaced with definitions of the rotor nonrotating degrees of freedom (β_{1S} etc.). Evaluating the expression for rotor thrust (B.133):

$$
\begin{aligned}
\frac{C_T}{\sigma a} &= \frac{1}{N}\sum_{m=1}^{N}\left[\int_0^1 \frac{\bar{F}_z}{a\bar{c}} d\bar{r}\right] \\
&= \frac{1}{N}\sum_{m=1}^{N}\left[T_0 + T_\mu \delta\bar{u}_T + T_{\dot\beta}\delta\bar{u}_{P1} + T_\lambda \delta\bar{u}_{P2} + T_\theta\delta\theta\right] \\
&= \frac{1}{N}\sum_{m=1}^{N}[T_0] + \frac{1}{N}\sum_{m=1}^{N}\left[T_\mu\delta\bar{u}_T\right] + \frac{1}{N}\sum_{m=1}^{N}\left[T_{\dot\beta}\delta\bar{u}_{P1}\right] + \frac{1}{N}\sum_{m=1}^{N}[T_\lambda\delta\bar{u}_{P2}] + \frac{1}{N}\sum_{m=1}^{N}[T_\theta\delta\theta] \\
&= \frac{T_0}{N}\sum_{m=1}^{N}[1] + \frac{T_\mu}{N}\sum_{m=1}^{N}[\delta\bar{u}_T] + \frac{T_{\dot\beta}}{N}\sum_{m=1}^{N}[\delta\bar{u}_{P1}] + \frac{T_\lambda}{N}\sum_{m=1}^{N}[\delta\bar{u}_{P2}] + \frac{T_\theta}{N}\sum_{m=1}^{N}[\delta\theta]
\end{aligned}
\tag{B.214}
$$

And these are now evaluated individually. The first term is trivial:

$$
\frac{T_0}{N}\sum_{m=1}^{N}[1] = T_0 \tag{B.215}
$$

The second term:

$$
\begin{aligned}
\frac{T_{\dot\zeta}}{N}\sum_{m=1}^{N}\delta u_{T1} &= \frac{T_{\dot\zeta}}{N}\sum_{m=1}^{N}\left[\alpha'_z - \zeta'_m\right] \\
&= T_{\dot\zeta}\left(\frac{1}{N}\sum_{m=1}^{N}\left[\alpha'_z\right] - \frac{1}{N}\sum_{m=1}^{N}\left[\zeta'_m\right]\right) \\
&= T_{\dot\zeta}\left(\alpha'_z - \zeta'_0\right)
\end{aligned}
\tag{B.216}
$$

The third term:

$$
\begin{aligned}
\frac{T_\mu}{N}\sum_{m=1}^{N}[\delta\bar{u}_T] =& \frac{T_\mu}{N}\sum_{m=1}^{N}\Big[-\bar{h}\left(\alpha'_y\sin\psi_m + \alpha'_x\cos\psi_m\right) + \mu\left(\alpha_y\sin\psi_m + \alpha_x\cos\psi_m\right) \\
&+ \mu\left(\bar\beta_g\cos\psi_m + \bar\alpha_g\sin\psi_m\right) + \left(y'_P\cos\psi_m - x'_P\sin\psi_m\right)\Big] \\
=& \frac{T_\mu}{N}\Bigg[\sum_{m=1}^{N}\left[\left(-\bar{h}\alpha'_y + \mu\alpha_y + \mu\bar\alpha_g - x'_P\right)\sin\psi_m\right] \\
&+ \sum_{m=1}^{N}\left[\left(-\bar{h}\alpha'_x + \mu\alpha_x + \mu\bar\beta_g + y'_P\right)\cos\psi_m\right]\Bigg] \\
=& \frac{T_\mu}{N}(0+0) \\
=& 0
\end{aligned}
\tag{B.217}
$$

The fourth term:

$$
\begin{aligned}
\frac{T_{\dot\beta}}{N}\sum_{m=1}^{N}[\delta u_{P1}] &= \frac{T_{\dot\beta}}{N}\sum_{m=1}^{N}\left[\beta'_m - \alpha'_y\cos\psi_m + \alpha'_x\sin\psi_m\right] \\
&= T_{\dot\beta}\left(\frac{1}{N}\sum_{m=1}^{N}\left[\beta'_m\right] - \alpha'_y\frac{1}{N}\sum_{0}^{1}\left[\cos\psi_m\right] + \alpha'_x\frac{1}{N}\sum_{0}^{1}\left[\sin\psi_m\right]\right) \\
&= T_{\dot\beta}\left(\beta'_0 - 0 + 0\right) \\
&= T_{\dot\beta}\beta'_0
\end{aligned}
\tag{B.218}
$$

The fifth term:

$$\begin{aligned}\frac{T_\lambda}{N}\sum_{m=1}^{N}[\delta\bar{u}_{P2}] &= \frac{T_\lambda}{N}\sum_{m=1}^{N}\left[\mu\bar{u}_g + z'_P\right] \\ &= T_\lambda\left(\mu\bar{u}_g\frac{1}{N}\sum_{m=1}^{N}[1] + z'_P\frac{1}{N}\sum_{m=1}^{N}[1]\right) \\ &= T_\lambda\left(\mu\bar{u}_g + z'_P\right)\end{aligned} \tag{B.219}$$

And lastly, the sixth term:

$$\begin{aligned}\frac{T_\theta}{N}\sum_{m=1}^{N}[\delta\theta] &= \frac{T_\theta}{N}\sum_{m=1}^{N}\left[\theta_{C_m} - K_P\beta_m\right] \\ &= T_\theta\left(\frac{1}{N}\sum_{m=1}^{N}\left[\theta_{C_m}\right] - K_P\frac{1}{N}\sum_{n=1}^{N}\left[\beta_m\right]\right) \\ &= T_\theta\left(\theta_0 - K_P\beta_0\right)\end{aligned} \tag{B.220}$$

If all of these terms are combined, then the following is achieved for the thrust equation (B.214):

$$\frac{C_T}{\sigma a} = T_0 + T_{\dot\zeta}\left(\alpha'_z - \zeta'_0\right) + T_{\dot\beta}\beta'_0 + T_\lambda\left(\mu\bar{u}_g + z'_P\right) + T_\theta\left(\theta_0 - K_P\beta_0\right) \tag{B.221}$$

The evaluation of the vertical force H equation (B.134) is slightly more intensive and is therefore shown here:

$$\frac{2C_H}{\sigma a} = \frac{2}{N}\sum_{m=1}^{N}\left[\cos\left(\psi_m\right)\int_0^1\frac{\bar{F}_r}{a\bar{c}}d\bar{r} + \sin\left(\psi_m\right)\int_0^1\frac{\bar{F}_x}{a\bar{c}}d\bar{r}\right] \tag{B.222}$$

The blade radial force expression $\int_0^1\frac{\bar{F}_r}{a\bar{c}}d\bar{r}$ requires the trim value of the coefficient of β_m, which is $\int_0^1\frac{\bar{F}_z}{a\bar{c}}d\bar{r}$. At trim, when all perturbation quantities are 0, this is simply:

$$\int_0^1\frac{\bar{F}_z}{a\bar{c}}d\bar{r} = \frac{C_T}{\sigma a} \tag{B.223}$$

as obtained just previously. Therefore:

$$\begin{aligned}\frac{2C_H}{\sigma a} = \frac{2}{N}\sum_{m=1}^{N}\Big[&\cos\left(\psi_m\right)\left(R_\mu\delta\bar{u}_R - \frac{C_T}{\sigma a}\beta_m\right) \\ &+ \sin\left(\psi_m\right)\left(H_0 + H_{\dot\zeta}\delta\bar{u}_{T1} + H_\mu\delta\bar{u}_{T2} + H_{\dot\beta}\delta\bar{u}_{P1} + H_\lambda\delta\bar{u}_{P2} + H_\theta\delta\theta\right)\Big]\end{aligned} \tag{B.224}$$

Each of the terms within the summation can be evaluated separately:

(B.225)
$$\begin{aligned}\frac{2}{N}\sum_{m=1}^{N}\left[R_\mu \delta\bar{u}_R\cos\psi_m\right] = R_\mu\frac{2}{N}\sum_{m=1}^{N}\Big[\Big(\bar{h}\left(-\alpha'_y\cos\psi_m+\alpha'_x\sin\psi_m\right)\\ +\mu\left(\alpha_y\cos\psi_m-\alpha_x\sin\psi_m\right)\\ +\mu\left(-\bar{\beta}_g\sin\psi_m+\bar{\alpha}_g\cos\psi_m\right)\\ -\left(y'_P\sin\psi_m+x'_P\cos\psi_m\right)\Big)\cos\psi_m\Big]\\ = R_\mu\frac{2}{N}\sum_{m=1}^{N}\Big[\bar{h}\left(-\alpha'_y\cos^2\psi_m+\alpha'_x\sin\psi_m\cos\psi_m\right)\\ +\mu\left(\alpha_y\cos^2\psi_m-\alpha_x\sin\psi_m\cos\psi_m\right)\\ -\mu\bar{\beta}_g\sin\psi_m\cos\psi_m+\mu\bar{\alpha}_g\cos^2\psi_m\\ -y'_P\sin\psi_m\cos\psi_m-x'_P\cos^2\psi_m\Big]\end{aligned}$$

We have from (B.70) that $\sin\psi_m\cos\psi_m$ summations are equal to 0, and from (B.71) that $\cos^2\psi_m$ summations are equal to 1, leading to great simplification:

(B.226)
$$\frac{2}{N}\sum_{m=1}^{N}\left[R_\mu\delta\bar{u}_R\cos\psi_m\right] = R_\mu\left(-\bar{h}\alpha'_y+\alpha_y\mu+\mu\bar{\alpha}_g-x'_P\right)$$

The next term is simple:

(B.227)
$$\begin{aligned}\frac{2}{N}\sum_{m=1}^{N}\left[-\frac{C_T}{\sigma a}\beta_m\cos\psi_m\right] &= -\frac{C_T}{\sigma a}\frac{2}{N}\sum_{m=1}^{N}\left[\beta_m\cos\psi_m\right]\\ &= -\frac{C_T}{\sigma a}\beta_{1C}\end{aligned}$$

As is the first of the sine summations:

(B.228)
$$\frac{2}{N}\sum_{m=1}^{N}\left[H_0\sin\psi_m\right] = H_0\frac{2}{N}\sum_{m=1}^{N}\left[\sin\psi_m\right] = 0$$

The second sine term:

(B.229)
$$\begin{aligned}\frac{2}{N}\sum_{m=1}^{N}\left[H_{\dot{\zeta}}\delta\bar{u}_{T1}\sin\psi_m\right] &= H_{\dot{\zeta}}\frac{2}{N}\sum_{m=1}^{N}\left[\left(\alpha'_z-\zeta'_m\right)\sin\psi_m\right]\\ &= H_{\dot{\zeta}}\left(\alpha'_z\frac{2}{N}\sum_{m=1}^{N}\left[\sin\psi_m\right]-\frac{2}{N}\sum_{m=1}^{N}\left[\zeta'_m\sin\psi_m\right]\right)\\ &= H_{\dot{\zeta}}\left(0-\zeta'_{1S}\right)\\ &= -H_{\dot{\zeta}}\zeta'_{1S}\end{aligned}$$

Then:

$$
\begin{aligned}
\frac{2}{N}\sum_{m=1}^{N}\left[H_\mu \delta\bar{u}_{T2}\sin\psi_m\right] &= H_\mu \frac{2}{N}\sum_{m=1}^{N}\Big[\Big(-\bar{h}\left(\alpha'_y\sin\psi_m+\alpha'_x\cos\psi_m\right) \\
&\qquad +\mu\left(\alpha_y\sin\psi_m+\alpha_x\cos\psi_m\right) \\
&\qquad +\mu\left(\bar{\beta}_g\cos\psi_m+\bar{\alpha}_g\sin\psi_m\right) \\
&\qquad +\left(y'_P\cos\psi_m-x'_P\sin\psi_m\right)\Big)\sin\psi_m\Big] \\
&= H_\mu \frac{2}{N}\sum_{m=1}^{N}\Big[-\bar{h}\left(\alpha'_y\sin^2\psi_m+\alpha'_x\sin\psi_m\cos\psi_m\right) \\
&\qquad +\mu\left(\alpha_y\sin^2\psi_m+\alpha_x\sin\psi_m\cos\psi_m\right) \\
&\qquad +\mu\bar{\beta}_g\sin\psi_m\cos\psi_m+\mu\bar{\alpha}_g\sin^2\psi_m \\
&\qquad +y'_P\sin\psi_m\cos\psi_m-x'_P\sin^2\psi_m\Big]
\end{aligned}
\tag{B.230}
$$

and in addition to the $\sin\psi_m\cos\psi_m$ summations going to 0, it can be found via the continuous-discrete relationship shown in (B.69) that $\sin^2\psi_m$ summations go to 1, providing us with:

$$
\frac{2}{N}\sum_{m=1}^{N}\left[H_\mu \delta\bar{u}_T\sin\psi_m\right] = H_\mu\left(-\bar{h}\alpha'_y+\alpha_y\mu+\mu\bar{\alpha}_g-x'_P\right)
\tag{B.231}
$$

The remaining terms of (B.224) use similar operations and shortcuts, and following their full evaluation and the collection of like terms, we are left with the following whole expression for vertical force in coefficient form:

$$
\begin{aligned}
\frac{2C_H}{\sigma a} &= \left(H_\mu+R_\mu\right)\left(-\bar{h}\alpha'_y+\alpha_y\mu+\mu\bar{\alpha}_g-x'_P\right) \\
&\quad -H_{\dot{\zeta}}\zeta'_{1S}+H_{\dot{\beta}}\left(\beta'_{1S}+\alpha'_x\right)+H_\theta\left(\theta_{1S}-K_P\beta_{1S}\right)-\frac{C_T}{\sigma a}\beta_{1C}
\end{aligned}
\tag{B.232}
$$

The θ coordinates represent control inputs by means of the usual rotor swashplate mechanism; θ_0 is the rotor collective control, and θ_{1C} and θ_{1S} are the rotor lateral and longitudinal cyclic control (control plane tilt).

From helicopter rotor aerodynamics, the tilt of the tip path plane β_{1C} and β_{1S} is expected to tilt the rotor thrust vector and hence give an in-plane force component on the rotor hub. The tip path plane tilt terms in C_H and C_Y are, respectively:

$$
-\left(\frac{C_T}{\sigma a}+H_{\dot{\beta}}\right)\beta_{1C} \quad \text{to } C_H
\tag{B.233}
$$

$$
-\left(\frac{C_T}{\sigma a}+H_{\dot{\beta}}\right)\beta_{1S} \quad \text{to } C_Y
\tag{B.234}
$$

where the first terms (i.e. thrust coefficient) are the in-plane forces due to radial tilt of the blade mean thrust vector by the blade flapping, already included in the equations of motion. The second terms are due to tip path plane tilt causing a flapping velocity in the rotating frame. This flapping velocity changes the blade angle of attack and so tilts the blade mean thrust vector in the chordwise direction (like induced drag). Likewise, a similar increment to the equations is caused by lead-lag (ζ_{1C} and ζ_{1S}) due to the net rotor centre of gravity being off-centre. These additions to C_H and C_Y are, respectively:

$$+H_{\dot{\zeta}}\zeta_{1C} \quad \text{to } C_H \tag{B.235}$$

$$+H_{\dot{\zeta}}\zeta_{1S} \quad \text{to } C_Y \tag{B.236}$$

The C_H additions give the following equation:

$$\begin{aligned}\frac{2C_H}{\sigma a} &= (H_\mu + R_\mu)\left(-\bar{h}\alpha'_y + \alpha_y\mu + \mu\bar{\alpha}_g - x'_P\right) + H_{\dot{\zeta}}\left(-\zeta'_{1S} + \zeta_{1C}\right) \\ &\quad + H_{\dot{\beta}}\left(\beta'_{1S} - \beta_{1C} + \alpha'_x\right) + H_\theta\left(\theta_{1S} - K_P\beta_{1S}\right) - \frac{C_T}{\sigma a}\beta_{1C}\end{aligned} \tag{B.237}$$

The equation for the side force Y in coefficient form is generated in the same manner, and with the rotor thrust vector tilt addition:

$$\begin{aligned}\frac{2C_Y}{\sigma a} &= -\left(H_\mu + R_\mu\right)\left(-\bar{h}\alpha'_x + \alpha_x\mu + \mu\bar{\beta}_g + y'_P\right) + H_{\dot{\zeta}}\left(\zeta'_{1C} + \zeta_{1S}\right) \\ &\quad - H_{\dot{\beta}}\left(\beta'_{1C} + \beta_{1S} - \alpha'_y\right) - H_\theta\left(\theta_{1C} - K_P\beta_{1C}\right) - \frac{C_T}{\sigma a}\beta_{1S}\end{aligned} \tag{B.238}$$

Remembering from earlier that the coning, pitching and yawing aerodynamic moments on the rotor disc are, respectively:

$$\bar{M}_{F_0} = \frac{1}{N}\sum_{m=1}^{N}\left[\bar{M}_{F_m}\right]$$

$$\bar{M}_{F_{1C}} = \frac{2}{N}\sum_{m=1}^{N}\left[\bar{M}_{F_m}\cos\psi_m\right]$$

$$\bar{M}_{F_{1S}} = \frac{2}{N}\sum_{m=1}^{N}\left[\bar{M}_{F_m}\sin\psi_m\right]$$

These can be evaluated by applying the (B.48 - B.50) summation operators to the equation for $\frac{\bar{M}_{Fm}}{a\bar{c}}$, (B.136). As the process is similar to obtaining (B.237) and (B.238), the intermediate steps are not shown. The coning moment is found to be:

$$\bar{M}_{F_0} = M_0 + M_{\dot{\zeta}}\left(\alpha'_z - \zeta'_0\right) + M_{\dot{\beta}}\beta'_0 + M_\lambda\left(\mu\bar{u}_g + z'_P\right) + M_\theta\left(\theta_0 - K_P\beta_0\right) \tag{B.239}$$

The application of the (B.49) summation operator gives the following for $\bar{M}_{F_{1C}}$:

$$\bar{M}_{F_{1C}} = -M_{\dot{\zeta}}\zeta'_{1C} + M_\mu\left(-\bar{h}\alpha'_x + \alpha_x\mu + \mu\bar{\beta}_g + y'_P\right) + M_{\dot{\beta}}\left(\beta'_{1C} - \alpha'_y\right) + M_\theta\left(\theta_{1C} - K_P\beta_{1C}\right) \tag{B.240}$$

However, the tilt of the thrust vector and the displacement of the net rotor centre of gravity also impart additional components to the rotor disc pitch and yaw moments, in the same manner as that discussed previously:

$$+M_{\dot{\beta}}\beta_{1S} - M_{\dot{\zeta}}\zeta_{1S} \quad \text{to pitch moment} \tag{B.241}$$

(B.242) $$-M_{\dot{\beta}}\beta_{1C}+M_{\dot{\zeta}}\zeta_{1C} \quad \text{to yaw moment}$$

and these additions produce the following final expressions for rotor disc pitching and yawing moments, respectively:

(B.243)
$$\bar{M}_{F_{1C}}=-M_{\dot{\zeta}}\left(\zeta'_{1C}+\zeta_{1S}\right)+M_{\mu}\left(-\bar{h}\alpha'_x+\alpha_x\mu+\mu\bar{\beta}_g+y'_P\right)+M_{\dot{\beta}}\left(\beta'_{1C}+\beta_{1S}-\alpha'_y\right)+M_{\theta}\left(\theta_{1C}-K_P\beta_{1C}\right)$$

(B.244)
$$\bar{M}_{F_{1S}}=M_{\dot{\zeta}}\left(-\zeta'_{1S}+\zeta_{1C}\right)+M_{\mu}\left(-\bar{h}\alpha'_y+\alpha_y\mu+\mu\bar{\alpha}_g-x'_P\right)+M_{\dot{\beta}}\left(\beta'_{1S}-\beta_{1C}+\alpha'_x\right)+M_{\theta}\left(\theta_{1S}-K_P\beta_{1S}\right)$$

The lead-lag aerodynamic moment expressions are generated by applying the same process to (B.137):

(B.245) $$\bar{M}_{L_0}=Q_0+Q_{\dot{\zeta}}\left(\alpha'_z-\zeta'_0\right)+Q_{\dot{\beta}}\beta'_0+Q_{\lambda}\left(\mu\bar{u}_g+z'_P\right)+Q_{\theta}\left(\theta_0-K_P\beta_0\right)$$

(B.246)
$$\bar{M}_{L_{1C}}=-Q_{\dot{\zeta}}\left(\zeta'_{1C}+\zeta_{1S}\right)+Q_{\mu}\left(-\bar{h}\alpha'_x+\alpha_x\mu+\mu\bar{\beta}_g+y'_P\right)+Q_{\dot{\beta}}\left(\beta'_{1C}+\beta_{1S}-\alpha'_y\right)+Q_{\theta}\left(\theta_{1C}-K_P\beta_{1C}\right)$$

(B.247)
$$\bar{M}_{L_{1S}}=Q_{\dot{\zeta}}\left(-\zeta'_{1S}+\zeta_{1C}\right)+Q_{\mu}\left(-\bar{h}\alpha'_y+\alpha_y\mu+\mu\bar{\alpha}_g-x'_P\right)+Q_{\dot{\beta}}\left(\beta'_{1S}-\beta_{1C}+\alpha'_x\right)+Q_{\theta}\left(\theta_{1S}-K_P\beta_{1S}\right)$$

The aerodynamic torque equation is generated in a very similar manner to the thrust equation and thus also has a similar final form:

(B.248) $$\frac{C_Q}{\sigma a}=Q_0+Q_{\dot{\zeta}}\left(\alpha'_z-\zeta'_0\right)+Q_{\dot{\beta}}\beta'_0+Q_{\lambda}\left(\mu\bar{u}_g+z'_P\right)+Q_{\theta}\left(\theta_0-K_P\beta_0\right)$$

B.2.1.5 Aerodynamic coefficients

There are quite a variety of coefficients that are required, as shown in the previous section. There, the aerodynamic integrals for the thrust equation were identified in their un-integrated form, arranged into a linear combination and named according to origin and direction of action. Expressions of similar structure were generated for the other forces and moments in the system. The coefficients could be calculated by fully evaluating the necessary integrals, however, in their current form they are large and complex, and so some simplifications are made to make them tractable. Firstly, the effects of drag (c_d terms) and of compressibility (M terms) are neglected. The drag is retained in the torque equation, however, as it is a key feature of the model given the inclusion of lead-lag dynamics in the rotor. Note also that as all the aerodynamic coefficients are evaluated at the trim condition (i.e. no perturbation), they are independent of blade azimuth position, and therefore the process of summing all blade contributions and dividing by blade number can be dropped wherever it appears. The process of matching terms to identify specific integrals is demonstrated here for the flapping moment equation $\int_0^1 \bar{r}\frac{\bar{F}_z}{a\bar{c}}$. Note that the drag and compressibility terms have already been removed:

$$
\begin{aligned}
\int_0^1 \bar{r}\frac{\bar{F}_z}{a\bar{c}} =& \int_0^1 \bar{r}\frac{c_{lT}}{2a}\bar{U}_T\bar{u}_{TT}d\bar{r} \\
&+\int_0^1 \bar{r}^2\left[\frac{c_{lT}}{2a}\left(\frac{\bar{u}_{TT}^2}{\bar{U}_T}+\bar{U}_T\right)+\frac{\partial c_l}{\partial\alpha}\frac{\bar{u}_{TT}\bar{u}_{PT}}{2a\bar{U}_T}\right]\delta\bar{u}_{T1}d\bar{r} \\
&+\int_0^1 \bar{r}\left[\frac{c_{lT}}{2a}\left(\frac{\bar{u}_{TT}^2}{\bar{U}_T}+\bar{U}_T\right)+\frac{\partial c_l}{\partial\alpha}\frac{\bar{u}_{TT}\bar{u}_{PT}}{2a\bar{U}_T}\right]\delta\bar{u}_{T2}d\bar{r} \\
&+\int_0^1 \bar{r}^2\left[\frac{c_{lT}}{2a}\frac{\bar{u}_{PT}\bar{u}_{TT}}{\bar{U}_T}-\frac{\partial c_l}{\partial\alpha}\frac{\bar{u}_{TT}^2}{2a\bar{U}_T}\right]\delta\bar{u}_{P1}d\bar{r} \\
&+\int_0^1 \bar{r}\left[\frac{c_{lT}}{2a}\frac{\bar{u}_{PT}\bar{u}_{TT}}{\bar{U}_T}-\frac{\partial c_l}{\partial\alpha}\frac{\bar{u}_{TT}^2}{2a\bar{U}_T}\right]\delta\bar{u}_{P2}d\bar{r} \\
&+\int_0^1 \bar{r}\frac{\partial c_l}{\partial\alpha}\frac{\delta\theta}{2a}\bar{U}_T\bar{u}_{TT}d\bar{r} \\
=& M_0+M_{\dot{\zeta}}\delta\bar{u}_{T1}+M_\mu\delta\bar{u}_{T2}+M_{\dot{\beta}}\delta\bar{u}_{P1}+M_\lambda\delta\bar{u}_{P2}+M_\theta\delta\theta
\end{aligned}
\tag{B.249}
$$

Allowing the unintegrated form of each coefficient to be identified easily. Note that this expression is very similar to (B.205), differing only by the absence of the compressibility (M) terms and a factor of $\bar{r}$. From a similar evaluation of the blade normal force $\int_0^1 \frac{\bar{F}_z}{a\bar{c}}$ with only trim terms considered (i.e. no perturbation terms are necessary) we obtain:

$$
\frac{C_T}{\sigma a} = T_0 = \int_0^1 \bar{U}_T\bar{u}_{TT}\frac{c_{lT}}{2a} \tag{B.250}
$$

And from evaluating blade drag torque $\int_0^1 \bar{r}\frac{\bar{F}_x}{a\bar{c}}$ in the same way:

$$
\frac{C_Q}{\sigma a} = Q_0 = \int_0^1 \bar{r}\bar{U}_T\left(\bar{u}_{PT}\frac{c_{lT}}{2a}-\bar{u}_{TT}\frac{c_{dT}}{2a}\right) \tag{B.251}
$$

Lastly, after the expansion and comparison is performed with blade drag force $\int_0^1 \frac{\bar{F}_x}{a\bar{c}}$ we obtain the following insight for all the coefficients:

$$
M_\mu = \int_0^1 \bar{r}\left[\frac{c_{lT}}{2a}\left(\frac{\bar{u}_{TT}^2}{\bar{U}_T}+\bar{U}_T\right)+\frac{\partial c_l}{\partial\alpha}\frac{\bar{u}_{TT}\bar{u}_{PT}}{2a\bar{U}_T}\right]d\bar{r} \tag{B.252}
$$

$$
M_{\dot{\beta}} = \int_0^1 \bar{r}^2\left[\frac{c_{lT}}{2a}\frac{\bar{u}_{PT}\bar{u}_{TT}}{\bar{U}_T}-\frac{\partial c_l}{\partial\alpha}\frac{\bar{u}_{TT}^2}{2a\bar{U}_T}\right]d\bar{r} \tag{B.253}
$$

$$
M_\theta = \int_0^1 \left[\bar{r}\frac{\partial c_l}{\partial\alpha}\frac{\bar{U}_T\bar{u}_{TT}}{2a}\right]d\bar{r} \tag{B.254}
$$

$$
H_\mu + R_\mu = \int_0^1 \left[\frac{c_{lT}}{2a}\frac{\bar{u}_{PT}\bar{u}_{TT}}{\bar{U}_T}-\frac{\partial c_l}{\partial\alpha}\frac{\bar{u}_{PT}^2}{2a\bar{U}_T}\right]d\bar{r} \tag{B.255}
$$

$$H_{\dot{\beta}} = \int_0^1 \bar{r}\left[\frac{c_{lT}}{2a}\left(\frac{\bar{u}_{PT}^2}{\bar{U}_T} + \bar{U}_T\right) - \frac{\partial c_l}{\partial \alpha}\frac{\bar{U}_T \bar{u}_{TT} \bar{u}_{PT}}{2a\bar{U}_T^2}\right] d\bar{r} \tag{B.256}$$

$$H_\theta = \int_0^1 \left[\frac{\partial c_l}{\partial \alpha}\frac{\bar{U}_T \bar{u}_{PT}}{2a}\right] d\bar{r} \tag{B.257}$$

As stated earlier, the torque coefficients (Q terms) are simply the drag force coefficients (H terms) with an extra factor of $\bar{r}$ in the integrand, while the other thrust coefficients (T terms) are just the flapping moment coefficients (M terms) less a factor of $\bar{r}$ in the integrand.

Expressions for the trim values of the sectional velocities are already defined, though trim values of the sectional lift coefficient c_l and lift curve slope $\frac{\partial c_l}{\partial \alpha}$ are still required. If angle of attack is assumed to be small then the lift curve slope can be assumed to be uniformly linear and equal in gradient to the 2D lift slope a, then the following simplification is possible:

$$\frac{\partial c_l}{\partial \alpha}\frac{1}{2a} = a\frac{1}{2a} = \frac{1}{2} \tag{B.258}$$

And therefore if:

$$c_{lT} = c_{l0} + \frac{\partial c_l}{\partial \alpha}\alpha_T \tag{B.259}$$

Then, when zero lift coefficient c_{l0} is neglected due to its very small size:

$$\begin{aligned} \frac{c_{lT}}{2a} &= 0 + \frac{\partial c_l}{\partial \alpha}\frac{1}{2a}\alpha_T \\ &= \frac{1}{2}\alpha_T \end{aligned} \tag{B.260}$$

And furthermore, the trim angle of attack α_T can be expressed in terms of the trim collective angle θ_T and the trim velocities (which comprise the trim inflow angle):

$$\frac{\alpha_T}{2} = \frac{1}{2}\left(\theta_T - \arctan\left(\frac{\bar{u}_{PT}}{\bar{u}_{TT}}\right)\right) \tag{B.261}$$

By evaluating the integrands at an effective radius, approximate expressions for the aerodynamic coefficients can be derived to show which terms are most influential and therefore must be retained. Since it is known that, for the trim inflow angle ϕ_T:

$$\tan\left(\phi_T\right) = \frac{\bar{u}_{PT}}{\bar{u}_{TT}} \tag{B.262}$$

Then it also follows that:

$$\sin\left(\phi_T\right) = \frac{\bar{u}_{PT}}{\bar{U}_T} \tag{B.263}$$

$$\cos\left(\phi_T\right) = \frac{\bar{u}_{TT}}{\bar{U}_T} \tag{B.264}$$

And from this it is possible to substitute $\bar{u}_{PT}$ and $\bar{U}_T$ out for $\bar{u}_{TT}$ and ϕ_T. Finally, $\bar{u}_{TT} = \bar{r}$ is substituted, and using all these substitutions gives:

$$\begin{aligned}
\frac{C_T}{\sigma a} &= \int_0^1 \bar{U}_T \bar{u}_{TT} \frac{c_l}{2a} d\bar{r} \\
&= \int_0^1 \left(\frac{\bar{u}_{TT}}{\cos\phi_T}\right)(\bar{r})\left(\frac{\alpha_T}{2}\right) d\bar{r} \\
&= \frac{1}{\cos\phi_T}\int_0^1 \bar{r}^2 \frac{\alpha_T}{2} d\bar{r}
\end{aligned} \tag{B.265}$$

and here a mean (along the span of the blade) trim angle of attack $\tilde{\alpha}_T$ can be defined to remove the dependency on $\bar{r}$ and allow the term to be brought outside the integral:

$$\frac{C_T}{\sigma a} = \frac{\tilde{\alpha}_T}{2\cos\phi_T}\int_0^1 \bar{r}^2 d\bar{r} = \frac{1}{\cos\phi_T}\frac{\tilde{\alpha}_T}{6} \tag{B.266}$$

Now, some of the aerodynamic integrals can be evaluated. Starting with M_μ:

$$\begin{aligned}
M_\mu &= \int_0^1 \bar{r}\left[\frac{c_{lT}}{2a}\left(\frac{\bar{u}_{TT}^2}{\bar{U}_T} + \bar{U}_T\right) + \frac{\partial c_l}{\partial \alpha}\frac{\bar{u}_{TT}\bar{u}_{PT}}{2a\bar{U}_T}\right] d\bar{r} \\
&= \int_0^1 \bar{r}\left[\frac{\alpha_T}{2}\left(\bar{r}\cos\phi_T + \frac{\bar{r}}{\cos\phi_T}\right) + \frac{1}{2}\bar{r}\sin\phi_T\right] d\bar{r} \\
&= \int_0^1 \bar{r}\left[\frac{\alpha_T}{2}\frac{\bar{r}}{\cos\phi_T}\left(\cos^2\phi_T + 1\right) + \frac{1}{2}\bar{r}\sin\phi_T\right] d\bar{r} \\
&= \left[\frac{\tilde{\alpha}_T}{2}\frac{1}{\cos\phi_T}\left(\cos^2\phi_T + 1\right) + \frac{1}{2}\sin\phi_T\right]\int_0^1 \bar{r}^2 d\bar{r} \\
&= \frac{1}{\cos\phi_T}\frac{\tilde{\alpha}_T}{6}\left(\cos^2\phi_T + 1\right) + \frac{\sin\phi_T}{6}
\end{aligned} \tag{B.267}$$

In low inflow, ϕ_T is small, so $\cos^2\phi_T \cong 1$, and substituting in (B.266) gives:

$$M_\mu \cong 2\frac{C_T}{\sigma a} + \frac{\sin\phi_T}{6} \tag{B.268}$$

Additionally, the C_T term is significant only for low inflow; in high inflow $\frac{C_T}{\sigma a} << 1$. If the same kind of process is followed for the other expressions, then it is seen that a c_{lT} term results in a C_T term and the $\frac{\partial c_l}{\partial \alpha}$ term results in a ϕ term. Furthermore, it is seen that thrust coefficient terms ultimately may be neglected. They are negligible in $M_{\dot{\beta}}$ (flap damping), and not present in M_θ and H_θ. On this basis, if high inflow operation is assumed, the thrust coefficient terms may reasonably be neglected and therefore the c_{lT} terms may be removed from the integrands. The reason the $\frac{\partial c_l}{\partial \alpha}$ terms dominate the coefficients is that with high inflow both in-plane and out-of-plane velocity perturbations give large angle of attack changes. Therefore, through the lift slope $\frac{\partial c_l}{\partial \alpha}$ they give large section lift perturbations, which have significant components in both the in-plane and out-of-plane directions. The high inflow – where μ is of order 1 – thus allows a great simplification of the rotor aerodynamic derivatives.

Retaining now only the $\frac{\partial c_l}{\partial \alpha}$ terms in the integral expressions and substituting in the expressions for the trim velocity components $\bar{u}_{TT}$, $\bar{u}_{PT}$ and $\bar{U}_T$, the following is obtained:

$$M_\mu = \int_0^1 \frac{\partial c_l}{\partial \alpha} \frac{1}{2a} \frac{\bar{r}^2 \mu}{\sqrt{\bar{r}^2 + \mu^2}} \tag{B.269}$$

$$M_{\dot{\beta}} = -\int_0^1 \frac{\partial c_l}{\partial \alpha} \frac{1}{2a} \frac{\bar{r}^4}{\sqrt{\bar{r}^2 + \mu^2}} \tag{B.270}$$

$$M_\theta = \int_0^1 \frac{\partial c_l}{\partial \alpha} \frac{1}{2a} \bar{r}^2 \sqrt{\bar{r}^2 + \mu^2} \tag{B.271}$$

$$H_\mu + R_\mu = \int_0^1 \frac{\partial c_l}{\partial \alpha} \frac{1}{2a} \frac{\mu^2}{\sqrt{\bar{r}^2 + \mu^2}} \tag{B.272}$$

$$H_{\dot{\beta}} = -\int_0^1 \frac{\partial c_l}{\partial \alpha} \frac{1}{2a} \frac{\bar{r}^2 \mu}{\sqrt{\bar{r}^2 + \mu^2}} \tag{B.273}$$

$$H_\theta = \int_0^1 \frac{\partial c_l}{\partial \alpha} \frac{1}{2a} \mu \sqrt{\bar{r}^2 + \mu^2} \tag{B.274}$$

With the thrust T and torque Q coefficients related to these in the manner described previously. The thrust coefficient expression contains only c_{lT} terms (and no $\frac{\partial c_l}{\partial \alpha}$ terms), the simplification of retaining only lift slope terms is not applied to it as it would create a trivial result. Instead it is defined as:

$$\frac{C_T}{\sigma a} = \int_0^1 \frac{\alpha_T}{2} \bar{r} \sqrt{\bar{r}^2 + \mu^2} \tag{B.275}$$

With the assumption that $\frac{\partial c_l}{\partial \alpha} \frac{1}{2a} = \frac{1}{2}$ as previously discussed, then the integrals may be evaluated exactly and the following definitions obtained for all aerodynamic integrals:

$$M_{\dot{\zeta}} = \frac{\mu}{6} \left[\sqrt{1+\mu^2} \left(1 - 2\mu^2\right) + 2\mu^3 \right] \tag{B.276}$$

$$M_\mu = \frac{\mu}{4} \sqrt{1+\mu^2} - \frac{\mu^3}{4} \ln \left[\frac{1 + \sqrt{1+\mu^2}}{\mu} \right] \tag{B.277}$$

$$M_{\dot{\beta}} = -\frac{1}{2} \sqrt{1+\mu^2} \frac{2 - 3\mu^2}{8} - \frac{3\mu^4}{16} \ln \left[\frac{1 + \sqrt{1+\mu^2}}{\mu} \right] \tag{B.278}$$

$$M_\lambda = -\frac{1}{6} \left[\sqrt{1+\mu^2} \left(1 - 2\mu^2\right) + 2\mu^3 \right] \tag{B.279}$$

(B.280)
$$M_\theta = \frac{1}{16}\left(2+\mu^2\right) - \frac{\mu^4}{16}\ln\left[\frac{1+\sqrt{1+\mu^2}}{\mu}\right]$$

(B.281)
$$H_{\dot{\zeta}} = \frac{\mu^2}{2}\left(\sqrt{1+\mu^2} - \mu\right)$$

(B.282)
$$H_\mu + R_\mu = \frac{\mu^2}{2}\ln\left[\frac{1+\sqrt{1+\mu^2}}{\mu}\right]$$

(B.283)
$$H_{\dot{\beta}} = -\frac{\mu}{4}\sqrt{1+\mu^2} + \frac{\mu^3}{4}\ln\left[\frac{1+\sqrt{1+\mu^2}}{\mu}\right]$$

(B.284)
$$H_\lambda = -\frac{\mu}{2}\left(\sqrt{1+\mu^2} - \mu\right)$$

(B.285)
$$H_\theta = \frac{\mu}{4}\sqrt{1+\mu^2} + \frac{\mu^3}{4}\ln\left[\frac{1+\sqrt{1+\mu^2}}{\mu}\right]$$

(B.286)
$$T_{\dot{\zeta}} = \frac{\mu}{4}\sqrt{1+\mu^2} - \frac{\mu^3}{4}\ln\left[\frac{1+\sqrt{1+\mu^2}}{\mu}\right]$$

(B.287)
$$T_\mu = \frac{\mu}{2}\left(\sqrt{1+\mu^2} - \mu\right)$$

(B.288)
$$T_{\dot{\beta}} = -\frac{1}{6}\left[\sqrt{1+\mu^2}\left(1-2\mu^2\right) + 2\mu^3\right]$$

(B.289)
$$T_\lambda = -\frac{1}{4}\sqrt{1+\mu^2} - \frac{\mu^2}{4}\ln\left[\frac{1+\sqrt{1+\mu^2}}{\mu}\right]$$

(B.290)
$$T_\theta = \frac{1}{6}\left[\left(\sqrt{1+\mu^2}\right)^3 - \mu^3\right]$$

(B.291)
$$Q_{\dot{\zeta}} = \frac{\mu^2}{4}\sqrt{1+\mu^2} - \frac{\mu^4}{4}\ln\left[\frac{1+\sqrt{1+\mu^2}}{\mu}\right]$$

(B.292)
$$Q_\mu = \frac{\mu^2}{2}\left(\sqrt{1+\mu^2} - \mu\right)$$

$$Q_{\dot{\beta}} = -\frac{\mu}{6}\left[\sqrt{1+\mu^2}\,(1-2\mu^2)+2\mu^3\right] \tag{B.293}$$

$$Q_{\lambda} = -\frac{\mu}{4}\sqrt{1+\mu^2}+\frac{\mu^3}{4}\ln\left[\frac{1+\sqrt{1+\mu^2}}{\mu}\right] \tag{B.294}$$

$$Q_{\theta} = \frac{\mu}{6}\left[\left(\sqrt{1+\mu^2}\right)^3-\mu^3\right] \tag{B.295}$$

The flap damping coefficient $M_{\dot{\beta}}$ is negative (which is positive damping). The speed stability coefficients M_{μ} and H_{μ} and pitch control power coefficients M_{θ} and H_{θ} are all positive. All coefficients are of order 1 for high inflow. For low inflow only, the flap damping and control, $M_{\dot{\beta}}$ and M_{θ}, are of order 1; the flap moment due to in-plane velocity is an order μ smaller in low inflow, and all in-plane force coefficients are an order μ smaller than the corresponding flap moment coefficients. Flap damping $M_{\dot{\beta}}$ and the mean blade angle of attack (for a given rotor thrust) are decreased by high inflow, but remain the same order as for low inflow; the other coefficients increase with increased inflow ratio. For low inflow, the rotor thrust coefficient terms must be retained for M_{μ}, H_{μ} and $H_{\dot{\beta}}$, while H_{θ} only has $\frac{\partial c_l}{\partial \alpha}$ terms anyway. For high inflow however, they may be neglected for all coefficients.

B.2.2 9-DoF rotor – wing model

B.2.2.1 Preliminaries

The derivation of the rotor dynamics, that is, the equations pertaining to the blade collective and cyclic flap and lag motions, are already developed in Section B.2.1, which yields a 12-DoF system including a generalised support/pivot point with 3 translational degrees of freedom and 3 rotational degrees of freedom. In this section, the equations of motion for the wing elastic bending and torsion motion are derived, and are integrated into the aforementioned rotor dynamics by substituting the wing degrees of freedom for the shaft motion degrees of freedom wherever they appear. The rotor hub forces and moments force the rotor degrees of freedom via the "mast", another name for the shaft of the rotor.

Some principal selection of the model's features is based on the consideration of the natural frequencies of various available degrees of freedom. For instance, only the lowest frequency wing modes are considered, as any higher frequency modes are less important to the coupled wing and rotor motion. That is, the rotor will not excite these higher frequency modes to any significant degree, nor be excited by them. In a similar vein, elastic motion of the pylon with respect to the wing is also neglected due to it usually having a much higher natural frequency than the lowest wing modes. Also neglected are the aircraft's rigid body motions, since these typically have low frequency and are not highly coupled with the wing and rotor motions. Modelling the system in this way – as a cantilever wing with a fixed end – is also useful as it corresponds to the configuration of many proprotor models that have been tested in wind tunnels.

The model consists of a wing and rotor operating in a freestream velocity V with the shaft in its undeformed state parallel to V, so that in the trim state the rotor equilibrium flow is purely axial. The rotor operates in high inflow. The wing root is attached to an immovable support with cantilever root restraint. The wing motion consists of elastic bending, vertical and chordwise, and elastic torsion. A pylon with large mass and moment of inertia (due to the engine and transmission typically being located at this location on a tiltrotor aircraft) is rigidly attached to the wing tip. The rotor is mounted on the pylon with the hub forward of the wing elastic axis, with the rotor shaft horizontal (parallel to V). The rotor has three or more blades, with first mode flap and lag motion for each blade. The rotor hub forces and moments are transmitted through the pylon to the wing tip.

The wing is assumed to have a high aspect ratio so that strip theory can be used for the wing aerodynamics and engineering beam theory for the elastic bending. This assumption is well justified for the tiltrotor aircraft, which typically have a wing aspect ratio of around 6.

The wing geometry is defined by a straight spar line that is the locus of the local elastic axis. The wring root is supported with cantilever restraint; the rotor shaft is attached rigidly to the wing tip. The wing geometry is shown in Figure B.9. The wing has constant chord c_w and a length y_{T_w} from root to tip (semispan). The distance along the spar is y_w, measured from the root. The shaft has length h, the distance the rotor hub is forward of the wing tip elastic axis. The wing spar is basically perpendicular to the forward velocity V, but small wing sweep, dihedral and angle of attack are considered. The wing root is attached to a plane defined by the forward velocity V and the vertical; then three rotation angles define the orientation of the spar with respect to the freestream velocity: dihedral angle δ_{w_1} (positive for wingtip moving upwards), wing angle of attack δ_{w_2} (positive for leading edge rising) and wing sweep angle δ_{w_3} (positive for wingtip moving rearward). All these angles are assumed to be small, an appropriate assumption for proprotor aircraft in cruise. The rotor shaft must then be rotated by the angles $-\delta_{w_1}$, $-\delta_{w_2}$ and $-\delta_{w_3}$ to keep the shaft parallel to the freestream velocity.

B.2.2.2 Coordinates and degrees of freedom

The wing motion is described by elastic bending and torsion of the wing spar. The wing displacement is shown in Figure B.9. The pylon (and with it the shaft) is rigidly attached to the wing tip. The existence of the elastic axis of the wing (assumed to be a straight line) means that the wing distortion may be described first by elastic torsion of the wing about the local elastic axis, without bending the wing, and then by elastic bending of the spar, which deflects the elastic axis from the undistorted position without changing the torsional deflection.

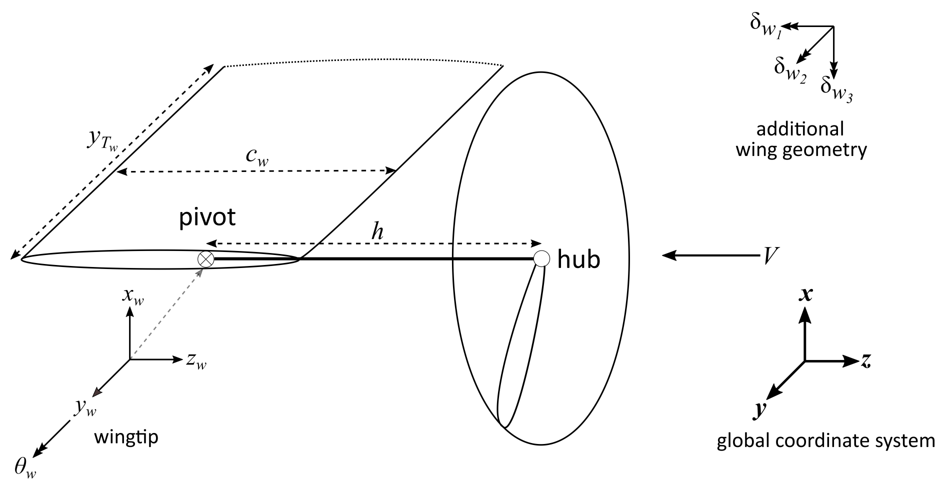

FIGURE B.9. Wing geometry

A modal description of the wing elastic deformation (in all three aforementioned manners) is used. The elastic torsion of the wing results in a pitch change $\theta_w(t, y_w)$, where t is time and y_w is a spatial coordinate along the wing elastic axis, where positive θ_w is nose-up. With a modal representation, this motion is written

$$\theta_w(t, y_w) = \sum_i p_i(t)\xi_{w_i}(y_w) \tag{B.296}$$

Which is an expansion of θ_w in a series of i modes. The generalised coordinates p_i are the degrees of freedom. Associated with each degree of freedom p_i is an equation of motion with appropriate generalised mass and stiffness, and hence a natural frequency of each mode, making p some time-varying quantity. $\xi_{w_i}(y_w)$ is the mode shape of the i^{th} mode, some function of y_w. The modal representation is useful because it separates the time and space dependencies of θ_w.

As mentioned before, only the lowest frequency degrees of freedom are retained in this model (due to the lack of significance/contribution of higher frequency degrees of freedom). Then:

$$\theta_w(t, y_w) = p(t)\xi_w(y_w) \tag{B.297}$$

The mode shape is normalised to unity at the wingtip ($y_w = y_{T_w}$), giving $\xi_w(y_{T_w}) = 1$, and we define p such that it gives the torsion angle in radians at the wingtip.

The elastic bending of the wing results in the deflection of the wing spar with components both perpendicular to the wing surface (vertical/beamwise bending) and parallel to the wing surface (chordwise). The deflection of the spar line normal to the wing surface is $z_w(t, y_w)$, positive for upward deflection. The deflection in the plane of the wing is $x_w(t, y_w)$, positive for rearward deflection. Both these quantities are defined with respect to the direction of the local principal axes of the section. With no built-in wing twist, these axes are the same all along the wing spar, but they are not vertical or horizontal because of the wing sweep, dihedral, and angle of attack. A modal representation is used for the bending deflections, both vertical and chordwise, and only the lowest frequency modes are retained. For this analysis it is sufficient to retain only one mode for each of the z_w and y_w representations; hence

$$z_w = q_1(t)\eta_w(y_w) \tag{B.298}$$

$$x_w = q_2(t)\eta_w(y_w) \tag{B.299}$$

where η_w is the mode shape of the elastic bending of the wing. For the present purposes, it is sufficient to use the same mode shape for both vertical and chordwise bending, but including different mode shapes would be straightforward. The generalised coordinates q_1 and q_2 are the degrees of freedom that represent wing vertical and chordwise bending, respectively. If the mode shape is normalised to y_{T_w} at the tip, i.e. $\eta_w(y_{T_w}) = y_{T_w}$, then the degree of freedom q_1 represents the ratio of the tip vertical deflection to the semi-span y_{T_w}, and q_2 represents the ratio of the tip chordwise deflection to y_{T_w}.

$$q_1(t) = \frac{x_w(y_{T_w})}{y_{T_w}} \tag{B.300}$$

$$q_2(t) = -\frac{z_w(y_{T_w})}{y_{T_w}} \tag{B.301}$$

These are shown in Figure B.10. The assumption of a cantilever root restraint imposes the

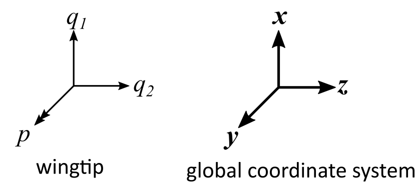

FIGURE B.10. Wing degrees of freedom

following boundary conditions:

$$\xi_w(0) = \eta_w(0) = \eta'_w(0) = 0 \tag{B.302}$$

That is, the torsion angle, and the wing bending deflection and bending slope (angle) of both flapwise and chordwise directions, are all zero at the root ($y_w = 0$).

Consider the motion of the rotor shaft in terms of the wing degrees of freedom. Specifically, the shaft displacement (x_P, y_P, z_P) and rotation (α_x, α_y, α_z) at a point a distance h aft of the rotor hub, (that is, at the connection of the rotor shaft with the wingtip), in terms of q_1, q_2 and p.

Neglecting for the moment the effects of the rotor rotation direction and wing sweep, dihedral and angle of attack, the following shaft motion is produced. The wing torsion deflection p results in shaft pitch α_y. The wing vertical bending q_1 results in vertical displacement x_P of the shaft; and since bending also produces a slope of the elastic axis at the tip, it results in shaft roll α_z. The wing chordwise bending q_2 results in longitudinal displacement z_P of the shaft and also shaft yaw angle α_x. With this model there is no first-order source of shaft lateral displacement y_P. If the magnitude of the displacement and rotation at the tip due to the wing degrees of freedom (given by the mode shapes) are accounted for, the shaft motion (for a clockwise rotating rotor on the right wing, see schematic, with dihedral angle δ_{w_1}, wing angle of attack δ_{w_2} and wing sweep angle δ_{w_3} all zero), is:

(B.303) $$\alpha_x = -q_2 \eta'_w(y_{T_w})$$

(B.304) $$\alpha_y = p$$

(B.305) $$\alpha_z = -q_1 \eta'_w(y_{T_w})$$

(B.306) $$x_P = q_1 y_{T_w}$$

(B.307) $$y_P = 0$$

(B.308) $$z_P = -q_2 y_{T_w}$$

Note that the wing bending motion produces coupling of the longitudinal and the lateral/vertical groups of the rotor, q_1 and q_2, giving them both longitudinal motion of the shaft (z_P and α_z) and lateral/vertical motion (x_P and α_x). The coupling is not strong, however, and it is found from the behaviour of the system that wing chordwise bending q_2 is basically a longitudinal motion, and vertical bending and torsion (q_1 and p) belong with the lateral/vertical group.

B.2.2.3 Contributions from wing dihedral, angle of attack and sweep angle

Consider the effect of the aforementioned wing geometry alterations. The wing tip displacement and rotations, along with the wing motion, are defined with respect to the wing spar and the section principal axes - which are rotated by δ_{w_1}, δ_{w_2} and δ_{w_3} with respect to the wind axes. That is, the wing degrees of freedom are applied relative to the principal axes once they have been rotated by the δ_w angles. For example, vertical bending q_1 produces, in addition to vertical displacement x_P and shaft roll α_z as given previously, some lateral displacement y_P due to wing dihedral δ_{w_1}, some shaft yaw α_x and axial displacement z_P due to angle of attack δ_{w_2}, and some shaft pitch α_y due to the wing sweep δ_{w_3}. After a consideration of the complete set of wing and shaft motions in this way, the result is:

$$\alpha_x = -q_2\eta'_w(y_{T_w}) + p\delta_{w_1} - q_1\delta_{w_2}\eta'_w(y_{T_w}) \tag{B.309}$$

$$\alpha_y = p + q_2\delta_{w_1}\eta'_w(y_{T_w}) - q_1\delta_{w_3}\eta'_w(y_{T_w}) \tag{B.310}$$

$$\alpha_z = -q_1\eta'_w(y_{T_w}) - p\delta_{w_3} + q_2\delta_{w_2}\eta'_w(y_{T_w}) \tag{B.311}$$

$$x_P = q_1 y_{T_w} - q_2\delta_{w_2} y_{T_w} \tag{B.312}$$

$$y_P = -q_1\delta_{w_1} y_{T_w} - q_2\delta_{w_3} y_{T_w} \tag{B.313}$$

$$z_P = -q_2 y_{T_w} - q_1\delta_{w_2} y_{T_w} \tag{B.314}$$

The influence of the wing sweep (and dihedral) requires more attention than given above. Consider the unswept wing, represented by a straight unswept elastic axis line with cantilever restraint at the root. This structure has these characteristics: elastic torsion (in-plane with XZ) at an inboard wing section results in pitch changes at outboard sections, but produces no vertical or chordwise displacement of the elastic axis from its undistorted position; and a force applied to the wing tip at the elastic axis results in bending of the wing, but produces no torsion motion since there is no torsion moment about any section due to this force. Thus, there is no elastic coupling of the wing bending and torsion motions.

If the wing is now swept, that behaviour would be maintained if the root restraint were also swept. In that case, the description developed for the shaft motion produced by the wing torsion and bending would be correct, including the effects of sweep and dihedral. However, this is not the way swept wings (of the type used for proprotor aircraft) are built. The wings are usually built with a centre box structure in the fuselage, where the spars are unswept, and only the wing structure outside the fuselage has swept spars. The wing is restrained at several points, where the wing box is tied to the fuselage. One approach to treating such a structure is to use a good structural dynamics analysis to calculate the coupled bending and torsion modes of the wing and pylon, including the influence of the root restraint and sweep. Such an approach is useful if available, and, in fact, it is probably necessary if an accurate representation of a specific design is required. Such an analysis is not desired here, however, rather the simplest representation that includes only the elements most fundamental to the behaviour. Since this report is aimed at a general examination of proprotor dynamics, rather than the design of a specific vehicle (with a swept wing), such a representation is adequate.

The model used to represent a swept wing has a straight elastic axis line except for a bend at span station $y_w = y_{B_w}$, where the wing sweep and dihedral are entered. Inboard of this location is unswept. The influence of the bent elastic axis model on the rotor shaft motion due to the wing degrees of freedom can now be determined from simple geometric considerations. Wing pitch deflection at y_{B_w} rotates the entire outboard portion of the wing about the inboard spar line, so torsion of the wing produces displacements at the wing tip – vertically due to sweep of the wing and longitudinally due to dihedral. The rotation angle is:

$$\theta_w(y_{B_w}) = p\xi_w(y_{B_w}) \tag{B.315}$$

and the arm at the tip is

$$\left(y_{T_w} - y_{B_w}\right)\delta_{w_3} \quad \text{for sweep}$$

$$\left(y_{T_w} - y_{B_w}\right)\delta_{w_1} \quad \text{for dihedral}$$

However for small y_{B_w}/y_{T_w} the terms involving y_{B_w} may be neglected:

$$y_{T_w}\delta_{w_3} \quad \text{for sweep}$$

$$y_{T_w}\delta_{w_1} \quad \text{for dihedral}$$

The increments in the shaft vertical and longitudinal displacement, x_P and z_P respectively, are then:

$$-p\xi_w(y_{B_w})y_{T_w}\delta_{w_3} \quad \text{for } x_P$$

$$-p\xi_w(y_{B_w})y_{T_w}\delta_{w_1} \quad \text{for } z_P$$

Note that a negative sign is introduced into each, as positive rotation in p (leading edge upward) about the inboard spar line will cause a positively swept (i.e. rearward) wingtip to move downward in x_P, and cause a wingtip with positive dihedral (i.e. upward) to move rearward in z_P.

B.2.2.4 Full transformation equations

The complete equations for the shaft motion induced by motion in the wing degrees of freedom are, in matrix form:

$$\begin{bmatrix} \alpha_x \\ \alpha_y \\ \alpha_z \end{bmatrix} = \begin{bmatrix} -\eta'_w(y_{T_w})\delta_{w_2} & -\eta'_w(y_{T_w}) & \delta_{w_1} \\ -\eta'_w(y_{T_w})\delta_{w_3} & \eta'_w(y_{T_w})\delta_{w_1} & 1 \\ -\eta'_w(y_{T_w}) & \eta'_w(y_{T_w})\delta_{w_2} & -\delta_{w_3} \end{bmatrix} \begin{bmatrix} q_1 \\ q_2 \\ p \end{bmatrix} \tag{B.316}$$

$$\begin{bmatrix} x_P \\ y_P \\ z_P \end{bmatrix} = \begin{bmatrix} y_{T_w} & -\delta_{w_2}y_{T_w} & -\xi_w(y_{B_w})\delta_{w_3}y_{T_w} \\ -\delta_{w_1}y_{T_w} & -\delta_{w_3}y_{T_w} & 0 \\ -\delta_{w_2}y_{T_w} & -y_{T_w} & -\xi_w(y_{B_w})\delta_{w_1}y_{T_w} \end{bmatrix} \begin{bmatrix} q_1 \\ q_2 \\ p \end{bmatrix} \tag{B.317}$$

B.2.2.5 Wing equations of motion

The dimensional equations of motion for the wing degrees of freedom, lowest mode elastic bending and torsion, are:

$$\left(I_{q_w} + m_P y_{T_w}^2\right)\ddot{q}_1 + C_{q_1}\dot{q}_1 + K_{q_1} q_1 + S_w \ddot{p} = M_{q_{1_{aero}}} + M_{q_{1_{rotor}}} \tag{B.318}$$

$$\left(I_{q_w} + I_{P_x}\eta_w'(y_{T_w})^2 + m_P y_{T_w}^2\right)\ddot{q}_2 + C_{q_2}\dot{q}_2 + K_{q_2} q_2 + S_w \delta_{w_2}\ddot{p} = M_{q_{2_{aero}}} + M_{q_{2_{rotor}}} \tag{B.319}$$

$$\left(I_{p_w} + I_{P_y}\right)\ddot{p} + C_p\dot{p} + K_p p + S_w \ddot{q}_1 - S_w \delta_{w_2}\ddot{q}_2 = M_{p_{aero}} + M_{p_{rotor}} \tag{B.320}$$

for the vertical bending, chordwise bending and torsion motions, respectively. Each equation has inertia, structural damping and structural spring terms, forced by wing aerodynamic forces and moments (subscript 'aero') and by the rotor hub forces and moments (subscript 'rotor') acting on the wingtip via the hub. The generalised inertia of the wing bending modes I_{q_w} is:

$$I_{q_w} = \int_0^{y_{T_w}} m_w \eta_w^2 dy_w \tag{B.321}$$

where m_w is the mass per unit length of the wing. This bending mode inertia applies to both of the bending modes, flapwise bending q_1 and chordwise bending q_2. Similarly, the generalised inertia of the torsion mode I_{p_w} is:

$$I_{p_w} = \int_0^{y_{T_w}} I_{\theta_w} \xi_w^2 dy_w \tag{B.322}$$

where I_{θ_w} is the moment of inertia per unit length of the wing.

To these are added the pylon inertia terms: m_P is the pylon mass (without the rotor) and I_{P_x} and I_{P_y} are, respectively, the pylon yaw and pitch moments of inertia about the wing tip effective elastic axis. The inertia coupling of the bending and torsion of the wing is due to the offset of the pylon centre of gravity: $S_w = m_P y_{T_w} z_{P_{EA}}$, where $z_{P_{EA}}$ is the distance the pylon centre of gravity is ahead of the wing tip effective elastic axis.

For typical proprotor configurations, the pylon mass is so large that its moment of inertia dominates the wing inertias, that is, $I_{q_w} << m_P y_{T_w}^2$ in the bending equations and $I_{p_w} << I_{P_y}$ in the torsion equation. Hence the inertia is primarily that of the pylon and rotor, with the wing contributing only the elastic restraint of the motion. This is fortunate in that calculating the wing inertias requires an accurate estimate of the wing mode shapes, while the pylon mass and moments of inertia are well-defined characteristics that are easily determined. The wing structural spring constants (K_{q_1}, K_{q_2}, K_p) are best determined by adjusting their values so that the predicted frequencies of the modes match the frequencies measured experimentally. It is evident that (for the lowest wing modes at least) the wing mode shapes have only a secondary influence on the equations of motion.

Only a very rough approximation to the bending mode shape η_w and the torsional mode shape ξ_w is satisfactory to estimate the wing contributions I_{q_w} and I_{p_w} to the inertias in (B.321) and (B.322), since they are dominated by the pylon contributions as discussed above. The structural spring constants and other parameters such as the slope of the bending mode shape at the wingtip, $\eta'_w(y_{T_w})$, are determined by matching them to the measured characteristics of the wing (or those calculated by a more accurate method) rather than using their definitions in terms of the wing mode shapes, which are not readily available.

The wing structural damping constants (C_{q_1}, C_{q_2} and C_p) are determined in the same way as the spring constants, by matching the theoretical results to the measured characteristics. By definition, a general damping constant C is given by:

$$C = g_s\sqrt{KI}$$

where g_s is the measured structural damping coefficient of the wing (twice the fraction of critical damping: 2ζ in modern nomenclature), K is the associated spring constant and I is the associated inertia. To adopt the nondimensional *-nomenclature from earlier:

$$C^* = \frac{C}{I} = g_s\sqrt{\frac{K}{I}}$$

B.2.2.6 Rotor hub forces and moments

As stated earlier, the wing motion is excited by the rotor forces and moments acting on the wingtip via the hub. For the moment, if the influence of wing dihedral angle δ_{w_1}, wing angle of attack δ_{w_2} and wing sweep angle δ_{w_3} are all neglected, the rotor forcing terms are:

$$M_{q_{1_{rotor}}} = \eta'_w(y_{T_w})Q + y_{T_w}H \tag{B.323}$$

$$M_{q_{2_{rotor}}} = -\eta'_w(y_{T_w})(M_x - hY) - y_{T_w}T \tag{B.324}$$

$$M_{p_{rotor}} = M_y + hH - C^*_{pq}y_{T_w}q_1 \tag{B.325}$$

The excitation of wing vertical bending q_1 is due to rotor torque Q and vertical force H, with the effectiveness of the former determined by the slope of the bending mode shape at the tip $\eta'_w(y_{T_w})$. Similarly, the excitation of chordwise bending q_2 is due to the pivot yaw moment $(M_x - hY)$ and the thrust force T. The wing torsion motion is excited by the pivot pitch moment $(M_y + hH)$ and by the trim thrust. The thrust term results because wing vertical bending q_1 elevates the rotor trim thrust above the inboard sections and so gives an arm about which the trim thrust produces a torsion moment, whose influence is controlled by the constant C^*_{pq}, defined thus:

$$C^*_{pq} = \frac{1}{y_{T_w}}\int_0^{y_{T_w}} \xi_w(y_w)\eta'_w(y_w)dy_w \tag{B.326}$$

If the mode shapes are assumed to be:

$$\eta_w(y_w) = \frac{y_w^2}{y_{T_w}} \quad \text{for bending} \tag{B.327}$$

$$\xi_w(y_w) = \frac{y_w}{y_{T_w}} \quad \text{for torsion} \tag{B.328}$$

then this gives $\eta_w(y_{T_w}) = y_{T_w}$ and $\xi_w(y_{T_w}) = 1$ as specified earlier. For illustration, the mode shapes are shown in Figure B.11. Furthermore:

$$\eta'_w(y_w) = 2\frac{y_w}{y_{T_w}} \tag{B.329}$$

by differentiation, and evaluating C^*_{pq} gives:

$$\begin{aligned} C^*_{pq} &= \frac{1}{y_{T_w}}\int_0^{y_{T_w}} \frac{y_w}{y_{T_w}} 2\frac{y_w}{y_{T_w}} dy_w \\ &= \frac{2}{y_{T_w}^3}\int_0^{y_{T_w}} y_w^2 dy_w \\ &= \frac{2}{y_{T_w}^3}\left[\frac{y_w^3}{3}\right]_0^{y_{T_w}} \\ &= \frac{2}{3} \end{aligned} \tag{B.330}$$

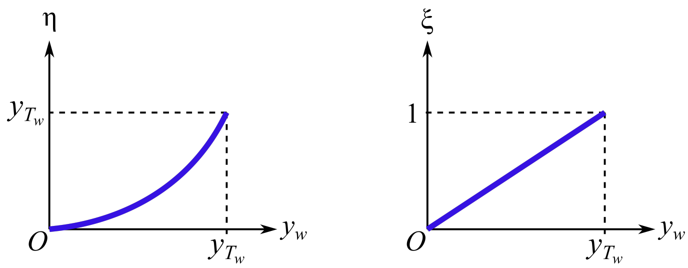

FIGURE B.11. Wing mode shapes

If dihedral, angle of attack and wing sweep are considered, the first influence is a slightly different decomposition of the rotor forces, which are defined with respect to the shaft (wind) axes, into the wing tip axes for determining the excitation of the wing bending and torsion. The equations then become:

$$\begin{aligned} M_{q_{1_{rotor}}} =& \eta'_w\left[Q - \delta_{w_3}(M_y + hH) - \delta_{w_2}(M_x - hY)\right] \\ &+ y_{T_w}\left[H - \delta_{w_1}Y - \delta_{w_2}T\right] \end{aligned} \tag{B.331}$$

$$\begin{aligned} M_{q_{2_{rotor}}} =& \eta'_w\left[-M_x + hY + \delta_{w_1}(M_y + hH) - \delta_{w_2}Q\right] \\ &+ y_{T_w}\left[-T - \delta_{w_3}Y - \delta_{w_2}H\right] \end{aligned} \tag{B.332}$$

$$\begin{aligned} M_{p_{rotor}} =& M_y + hH + \delta_{w_3} Q \\ & \delta_{w_1}(M_x - hY) + C^*_{pq} y_{T_w} T(-q_1 + \delta_{w_2} q_2) \end{aligned} \tag{B.333}$$

Additionally, the model considered here has the inboard portion unswept, and only the wing outboard of $y_w = y_{B_w}$ has sweep and dihedral. Firstly, the value of the bending mode shape at the wing sweeping point $\eta_w(y_{B_w})$ can be expressed in terms of the torsional mode shape value there, due to the similarity of the expressions:

$$\xi_w^2(y_w) = \frac{y_w^2}{y_{T_w}^2}$$

$$\Rightarrow y_{T_w} \xi_w^2(y_w) = \frac{y_w^2}{y_{T_w}} = \eta_w(y_w) \tag{B.334}$$

And now, using the shorthand nomenclature $\eta'_w = \eta'_w(y_{T_w})$ and $\xi_w = \xi_w(y_{B_w})$, the full equations are:

$$\begin{aligned} M_{q_{1_{rotor}}} =& \eta'_w \left[Q - \delta_{w_3}(1-\xi_w)(M_y + hH) - \delta_{w_2}(M_x - hY)\right] \\ & + y_{T_w}\left[H - \delta_{w_1}(1-\xi_w^2)Y - \delta_{w_2} T\right] \end{aligned} \tag{B.335}$$

$$\begin{aligned} M_{q_{2_{rotor}}} =& \eta'_w \left[-M_x + hY + \delta_{w_1}(1-\xi_w)(M_y + hH) - \delta_{w_2} Q\right] \\ & + y_{T_w}\left[-T - \delta_{w_3}(1-\xi_w^2)Y - \delta_{w_2} H\right] \end{aligned} \tag{B.336}$$

$$\begin{aligned} M_{p_{rotor}} =& M_y + (h - \xi_w)\delta_{w_3} y_{T_w} H - \xi_w \delta_{w_1} y_{T_w} T + \delta_{w_3}(1-\xi_w) Q \\ & + \delta_{w_1}(1-\xi_w)(M_x - hY) + C^*_{pq} y_{T_w} T(-q_1 + \delta_{w_2} q_2) \end{aligned} \tag{B.337}$$

As with the rotor equations of motion, the wing equations of motion are normalized by dividing by $\frac{N}{2} I_b$ and the asterisk notation (e.g. $I^*_{q_w}$) is once again employed to denote normalization in this way. Time is also nondimensionalised as in the rotor equations derivation, giving dash-derivatives rather than dot-derivatives.

(B.338)

$$\begin{aligned} &\begin{bmatrix} I^*_{q_w} + m^*_P & 0 & S^*_w \\ 0 & I^*_{q_w} + I^*_{P_x}\eta_w^2 + m^*_P & -S^*_w \delta_{w_2} \\ S^*_w & -S^*_w \delta_{w_2} & I^*_{p_w} + I^*_{P_y} \end{bmatrix} \begin{bmatrix} q''_1 \\ q''_2 \\ p'' \end{bmatrix} + \begin{bmatrix} C^*_{q_1} & 0 & 0 \\ 0 & C^*_{q_2} & 0 \\ 0 & 0 & C^*_p \end{bmatrix} \begin{bmatrix} q'_1 \\ q'_2 \\ p' \end{bmatrix} \\ &+ \begin{bmatrix} K^*_{q_1} & 0 & 0 \\ 0 & K^*_{q_2} & 0 \\ 0 & 0 & K^*_p \end{bmatrix} \begin{bmatrix} q_1 \\ q_2 \\ p \end{bmatrix} = \begin{bmatrix} M^*_{q_{1_{aero}}} \\ M^*_{q_{2_{aero}}} \\ M^*_{p_{aero}} \end{bmatrix} + \begin{bmatrix} M^*_{q_{1_{rotor}}} \\ M^*_{q_{2_{rotor}}} \\ M^*_{p_{rotor}} \end{bmatrix} \end{aligned}$$

Substituting in the rotor forcing expressions ($M_{q_{1_{rotor}}}$ etc.) and applying the rotor coefficient form directly to force and moment terms, as shown in (B.97), gives the following:

$$
\begin{aligned}
&\begin{bmatrix} I^*_{q_w} + m^*_P & 0 & S^*_w \\ 0 & I^*_{q_w} + I^*_{P_x}\eta_w^2 + m^*_P & -S^*_w\delta_{w_2} \\ S^*_w & -S^*_w\delta_{w_2} & I^*_{p_w} + I^*_{P_y} \end{bmatrix} \begin{bmatrix} q_1'' \\ q_2'' \\ p'' \end{bmatrix} + \begin{bmatrix} C^*_{q_1} & 0 & 0 \\ 0 & C^*_{q_2} & 0 \\ 0 & 0 & C^*_p \end{bmatrix} \begin{bmatrix} q_1' \\ q_2' \\ p' \end{bmatrix} \\
&+ \begin{bmatrix} K^*_{q_1} & 0 & 0 \\ 0 & K^*_{q_2} & 0 \\ C^*_{pq} y_{T_w} \gamma \frac{2C_T}{\sigma a} & -C^*_{pq} y_{T_w} \gamma \frac{2C_T}{\sigma a} \delta_{w_2} & K^*_p \end{bmatrix} \begin{bmatrix} q_1 \\ q_2 \\ p \end{bmatrix} = \begin{bmatrix} M^*_{q_{1aero}} \\ M^*_{q_{2aero}} \\ M^*_{p_{aero}} \end{bmatrix} \\
&+ \gamma \begin{bmatrix} \eta_w'\delta_{w_3}(1-\xi_w) & -\eta_w'\delta_{w_2} \\ -\eta_w'\delta_{w_1}(1-\xi_w) & -\eta_w' \\ -1 & -\delta_{w_1}(1-\xi_w) \end{bmatrix} \begin{bmatrix} -2\frac{C_{M_y}}{\sigma a} \\ 2\frac{C_{M_x}}{\sigma a} \end{bmatrix} \\
&+ \gamma \begin{bmatrix} \bar{y}_{T_w} - \eta_w'\delta_{w_3}\bar{h}(1-\xi_w) & -\eta_w'\delta_{w_2}\bar{h} + \bar{y}_{T_w}\delta_{w_1}(1-\xi_w^2) \\ -\delta_{w_2}\bar{y}_{T_w} + \eta_w'\delta_{w_3}\bar{h}(1-\xi_w) & -\eta_w'\bar{h} + \bar{y}_{T_w}\delta_{w_3}(1-\xi_w^2) \\ (\bar{h}-\xi_w)\delta_{w_3}\bar{y}_{T_w} & \delta_{w_1}(1-\xi_w)\bar{h} \end{bmatrix} \begin{bmatrix} 2\frac{C_H}{\sigma a} \\ -2\frac{C_Y}{\sigma a} \end{bmatrix} \\
&+ \gamma \begin{bmatrix} 2\eta_w' \\ -2\eta_w'\delta_{w_2} \\ 2\delta_{w_3}(1-\xi_w) \end{bmatrix} \frac{C_Q}{\sigma a} + \gamma \begin{bmatrix} -2\bar{y}_{T_w}\delta_{w_2} \\ -2\bar{y}_{T_w} \\ -2\xi_w\delta_{w_1}\bar{y}_{T_w} \end{bmatrix} \frac{C_T}{\sigma a}
\end{aligned}
\tag{B.339}
$$

where $\bar{y}_{T_w}$ is the nondimensional wing semispan, nondimensionalised by R as all other lengths. An exception to the asterisk notation for indicating nondimensionalisation is m^*_P. Rather than a factor of $\frac{N}{2}I_b$, the definition is:

$$m^*_P = \frac{m_P y^2_{T_w}}{\frac{N}{2}I_b} \tag{B.340}$$

where the additional $y^2_{T_w}$ converts the mass to a moment of inertia term prior to nondimensionalisation by $\frac{N}{2}I_b$. It also follows that:

$$S^*_w = \frac{S_w}{\frac{N}{2}I_b} = \frac{m^*_P z_{P_{EA}}}{y_{T_w}} \tag{B.341}$$

The Lock number γ appears as a factor of all the aerodynamic terms (the rotor forces and moments have inertia terms, too, but always with a factor γ^{-1}. This single parameter accounts for the relative influence of the aerodynamic and inertial forces; specifically, it is the only parameter that varies with air density ρ, all other constants being the ratio of inertias (that is, of course, the reason for the normalisation by $\frac{N}{2}I_b$). The spring and damping constants are also normalised in this way.

B.2.2.7 Wing aerodynamics

The wing aerodynamic forces and moments that excite the bending and torsion motions of the wing are defined by:

$$M_{q_{1aero}} = \int_0^{y_{T_w}} F_{z_w} \eta_w dy_w \tag{B.342}$$

$$M_{q_{2aero}} = \int_0^{y_{T_w}} F_{x_w} \eta_w dy_w \tag{B.343}$$

$$M_{p_{aero}} = \int_0^{y_{T_w}} M_w \xi_w dy_w \tag{B.344}$$

where F_{z_w} is the sectional vertical aerodynamic force (i.e. lift); F_{x_w} is the chordwise force (profile drag and induced drag); and M_w is the aerodynamic pitching moment about the local elastic axis. The section forces F_{z_w} and F_{x_w} are defined with respect to the section principal axes, not with respect to the freestream. The integrals of these section forces over the span, weighted by the appropriate mode shape, give the net forces and moments that excite the wing degrees of freedom. The velocity seen by the section has perturbations that result from the wing degrees of freedom and from aerodynamic gusts; any interference with the rotor is neglected. From the velocity perturbation, the perturbations of the section forces are found (following a procedure similar to that used for the rotor aerodynamics):

$$\begin{aligned}
\begin{bmatrix} M^*_{q_{1aero}} \\ M^*_{q_{2aero}} \\ M^*_{p_{aero}} \end{bmatrix} &= \gamma \begin{bmatrix} M^*_{q_1q'_1} & M^*_{q_1q'_2} & M^*_{q_1p'} \\ M^*_{q_2q'_1} & M^*_{q_2q'_2} & M^*_{q_2p'} \\ M^*_{pq'_1} & M^*_{pq'_2} & M^*_{pp'} \end{bmatrix} \begin{bmatrix} q'_1 \\ q'_2 \\ p' \end{bmatrix} \\
&+ \gamma \begin{bmatrix} M^*_{q_1q_1} & M^*_{q_1q_2} & M^*_{q_1p} \\ M^*_{q_2q_1} & M^*_{q_2q_2} & M^*_{q_2p} \\ M^*_{pq_1} & M^*_{pq_2} & M^*_{pp} \end{bmatrix} \begin{bmatrix} q_1 \\ q_2 \\ p \end{bmatrix} \\
&+ \gamma \begin{bmatrix} M^*_{q_1\bar{u}_g} & M^*_{q_1\bar{\beta}_g} & M^*_{q_1\bar{\alpha}_g} \\ M^*_{q_2\bar{u}_g} & M^*_{q_2\bar{\beta}_g} & M^*_{q_2\bar{\alpha}_g} \\ M^*_{p\bar{u}_g} & M^*_{p\bar{\beta}_g} & M^*_{p\bar{\alpha}_g} \end{bmatrix} \begin{bmatrix} \bar{u}_g \\ \bar{\beta}_g \\ \bar{\alpha}_g \end{bmatrix}
\end{aligned} \tag{B.345}$$

Consequently the wing aerodynamic coefficients are found. Note that the trim terms are dropped. From the first (damping) matrix:

$$M^*_{q_1q'_1} = -d_{13}\mu C_{L_\alpha} \frac{1}{y^3_{T_w}} \int_0^{y_{T_w}} \eta^2_w dy_w$$

$$M^*_{q_1q'_2} = -d_{13}\mu C_{L_0} \frac{1}{y^3_{T_w}} \int_0^{y_{T_w}} \eta^2_w dy_w$$

$$M^*_{q_1p'} = d_{22}\frac{\mu}{2}\left(\frac{3}{4}+\frac{x_{A_w}}{c_w}\right)C_{L_\alpha}\frac{1}{y_{T_w}}\int_0^{y_{T_w}}\eta_w\xi_w dy_w$$

$$M^*_{q_2q'_1} = -d_{13}\mu\left(C_{D_\alpha}-2C_{L_0}\right)\frac{1}{y^3_{T_w}}\int_0^{y_{T_w}}\eta^2_w dy_w$$

$$M^*_{q_2q'_2} = -d_{13}\mu\left(2C_{D_0}-\delta_{w_2}C_{L_\alpha}\right)\frac{1}{y^3_{T_w}}\int_0^{y_{T_w}}\eta^2_w dy_w$$

$$M^*_{q_2p'} = d_{22}\frac{\mu}{2}\left[\left(\frac{1}{2}+\frac{x_{A_w}}{c_w}\right)\left(C_{D_\alpha}-2C_{L_0}\right)-\frac{C_{L_0}}{4}\right]\frac{1}{y_{T_w}}\int_0^{y_{T_w}}\eta_w\xi_w dy_w$$

$$M^*_{pq'_1} = d_{22}\mu\frac{x_{A_w}}{c_w}C_{L_\alpha}\frac{1}{y_{T_w}}\int_0^{y_{T_w}}\eta_w\xi_w dy_w$$

$$M^*_{pq'_2} = -d_{22}\mu 2C_{m_{ac}}\frac{1}{y_{T_w}}\int_0^{y_{T_w}}\eta_w\xi_w dy_w$$

$$M^*_{pp'} = -d_{31}\frac{\mu}{2}\left(\frac{1}{4}+\frac{1}{2}\frac{x_{A_w}}{c_w}\right)C_{L_\alpha}\frac{1}{y_{T_w}}\int_0^{y_{T_w}}\xi^2_w dy_w$$

From the second (spring) matrix:

$$M^*_{q_1q_1} = -d_{12}\mu^2\delta_{w_3}C_{L_\alpha}\frac{1}{y^2_{T_w}}\int_0^{y_{T_w}}\eta_w\eta'_w dy_w$$

$$M^*_{q_1q_2} = -d_{12}\mu^2\delta_{w_3}C_{L_0}\frac{1}{y^2_{T_w}}\int_0^{y_{T_w}}\eta_w\eta'_w dy_w$$

$$M^*_{q_1p} = d_{12}\mu^2 C_{L_\alpha}\frac{1}{y_{T_w}}\int_0^{y_{T_w}}\eta_w\xi_w dy_w$$

$$M^*_{q_2q_1} = -d_{12}\mu^2\delta_{w_3}\left(C_{D_\alpha}-2C_{L_0}\right)\frac{1}{y^2_{T_w}}\int_0^{y_{T_w}}\eta_w\eta'_w dy_w$$

$$M^*_{q_2q_2} = -d_{12}\mu^2\delta_{w_3}\left(2C_{D_0}-\delta_{w_2}C_{L_\alpha}\right)\frac{1}{y^3_{T_w}}\int_0^{y_{T_w}}\eta^2_w dy_w$$

$$M^*_{q_2p} = d_{12}\mu^2\left(C_{D_\alpha}-C_{L_0}\right)\frac{1}{y_{T_w}}\int_0^{y_{T_w}}\eta_w\xi_w dy_w$$

$$M^*_{pq_1} = d_{12}\mu^2 C_{m_{ac}}\frac{1}{y^2_{T_w}}\int_0^{y_{T_w}}\xi_w\eta''_w\frac{\left(y_w-y_{T_w}\right)^2}{2}dy_w$$

$$M^*_{pq_2} = -d_{12}\mu^2 C_{L_0}\frac{1}{y^2_{T_w}}\int_0^{y_{T_w}}\xi_w\eta''_w\frac{\left(y_w-y_{T_w}\right)^2}{2}dy_w$$

$$M^*_{pp} = -d_{21}\mu^2\frac{x_{A_w}}{c_w}C_{L_\alpha}\frac{1}{y_{T_w}}\int_0^{y_{T_w}}\xi^2_w dy_w$$

And from the last (gusts) matrix:

$$M^*_{q_1\bar{u}_g} = d_{12}\mu^2 2C_{L_0}\frac{1}{y^2_{T_w}}\int_0^{y_{T_w}}\eta_w dy_w$$

$$M^*_{q_1\bar{\beta}_g} = \delta_{w_1} d_{12}\mu^2 C_{L_\alpha} \frac{1}{y^2_{T_w}} \int_0^{y_{T_w}} \eta_w dy_w + \delta_{w_3} d_{12}\mu^2 2C_{L_0} \frac{1}{y^2_{T_w}} \int_0^{y_{T_w}} \eta_w dy_w$$

$$M^*_{q_1\bar{\alpha}_g} = d_{12}\mu^2 C_{L_\alpha} \frac{1}{y^2_{T_w}} \int_0^{y_{T_w}} \eta_w dy_w$$

$$M^*_{q_2\bar{u}_g} = d_{12}\mu^2 2\left(C_{D_0} - \delta_{w_2} C_{L_0}\right) \frac{1}{y^2_{T_w}} \int_0^{y_{T_w}} \eta_w dy_w$$

$$M^*_{q_2\bar{\beta}_g} = \delta_{w_1} d_{12}\mu^2 \left(C_{D_\alpha} - 2C_{L_0}\right) \frac{1}{y^2_{T_w}} \int_0^{y_{T_w}} \eta_w dy_w + \delta_{w_3} d_{12}\mu^2 2\left(C_{D_0} - \delta_{w_2} C_{L_0}\right) \frac{1}{y^2_{T_w}} \int_0^{y_{T_w}} \eta_w dy_w$$

$$M^*_{q_2\bar{\alpha}_g} = d_{12}\mu^2 \left(C_{D_\alpha} - 2C_{L_0}\right) \frac{1}{y^2_{T_w}} \int_0^{y_{T_w}} \eta_w dy_w$$

$$M^*_{p\bar{u}_g} = d_{21}\mu^2 2C_{m_{ac}} \frac{1}{y_{T_w}} \int_0^{y_{T_w}} \xi_w dy_w$$

$$M^*_{p\bar{\beta}_g} = -\delta_{w_1} d_{21}\mu^2 \frac{x_{A_w}}{c_w} C_{L_\alpha} \frac{1}{y_{T_w}} \int_0^{y_{T_w}} \xi_w dy_w + \delta_{w_3} d_{21}\mu^2 2C_{m_{ac}} \frac{1}{y_{T_w}} \int_0^{y_{T_w}} \xi_w dy_w$$

$$M^*_{p\bar{\alpha}_g} = -d_{21}\mu^2 \frac{x_{A_w}}{c_w} C_{L_\alpha} \frac{1}{y_{T_w}} \int_0^{y_{T_w}} \xi_w dy_w$$

where C_{L_0} and C_{D_0} are the wing trim lift and drag (both profile and induced) coefficients respectively, and C_{L_α} and C_{D_α} are their respective derivatives, with respect to angle of attack. The section moment characteristics are given by x_{A_w}, the distance the aerodynamic centre is behind the elastic axis, and $c_{m_{ac}}$, the nose-up moment coefficient about the aerodynamic centre. The constant $d_{nm} = \frac{\bar{c}^n_w \bar{y}^m_{T_w}}{\pi\sigma a}$ accounts for the difference in the normalization between the wing and rotor coefficients. The integrals are evaluated using the mode shapes discussed earlier: (B.327) and (B.328), which are reasonably accurate given the large mass on the wing tip.

In the same manner as the derivation of the rotor aerodynamics, only the wing lift slope terms (C_{L_α}) are retained due to their dominance in the overall system dynamics compared to the contributions of the other terms.

B.2.2.8 Full equations of motion for proprotor and wing

All the elements are now available to construct the equations of motion for the proprotor and cantilever wing system: the rotor equations of motion, the rotor hub forces and moments (both inertial and aerodynamic), the shaft motion due to the wing degrees of freedom, and the wing equations of motion. it is only necessary to perform the matrix multiplications required because of the substitutions. The result is a set of linear ordinary differential equations for the nine degrees of freedom:

β_{1C} cyclic flap (longitudinal tip path plane tilt/pitch)

β_{1S} cyclic flap (lateral tip path plane tilt/yaw)

ζ_{1C} cyclic lead-lag (lateral rotor centre-of-gravity offset)

ζ_{1S} cyclic lead-lag (longitudinal/vertical rotor centre-of-gravity offset)

β_0 collective flap (coning)

ζ_0 collective lag (or rotor speed perturbation)

q_1 wing vertical/beamwise/flapwise bending

q_2 wing chordwise bending

p wing torsion

with the inputs

θ_{1C} cyclic pitch (lateral/pitch control plane tilt)

θ_{1S} cyclic pitch (longitudinal/yaw control plane tilt)

θ_0 collective pitch

$\bar{u}_g$ longitudinal gust

$\bar{\beta}_g$ lateral gust

$\bar{\alpha}_g$ vertical gust

which are arranged in the degree of freedom vector $\mathbf{x}$ and control vector $\mathbf{v}$ thus:

(B.346)
$$\mathbf{x} = \begin{bmatrix} \beta_{1C} & \beta_{1S} & \zeta_{1C} & \zeta_{1S} & \beta_0 & \zeta_0 & q_1 & q_2 & p \end{bmatrix}^T$$

(B.347)
$$\mathbf{v} = \begin{bmatrix} \theta_{1C} & \theta_{1S} & \theta_0 & \bar{u}_g & \bar{\beta}_g & \bar{\alpha}_g \end{bmatrix}^T$$

which allows the full equations to have the form:

(B.348)
$$\mathbf{A}_2\mathbf{x}'' + \mathbf{A}_1\mathbf{x}' + \mathbf{A}_0\mathbf{x} = \mathbf{B}\mathbf{v}$$

where $\mathbf{A}_{0,1,2}$ are the coefficient matrices for stiffness, damping and inertia, respectively, and $\mathbf{B}$ is the control coefficient matrix. Some final simplifications are made before the full equations are stated. In the parametric values given in the original literature, only the wing sweep angle δ_{w_3} is non-zero, and therefore all terms with wing dihedral angle δ_{w_1} and wing angle of attack δ_{w_2} go to 0 and disappear. As the '3' subscript is no longer necessary, the quantity is indicated here with just δ to save some space.

Furthermore, as the present work does not make use of either the gust terms or control inputs, all elements of $\mathbf{v}$ are 0 at all times and therefore the right hand side of (B.348) may simply become $\mathbf{0}$. Although the simplified equations are written in matrix form in the original text, the great number of additional terms that are present in the un-simplified equations makes this format impractical, and the equations are therefore written out separately as ordinary algebra. Specifically:

$$\begin{aligned}(\text{B.349})\quad & I^*_\beta \beta''_{1C} + I^*_{\beta\alpha}\delta\eta q''_1 - I^*_{\beta\alpha} p'' \\ & + \left(I^*_\beta g_\beta \sqrt{\nu^2_\beta - 1} - \gamma M_{\dot\beta}\right)\beta'_{1C} + 2I_\beta \beta'_{1S} + \gamma M_{\dot\zeta}\zeta'_{1C} - \gamma M_{\dot\beta}\delta\eta q'_1 - \left(2I^*_{\beta\alpha}\eta + \gamma M_\mu(\eta\bar h - \delta y_{T_w})\right) q'_2 + \gamma M_{\dot\beta} p' \\ & + \left(I^*_\beta(\nu^2_\beta - 1) + K_P\gamma M_\theta\right)\beta_{1C} - \gamma M_{\dot\beta}\beta_{1S} + \gamma M_{\dot\zeta}\zeta_{1S} + \gamma(\mu) M_\mu \eta q_2 = 0\end{aligned}$$

$$\begin{aligned}(\text{B.350})\quad & I^*_\beta \beta''_{1S} - \eta I^*_{\beta\alpha} q''_2 \\ & - 2I^*_\beta \beta'_{1C} + \left(I^*_\beta g_\beta \sqrt{\nu^2_\beta - 1} - \gamma M_{\dot\beta}\right)\beta'_{1S} + \gamma M_{\dot\zeta}\zeta'_{1S} + \left[\gamma M_\mu(y_{T_w} - \delta\eta\bar h) - 2I_{\beta\alpha}\delta\eta\right] q'_1 + \gamma M_{\dot\beta}\eta q'_2 \\ & + \left(2I_{\beta\alpha} + \gamma M_\mu(\bar h - \delta\xi y_{T_w})\right) p' \\ & + \gamma M_{\dot\beta}\beta_{1C} + \left(I^*_\beta(\nu^2_\beta - 1) + K_P\gamma M_\theta\right)\beta_{1S} - \gamma M_{\dot\zeta}\zeta_{1C} + \gamma M_\mu \delta\eta\mu q_1 - \gamma M_\mu \mu p = 0\end{aligned}$$

$$\begin{aligned}(\text{B.351})\quad & I^*_\zeta \zeta''_{1C} - S^*_\zeta(\eta\bar h - \delta y_{T_w}) q''_2 \\ & + \gamma Q_{\dot\beta}\beta'_{1C} + \left(\gamma Q_{\dot\zeta} + I^*_\zeta g_\zeta \nu_\zeta\right)\zeta'_{1C} + 2I^*_\zeta \zeta'_{1S} - \gamma Q_{\dot\beta}\delta\eta q'_1 - \gamma Q_\mu(\eta\bar h - \delta y_{T_w}) q'_2 + \gamma Q_{\dot\beta} p' \\ & + \gamma K_P Q_\theta \beta_{1C} - \gamma Q_{\dot\beta}\beta_{1S} + I^*_\zeta(\nu^2_\zeta - 1)\zeta_{1C} + \gamma Q_{\dot\zeta}\zeta_{1S} + \gamma Q_\mu \eta\mu q_2 = 0\end{aligned}$$

$$\begin{aligned}(\text{B.352})\quad & I^*_\zeta \zeta''_{1S} + S\zeta^*(y_{T_w} - \delta\eta\bar h) q''_1 + S^*_\zeta(\bar h - \delta\xi y_{T_w}) p'' \\ & - \gamma Q_{\dot\beta}\beta'_{1S} - 2I^*_\zeta \zeta'_{1C} + \left(\gamma Q_{\dot\zeta} + I^*_\zeta g_\zeta \nu_\zeta\right)\zeta'_{1S} + \gamma Q_\mu(y_{T_w} - \delta\eta\bar h) q'_1 + \gamma Q_{\dot\beta}\eta q'_2 + \gamma Q_\mu(\bar h - \delta\xi y_{T_w}) p' \\ & + \gamma Q_{\dot\beta}\beta_{1C} + \gamma Q_\theta K_P \beta_{1S} - \gamma Q_{\dot\zeta}\zeta_{1C} + I^*_\zeta(\nu^2_\zeta - 1)\zeta_{1S} + \gamma Q_\mu \delta\eta\mu q_1 - \gamma Q_\mu \mu p = 0\end{aligned}$$

$$\begin{aligned}(\text{B.353})\quad & I^*_{\beta_0}\beta''_0 - S^*_{\beta_0} y_{T_w} q''_2 \\ & + \left(I^*_{\beta_0} g_{\beta_0}\sqrt{\nu^2_{\beta_0} - 1} - \gamma M_{\dot\beta}\right)\beta'_0 + \gamma M_{\dot\zeta}\zeta'_0 + \gamma M_{\dot\zeta}\eta q'_1 + \gamma M_\lambda y_{T_w} q'_2 + \gamma M_{\dot\zeta}\delta p' \\ & + \left(I^*_{\beta_0}\nu^2_{\beta_0} + \gamma K_P M_\theta\right)\beta_0 = 0\end{aligned}$$

$$\begin{aligned}(\text{B.354})\quad & I^*_{\zeta_0}\zeta''_0 + \eta I^*_{\zeta_0\alpha} q''_1 + I_{\zeta_0\alpha}\delta p'' \\ & - \gamma Q_{\dot\beta}\beta'_0 + \left(I^*_{\zeta_0} g_{\zeta_0}\nu_{\zeta_0} + \gamma Q_{\dot\zeta}\right)\zeta'_0 + \gamma Q_{\dot\zeta}\eta q'_1 + \gamma Q_\lambda y_{T_w} q'_2 + \gamma Q_{\dot\zeta}\delta p' \\ & + \gamma K_P Q_\theta \beta_0 + I^*_{\zeta_0}\nu^2_{\zeta_0}\zeta_0 = 0\end{aligned}$$

(B.355)

$$
\begin{gathered}
S_\zeta^*(y_{T_w}+\delta\eta\bar{h}(\xi-1))\zeta''_{1S}+2\eta I_{\zeta_0\alpha}\zeta''_0+\left(I_{q_w}+m_P^*+2M_b(y_{T_w}+\delta\eta\bar{h}(\xi-1))(y_{T_w}-\delta\eta\bar{h})+2\eta^2\right)q''_1\\
+\left(S_w^*+2\delta\eta+2M_b(y_{T_w}+\delta\eta\bar{h}(\xi-1))(\bar{h}-\delta\xi y_{T_w})\right)p''\\
-\gamma H_{\dot\beta}\left(y_{T_w}+\delta\eta\bar{h}(\xi-1)\right)\beta'_{1S}+\gamma H_{\dot\zeta}(y_{T_w}+\delta\eta\bar{h}(\xi-1))\zeta'_{1S}-2\gamma Q_{\dot\beta}\eta\beta'_0+2\gamma Q_{\dot\zeta}\eta\zeta'_0\\
+\left(C_{q_1}^*+2\eta^2\gamma Q_{\dot\zeta}+\gamma\left(H_\mu+R_\mu\right)(y_{T_w}+\delta\eta\bar{h}(\xi-1))(y_{T_w}-\delta\eta\bar{h})-\gamma M_{q_1q'_1}\right)q'_1\\
+\left(2\eta y_{T_w}\gamma Q_\lambda+\gamma H_{\dot\beta}\eta\left(y_{T_w}+\delta\eta\bar{h}(\xi-1)\right)\right)q'_2\\
+\left(\gamma\left(H_\mu+R_\mu\right)\left(y_{T_w}+\delta\eta\bar{h}(\xi-1)\right)(\bar{h}-\delta\xi y_{T_w})+2\gamma Q_{\dot\zeta}\delta\eta-\gamma M_{q_1p'}\right)p'\\
+\left(\gamma H_{\dot\beta}\left(y_{T_w}+\delta\eta\bar{h}(\xi-1)\right)+I_\beta^*\delta\eta(\nu_\beta^2-1)(\xi-1)\right)\beta_{1C}+\gamma K_PH_\theta\left(y_{T_w}+\delta\eta\bar{h}(\xi-1)\right)\beta_{1S}\\
-\gamma H_{\dot\zeta}\left(y_{T_w}+\delta\eta\bar{h}(\xi-1)\right)\zeta_{1C}+2\gamma Q_\theta\eta K_P\beta_0\\
+\left(K_{q_1}+\gamma\left(H_\mu+R_\mu\right)\delta\eta\mu\left(y_{T_w}+\delta\eta\bar{h}(\xi-1)\right)-\gamma M_{q_1q_1}\right)q_1-\left(\gamma\left(H_\mu+R_\mu\right)\mu\left(y_{T_w}+\delta\eta\bar{h}(\xi-1)\right)+\gamma M_{q_1p}\right)p=0
\end{gathered}
$$

(B.356)

$$
\begin{gathered}
-S_\zeta^*\left(\eta\bar{h}+\delta y_{T_w}(\xi^2-1)\right)\zeta''_{1C}-S_\zeta^*\delta\eta\bar{h}(\xi-1)\zeta''_{1S}-2y_{T_w}S_{\beta_0}\beta''_0-2M_b\delta\eta\bar{h}\left(y_{T_w}-\delta\eta\bar{h}\right)(\xi-1)q''_1\\
+\left(I_{q_w}^*+m_P+I_{P_x}\eta^2+2M_b(\eta\bar{h}-\delta y_{T_w})(\eta\bar{h}+\delta y_{T_w}(\xi^2-1))+2y_{T_w}^2M_b\right)q''_2-2M_b\delta\eta\bar{h}\left(\bar{h}-\delta\xi y_{T_w}\right)(\xi-1)p''\\
+\gamma H_{\dot\beta}\left(\eta\bar{h}+\delta y_{T_w}(\xi^2-1)\right)\beta'_{1C}+\gamma H_{\dot\beta}\delta\eta\bar{h}(\xi-1)\beta'_{1S}-\gamma H_{\dot\zeta}\left(\eta\bar{h}\delta y_{T_w}(\xi^2-1)\right)\zeta'_{1C}-\gamma H_{\dot\zeta}\delta\eta\bar{h}(\xi-1)\zeta'_{1S}\\
+2\gamma T_{\dot\beta}y_{T_w}\beta'_0-2\gamma T_{\dot\zeta}y_{T_w}\zeta'_0\\
+\left(\gamma H_{\dot\beta}\delta\eta\left(\eta\bar{h}+\delta y_{T_w}(\xi^2-1)\right)-2\gamma T_{\dot\zeta}\eta y_{T_w}-\gamma\left(H_\mu+R_\mu\right)\delta\eta\bar{h}\left(y_{T_w}-\delta\eta\bar{h}\right)(\xi-1)\right)q'_1\\
+\left(C_{q_2}^*+\gamma\left(H_\mu+R_\mu\right)\left(\eta\bar{h}+\delta y_{T_w}(\xi^2-1)\right)-2\gamma T_\lambda y_{T_w}^2-\gamma H_{\dot\beta}\delta\eta^2\bar{h}(\xi-1)\right)q'_2\\
-\left(\gamma H_{\dot\beta}\left(\eta\bar{h}+\delta y_{T_w}(\xi^2-1)\right)+2\gamma T_{\dot\zeta}\delta y_{T_w}+\gamma\left(H_\mu+R_\mu\right)\delta\eta\bar{h}\left(\bar{h}-\delta\xi y_{T_w}\right)(\xi-1)\right)p'\\
-\left(\gamma H_\theta K_P\left(\eta\bar{h}+\delta y_{T_w}(\xi^2-1)\right)+\gamma H_{\dot\beta}\delta\eta\bar{h}(\xi-1)\right)\beta_{1C}\\
+\left(\eta I_\beta^*(\nu_\beta^2-1)+\gamma H_{\dot\beta}\left(\eta\bar{h}+\delta y_{T_w}(\xi^2-1)\right)-\gamma H_\theta K_P\delta\eta\bar{h}(\xi-1)\right)\beta_{1S}\\
+\gamma H_{\dot\zeta}\delta\eta\bar{h}(\xi-1)\zeta_{1C}-\gamma H_{\dot\zeta}\left(\eta\bar{h}+\delta y_{T_w}(\xi^2-1)\right)\zeta_{1S}-2\gamma T_\theta K_Py_{T_w}\beta_0-\gamma\left(H_\mu+R_\mu\right)\delta^2\eta^2\bar{h}\mu(\xi-1)q_1\\
+\left(K_{q_2}^*-\gamma\left(H_\mu+R_\mu\right)\eta\mu\left(\eta\bar{h}+\delta y_{T_w}(\xi^2-1)\right)\right)q_2+\gamma\left(H_\mu+R_\mu\right)\delta\eta\bar{h}\mu(\xi-1)p=0
\end{gathered}
$$

$$
\begin{aligned}
\text{(B.357)}\quad & S^*_{\zeta}\zeta''_{1S} - 2I^*_{\zeta_0\alpha}\delta(\xi-1)\zeta_0 + \left(S^*_w + 2M^*_b\bar{h}\left(y_{T_w} - \delta\eta\bar{h}\right) - 2\delta\eta(\xi-1)\right)q''_1 \\
& + \left(I^*_{p_w} + I^*_{P_y} + 2M^*_b\bar{h}\left(\bar{h} - \delta\xi y_{T_w}\right) - 2\delta^2(\xi-1)\right)p'' \\
& - \gamma H_{\dot{\beta}}\bar{h}\beta'_{1S} + \gamma H_{\dot{\zeta}}\bar{h}\zeta'_{1S} + 2\gamma Q_{\dot{\beta}}\delta(\xi-1)\beta'_0 - 2\gamma Q_{\dot{\zeta}}\delta(\xi-1)\zeta'_0 \\
& + \left(\gamma\left(H_\mu + R_\mu\right)\bar{h}\left(y_{T_w} - \delta\eta\bar{h}\right) - 2\gamma Q_{\dot{\zeta}}\delta\eta(\xi-1) - \gamma M^*_{pq'_1}\right)q'_1 + \left(\gamma H_{\dot{\beta}}\eta\bar{h} - 2\gamma Q_\lambda\delta y_{T_w}(\xi-1) - \gamma M^*_{pq'_2}\right)q'_2 \\
& + \left(C^*_p + \gamma\left(H_\mu + R_\mu\right)\bar{h}\left(\bar{h} - \delta\xi y_{T_w}\right) - 2\gamma Q_{\dot{\zeta}}\delta^2(\xi-1) + M^*_{pp'}\right)p' \\
& + \left(I^*_{\beta}(\nu^2_{\beta} - 1) + \gamma H_{\dot{\beta}}\bar{h}\right)\beta_{1C} + \gamma H_\theta K_P\bar{h}\beta_{1S} - \gamma H_{\dot{\zeta}}\bar{h}\zeta_{1C} \\
& - 2\gamma Q_\theta K_P\delta(\xi-1)\beta_0 + \left(\gamma\left(H_\mu + R_\mu\right)\delta\eta\bar{h}\mu - \gamma M^*_{pq_1} + C^*_{pq}\right)q_1 - \left(\gamma\left(H_\mu + R_\mu\right)\bar{h}\mu + \gamma M^*_{pp}\right)p = 0 \quad \blacksquare.
\end{aligned}
$$

BIBLIOGRAPHY

[1] C. Sheng and J. C. Narramore.
Computational Simulation and Analysis of Bell Boeing Quad Tiltrotor Aero Interaction.
Journal of the American Helicopter Society, 54(4), 2009.

[2] M. W. Floros, J. Shen, M. K. Lee, and S. Hwang.
Loads and Stability Analysis of an Unmanned Tilt Rotor.
Presented at the 62nd Annual Forum of the American Helicopter Society, 2006.

[3] J. Shen, M. Floros, M. K. Lee, and J. M. Kim.
Multibody Dynamics Simulation of a Tiltrotor UAV.
Presented at the 2nd International Basic Research Conference on Rotorcraft Technology, Nanjing, China, November 7-9, 2005.

[4] R. J. Peyran and O. Rand.
Effect of Design Requirements on Conceptual Tiltrotor Wing Weight.
American Helicopter Society 55th Annual Forum, Montreal, Canada, 1999.

[5] C. W. Acree and W. Johnson.
Aeroelastic Stability of the LCTR2 Civil Tiltrotor.
AHS Technical Specialists' Meeting, Dallas, TX, USA, 2008.

[6] E. S. Taylor and K. A. Browne.
Vibration Isolation of Aircraft Power Plants.
Journal of Aeronautical Sciences, 6(2):43–49, 1938.

[7] W. H. Reed III and R. M. Bennett.
Propeller Whirl Flutter Considerations for V/STOL Aircraft.
Presented at the CAL-TRECOM Symposium on Dynamics Loads Problems Associated With Helicopters and V/STOL Aircraft, Buffalo, NY, USA, 1963.

[8] R. H. Scanlan and J. C. Truman.
The Gyroscopic Effect of a Rigid Rotating Propeller on Engine and Wing Vibration Modes.
Journal of the Aeronautical Sciences, 17(10):653–659, 1950.

[9] D. G. Koenig, R. K. Greif, and M. W. Kelly.
Full-Scale Wind-Tunnel Investigation of the Longitudinal Characteristics of a Tilting-rotor Convertiplane.
NASA Technical Note D-35, 1959.

[10] W. H. Deckert and R. G. Ferry.
Limited Flight Evaluation of the XV-3 Aircraft.
Air Force Flight Test Center, Air Research and Development Command, United States Air Force, 1960.

[11] Civil Aeronautics Board.
Braniff Airways Flight 542 Accident Report SA-346.
1961.

[12] Civil Aeronautics Board.
Northwest Airlines Flight 710 Accident Report SA-354.
1961.

[13] U.S. Civil Air Regulations 4b.308 Amendment 4b-16, effective October 5 1964.

[14] Johnson Aeronautics.
CAMRAD/JA: A Comprehensive Analytical Model of Rotorcraft Aerodynamics and Dynamics, Theory Manual.
1988.

[15] J. Cecrdle.
Determination of Twin Turboprop Utility Aircraft Whirl Flutter Stability Boundaries.
Presented at the 27th Congress of the International Council of the Aeronautical Sciences (ICAS 2010), Nice, France, September 19-24, 2010.

[16] C. C. Pate, M. K. Punatar, and R. W. Winn.
Some Special Investigation Areas in Light Aircraft Flutter.
SAE Technical Paper 720309, National Business Aircraft Meeting and Engineering Display, Wichita, Kansas, USA, 1972.

[17] C. B. Hoover and J. Shen.
Parametric Study of Whirl Flutter Stability of the NASA Aircraft X-57.
Presented at the 2018 AIAA Aerospace Sciences Meeting, page 276, 2018.

[18] C. B. Hoover and J. Shen.
Whirl Flutter Analysis of a Free-Flying Electric-Driven Propeller Aircraft.
Journal of Aircraft, 56(2):831–836, 2019.

[19] J. Cecrdle.
Whirl Flutter-related Certification according to FAR/CS 23 and 25 Regulation Standards.
Presented at the 2019 International Forum on Aeroelasticity and Structural Dynamics (IFASD 2019), Savannah, Georgia, USA, June 9-13, 2019.

[20] J. Cecrdle.
Exploitation of Optimization Solution for Determination of Whirl Flutter Stability Boundaries.
Presented at the 26th International Congress of the Aeronautical Sciences, Anchorage, Alaska, USA, 14-19 September, 2008.

[21] J. Cecrdle and J. Malecek.
Conceptual Design of Aeroelastic Demonstrator for Whirl Flutter Simulation.
International Journal of Aerospace and Mechanical Engineering, 6(8):1365–1369, 2012.

[22] National Transportation Safety Board.
Aircraft Accident/Incident Summary Report PB93-910405.
NTSB/AAR-93/01/SUM, 1993.

[23] D. C. Janetzke and K. R. V. Kaza.
Whirl Flutter Analysis of a Horizontal-axis Wind Turbine with a Two-Bladed Teetering Rotor.
Solar Energy, 31(2):173–182, 1983.

[24] P. P. Friedmann.
Aeroelastic Modeling of Large Wing Turbines.
Journal of the American Helicopter Society, 21(4):17–27, 1976.

[25] P. Crimi.
A Method for Analyzing the Aeroelastic Stability of a Helicopter Rotor in Forward Flight.
NASA Contractor Report 1332, 1969.

[26] E. Breitbach.
Effects of Structural Non-Linearities on Aircraft Vibration and Flutter.
AGARD Report 665, NATO, 1977.

[27] H. K. Edenborough.
Investigation of Tilt-Rotor VTOL Aircraft Rotor-Pylon Stability.
Journal of Aircraft, 5(6), 1968.

[28] D. S. Woolston, H. L. Runyan, and T. A. Byrdsong.
Some Effects of System Nonlinearities in the Problem of Aircraft Flutter.
NACA Technical Note 359, 1955.

[29] D. S. Woolston, H. L. Runyan, and R. E. Andrews.
An Investigation of Effects of Certain Types of Structural Nonlinearities on Wing and Control Surface Flutter.
Journal of the Aeronautical Sciences, 24.1:57–63, 1957.

[30] W. H. Reed III and S. R. Bland.
An Analytical Treatment of Aircraft Propeller Precession Instability.
NASA TN D-659, 1961.

[31] J. C. Houbolt and W. H. Reed III.
Propeller-nacelle Whirl Flutter.
Journal of Aeronautical Sciences, 29(3), 1962.

[32] J. L. Sewall.
An Analytical Trend Study of Propeller Whirl Instability.
NASA Technical Note D-996, 1962.

[33] R. J. Zwaan and H. Bergh.
Propeller-Nacelle Flutter of the Lockheed Electra Aircraft.
Report F.288, Natl. Luchten Ruimtevaartlab., Amsterdam, 1962.

[34] J. R. Richardson and H. F. W. Naylor.
Whirl Flutter of Propellers With Hinged Blades.
Report No. 24, Directorate Eng. Res., Defence Board (Can.), 1962.

[35] S. R. Bland and R. M. Bennett.
Wind-Tunnel Measurement of Propeller Whirl-Flutter Speeds and Static Stability Derivatives and Comparison with Theory.
NASA Technical Note D-1807, 1963.

[36] F. T. Abbott Jr., H. N. Kelly, and K. D. Hampton.
Investigation of Propeller-Powerplant Autoprecession Boundaries for a Dynamic-Aeroelastic Model of a Four-Engine Turboprop Transport Airplane.
NASA Technical Note D-1806, 1963.

[37] R. J. Ravera.
Effects of Steady State Blade Angle of Attack on Propeller Whirl Flutter.
Grumann Aircraft Eng. Corp. Report No. ADR 06-01-63.1, 1963.

[38] R. M. Bennett and S. R. Bland.
Experimental and Anlaytical Investigation of propeller Whirl FLutter of a Power Plant on a Flexible Wing.
NASA Technical Note D-2399, 1964.

[39] G. E. Smith.
Whirl of an Aircraft Power-plant Installation and its Interaction with the Flutter Motion of a Flexible Wing.
Ministry of Technology Report No. 3636, 1966.

[40] W. H. Reed III.
Propeller-Rotor Whirl Flutter: A State-of-the-Art Review.
Symposium on the Noise and Loading Actions on Helicopter V/STOL Aircraft and Ground Effect Machines, 1965.

[41] W. H. Reed III.
Review of Propeller-Rotor Whirl Flutter.
NASA TR R-264, 1967.

[42] H. C. Quigley and D. G. Koenig.
The Effect of Blade Flapping on the Dynaic Stability of a Tilting-Rotor Convertiplane.
NASA Conference on V/STOL Aircraft, Paper 13, 1960.

[43] H. C. Quigley and D. G. Koenig.
A Flight Study of the Dynamic Stability of a Tilting-Rotor Convertiplane.
NASA Technical Note D-778, 1961.

[44] W. E. Hall Jr.
Prop-Rotor Stability at High Advance Ratios.
Journal of the American Helicopter Society, 11(2):11–26, 1966.

[45] M. I. Young and R. T. Lytwyn.
The Influence of Blade Flapping Restraint on the Dynamic Stability of Low Disk Loading Propeller-Rotors.
Presented at the 23rd American Helicopter Society Annual Forum, Washington D.C., USA, 1967.

[46] T. M. Gaffey, J. G. Yen, and R. G. Kvaternik.
Analysis and Model Tests of the Proprotor Dynamics of a Tilt-Proprotor VTOL Aircraft.
Air Force V/STOL Technology and Planning Conference, Las Vegas, NV, USA, pages 23–25, 1969.

[47] L. N. DeLarm.
Whirl flutter and divergence aspects of tilt-wing and tilt-rotor aircraft.
Air Force V/STOL Technology and Planning Conference, Las Vegas, NV, USA, 1969.

[48] R. A. Johnston.
Parametric Studies of Instabilities Associated With Large, Flexible Rotor Propellers.

Preprint No. 615, American Helicopter Society 28th Annual National Forum, 1972.

[49] K. R. V. Kaza.
Effect of Steady State Coning Angle and Damping on Whirl Flutter Stability.
Journal of Aircraft, 10(11), 1973.

[50] R. G. Loewy.
Review of Rotary-Wing V/STOL.
Journal of the American Helicopter Society, 14(3):3–23, 1969.

[51] K. G. Wernicke.
Tilt Proprotor Composite Aircraft, Design State of the Art.
Journal of the American Helicopter Society, 14(2):10–25, 1969.

[52] J. K. D. Frick and W. Johnson.
Optimal Control Theory Investigation of Proprotor/Wing Response to Vertical Gust.
NASA Technical Memorandum X-62,384, 1974.

[53] W. Johnson.
Optimal Control Alleviation of Tilting Proprotor Gust Response.
Journal of Aircraft, 3(14):301–308, 1977.

[54] M. Yasue.
A Study of Gust Response for a Rotor-Propeller in Cruising Flight.
MSc. Dissertation, Massachusetts Institute of Technology, 1974.

[55] H. C. Curtiss Jr., T. Komatsuzaki, and J. J. Traybar.
The Influence of Feedback on the Aeroelastic Behavior of Tilt Proprotor Aircraft including the Effects of Fuselage Motion.
NASA Contractor Report 158778, 1979.

[56] K. Nasu.
Tilt-Rotor Flutter Control in Cruise Flight.
NASA Technical Memorandum 88315, 1986.

[57] J. G. Vorwald and I. Chopra.
Stabilizing Pylon Whirl Flutter on a Tilt-Rotor Aircraft.
32nd Structures, Structural Dynamics, and Materials Conference, Baltimore, MD, USA, 1991.

[58] J. M. van Aken.
Alleviation of Whirl-Flutter on Tilt-Rotor Aircraft Using Active Controls.
Presented at the 47th Annual Forum of the American Helicopter Society, Phoenix, Arizona, USA, May 6-8, 1991.

[59] F. Nitzsche.
Whirl-Flutter Suppression in Advanced Turboprops and Propfans by Active Control Techniques.
Journal of Aircraft, 31(3), 1994.

[60] E. L. Hathaway and F. Gandhi.
Tiltrotor Whirl Flutter Alleviation Using Actively Controlled Wing Flaperons.
AIAA Journal, 44(11):2524–2534, 2006.

[61] J. Paik, R. Singh, F. Gandhi, and E. Hathaway.
Active Tiltrotor Whirl-Flutter Stability Augmentation Using Wing-Flaperon and Swash-Plate Actuation.
Journal of Aircraft, 44(5):1439–1446, 2007.

[62] T. Richter, T. Rath, O. Oberinger, and W. Fichter.
Investigation of Whirl Flutter Stabilization using Active Trailing Edge Flaps.
Presented at the 71st Annual Forum of the American Helicopter Society, Virginia Beach, VA, May 5-7, 2015.

[63] M. W. Floros and H. Kang.
Tiltrotor Whirl Flutter Stability Augmentation Using Active Wing Tips.
Presented at American Helicopter Society 73rd Annual Forum, Fort Worth, TX, USA, May 9-11, 2017.

[64] D. G. Miller and N. D. Ham.
Active Control of Tiltrotor Blade In-plane Loads During Maneuvers.
Presented at the 14th European Rotorcraft Forum, Milan, Italy, 1988.

[65] A. Agnihotri, W. Schuessler, and R. Marr.
V-22 Aerodynamic Loads Analysis and Development of Loads Alleviation Flight Control System.
Presented at the 45th Annual Forum of the American Helicopter Society, Boston, Massachusetts, USA, May 22-24, 1989.

[66] D. G. Miller, T. M. Black, and M. Joglekar.
Tiltrotor Control Law Design for Rotor Loads Alleviation Using Modern Control Techniques.
Presented at the 1991 American Control Conference, Boston, Massachusetts, June 26-28, pages 2488–2493, 1991.

[67] B. Manimala, G. D. Padfield, D. Walker, M. Naddei, L. Verde, U. Ciniglio, P. Rollet, and F. Sandri.

Load Alleviation in Tilt Rotor Aircraft through Active Control; Modelling and Control Concepts.
The Aeronautical Journal, 108(1082), 2004.

[68] T. B. Settle and M. W. Nixon.
MAVSS Control of an Active Flaperon for Tiltrotor Vibration Reduction.
Presented at the 53rd Annual Forum of the American Helicopter Society, Virginia Beach, Virginia, USA, April 29 - May 1, 1997.

[69] M. W. Nixon, R. G. Kvaternik, and T. B. Settle.
Tiltrotor Vibration Reduction Through Higher Harmonic Control.
Journal of the American Helicopter Society, 43(3):235–245, 1998.

[70] D. J. Piatak, R. G. Kvaternik, M. W. Nixon, C. W. Langston, J. D. Singleton, R. L. Bennett, and R. K. Brown.
A Wind-Tunnel Parametric Investigation of Tiltrotor Whirl-Flutter Stability Boundaries.
Presented at the 57th Annual Forum of the American Helicopter Society, Washington, D. C., USA, May 9-11, 2001.

[71] D. J. Piatak, R. G. Kvaternik, M. W. Nixon, C. W. Langston, J. D. Singleton, R. L. Bennett, and R. K. Brown.
A Parametric Investigation of Whirl-Flutter Stability on the WRATS Tiltrotor Model.
Journal of the American Helicopter Society, 47(2):134–144, 2002.

[72] K. Nguyen, M. Betzina, and C. Kitaplioglu.
Full-Scale Demonstration of Higher Harmonic Control for Noise and Vibration Reduction.
Journal of the American Helicopter Society, 46(3):182–191, 2001.

[73] D. Muro, M Molica Colella, J. Serafini, and M. Gennaretti.
An Optimal Control Approach for Alleviation of Tiltrotor Gust Response.
The Aeronautical Journal, 116(1180):651–666, 2012.

[74] D. A. Popelka, D. Lindsay, T. Parham Jr, V. Berry, and D. J. Baker.
Results of an Aeroelastic Tailoring Study for a Composite Tiltrotor Wing.
Presented at the 51st Annual Forum of the American Helicopter Society, Fort Worth, Texas, USA, May 9-11, 1995.

[75] D. A. Popelka, D. Lindsay, T. Parham Jr, V. Berry, and D. Baker.
Results of an Aeroelastic Tailoring Study for a Composite Tiltrotor Wing.
Journal of the American Helicopter Society, 42(2):126–136, 1997.

[76] L. M. Corso, D. A. Popelka, and M. W. Nixon.
Design, Analysis and Test of a Composite Tailored Tiltrotor Wing.

Presented at the 53rd Annual Forum of the American Helicopter Society, Virginia Beach, Virginia, USA, April 29 - May 1, 1997.

[77] J. Zhang and E. C. Smith.
Influence of Aeroelastically Tailored Wing Extensions and Winglets on Whirl Flutter Stability.
Presented at the 2nd Asian/Australian Rotorcraft Forum, ARF 2013 and the 4th International Basic Research Conference on Rotorcraft Technology 2013, IBRCRT, Tianjin, China, 2013.

[78] J. Zhang and E. C. Smith.
Parametric Studies of Wing Extensions and Winglets on Whirl Flutter Stability.
Presented at the 5th Decennial AHS Aeromechanics Specialists' Conference, San Francisco, California, USA, January 22-24, 2014.

[79] J. Zhang and E. C. Smith.
Advanced Composite Wings for Whirl Flutter Augmentation: Wind Tunnel Model Design.
Presented at the 56th AIAA/ASCE/AHS/ASC Structures, Structural Dynamics, and Materials Conference, Kissimmee, Florida, USA, January 9-15, page 1414, 2015.

[80] J. Zhang, H. Kang, and E. C. Smith.
Stability Analysis of a Scaled Tiltrotor Model with Wing Extensions and Winglets.
Presented at the AHS Technical Conference on Aeromechanics Design for Transformative Vertical Flight, San Francisco, California, USA, January 16-19, 2018.

[81] C. W. Acree, R. J. Peyran, and W. Johnson.
Rotor Design for Whirl Flutter: An Examination of Options for Improving Tiltrotor Aeroelastic Stability Margins.
Presented at the 55th Annual Forum of the American Helicopter Society, Montreal, Quebec, Canada, May 25-27, 1999.

[82] C. W. Acree, R. J. Peyran, and W. Johnson.
Improving Tiltrotor Whirl-Mode Stability with Rotor Design Variations.
Presented at the 26th European Rotorcraft Forum, The Hague, The Netherlands, September 26-29, 2000.

[83] C. W. Acree.
Effects of Rotor Design Variations on Tiltrotor Whirl-Mode Stability.
Tiltrotor/Runway Independent Aircraft Technology and Applications Specialists' Meeting of the American Helicopter Society, Arlington, TX, USA, 2001.

[84] C. W. Acree, R. J. Peyran, and W. Johnson.

Rotor Design Options for Improving Tiltrotor Whirl-Flutter Stability Margins.
Journal of the American Helicopter Society, 46(2):87–95, 2001.

[85] C. W. Acree.
Rotor Design Options for Improving V-22 Whirl-Mode Stability.
Presented at the 58th Annual Forum of the American Helicopter Society, Montreal, Quebec, Canada, June 11-13, 2002.

[86] C. W. Acree, R. J. Peyran, and W. Johnson.
Rotor Design Options for Improving XV-15 Whirl Flutter Stability Margins.
NASA Technical Publication TP-2004-21226, 2004.

[87] C. W. Acree.
Effects of V-22 Blade Modifications on Whirl Flutter and Loads.
Journal of the American Helicopter Society, 50(3):269–278, 2005.

[88] J. Liu and M. A. McVeigh.
Design of Swept Blade Rotors for High-Speed Tiltrotor Application.
Presented at the AIAA, AHS, and ASEE, Aircraft Design Systems and Operations Meeting, Baltimore, Maryland, USA, September 23-25, AIAA 91-3147, 1991.

[89] V. Srinivas, I. Chopra, and M. W. Nixon.
Aeroelastic Analysis of Advanced Geometery Tiltrotor Aircraft.
Journal of the American Helicopter Society, 43(3):212–221, 1998.

[90] Oe. Soykasap and D. H. Hodges.
Performance Enhancement of a Composite Tilt-Rotor Using Aeroelastic Tailoring.
Journal of Aircraft, 37(5):805–858, 2000.

[91] S. M. Barkai, O. Rand, R. J. Peyran, and R. M. Carlson.
Modeling and Analysis of Tilt-Rotor Aeromechanical Phenomena.
Mathematical and Computer Modelling, 27(12):17–43, 1998.

[92] S. M. Barkai and O. Rand.
The Influence of Composite Induced Couplings on Tiltrotor Whirl Flutter Stability.
Journal of the American Helicopter Society, 43(2):133–145, 1998.

[93] M. W. Nixon, D. J. Piatak, L. M. Corso, and D. A. Popelka.
Aeroelastic Tailoring for Stability Augmentation and Performance Enhancements of Tiltrotor Aircraft.
Journal of the American Helicopter Society, 45(4):270–279, 2000.

[94] L. M. Corso, D. A. Popelka, and M. W. Nixon.

Design, Analysis and Test of a Composite Tailored Tiltrotor Wing.
Journal of the American Helicopter Society, 45(3):207–215, 2000.

[95] B. Singh and I. Chopra.
Whirl Flutter Stability of Two-Bladed Proprotor/Pylon Systems in High Speed Flight.
Journal of the American Helicopter Society, 48(2):99–107, 2003.

[96] C. Yang and P. Xia.
Aeroelastic Stability of Wing/Pylon/Rotor Coupled System for Tiltrotor Aircraft in Forward Flight.
Science China Technological Sciences, 54(10):2708–2715, 2011.

[97] T. Kim, S. Shin, and D. Kim.
Influence of Geometric Coupling on the Whirl Flutter Stability in Tiltrotor Aircraft with Unsteady Aerodynamics.
Journal of Aerospace Engineering, 25(1):143–148, 2012.

[98] S. Kambampati, J. Zhang, and E. C. Smith.
Aeroelastic Optimization for High-Speed, High-Efficiency Tiltrotors with Wing Extensions and Winglets.
Presented at the 56th AIAA/ASCE/AHS/ASC Structures, Structural Dynamics, and Materials Conference, Kissimmee, Florida, USA, January 9-15, 2015.

[99] S. Kambampati, T. Hoover, E. C. Smith, and M. D. Maughmer.
Multidisciplinary Optimization for High Speed, High Efficiency Tiltrotors with Wing Extensions and Winglets.
Presented at the 72nd Annual Forum of the American Helicopter Society, West Palm Beach, Florida, USA, May 17-19, 2016.

[100] S. Kambampati and E. C. Smith.
Aeroelastic Optimization of High-Speed Tiltrotor Wings with Wing Extensions and Winglets.
Journal of Aircraft, 54(5):1718–1727, 2017.

[101] V. Muscarello and G. Quaranta.
Optimization of Tiltrotor Blade Twist to Increase Whirl-Flutter Stability.
Presented at the AIAA SciTech Forum, San Diego, California, USA, January 7-11, 2019.

[102] D. A. Richardson.
The Application of Hingeless Rotors to Tilting Prop/Rotor Aircraft.
Journal of the American Helicopter Society, 16(3), 1971.

[103] J. P. Magee and H. R. Alexander.
Wind Tunnel Tests of a Full Scale Hingeless Prop/Rotor Designed for the Boeing Model 222 Tilt Rotor Aircraft.
NASA Contractor Report 114664, 1973.

[104] H. K. Edenborough, T. M. Gaffey, and J. A. Weiberg.
Analyses and tests confirm design of proprotor aircraft .
4th Aircraft Design, Flight Test, and Operations Meeting, page 803, 1972.

[105] H. R. Alexander, L. M. Hengen, and J. A. Weiberg.
Aeroelastic-Stability Characteristics of a V/STOL TiltRotor Aircraft with Hingeless Blades: Correlation of Analysis and Test.
Journal of the American Helicopter Society, 20(2):12–22, 1975.

[106] P. B. Harendra, M. J. Joglekar, T. M. Gaffey, and R. L. Marr.
V/STOL Tilt Rotor Study. Volume 5: A Mathematical Model for Real Time Flight Simulation of the Bell Model 301 Tilt Rotor Research Aircraft.
NASA Contractor Report 114614, 1973.

[107] K. G. Wernicke and H. K. Edenborough.
Full-Scale Proprotor Development.
Journal of the American Helicopter Society, 17(1):31–40, 1972.

[108] R. A. Ormiston.
Aeromechanical Stability of Soft Inplane Hingeless Rotor Helicopters.
Presented as Paper No. 25 at the 3rd European Rotorcraft Forum, Aix-en-Provence, September 7-9, France, 1977.

[109] V. Kloeppel, K. Kampa, and B. Isselhorst.
Aeromechanical Aspects in the Design of Hingeless/Bearingless Rotor Systems.
Presented as Paper No. 57 at the 9th European Rotorcraft Forum, September 13–15, Stresa, Italy, 1983.

[110] M. W. Nixon, C. W. Langston, J. D. Singleton, D. J. Piatak, R. G. Kvaternik, L. M. Corso, and R. Brown.
Aeroelastic Stability of a Soft-Inplane Gimballed Tiltrotor Model in Hover.
Presented at the AIAA/ASME/ASCE/AHS/ASC Structures, Structural Dynamics and Materials Conference, Seattle, Washington, USA, April 16-19, 2001.

[111] R. G. Kvaternik, D. J. Piatak, M. W. Nixon, C. W. Langston, J. D. Singleton, R. L. Bennett, and R. K. Brown.
An Experimental Evaluation of Generalized Predictive Control for Tiltrotor Aeroelastic Stability Augmentation in Airplane Mode of Flight.

Journal of the American Helicopter Society, 47(3):198–208, 2002.

[112] M. W. Nixon, C. W. Langston, J. D. Singleton, D. J. Piatak, R. G. Kvaternik, L. M. Corso, and R. K. Brown.
Aeroelastic Stability of a Four-Bladed Semi-Articulated Soft-Inplane Tiltrotor Model.
International Forum on Aeroelasticity and Structural Dynamics, 4-6 June 2003, Amsterdam, Netherlands, 2003.

[113] J. A. Detore and T. M. Gaffey.
The Stopped-Rotor Variant of the Proprotor VTOL Aircraft.
Journal of the American Helicopter Society, 15(3):45–56, 1970.

[114] J. G. Yen, G. E. Weber, T. M. Gaffey, H. E. Losey, and P. Y. Hsieh.
A Study of Folding Proprotor VTOL Aircraft Dynamics, Vols. I and II.
Technical Report AFFDL-TR-71-7, 1971.

[115] F. E. Tiller and R. Nicholson.
Stability and Control Considerations for a Tilt-Fold-Proprotor Aircraft.
Journal of the American Helicopter Society, 16(3):22–33, 1971.

[116] D. van Wagensfeld, F. J. McHugh, L. N. DeLarm, W. L. Lapinski, and J. F. Magee.
Wind Tunnel Test of the Aerodynamics and Dynamics of Rotor Spinup, Stopping and Folding on a Semispan Folding Tilt-Rotor Mode.
Technical Report AFFDL-TR-71-62, 1971.

[117] J. C. Slaby and E. C. Smith.
Aeroelastic Stability of Folding Tiltrotor Aircraft in Cruise Flight with Composite Wings.
Presented at the 52nd AIAA/ASME/ASCE/AHS/ASC Structures, Structural Dynamics and MAterials Conference, Denver, Colorado, USA, April 4-7, 2011.

[118] J. Wolkovitch, B. Wainfan, Y. Ben-Harush, and W. Johnson.
Application of the Joined Wing to Tiltrotor Aircraft.
NASA Contractor Report 177543, 1989.

[119] H. R. Alexander, P. F. Leone, A. K. Amos, and F. J. Tarzanin.
V/STOL Dynamics and Aeroelastic Rotor-Airframe Technology, Vols I-III.
Technical Report AFFDL-TR-72-40, 1972.

[120] R. G. Kvaternik.
Experimental and Analytical Studies in Tilt-Rotor Aeroelasticity.
Presented at the AHS/NASA Ames Specialists' Meeting on Rotorcraft Dynamics, February 13-15, Moffett Field, California, USA, 1974.

[121] W. Johnson.
Dynamics of Tilting Proprotor Aircraft in Cruise Flight.
NASA Technical Note D-7677, 1974.

[122] W. Johnson.
Theory and Comparisons with Tests of Two Full-Scale Proprotors.
Presented at the AHS/NASA-Ames Specialists' Meeting on Rotorcraft Dynamics, February 13-15, Moffett Field, California, USA, 1974.

[123] H. B. Huber.
Effect of Torsion-Flap-Lag Coupling on Hingeless Rotor Stability.
Presented at the American Helicopter Society 29th Annual Forum, Washington D. C., USA, 1973.

[124] W. Johnson.
Analytical Model for Tilting Proprotor Aircraft Dynamics, Including Blade Torsion and Coupled Bending Modes, and Conversion Mode Operation.
NASA Technical Memorandum X-62,369, 1974.

[125] W. Johnson.
Analytical Modeling Requirements for Tilting Proprotor Aircraft Dynamics.
NASA Technical Note D-8013, 1975.

[126] H. C. Curtiss Jr.
The Longitudinal Equations of Motion of a Tilt Prop/Rotor Aircraft Including the Effects of Wing and Prop/Rotor Blade Flexibility.
NASA Contractor Report 137855, 1976.

[127] W. Johnson.
The Influence of Engine/Transmission/Governor on Tilting Proprotor Aircraft Dynamics.
NASA Technical Memorandum X-62,455, 1975.

[128] W. Johnson.
Predicted Dynamic Characteristics of the XV-15 Tilting Proprotor Aircraft in Flight and in the 40- by 80-ft Wind Tunnel.
NASA Technical Memorandum X-73,158, 1976.

[129] R. G. Kvaternik.
A Review of some Tilt-Rotor Aeroelastic Research at NASA-Langley.
Journal of Aircraft, 13(5):357–363, 1976.

[130] L. Kingston and J. DeTore.
Tilt Rotor V/STOL Aircraft Technology.

Presented as Paper No. 36 at the 2nd European Rotorcraft Forum, September 20–22, Bueckeburg, Federal Republic of Germany, 1976.

[131] R. G. Kvaternik and J. S. Kohn.
An Experimental and Analytical Investigation of Proprotor Whirl Flutter.
NASA Technical Paper 1047, 1977.

[132] D. D. Few and H. K. Edenborough.
Tilt-Proprotor Perspective.
Astronautics and Aeronautics, 15:28–31, 1977.

[133] J. P. Magee and K. G. Wernicke.
XV-15 Tilt Rotor Research Aircraft-Program report.
Presented at Atlantic Aeronautical Conference, page 704, 1979.

[134] R. Carlson and W. Miao.
Aeroelastic Analysis of the Elastic Gimbal Rotor.
NASA Contract Report 166287, 1981.

[135] M. W. Nixon.
Parametric Studies for Tiltrotor Aeroelastic Stability in Highspeed Flight.
Journal of the American Helicopter Society, 38(4):71–79, 1993.

[136] A. I. Abrego, M. D. Betzina, and K. L. Long.
A Small-Scale Tiltrotor Model Operating in Descending Flight.
Presented as Paper No. 39 at the 28th European Rotorcraft Forum, Bristol, UK, September 17-20, 2002.

[137] M. D. Betzina.
Tiltrotor Descent Aerodynamics: A Small-Scale Experimental Investigation of Vortex Ring State.
Presented at the 57th Annual Forum of the American Helicopter Society, Washington, D. C., USA, May 9-11, 2001.

[138] W. Johnson.
Influence of Wake Models on Calculated Tiltrotor Aerodynamics.
Presented at the American Helicopter Society Aerodynamics, Acoustics, and Test and Evaluation Technical Specialists' Meeting, San Francisco, California, January 23-25, 2002.

[139] G. K. Yamauchi, W. Johnson, and A. J. Wadcock.
Vortex Wake Geometry of a Model Tilt Rotor in Forward Flight.
Presented at Heli Japan 2002, AHS International Meeting on Advanced Rotorcraft Technology and Life Saving Activities, Tochigi, Japan, November 11-13, 2002.

[140] C. Barla, D. Favier, C. Rondot, C. Maresca, M. Raffel, H. Richard, J. Bosbach, and H. Henning.
PIV Measurements of the Vortical Wake Behind Tilt-rotor Blades.
Presented at the 13th International Symposium on Applications of Laser Techniques to Fluid Mechanics, Lisbon, Portugal, June 26-29, 2006.

[141] C. Barla, T. Lefebvre, E. Berton, P. Beaumier, and D. Favier.
Experimental and Numerical Investigation of Aerodynamic Interactions on a Tilt-rotor Configuration.
Presented at the 32nd European Rotorcraft Forum, Maastricht, The Netherlands, September 12-14, 2006.

[142] T. Kim and S. Shin.
Advanced Analysis on Tiltrotor Aircraft Flutter Stability Including Unsteady Aerodynamics.
AIAA Journal, 46(4):1002–1012, 2008.

[143] J. M. Greenberg.
Airfoil in Sinusoidal Motion in a Pulsating Stream.
NACA Technical Note 1326, 1947.

[144] T. Kim, S. Shin, and T. Kim.
Analysis of Tiltrotor Whirl Flutter in Time and Frequency Domain.
Journal of Mechanical Science and Technology, 23(12):3281–3291, 2009.

[145] H. L. Yue and P. Q. Xia.
A Wake Bending Unsteady Dynamic Inflow Model of Tiltrotor in Conversion Flight of Tiltrotor Aircraft.
Science in China Series E: Technological Sciences, 52(11):3188–3197, 2009.

[146] M. Gennaretti and L. Greco.
A Time-Dependent-Coefficient Reduced-Order Model for Unsteady Aerodynamics of Proprotors.
Journal of Aircraft, 42(1):138–147, 2005.

[147] M. Gennaretti and L. Greco.
Whirl Flutter Analysis of Prop-Rotors Using Unsteady Aerodynamics Reduced-Order Models.
The Aeronautical Journal, 112(1131):261–270, 2008.

[148] M. Gennaretti, M. Molica Collela, and G. Bernardini.
Prediction of Tiltrotor Vibratory Loads with Inclusion of Wing-Proprotor Aerodynamic Interaction.

Journal of Aircraft, 47(1):71–79, 2010.

[149] G. Droandi, G. Gibertini, M. Lanz, G. Campardini, D. Grassi, and S. Garbaccio.
Wing-Rotor Interactions on a 1/4-Scale Tiltrotor Half-Model.
Presented at the 39th European Rotorcraft Forum, Moscow, Russia, September 3-6, 2013.

[150] G. Droandi, A. Zanotti, G. Gibertini, D. Grassi, and G. Campardini.
Experimental Investigation of the Rotor-Wing Aerodynamic Interaction in a Tiltwing Aricraft in Hover.
The Aeronautical Journal, 119(1215):591–612, 2015.

[151] G. Droandi, G. Gibertini, D. Grassi, G. Campanardi, C. Liprino, and M. Bertagnini.
Wing-rotor Aerodynamic Interference on a Tiltwing Aircraft in the First Part of Conversion Manoeuvre.
Presented as Paper no. 103 at the 42nd European Rotorcraft Forum, Lille, France, September 5-8, 2016.

[152] W. Staruk, I. Chopra, and A. Datta.
Loads Prediction for a Gimbaled Tiltrotor in Conversion Flight Using CAD-Based 3-D Structural Analysis Models.
Presented at American Helicopter Society 73rd Annual Forum, Fort Worth, TX, USA, May 9-11, 2017.

[153] W. Appleton, A. Filippone, and N. Bojdo.
Low-Order Aeromechanics of Tilt-Rotor Helicopters.
Presented as Paper No. 39 at the 44th European Rotorcraft Forum, Delft, The Netherlands, September 18-21, 2018.

[154] Z. Li and P. Xia.
Aeroelastic modelling and stability analysis of tiltrotor aircraft in conversion flight.

[155] A. J. Garcia and G. N. Barakos.
Aerodynamic Study of Tiltrotor Blades.
Presented as Paper No. 56 at the 42nd European Rotorcraft Forum, Lille, France, September 5-8, 2016.

[156] F. Dehaeze, B. Allen, and G. Barakos.
The HiPerTilt Project: Developing New Aerodynamics Methods Adapted for Tilt Rotor Aircraft.
Presented as Paper No. 90 at the 42nd European Rotorcraft Forum, Lille, France, September 5-8, 2016.

[157] D. H. Hodges.
Nonlinear Composite Beam Theory.
American Institute of Aeronautics and Astronautics, 2006.

[158] R. A. Ormiston and W. G. Warmbrodt.
(Survey of Army/NASA) Rotorcraft Aeroelastic Stability.
NASA Conference Publication 2495, NASA/Army Rotorcraft Technology, Volume I - Aerodynamics, and Dynamics and Aeroelasticity, 1988.

[159] A. Rigo, M. Favale, A. A. Trezzini, and G. Quaranta.
Numerical Evaluation of Gust Loads on a Tiltrotor.
Presented at the 74th Annual Forum of the American Helicopter Society, Phoenix, AZ, USA, May 14-17, 2018.

[160] M. Gupta and D. H. Hodges.
Nonlinear Analysis of Composite Beams with Structural Damping.
Presented at the 74th Annual Forum of the American Helicopter Society, Phoenix, AZ, USA, May 14-17, 2018.

[161] T. Parham Jr.
V-22 Pilot-in-the-Loop Aeroelastic Stability Analysis.
Presented at the 47th Annual Forum of the American Helicopter Society, Phoenix, Arizona, USA, May 6-8, 1991.

[162] T. Parham Jr. and L. M. Corso.
Aeroelastic and Aeroservoelastic Stability of the BA 609.
Presented as Paper No. G3 at the 25th European Rotorcraft Forum, Rome, Italy, September 14-16, 1999.

[163] J. Serafini, D. Muro, and M. Gennaretti.
Pilot-in-the-Loop Influence on Controlled Tiltrotor Stability and Gust Response.
Presented at the 27th Congress of the International Council of the Aeronautical Sciences (ICAS 2010), Nice, France, September 19-24, 2010.

[164] M. Gennaretti, J. Serafini, P. Masarati, and G. Quaranta.
Effects of Biodynamic Feedthrough in Rotorcraft/Pilot Coupling: Collective Bounce Case.
Journal of Guidance, Control and Dynamics, 36(6):1709–1721, 2013.

[165] V. Muscarello, P. Massarati, and G. Quaranta.
Collective Bounce in Tiltrotors.
Presented as Paper No. 121 at the 42nd European Rotorcraft Forum, Lille, France, September 5-8, 2016.

[166] M. Rais-Rohani.
Wing Design for a Civil Tiltrotor Transport Aircraft.
NASA Contractor Report 197523, 1994.

[167] M. Rais-Rohani.
Global-Local Analysis and Optimization of a Composite Civil Tilt-Rotor Wing.
Final report of NASA Langley Grant NAG 1-1571, 1999.

[168] S. L. Brunson and M. Rais-Rohani.
A Thin Tailored Composite Wing box for a Civil Tiltrotor Transport Aircraft.
Presented at the 37th AIAA/ASME/ASCE/AHS/ASC Structures, Strucural Dynamics, and Materials Conferences and Exhibit, Salt Lake City, Utah, USA, April 15-17, 1996.

[169] T. M. Clements and M. Rais-Rohani.
Design Optimization of a Composite Tilt-Rotor Wing with Stability Approximations.
Presented at the 41st Structures, Structural Dynamics, and Materials Conference and Exhibit, Atlanta, Georgia, USA, April 3-6, page 1454, 2000.

[170] M. Stettner and D. P. Schrage.
An Approach to Tiltrotor Wing Aeroservoelastic Optimization through Increased Productivity.
Presented at the 4th Symposium on Multidisciplinary Analysis and Optimization, Cleveland, Ohio, USA, September 21-23, page 4781, 1992.

[171] T. R. McCarthy.
A Coupled Rotor/Wing Optimization Procedure for High Speed Tilt-Rotor Aircraft.
Journal of the American Helicopter Society, 41(4):360–369, 1996.

[172] J. S. Park, N. J. Sung, L. Myeong-Kyu, and J. M. Kim.
Design Optimization Framework for Tiltrotor Composite Wings Considering Whirl Flutter Stability.
Composites Part B: Engineering, 41(4):257–267, 2010.

[173] A. Chattopadhyay and T. R. McCarthy.
Design of High Speed Proprotors using Multiobjective Optimization Techniques.
Engineering Optimization, 23(2):155–172, 1994.

[174] A. Chattopadhyay, T. R. McCarthy, and J. F. Madden III.
An Optimization Procedure for the Design of Prop-Rotors in High Speed Cruise including the Coupling of Performance, Aeroelastic Stability, and Structures.
Mathematical and Computer Modelling, 19(3-4):75–88, 1994.

[175] T. Kim, J. Lim, S. Shin, and D. Kim.
Structural Design Optimization of a Tiltrotor Aircraft Composite Wing to enhance Whirl Flutter Stability.
Composite Structures, 95:283–94, 2013.

[176] J. Cecrdle.
Determination of Aircraft Structure Whirl Flutter Stability Boundaries by means of Optimization Based Solution.
Presented at Engineering Mechanics 2008, Svratka, Czech Republic, May 12-15, 2008.

[177] W. Johnson.
A History of Rotorcraft Comprehensive Analyses.
Presented at the 69th Annual Forum of the American Helicopter Society, Phoenix, Arizona, USA, May 21-23, 2013.

[178] J. Shen, P. Masarati, B. Roget, D. J. Piatak, M. W. Nixon, and J. D. Singleton.
Stiff-inplane Tiltrotor Aeromechanics Investigation Using Two Multibody Analyses.
Proceedings of MULTIBODY DYNAMICS 2007, ECCOMAS Thematic Conference, Milan, Italy, June 25-28, 2007.

[179] W. Johnson.
A Comprehensive Analytical Model of Rotorcraft Aerodynamics and Dynamics, Vols I-III.
NASA Technical Memorandum 81182, 1980.

[180] W. Johnson.
Elementary Applications of a Rotorcraft Dynamic Stability Analysis.
NASA Technical Memorandum X-73,161, 1976.

[181] W. Johnson.
CAMRAD/JA. A Comprehensive Analytical Model of Rotorcraft Aerodynamics and Dynamics, Johnson Aeronautics Version.
Johnson Aeronautics, Palo Alto, California, USA, 1988.

[182] W. Johnson.
Technology Drivers in the Development of CAMRAD II.
American Helicopter Society Aeromechanics Specialists Conference, San Francisco, California, USA, January, 1994.

[183] D. A. Popelka, M. Sheffler, and J. Bilger.
Correlation of Test and Analysis for the 1/5-Scale V-22 Aeroelastic Model.
Journal of the American Helicopter Society, 32(2):21–33, 1987.

[184] G. Bir, I. Chopra, and K. Nguyen.
Development of UMARC (University of Maryland Advanced Rotorcraft Code).
Presented at the 46th Annual Forum of the American Helicopter Society, Washington, DC, USA, May 21-23, 1990.

[185] V. Srinivas and I. Chopra.
Validation of a Comprehensive Aeroelastic Analysis for Tiltrotor Aircraft.
Presented at the 52nd Annual Forum of the American Helicopter Society, 1998.

[186] H. Saberi, M. Khoshlahjeh, R. A. Ormiston, and M. J. Rutkowski.
Overview of RCAS and Application to Advanced Rotorcraft Problems.
American Helicopter Society 4th Decennial Specialists' Conference on Aeromechanics, 2004.

[187] J. C. Ho, B. Jayaraman, and H. Yeo.
Coupled Computational Fluid Dynamics and Comprehensive Analysis Calculations of a Gimballed Tiltrotor.
AIAA Journal, 57(10):4433–4446, 2019.

[188] O. A. Bauchau, C. L. Bottasso, M. Dindar, H. S. Murty, Z. Rusak, and M. S. Shephard.
Aeroelastic Stability of Rotor Blades using a Parallel Adaptive Finite Element Solver.
American Helicopter Society 2nd International Aeromechanics Specialists' Conference, Bridgeport, Connecticut, USA, 1995.

[189] G. Quaranta, G. Bindolino, P. Masarati, and P. Mantegazza.
Toward a Computational Framework for Rotorcraft Multi-Physics Analysis Adding Computational Aerodynamics to Multibody Rotor Models.
Paper No. 18 at the 30th European Rotorcraft Forum, Marseilles, France, September, 2004.

[190] E. L. Hathaway and F. S. Gandhi.
Modeling Refinements in Simple Tiltrotor Aeroelastic Stability Analyses.
Presented at the 43rd AIAA/ASME/ASCE/AHS/ASC Structures, Structural Dynamics, and Materials Conference, page 1604, 2002.

[191] E. L. Hathaway and F. S. Gandhi.
Modeling Refinements in Simple Tiltrotor Whirl Flutter Analyses.
Journal of the American Helicopter Society, 48(3):186–198, 2003.

[192] P. Hylton.
Analyzing a Simple Prop-Whirl-Flutter Model using Modern Analysis Tools.
Presented as Paper No. 005 at 2006 IJME-INTERTECH Conference, Kean University, Union, New Jersey, USA, October 18-21, 2006.

[193] Z. Li and P. Xia.
Whirl Flutter and Rotor Hub Center's Motion Image of Tiltrotor Aircraft.
Scientia Sinica (Technologica), (3):8, 2015.

[194] W. Johnson.
An Assessment of the Capability to Calculate Tilting Prop-Rotor Aircraft Performance, Loads, and Stability.
NASA Technical Paper 2291, 1984.

[195] W. Johnson.
Rotorcraft Dynamics Models for a Comprehensive Analysis.
Presented at the 54th Annual Forum of the American Helicopter Society, Washington, DC, USA, May 20-22, 1998.

[196] J. Shen and H. Kang.
Comparison Study of Tiltrotor Whirl Flutter Using Two Rotorcraft Comprehensive Analyses.
Journal of Aircraft, 54(2):841–846, 2016.

[197] H. Kang, J. Shen, and A. R. Kreshock.
Validation of Comprehensive Analysis for Tiltrotor Whirl Flutter Predictions.
Journal of Aircraft, 54(4), 2017.

[198] C. Hoover, J. Shen, H. Kang, and A. R. Kreshock.
Proprotor Loads and Whirl-Flutter Stability of a Tiltrotor Wind Tunnel Model.
Presented at the 72nd Annual Forum of the American Helicopter Society, West Palm Beach, Florida, USA, May 17-19, 2017.

[199] H. Yeo, J. Bosworth, C. W. Acree, and A. R. Kreshock.
Comparison of CAMRAD II and RCAS Predictions of Tiltrotor Aeroelastic Stability.
Presented at American Helicopter Society 73rd Annual Forum, Fort Worth, TX, USA, May 9-11, 2018.

[200] A. R. Kreshock, R. P. Thornburgh, and H. Yeo.
Comparison of Comprehensive Analyses Predicting Aeroelastic Stability of the Wing and Rotor Aeroelastic Test System.
Presented at the 74th Annual Forum of the American Helicopter Society, Phoenix, AZ, USA, May 14-17, 2018.

[201] A. R. Kreshock, R. P Thornburgh, and H. Yeo.
Comparison of Comprehensive Analyses Predicting Whirl Flutter Stability of the Wing and Rotor Aeroelastic Test System.
Journal of the American Helicopter Society, 64(4):1–12, 2019.

[202] W. Johnson and A. Datta.
Requirements for Next Generation Comprehensive Analysis of Rotorcraft.
Presented at the AHS Specialists' Conference on Aeromechanics, San Francisco, California, USA, January 23-25, 2008.

[203] G. L. Ghiringelli, P. Masarati, P. Mategazza, and M. W. Nixon.
Multi-Body Analysis of the 1/5 Scale Wind Tunel Model of the V-22 Tiltrotor.
Presented at the 55th Annual Forum of the American Helicopter Society, Montreal, Quebec, Canada, May 25-27, 1999.

[204] E. J. Haug.
Computer Aided Kinematics and Dynamics of Mechanical Systems. Vol. 1: Basic Methods.
Allyn and Bacon, Boston, 1989.

[205] A. Cardona.
An Integrated Approach to Mechanism Analysis.
Doctoral thesis, University of Liege, 1989.

[206] W. Schiehlen.
Multibody Systems Handbook.
Springer-Verlag, Berlin, 1990.

[207] G. L. Ghiringelli, P. Masarati, P. Mantegazza, and M. W. Nixon.
Multi-Body Analysis of a Tiltrotor Configuration.
Nonlinear Dynamics, 19(4):333–357, 1999.

[208] G. L. Ghiringhelli, P. Masarati, P. Mantegazza, and M. W. Nixon.
Multi-Body Analysis of an Active Control for a Tiltrotor.
CEAS International Forum on Aeroelasticity and Structural Dynamics 1999, Williamsburg, Virginia, USA, June 22-25, pages 149–158, 1999.

[209] Y. Gourinat, J. P. Mueller, R. Ferrer, T. Krysinski, and B. Kerdreux.
A Numerical Study on Active Control for Tiltrotor Whirl Flutter Stability Augmentation.
Presented at the American Helicopter Society 4th Decennial Specialists' Conference on Aeromachanics, San Francisco, California, USA, January 21-23, 2004.

[210] J. P. Mueller, Y. Gourinat, R. Ferrer, T. Krysinski, and B. Kerdreux.
A Numerical Study on Active Control for Tiltrotor Whirl Flutter Stability Augmentation.
Journal of the American Helicopter Society, 51(3):244–254, 2006.

[211] G. Quaranta, P. Masarati, M. Lanz, G. L. Ghiringhelli, and P. Mantegazza.
Dynamic Stability of Soft-In-Plane Tiltrotors by Parallel Multibody Analysis.

Presented at the 26th European Rotorcraft Forum, The Hague, The Netherlands, September 26-29, 2000.

[212] G. Quaranta, P. Mantegazza, and P. Masarati.
Assessing the Local Stability of Periodic Motions for Large Multibody Non-linear Systems using Proper Orthogonal Decomposition.
Journal of Sound and Vibration, 271(3–5):1015–1038, 2004.

[213] P. Masarati, G. Quaranta, M. Lanz, and P. Mantegazza.
Dynamic Characterization and Stability of a Large Size Multibody Tiltrotor Model by POD Analysis.
ASME 2003 International Design Engineering Technical Conferences and Computers and Information in Engineering Conference, Chicago, Illinois, USA, September 2-6, pages 1145–1154, 2003.

[214] J. Shen, J. D. Singleton, D. J. Piatak, and O. A. Bauchau.
Multibody Dynamics Simulation and Experimental Investigation of a Model-Scale Tiltrotor.
Presented at the 61st Annual Forum of the American Helicopter Society, Grapevine, Texas, USA, June 1-3, 2005.

[215] J. Shen, J. D. Singleton, D. J. Piatak, O. A. Bauchau, and P. Masarati.
Multibody Dynamics Simulation and Experimental Investigation of a Model-Scale Tiltrotor.
Modified version of that presented at the 61st Annual Forum of the American Helicopter Society, Grapevine, Texas, USA, June 1-3, 2016.

[216] J. Shen, P. Masarati, B. Roget, D. J. Piatak, J. D. Singleton, and M. W. Nixon.
Modeling a Stiff-Inplane Tiltrotor Using Two Multibody Analyses: A Validation Study.
Journal of the American Helicopter Society, 64(3):2307, 2008.

[217] P. Masarati, G. Quaranta, D. J. Piatak, J. D. Singleton, and J. Shen.
Further Results of Soft-Inplane Tiltrotor Aeromechanics Investigation using Two Multibody Analyses.
Presented at the 60th Annual Forum of the American Helicopter Society, Baltimore, Maryland, USA, June 7-10, 2004.

[218] P. Masarati, D. J. Piatak, and G. Quaranta.
Soft-inplane Tiltrotor Aeromechanics Investigation Using Two Comprehensive Multibody Solvers.
Journal of the American Helicopter Society, 53(2):179–192, 2008.

[219] M. Mattaboni, P. Masarati, G. Quaranta, and P. Mantegazza.
Multibody Simulation of Integrated Tiltrotor Flight Mechanics, Aeroelasticity, and Control.
Journal of Guidance, Control and Dynamics, 35(5):1391–1405, 2012.

[220] M. Mattaboni, P. Masarati, and P. Mantegazza.
Multibody Simulation of a Generalized Predictive Controller for Tiltrotor Active Aeroelastic Control.
Proceedings of the Institution of Mechanical Engineers, Part G: Journal of Aerospace Engineering, 226(2):197–216, 2012.

[221] W. R. Krueger.
Multibody Analysis of Whirl Flutter Stability on a Tiltrotor Wind Tunnel Model.
Proc. of the Institution of Mechanical Engineers, Part K: Journal of Multi-body Dynamics, 230(2):121–133, 2014.

[222] G. Quaranta, A. tamer, V. Muscarello, P. Masarati, M. Gennaretti, J. Serafini, and M. Molica Collela.
Evaluation of Rotorcraft Aeroelastic Stability Using Robust Analysis.
Presented as Paper No. 93 at the 38th European Rotorcraft Forum, Amsterdam, The Netherlands, September 4-7, 2012.

[223] L. Colo, G. Broux, and E. Garrigues.
A New Flutter Prediction Algorithm to Avoid P-K Method Shortcomings.
Presented at the 2019 International Forum on Aeroelasticity and Structural Dynamics (IFASD 2019), Savannah, Georgia, USA, June 9-13, 2019.

[224] Y. Karniel, D. Kariv, and M. Iovnovich.
Flutter Mechanisms Characterization using Distributed Aeroelastic Energy Analysis.
Presented at the 2019 International Forum on Aeroelasticity and Structural Dynamics (IFASD 2019), Savannah, Georgia, USA, June 9-13, 2019.

[225] M. Manetti, G. Quaranta, and P. Mantegazza.
Numerical Evaluation of Limit Cycles of Aeroelastic Systems.
Journal of Aircraft, 46(5):1759–1769, 2010.

[226] V. Muscarello and G. Quaranta.
Multiple Input Describing Function for Non-Linear Analysis of Ground and Air Resonance.
Presented as Paper No. 111 at the 37th European Rotorcraft Forum, Vergiate and Gallarate, Italy, Stepmber 13-15, 2011.

[227] A. H. Nayfeh and D. T. Mook.
Nonlinear Oscillations.
John Wiley & Sons, 2008.

[228] M. A. Razzak.
A Simple Harmonic Balance Method for Solving Strongly Nonlinear Oscillators.

Journal of the Association of Arab Universities for Basic and Applied Sciences, 21:68–76, 2016.

[229] D. L. Kunz.
Analysis of Proprotor Whirl Flutter: Review and Update.
Journal of Aircraft, 42(1):172–178, 2005.

[230] B. H. Tongue.
Limit Cycle Oscillations of a Nonlinear Rotorcraft Model.
AIAA Journal, 22(7):967–974, 1984.

[231] B. H. Tongue.
Reponse of a Rotorcraft Model with Damping Non-Linearities.
Journal of Sound and Vibration, 103(2):211–224, 1985.

[232] S. J. Price, B. H. K. Lee, and H. Alighanbari.
Postinstability Behavior of a Two-Dimensional Airfoil with a Structural Nonlinearity.
Journal of Aircraft, 31(6):1395–1401, 1994.

[233] M. D. Conner, D. M. Tang, E. H. Dowell, and L. N. Virgin.
Nonlinear Behaviour of a Typical Airfoil Section with Control Surface Freeplay: a Numerical and Experimental Study.
Journal of Fluids and Structures, 11(1):89–109, 1997.

[234] E. H. Dowell and D. Tang.
Nonlinear Aeroelasticity and Unsteady Aerodynamics.
AIAA Journal, 40(9):1697–1707, 2002.

[235] E. H. Dowell, J. Edwards, and T. Strganac.
Nonlinear Aeroelasticity.
Journal of Aircraft, 40(5):857–874, 2003.

[236] I. Garrick and W. H. Reed III.
Historical Development of Aircraft Flutter.
Journal of Aircraft, 18(11):897–912, 1981.

[237] S. Irani, H. Sarrafzadeh, and M. R. Amoozgar.
Bifurcation in a 3-DOF Airfoil with Cubic Structural Nonlinearity.
Chinese Journal of Aeronautics, 24(3):265–378, 2011.

[238] Y. Ning, W. Zhigang, and Y. Chao.
Structural Nonlinear Flutter Characteristics Analysis for an Actuator-Fin System with Dynamic Stiffness.
Chinese Journal of Aeronautics, 24(5):590–599, 2011.

[239] Y. Seo, S. Lee, J. Bae, and I. Lee.
Effects of Multiple Structural Nonlinearities on Limit Cycle Oscillation of Missile Control Fin.
Journal of Fluids and Structures, 27(4):623–635, 2011.

[240] D. Li, S. Guo, and J. Xiang.
Study of the Conditions That Cause Chaotic Motion in a Two-Dimensional Airfoil with Structural Nonlinearities in Subsonic Flow.
Journal of Fluids and Structures, 33:109–126, 2012.

[241] A. Abdelkefi, R. Vasconcellos, F. D. Marques, and M. R. Hajj.
Modeling and Identification of Freeplay Nonlinearity.
Journal of Sound and Vibrations, 331(8):1898–1907, 2012.

[242] M. Ghommem, A. Abdelkefi, A. O. Nuhait, and M. R. Hajj.
Aeroelastic Analysis and Nonlinear Dynamics of an Elastically Mounted Wing.
Journal of Sound and Vibration, 331(26):5774–5787, 2012.

[243] R. Vasconcellos, A. Abdelkefi, F. D. Marques, and M. R. Hajj.
Representation and Analysis of Control Surface Freeplay Nonlinearity.
Journal of Fluids and Structures, 31:79–91, 2012.

[244] D. M. Tang and E. H. Dowell.
Nonlinear Dynamics of a Helicopter Model in Ground Resonance.
Presented as Paper No. 4, Session no. 1 at the 2nd Decennial Specialists' Meeting on Rotorcraft Dynamics, NASA Ames Research Center, California, USA, November 7-9, 1985.

[245] G. T. Flowers and B. H. Tongue.
Nonlinear Rotorcraft Analysis using Symbolic Manipulation.
Applied Mathematical Modelling, 12(2):154–160, 1988.

[246] D. M. Tang and E. H. Dowell.
Nonlinear Aeroelasticity in Rotorcraft.
Mathematical and Computer Modelling, 18(3-4):157–184, 1993.

[247] C. S. Robinson.
Modeling and Analysis of Helicopter Ground Resonance utlizing Symbolic Processing and Dynamic Simulation Software.
Postgraduate Thesis, United States Navy Naval Postgraduate School, 1997.

[248] D. L. Kunz.
Nonlinear Analysis of Helicopter Ground Resonance.

Presented at the 41st Structures, Structural Dynamics, and Materials Conference and Exhibit, Atlanta, Georgia, USA, April 3-6, page 1690, 2000.

[249] P. Andersch and M. Hajek.
Lead-Lag Dynamics of a Rotor with Stick-Slip Nonlinearity.
Presented as Paper No. 47 at the 41st European Rotorcraft Forum, Munich, Germany, September 1-4, 2015.

[250] F. Gandhi and I. Chopra.
Analysis of Bearingless Main Rotor Aeroelasticity using an Improved Time Domain Nonlinear Elastomeric Damper Model.
Journal of the American Helicopter Society, 41(3):267–277, 1996.

[251] C. Howcroft, M. Lowenberg, S. Neild, B. Krauskopf, and E. Coetzee.
Shimmy of an Aircraft Main Landing Gear with Geometric Coupling and Mechanical Freeplay.
Journal of Computational and Nonlinear Dynamics, 10(5), 2015.

[252] C. V. Jutte and S. Kota.
Design of Nonlinear Springs For Prescribed Load-Displacement Functions.
Journal of Mechanical Design, 130(8), 2008.

[253] B. H. K. Lee and A. Tron.
Effects of Structural Nonlinearities on Flutter Characteristics of the CF-18 Aircraft.
Journal of Aircraft, 26(8):781–786, 1989.

[254] C. W. Acree, H. Yeo, and J. D. Sinsay.
Performance Optimization of the NASA Large Civil Tiltrotor.
Presented at the International Powered Lift Conference, London, UK, July 22-24, 2008.

[255] H. Yeo, J. D. Sinsay, and C. W. Acree.
Blade Loading Criteria for Heavy Lift Tiltrotor Design.
AHS Technical Specialists' Meeting, Dallas, Texas, USA, 2008.

[256] C. W. Acree.
Integration of Rotor Aerodynamic Optimization with the Conceptual Design of a Large Civil Tiltrotor.
Presented at the AHS Aeromechanics Conference, San Francisco, California, USA, January 20-22, 2010.

[257] C. W. Acree.
Aerodynamic Limits on Large Civil Tiltrotor Sizing and Efficiency.

Presented at the 5th Decennial AHS Aeromechanics Specialists' Conference, San Francisco, California, USA, January 22-24, 2014.

[258] C. W. Acree and W. Johnson.
Performance, Loads and Stability of Heavy Lift Tiltrotors.
AHS Vertical Lift Aircraft Design Conference, San Francisco, CA, USA, 2006.

[259] Y. A. Kuznetsov.
Elements of Applied Bifurcation Theory.
Springer Science & Business Media, 3rd edition, 2004.

[260] S. H. Strogatz.
Nonlinear Dynamics and Chaos.
Addison-Wesley, 1998.

[261] J. M. T. Thompson and H. B. Stewart.
Nonlinear Dynamics and Chaos.
John Wiley & Sons, Ltd, Chichester, UK, 2002.

[262] K. Sibilski.
Prediction of Helicopter Critical Flight Regimen by Continuation and Bifurcation Methods.
Presented at the AIAA Atmospheric Flight Mechanics Conference and Exhibit, South Carolina, USA, August 20-23, 2007.

[263] R. K. Mehra, W. C. Kessel, and J. V. Carroll.
Global Stability and Control Analysis of Aircraft at High Angles-of-Attack.
Scientific Systems, Inc. Report ONR-CR215-248-1, 1977.

[264] R. K. Mehra and J. V. Carroll.
Global Stability and Control Analysis of Aircraft at High Angles-of-Attack.
Scientific Systems, Inc. Report ONR-CR215-248-2, 1978.

[265] R. K. Mehra and J. V. Carroll.
Global Stability and Control Analysis of Aircraft at High Angles-of-Attack.
Scientific Systems, Inc. Report ONR-CR215-248-3, 1979.

[266] K. Sibilski.
An Agile Aircraft Non-linear Dynamics by Continuation Methods and Bifurcation Theory.
Proceedings of the 22nd International Congress of Aeronautical Sciences, 2000.

[267] C. C. Jahnke and F. E. C. Culick.
Application of Bifurcation Theory to the High-Angle-of-Attack Dynamics of the F-14.
Journal of Aircraft, 31(1):26–34, 1994.

[268] J. T. Gordon, E. E. Meyer, and R. L. Minogue.
Nonlinear Stability Analysis of Control Surface Flutter with Free-Play Effects.
Journal of Aircraft, 45(6):1904–1916, 2008.

[269] L. Salles, B. Staples, N. Hoffmann, and C. Schwingshackl.
Continuation Techniques for Analysis of Whole Aeroengine Dynamics with Imperfect Bifurcations and Isolated Solutions.
Journal of Nonlinear Dynamics, 86(3):1897–1911, 2016.

[270] P. A. Cummings.
Continuation Methods for Qualitative Analysis of Aircraft Dynamics.
NASA Contractor Report 2004-213035, 2005.

[271] S. Pauck and J. Engelbrecht.
Bifurcation Analysis of the Generic Transport Model with a view to Upset Recovery.
Presented at the AIAA Atmospheric Flight Mechanics Conference, Minneapolis, Minnesota, USA, August 13-16, page 4646, 2012.

[272] D. Rezgui and M. H. Lowenberg.
On the Nonlinear Dynamics of a Rotor in Autorotation: a Combined Experimental and Numerical Approach.
Phil. Trans. R. Soc. A, 373.2051 20140411, 2015.

[273] K. Sibilski.
Bifurcation Analysis of a Helicopter Non-Linear Dynamics.
Presented at the 24th European Rotorcraft Forum, Marseilles, France, 15-17 September, 1998.

[274] K. Sibilski.
Non-Linear Flight Mechanics of a Helicopter Analysis by Application of a Continuation Methods.
Presented as Paper No. H4 at the 25th European Rotorcraft Forum, Rome, Italy, 14-16 September, 1999.

[275] G. Avanzini and G. de Matteis.
Effects of Nonlinearities on Ground Resonance Instability.
Presented at the 34th European Rotorcraft Forum, Liverpool UK, September 16-19, pages 2327–2378, 2008.

[276] K. Sibilski.
A Study of the Flight Dynamics Helicopter Carrying an External Load using Bifurcation Theory and Continuation Methods.
Journal of Theoretical and Applied Mechanics, 41(4):823–852, 2003.

[277] P. M. Basset and J. V. R. Prasad.
Study of the Vortex Ring State using Bifurcation Theory.
Presented at the 58th Annual Forum of the American Helicopter Society, Montreal, Quebec, Canada, June 11-13, 2002.

[278] D. Rezgui, M. H. Lowenberg, M. Jones, and C. Monteggia.
Continuation and Bifurcation Analysis in Helicopter Aeroelastic Stability Problems.
Journal of Guidance, Control and Dynamics, 37(3):889–897, 2014.

[279] D. Rezgui and M. H. Lowenberg.
Nonlinear Blade Stability for a Scaled Autogyro Rotor at High Advance Ratios.
Journal of the American Helicopter Society, 65(1):1–19, 2020.

[280] M. Jones, A. Bernascone, P. Masarati, G. Quaranta, and D. Rezgui.
Ongoing Developments in the Use of Continuation-Bifurcation Methodology at AgustaWestland.
Proc. 40th European Rotorcraft Forum, Southampton, UK, pages 905–918, 2014.

[281] R. Yurkovich.
Status of Unsteady Aerodynamic Prediction for Flutter of High-Performance Aircraft.
Journal of Aircraft, 40(5):832–842, 2003.

[282] C. Mair, D. Rezgui, and B. Titurus.
Nonlinear Stability Analysis of Whirl Flutter in a Tiltrotor Rotor-Nacelle System.
Presented as Paper No. 707 at the 43rd European Rotorcraft Forum, Milan, Italy, September 12-15, 2017.

[283] C. Mair, D. Rezgui, and B. Titurus.
Nonlinear Stability Analysis of Whirl Flutter in a Rotor-Nacelle System.
Journal of Nonlinear Dynamics, 94(3):2013–2032, 2018.

[284] C. Mair, D. Rezgui, and B. Titurus.
Stability Analysis of Whirl Flutter in a Nonlinear Gimballed Rotor-Nacelle System.
Presented as Paper No. 389 at the 75th Annual Forum of the Vertical Flight Society, Philadelphia, Pennsylvania, USA, May 13-16, 2019.

[285] C. Mair, D. Rezgui, and B. Titurus.
Stability Analysis of Whirl Flutter in a Rotor-Nacelle System with Freeplay Nonlinearity.
Presented as Paper No. 170 at the 45th European Rotorcraft Forum, Warsaw, Poland, September 17-20, 2019.

[286] C. Mair, B. Titurus, and D. Rezgui.
Stability Analysis of Whirl Flutter in Rotor-Nacelle Systems with Freeplay Nonlinearity.

Journal of Nonlinear Dynamics, 104(1):65–89, 2021.

[287] ICAO.
iSTARS Accident Statistics Repository.
1947–present.

[288] D. Matuska, A. Saccullo, and K. Studebaker.
Reduced Tip Speed Testing of a Variable Diameter Tiltrotor.
Presented as Paper No. D10 at the 19th European Rotorcraft Forum, Cernobbio, Italy, September 14-16, 1993.

[289] R.G. Kvaternik.
Studies in Tilt-Rotor Aircraft Aeroelasticity.
Doctoral Thesis, Case Western Reserve University, 1973.

[290] G. White.
V-22 Nacelle Conversion Actuator.
Proceedings of the Institution of Mechanical Engineers, Part G: Journal of Aerospace Engineering, 207(1):61–72, 1993.

[291] G. White.
A Tilt-rotor Actuator.
Proceedings of the Institution of Mechanical Engineers, Part G: Journal of Aerospace Engineering, 224(6):657–672, 2009.

[292] M. A. Padmanabhan.
Sliding Wear and Freeplay Growth due to Control Surface Limit Cycle Oscillations.
Journal of Aircraft, 56(5):1973–1979, 2019.

[293] S. A. Safi, D. W. Kelly, and R. D. Archer.
Interaction between Wear Processes and Limit Cycle Oscillations of a Control Surface with Free-Play Non-Linearity.
Proceedings of the Institution of Mechanical Engineers, Part G: Journal of Aerospace Engineering, 216(3):143–153, 2002.

[294] The MathWorks Inc.
MATLAB R2015a.
2015.

[295] P. J. Prince J. R. Dormand.
A Family of Embedded Runge-Kutta Formulae.
Journal of Computational and Applied Mathematics, 6:19–26, 1980.

[296] R. A. Beauregard and J. B. Fraleigh.
A First Course in Linear Algebra.
Houghton Mifflin, Boston, USA, 1973.

[297] H. Dankowicz and F. Schilder.
Recipes for Continuation.
Society for Industrial and Applied Mathematics, Pennsylvania, USA, 2013.

[298] B. Krauskopf, H. M. Osinga, and J. Galán-Vioque.
Numerical Continuation Methods for Dynamical Systems.
Springer, Dordrecht, The Netherlands, 2007.

[299] P. A. Kuchment.
Floquet Theory for Partial Differential Equations.
Birkäuser, Basel, 2012.

[300] E. L. Allgower and K. Georg.
Introduction to Numerical Continuation Methods.
Society for Industrial and Applied Mathematics, 2003.

[301] E. Coetzee, B. Krauskopf, and M. Lowenberg.
The Dynamical Systems Toolbox: Integrating AUTO into MATLAB.
Proc. 16th US National Congress of Theoretical and Applied Mechanics USNCTAM2010-827, 2010.

[302] E. J. Doedel, A. R. Champneys, and F. Dercole.
AUTO07P: Continuation and Bifurcation Software for Ordinary Differential Equations.
University of Concordia, 2007.

[303] E. J. Doedel, H. B. Keller, and J. P. Kernevez.
Numerical Analysis and Control of Bifurcation Problems: (I) Bifurcation in Finite Dimensions.
International Journal of Bifurcation and Chaos, 1(3):493–520, 1991.

[304] E. J. Doedel, H. B. Keller, and J. P. Kernevez.
Numerical Analysis and control of Bifurcation Problems: (II) Bifurcation in Infinite Dimensions.
International Journal of Bifurcation and Chaos, 1(4):745–772, 1991.

[305] A. Champneys and Y. Kuznetsov.
Numerical Detection and Continuation of Codimension-Two Homoclinic Bifurcations.
International Journal of Bifurcation and Chaos, 4(4):785–822, 1994.

[306] A. Champneys, Y. Kuznetsov, and B. Sandstede.
A Numerical Toolbox for Homoclinic Bifurcation Analysis.
International Journal of Bifurcation and Chaos, 6(5):867–887, 1996.

[307] F. Dercole.
BPcont: An AUTO Driver for the Continuation of Branch Points of Algebraic and Boundary-Value Problems.
SIAM Journal on Scientific Computing, 30(5):2405–2426, 2008.

[308] T. F. Fairgrieve.
The Computation and Use of Floquet Multipliers for Bifurcation Analysis.
PhD thesis, University of Toronto, 1994.

[309] T. F. Fairgrieve and A. D. Jepson.
O.K. Floquet Multipliers.
SIAM Journal on Numerical Analysis, 28(5):1446–1462, 1991.

[310] R. L. Bielawa.
Rotary Wing Structural Dynamics and Aeroelasticity, 2nd Ed.
AIAA Education Series, Washington, DC, USA, 2005.

[311] A. J. Homburg and B. Sandstede.
Homoclinic and Heteroclinic Bifurcations in Vector Fields.
In *Handbook of Dynamical Systems Vol. 3*. Elsevier, 2010.

[312] V. I. Arnold.
Mathematical Method of Classical Mechanics.
Springer-Verlag, New York, 2nd edition, 1989.

[313] G. Dimitriadis.
Introduction to Nonlinear Aeroelasticity.
John Wiley & Sons, Ltd, Chichester, UK, 2017.

[314] M. Golubitsky and D. G. Schaeffer.
Singularities and Groups in Bifurcation Theory.
Springer, Berlin, 1985.

[315] Federal Aeronautics Administration.
FAR Part 23: Airworthiness Standards: Normal Category Airplanes, 14 C.F.R. §23.2245.
2021.

[316] P. Thota and H. Dankowicz.
TC-HAT ($\widehat{TC}$): A Novel Toolbox for the Continuation of Periodic Trajectories in Hybrid Dynamical Systems.

7(4):1283–1322, 2008.

[317] K. Sibilski, J. Żurek, and W. Wróblewski.
The Influence of Free-Play and Friction in Elevator Control System on Aircraft Dynamics.
Presented at the 26th International Congress of the Aeronautical Sciences, Anchorage, Alaska, USA, 14-19 September, 2008.

[318] W. Anderson and S. Mortara.
Maximum Control Surface Freeplay, Design and Flight Testing Approach on the F-22.
Presented at the 48th AIAA/ASME/ASCE/AHS/ASC Structures, Structural Dynamics, and Materials Conference, Honolulu, HI, USA, April 23-26, 2007.

[319] R. I. Leine and H. Nijmeijer.
Dynamics and Bifurcations of Non-Smooth Mechanical Systems.
Springer-Verlag, New York, USA, 2004.

[320] H. S. Ribner.
Propellers in Yaw.
NACA Report 820, 1945.